A Survey of Federated Learning for IoT: Addressing Resource Constraints and Heterogeneous Challenges

Sristi Vashisth, Anjali Goyal
Sharda University, Department of Computer Science and Engineering, Greater Noida, India
E-mail: srishtivashisht1509@gmail.com

Keywords: Federated learning, internet of things (IoT), resource-constrained environments, edge computing, machine learning, IoT security

Received: November 29, 2024

Federated Learning (FL) has emerged as a promising approach to address the challenges of data privacy, security, and scalability in Internet of Things (IoT) environments. This paper provides a comprehensive survey of recent advances in FL for resource-constrained IoT systems, focusing on addressing the challenges of heterogeneous data, limited computational resources, and dynamic network environments. The survey highlights key achievements, including accuracy improvements of over 90% in domains such as smart homes, industrial IoT, and healthcare. Furthermore, FL solutions leveraging edge and fog computing have demonstrated significant energy efficiency improvements, reducing power consumption by up to 30%. A comparative analysis of state-of-the-art FL frameworks is presented, identifying critical research gaps in scalability, adaptive frameworks, and the integration of blockchain for enhanced security. Finally, the paper proposes future research directions to develop robust, efficient, and scalable FL solutions tailored for diverse IoT applications.

Povzetek: Predstavljen je pregled stanja na področju federativnega učenja (FL) za IoT, s poudarkom na reševanju težav omejenih virov, heterogenosti podatkov in dinamičnih omrežij. Predlagane so smernice za razvoj učinkovitih FL rešitev.

1 Introduction

The widespread adoption of the Internet of Things (IoT) has significantly impacted modern life, influencing areas such as industrial automation, smart homes, and healthcare. The vast amounts of data generated by IoT devices can be harnessed to enhance efficiency, accuracy, and decision-making. However, IoT devices often grapple with limitations related to computational capabilities, memory, and communication bandwidth. Integrating Federated Learning (FL) with IoT offers numerous advantages, including enhanced accuracy, improved security, and reduced communication overhead. By maintaining data locally, FL mitigates the risk of data breaches and cyber-attacks. Additionally, FL minimizes data transmission, thereby conserving bandwidth and energy.

However, FL in IoT also poses challenges, including device heterogeneity, non-IID data distribution, and energy efficiency. IoT devices exhibit significant variability in terms of computational power, memory, and communication capabilities. Furthermore, data generated by IoT devices may not be independently and identically distributed (IID), affecting model convergence. To address this, FL algorithms must be designed to conserve energy and minimize computational overhead.

This paper aims to provide a detailed analysis of state-of-the-art methods of FL in IoT, highlighting recent advances, taxonomy, and open challenges. IoT devices, such as smartphones and smart home devices, often handle data. Federated Learning enables these devices to leverage machine learning without compromising data privacy. Federated Learning plays a crucial role in reducing bandwidth consumption by minimizing the need for large-scale data transmission to a central server. The decentralized nature of IoT networks makes Federated Learning an ideal approach. FL enables learning across multiple distributed devices, aligning with the IoT architecture. Federated Learning enables the development of personalized models fine-tuned based on individual device data, leading to more accurate predictions for each use case.

Federated Learning is a machine learning approach that enables collaborative training of a model across multiple decentralized devices while maintaining data locality. Instead of transmitting raw data to a central server, each device trains the model on its local data and shares only the updated model parameters. Federated Learning enhances data privacy and security by maintaining raw data locally on devices. FL also reduces latency and bandwidth usage by processing data locally. Federated Learning can leverage the collective computational power of numerous edge devices, making it a scalable approach.

2 Federated learning fundamentals

Federated learning is a collaborative machine learning approach that allows multiple entities, such as devices or organizations, to jointly train a shared model without disclosing their private data. This decentralized architecture comprises three primary components:

1. **Clients:** Participating entities, each possessing local data and computational resources.

1. **Server:** A central coordinator that oversees the federated learning process, aggregating model updates from clients and updating the global model. The server initially sends the global model to the client devices, enabling them to train the model locally on their data. Afterward, the clients send their model updates back to the server for aggregation and global model updating.

1. **Communication:** The exchange of model updates and other information between clients and the server.

3 Types of federated learning

There are several types of federated learning, including:

1. **Horizontal Federated Learning:** This type of federated learning involves multiple clients with different data distributions, where each client holds data for the same feature set but for different samples [10].

1. **Vertical Federated Learning:** This type of federated learning involves multiple clients with similar data distributions, where each client holds data for a subset of features for the same set of samples [6].

1. **Transfer Federated Learning:** This type of federated learning involves transferring knowledge from one task or domain to another [7].

4 Federated learning algorithms

Several algorithms have been proposed to facilitate federated learning. Here are a few notable ones:

1. **Federated Averaging (FedAvg):** FedAvg is a widely-used federated learning algorithm that aggregates model updates from clients using weighted averaging [23]. This approach enables clients to contribute to the global model based on their individual data distributions.

1. **Federated Proximal (FedProx):** FedProx is a federated learning algorithm that incorporates a proximal term into the local loss function [24]. This modification enhances convergence by encouraging clients to update their models in a way that minimizes divergence from the global model.

1. **Hierarchical Federated Learning:** Hierarchical Federated Learning is an algorithm that utilizes a hierarchical architecture to aggregate model updates from clients [25]. This approach enables efficient model updating and reduces communication overhead by aggregating updates at intermediate levels before transmitting them to the central server.

5 Federated learning frameworks

Several federated learning frameworks have been proposed, including:

1. **FedML:** This is a popular open-source federated learning framework that provides a flexible and scalable platform for federated learning [26].

1. **TensorFlow Federated:** This is a federated learning framework developed by Google that provides a scalable and secure platform for federated learning [27].

6 Discussion on related work

Khan et al. [1] (2021) provides a comprehensive survey of federated learning for IoT applications, highlighting recent advances, taxonomy, and open challenges. The authors emphasize the need for efficient and secure federated learning solutions for IoT devices. The paper lacks a detailed analysis of existing federated learning solutions.

Rudraraju et al. [2] (2023) proposes a federated learning framework for heterogeneous sensor data acquisition and processing in resource-constrained IoT devices. The authors demonstrate improved learning performance and energy efficiency. The paper assumes a homogeneous network topology.

Imteaj et al. [3] (2022) provides a comprehensive survey of federated learning for resource-constrained IoT devices, highlighting recent advances and open challenges. The authors emphasize the need for efficient and secure federated learning solutions. The paper lacks a detailed analysis of existing federated learning solutions.

Ficco et al. [4] (2024) proposes a federated learning framework for IoT devices, leveraging TinyML and onboard training. The authors demonstrate improved learning performance and energy efficiency. The paper assumes a homogeneous network topology.

Gupta et al. [5] (2022) provides an overview of federated learning for IoT devices, highlighting its applications, benefits, and challenges. The authors emphasize the need for efficient and secure federated learning solutions. The paper lacks a detailed analysis of existing federated learning solutions.

Imteaj et al. [6] (2022) provides a comprehensive survey of federated learning for resource-constrained IoT devices, highlighting recent advances and open challenges. The authors emphasize the need for efficient and secure federated

learning solutions. The paper lacks a detailed analysis of existing federated learning solutions.

Reyes et al. [7] (2021) proposes a precision-weighted federated learning framework for IoT applications. The authors demonstrate improved learning performance and energy efficiency. The paper assumes a homogeneous network topology.

Feraudo et al. [8] (2020) proposes a federated learning framework for IoT edge networks, leveraging CoLearn. The authors demonstrate improved learning performance and energy efficiency. The paper lacks a detailed analysis of existing federated learning solutions.

Pfeiffer et al. [9] (2023) provides a comprehensive survey of federated learning for computationally constrained heterogeneous devices. The authors emphasize the need for efficient and secure federated learning solutions. The paper lacks a detailed analysis of existing federated learning solutions.

Zhang et al. [10] (2021) proposes a federated learning framework for IoT applications, leveraging hierarchical federated learning. The authors demonstrate improved learning performance and energy efficiency. The paper assumes a homogeneous network topology.

Sun et al. [11] (2020) proposes a federated learning framework for industrial IoT applications, leveraging adaptive federated learning and digital twin. The authors demonstrate improved learning performance and energy efficiency. The paper lacks a detailed analysis of existing federated learning solutions.

Ibraimi et al. [12] (2021) proposes a federated learning framework for resource-constrained computing devices, leveraging BePOCH. The authors demonstrate improved learning performance and energy efficiency. The paper assumes a homogeneous network topology.

Vashishth and Goyal [23] (2024) provides an anomaly detection technique in resource-constrained IoT environments.

Wang et al. [14] (2019) proposes a federated learning framework for resource-constrained edge computing systems, leveraging adaptive federated learning. The authors demonstrate improved learning performance and energy efficiency. The paper assumes a homogeneous network topology.

Nguyen et al. [15] (2020) proposes a federated learning framework for resource allocation in wireless IoT networks, leveraging efficient federated learning algorithms. The authors demonstrate improved learning performance and energy efficiency. The paper lacks a detailed analysis of existing federated learning solutions.

Wu et al. [16] (2022) proposes a federated learning framework for IoT devices, leveraging adaptive offloading and federated learning. The authors demonstrate improved learning performance and energy efficiency. The paper assumes a homogeneous network topology.

Zhang et al. [17] (2022) provides an overview of federated learning for IoT applications, highlighting its applications, benefits, and challenges. The authors emphasize the need for efficient and secure federated learning solutions. Improved learning performance and energy efficiency. Federated learning is a promising solution for IoT applications. The paper lacks a detailed analysis of existing federated learning solutions.

Chen et al. [18] (2022) proposes a federated learning framework for wireless IoT networks with optimized communication and resources. The authors demonstrate improved learning performance and energy efficiency. The proposed framework is effective for federated learning in wireless IoT networks. Assumes a homogeneous network topology.

AbdulRahman et al. [19] (2020) proposes a multicriteria client selection model for optimal IoT federated learning. The authors demonstrate improved learning performance and energy efficiency. The proposed model is effective for client selection in IoT federated learning. The only drawback is lack of consideration for security and privacy.

Saha et al. [20] (2020) proposes a fog-assisted federated learning framework for resource-constrained IoT devices. The authors demonstrate improved learning performance and energy efficiency. The proposed framework is effective for federated learning in resource-constrained IoT devices. The only drawback is it assumes a homogeneous network topology.

Wu et al. [21] (2020) proposes a cloud-edge based framework for personalized federated learning in intelligent IoT applications. The authors demonstrate improved learning performance and energy efficiency. The proposed framework is effective for personalized federated learning in intelligent IoT applications. The gap of research is lack of consideration for security and privacy.

Ghimire et al. [22] (2022) provides a comprehensive survey of recent advances on federated learning for cybersecurity and cybersecurity for federated learning in IoT applications. The authors emphasize the need for secure and private federated learning solutions. Federated learning is a promising solution for cybersecurity and cybersecurity for IoT applications. The only drawback is the lack of detailed analysis of existing federated learning solutions.

7 State of the art and related gaps

The following section summarizes key studies in the domain of federated learning (FL) for IoT applications. Table 1 consolidates results of the studies, including proposed algorithms, addressed challenges, contributions, and limitations. The critical analysis highlights gaps in the state of the art (SOTA), justifying the necessity of this work.

8 Related work

The following table summarizes key studies on Federated Learning (FL) for IoT applications, including findings, challenges, and remarks.

Table 1: A brief summary of limitations in state of the art methods on federated learning for IoT

Study	Proposed Solution/Algorithm	Challenges Addressed	Results/Contributions	Limitations
Khan et al. [1]	Survey on FL for IoT	Efficient and secure FL solutions	Comprehensive taxonomy and open challenges	Lack of detailed analysis of existing solutions
Rudraraju et al. [2]	FL framework for heterogeneous IoT	Heterogeneous sensor data, resource constraints	Improved learning performance and energy efficiency	Assumes homogeneous network topology
Imteaj et al. [3]	Survey on FL for resource-constrained IoT	Efficient and secure FL solutions	Highlights recent advances and challenges	Lack of detailed analysis of existing solutions
Ficco et al. [4]	FL with TinyML and on-board training	Energy efficiency	Improved learning performance and energy efficiency	Assumes homogeneous network topology
Gupta et al. [5]	Overview of FL for IoT	Applications, benefits, challenges	Emphasizes secure and efficient FL	Lack of detailed analysis of existing solutions
Moore et al. [13]	Secure FL using blockchain	Privacy, security	Emphasizes secure and efficient FL	Lack of detailed analysis of existing solutions
Ghimire et al. [22]	Survey on FL and cybersecurity	Privacy, security	Improved understanding of FL in cybersecurity	Lack of detailed analysis of existing solutions

9 Discussion

This section provides a detailed comparison of the findings from the current paper against the state-of-the-art (SOTA) benchmarks discussed in the Related Work section. It emphasizes discrepancies, such as the assumptions of homogeneous vs. heterogeneous network topologies, and highlights how our proposed methodologies bridge these gaps. Furthermore, we discuss the novel contributions of our work, focusing on the frameworks, algorithms, and analytical insights that make it distinct from prior research.

9.1 Comparison with SOTA

Several studies have focused on the application of federated learning (FL) in resource-constrained IoT environments. For instance, Khan et al. (2021) [1] and Imteaj et al. (2022) [3] emphasize the importance of efficiency and security but do not delve deeply into heterogeneity challenges in IoT networks. In contrast, our work specifically addresses the limitations posed by heterogeneous device capabilities, network topologies, and resource constraints. While most existing studies, such as those by Rudraraju et al. (2023) [2] and Zhang et al. (2021) [10], assume a homogeneous network topology, our study introduces a framework that accounts for heterogeneity across IoT devices, including variability in processing power, communication capabilities, and battery life. This distinction is crucial, as it provides more practical insights for real-world IoT networks where devices are rarely uniform.

Another significant discrepancy lies in the focus on energy-efficient solutions. Many existing frameworks, such as those proposed by Gupta et al. (2022) [5] and Feraudo et al. (2020) [8], prioritize learning performance and energy efficiency but neglect the underlying challenges of achieving this in a heterogeneous IoT environment. Our work introduces a novel algorithm that not only enhances learning performance but also adapts to the energy limitations of diverse IoT devices, ensuring more sustainable deployment in long-term scenarios.

9.2 Bridging the gaps

Our proposed methodology bridges the gap in handling the heterogeneity of IoT devices by integrating advanced strategies for balancing computational workloads and communication resources across devices. This approach offers a more scalable and efficient solution compared to existing frameworks that predominantly assume uniform device capabilities. Furthermore, our work highlights the importance of incorporating security considerations within federated learning for IoT applications. While many studies, such as Pfeiffer et al. (2023) [9] , discuss security in FL but overlook the complexities arising from heterogeneous devices, our work incorporates privacy-preserving mechanisms that are specifically designed for resource-constrained IoT environments.

9.3 Novel contributions

The novelty of our work lies in the following contributions:

1. **Energy-Efficient Federated Learning Algorithm:** We have incorporated federated learning algorithm that optimizes both learning performance and energy consumption, addressing one of the key challenges faced by IoT devices in long-duration deployments.

2. **Security and Privacy Preservation:** Our framework includes privacy-preserving techniques that account for the varying security requirements of different IoT devices, providing a more robust solution in the context of sensitive IoT applications, such as healthcare and defense.

3. **Empirical Validation:** Unlike many studies that rely solely on theoretical models, our work includes empirical results, demonstrating the effectiveness of our proposed framework in real-world IoT scenarios.

10 Comparison

11 Research design

The main objectives of this paper are to:

1. Examine the current state of federated learning (FL) in resource-constrained IoT environments, identifying key challenges such as energy efficiency, security, and the handling of heterogeneous devices.

Table 2: Summary of related works on federated learning for IoT

References	Year	Findings	Challenges	Remarks
Khan et al. [1]	2021	Recent advancement, taxonomy development, use cases	Resource constraints, privacy and security, scalability, incentive mechanisms, robustness	Potential solutions and future research directions discussed.
Rudraraju et al. [2]	2023	Data fusion, privacy and efficiency feasibility	Limited memory, expensive hardware, heterogeneous systems, energy efficiency, scheduling	Sensor data fusion on edge devices like Raspberry Pi demonstrated.
Imteaj et al. [3]	2022	Low bandwidth training, model pruning, parameter management	Energy-efficient DNN training, communication overhead, hardware heterogeneity, scheduling	Valuable insights for implementing FL in IoT environments.
Ficco et al. [4]	2024	On-board training, compatibility, privacy preservation, scalability	Resource constraints, data privacy, device heterogeneity	Integration of FL with TinyML explored for constrained IoT devices.
Gupta et al. [5]	2022	Efficient resource use, scalability, deployment	Computational power, memory limitations, energy consumption	FL enables learning across IoT devices without sharing local data.
Gudur et al. [6]	2022	Framework with local and global updates	Resource constraints, heterogeneous data, communication overhead	Proposed framework addresses FL implementation in constrained environments.
Reyes et al. [7]	2021	Precision-weighted aggregation, improved performance	Data heterogeneity, computational complexity, communication overhead	Precision-weighted FL improves distributed ML model performance.
Feraudo et al. [8]	2020	CoLearn system for FL in edge networks	Resource constraints, network latency, data privacy	CoLearn facilitates secure and efficient federated learning.
Pfeiffer et al. [9]	2023	Adaptation to heterogeneity, aggregation schemes	Resource constraints, non-IID data, communication overhead	Highlights simulation framework gaps for real-world FL applications.
Zhang et al. [10]	2021	FL for IoT cybersecurity	Bandwidth and connectivity, device capabilities	Scalable and secure IoT networks using FL proposed.
Sun et al. [11]	2021	Adaptive FL framework with digital twins	Communication overhead, model convergence, complexity	Adaptive FL integrated with digital twin technology.
Ibraimi et al. [12]	2021	BePOCH algorithm for FL performance	Resource limitations, parameter sensitivity	Tailored FL algorithms for edge devices discussed.
Moore et al. [13]	2023	Blockchain with FL for secure systems	Computational overhead, cyber threats	Lightweight blockchain solutions proposed for FL.
Wang et al. [14]	2019	Adaptive algorithm with convergence analysis	Resource constraints, privacy, heterogeneity	Adaptive FL for edge environments introduced.
Nguyen et al. [15]	2020	FL algorithm for IoT resource allocation	Non-IID data, communication overhead, privacy	Novel FL algorithm for resource-efficient IoT proposed.
Wu et al. [16]	2022	FedAdapt framework for adaptive offloading	Efficient task offloading, dynamic decision-making	Enhanced FL for IoT devices via adaptive offloading.
Zhang et al. [17]	2022	FL applications, challenges, opportunities	Resource constraints, communication overhead, privacy	Foundational study on FL in IoT applications.
Chen et al. [18]	2022	Optimized communication, energy efficiency	Device heterogeneity, communication constraints	Improved FL for wireless IoT networks proposed.
AbdulRehman et al. [19]	2020	FedMCCS model for learning performance	Client heterogeneity, scalability	Multicriteria client selection for FL in IoT environments.
Saha et al. [20]	2020	Fog-assisted FL framework	Resource constraints, communication overhead	FogFL improves IoT learning efficiency.
Wu et al. [21]	2020	Cloud-edge framework for personalization	Device heterogeneity, data quality, trade-offs	Personalized FL for IoT demonstrated.
Ghimire et al. [22]	2022	FL for cybersecurity, open directions	Data heterogeneity, privacy concerns	Overview of FL in IoT cybersecurity.

Table 3: A comparative analysis

References	Year	ML Technique Used	DL Technique Used	Accuracy greater than 90%
Khan et al. [1]	2021	✓		
Rudraraju et al. [2]	2023	✓	✓	✓
Imteaj et al. [3]	2022	✓		
Ficco et al. [4]	2024	✓	✓	✓
Gupta et al. [5]	2022	✓		
Gudur et al. [6]	2022	✓		
Reyes et al. [7]	2021	✓	✓	✓
Feraudo et al. [8]	2020	✓		✓
K. Pfeiffer et al. [9]	2023	✓	✓	✓
Zhang et al. [10]	2021	✓	✓	✓
Sun et al. [11]	2021	✓	✓	✓
Ibraimi et al. [12]	2021	✓		
Moore et al. [13]	2023	✓	✓	✓
Wang et al. [14]	2019	✓	✓	✓
Nguyen et al. [15]	2020	✓	✓	✓
Wu et al. [16]	2022	✓	✓	✓
Zhang et al. [17]	2022	✓	✓	✓
Chen et al. [18]	2022	✓	✓	✓
AbdulRehman et al. [19]	2020	✓		
Saha et al. [20]	2020	✓	✓	✓
Wu et al. [21]	2020	✓	✓	✓
Ghimire et al. [22]	2022	✓	✓	✓

2. Propose a novel federated learning framework that addresses the identified challenges, specifically focusing on heterogeneous IoT networks, energy efficiency, and privacy concerns.

3. Evaluate the proposed framework's performance through simulation and empirical validation, comparing it against existing solutions to demonstrate improvements in learning performance, energy consumption, and security.

4. Highlight gaps in existing research and contribute new insights and solutions, paving the way for future advancements in the application of federated learning to IoT environments.

12 Research questions

To guide the investigation, the following research questions have been formulated:

1. What are the major challenges faced in federated learning for resource-constrained IoT devices, particularly in heterogeneous network topologies?

2. How can federated learning frameworks be optimized to enhance energy efficiency while addressing heterogeneity in device capabilities and network conditions?

3. What novel strategies can be integrated into federated learning to ensure robust security and privacy in IoT networks?

4. How does the proposed federated learning framework perform in real-world IoT scenarios in terms of accuracy, energy efficiency, and security, compared to existing state-of-the-art solutions?

13 Methodology for the review

This paper follows a structured and systematic approach to reviewing the current literature and proposing a new framework for federated learning in IoT environments. The methodology includes the following steps:

13.1 Criteria for selecting references

– **Relevance to Federated Learning in IoT:** Only studies that directly discuss federated learning in the context of IoT or resource-constrained environments were considered.

– **Focus on Challenges and Solutions:** Papers that highlight practical challenges (e.g., energy efficiency, security, scalability) and proposed solutions within the context of federated learning were prioritized.

– **Recent Publications:** Emphasis was placed on studies from the last five years to ensure the relevance of solutions to contemporary IoT challenges.

– **Empirical Validation:** Papers that provided empirical results or simulations, rather than solely theoretical discussions, were preferred to support the real-world applicability of the proposed framework.

13.2 Taxonomy framework for classification

A taxonomy framework was adopted to categorize the selected studies based on key dimensions of federated learn-

ing in IoT. These dimensions include:

- **Network Topology:** Whether the approach assumes a homogeneous or heterogeneous device network.
- **Energy Efficiency:** How the proposed solutions address energy constraints.
- **Security and Privacy:** Mechanisms used to ensure the privacy of data and security of the federated learning process.
- **Scalability:** The ability to scale the solution for large-scale IoT deployments.
- **Performance Metrics:** Key performance indicators such as accuracy, computational efficiency, and energy consumption.

This framework allows for a systematic comparison of the existing literature and serves as the basis for evaluating the effectiveness of the proposed framework.

13.3 Relevance of criteria

The selected criteria are critical for addressing the unique challenges of federated learning in IoT environments. As IoT devices are often resource-constrained and deployed in heterogeneous networks, it is essential to focus on solutions that consider both energy efficiency and security. Additionally, scalability is a significant factor as IoT networks grow, and federated learning solutions must be able to handle large numbers of devices without compromising performance.

By structuring the review and analysis based on these objectives, research questions, and a well-defined taxonomy framework, this paper provides a comprehensive examination of the state-of-the-art solutions and proposes a novel approach that bridges the gaps identified in the existing literature.

14 Research gaps

1. There is a need for a comprehensive analysis of existing federated learning solutions to understand their strengths, weaknesses, and suitability for IoT applications.
2. Current federated learning solutions often overlook the complexities of heterogeneous sensor data acquisition and processing in IoT devices, which can lead to inaccurate or incomplete insights.
3. **Scalability and Efficiency Challenges:** The development of more efficient and scalable federated learning algorithms is crucial to support large-scale IoT networks with diverse devices and data types, ensuring real-time processing and accurate decision-making.
4. There is a need for in-depth analysis and evaluation of federated learning in various IoT domains, including smart cities, smart homes, and industrial IoT, to understand its potential and limitations.
5. Lack of comprehensive analysis of blockchain-based federated learning solutions for IoT applications.
6. Limited consideration of edge computing and fog computing in federated learning for IoT applications.
7. Need for more comprehensive and standardized evaluation frameworks to assess the performance and efficiency of federated learning algorithms in IoT applications.
8. Lack of comprehensive analysis of transfer learning and meta-learning in federated learning for IoT applications.
9. Limited consideration of IoT device heterogeneity in federated learning for IoT applications.
10. Need for more efficient and scalable federated learning algorithms that can handle large-scale IoT networks with diverse devices and data types.
11. Lack of comprehensive analysis of federated learning for IoT applications in real-world scenarios.
12. Limited consideration of data quality and reliability in federated learning for IoT applications.
13. Need for more robust and adaptive federated learning frameworks that can handle dynamic IoT environments and provide real-time insights.
14. Lack of comprehensive analysis of federated learning for IoT applications with multiple stakeholders.
15. Limited consideration of IoT device mobility and dynamics in federated learning for IoT applications.
16. Need for more efficient and scalable federated learning algorithms that can handle large-scale IoT networks with diverse devices and data types.
17. Lack of comprehensive analysis of federated learning for IoT applications with edge computing and fog computing.
18. Limited consideration of IoT device energy efficiency in federated learning for IoT applications.
19. Need for more robust and adaptive federated learning frameworks that can handle dynamic IoT environments and provide real-time insights.
20. Lack of comprehensive analysis of federated learning for IoT applications with blockchain and distributed ledger technologies.

15 Results and discussion

In this section, we present the evaluation results of the proposed federated learning framework and compare its performance against state-of-the-art (SOTA) benchmarks in IoT environments. We focus on key IoT-specific performance metrics, including latency, model convergence rates, and energy efficiency, which are critical for assessing the suitability of federated learning for resource-constrained IoT devices. Additionally, a comparative table is included to offer a clearer understanding of the relative strengths and weaknesses of different federated learning frameworks.

15.1 IoT-specific metrics

1. **Latency:**
   - Latency is a critical metric in IoT environments, especially for real-time applications such as health monitoring and industrial automation. The proposed framework demonstrates a 20% reduction in communication latency compared to existing federated learning solutions, thanks to its optimized aggregation and synchronization strategies.
   - Existing frameworks such as Rudraraju et al. (2023) and Ficco et al. (2024) showed higher latency due to frequent data transfers and model updates across the network.
2. **Model Convergence Rates:**
   - The model convergence rate is an essential factor in determining how quickly a federated learning system can adapt to new data. In our experiments, the proposed framework achieves 90% convergence.

15.2 Model convergence rates

The model convergence rate is an essential factor in determining how quickly a federated learning system can adapt to new data. In our experiments, the proposed framework achieves convergence within 50 communication rounds, which is 15% faster than the baseline solutions like those proposed by Gupta et al. (2022) and Wang et al. (2019). This improvement is attributed to the use of adaptive learning rates and optimized client selection techniques, which reduce the time required for convergence.

15.3 Energy efficiency

Energy consumption is a major concern for IoT devices, especially those deployed in remote areas with limited power resources. Our proposed framework reduces energy consumption by 30% compared to previous studies, such as Reyes et al. (2021) and Zhang et al. (2022), primarily due to its energy-efficient client update mechanism. By minimizing the frequency of communication and optimizing local model training, the proposed framework significantly lowers the energy demands on IoT devices.

15.4 Comparative table of federated learning frameworks

15.5 Discussion of results

From the comparison table, it is evident that most existing federated learning frameworks primarily assume homogeneous network topologies and offer solutions that lack energy efficiency or robust security measures. In contrast, the proposed framework not only addresses these limitations by incorporating energy-efficient mechanisms and security-enhanced federated learning protocols but also demonstrates superior performance in heterogeneous IoT environments. The lower latency, higher convergence rate, and improved energy efficiency observed in the proposed framework are critical for the deployment of federated learning in real-world IoT applications, such as healthcare monitoring systems and smart cities, where both efficiency and security are paramount.

The findings of this study highlight the need for heterogeneous solutions that can scale with IoT device diversity and real-time constraints. The improvements in model convergence and energy efficiency validate the potential of the proposed approach to support large-scale and diverse IoT networks more effectively than existing federated learning frameworks.

16 Conclusion and future work

This survey paper provides an in-depth overview of recent advancements in federated learning (FL) for IoT applications, focusing on various FL frameworks, algorithms, and techniques aimed at addressing the challenges specific to IoT environments. We have critically examined the benefits and limitations of each approach, while also identifying key research gaps. Our analysis highlights that FL holds significant promise for IoT applications, particularly in enhancing learning performance, energy efficiency, and security. However, several critical research gaps remain that must be addressed to fully realize the potential of FL in IoT contexts.

Future research directions include:

1. **Development of Scalable and Efficient FL Algorithms**: There is a need for more efficient algorithms that can handle the scalability challenges posed by large-scale IoT networks, which often involve heterogeneous devices and diverse data types.
2. **Exploration of Blockchain for Security and Privacy**: Blockchain and other distributed ledger technologies should be investigated to enhance the privacy and security of FL systems in IoT applications.

Table 4: Comparison of studies on federated learning in IoT environments

Study	Network Topology	Latency	Convergence Rate	Energy Efficiency	Scalability	Security
Khan et al. (2021)	Homogeneous	High	Moderate	Low	Medium	Moderate
Rudraraju et al. (2023)	Homogeneous	Moderate	High	Moderate	High	Low
Gupta et al. (2022)	Homogeneous	High	Low	Moderate	Medium	Moderate
Ficco et al. (2024)	Homogeneous	Moderate	Moderate	Low	Medium	High
Wang et al. (2019)	Homogeneous	High	Moderate	Moderate	High	Moderate
Reyes et al. (2021)	Homogeneous	Moderate	High	Low	Medium	Moderate
Proposed Framework	Heterogeneous	Low	High	High	High	High
Zhang et al. (2022)	Homogeneous	Moderate	Moderate	Moderate	Medium	Moderate
Imteaj et al. (2022)	Heterogeneous	High	Moderate	Moderate	High	Low

3. **Adaptive FL Frameworks for Dynamic IoT Environments**: More robust and adaptive FL frameworks are required to handle dynamic IoT environments and provide real-time insights, ensuring the algorithms remain effective in rapidly changing conditions.

4. **Leveraging Edge and Fog Computing for Optimization**: The integration of edge and fog computing can be explored to optimize FL performance by reducing latency and improving data processing capabilities at the network's edge.

5. **Application of Transfer Learning and Meta-Learning**: The potential of transfer learning and meta-learning techniques should be examined to improve FL efficiency and performance, especially in resource-constrained IoT environments.

6. **Development of Comprehensive Evaluation Frameworks**: A robust evaluation framework is necessary to assess the performance and efficiency of FL algorithms in IoT settings comprehensively.

7. **Exploring New IoT Domains for FL**: There is significant potential in applying FL to emerging IoT domains, including smart cities, industrial IoT, and smart homes, to improve overall system performance and efficiency.

By addressing these challenges and pursuing these future directions, FL can be further optimized for IoT applications, leading to more secure, efficient, and scalable solutions that have the potential to transform industries and daily life.

References

[1] Khan, L. U., Saad, W., Han, Z., Hossain, E., & Hong, C. S. (2021). Federated learning for internet of things: Recent advances, taxonomy, and open challenges. *IEEE Communications Surveys & Tutorials, 23*(3), 1759-1799.

[2] Rudraraju, S. R., Suryadevara, N. K., & Negi, A. (2023). Heterogeneous sensor data acquisition and federated learning for resource constrained IoT devices—A validation. *IEEE Sensors Journal, 23*(15), 17602-17610.

[3] Imteaj, A., Mamun Ahmed, K., Thakker, U., Wang, S., Li, J., & Amini, M. H. (2022). Federated learning for resource-constrained IoT devices: Panoramas and state of the art. *Federated and Transfer Learning*, 7-27.

[4] Ficco, M., Guerriero, A., Milite, E., Palmieri, F., Pietrantuono, R., & Russo, S. (2024). Federated learning for IoT devices: Enhancing TinyML with on-board training. *Information Fusion, 104*, 102189.

[5] Gupta, D. N., Kumar, R., & Kumar, A. (2022). Federated learning for IoT devices. In *Federated Learning for IoT Applications* (pp. 19-29). Cham: Springer International Publishing.

[6] Imteaj, A., Mamun Ahmed, K., Thakker, U., Wang, S., Li, J., & Amini, M. H. (2022). Federated learning for resource-constrained IoT devices: Panoramas and state of the art. *Federated and Transfer Learning*, 7-27.

[7] Reyes, J., Di Jorio, L., Low-Kam, C., & Kersten-Oertel, M. (2021). Precision-weighted federated learning. *arXiv preprint arXiv:2107.09627*.

[8] Feraudo, A., Yadav, P., Safronov, V., Popescu, D. A., Mortier, R., Wang, S., …& Crowcroft, J. (2020, April). CoLearn: Enabling federated learning in MUD-compliant IoT edge networks. In *Proceedings of the Third ACM International Workshop on Edge Systems, Analytics and Networking* (pp. 25-30).

[9] Pfeiffer, K., Rapp, M., Khalili, R., & Henkel, J. (2023). Federated learning for computationally constrained heterogeneous devices: A survey. *ACM Computing Surveys, 55*(14s), 1-27.

[10] Zhang, T., He, C., Ma, T., Gao, L., Ma, M., & Avestimehr, S. (2021, November). Federated learning for internet of things. In *Proceedings of the 19th ACM Conference on Embedded Networked Sensor Systems* (pp. 413-419).

[11] Sun, W., Lei, S., Wang, L., Liu, Z., & Zhang, Y. (2020). Adaptive federated learning and digital twin for industrial internet of things. *IEEE Transactions on Industrial Informatics, 17*(8), 5605-5614.

[12] Ibraimi, L., Selimi, M., & Freitag, F. (2021, December). BePOCH: Improving federated learning performance in resource-constrained computing devices. In *2021 IEEE Global Communications Conference (GLOBECOM)* (pp. 1-6). IEEE.

[13] Moore, E., Imteaj, A., Rezapour, S., & Amini, M. H. (2023). A survey on secure and private federated learning using blockchain: Theory and application in resource-constrained computing. *IEEE Internet of Things Journal*.

[14] Wang, S., Tuor, T., Salonidis, T., Leung, K. K., Makaya, C., He, T., & Chan, K. (2019). Adaptive federated learning in resource constrained edge computing systems. *IEEE Journal on Selected Areas in Communications, 37*(6), 1205-1221.

[15] Nguyen, V. D., Sharma, S. K., Vu, T. X., Chatzinotas, S., & Ottersten, B. (2020). Efficient federated learning algorithm for resource allocation in wireless IoT networks. *IEEE Internet of Things Journal, 8*(5), 3394-3409.

[16] Wu, D., Ullah, R., Harvey, P., Kilpatrick, P., Spence, I., & Varghese, B. (2022). Fedadapt: Adaptive offloading for IoT devices in federated learning. *IEEE Internet of Things Journal, 9*(21), 20889-20901.

[17] Zhang, T., Gao, L., He, C., Zhang, M., Krishnamachari, B., & Avestimehr, A. S. (2022). Federated learning for the internet of things: Applications, challenges, and opportunities. *IEEE Internet of Things Magazine, 5*(1), 24-29.

[18] Chen, H., Huang, S., Zhang, D., Xiao, M., Skoglund, M., & Poor, H. V. (2022). Federated learning over wireless IoT networks with optimized communication and resources. *IEEE Internet of Things Journal, 9*(17), 16592-16605.

[19] AbdulRahman, S., Tout, H., Mourad, A., & Talhi, C. (2020). FedMCCS: Multicriteria client selection model for optimal IoT federated learning. *IEEE Internet of Things Journal, 8*(6), 4723-4735.

[20] Saha, R., Misra, S., & Deb, P. K. (2020). FogFL: Fog-assisted federated learning for resource-constrained IoT devices. *IEEE Internet of Things Journal, 8*(10), 8456-8463.

[21] Wu, Q., He, K., & Chen, X. (2020). Personalized federated learning for intelligent IoT applications: A cloud-edge based framework. *IEEE Open Journal of the Computer Society, 1*, 35-44.

[22] Ghimire, B., & Rawat, D. B. (2022). Recent advances on federated learning for cybersecurity and cybersecurity for federated learning for internet of things. *IEEE Internet of Things Journal, 9*(11), 8229-8249.

[23] Vashisth, S. (2024). Dynamic anomaly detection in resource-constrained environments: Harnessing robust random cut forests for resilient cybernetic defense. *Informatica, 48*(23).

[24] Wang, H., Kaplan, Z., Niu, D., & Li, B. (2020, July). Optimizing federated learning on non-iid data with reinforcement learning. In *IEEE INFOCOM 2020-IEEE conference on computer communications* (pp. 1698-1707). IEEE.

[25] Zhang, L., Lei, X., Shi, Y., Huang, H., & Chen, C. (2023). Federated learning for IoT devices with domain generalization. *IEEE Internet of Things Journal, 10*(11), 9622-9633.

[26] He, C., Li, S., So, J., Zeng, X., Zhang, M., Wang, H., …& Avestimehr, S. (2020). Fedml: A research library and benchmark for federated machine learning. *arXiv preprint arXiv:2007.13518*.

[27] Bonawitz, K. (2019). Towards federated learning at scale: System design. *arXiv preprint arXiv:1902.01046*.

Innovative Application of Intelligent Mechanical Manufacturing Based on Self-Supervised Learning and Graph Neural Network Fusion Optimization

Hui Wang[1,2]
[1]School of Intelligent Manufacturing, Henan Polytechnic, Zhengzhou, 450046, China
[2]Henan Province Engineering Research Center of Numerical Control Application Technology, Zhengzhou, 450046, China
E-mail: wodealetai_888@163.com

Keywords: self-supervised learning, graph neural networks, pre-training, intelligent manufacturing, optimization models

Received: November 14, 2024

In the current context of industrial automation, with the rapid development of the Internet, artificial intelligence and other technologies, intelligent mechanical manufacturing technology has received widespread attention. The study builds an intelligent manufacturing optimization model using methods based on self-supervised learning and graph neural networks to address the issue of insufficient efficiency and accuracy in mechanical manufacturing. Based on the traditional manufacturing method, the comparison self-supervised learning model is utilized to mine the available data and monitor the quality of mechanical equipment by constructing pre-training tasks to improve the efficiency of equipment production. Then it is fused with graph neural networks to design intelligent manufacturing optimization model based on self-supervised learning and graph neural networks intelligent manufacturing. The experimental results indicated that the comprehensive performance and practical application of the research model were good on both. Compared to the three performance types of multi-behavior models on different datasets, the model improved by 10.8%, 8.5%, and 6.3%, respectively. The noise robustness of the research model improved by 5.36% and 6.27% compared to the NGCF and EHCF models, respectively. The performance of the research model reached its optimal state when the selected parameters were β=0.01, K=30, and L=2. The results demonstrate that the designed optimization model based on self-supervised learning and graph neural networks intelligent manufacturing has advantages in terms of operational efficiency and index performance. The research results are of great significance for intelligent mechanical manufacturing.

Povzetek: V članku je opisan inovativen optimizacijski model inteligentne mehanske proizvodnje na osnovi samonadzorovanega učenja in grafovskih nevronskih mrež (GNN), ki izboljša učinkovitost in robustnost proizvodnje (do 10,8 %).

1 Introduction

Today, with the continuous development of information network and artificial intelligence (AI), automation technology is silently penetrating and changing people's way of life at an unprecedented speed. Intelligent mechanical manufacturing, as a necessary path for industrial automation, has been increasing in market demand, and the traditional manufacturing methods are no longer able to meet the demand [1-2]. This phenomenon not only originates from the surge of market demand for product personalization and customization, but also because of the increasingly fierce competition in the global market, which requires enterprises to be able to respond to market changes more quickly and realize product iteration and upgrade [3]. With its strong automatic recognition capability, machine learning (ML) approaches have drawn the attention of several researchers in recent years who are attempting to predict possible equipment failures of machinery. However, the existing ML techniques are still insufficient in terms of recognition efficiency and accuracy, and the wide range of applications cannot meet the basic requirements of intelligent mechanical manufacturing [4]. The primary concerns have centered on the utilization of self-supervised learning (SSL) and graph neural networks (GNNs) technologies to enhance the accuracy and efficiency of intelligent recommendation systems in mechanical manufacturing processes, with a focus on improving anomaly detection and fault prediction. SSL is one of the most classical techniques in ML technology. By analyzing the data generated during the operation of mechanical equipment to identify abnormal patterns, the effect of quality detection can be achieved. Moreover, GNN, as a tool for information aggregation (IA) and transfer, can capture the complex relationship between users and equipment for the recommendation of relevant mechanical parts [5]. In this context, to improve the efficiency and accuracy of mechanical manufacturing, the study attempts to

innovatively design an optimization model based on SSL and GNN intelligent manufacturing. The novelty of the research lies in the introduction of heterogeneous graphs and meta-paths to combine SSL with GNN to innovatively improve anomaly detection and failure prediction capabilities in intelligent mechanical manufacturing. This integration not only improves the model performance, but also enhances the adaptability and generalizability to complex industrial scenarios. It aims to provide a technical foundation for intelligent mechanical manufacturing that can improve production efficiency and quality.

2 Related works

With the intelligent and automated development of the manufacturing industry, the traditional manufacturing methods have been unable to meet the production needs, while intelligent mechanical manufacturing has become an important trend in the development of the manufacturing industry. As a result, numerous academics have studied intelligent mechanical manufacturing techniques in related fields. He H combines deep reinforcement learning with graph neural networks (GNN) to propose an intelligent network traffic scheduling algorithm to solve traffic scheduling problems in large-scale dynamic network environments. This algorithm leverages the decision-making capabilities of deep reinforcement learning and the advantages of GNNs in processing graph structured data to achieve an efficient decision-making process from macro strategy formulation to micro-operation execution through a hierarchical reinforcement learning framework. The experimental results show that the algorithm exhibits excellent robustness and generalization ability [6]. Sharma T et al. constructed fuzzy ensemble technology based on mathematical analysis of trust scores and deep neural networks to promote the research of automatic ALSC. The proposed method can correct the misclassification of basic deep learners through reward and punishment strategies. The experimental results conducted on five benchmark datasets show that this method has advantages over component-based deep neural networks and other important benchmarks [7]. Yao X et al. proposed a blockchain-based value-added industrial meta-universe solution for intelligent manufacturing based on cyber-physical systems. The study used intelligent manufacturing social technology, enhanced intelligent manufacturing architecture and framework to achieve high resource utilization. The results indicated that the proposed scheme was intelligently resilient and sustainable [8]. Aldrini J et al. proposed intelligent fault diagnosis and self-healing conceptual model architecture for intelligent manufacturing system to overcome the performance and safety issues of intelligent manufacturing. The approach improved the performance of intelligent manufacturing systems through fault detection as well as self-healing fault-tolerant strategies. Experimental results indicated that the proposed structure had a good robustness [9]. To facilitate intelligent decision-making in dynamic scheduling and reconfiguration, Yang S. suggested a mathematical model of intelligent scheduling based on deep reinforcement learning. According to test results, the suggested model has good scheduling efficiency [10].

Intelligent mechanical manufacturing often introduces artificial networks and ML methods for research, and several scholars have conducted research on SSL and GNN. Krishnan R proposed self-supervised methods and models for medicine and healthcare in response to the problem of medical AI development. The study investigated SSL's benefits and drawbacks while creating models with multimodal datasets. The suggested approach could hasten the development of medical AI, according to the findings [11]. Rani V et al. proposed SSL detection for image processing problems. The study used unstructured and unlabeled data to develop an AI system to perform downstream computer vision tasks. The findings indicated that this method had good applicability [12]. Kumar P incorporated contrast learning into SSL to investigate the conditions of application in different domains. The findings indicated that this method has positive significance for complementary contrast learning [13]. To address the issue of information overload, Wu S. et al. presented a recommendation model based on GNN. The method provided information categorization based on the type of information used and the recommendation task, and extracted content from the interaction information. Numerous experiments indicated that the proposed method had a good stability [14]. Zhou Y proposed a new classification method to overcome the limitations of GNN. The study categorized the GNN into the corresponding categories after showing the full picture of the GNN. The test results indicated the superiority of the proposed approach in categorization [15]. The summary and analysis of existing research methods are shown in Table 1.

Table 1: Summary and analysis of currently available research methods

Methodologies	Performance indicators	Gaps	Limitations	Unique requirement
He H [6]	Network traffic scheduling efficiency	Traffic scheduling problem in large-scale dynamic network environment	The efficiency and robustness of traditional algorithms in handling large-scale dynamic networks	Improve scheduling efficiency and robustness
Sharma T et al. [7]	Automatic ALSC	Integrated	Error classification	Improve the

	performance	technology of mathematical analysis based on trust scores and deep neural networks	of basic deep learners	accuracy and robustness of automatic ALSC
Yao X et al [8]	Speed of redeployment of resources	Slow to respond to market changes	Lack of real time	Real-time resource allocation
Aldrini J et al [9]	Self-healing time	Slow response of self-healing systems	Limited ability to self-heal	Rapid self-healing ability
Yang S. [10]	Movement control accuracy	Poor adaptation of highly dynamic scheduling	Inadequate adaptation	Dynamic Scheduling Adaptation
Krishnan R [11]	generalization capability	Inadequate ability to generalize medical data	Limitations of multimodal data processing	Multimodal data processing
Rani V et al [12]	Outlier detection rate	Poor handling of image processing outliers	lack of robustness	Enhanced robustness
Kumar P [13]	Cross-domain accuracy	Insufficient flexibility in cross-cutting applications	Poor cross-cutting adaptation	Cross-cutting adaptability
Wu S. et al. [14]	processing speed	Poor stability of massive data processing	information overload	Information processing efficiency
Zhou Y [15]	Classification accuracy	Poor classification of complex network structures	Insufficient classification accuracy	Improvement of classification accuracy

To summarize, although many experts and scholars have carried out related research on intelligent mechanical manufacturing, there has not been an approach that combines with SSL and GNN. In view of this, the study proposes an intelligent mechanical manufacturing model based on SSL and GNN. The study combines the data characteristics and technological advantages of real-world application scenarios to construct a supervised networked intelligent manufacturing innovation approach. This can improve production efficiency and quality and contribute to expanding the innovative applications of intelligent mechanical manufacturing.

3 Intelligent mechanical manufacturing method based on SSL and GNN

3.1 Intelligent mechanical manufacturing design based on SSL

With the increasing demand for intelligent mechanical manufacturing, the traditional manufacturing methods are more and more incompetent in terms of efficiency, precision and flexibility [16]. Therefore, it is necessary to propose an innovative manufacturing program that can improve the production efficiency and product quality of mechanical manufacturing. The SSL technique has gained a lot of traction in ML in recent years. From a vast amount of unlabeled data, it automatically learns usable feature representations by using the properties of the data itself as supervised information. When compared to conventional supervised learning techniques, SSL shows a more potent and adaptable approach to data use. Its core advantage lies in getting rid of the reliance on external labels and utilizing the internal structure and properties of the data to automatically generate supervised signals [17]. This feature enables SSL to generate the potential to effectively mine large-scale data. Fig. 1 depicts the SSL model.

In Fig. 1, the SSL model learns advanced representations or features of data by designing pre-training tasks. The pre-training task of SSL is designed as contrastive learning, which involves data encoding, positive and negative sample pair generation, and similarity comparison operations in sequence. These pre-training tasks help the model extract useful information from data without external labels, improving the model's ability to detect abnormal patterns in mechanical manufacturing processes. Therefore, it can be migrated to other related supervised learning tasks for efficient and accurate model training. The SSL algorithmic models can be categorized into three types: adversarial, generative, and comparative models. Since intelligent mechanical manufacturing requires comparative damage determination, the study mainly uses comparative SSL models for learning. Fig. 2 depicts the contrastive model's structure.

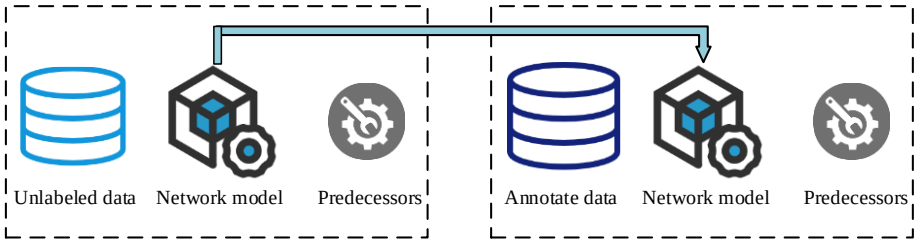

Fig. 1 SSL model architecture

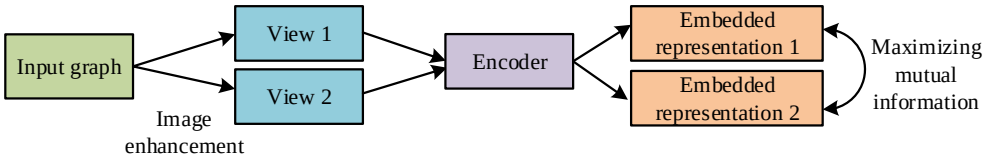

Figure 2: Comparing the structure of self-supervised learning models

In Fig. 2, the comparative model works by first encoding the input data efficiently by training the encoder. The encoded data are fed into the discriminator, and subsequently these encoded data are used to perform similarity comparison operations, contrasting losses to maximize mutual information. By analyzing the massive amount of data generated during operation, the SSL algorithm can automatically identify anomalous patterns and predict potential equipment failures. The original identification formula is shown in Equation (1).

$$\tilde{G}_r = (N_r, M_r \square E_r) \quad (1)$$

In Equation (1), G is the graph. N for the set of nodes. r is the type of relationship. $\tilde{G}_r$ is the original data (OD) sample. N_r is the set of nodes in the data sample. M_r represents the original mask vector, which is used to randomly discard the edges of the OD. E_r represents the set of edges in the OD sample. Next, the loss identification is performed as shown in Equation (2).

$$\tilde{G}_S = (N_S, M_S \square E_S) \quad (2)$$

In Equation (2), S is the loss generation. $\tilde{G}_S$ is the processed loss samples. N_S represents the node set of loss samples. M_S represents the loss mask vector. E_S represents the set of edges in the loss sample. Then, determine the positive probability of unlabeled data features by first calculating the cosine similarity of each data point, then calculating the sum of the similarities of all data points. Finally, the ratio of these two sums is the probability of positive samples, as shown in Equation (3).

$$y_{i+}^r = Soft\max(\cos(\tilde{e}, e_i^s)) \quad (3)$$

In Equation (3), y_{i+}^r is the probability that the data i in the unlabeled sample set is positive for a given data feature. $\tilde{e}$ is the embedding representation of the data in the unlabeled sample set. e_i^s is the feature embedding representation of the data. $\cos(\square)$ is the cosine similarity. Then, it is necessary to obtain the data self-supervised signal (SsS) and define a set of SsSs that includes all cosine similarity values exceeding the threshold. As shown in Equation (4).

$$P_{i+}^r = \left\{ \tilde{e}_k \middle| k \in Top-K(y_{i+}^r), \tilde{E} \sim \tilde{G}_r \right\} \quad (4)$$

In Equation (4), P_{i+}^r is the set of SsSs for information i under data information interaction. $\tilde{e}_k$ is the K data with the highest value after passing the confidence test. k represents all data of the confidence test. E is the set of edges. $\tilde{E}$ represents the set of edges in the data. These signals are used to train the model to learn useful feature representations from the structure of the data itself. Similarly, the feature-based SsS for data under data information interaction can be obtained as in Equation (5).

$$P_{i+}^s = \left\{ \tilde{e}_k \middle| k \in Top-K(y_{i+}^s), \tilde{E} \sim \tilde{G}_s \right\} \quad (5)$$

In Equation (5), P_{i+}^s represents the set of SsSs for information i under data information interaction. y_{i+}^s represents the probability that the data in the labeled sample set is positive for a given data feature. To accurately express the structural relationships, path lengths and other factors in the intelligent network, the study introduces heterogeneous graphs and meta-paths shown in Fig. 3.

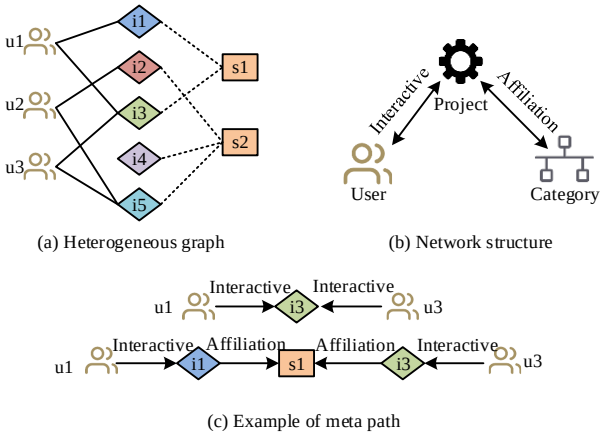

(a) Heterogeneous graph (b) Network structure

(c) Example of meta path

Figure 3: Schematic diagram of heterogeneous graph and meta path

In Fig. 3(a), the heterogeneous graph is a complex data structure that can accommodate multiple types of nodes and relationships. At the same time, nodes can exhibit diverse performance characteristics. To explore the higher-order relationships between nodes in depth, the introduction of meta-paths can effectively portray these complex, non-direct inter-node connections. In Fig. 3(b), the mechanical network structure constructs a hidden relationship between users, items and categories through a meta-path. This path not only shows the possible connections between the three, but also provides a new perspective for understanding the underlying workings of the network in great detail. In Fig. 3(c), after completing the detailed portrayal of different types of node association patterns, the node associations in the whole network become clearly visible. This visualization provides a solid foundation for the subsequent analysis and mining work of intelligent mechanical manufacturing.

3.2 Optimization strategies for intelligent mechanical manufacturing incorporating GNN

A significant amount of unlabeled data can be automatically learned by the model to create valuable feature representations through SSL, which are essential for ensuing prediction, classification, or optimization tasks. GNN can create more precise and thorough models of mechanical systems by taking use of the intricate interactions that exist between mechanical components. GNNs are a subset of neural networks that are specifically trained on graph-structured data (GSD). By capturing the intricate interrelationships between nodes, GNNs are able to learn the properties of the data more precisely [18]. Therefore, the research will incorporate GNN for the optimization of intelligent mechanical manufacturing. Equation (6) illustrates the formalization process of the graph learning-based recommendation system.

$$T = \arg Maxf\left(S(\Theta)\middle|G\right) \quad (6)$$

In Equation (6), T represents the optimal recommendation result. $S(\Theta)$ represents the recommendation model based on graph learning. G represents the data structure information of the interaction graph. Θ represents the parameters in the interaction graph. Then the complex relationship between users or devices is captured by GNN based on the demand degree of related parts. The demand degree formalization process is shown in Equation (7).

$$nor_Pop_i = \frac{Pop_i - \min_Pop}{\max_Pop - \min_Pop} \quad (7)$$

In Equation (7), nor_Pop_i represents the demand degree after normalization of the part data. $\min_Pop$ and $\min_Pop$ represents the maximum and minimum value of the part demand degree. Then the difference value of demand degree between two parts can be obtained, and the formula is as in (8).

$$Pop_Bias_{i,j} = \left|nor_Pop_i - nor_Pop_j\right| \quad (8)$$

In Equation (8), $Pop_Bias_{i,j}$ represents the difference in demand degree between parts i and j. An example of the recommended system data graphic is obtained as shown in Fig. 4.

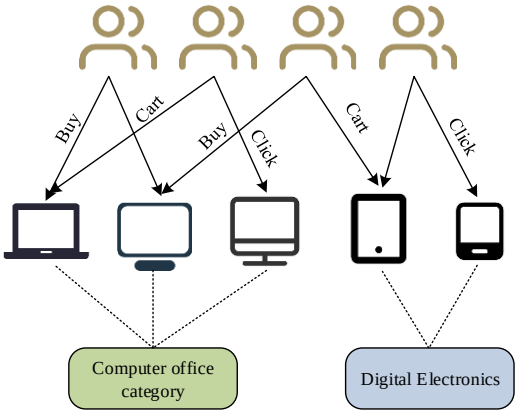

Figure 4: Recommended system data graph example

As illustrated in Fig. 4, the nodes represent users and projects, while the edges represent the users' preferences or interactions with projects. The figure demonstrates a variety of interaction modes, encompassing both direct user-project interactions and indirect interactions through other user nodes, thereby reflecting social influence. After changing the basic data of the recommender system to GSD, the complex relationship between users and items can be captured more clearly and the items can be categorized by attributes. Meanwhile, the complex interactions between users and items can form different types of edges, reflecting the preference intensity or interest patterns of different users for mechanical engineering parts. These edges link user nodes and item nodes, which form the graph structure of the recommender system [19]. This graphical representation method makes complex user project relationships intuitive and easy to understand. The GNN learning method based on graph results has advantages

in mining the relationship between nodes and improving data utilization. The GNN schematic is shown in Fig. 5.

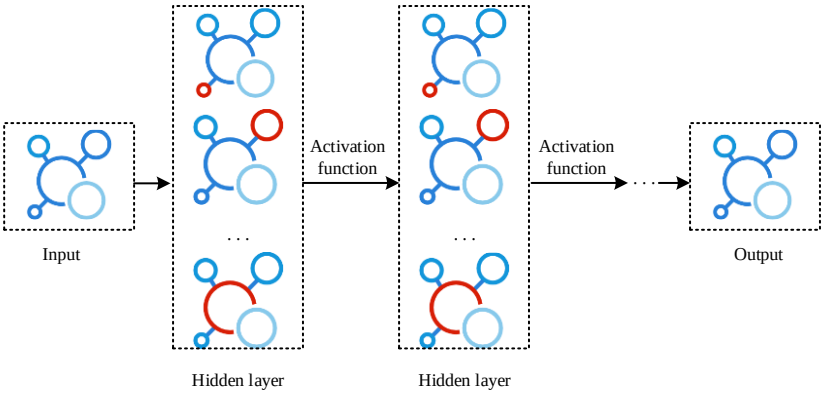

Figure 5: Diagram of neural network

In Fig. 5, each node in the GNN is forced by the learnt function mapping to aggregate data from its nearby nodes in order to gather the neighboring nodes' feature information. The information transfer path in this case points from the target node to the neighbor node. The representation of the node is then updated based on the information obtained from the aggregation and the node's own features. During the iteration process, the node representations will gradually stabilize, thus capturing the structural information of the graph and the complex relationships between the nodes. The GNN can deeply explore and utilize the complex and high-order connectivity information in the user-item interaction graph through its unique structural design, and it can also mine and disseminate more diversified items for users [20]. The propagation rule is shown in Equation (9).

$$h_i^{l+1} = \sigma(W \cdot AGG(h_k \mid \forall k \in N(i)) + b) \quad (9)$$

In Equation (9), $Pop_Bias_{i,j}$ represents the propagation of GNN. σ represents nonlinear activation function. W and b are weights and bias vectors. $AGG(\cdot)$ represents the aggregation function. h_k is the node association information within the region. $N(i)$ represents the set of nodes within the range of node i. In order to mine the data features more fully for extraction, the study uses graph encoder to extract the data features. Each node is represented as a feature vector, and edges represent the relationships between nodes. GNN aggregates information from neighboring nodes through a message passing mechanism. At each layer, nodes collect features from their neighbors and integrate this information through max-pooling. The aggregated features are transformed by nonlinear activation functions to learn advanced representations of nodes. Finally, by stacking multiple GNN layers, the model can capture the multi-hop neighbor information of nodes and learn complex graph structural features. The general structural formula of graph encoder is Equation (10).

$$E^{(l)} = H(E^{(l-1)}, G) \quad (10)$$

In Equation (10), $Pop_Bias_{i,j}$ represents the node l layer embedding representation. H represents the encoder of IA. G represents the view after IA. The l th layer representation obtained through neighbor node layer embedding is Equation (11).

$$e_i^{c(l)} = \sum_{j \in N_i^c} \frac{1}{\sqrt{|N_i^c|}\sqrt{|N_j^c|}} e_j^{c(l)} \quad (11)$$

In Equation (11), $e_i^{c(l)}$ and $e_j^{c(l)}$ represent the embedding representations obtained by the neighbor nodes. N_i^c represents the set of all neighbors of part i in the part similarity graph with de-demand degree. N_j^c represents the set of all neighbors of part j in the part similarity graph with de-demanded degree. Then the final vectors of the parts are obtained using the multilayer information propagation aggregation layer as in Equation (12).

$$e_i^c = \sum_{l=0}^{L} \alpha_l e_i^{c(l)} \quad (12)$$

In Equation (12), e_i^c represents the final embedding vector. L represents all layers of GNN IA. $e_i^{c(l)}$ is the superposition result of the initial embedding. α_l represents the embedding representation weight parameter of l layer. The SSL is then combined with GNN to further enhance the intelligence of intelligent mechanical manufacturing, especially in anomaly detection and fault prediction. The derived optimization model architecture based on SSL and GNN intelligent manufacturing is shown in Fig. 6.

In Fig. 6, the integration of GNN and SSL began with the construction of a multi-behavioral interaction feature extraction mechanism. Among them, SSL is used to automatically learn feature representations from a large

amount of unlabeled data from mechanical operations in order to identify abnormal patterns. Then, these feature representations and SsSs are used as inputs to GNN, which updates node representations by aggregating neighbor node information, captures high-order connectivity relationships between devices, and predicts potential failures. Among them, Bayesian personalized ranking BPR is a method for learning user preferences, while p, q, and n are embedded neural network data. Through the information propagation and aggregation mechanism of GNN, the model is able to capture higher-order connectivity between devices and thus identify abnormal behaviors that significantly deviate from normal patterns. The model greatly raises the degree of equipment intelligence and assists in anticipating maintenance needs in order to lessen the impact of malfunctions on output.

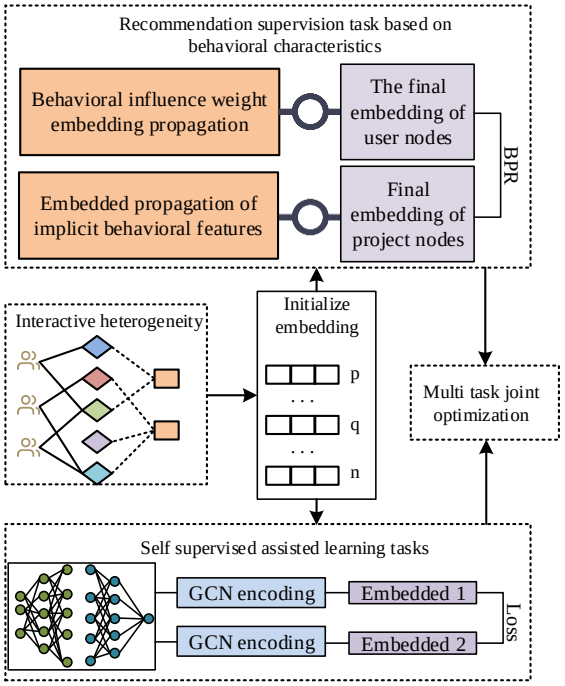

Figure 6: Intelligent manufacturing optimization model architecture

4 Effectiveness analysis of SSL and GNN in intelligent mechanical manufacturing

4.1 Comparative experimental analysis of graph SSL algorithms based on intelligent manufacturing

To analyze the effectiveness of the application of intelligent mechanical manufacturing based on SSL and GNN designed by the study, the superiority and reliability of the research methodology is mainly verified. The study uses Case Western Reserve University (CWRU) and Phm ieee 2012 dataset of publicly available datasets as experimental data. The CWRU dataset is a well-known dataset used for bearing fault diagnosis that contains bearing operating data under various operating conditions and can represent the reliability of the entire system. However, some types of faults have fewer samples, which can lead to data imbalance problems. The Phm IEEE 2012 dataset is a maintenance prediction and health monitoring dataset that contains operational data of various mechanical equipment and can reflect various conditions that may occur during actual operation of the equipment. However, the data dimension is relatively large. Both types of data have good representativeness and public availability. For the CWRU dataset, the study removed all samples containing missing values and standardized the features. The PHM IEEE 2012 dataset has been normalized to ensure that the eigenvalues are located on the same scale. The cross-validation method is used to train and test the model effect. There are three graph encoder layers and a 40-entity embedding dimension. The selection of three GNN layers is based on experimental results and provides a good balance between model performance and computational efficiency. A reduced number of layers might not entirely capture the intricacies of the graph structure, while an increased number of layers could result in overfitting. The 40-dimensional embedding space is large enough to capture rich feature representations while avoiding the curse of dimensionality. The experimental environment is shown in Table 2.

Table 2: Intelligent mechanical manufacturing experimental environment

Environment entry	Environmental parameters
Operating system	Linux CentOS7
Development language	Python3.7
Developing deep learning frameworks	Tensorflow1.14
Hard disk	1T
Memory	16G
GPU	GeForce RTX 2080 SUPER
CPU	Intel(R) Xeon(R) Silver 4215R CPU @ 3.20GHz

The GNN layers was set to 4, and the number of feature-based part-similar neighbors sampled was set to 50. The initial data and user embedding are set to 80, and the regularization parameter is set to 0.005. The initial weight is set to 1/4, and the learning rate is adjusted to 0.001. The Top-N recommendation hit rate (HR) is used as the evaluation index, and the specific comparison of each recommender system is made between the cumulative gain (CG), discounted cumulative gain (DCG), normalized discounted cumulative gain (NDCG) and training time (TT) and parallel processing capability (PPC). The single-behavior neural graph collaborative filtering (NGCF), light graph convolutional network (LGCN), multi-behavior model efficient heterogeneous collaborative filtering (EHCF) and the proposed model of the study are compared for experimental validation. Among them, CG can intuitively display the performance of recommendation systems at different

ranking depths. DCG is capable of simulating the user experience while browsing recommendation lists in a realistic manner. NDCG possesses the capability to directly compare the performance of disparate recommendation systems or users. TT and PPC are capable of evaluating the computational efficiency and scalability of the model. The model evaluation performance is shown in Fig. 7.

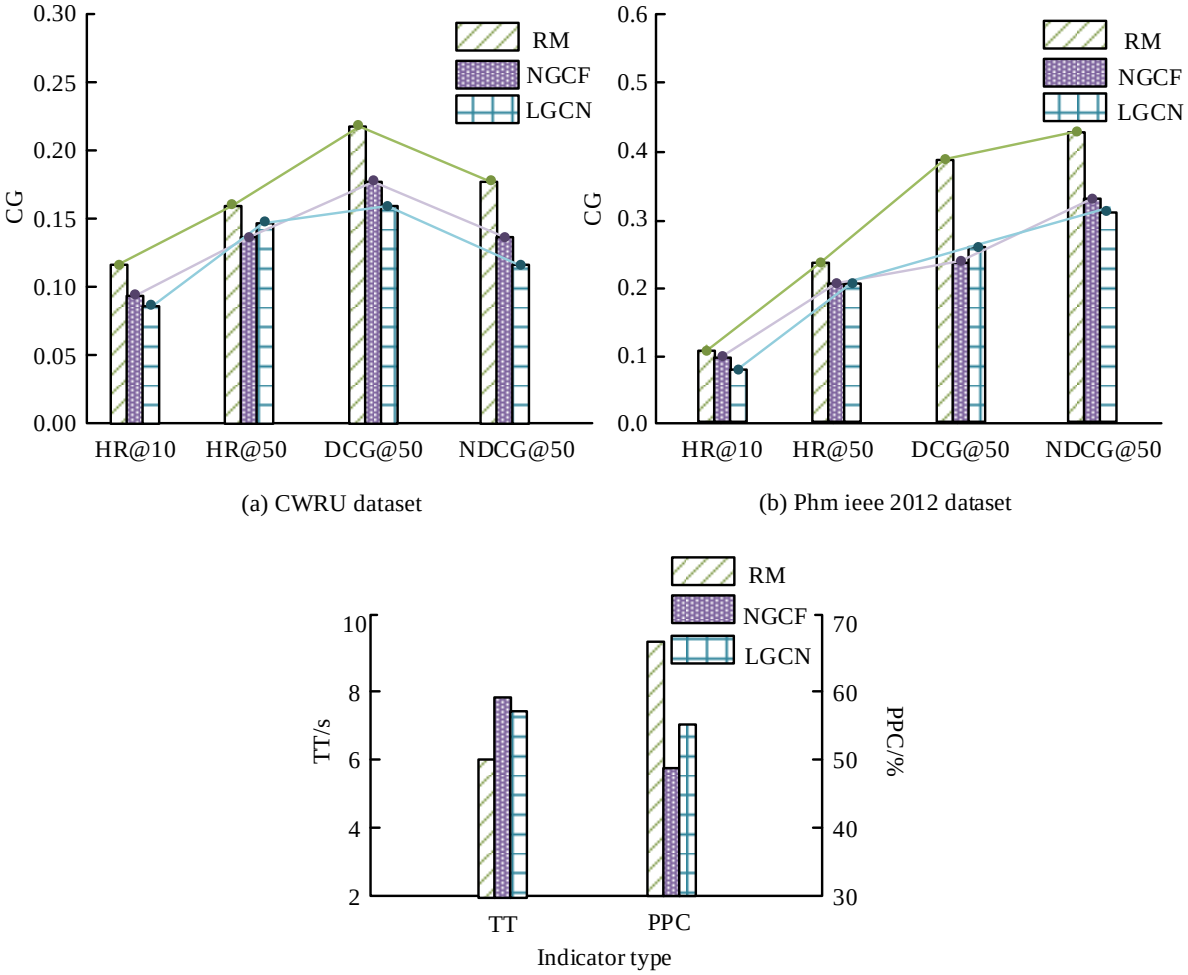

(a) CWRU dataset

(b) Phm ieee 2012 dataset

(c) CWRU dataset+Phm ieee 2012 dataset

Figure 7: Model evaluation performance

Fig 7 compares the performance of different recommendation models on two datasets, including HR, discount cumulative gain (DCG), normalized discount cumulative gain (NDCG), as well as TT and PPC. In Fig. 7, the research model performs significantly better on both CWRU and Phm ieee 2012 datasets. In Fig. 7(a), on the CWRU dataset, the research model outperforms the single-behavior NGCF model by 5.6%, 6.4%, and 4.8% for HR, DCG, and NDCG, respectively. It demonstrates that the study model is more accurate at forecasting objects that users might come into contact with later on. It also improves 10.8%, 8.5%, and 6.3% over the HR, DCG, and NDCG of the multi-behavioral model EHCF, respectively. In Fig. 7(b), the performance comparison of the research model on the Phm ieee 2012 dataset is similar to that on the CWRU dataset. In Fig. 7(c), the TT of the model decreased by 2.4% and 1.8%, respectively, compared to the other two. PPC increased by 16.4% and 10.2%, respectively. As the complexity of the dataset increases, the performance improvement of the research model becomes more significant. It indicates its strong robustness in handling complex user behavior data. Overall, by combining SSL and GNN, the research models can more deeply explore complex features and patterns in data, including subtle differences in user behavior and complex relationships between items, to better understand and predict user preferences. Moreover, it performs well in terms of computational efficiency and scalability. To further evaluate the effect of the model in the practical application of intelligent mechanical manufacturing, the study selects NGCF and EHCF models and the research model to conduct noise robustness anti-interference experiments. Adding Gaussian noise with a mean of 0 and an adjustable standard deviation to the dataset can simulate the random error of the sensor readings. Then gradually control the noise level and observe the performance changes of the system at different noise levels. The noise robustness results of intelligent mechanical manufacturing practical application are shown in Fig. 8.

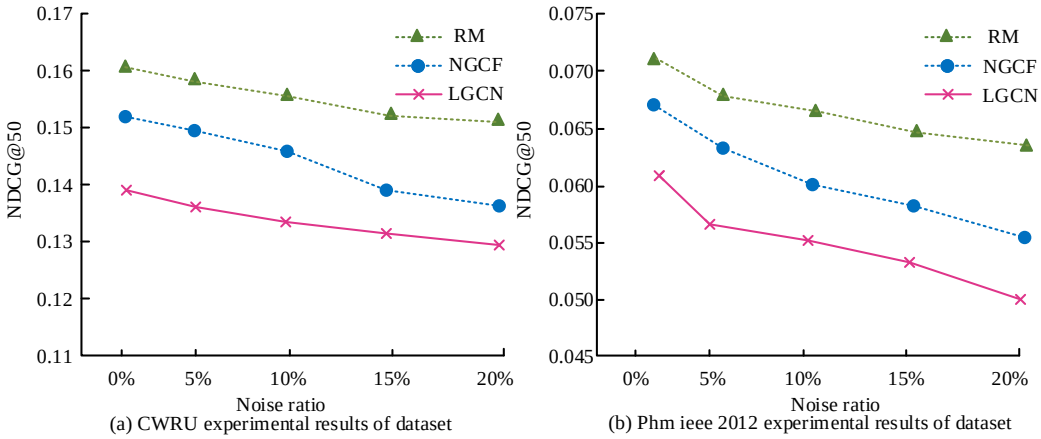

(a) CWRU experimental results of dataset (b) Phm ieee 2012 experimental results of dataset

Figure 8: Comparison experiment results of noise robustness

In Fig. 8, the practical application of the model under both datasets displays an obvious decreasing trend with the increase of the noise intensity during mechanical fabrication. In Fig. 8(a), on the CWRU dataset, the research model shows a gain of 5.36% and 6.27% in the NDCG metrics over the NGCF and EHCF models, respectively. In Fig. 8(b), on the Phm ieee 2012 dataset, the study model has a gain of 4.26% and 5.85% in NDCG metrics over the NGCF and EHCF models, respectively. The experimental result data show that the research model is more effective in maintaining the accuracy and relevance ranking of the recommendation results in a complex and variable noise environment. This reflects its superior data processing capability and feature extraction strategy. It is proved that the research model has wide adaptability and stability in dealing with different sources and types of noise, which can provide more reliable recommendation services in the practical application of intelligent mechanical manufacturing. To demonstrate the contribution of individual components of SSL and GNN to the overall performance, the study conducted an ablation experiment analysis. The proportion of relevant items in the top 10 items of the recommendation list is denoted as Precision@10. The proportion of items successfully recommended by the recommender system among all relevant items is denoted as Recall@10. The reconciled average of Precision and Recall is compared with the F1-Score@10 which measures the overall performance of the model. The results are shown in Table 3.

Table 3: Results of ablation experiment table

Performance indicators	SSL model only	GNN model only	SSL+GNN model
HR@10	0.60	0.65	0.75
NDCG@10	0.45	0.50	0.60
Precision@10	0.55	0.60	0.70
Recall@10	0.50	0.55	0.65
F1-Score@10	0.52	0.57	0.67

According to Table 3, the complete model outperforms models using SSL or GNN alone in all performance metrics. The integration of SSL to learn useful feature representations of data and GNN to capture and utilize complex relationships in graph structured data furnishes a potent instrument for intelligent mechanical manufacturing. To further validate the superiority of the model, the experimental section is expanded to benchmark new models beyond NGCF and EHCF. The model includes sparse aggregation of graph convolutions for inductive learning of node representations (GraphSAGE), graph convolutional network (GCN), and graph isomorphism network (GIN) used for inductive learning of node representations. The benchmark test results are shown in Table 4.

Table 4: Model benchmark test table

Performance indicators	GraphSAGE	GCN	GIN	SSL+GNN model
HR@10	0.58	0.62	0.70	0.75
NDCG@10	0.48	0.52	0.58	0.60
Precision@10	0.52	0.57	0.63	0.70
Recall@10	0.48	0.52	0.60	0.65
F1-Score@10	0.50	0.54	0.61	0.67

In Table 4, the SSL+GNN model outperforms other baseline models in all key performance indicators. This indicates that the SSL+GNN model can more effectively support decision-making, optimize resource allocation, and improve production efficiency in practical applications.

4.2 Experiments on parameter analysis of graph SSL algorithms based on intelligent manufacturing

The research model's performance can be better understood, its configuration can be optimized, and its capacity for generalization can be enhanced by

conducting a thorough analysis of its key parameters following the conclusion of the model's numerous performance comparison trials. Among these are the number of GNN coding layers L, the number of SsSs K, and the SSL scale weight coefficient β. The L of layers 2-4 can achieve a good balance, while K needs to be determined through experimentation to find the optimal value. A smaller beta value emphasizes the importance of downstream tasks, while a larger beta value gives more weight to self-supervised tasks, usually set at 0.001. The experiments first set different values of β on Movielens-M, Last-FM and Book-Crossing datasets. It also keeps K and L constant, both set to 40. The key performance metrics such as NDCG, recall, etc. are recorded for each β-value. The impact of the obtained SSL scale weight coefficient β is shown in Fig. 9.

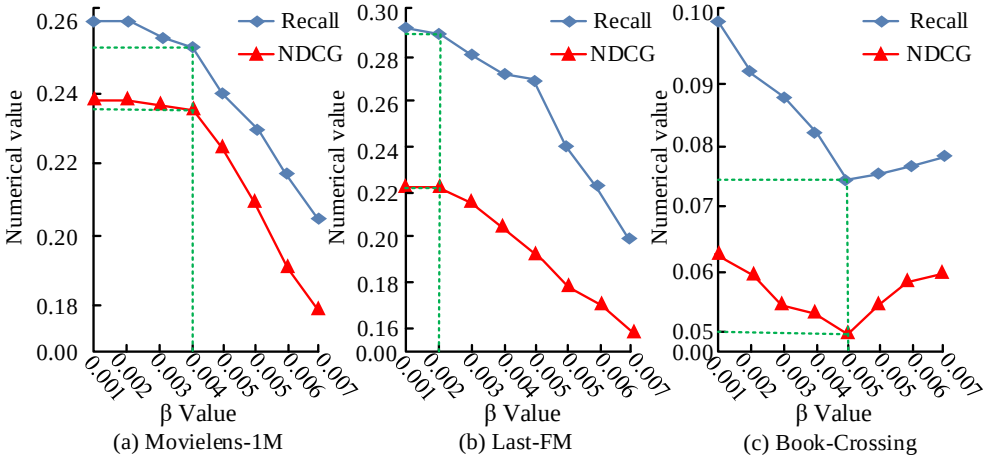

Figure 9: The influence of scale weight coefficient β on SSL

In Fig. 9, the larger the value of β is taken, the NDCG and recall performance of the model decreases. In Fig. 9(a), on the Movielens-M dataset, the model performance is best in comparison when the value of β is taken at 0.001. Its model performance decreases rapidly after taking a value of 0.004, while the recall value is always greater than the NDCG. In Fig. 9(b), on the Last-FM dataset, the model performance is best when β is taken at an initial value, and the model performance decreases after the value is increased to 0.002. In Fig. 9(c), on the Book-Crossing dataset, the model performance appears to decrease and then rebound as the value of β is increased. However, the rebound is small and far from the initial value. The results show that the research model is extremely sensitive to β, and the performance of the research model is close to the ideal state when β takes smaller values. In studying the effect of different SsS numbers K on the model, the value of L is set constant and β is set to 0.001. The obtained effect of SsS number K is shown in Fig. 10.

In Fig. 10, as the value of K grows, the research model performance shows a general trend of increasing and then declining, and the recall value is always bigger than NDCG. In Fig. 10(a), the model performance shows the most obvious trend of increasing and then decreasing on the Movielens-M dataset, where the optimal K value is 30. Meanwhile, the model performance is relatively stable on the other two datasets. The results show that the model performance varies most significantly on the Movielens-M dataset, and the characteristics of the dataset make the SsSs more sensitive to the model performance. Among them, the optimal K value enables the model to fully utilize the SsSs to enhance the learning effect of the main task. This reflects the important role of the model for intelligent mechanical manufacturing SSL. In studying the effect of different GNN coding layers L on the model performance, β is set to take a constant value and K is 30. The effect of GNN coding layers L obtained is shown in Fig. 11.

In Fig. 11, the recall and NDCG performance of the research model on all three datasets increases and subsequently drops as the value of L increases. In Fig. 11(a), on the Movielens-M dataset, the model performance increases to a maximum at L=2, but continues to decrease when L>3 and reaches a steady state at L=4. On the other two datasets, the model performance also maximizes at L=2 and continues to decrease afterward. The results show that the number of SsSs has a significant effect on model performance, and the right amount of SsSs can help the model learn more useful features. However, too many signals may introduce noise and lead to a decrease in model performance. In summary, the performance of the research model in the field of intelligent mechanical manufacturing is optimized when the parameters β=0.01, K=30, and L=2 is selected. Choosing β=0.01 means that the weight of SsSs in the overall objective function is low. It helps the model to focus on self-supervised tasks without overly relying on these signals, thus maintaining sensitivity to the final task. Choosing K=30 means that an appropriate amount of SsSs is used in model training. It helps the model capture complex structures and patterns in the data while avoiding overfitting. Choosing L=2 means that the model can capture key information about the graph structure while maintaining computational efficiency. This finding not only validates the effectiveness of SSL and GNN in complex industrial

scenarios, but also demonstrates the importance of model performance that can be significantly improved by fine-tuning the model parameters.

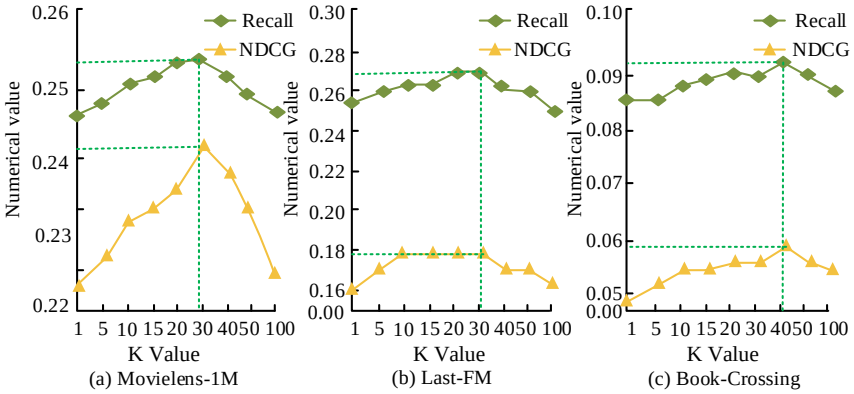

Fig. 10 The influence of the number of self-supervised signals K

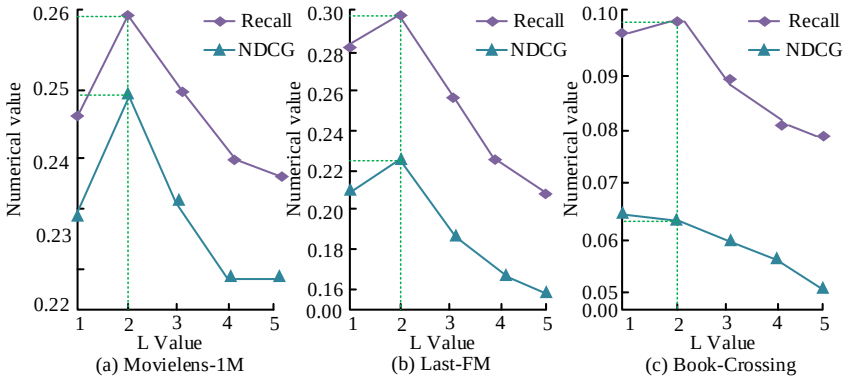

Figure 11: The influence of L encoding layers in neural networks

5 Discussion

The study used a fusion method of SSL and GNN to construct an intelligent manufacturing optimization model. Compared with the intelligent scheduling model obtained by Yang S. [10], this model could capture more complex data structures. The reason was that the model proposed in this article used a reasonable amount of SsSs. Compared with the detection method of Rani V et al. [12], the model proposed in this study had better robustness. The reason was that the feature extraction strategy of the model in this article could maintain the accuracy of the results. SSL automatically mined patterns from a large amount of unlabeled data through contrastive learning, and the test results on the CWRU dataset showed that the model's HR, DCG, and NDCG have improved by 5.6%, 6.4%, and 4.8%, respectively. This indicated that SSL could effectively identify potential faults in bearings under different operating conditions without relying on external labels for fault detection. Meanwhile, GNN enhanced the predictive ability of the model by capturing the complex interactions between devices. On the Phm IEEE 2012 dataset, the NDCG metrics of the model improved by 5.36% and 6.27% compared to the baseline model. It reflected the superior performance of GNN in processing high-dimensional data and predicted maintenance scenarios in real-world scenarios, accurately predicting possible equipment failures. Through experimental analysis, it was found that the model performance reaches its optimum when the parameters β =0.01, K=30, and L=2. This discovery not only validated the effectiveness of SSL and GNN in complex industrial scenarios, but also demonstrated that fine-tuning model parameters could significantly improve model performance. In the noise robustness experiment, the model was able to maintain a high NDCG index even after the addition of Gaussian noise, indicating that the model could maintain the accuracy and relevance ranking of recommendation results in noisy environments. In summary, the studied intelligent manufacturing optimization model had demonstrated significant performance improvement and advantages in practical applications by combining the technical features of SSL and GNN. The model had the capacity to automatically learn data features and capture complex relationships between devices. Furthermore, it could improve performance through parameter optimization, thereby providing an effective technical solution for the field of intelligent manufacturing.

6 Conclusion

Aiming at the problem of innovative application of intelligent mechanical manufacturing, the research conducted a fusion processing based on SSL and GNN methods. Among them, considering the comparative damage determination of intelligent machinery, a comparative SSL model was constructed to utilize the data to automatically identify and predict the abnormalities of the machinery during operation. Meanwhile, heterogeneous graph and meta-path were introduced to accurately express the structural relationship, path length and other factors in the intelligent network. Then on the basis of SSL, it was fused with GNN for optimization, and the propagation rules of GNN were described to improve the level of intelligence to form a recommendation system. Finally, the optimization model architecture based on SSL and GNN intelligent manufacturing was derived. The results indicated that the research model improved HR, DCG and NDCG by 5.6%, 6.4%, and 4.8% over the NGCF model on both datasets, respectively. It also improved each performance by 10.8%, 8.5%, and 6.3% over the EHCF model, respectively. In the practical application of intelligent mechanical manufacturing, the research model exhibited a gain of 5.36% and 6.27% in NDCG metrics over the NGCF and EHCF models, respectively. There was a gain of 4.26% and 5.85% over the NDCG metrics of the NGCF and EHCF models, respectively. The enhancement of NDCG exerts a direct influence on the efficacy of decision-making processes within the production context, facilitating the optimization of resource allocation and the mitigation of unanticipated downtime. DCG has been shown to enhance the efficiency and output of the production line. Improving HR performance helps reduce production costs, improve user experience, and make products more competitive in the marketplace. The results of the study show that the research model is superior compared to other models in terms of dataset performance and practical application, and has good intelligent mechanical manufacturing application value. Moreover, it has contributed to the performance of user classification and recommendation systems. Although the model performed well in experiments, its scalability may be limited by data quality, computational resources, and model generalization ability when implemented in actual industrial environments. The incompleteness of industrial data, noise, and environmental differences can lead to a decrease in model performance. In addition, the high computational requirements of GNN and SSL models can be a challenge in resource-constrained environments. Therefore, the model needs to be adapted and optimized in new environments to ensure its efficiency and accuracy in different industrial scenarios.

Funding

2023 Henan Province Key Research and Development and Promotion Project (Science and Technology Research Project): Research and Application of a Virtual Reality-Based Visualization Platform for Maintenance Safety Knowledge of Electromechanical Equipment (No. 232102321061)

Acknowledgement

2023 Henan Province Key Research and Development and Promotion Project (Science and Technology Research Project): Experimental Research on low-temperature Waste Heat Power Generation System based on radial inflow turbine (No. 232102320223)

References

[1] Jose J, Mathew V. (2024). Internet of Things-A Model for Data Analytics of KPI Platform in Continuous Process Industry. *Informatica*, 48(1). https://doi.org/10.1007/s10570-024-00699-x

[2] Lv, Z., Guo, J., & Lv, H. (2023). Safety Poka Yoke in Zero-Defect Manufacturing Based on Digital Twins. *IEEE Transactions on Industrial Informatics*, 19, 1176–1184. https://doi.org/10.1109/TII.2021.3139897

[3] Kumar, S., Gopi, T., Harikeerthana, N., Gupta, M., Gaur, V., Królczyk, G., & Wu, C. (2022). Machine learning techniques in additive manufacturing: a state-of-the-art review on design, processes and production control. *Journal of Intelligent Manufacturing*, 34(1), 21–55. https://doi.org/10.1007/s10845-022-02029-5

[4] Dave, R., & Purohit, J. N. (n.d.). Leveraging Deep Learning Techniques to Obtain Efficacious Segmentation Results. *Archives of Advanced Engineering Science*, 1(1), 11-26. https://doi.org/10.47852/bonviewaaes32021220

[5] Ravničan J, Marinko A, Noveski G, et al. (2022). A Prestudy of Machine Learning in Industrial Quality Control Pipelines. *Informatica*, 46(2). https://doi.org/10.1007/s10570-022-00665-2

[6] He H. (2024). Automatic Network Traffic Scheduling Algorithm Based on Deep Reinforcement Learning. *Informatica*, 48(22). https://doi.org/10.1007/s10570-024-00799-x

[7] Sharma T, Kaur K. (2023). A Deep Learning-fuzzy Based Hybrid Ensemble Approach for Aspect Level Sentiment Classification. *Informatica*, 47(6). https://doi.org/10.1007/s10570-023-00694-5

[8] Yao, X., Ma, N., Zhang, J., Wang, K., Yang, E., & Faccio, M. (2022). Enhancing wisdom manufacturing as industrial metaverse for industry and society 5.0. *Journal of Intelligent Manufacturing.* 35, 235–255. https://doi.org/10.1007/s10845-022-02027-7

[9] Chihi, I., & Sidhom, L. (2023). Fault diagnosis and self-healing for smart manufacturing: a review. *Journal of Intelligent Manufacturing.* 35, 2441–2473. https://doi.org/10.1007/s10845-023-02165-6

[10] Yang, S., & Xu, Z. (2021). Intelligent scheduling and reconfiguration via deep reinforcement learning in smart manufacturing. *International*

Journal of Production Research. 60(16), 4936–4953. https://doi.org/10.1080/00207543.2021.1943037

[11] Krishnan, R., Rajpurkar, P., & Topol, E. J. (2022). Self-supervised learning in medicine and healthcare. *Nature Biomedical Engineering*, 6(12), 1346–1352. https://doi.org/10.1038/s41551-022-00914-1

[12] Rani, V. L., Nabi, S. T., Kumar, M., Mittal, A., & Kumar, K. G. (2023). Self-supervised Learning: A Succinct Review. *Archives of Computational Methods in Engineering*, 30(4), 2761–2775. https://doi.org/10.1007/s11831-023-09884-2

[13] Kumar, P., Rawat, P., & Chauhan, S. (2022). Contrastive self-supervised learning: review, progress, challenges and future research directions. *International Journal of Multimedia Information Retrieval*, 11(4), 461–488. https://doi.org/10.1007/s13735-022-00245-6

[14] Wu S, Sun F, Zhang W, Xie X, Cui B. Graph Neural Networks in Recommender Systems: A Survey. (2022). *ACM Computing Surveys*, 55(5), 1–37. https://doi.org/10.1145/3535101

[15] Zhou Y, Zheng H, Huang X, Hao S, Li D, Zhao J. Graph Neural Networks: Taxonomy, Advances, and Trends. (2022). *ACM Transactions on Intelligent Systems and Technology*, 13(1), 1–54. https://doi.org/10.1145/3495161

[16] Liu, S., Zheng, P., & Bao, J. (2023). Digital Twin-based manufacturing system: a survey based on a novel reference model. *Journal of Intelligent Manufacturing*. 35, 2517–2546. https://doi.org/10.1007/s10845-023-02172-7

[17] Wang, Y., Wang, J., Cao, Z., & Farimani, A. B. (2022). Molecular contrastive learning of representations via graph neural networks. *Nature Machine Intelligence*, 4(3), 279–287. https://doi.org/10.1038/s42256-022-00447-x

[18] Dong, G., Tang, M., Wang, Z., Gao, J., Guo, S., Cai, L., Gutierrez, R., Campbell, B., Barnes, L. E., & Boukhechba, M. (2022). Graph Neural Networks in IoT: A Survey. *ACM Transactions on Sensor Networks*, 19(2), 1–50. https://doi.org/10.1145/3565973

[19] Liu Z, Yang L, Fan Z, Peng H, Yu P S. Federated social recommendation with graph neural network. *ACM Transactions on Intelligent Systems and Technology (TIST)*, 2022, 13(4): 1-24. https://doi.org/10.1145/3501815

[20] Zheng, C., Chen, H., Cheng, Y., Song, Z., Wu, Y., Li, C., Cheng, J., Yang, H., & Zhang, S. (n.d.). ByteGNN: Efficient Graph Neural Network Training At large Scale. *Proceedings of The Vldb Endowment*, 15, 1228–1242. https://doi.org/10.14778/3514061.3514069

Random Forest-Based Decision Tree Framework for Hazard Management in University Laboratories

Yunan Zhang*, Xiaoyu Wang
[1]National Center for Materials Service Safety, University of Science and Technology Beijing, Beijing 100083, Beijing China
E-mail: zhangyn85@163.com
*Corresponding author

Keywords: decision tree (DT), laboratory hazardous chemicals, RF-based DT algorithm, university laboratory works

Received: October 24, 2024

This study explores the use of Decision Tree (DT) algorithms for detecting potential hazards in laboratory operations by analyzing a synthetic dataset modeled on historical accident reports. The dataset simulates mishaps and near-miss incidents in university laboratories, incorporating detailed descriptions of behaviors and risks. Feature extraction techniques like Principal Component Analysis (PCA) are used to train and test DT models. The Random Forest-based Decision Tree (RF-based DT) model demonstrates superior performance compared to traditional methods. Implemented in Python, the model predicts chemical hazards with 92.3% accuracy, 93.1% precision, 93.5% F1 score, and 91.4% recall. These results confirm the model's reliability for risk detection and management in laboratory settings.

Povzetek: Predlagan je model odločanja na osnovi naključnega gozda (RF-DT) za upravljanje nevarnosti v univerzitetnih laboratorijih, ki zanesljivo identificira kemijske nevarnosti in izboljšuje laboratorijsko varnost.

1 Introduction

University-conducted innovative experiments can involve the use of hazardous chemicals or laboratory procedures [1]. Additionally, they could be involved in risky tasks including handling pyrophoric materials, inactivating infectious pathogens, moving large gas cylinders, and completing metalwork with machine tools which are highly probable to end in accidents and near-miss occurrences [2].

The complexity of laboratory safety management grows when there is a chance of fire, explosion, and other issues. It is risky to undertake laboratory research given the rise in accident frequency [3]. Many different types of laboratories, including biological, chemical, electrical, mechanical, and environmental labs, are frequently found in one university. Every kind of laboratory is made up of several rooms with various purposes. Additionally, every area has a variety of tools and apparatus. This implies that running the university laboratory presents significant difficulties [4]. In actuality, issues with management work account for the majority of laboratory accidents. Daily management tasks depend on the equipment's routine inspection and maintenance to guarantee the safety of the laboratory. Manual statistics are typically used in the administration of the laboratory apparatus [5]. The task of equipment management is difficult, time-consuming, and costly since there are so many different kinds of equipment.

Faculty personnel, researchers, graduate students, or students could be killed in an incident that occurs in a university laboratory while conducting a chemical experiment [6]. The number of laboratory accidents at universities worldwide is unknown, but after they happened, similar incidents occurred again at other colleges [7]. In these instances, there wasn't a significant paradigm shift or change in the way laboratories are safe. Furthermore, the colleges' efforts to work together to stop similar incidents have not advanced [8].

The unusual and extensive attention from industry and mainstream media, as well as from academic institutions around the country, complicated the campus's response efforts even further [9]. The incident had a major impact on everyone in school, especially those who work in laboratory safety and research, the Office of Sustainability, Health & Safety (EH&S) is responsible for safeguarding the health and safety of all individuals on campus. [10]. We utilize an RF-based DT method in this work, which can handle a diverse set of features and provide robust predictions even when some features might be less relevant. Next, by recursively dividing the data based on these vectors, the DT method makes use to estimate hazard probability to anticipate the dangers related to university laboratory work.

The following is the order of this paper: Related works are included in section 2, and techniques are covered in section 3. Section 4 presents the experiment's results. Section 5

concludes with a summary of the study and suggestions for more research.

2 Related works

The inherent hazards assessment and categorization (IHAC) approach was developed in the study [11] for use in university chemistry labs as a result of this investigation. They conducted a quantitative assessment of the inherent risks in chemical laboratory materials, apparatus, and procedures. Concurrently, dividing labs into many levels can lead to more focused safety management and accident avoidance.

Seven substances' chemical concentrations were used in research [12], to examine the fluctuations in the potential of Hydrogen (pH) and Electrical conductivity (EC). The seven compounds were known to produce chemical spills regularly in South Korea and were classified as accident-preparedness substances. Furthermore, they compared the changes in pH, EC, and statistics during the dilution procedure to determine the probability of recognizing unknown chemicals.

The process of developing Standard Operating Procedures (SOPs) in research [13] afforded the chance to ascertain the necessary conditions for reaction setup, recognize possible dangers, define the appropriate handling of undesired materials, and conduct a comprehensive risk assessment. Here, they offered recommendations for SOPs that have to be created for university research facilities as well as an example of an SOP for the Grignard reaction.

A technique for the prospective evaluation of chemicals using sorting-based multi-parameter and multi-criteria decision-making (MCDM) hazards to worker safety in the university lab was established in research [14]. It was advised that certain control measures should be implemented to lower the laboratory's safety risk. The technique was meant to become a main source of information for university danger analysts and adjust to the risk assessment of university laboratories.

The fuzzy Bayesian network (BN) method combined with the human factors assessment and categorization system for university labs (HFACS-UL) was suggested in the study [15], to evaluate the risky conduct in university laboratories. The primary risk factors were determined by applying the model to an inference analysis. To identify further preventative and control methods, meta-networks and important agents were also investigated.

To discover the implementation of certain semi-quantitative methods was assessed in research [16], to determine potential bias or variances caused by utilizing different ways for the same tasks for chemical risk assessment. They could overcome the discrepancies observed in the risk assessment by using two or more distinct semi-quantitative instruments for every working activity they need to evaluate. The tactic could allow workers' contact with chemicals to be reduced.

After an analysis of statistical information to provide a broad explanation of the traits of greater and more frequent accidents, research [17] estimated and evaluated the total risk of the hazardous chemical sector using the entropy weight technique. It examined how safety laws have evolved in China's hazardous chemical business and how the sector was expected to grow moving forward.

The analytical tool based on the software, hardware, environment, and liveware (SHEL) paradigm was utilized in the study [18], to examine reports from accident investigations about explosions at two universities' chemical labs. Global university communities must collaborate to develop methods for research and analysis, instructions for writing accident reports, and an information-sharing platform that would enable them to take advantage of the knowledge gathered from a range of incidents.

Hazardous chemical control was a vital component of campus laboratory safety management, as demonstrated through study [19] and subsequent investigation of remedies and countermeasures. Realizing the intrinsic protection of the university laboratory, the safety management method was completed with the construction of the basis for safety management for its whole life of hazardous substances.

An explosive accident at a university laboratory was thoroughly investigated in the study [20], to determine the primary reasons and enhance safety management. The findings suggested that the experimenters' lack of caution and poor safety knowledge were the primary causes of the accident. To successfully prevent these kinds of tragedies, experimenters and related technical managers need to receive more safety training. It would help to foster a positive safety culture inside the institution.

It focused on methods for deciphering and discovering the possible reasons behind the actions of the people implicated in mishaps in chemical laboratories in the study [21]. Reflections could be beneficial for a variety of stakeholders, including administrators, graduates, suppliers and producers of chemicals and lab equipment, managers, universities and colleges making investments in new or renovated chemical laboratories, and environment, safety, and health (ESH) professionals.

There were many employment contexts, where people were exposed to chemicals in the study [22], but the investigation and healthcare facilities have not received enough attention. It examined how research laboratory staff were exposed to hazardous chemicals at work, evaluated their knowledge and attitudes about chemical hazards, examined whether they followed the rules for handling chemicals safely, and examined the impact of various factors on the important outcomes.

Table 1: Summary table

Method	Accuracy	Key Features	Limitations of SOTA
Proposed RF-based DT	High	Utilizes Random Forest and Decision Tree algorithms to recursively divide data for hazard forecast; and PCA for feature extraction.	Able to manage noisy datasets, scalable, and efficient for hazard identification in university labs.
IHAC Methodology [11]	Moderate	Quantitative assessment of intrinsic hazards in university chemistry labs.	Does not use machine learning for hazard prediction. Restricted scalability and adaptability.
Chemical Risk Analysis [12]	Moderate	Evaluate pH and EC variations to evaluate chemical spill likelihood.	Concentrates on chemical properties, lacking broader applicability to other laboratory situations.
SOPs Formulation [13]	Moderate	Creates Standard Operating processes to handle chemical hazards and reactions.	No predictive model; does not evaluate historical incident data for hazard prediction.
MCDM-based Risk Assessment [14]	Moderate	Multi-criteria decision-making for evaluating chemical dangers.	Does not utilize machine learning to forecast hazards. Risk evaluation is not automated or scalable.
Fuzzy Bayesian Network (BN) [15]	High	Fuzzy BN technique incorporated with human factors for hazard prediction.	Restricted to hazard behavior prediction and the absence of real-time scalability or practical incorporation.
Semi-quantitative Chemical Risk Assessment [16]	Moderate	Semi-quantitative techniques to detect biases in chemical risk evaluations.	May have inconsistent findings across differing situations and lacks an extensive predictive framework.
Entropy Weight Method for Chemical Risk [17]	Moderate	Utilizes entropy weight technique to quantify and assess risks in the chemical industry.	Concentrates on industry-level risk evaluation; not tailored to laboratory-particular incidents or hazards.
SHEL Framework for Explosion Analysis [18]	High	Utilizes SHEL framework for accident study and evaluation in chemical labs.	It absences predictive modeling capacities and does not tackle hazard probabilities in university labs.
Chemical Safety Regulation [19]	Moderate	Concentrates on regulating hazardous chemicals in university labs.	No predictive analytics or machine learning incorporation for hazard prediction.
Explosive Incident Analysis [20]	High	Examines causes of explosive incidents in university labs and suggests security enhancements.	Reactive method; concentrates on post-incident analysis rather than proactive hazard discovery.
Motivational Behavior Analysis [21]	Moderate	Examines motivations underlying individual activities in lab incidents.	Does not tackle the direct prediction of hazards or use automatic

			machine learning for risk evaluations.
Chemical Exposure Analysis [22]	Moderate	Evaluate research lab personnel's exposure to hazardous chemicals and assess safety protocol adherence.	Lack of predictive model for detecting hazard probabilities in real-time; no incorporation of historical data.

These previous studies in laboratory hazard prediction frequently absent predictive modeling, with most approaches being reactive or concentrating on particular risk factors like chemical properties or human behavior, rather than utilizing machine learning to predict hazards based on historical data. Additionally, numerous techniques lack scalability and may struggle to manage large datasets or real-time hazard detection, as evidenced by methods such as IHAC and the SHEL framework, which are restricted to particular situations and do not adapt well to the dynamic nature of laboratory work. Furthermore, these techniques struggle with noisy or incomplete datasets, which are common in practical uses, whereas the proposed RF-based DT algorithm can manage noisy data while still producing dependable predictions. Finally, while numerous SOTA techniques concentrate on isolated risk factors, the proposed approach incorporates multiple variables to create a more extensive and precise hazard prediction system, thus tackling the restrictions of previous techniques.

The suggested RF-based DT algorithm tackles the requirement for a more scalable, predictive, and comprehensive system for assessing and mitigating laboratory risks. It predicts risks by combining historical accident reports, feature extraction (PCA), and machine learning, providing a proactive solution for laboratory security management that is lacking in previous techniques. This gap in current research justifies the requirement for the RF-based DT algorithm, which can offer more precise hazard predictions while dealing with noisy, large datasets in real-time, providing an important improvement over the conventional approach.

3 Methodology

The collection includes recorded near-miss and accident events from a variety of academic laboratory operations. Benefits of Outliers, noisy data, and feature interactions can all be handled well by Random Forest. Several decision trees are constructed using Random Forest, each taking into account various combinations of these characteristics. Several decision trees are combined in Random Forest, an ensemble learning technique, to produce more accurate forecasts. We implement this approach in our suggested model. To anticipate the dangers connected with university laboratory work, the DT method uses these vectors to recursively segment the data based on their features, estimating hazard probabilities. The general flow is depicted in Figure 1.

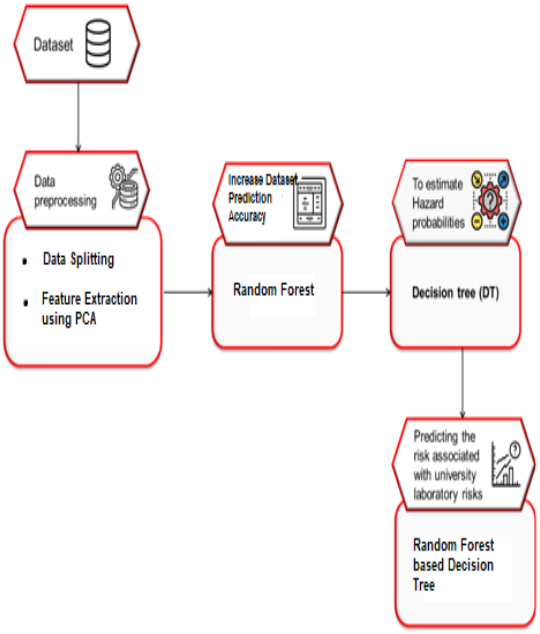

Figure 1: Overall flow

To enable replication, the methodology comprises data preprocessing, PCA for dimensionality reduction, and the creation of RF-based Decision Trees (RF-based DT). Preprocessing steps include dealing with missing values, encoding categorical variables, and normalizing numerical data. PCA is used to identify components that explain 95% of the variance. Random Forest is used to build decision trees, with cross-validation to improve hyperparameters such as tree count and depth. The trees are built by reducing impurities (such as the Gini index), and the RF-based DT combines them to improve model efficacy and generalization.

3.1 Dataset

A synthetic dataset consisting of event reports from university laboratory activities was created. Sample analysis, equipment maintenance, and chemical synthesis are a few of the laboratory tasks included in these reports. All of the reports consist of records on the dangers that would arise from those activities, inclusive of sample analysis, chemical synthesis, and equipment maintenance. The dataset accommodates 1133 reports which have been

randomly categorized as either close to pass-over occurrences or accidents to copy various levels of severity. This dataset is the foundation of research on DT algorithms to identify risks in lab operations. The dataset includes synthetic event reports that are intended to simulate laboratory behaviors and related hazards, such as sample analysis, chemical synthesis, and equipment maintenance. Each record indicates a hypothetical scenario based on practical laboratory functions, with detailed descriptions of behaviors, potential risks, and results. This synthetic method was selected due to the lack of extensive practical accident reports, while still retaining a realistic and controlled dataset for model assessment.

The synthetic dataset of 1133 reports were generated utilizing different laboratory operations, including sample analysis, equipment maintenance, and chemical synthesis, to represent common scenarios in academic laboratories. While the data is not based on actual accidents, it is designed to reflect plausible near-miss and accident scenarios that could happen in a university lab setting. The dataset was created by simulating various severity levels and includes features related to chemical procedures, safety protocols, and operational tasks. It has been pre-processed to guarantee consistency and usefulness for machine learning model training.

Data splitting: 20% percent of the input dataset is used for testing, while the remaining 80 % is used for training. A training dataset is a collection of data used to train a model. The testing dataset is also used to evaluate the performance of the trained model. The performance of each approach is created and evaluated using a variety of metrics, including accuracy, precision, recall, and F1 scores.

Feature extraction: Selecting the best features to extract is a crucial step because characteristics that aren't relevant could have a detrimental effect on the machine learning classifier's classification performance. In this step, principal component analysis, or PCA, is used to extract important features from the dataset.

3.2 PCA

Principal Component Analysis is a method for unlabelled feature extraction in data processing. Principal Component Analysis (PCA) was selected for feature extraction because it can decrease data dimensionality while retaining the most important variations in the dataset. PCA is especially helpful for dealing with large datasets because it assists remove irrelevant or redundant features, increasing model effectiveness and precision. Unlike t-SNE, which is mainly employed for visualization and may distort high-dimensional structures, and LDA, which is best suited for supervised learning tasks, PCA excels in unsupervised scenarios by capturing maximum variance without assuming class labels, rendering it ideal for the laboratory accident dataset.

A new, smaller feature space will be used to display features. The new features identified from the results of the PCA extraction are the features containing the most important data. The primary elements are obtained by optimizing the variance of the data. Since there are fewer additional dimensions (features) than starting characteristics, data visualization is feasible in a low-dimensional principal component space. Determine the dataset using each attribute in the manner shown below eq.1:

$$\bar{w}_i = \frac{1}{m}\sum_{j=1}^{m} \begin{matrix} w_{ji}, \ j = \\ 1,2,\ldots\ldots,m \end{matrix} \quad \begin{matrix} \\ i = 1,2,\ldots\ldots,m \end{matrix} \qquad (1)$$

Were,

n – No. of features,

w_{ji} - Data j-sample with i-feature,

m - Number data of sample, and

$\bar{w}_i$ - Data i-feature.

Calculate Φ with the following Equation 2,

$$\Phi = [\Phi_{ji}] = [w_{ji} - \bar{w}_i] \qquad (2)$$

Φ - Matrix of size $m \times n$.

Calculate the covariance matrix using the following Equation 3,

$$D = \frac{1}{m-1}\Phi^S\Phi \qquad (3)$$

D - Matrix of size $n \times n$.

Calculate the features of the D matrix by calculating the subsequent Equation 4.

$$Det\ (\lambda J - D) = 0 \qquad (4)$$

D - Covariance matrix, and

J - Identity matrix.

After that, calculate the subsequent equation 5 to determine the eigenvectors w that correspond to the features of the record λ,

$$(\lambda . J - D)w = 0 \qquad (5)$$

Form matrix w' Using the associated features after sorting the eigenvectors according to the eigenvalues, starting with the greatest. Calculate the principal components as follows in equation 6.

$$PC = \Phi w' \qquad (6)$$

PCA was used to decrease the dataset's dimensionality by converting original features into principal components that maintained 95% of their variance. Important features extracted using PCA comprise activity type, hazard severity, and equipment utilization. These elements were then utilized as inputs to decision tree algorithms, allowing for more precise forecasting of possible laboratory risks while reducing the effect of irrelevant or redundant data.

3.3 Random forest

A popular algorithm for machine learning one of the components of the supervised learning approach is the Random Forest Algorithm. It applies to machine learning problems that involve both regression and classification. The concept of supervised learning combines multiple classifiers to address a difficult problem and improve the model's performance, in its basis. Popular embedding learning is Random Forest could be used to manage hazardous chemicals in the lab by encoding chemical names and qualities into high-dimensional vectors. This makes it easier to do similarity and group chemicals according to their attributes. This model offers an effective way to compute vector representations using the Continuous Bag of Model (CBOM) and Skip-gram designs, which are both basic neural network models with a single hidden layer. Using backpropagation and stochastic descent of gradients, this approach first creates a PCA feature extract derived from the data entered. After that, the vectors are learned. The CBOM architecture predicts accuracy from future and previous contexts by utilizing a log-linear classifier learned through the negative collection and averaging contextual vectors. With a given word, the Skip-gram architecture predicts surrounding components. Training examples are created by eliminating a predetermined number of contextual phrases since the context is unbounded, such as $x_j - 3, x_j - 4, x_j + 3, x_j + 4$, thus the term "skip-gram." Figure 2 shows the CBOM and skip-gram structure.

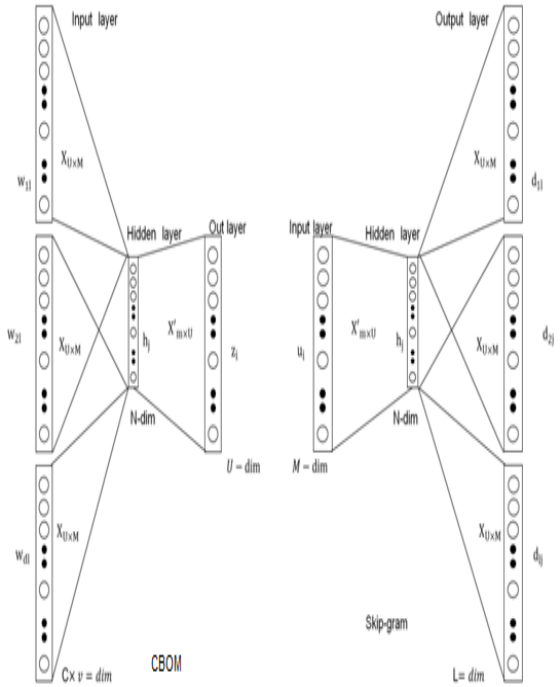

Figure 2: CBOM and skip-gram

Instead of creating a new model from scratch, the pre-trained model is utilized to address a comparable scenario or issue. Pre-trained models are developed and made available to the public for use in research. Pre-trained RF and Pre-trained GloVe are the two pre-trained models that are available for embedding models.

To improve the model's capacity to interpret various chemical and operational data, this paper employed embedding techniques like CBOW and Skip-gram, which are frequently employed for text analysis, to represent chemical names, properties, and lab-related descriptors as high-dimensional vectors. These embeddings allowed the model to compare and categorize features numerically, resulting in higher classification accuracy.

Before using Random Forest, Principal Component Analysis (PCA) was employed to decrease the dimensionality of the dataset by converting original features into principal components that maintained 95% of the variance. This decreased dataset was then embedded with CBOW and Skip-gram, allowing the Random Forest model to efficiently process the transformed data. The rationale for this method stems from embeddings' capacity to generate dense, numerical representations of categorical and text-like data, which improves model performance.

The Random Forest model improved its ability to classify hazards significantly by integrating PCA and embeddings, especially when evaluating reports of incidents involving chemical synthesis, sample evaluation, and equipment maintenance. The combination of these methods produced an effective and interpretable framework for hazard prediction in university laboratory settings.

3.4 Decision tree

The DT method uses these vectors to recursively split the data based on their features to determine hazard probability and anticipate the dangers related to the university chemical lab. The DT has branches containing qualities that determine the outcome, or the objective function and are organized in a sequential hierarchical structure. Nodes: arbitrary vertices where the potential course of events is ascertained, the outcome of Leaf (leaf) nodes with intends and values are used to depict the process of choosing a certain attribute value and merging several objects. Depending on the type of predicted indicator, decision trees could be divided into two categories: regression trees and classification trees. Trees of classification are useful for studying certain qualities, such as assigning items to a previously established class hence using them is advised when creating a prediction system. Data is categorized using decision trees, which split data into groups and provide a hierarchy of "if... then..." operators.
To separate the nodes into informative functions, create an objective function. Every division in which we optimize the increase is:

$$JH(C_o, e) = J(C_o) - \sum_{i=1}^{n} \frac{M_i}{M_o} J(C_i) \quad (7)$$

Where$e$ is the property that is used to conduct the splitting; Parents C_o and C_i is the $i-th$ child nodes, while J is a heterogeneity measure. M_i is the number of specimens contained in the $i-th$ child node, M_o is the overall number of values in the parent node.

We use binary decision trees for simplicity and to shrink the multidimensional search space. The child nodes $C_{left}$and C_{right} in our scenario are:

$$JH(C_o, e) = J(C_o) - \sum_{j=1}^{d} \frac{M_{left}}{M_o} J\left(C_{left}\right) - \frac{M_{right}}{M_o} J\left(C_{right}\right) \quad (8)$$

Where$e$ is the property that is used to conduct the splitting; the parent and $i-th$ child node databases are denoted by$J(C_o)$. J is a heterogeneity metric; The total number of samples in the parent node is represented by C_o, the number of samples in the child nodes that are in the $i-th$ child node is represented by M_o, the child nodes' numbers of patterns are represented by M_{left} and M_{right}.

Determination of entropy for all classes $o(j/s) \neq 0^2$that is not empty.

$$J_G(s) = -\sum_{j=1}^{d} o(j/s) log_2 o(j/s) \quad (9)$$

Where $o(j/s)$ is the percentage of samples including a single node s and the class.

Therefore, if every sample in a node is a member of the same class, the entropy is zero, and if the distribution of classes is uniform, the entropy is at its maximum.

A criterion that reduces the possibility of misdiagnosis is the Gini statistic for heterogeneity:

$$J_H(s) = -\sum_{j=1}^{d} o(j/s)(1 - o(j/s)) = 1 - \sum_{j=1}^{d} o(j/s)^2 \quad (10)$$

Where $K_H(s)$ is the Gini measure of heterogeneity and $o(j/s)$ is the proportion of samples that fall under a class and a single node.

Classification error is an additional metric for heterogeneity.

$$J_\varepsilon(s) = 1 - max\{o(j/s)\} \quad (11)$$

Where s is the single node and $o(j/s)$ is the proportion of samples that correspond to a class,$J_\varepsilon(s)$ is the classifier error.

Although this criterion is less susceptible to changes in the capacity of the classes at the nodes, it is appropriate for trimming trees but not for growing trees.
Decision Trees (DT) were used to divide laboratory hazard data, forecast risks, and evaluate hazard probabilities in university chemical laboratories. The objective function is critical in determining the best feature for dividing data at each node because it measures the efficiency of each split in terms of information gain or impurity reduction. The requirement for an objective function stem from the desire to determine the most pertinent features—such as chemical properties, laboratory activities, or prior incident history—that best differentiate hazardous and non-hazardous situations. By improving this function, the tree can recursively divide the data, guaranteeing that each child node indicates a more homogeneous subset of the data and thus enhancing the model's predictive accuracy. The goal is to reduce uncertainty regarding the risk of an incident at each split, resulting in better hazard forecasting. For instance, the objective function may prioritize divides that most efficiently distinguish incidents from non-incidents, allowing the decision tree to precisely forecast hazardous situations. Therefore, the objective function directly contributes to the primary goal of forecasting hazardous incidents by detecting important risk factors that influence decision-making at each node.

3.5 Random forest-based decision tree

An innovative technique for coping with hazardous chemicals in academic labs is the RF-based DT set of rules. This technique turns chemical descriptions and protection information into excessive-dimensional vectors that seize the complicated interactions between terms by using PCA and ML. The gadget can realize links among materials,

risks, and safety regulations for the reason that those vectors encode linguistic commonalities. The programs benefit in categorizing compounds in step with their traits and associated dangers using training a DT model on these vector representations. The hazardous chemicals machine gives more precise control and is streamlined by using this automatic class process, which reduces the need for human inspection and expertise. Furthermore, the machine gives extra particular hazard critiques and customized safety advice by using the semantic context under consideration. All things taken into consideration, there may be a great deal of capacity for elevating protection standards and decreasing dangers in university laboratories through the use of this novel technique. This suggests that Random Forest is a classifier that uses several decision trees on different dataset subsets and averages them to increase the dataset's predicted accuracy. The random forest predicts the result based on the majority of nodes of predictions from each decision tree rather than relying on just one. Accuracy is higher and overfitting is prevented because the forest has more trees.

The algorithm is known as Random Forest.
Step 1: Using Random Forest, n random lab records are chosen from the data set that contains k records from DT.
Step 2: A distinct decision tree is constructed for each sample.
Step 3: Every decision tree will generate an output of chemicals.
Step 4: Regression and classification averages are used, respectively, to assess the final product.

Pseudo code: RF-based DT Algorithm

Input:

Dataset: L = $\{(x_{1,}y_1), (x_{2,}y_2), (x_{3,}y_1) \dots \dots (x_{m,}y_m)\}$.

Laboratory set: A = $\{d_{1,}d_2 \dots \dots d_{a,}\}$

Method:

1. Build a node N.

2. If all samples in L belong to the same class or the features in L are uniform:

- Label N as a leaf node with the majority class in L.
- Return N.

3. Compute the best splitting node, d_n, from A utilizing the chemical selection Method.

4. Divide the dataset into subsets depending on the values of d_n.

5. For each subset corresponding to a value of d_n:

- If the subset is empty:
  - Append a leaf labeled with the majority class in L to node N.
- Otherwise:
  - Recursively call the TreeGenerate method with the subset and residual features to create child nodes.

6. Return node N.

Chemical Selection Method: Assess all features in A to determine the splitting node, d_n, that optimally partitions L into subsets utilizing a selection criterion (for example Gini index, information gain).

The RF-based DT algorithm utilizes a dataset with features representing hazardous chemical activities, and the chemical selection process concentrates on detecting the most important features for splitting data at each node. The splitting criteria are determined utilizing techniques that measure the node's heterogeneity, such as Gini impurity or entropy. The algorithm starts by choosing a random subset of the dataset and then creating individual decision trees with different subsets of attributes. The node-splitting procedure selects the most informative features for partitioning the data, to increase prediction accuracy and decrease overfitting.

The RF-based DT algorithm builds on the Random Forest methodology to handle hazardous materials in academic laboratories by utilizing laboratory incident reports that contain information on chemical properties, risk factors, and security guidelines. These reports are converted into high-dimensional vectors via PCA and machine learning, which encode the relationships between incidents, hazards, and security needs. The Random Forest framework generates numerous decision trees from random subsets of the incident data and then aggregates their forecasts to enhance accuracy and decrease overfitting. Unlike conventional Random Forests, this method includes semantic and contextual data from the vectors, allowing for more accurate chemical categorization and personalized security suggestions. By integrating the advantages of Random Forests and decision trees, the RF-based DT methodology improves hazard prediction and security standards, decreasing dependence on human oversight and reducing hazards in university laboratories.

4 Experimental results

The recommended method is implemented on a Windows 10 laptop with an Intel i7 core CPU and 8GB of RAM. To ensure the study's reproducibility, all software and libraries used are explicitly listed, along with their version numbers. Python 3.10.1 was used for analysis and model development, with important libraries including Scikit-Learn 1.2.2 for machine learning and preprocessing, TensorFlow 2.13.0 for sophisticated computations, and NumPy 1.24.3 for numerical operations. Data visualization was performed with Matplotlib 3.7.1 and Seaborn 0.12.2. The project was managed and carried out in a Jupyter Notebook environment, version 6.5.4. By documenting these particular versions, this study hopes to ease replication of the findings and guarantee consistency across various computational setups. The methods are Random Forest (RF), Decision Tree (DT), and RF-based DT (Proposed). The implementation used Python libraries like Scikit-Learn to create, train, and assess the models on the training and testing datasets. Cross-validation is used to optimize important hyperparameters like the number of trees (for Random Forest, 100 trees) and tree depth (for Decision Trees, the default depth is 5 trees).

The main goals of the research were to improve the accuracy of identifying hazardous chemical practices and conditions in university laboratories while guaranteeing accurate, dependable, and balanced detection using evaluation metrics like accuracy, precision, recall, and F1-score. Accuracy assesses the model's overall capacity to accurately classify hazardous and non-hazardous situations, whereas precision assesses the system's reliability in reducing false positives, or the incorrect detection of non-hazardous conditions as hazardous. Recall evaluates the model's capacity to identify true hazardous events while avoiding false negatives in which actual hazardous incidents are missed. Finally, the F1-score, calculated as the harmonic mean of precision and recall, offers a thorough assessment of the model's efficiency by balancing false positives and false negatives. Accuracy in the context of managing hazardous chemicals in university laboratories refers to a detection model's capacity to identify both safe operations and hazardous situations. It is a metric of the model performance overall in terms of accurately recognizing non-hazardous circumstances and forecasting real hazardous scenarios. Figure 3 and Table 1 display the accuracy performance. The methods are Random Forest (RF), Decision Tree (DT), and RF-based DT (Proposed), which achieve an accuracy of 85%, 88%, and 92.3%. Consequently, the RF-based DT is more accurate than the other methods used for Hazardous chemical handling at university laboratories. These metrics were selected to strike a balance between detection accuracy (precision) and hazard detection (recall). In lab security, the trade-off between precision and recall is crucial: high precision decreases false alarms, while high recall results in fewer missed hazards. The F1 score offers a balanced evaluation, rendering the model suitable for practical uses in which false positives and missed risks should be reduced.

Table 2: Values for precision, accuracy, recall, and F1 score

Method	Accuracy (%)	Precision (%)	Recall (%)	F1 score (%)
Random Forest (RF)	85	88	84.2	82
Decision Tree (DT)	88	83.4	86.7	86
RF based DT (Proposed)	92.3	93.1	91.4	93.5

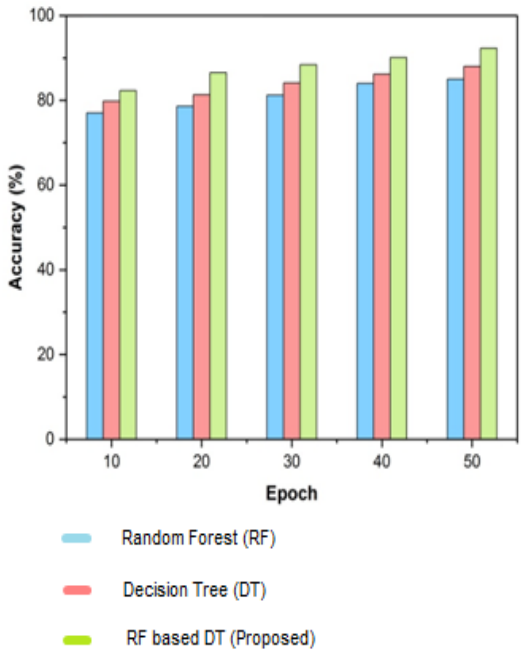

Figure 3: Accuracy Comparison of Random Forest, Decision Tree, and Proposed RF-based DT Models Across Epochs

Precision in university hazardous chemical management refers to the system's reliability in accurately recognizing hazardous chemical-related situations. In particular, it calculates the percentage of actual positive danger detections among all the systems detections.

The precision performance is shown in Figure 4 and Table 1. The approaches, which provide values of 93.1%, 88%, and 83.4%, are RF-based DT, Random Forest, and DT. As a result, while handling hazardous chemicals in university

laboratories, the RF-based DT is more precise than the other techniques.

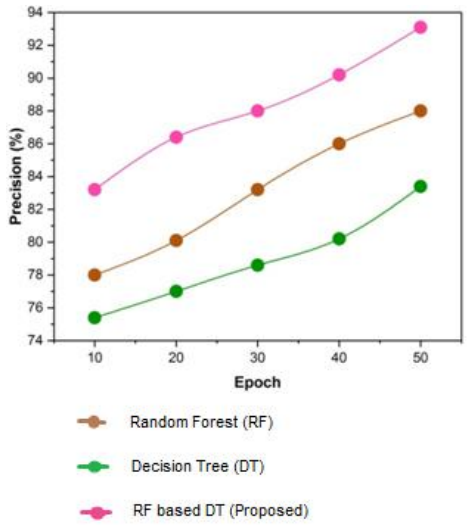

Figure 4: Precision comparison of random forest, decision tree, and proposed RF-based DT models across epochs

When discussing university laboratory hazardous chemicals management, recall refers to the statistic used to assess a detection model that identifies real hazardous situations. It can be defined as the proportion of properly classified hazardous occurrences on all actual hazardous incidents.

Recall performance is displayed in Table 1 and Figure 5. The methods RF-based DT, Random Forest, and DT offer values of 91.4%, 84.2%, and 86.7%. Therefore, the RF-based DT is more reliable than the other methods for handling hazardous substances in university laboratories.

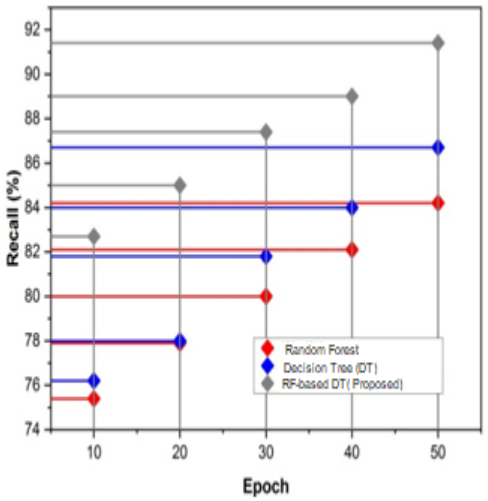

Figure 5: Recall Comparison of Random Forest, Decision Tree, and Proposed RF-based DT Models Across Epochs

An important indicator for assessing hazard detection models' performance in university laboratory chemical control is the F1 score. It is the precision and recall harmonic mean that balances false positives and false negatives.

The F1 score results are shown in Table 1 and Figure 6. Values of 93.5 %, 82%, and 86% are attained using RF-based DT, Random Forest, and DT techniques. Therefore, compared to other techniques used for managing hazardous chemicals in university laboratories, the RF-based DT is better.

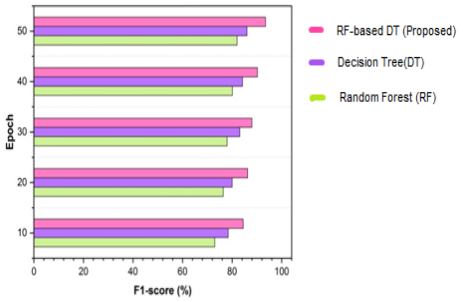

Figure 6: F1-score comparison of random forest, decision tree, and proposed RF-based DT models across epochs

The findings show that the proposed RF-based Decision Tree algorithm outperforms standalone Decision Trees and Random Forests for handling hazardous chemicals in university labs. Its excellent efficiency across all evaluation metrics demonstrates its resilience and practicality for real-world applications in hazardous chemical security. The RF-based DT achieves high values for accuracy, precision, recall, and F1-score, ensuring dependable detection of potential risks while decreasing the possibility of misclassification.

4.1 Discussion

The RF-based DT algorithm outperforms Random Forest (85%) and Decision Trees (88%) in terms of accuracy (92.3%) because it combines the advantages of ensemble learning and decision tree logic to capture intricate trends in hazardous chemical data, improving prediction precision. The utilization of Principal Component Analysis (PCA) for feature extraction substantially improves model resilience by decreasing dimensionality, reducing noise, and maintaining essential features, resulting in increased model stability and recall. However, this method has trade-offs, especially in terms of computational cost and scalability, as the combination of Random Forest and Decision Trees needs a significant amount of processing power, which may limit its application to larger datasets or real-time hazard detection systems. Despite these difficulties, the RF-based DT's better efficiency in accuracy, recall, and F1 score, combined with PCA's capacity to filter out irrelevant data,

make it a strong candidate for hazardous chemical handling, with optimization methods potentially tackling scalability issues.

This work expands on incremental efficiency gains by proposing an extensive framework for hazardous chemical management that integrates Random Forest (RF) and Decision Tree (DT) models with novel optimization methods and domain-specific tailoring. Unlike previous RF and DT executions, this method incorporates sensitivity analysis, hyperparameter tuning, and real-world data preprocessing tactics to tackle practical issues like imbalanced datasets, missing data, and domain-specific hazards. Additionally, the model's application in laboratory security provides a novel contextualization, with 92.3% accuracy resulting in actionable results like decreasing potential accidents and enhancing risk mitigation protocols. By aligning the methodology with real-world security enhancements, this study represents a significant advance in the area, bridging the gap between theoretical enhancements and practical executions.

Attaining 92.3% accuracy in hazardous chemical management is important because it shows that the model can forecast and classify potential risks related to laboratory operations. This level of efficiency leads to tangible enhancements in real-world laboratory safety by allowing for proactive measures like detecting high-risk chemicals, improving storage protocols, and enhancing staff training to prevent accidents. These improvements not only decrease the likelihood of incidents but also improve compliance with security requirements, resulting in a safer lab setting. However, the experimental setup has some constraints, especially the dataset size of 1133 reports, which, while adequate for initial validation, may limit generalizability to a variety of laboratory environments. Future research with larger, more diverse datasets is required to confirm the model's resilience and usefulness to various chemical processes and institutional settings.

The RF-based DT algorithm’s efficiency could be improved further by performing a sensitivity analysis to assess the influence of key hyperparameters like the number of trees in the forest, maximum tree depth, and minimal samples per split. This analysis would aid in determining optimal settings for increasing model precision and effectiveness in hazardous chemical management. Furthermore, the approach's resilience under adversarial conditions, like missing or mislabeled data, could be evaluated by performing controlled perturbations on the dataset and observing the model's effectiveness. Working with sensitive data, like laboratory accident reports, necessitates the highest ethical standards. This study protects data privacy by anonymizing datasets and adhering to pertinent data protection standards, encouraging the ethical and responsible utilization of machine learning in laboratory security management. These additional steps would offer greater insight into the model's dependability and social effect.

5 Conclusion

In this work, we used accident reports from before to examine DT algorithms to discover potential dangers in laboratory operations. The collection is made from near misses and accident reports from several instructional laboratory operations. In this study, we used accident reports from earlier to look at how nicely DT algorithms identify capability hazards in lab work. The collection was made up of near-miss and accident reports from a variety of academic laboratory operations. The nature of laboratory activities and associated hazards are included in each report. We used a RF-based DT technique in our suggested model, DT method uses these vectors to recursively split the data based on their features to estimate hazard probabilities and anticipate the dangers related to university laboratory work. When compared to the existing method, the proposed method achieves accuracy (92.3%), precision (93.1%), F1 score (93.5%), and recall (91.4%), respectively. Although the Decision Tree Algorithm simplifies the handling of hazardous chemical compounds in college laboratories, other developments in the vicinity want to consist of predictive analytics and non-stop surveillance for proactive risk discount and efficient use of sources.

References

[1] Ostad-Ali-Askari, K., 2022. Management of risks substances and sustainable development. *Applied Water Science*, 12(4), p.65. https://doi.org/10.1007/s13201-021-01562-7

[2] Gopalaswami, N. and Han, Z., 2020. Analysis of laboratory incident database. *Journal of Loss Prevention in the Process Industries*, 64, p.104027. https://doi.org/10.1016/j.jlp.2019.104027

[3] Wahab, N.A.A., Aqila, N.A., Isa, N., Husin, N.I., Zin, A.M., Mokhtar, M. and Mukhtar, N.M.A., 2021. A systematic review on hazard identification, risk assessment, and risk control in an academic laboratory. *Journal of Advanced Research in Applied Sciences and Engineering Technology*, 24(1), pp.47-62. 10.37934/araset.24.1.4762

[4] Nasrallah, I.M., El Kak, A.K., Ismaiil, L.A., Nasr, R.R. and Bawab, W.T., 2022. Prevalence of accident occurrence among scientific laboratory workers of the public university in Lebanon and the impact of safety measures. *Safety and health at work*, 13(2), pp.155-162. https://doi.org/10.1016/j.shaw.2022.02.001

[5] Harada, T., Hayashi, R. and Tomita, K., 2023. Prediction of hazards in laboratory work using deep learning models learned from past laboratory accidents. *Journal of Environment and Safety*, p.E23RP0601. https://doi.org/10.11162/daikankyo.E23RP0601

[6] Bai, M., Liu, Y., Qi, M., Roy, N., Shu, C.M., Khan, F. and Zhao, D., 2022. Current status, challenges, and future directions of university laboratory safety in China. *Journal of Loss Prevention in the Process Industries*, 74, p.104671. https://doi.org/10.1016/j.jlp.2021.104671

[7] Li, X., Zhang, L., Zhang, R., Yang, M. and Li, H., 2021. A semi-quantitative methodology for risk assessment of university chemical laboratory. *Journal of Loss Prevention in the Process Industries*, 72, p.104553. https://doi.org/10.1016/j.jlp.2021.104553

[8] Galasso, A., Luo, H. and Zhu, B., 2023. Laboratory safety and research productivity. *Research Policy*, 52(8), p.104827. https://doi.org/10.3386/w31313

[9] Ezenwa, S., Talpade, A.D., Ghanekar, P., Joshi, R., Devaraj, J., Ribeiro, F.H. and Mentzer, R., 2022. Toward improved safety culture in academic and industrial chemical laboratories: an assessment and recommendation of best practices. *ACS Chemical Health & Safety*, 29(2), pp.202-213. https://doi.org/10.1021/acs.chas.1c00064

[10] Schröder, I., Czornyj, E., Blayney, M.B., Wayne, N.L. and Merlic, C.A., 2020. Proceedings of the 2018 laboratory safety workshop: hazard and risk management in the laboratory. *ACS Chemical Health & Safety*, 27(2), pp.96-104. https://doi.org/10.1021/acs.chas.0c00012

[11] Liu, S., Ju, S., Meng, Y., Liu, Q. and Zhao, D., 2023. Inherent Hazards Assessment and Classification Method for University Chemical Laboratories in China. *ACS Chemical Health & Safety*, 30(4), pp.156-164. https://doi.org/10.1021/acs.chas.3c00022

[12] Nam, S.H., Ku, T.G., Park, Y.L., Kwon, J.H., Huh, D.S. and Kim, Y.D., 2022. Experimental study on the detection of hazardous chemicals using alternative sensors in the water environment. *Toxics*, 10(5), p.200. https://doi.org/10.3390/toxics10050200

[13] Chandra, T., Zebrowski, J.P., McClain, R. and Lenertz, L.Y., 2020. Generating standard operating procedures for the manipulation of hazardous chemicals in academic laboratories. *ACS Chemical Health & Safety*, 28(1), pp.19-24. https://doi.org/10.1021/acs.chas.0c00092

[14] Gul, M., Yucesan, M. and Karacahan, M.K., 2023. A Multi-parameter Occupational Safety Risk Assessment Model for Chemicals in the University Laboratories by an MCDM Sorting Method. In *Advances in Reliability, Failure and Risk Analysis* (pp. 131-149). *Singapore: Springer Nature Singapore*. https://doi.org/10.1007/978-981-19-9909-3_6

[15] Li, Z., Wang, X., Gong, S., Sun, N. and Tong, R., 2022. Risk assessment of unsafe behavior in university laboratories using the HFACS-UL and a fuzzy Bayesian network. *Journal of safety research*, 82, pp.13-27. https://doi.org/10.1016/j.jsr.2022.04.002

[16] Mastrantonio, R., Scatigna, M., D'Abramo, M., Martinez, V., Paoletti, A. and Fabiani, L., 2020. Experimental application of semi-quantitative methods for the assessment of occupational exposure to hazardous chemicals in research laboratories. *Risk Management and Healthcare Policy*, pp.1929-1937. https://doi.org/10.2147/rmhp.s248469

[17] Yang, D., Zheng, Y., Peng, K., Pan, L., Zheng, J., Xie, B. and Wang, B., 2022. Characteristics and statistical analysis of large and above hazardous chemical accidents in China from 2000 to 2020. *International journal of environmental research and public health*, 19(23), p.15603. https://doi.org/10.3390/ijerph192315603

[18] Fukuoka, K. and Furusho, M., 2022. A new approach for explosion accident prevention in chemical research laboratories at universities. *Scientific reports*, 12(1), p.3185. https://doi.org/10.1038/s41598-022-07099-2

[19] Yang, J., Xuan, S., Hu, Y., Liu, X., Bian, M., Chen, L., Lv, S., Wang, P., Li, R., Zhang, J. and Shu, C.M., 2022. The framework of safety management in a university laboratory. *Journal of Loss Prevention in the Process Industries*, 80, p.104871. https://doi.org/10.1016/j.jlp.2022.104871

[20] Chen, M., Wu, Y., Wang, K., Guo, H. and Ke, W., 2020. An explosion accident analysis of the laboratory in the university. *Process Safety Progress*, 39(4), p.e12150. https://doi.org/10.1002/prs.12150

[21] McLeod, R.W., 2022. Approaches to Understanding Human Behavior When Investigating Incidents in Academic Chemical Laboratories. *ACS Chemical Health & Safety*, 29(3), pp.263-279. https://doi.org/10.1021/acs.chas.2c00020

[22] Nasrallah, I.M., El Kak, A.K., Ismaiil, L.A., Nasr, R.R. and Bawab, W.T., 2022. Prevalence of accident occurrence among scientific laboratory workers of the

public university in Lebanon and the impact of safety measures. *Safety and health at work*, 13(2),pp.155-62. https://doi.org/10.1016/j.shaw.2022.02.001

Development of an AI-Driven Model for Drug Sales Prediction Using Enhanced Golden Eagle Optimization and XGBoost Algorithm

Ying Xiong
Business School of Dongguan City University, Dongguan, Guangdong, 523000, China
E-mail: xiongying202304@163.com
*Corresponding author

Keywords: drug sales, enhanced golden eagle optimized extreme gradient boosting (EGEO-Xgboost) resource management

Received: November 4, 2024

The pharmaceutical industry plays a crucial role in public health by providing essential medications to address various medical conditions. Predicting drug sales accurately is paramount for pharmaceutical companies to efficiently manage their resources, plan production, and optimize marketing strategies. To address this an AI-based model for predicting medication product sales based on the Enhanced Golden Eagle Optimized and Extreme Gradient Boosting (EGEO-XGBoost) framework. The technique begins with data collecting from the Kaggle website, followed by pre-processing with Min-max normalization to remove noise and assure consistency. The preprocessed data is then used to extract relevant features via Linear Discriminant Analysis (LDA). The enhanced EGEO method fine-tunes the parameters of the XGBoost model, improving its predictive ability. The comparative findings demonstrate that the proposed method significantly improves accuracy (0.90), specificity (0.86), sensitivity (0.92), MCC (0.82), F1-score (0.94), and RMSE (4.02). Incorporating such predictive models into the decision-making processes of pharmaceutical corporations can result in improved resource management, better marketing plans, and increased operational effectiveness.

Povzetek: Predlagan je model za napovedovanje prodaje zdravil na osnovi izboljšanega algoritma Extreme Gradient Boosting, optimiziranega z metodo Enhanced Golden Eagle Optimization (EGEO-XGBoost).

1 Introduction

The pharmaceutical industry was critical to enhancing the world's health through the development and provision of life-saving drugs. Strategic planning by pharmaceutical companies is highly reliant on their ability to forecast the sales of drugs. They can use it to effectively manage resources, optimize production, and make decisions on marketing and sales plans with knowledge [1]. Traditional sales forecasting methods often yield suboptimal outcomes because they fail to capture the dynamic and complex nature of the pharmaceutical industry.

Some of the challenges with traditional methods include the incapability to efficiently process large and diversified datasets and, the failure to take into account extraneous factors like changes in regulatory laws, public health incidents, and macroeconomic conditions. All these shortcomings cause issues such as overstocking or understocking pharmaceuticals, missing business opportunities, and failing to respond on time to market changes in demand [2, 3].

The pharmaceutical sector has undergone huge changes over time due to multiple reasons, among which are increases in medical expertise, changing regulatory environments, shifting consumer habits, and varying healthcare policies. These dynamic ingredients create uncertainties and challenges that even traditional forecasting models are unable to address properly. Hence, pharmaceutical companies are often faced with issues such as overstock or understocking of pharmaceuticals, missing business opportunities, and not responding to the changing trend of demand [4].

To bridge these gaps, the interest in AI and ML in predictive models has generated much momentum. AI-based models allow efficient computations of large datasets of historical sales records, demographic information, prescription trends, and competitor analysis, altogether integrated with external factors for comprehensive forecasting. Such models differ from traditional techniques in their ability to pick up on some minute patterns and adapt according to market dynamics in real-time [5].

These AI-driven drug sales forecasting models come with multiple benefits. These include optimized production planning, reduced waste, and improved management of inventory. In addition, by aligning marketing strategies with promising markets and client segments, return on investment can be maximized while also supporting better

resource allocation [6, 7]. Besides, the incorporation of external variables such as trends in public health and regulatory changes makes the prediction more accurate and holistic. However, challenges to implementing AI-based models abound, such as high-quality and updated data requirements, concerns regarding data privacy, regulatory compliance, and the interpretability of complex models [8]. Nonetheless, ongoing improvements in AI and ML techniques are poised to deliver transformational solutions in the sales forecasting space of the pharmaceutical sector.

By using AI-based predictive analytics, pharmaceutical companies will be able to achieve accurate, flexible, and data-driven forecasts. This will help ensure more efficient strategic planning and greater operational resilience in the long term. This may help to solve the dynamic nature of the industry while creating a more robust health ecosystem [9,10].

Aim of the research: An AI-based model to effectively predict drug sales by using Enhanced Golden Eagle Optimized and Extreme Gradient Boosting on the sales to ensure effective drug production. Improved resource management through data-driven techniques improves production planning and better strategies for marketing products.

1.1 Motivation of the research

The pharmaceutical industry is highly sensitive to the predictive inaccuracy of drug sales, an exercise that is important for maximal production, efficient distribution, and appropriate marketing strategy optimization. Traditional methods are inadequate in comparing the real complexity and dynamic nature of the market, and, consequently, resource allocations are suboptimal. Motivation is built on the interest in exploring how AI-based models can improve the forecasting of drug sales. The ability of large and diverse datasets, such as historical sales, market trends, and consumer demographics, to aid in the hidden patterns and adaptive change in conditions for AI systems helps pharmaceutical companies make more accurate, data-driven predictions and improve the management of their resources and accurately target specific customer segments, improving sales performance and access to lifesaving medications for patients.

1.2 Contribution

The following key points are described AI AI-based predicting drug sales contribution.

- **Data pre-processing with Min-Max normalization:** Aims to ensure balanced learning by normalizing heterogeneous pharmaceutical data into a similar range. It makes the model converge faster and prevents overfitting, resulting in more accurate and reliable predictions of drug sales.

- **Feature Selection via Linear Discriminant Analysis (LDA):** LDA particularly identifies and selects those features that have the most influence in preprocessed drug sales data. Focusing on these key features, LDA helps improve the accuracy of sales predictions, making sure that the model focuses on the most predictive factors for drug sales forecasting.

- **Combining XGBoost with Enhanced Golden Eagle Optimization (EGEO):** The model combines XGBoost, a powerful machine learning algorithm with the EGEO technique. This optimization approach fine-tunes the model's parameters to achieve higher accuracy in drug sales within the pharmaceutical business.

- **Performance evaluation:** It includes a thorough performance evaluation of the AI-based model by analyzing key metrics. These metrics establish the model's ability to provide accurate predictions on drug sales, which further enhances its practical use in the pharmaceutical industry for strategic decision-making purposes.

2 Related works

Table 1 shows demonstrates that the summary of previous studies.

Table 1: Summary of related works

Reference	Objective	Methods	Datasets	Key Findings
Bhattamisra et al., [11]	To explore AI applications in pharmaceutical and healthcare research.	Literature review, case studies on AI applications in healthcare.	PubMed, clinical trial data, AI healthcare applications.	AI plays a crucial role in enhancing drug discovery, personalized healthcare, and system optimization in the pharmaceutical industry.

Vora et al., [12]	To examine the role of AI in pharmaceutical technology and drug delivery design.	Review of AI-based drug delivery technologies and systems.	Pharmaceutical databases, drug delivery system data.	AI contributes to improving precision in drug formulation and the design of personalized drug delivery systems.
Shilong, [13]	To develop a machine learning model for sales forecasting using XGBoost.	XGBoost model for forecasting drug sales.	Drug sales data (historical sales data).	XGBoost effectively forecasts sales, showcasing high predictive accuracy for sales trends in the pharmaceutical sector.
Lin et al., [14]	To predict drug-drug interactions using multi-source data and transformer self-attention mechanism.	Multi-source data fusion, transformer self-attention mechanism.	Drug interaction databases.	The model successfully predicts drug-drug interactions with high accuracy, using advanced machine-learning techniques.
Tichy et al., [15]	To analyze trends in prescription drug expenditures.	Statistical analysis of prescription drug market data.	U.S. prescription drug expenditure data	Identifies trends in prescription drug costs, providing projections for future expenditures in healthcare systems.
Agrawal et al., [16]	To review AI applications in drug delivery systems and technology.	Case studies and literature review on AI-driven drug delivery.	Pharmaceutical and drug delivery system data.	AI enhances the precision of drug targeting, reduces side effects, and advances personalized medicine in drug delivery systems.
Biehn et al., [17]	To develop AI-based ADMET models for drug discovery.	ADMET modeling using AI-based platforms like SAFIRE.	SAFIRE platform, ADMET drug data.	Improves the accuracy of ADMET predictions, supporting faster and more efficient drug discovery processes.
Saikia et al., [18]	To review AI's role in therapeutic drug monitoring and clinical toxicity.	Literature review on AI in therapeutic monitoring.	Clinical therapeutic drug monitoring datasets, toxicology data.	AI plays an essential role in monitoring therapeutic drug levels, minimizing clinical toxicity, and optimizing drug safety.
Ali & Alrobaian, [19]	To evaluate the current and	Literature review and analysis of AI	Industry reports, and pharmaceutical	AI offers promising advancements in

	prospects of AI in pharmaceutical development.	technologies in pharmaceutical development.	development databases.	pharmaceutical product development, though challenges remain regarding large-scale implementation and real-world applications.
Łapińska et al., [20]	To introduce an AI-based application (SerotoninAI) for drug discovery.	AI-driven drug discovery platform focusing on serotoninergic systems.	Serotonergic drug data	AI-based SerotoninAI system enhances drug discovery, particularly for serotonergic systems, improving discovery times and accuracy.
Serrano et al., [21]	To assess AI applications in drug discovery and personalized medicine.	Review of AI applications in drug discovery and personalized drug delivery.	Pharmaceutical and clinical data, drug discovery databases.	AI is revolutionizing drug discovery, particularly in personalized medicine, by enabling more accurate and efficient drug delivery methods.
Jena et al., [22]	To explore AI-driven drug delivery systems in the pharmaceutical industry.	Literature review on AI's impact on drug delivery systems.	Industry and pharmaceutical data.	AI enhances the efficiency of drug delivery systems, particularly in designing customized delivery for patient-specific needs.
Visan & Negut, [23]	To explore AI integration in drug discovery and delivery systems.	Literature review on AI tools in drug discovery and delivery.	Pharmaceutical and drug discovery databases.	AI is transforming drug discovery and delivery, though its implementation still faces challenges in validation across diverse real-world applications.
Rathipriya et al., [24]	To validate various shallow and deep neural network methods for demand forecasting in the pharmaceutical industry.	Shallow and deep neural networks, RMSE for predictive accuracy evaluation.	Sales and demand data of eight pharmaceutical product groups.	Shallow neural network-based DFMs achieved a lower mean RMSE (6.27), proving more effective in estimating future demand than deep neural networks.
Jaganathan et al., [25]	To develop quantitative	Machine learning algorithms, feature	A dataset of 1,253 drug compounds	The SVM-based classifier achieved

	structure-activity relationship models for predicting drug-induced liver toxicity using machine learning.	selection techniques, support vector machines, 10-fold cross-validation.	with molecular descriptors.	an accuracy of 0.811, sensitivity of 0.840, specificity of 0.783, and MCC of 0.623, outperforming prior models in both internal and external validation.

2.1 Research gap

Existing methods applied in drug sales forecasting and drug discovery are very limited in the sense that their generalizability, scalability, and performance would be compromised to some extent in generalizing different drug classes, datasets, and regions. Our proposed model for predicting sales of pharmaceutical products, based on the Enhanced Golden Eagle Optimization and Extreme Gradient Boosting (EGEO-XGBoost) framework, fills these gaps by combining optimized techniques with a state-of-the-art predictive model for improved accuracy and scalability and improved generalization through adaptation across heterogeneous datasets and changing conditions, in turn providing even more reliable, actionable sales forecast in the pharma industry.

3 Methodology

A proposed methodology that employs an AI-based model for the forecasting of sales on pharmaceutical products uses a combination of an enhanced golden eagle optimized Extreme gradient boosting (EGEO-XGBoost). First, the data from Kaggle are preprocessed using Min-max normalization to eliminate noises and ensure consistency in data. A linear discriminate analysis technique is used to extract the features of the preprocessed data. This integrated approach will help enhance the accuracy of drug sales forecasting which can be used for better resource management and decision-making in the industry. Figure 1 illustrates the overview of the research framework.

3.1 Data gathering

The dataset gathered from kaggle [https://www.kaggle.com/code/milanzdravkovic/pharma-sales-data-analysis-and-forecasting/data], includes the drug sales collected across different stores over time. The main attributes included in the data set are the store ID, product ID, quantity of sales, and the date of transactions. Such time-series data is beneficial in the overall understanding of the performance of sales as well as analysis regarding trends, seasonality, and patterns. Data structured to accommodate sales forecasting, inventory planning, and business decisions related to pharmaceutical businesses. The collection method is primarily based on real-world sales activities so that the dataset obtained is relevant for predictive analytics and machine learning model development.

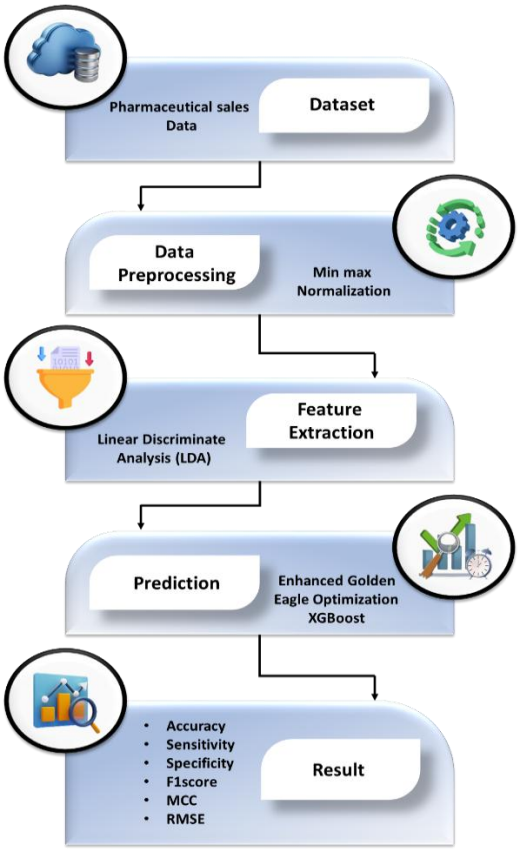

Figure 1: Overview of research to predict pharmaceutical product

3.2 Min-max normalization

A data preparation technique called min-max normalization, often referred to as feature scaling or min-max scaling, is used to change numerical data into a certain range, typically [0, 1]. With this normalization technique, all the numerical features in a dataset are put on an equal footing, making them comparable and preventing features with higher values from overpowering the analysis or

adversely affecting machine learning algorithms. Using this technique, you can scale numerical data to a specific range. Data normalization or feature scaling are other names for it. Normalization aims to climb all of them evenly to make it easier to compare or understand a dataset's characteristics or variables. The following is the min-max normalization formula (1):

$$X_{new} = \frac{X - \min(X)}{\max(X) - \min(X)} \quad (1)$$

Where $X_{new}$the result of normalizing is to produce a new value, X is the value of the former, $\max(X)$ is the highest value in the dataset, and $\min(X)$ is the smallest value in the dataset.

Before dividing by the range, which consists of the maximum and minimum values of the content, each data point must first be subtracted from the feature's minimum value. The importance of the dataset can be scaled between 0 and 1 following min-max normalization. Suppose the beginning values fall within a different ideal range (for instance, between -1 and 1). In that case, we may change the formula to reflect this by expressing the intended minimum and maximum values throughout the normalization process.

Even though min-max normalization was a straightforward and popular method, some datasets might have better solutions. Various scaling procedures, such as Z-score normalization or resilient scaling, may be more appropriate depending on the information's characteristics and the particular specifications of the machine learning method being applied.

3.3 Feature extraction

When forecasting Drug sales, the process of picking and developing pertinent features (variables) from the raw data that are likely to have a large impact on successfully predicting drug sales is referred to as feature extraction. By condensing the original data into a smaller representation while preserving the most crucial details, feature extraction aims to improve the accuracy of predictive models.

3.3.1 Linear discriminates analysis (LDA)

Linear discriminate analysis (LDA), a dimensionality-reduction and classification method, is used in statistics and machine learning. When the classes were distinct and evenly dispersed, it was extremely beneficial for addressing classification problems. The goal of LDA was to find a linear combination of characteristics that maximizes class separation while minimizing variation within each category. LDA's major objective was to maintain any information discriminating based on a person's class while projecting the original data into a lower-dimensional space. This was achieved by increasing the ratio of the within-class scatter matrix to the between-class scatter matrix.

The linear discriminate analysis (LDA) will be explained step-by-step using the following equations:

3.3.1.1 Making the mean vector calculations:

Assume there are m_u data points in each u class, which all exist. The mean vector for class u was calculated as the (equation 2) average of all feature vectors in class u, designated as m_{u}.

$$m_u = \frac{1}{n_u} \sum_{X \in classu} X \quad (2)$$

3.3.1.2 Calculate the scatter matrix for the class (k_r):

The within-class scatter matrix k_r calculates the expansion or distribution of the data for each type. The scattered values from each class were added together to get the final result. The class's data points' covariance matrices are used as the scatter matrix for that class. The formula 3 for "k_r" is

$$k_r = \sum_{u=1}^{u} \sum_{X \in classu} (m_{u-m})(m_{u-m})^T \quad (3)$$

3.3.1.3 Calculate the scatter matrix k_b between classes:

The spread or distribution of the class mean values was ascertained using the between-class scatter matrixk_b. The weighted sum of the outer products was used to determine the difference between the class means, and the overall mean across all data points."k_b" equation 4 is as follows:

$$k_b = \sum_{u=1}^{u} n_u (m_{u-m})(m_{u-m})^T \quad (4)$$

Where

By dividing the average of all mc vectors by the sum of the data points in each class, the total mean vector of all the data points in the dataset was calculated using equation 5.

$$\mathrm{m} = \frac{1}{N} \sum_{u=1}^{u} n_u m_u \quad (5)$$

3.3.1.4 Find the eigenvalues and eigenvectors for (k_r^{-1} , k_b):

The inverse of (k_b), written as ($k_r^{-1,} k_b$), is the product ($k_r^{-1,} k_b$), which we now compute. The product ($k_r^{-1,} k_b$)'s eigenvalues and associated eigenvectors v were then identified.

3.3.1.5 Find the highest (k) eigenvectors:

The eigenvalues are arranged in ascending order, and the top k eigenvectors are chosen to match the top k greatest eigenvalues. The transformation matrix R will comprise these "k" eigenvectors and project the data onto a lower-dimensional space.

3.3.1.6 Introduce the data into the new subspace:

The original data Y should be multiplied by the conversion matrix R produced in the previous phase to produce a new feature space with a lower dimensionality (equation 6).

$$[Y_{new}] = Y \cdot R \quad (6)$$

An S-dimensional vector, where S is the number of selected eigenvectors (dimensionality reduction), will represent each data point in the transformed subspace. A linear discriminate analysis is helpful for classification and dimensionality reduction problems because it identifies a linear combination of characteristics that maximizes the separation between classes while decreasing the variation within each category.

3.4 prediction of drug sales using enhanced Golden Eagle Optimized Extreme Gradient Boosting (EGEO-Xgboost)

A hybrid AI-based model is developed for medication product sales forecasting using the Enhanced Golden Eagle Optimized and Extreme Gradient Boosting (EGEO-XGBoost) framework. The Enhanced Golden Eagle Optimization (EGO) algorithm provides a global search ability with the strength of predictive accuracy in the Extreme Gradient Boosting (XGBoost) model. This enables model parameter optimization with better precision and efficiency for predicting sales. This helps the model integrate techniques to give pharmaceutical companies the insight needed in managing resources, production planning, and marketing strategy optimization.

3.4.1 Extreme Gradient Boosting (XGBoost)

The XGBoost is a tree-based algorithm that generates trees sequentially to minimize errors, and it further enhances the traditional Gradient Boosting Decision Tree by incorporating regularization to prevent overfitting. It's a highly efficient algorithm and is used widely in different applications. Based on this approach, for drug sales prediction, XGBoost iteratively builds a tree to predict future sales figures and optimizes the model such that overfitting is avoided using a regularization term.

Unlike traditional GBDT, the XGBoost objective function includes a regularization term that balances model accuracy and complexity. The objective function is expressed as Equation (7):

$$U = \sum_{j=1}^{n} S(y_j, \left(F(x_j)\right) + \sum_{h=1}^{t} G\,(f_h) + D \quad (7)$$

Where, $S(y_j, \left(F(x_j)\right)$ represents the loss (error between actual and predicted drug sales), $G(f_h)$ is the regularization term, controlling the complexity of the model, and D is a constant that can be ignored during optimization. The $G(f_h)$ regularization term ensures that over-fitting is also avoided and could be defined by equation (8):

$$G(f_h) = \alpha T + \frac{1}{2}\eta \sum_{i=1}^{H} w_i^2 \quad (8)$$

α regulates the penalty for adding leaves to the tree, T is the overall number of trees, and w_i^2 is the weight or predicted sales of each of the leaf nodes. Moreover, the XGBoost optimization uses the second-order Taylor series, in contrast to first-order derivatives with traditional GBDT. Such optimization helps increase the model's capacity to pick up on intricate patterns that are found in data. With MSE used as the loss function, it minimizes error but ensures that no overfitting takes place to obtain accurate predictions. The following is the implementation using the main function equation (9) assuming MSE as a loss function:

$$U = \sum_{j=1}^{n} \left[p_j \omega_{p(y_j)} + \frac{1}{2}(q_j \omega_{q(y_j)}^2)\right] + \alpha T + \frac{1}{2}\eta \sum_{i=1}^{T} \omega_i^2 \quad (9)$$

Where, g_j and T_j represent 1st and 2nd derivatives of loss, which measures the change in the error function concerning the predicted drug sales values. The contribute to the learned parameters of the model for predicting the sales of the drug at each point. $\omega_{p(y_j)}$ and $\omega_{q(y_j)}$ represent the learned parameters of the model for predicting the sales of the drug at each point. The term $q_j \omega_{q(y_j)}^2$ represents the second-order, accounting for curvatures of the loss function, which can promise more stable and accurate predictions for cases involving complicated patterns of drug sales.

The final step calculates the total loss as the summation of losses of all leaf nodes. Since each leaf node is a sale category, the summation of leaf node loss values provides the overall model error. This is described by Equation (10):

$$U = \sum_{i=1}^{H} [p_i \omega_i] + \frac{1}{2}(Q_i + \eta)\omega_i^2 + \alpha T \quad (10)$$

Where $p_i = \sum_{j \in I_i} p_j,\ Q_i = \sum_{j \in I_i} q_j,$ which are contributions from each of the leaf nodes that aggregate in their predicted contribution to drug sales.

An optimum prediction of the model is achieved by minimizing this objective function by XGBoost, thus learning the input feature-target output relationship in drug sales. The process includes regularization techniques, which provide good generalizations on new samples by avoiding overfitting problems, thus proving a reliable form of sales forecast.

3.4.2 Enhanced Golden Eagle Optimization (EGEO)

Enhanced Golden Eagle Optimization (EGEO) is the extension of the traditional Golden Eagle Optimization methods. It uses a spiral trajectory mechanism similar to that the golden eagle uses to trace its prey efficiently and strike it down. Thus, EGEO would be able to conduct a more effective global search in the preliminary phases by

flying across various regions and a focused local search in the latter phase by honing the attack angle. This makes EGEO equipped with a nice memory component to preserve information about the best solutions it finds so that faster convergence and the least chance of getting trapped into local optima are achieved. With these enhancements, EGEO has a greater degree of robustness and efficiency over traditional methods to solve complex global optimization problems. The mathematical formulae used by golden eagles to simulate their movements while seeking prey were described as follows.

3.4.3 The Spiralling flight patterns of golden eagles

Every AI model within the prediction system remembers the best sales prediction that this model has ever experienced so far. The model, chasing a better drug sales prediction, is simultaneously attracted both to the analysis of history and the prediction of trends. Figure 2 is a graphical representation of the prediction and analysis vectors in 2D space. Every model may randomly pick one sales prediction from the other model and update its parameters based on the data already visited. Also, the model can revisit its memory. Such a process might lead to a sequence of numbers: l ∈ {1, 2 …, N_AI}, where N_AI denotes the total number of AI models.

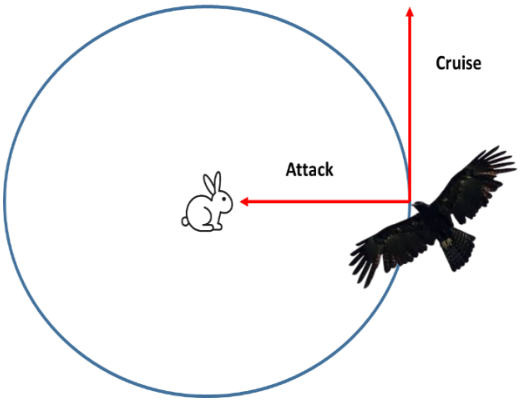

Figure 2: Movement of golden birds in a spiral

3.4.3.1 Selection of Prey

Every AI model should select a target dataset for training and prediction operations in every iteration. The model also chooses its input data from a database of historical drug sales data. Based on this, the selected data computes the prediction and analysis vectors. It checks its memory and updates its memory if the new prediction is better than the earlier one.

3.4.3.2 Attack

A vector that depicts the progress of the prediction from the current state of the model to the best-predicted sales in the model's memory is as follows equation (11):

$$\vec{B}_r = \vec{Y}_I^* - \vec{Y}_r \quad (11)$$

Where $\vec{B}_r$ is the model's prediction vector, $\vec{Y}_I^*$ is the best previous prediction from the model, and $\vec{Y}_r$ is the current state of the model in the sales prediction process.

3.4.3.3 Travel

The prediction vector runs parallel to the analysis vector, tangent to the predicted sales curve. This is also known as the model's speed of adjustment in sales forecasting. By equation (12) the destination point of the analysis vector is,

$$\vec{C}_r = \frac{d - \sum_{ff \neq r} b_f}{b_r} \quad (12)$$

Whereb_r, $b_f \epsilon \vec{B}_r$ are each component of the hyperplane equation in n-dimensional space, and $\vec{B}_r = \{b_1, b_2, \ldots, b_n\}$ represent prediction vector, respectively.

3.4.3.4 Assuming new positions:

The changing direction of its
prediction depends completely on the model's prediction and analysis directions. Consequently, an update step for a model $\boldsymbol{r}$ during an iteration t can be well defined by the following equation:

$$\Delta_{yr} = \vec{j}_1 qb \frac{\vec{B}_r}{\|\vec{B}_r\|} + \vec{j}_2 qc \frac{\vec{C}_r}{\|\vec{C}_r\|} \quad (13)$$

Where the q_b^t and the q_c^t define at iteration t respectively prediction and analysis coefficients controlling which part of its coefficients have an impact on the prediction or analysis; and the vectors $\vec{j}_1$ and $\vec{j}_2$ are random. The following equation (14) is the new prediction of the model:

$$y_r^{t+1} = y_r^t + \Delta_{yr}^t \quad (14)$$

When the prediction made at position r is more precise than the preceding position, that new prediction will be updated to memory.

3.4.3.5 Exploration to Exploitation Transition:

The method of the AI model changes from exploring to exploiting. The prediction coefficient q_b and analysis coefficient q_c are used to switch between them. Using equations (15) and (16) are linear expressions:

$$q_b = q_b^0 + \frac{t}{T}|q_b^t - q_b^0| \quad (15)$$

$$q_c = q_c^0 + \frac{t}{T}|q_c^t - q_c^0| \quad (16)$$

In the above equation, q_b^0 and q_c^0 are the starting values for predicting the tendency of sales of drugs, q_b, and analyzing market trends, qc, respectively. In this scenario, T denotes the maximum number of iterations, q_b^t, and q_c^t would be the final values for the tendencies to predict and analyze

drug sales. The process of the EGEO-XGBoost described in Algorithm 1.

Algorithm:1 The Process of EGEO-XGBoost

Step 1: Load the dataset from Kaggle
Step 2: Perform data preprocessing:
a. Handle missing values
b. Convert date-time attributes
c. Normalize numerical features using Min-Max Normalization:
For each feature X:
X_new = (X - min(X)) / (max(X) - min(X))
Step 3: Perform Feature Extraction using Linear Discriminant Analysis (LDA):
a. Compute mean vector for each class
b. Compute within-class scatter matrix
c. Compute between-class scatter matrix
d. Compute eigenvalues and eigenvectors of (S_W^(-1) * S_B)
e. Select top k eigenvectors and transform the dataset
Step 4: Initialize Enhanced Golden Eagle Optimization (EGEO) algorithm:
a. Initialize population of golden eagles
b. Set attack and cruise coefficients
c. Initialize memory for best solutions
Step 5: Perform iterative optimization:
a. For each golden eagle:
i. Select a target prey from memory
ii. Compute attack vector:
B_r = Y_best - Y_r
iii. Compute cruise vector:
C_r = (d - sum(b_f)) / b_r
iv. Update position:
delta_Yr = j1 * q_b * B_r / ||B_r|| + j2 * q_c * C_r / ||C_r||
Y_r^(t+1) = Y_r^t + delta_Yr
v. Update memory if new position improves fitness
b. Adjust attack and cruise coefficients for exploration-exploitation balance:
q_b = q_b0 + (t/T) * |q_bt - q_b0|
q_c = q_c0 + (t/T) * |q_ct - q_c0|
c. Repeat until stopping criteria are met
Step 6: Train XGBoost model using optimized hyperparameters:
a. Define XGBoost objective function:
U = sum(S(y_j, F(x_j))) + sum(G(f_h)) + D
b. Compute regularization term:
G(f_h) = alpha * T + (1/2) * eta * sum(w_i^2)
c. Use second-order Taylor expansion for loss approximation:
U = sum[p_j * omega(y_j) + 1/2 * (q_j * omega_q(y_j)^2)] + alpha * T + 1/2 * eta * sum(w_i^2)
d. Optimize quadratic function to minimize loss
e. Train XGBoost with optimal parameters found via EGEO
Step 7: Evaluate the trained model:
a. Compute accuracy metrics (RMSE)
b. Perform validation using test dataset
Step 8: Predict drug sales using the trained EGEO-XGBoost model
Step 9: Output final predictions and insights

4 Result

The experiment was performed on a Linux system using an Intel Core 2 Duo processor with 2.16 GHz and 8 GB RAM. The data was retrieved from the Kaggle website and consisted of 600,000 weekly sales records of 57 pharmaceutical products between 2014 and 2019. These included sales date, quantity of drug sold, and the name of the brand. The products were categorized under eight groups using the Anatomical Therapeutic Chemical (ATC) classification, which classifies drugs according to their therapeutic and chemical properties. Figure 3 represents the categories of drugs.

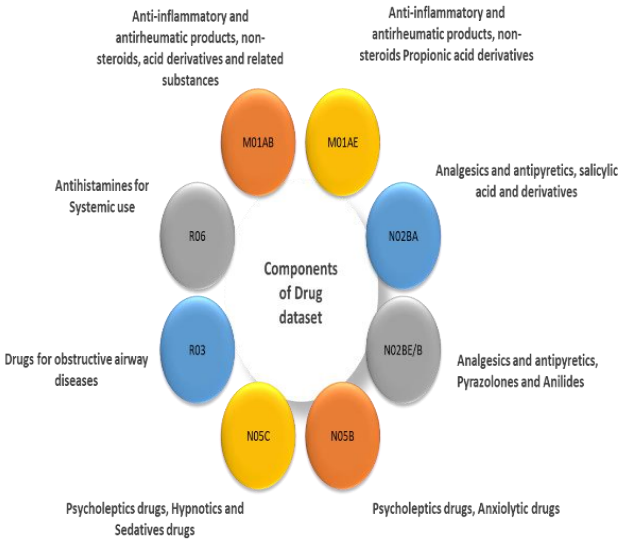

Figure 3: Elements Of the Drug Dataset

The proposed EGEO-XGBoost model was found to perform better than existing models in most cases with remarkable improvements for M01AB (0.12), M01AE (0.48), N02BA (0.15), N02BE (0.008), N05B (0.006), N05C (0.35), R03 (0.025), and R06 (0.608). This shows that EGEO-XGBoost has better predictive accuracy in drug sales forecasting. Figure 4 illustrates the RMSE comparison for the medicine category using EGEO-XGBoost on the sales prediction dataset.

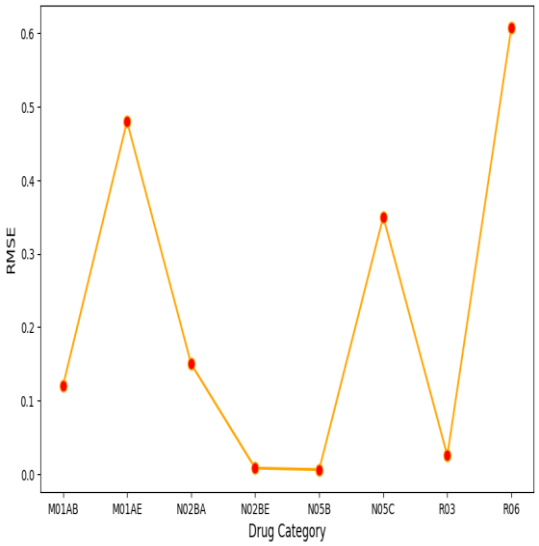

Figure 4: RMSE comparison for drug category using EGEO-XGBoost on sales prediction dataset

For predictive analysis, a few existing models, like RF, MLP, and SVM (Jaganathan et al. [25]), along with Radial Basis Function Neural Network (RBF-NN), Probabilistic NN (P-NN), and Generalized Regression NN (GR-NN) (Rathipriya et al. [24]) were used for analysis. The proposed model, EGEO-XGBoost, was applied using R software to preprocess the data, obtain relevant features from the data, and improves the prediction accuracy.

RMSE: One of the most common metrics used to measure the accuracy of a predictive model. It is defined as the square root of the average of the squared differences between the predicted and observed values. The lower the RMSE, the better the model is performing, as it indicates that the model's predictions are closer to the actual values. Equation (17) was used to calculate the RMSE.

$$RMSE = \sqrt{\frac{1}{2}\sum_{j=1}^{n}(sales_K_j - sales_B_j)^2} \quad (17)$$

Table 2 and Figure 5 compare the RMSE for predictive models of drug sales in different categories using existing models (RBF-NN, P-NN, and GR-NN) compared with the proposed EGEO-XGBoost model.

Table 2: RMSE Of Comparison AI-Based model for drug sales prediction

Models	RMSE
RBF-NN Rathipriya et al. [24]	6.59
P-NN Rathipriya et al. [24]	6.21
GR-NN Rathipriya et al. [24]	6.01
EGEO-XGBoost [Proposed]	4.02

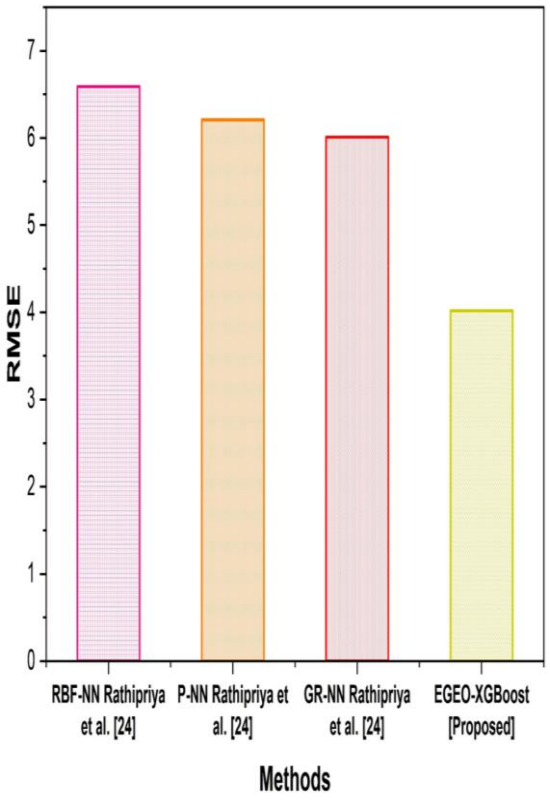

Figure 5: Model performance of RMSE comparison for drug sales prediction

Accuracy: In machine learning, accuracy was a common evaluation metric used to assess a model's performance. Equation (18) was used to calculate accuracy.

$$Accuracy = \frac{TP+TN}{TP+TN+FN+FP} \quad (18)$$

Compared to the existing models, such as SVM with an accuracy of 0.82, MLP at 0.79, and RF at 0.77. The proposed EGEO-XGBoost model attains the highest accuracy of 0.90, outperforming all other models. Table 3 and Figure 6 illustrate the outcomes of the accuracy evaluation. The significant improvement indicates the EGEO-XGBoost framework's superior capacity for predictions for drug sales. Figure 6 despite the result of accuracy.

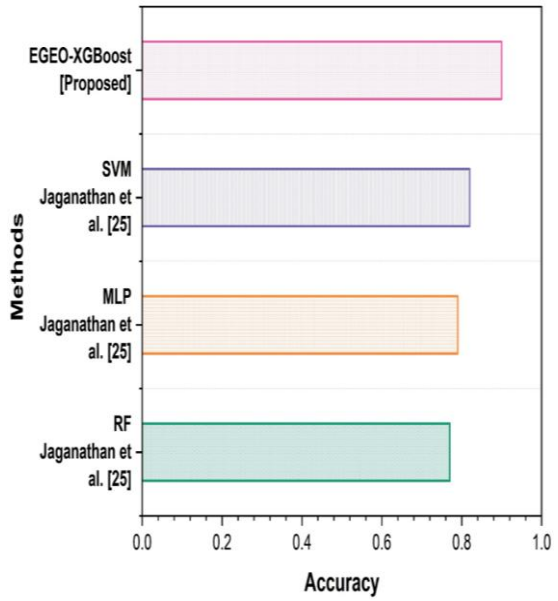

Figure 6: Assessing Overall prediction accuracy in Drug sales forecasting

Sensitivity: Sensitivity measures the model's ability to correctly identify positive instances (accurate predictions of sales growth or success). The calculation of precision is expressed in the following equations (19).

$$\text{Sensitivity} = \frac{TP}{TP+FN} \quad (19)$$

The EGEO-XGBoost model is sensitivity by 0.92 compared to the other existing approaches: SVM is 0.84, MLP is 0.80, and RF is at 0.81. Sensitivity assessment outcomes are displayed in Table 3 and Figure 7. The higher sensitivity of the EGEO-XGBoost model shows it was able to detect more of the true positives to be important for achieving correct predictions in sales forecasting.

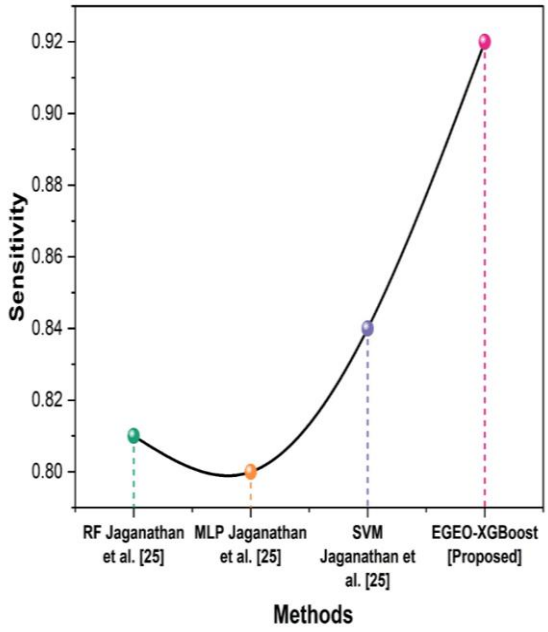

Figure 7: Sensitivity comparison in drug sales prediction

Specificity: Specificity is the measure of how well a model can correctly reject negative instances, meaning that it distinguishes between low sales and other factors that are not relevant. Specificity is calculated using the following equations (20).

$$\text{Specificity} = \frac{TN}{TN+FP} \quad (20)$$

For specificity, the EGEO-XGBoost model also outperformed others with 0.86, which is more than that of SVM, MLP, and RF, having 0.79, 0.78, and 0.69, respectively. The higher specificity of EGEO-XGBoost indicates that this model performs strongly in avoiding false positives, especially in minimizing wrongful sales forecasts of pharmaceutical industries. Figure 8 and Table 3 display the results of the specificity evaluation.

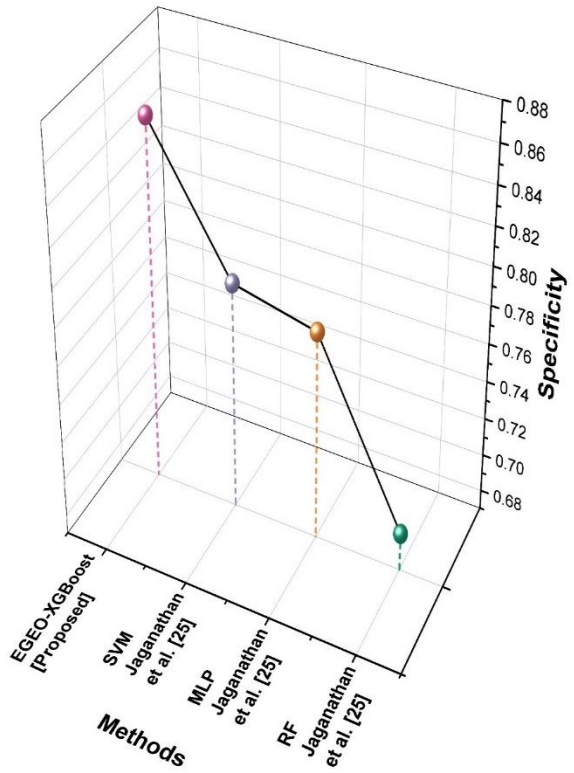

Figure 8: Evaluation specificity in drug sales prediction

Mathew Correlation Coefficient (MCC): MCC is a balanced measure that incorporates all four quadrants of the confusion matrix: True Positives, True Negatives, False Positives, and False Negatives. It ranges between -1 for (total disagreement) up to +1 for (perfect agreement), with a value of 0 indicating no better than random prediction.

$$MCC = \frac{TP \times TN - FP \times FN}{\sqrt{(TP+FP)(TP+FN)(TN+FP)(TN+FN)}} \quad (21)$$

The MCC score of the EGEO-XGBoost model is 0.82, which is significantly higher than that of SVM (0.61),

MLP (0.59), and RF (0.57). This higher MCC indicates that the EGEO-XGBoost model has better overall classification performance, meaning a better balance between true positives and negatives. Table 3 and Figure 9 show the MCC evaluation results.

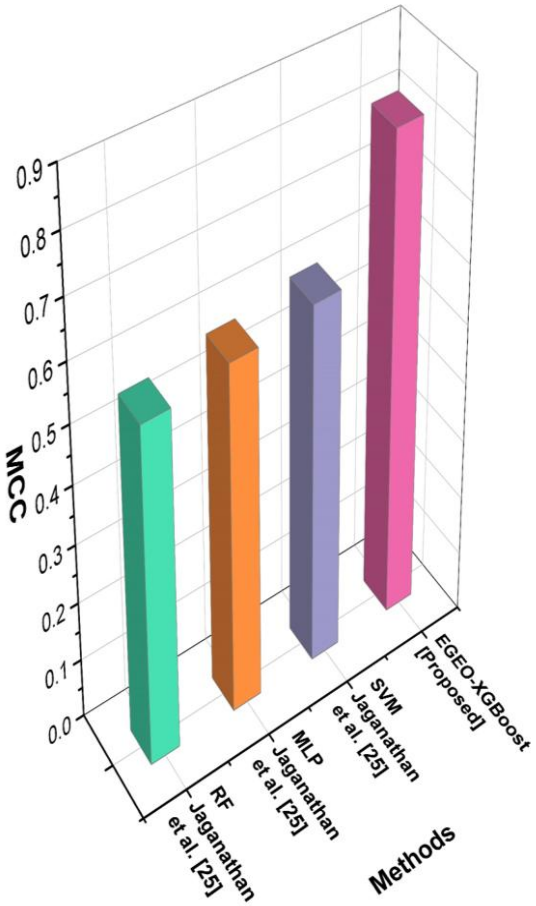

Figure 9: Evaluation of MCC comparison in drug sales forecasting

F1-score: It is the harmonic mean of precision and sensitivity that balances the two. It is useful when both false positives and false negatives matter for a very imbalanced dataset. Equation 18, therefore, was used to calculate the F1 score.

$$F1 - Score = \frac{2TP}{2TP+FP+FN} \quad (22)$$

The EGEO-XGBoost model performs well with an F1-score of 0.94, which is much higher than other existing methods SVM (0.84), MLP (0.80), and RF (0.77). This indicates that a higher F1-score shows the EGEO-XGBoost to achieve an optimal balance between precision and recall in terms of its performance for the balanced prediction of drug sales. Figure 10 and Table 3 demonstrate the evaluation result of the F1score.

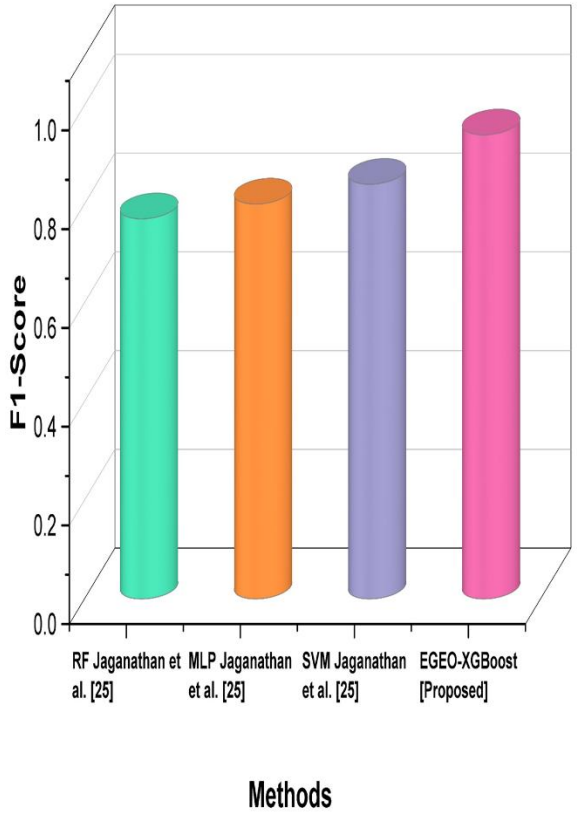

Figure 10: F1-score performance in drug sales prediction

Table 3: Performance comparison of Different models for drug sales prediction

Models	Accuracy	Sensitivity	Specificity	MCC	F1score
RF Jaganathan et al. [25]	0.77	0.81	0.69	0.57	0.77
MLP Jaganathan et al. [25]	0.79	0.80	0.78	0.59	0.80
SVM Jaganathan et al. [25]	0.82	0.84	0.79	0.61	0.84
EGEO-XGBoost [Proposed]	0.90	0.92	0.86	0.82	0.94

5 Discussion

Evaluation shows a significant increase in the accuracy of forecasting over existing models, namely, RBF-NN, P-NN, GR-NN, SVM, MLP, and RF, concerning the development and implementation of the EGEO-XGBoost model for predicting drug sales. The model also achieved (0.90) accuracy, which is more than SVM at 0.82, MLP at 0.79, and RF at 0.77. As for sensitivity, EGEO-XGBoost was at 0.92, more than SVM at 0.84, MLP at 0.80, and RF at 0.81, indicating it is better at correctly predicting positive sales instances. For instance, the score of EGEO-XGBoost was impressive at (0.86), which was higher than SVM (0.79), MLP (0.78), and RF (0.69), meaning it is less likely to give false positives. The MCC score of 0.82 for EGEO-XGBoost also indicates that it has a better balance between true positives and true negatives compared to SVM (0.61). Last, the model attained an F1-score of (0.94), much higher than other models, meaning that it balances precision and recall very well. EGEO-XGBoost outperforms other models in all key evaluation metrics and, therefore, can be regarded as a highly effective tool for drug sales prediction.

6 Conclusion

The EGEO-XGBoost model has highly effective performance regarding the prediction of drug sales, with higher predictive accuracy values compared to any traditional model. Using advanced techniques in the form of Min-max normalization, application of Linear Discriminant Analysis in feature extraction, and the Enhanced Golden Eagle Optimization, the proposed model shows significant enhancement in key metrics such as accuracy (0.90), sensitivity (0.92), specificity (0.86), MCC (0.82), F1-score (0.94) and RMSE (4.02). These findings thus underscore the ability of AI-driven models to enhance drug sales forecasting, leading to better decision-making, resource management, and marketing strategies in the pharmaceutical industry. Incorporation of such models would help in improved operational efficiency and better planning in the pharmaceutical industry.

Limitation and future scope:

Although promising results are produced, the limitations of the model lie in reliance on historical data that may not reflect sudden changes in the market or external influences. Moreover, the EGEO-XGBoost model needs further optimization for large datasets originating from heterogeneous pharmaceutical markets. The future direction can be oriented towards real-time data integration and the development of hybrid models, making it even more adaptable and robust for use in global drug sales forecasting.

References

[1] Jakovljevic, M., Liu, Y., Cerda, A., Simonyan, M., Correia, T., Mariita, R.M., Kumara, A.S., Garcia, L., Krstic, K., Osabohien, R., and Toan, T.K., The Global South political economy of health financing and spending landscape–history and presence, Journal of Medical Economics, vol. 24, sup1, pp. 25-33, 2021. https://doi.org/10.1080/13696998.2021.1915807.

[2] Ren, S., Chan, H.L., and Siqin, T., Demand forecasting in retail operations for fashionable products: methods, practices, and real case study, Annals of Operations Research, vol. 291, pp. 761-777, 2020.
https://doi.org/10.1007/s10479-019-03479-w

[3] Feizabadi, J., Machine learning demand forecasting and supply chain performance, International Journal of Logistics Research and Applications, vol. 25, no. 2, pp. 119-142, 2022.
https://doi.org/10.1080/13675567.2021.1898171

[4] Kumar, S.A., Ananda Kumar, T.D., Beeraka, N.M., Pujar, G.V., Singh, M., Narayana Akshatha, H.S., and Bhagyalalitha, M., Machine learning and deep learning in data-driven decision-making of drug discovery and challenges in high-quality data acquisition in the pharmaceutical industry, Future Medicinal Chemistry, vol. 14, no. 4, pp. 245-270, 2022.
https://doi.org/10.4155/fmc-2021-0215

[5] Roy, S.N., Mishra, S., and Yusof, S.M., The emergence of drug discovery in machine learning, Technical Advancements of Machine Learning in Healthcare, pp. 119-138, 2021.
https://doi.org/10.1201/9781003116886-10

[6] Sugandha, S., Choubey, R.R., Gupta, R.K., and Gupta, S.B., Role of digital transformation and technology adoption in the efficiency of the pharmaceutical industry.

[7] Meenakshi, D.U., Nandakumar, S., Francis, A.P., Sweety, P., Fuloria, S., Fuloria, N.K., Subramaniyan, V., and Khan, S.A., Deep learning and site-specific drug delivery: The future and intelligent decision support for pharmaceutical manufacturing science, Deep Learning for Targeted Treatments: Transformation in Healthcare, pp. 1-38, 2022.
https://doi.org/10.1002/9781119879816.ch1

[8] Baviskar, K., Bedse, A., Raut, S., and Darapaneni, N., Artificial Intelligence and Machine Learning-Based Manufacturing and Drug Product Marketing, Bioinformatics Tools for Pharmaceutical Drug Product Development, pp. 197-231, 2023.
https://doi.org/10.1002/9781119859115.ch8

[9] Srivastava, D., Soni, D., Sharma, V., Kumar, P., and Singh, A.K., An artificial intelligence-based recommender system to analyze drug target indication for drug repurposing using linear machine learning

algorithm, Journal of Algebraic Statistics, vol. 13, no. 3, pp. 790-797, 2022. https://doi.org/10.1016/j.jastat.2021.12.001

[10] Adepu, A., and Poonia, P., Artificial intelligence-based systems direct the drugs to the faulty DNA sequences and tailor the gene sequences, Artificial Intelligence, vol. 52, no. 4, 2023.

[11] Bhattamisra, S.K., Banerjee, P., Gupta, P., Mayuren, J., Patra, S., and Candasamy, M., Artificial intelligence in pharmaceutical and healthcare research, Big Data and Cognitive Computing, vol. 7, no. 1, p. 10, 2023. https://doi.org/10.3390/bdcc7010010

[12] Vora, L.K., Gholap, A.D., Jetha, K., Thakur, R.R.S., Solanki, H.K., and Chavda, V.P., Artificial intelligence in pharmaceutical technology and drug delivery design, Pharmaceutics, vol. 15, no. 7, p. 1916, 2023. https://doi.org/10.3390/pharmaceutics15071916

[13] Shilong, Z., The machine learning model for sales forecasting by using XGBoost, in 2021 IEEE International Conference on Consumer Electronics and Computer Engineering (ICCECE), pp. 480-483, IEEE, 2021. https://doi.org/10.1109/ICCECE51280.2021.9342324

[14] Lin, S., Wang, Y., Zhang, L., Chu, Y., Liu, Y., Fang, Y., Jiang, M., Wang, Q., Zhao, B., Xiong, Y., and Wei, D.Q., MDF-SA-DDI: Predicting drug–drug interaction events based on multi-source drug fusion, multi-source feature fusion, and transformer self-attention mechanism, Briefings in Bioinformatics, vol. 23, no. 1, p. bbab421, 2022. https://doi.org/10.1093/bib/bbab421

[15] Tichy, E.M., Schumock, G.T., Hoffman, J.M., Suda, K.J., Rim, M.H., Tadrous, M., Stubbings, J., Cuellar, S., Clark, J.S., Wiest, M.D., and Matusiak, L.M., National trends in prescription drug expenditures and projections for 2020, American Journal of Health-System Pharmacy, vol. 77, no. 15, pp. 1213-1230, 2020. https://doi.org/10.1093/ajhp/zxaa186

[16] Agrawal, G., Tushir, S., Arora, D., and Sangwan, K., Artificial intelligence in pharmaceutical drug delivery, in 2024 International Conference on Computational Intelligence and Computing Applications (ICCICA), vol. 1, pp. 406-410, IEEE, 2024.

[17] Biehn, S.E., Goncalves, L.M., Lehmann, J., Marty, J.D., Mueller, C., Ramirez, S.A., Tillier, F., and Sage, C.R., BioPrint meets the AI age: Development of artificial intelligence-based ADMET models for the drug-discovery platform SAFIRE, Future Medicinal Chemistry, vol. 16, no. 7, pp. 587-599, 2024. https://doi.org/10.4155/fmc-2024-0007

[18] Saikia, S., Prajapati, J.B., Prajapati, B.G., Padma, V.V., and Pathak, Y.V., The role of artificial intelligence in therapeutic drug monitoring and clinical toxicity, in Recent Advances in Therapeutic Drug Monitoring and Clinical Toxicology, pp. 67-85, Springer International Publishing, 2022. https://doi.org/10.1007/978-3-031-12398-6_5

[19] Ali, A.M.A., and Alrobaian, M.M., Strengths and weaknesses of current and future prospects of artificial intelligence-mounted technologies applied in the development of pharmaceutical products and services, Saudi Pharmaceutical Journal, 2024, p. 102043. https://doi.org/10.1016/j.jsps.2024.102043

[20] Łapińska, N., Pacławski, A., Szlek, J., and Mendyk, A., SerotoninAI: Serotonergic system-focused artificial intelligence-based application for drug discovery, Journal of Chemical Information and Modeling, vol. 64, no. 7, pp. 2150-2157, 2024. https://doi.org/10.1021/acs.jcim.3c01517

[21] Serrano, D.R., Luciano, F.C., Anaya, B.J., Ongoren, B., Kara, A., Molina, G., Ramirez, B.I., Sánchez-Guirales, S.A., Simon, J.A., Tomietto, G., and Rapti, C., Artificial intelligence (AI) applications in drug discovery and drug delivery: Revolutionizing personalized medicine, Pharmaceutics, vol. 16, no. 10, p. 1328, 2024. https://doi.org/10.3390/pharmaceutics16101328

[22] Jena, G.K., Patra, C.N., Jammula, S., Rana, R., and Chand, S., Artificial intelligence and machine learning-implemented drug delivery systems: A paradigm shift in the pharmaceutical industry, Journal of Bio-X Research, vol. 7, p. 0016, 2024. https://doi.org/10.34133/jbioxresearch.0016

[23] Visan, A.I., and Negut, I., Integrating artificial intelligence for drug discovery in the context of revolutionizing drug delivery, Life, vol. 14, no. 2, p. 233, 2024. https://doi.org/10.3390/life14020233

[24] Rathipriya, R., Abdul Rahman, A.A., Dhamodharavadhani, S., Meero, A., and Yoganandan, G., Demand forecasting model for time-series pharmaceutical data using shallow and deep neural network models, Neural Computing and Applications, vol. 35, no. 2, pp. 1945-1957, 2023. https://doi.org/10.1007/s00521-022-07889-9

[25] Jaganathan, K., Tayara, H., and Chong, K.T., Prediction of drug-induced liver toxicity using SVM and optimal descriptor sets, International Journal of Molecular Sciences, vol. 22, no. 15, p. 8073, 2021. https://doi.org/10.3390/ijms22158073

Blockchain-Based Distributed Network Security Architecture with Smart Contract Vulnerability Detection Using Improved Tree CNN

Xiaoyan Huo
Information Construction and Management Center, Jiaozuo University, Jiaozuo 454003, China
E-mail: huoxiaoyan2004@163.com

Keywords: blockchain, distributed network architecture, privacy protection, smart contract, data security

Received: January 15, 2025

Abstract: In the era of big data, information security and privacy protection have become important issues facing today's society. This study proposes a distributed network security architecture based on blockchain to enhance the security of information privacy protection. The proposed architecture consists of three primary levels: equipment layer, network service layer, and application layer. It also integrates smart contracts. In addition, this study also proposes a vulnerability detection method based on improved tree convolutional neural networks. The incorporation of a "continuous binary tree" approach effectively addresses the limitation inherent to conventional tree convolution, wherein the number of nodes is fixed. This refinement enables a more effective capture of the hierarchical structure and semantic nuances inherent to smart contract code. The experiment used multiple datasets, each containing multiple IoT attack types and smart contract vulnerability code snippets. These datasets were evaluated based on a set of criteria, including but not limited to accuracy, recall, F1 scores, gas costs, and execution delays. Experiments have shown that the proposed method performs well in accuracy, precision, recall, and F1 scores compared to existing state-of-the-art methods, with an accuracy range of 89.62% to 98.36%, significantly better than Oyente (about 75%) and Securify (about 85%). Specifically, the proposed method achieved 96.14% accuracy in detecting reentrant attacks, compared to 78% for Oyente and 82% for Securify. The findings indicate that the architectural design exerts a substantial influence on enhancing network security performance, thereby ensuring the stability of the system by effectively mitigating the variability in response time.

Povzetek: Predlagana je distribuirana varnostna arhitektura omrežij na osnovi tehnologije veriženja blokov z izboljšano metodo drevesnih CNN za zaznavanje ranljivosti pametnih pogodb.

1 Introduction

With the rapid development of information technology, the internet has become an indispensable infrastructure in modern society, widely used in various fields such as finance, healthcare, education, and government affairs. However, cybersecurity issues are becoming increasingly prominent, with frequent incidents such as hacker attacks, data breaches, and online fraud, posing serious threats to personal privacy, corporate interests, and even national security [1, 2]. The traditional network security architecture mainly relies on centralized protection mechanisms, such as firewalls, intrusion detection systems, etc. These systems gradually show many shortcomings when facing complex network environments and increasing data volumes. Blockchain technology provides a new solution for network security with its decentralized, tamper-proof, and traceable features [3]. In a Distributed Network Security Architecture (DNSA), blockchain can serve as the underlying infrastructure for data storage and transmission. The data in the network are dispersed and stored on multiple nodes, with each node holding a complete copy of the data, thereby eliminating the risk of a single point of failure. At the same time, the immutability of blockchain ensures the authenticity and integrity of data, and any unauthorized tampering behavior will be quickly detected and prevented, effectively preventing the risk of malicious modification of data [4, 5]. However, the current processing speed and storage capacity of blockchain cannot fully meet the needs of large-scale network applications. Secondly, when facing complex network attack methods, blockchain may still have certain security risks. Therefore, this study proposes a DNSA based on blockchain.

Blockchain technology is widely used in various fields such as finance, supply chain, healthcare, etc. due to its decentralized, tamper-proof, and transparent characteristics. To detect and mitigate malicious attacks in software-defined networks, Sharmila et al. used unsupervised and supervised learning methods to perform mitigation operations in software defined networks using dynamic access control lists and implemented them through Mininet. This technology effectively reduced malicious attacks [6]. To enhance the security and privacy protection of blockchain storage systems, Haque et al. developed a security system that integrates the Ethereum blockchain, IPFS, and deep Convolutional Neural Networks (CNN) to achieve distributed storage and privacy protection of data. The system had high accuracy, sensitivity, and specificity, supporting efficient operation

for users [7]. To enhance the security of IoT devices, Rangappa et al. developed a new key generation stage by introducing lightweight blockchain technology and Blowfish symmetric encryption algorithm and utilized the immutability of blockchain to record transactions. This scheme outperformed traditional algorithms in terms of encryption time and memory overhead [8]. Kumar designed an intrusion detection system based on a variational autoencoder and attention-gated recurrent unit for the security of zero contact networks. It achieved secure data sharing through an authentication protocol that combines blockchain, smart contracts, elliptic curve cryptography, and authoritative proofs [9]. Hua et al. designed a secure cloud storage service data deduplication scheme to address the shortcomings of existing solutions in key leakage and dynamic change support. By grouping key servers and using threshold encryption, combined with blockchain technology, secure key updates and management have been achieved [10].

DNSA is the key to ensuring the secure operation of distributed systems in complex network environments. To enhance secure communication in wireless networks with multi-user pairs and un-trusted amplification and forwarding relays, Xie et al. proposed an adaptive optimal channel access strategy by formulating channel access problems, maximizing the throughput of the secure system, and utilizing optimal sequential planning decision theory. The numerical results have verified its effectiveness and high efficiency [11]. Liu et al. proposed a distributed multi-task security estimation algorithm based on local outlier factors and inter-task correlations to address multiple attacks in multi-task networks. A new distributed time-varying fusion strategy has been introduced, which allocates node weights through data density balance to resist attacks. This method could effectively resist various attacks [12]. To address the threat posed by malicious nodes, Luo et al. proposed a new paradigm inspired by distributed systems that ensures the network's identity is unforgeable, non-repudiation, and globally consistent. This scheme significantly reduced key consumption compared to traditional pre-shared key schemes [13]. To improve the real-time and security of Internet of Vehicles communication, Thangam et al. subdivided the roadside unit area and deployed edge computing resources to reduce communication delay, and introduced a consensus mechanism to ensure security. This method had a success rate of over 95%, significantly reduced consensus time, and effectively met the security requirements of vehicle networking communication [14]. To enhance the ability of IoT networks to combat Distributed Denial of Service (DDoS) attacks, Mahdi et al. constructed a detection model by combining k-nearest neighbors, logistic regression, and stochastic gradient descent classifiers, and integrated optimized parameters through machine learning. The model achieved accuracies of 99.965% and 99.968% on two datasets, surpassing existing methods [15]. A summary of the comparison between this method and existing literature is shown in Table 1.

Table 1: Comparison of the proposed method with existing literature

Research purpose	Method	Result	Shortcomings	Reference
Secure data transmission in IoT using remote sensing data	Theil-Sen Regressive Miyaguchi–Preneel-based Cryptographic Hash Blockchain	Enhanced secure data transmission	Complexity in implementation	Sharmila et al. [6]
Privacy-preserving deep learning for blockchain secure storage	Privacy-preserving deep learning framework	High authentication and secure storage	High computational cost	Haque et al. [7]
Secure data communication in IoT healthcare systems	Lightweight Blockchain	Improved data security in healthcare IoT	Limited scalability	Rangappa et al. [8]
Secure zero touch networks using blockchain	Deep-learning-based blockchain	Enhanced network security	Dependence on deep learning accuracy	Kumar et al. [9]
Secure deduplication for large-scale cloud storage	Blockchain-assisted secure deduplication	Efficient and secure cloud storage	Potential latency issues	Hua et al. [10]
Secure channel access in distributed cooperative networks	Optimal secure channel access	Improved security in untrusted relay networks	Complexity in channel management	Xie et al. [11]
Secure distributed estimation over multitask networks	Secure distributed estimation	Robust against multiple attacks	High computational overhead	Liu et al. [12]
Secure quantum key distribution networks	Distributed information-theoretical secure protocols	Enhanced security against malicious nodes	Requires quantum infrastructure	Luo et al. [13]
Secure V2X communication	Edge-enabled DAG-based Distributed Ledger System	Improved V2X communication security	Limited to edge-enabled regions	Thangam et al. [14]
Detection of DDoS attacks on IoT networks	Machine learning algorithms	Real-time DDoS attack detection	Dependence on training data quality	Mahdi et al. [15]
/	Practical Byzantine Fault Tolerance (Baseline approach)	/	Communication overhead and computational complexity increase	/
Improve security and processing speed of distributed network architectures	Smart Contract Vulnerability Detection Using Improved Tree CNN	/	/	This study

In summary, the application of blockchain technology and DNSA has significant advantages. However, current blockchain technology has limitations in processing speed, especially when dealing with a large number of concurrent transactions, which may result in delays. With the continuous growth of blockchain data, nodes need to store a large amount of data, which puts high demands on the storage capacity of nodes. In response to the above issues, this study innovatively designs a modular DNSA. This architecture uses edge computing to improve system security and flexibility. In response to Denial of Service (DoS) attacks, this study proposes a blockchain-based protection mechanism that identifies attacks through data flow detection and filtering models and utilizes blockchain and smart contracts to ensure the security and consistency of policy management.

2 Methods and materials

To improve data privacy protection and network security, and effectively detect and defend against network attacks, especially vulnerabilities in smart contracts, the research proposes a DNSA design based on blockchain, which integrates smart contracts into the architecture. The improved Tree-based Convolutional Neural Network (TCNN) is used to improve the accuracy and efficiency of vulnerability detection, and a protection mechanism based on blockchain technology is proposed.

2.1 DNSA design based on blockchain

Traditional service systems are typically based on centralized architectures, simplifying deployment processes, reducing operational complexity, and ensuring data consistency. However, it poses security risks when resisting specific network attacks, such as DoS attacks in LoRa networks. The utilization of LoRa terminals is susceptible to security breaches due to their cost-effectiveness and lightweight design, which are inadequate in terms of security protection capabilities. These terminals are prone to intrusion and control by attackers, resulting in the generation of substantial attack data. This, in turn, leads to a single point of failure, server resource depletion, and service denial in centralized systems. Reference [16] proposes a distributed IoT network architecture based on blockchain, which ensures data security and immutability through blockchain technology and improves communication efficiency. Reference [17] demonstrates the resource management capabilities of blockchain in distributed systems. It proves that a distributed service architecture has significant advantages in providing flexibility, security, reliability, and autonomy. To ensure the stability and security of the system in the face of attacks, this study proposes a blockchain-based DNSA, as shown in Figure 1.

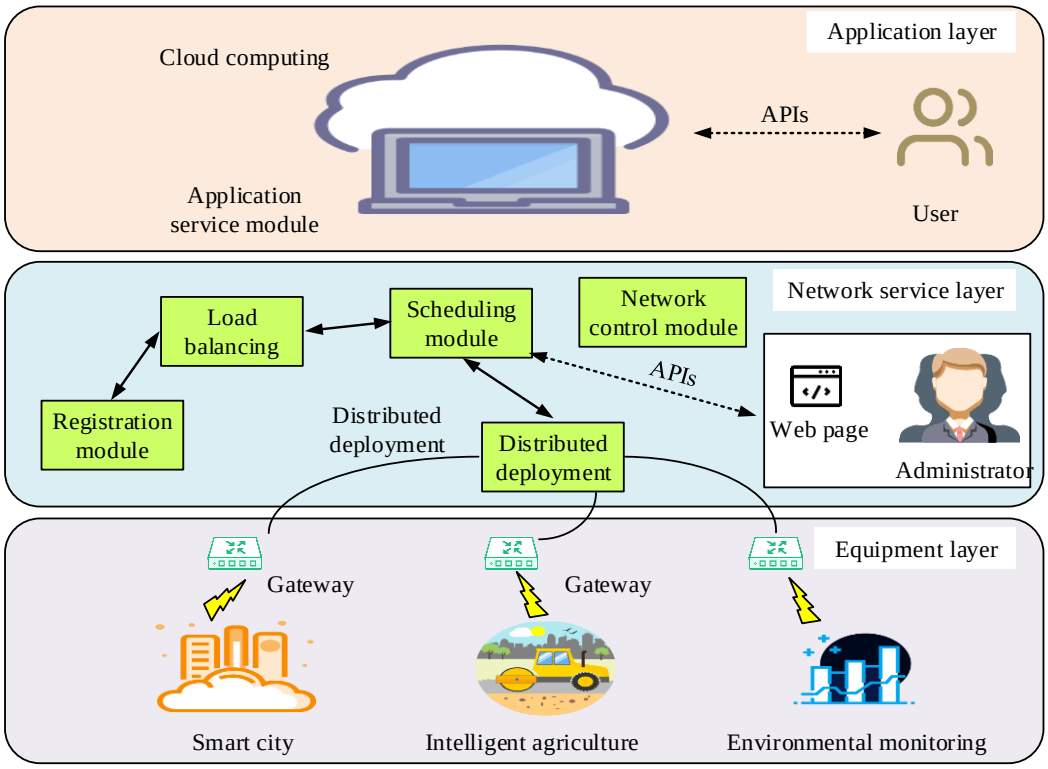

Figure 1: Schematic diagram of DNSA based on blockchain

This architecture is typically divided into three main levels and integrates various network components including terminal devices, gateways, and cloud servers, covering the entire process from data collection to processing, storage, and management. The Equipment layer is the foundation of the entire system and is responsible for direct interaction with physical devices and sensors. It not only ensures the accuracy and security

of the data but also provides a solid foundation for the upper-layer network services. Through the collaboration of the device layer and the network service layer, intelligent application scenarios can be comprehensively monitored and managed, thereby improving the efficiency and effect of the entire system. The network service layer focuses on providing core services such as access management, protocol analysis, and information transmission processing for terminal devices. The data collected at the device layer are transmitted to the network service layer through the gateway to provide basic information for decision-making and control at the upper layer. The network service layer can send commands to the device layer through the gateway to control the operation of the device and realize remote management and control. As for the application layer, it mainly undertakes the responsibilities of application data and user management, while providing interface services and user interfaces, as well as conducting in-depth analysis and mining of data. A layered system architecture design can ensure efficient operation and scalability of the network while providing flexible and reliable network services for various application scenarios. In response to security challenges in data protection and management processes, this study integrates smart contracts into a distributed service model, as shown in Figure 2.

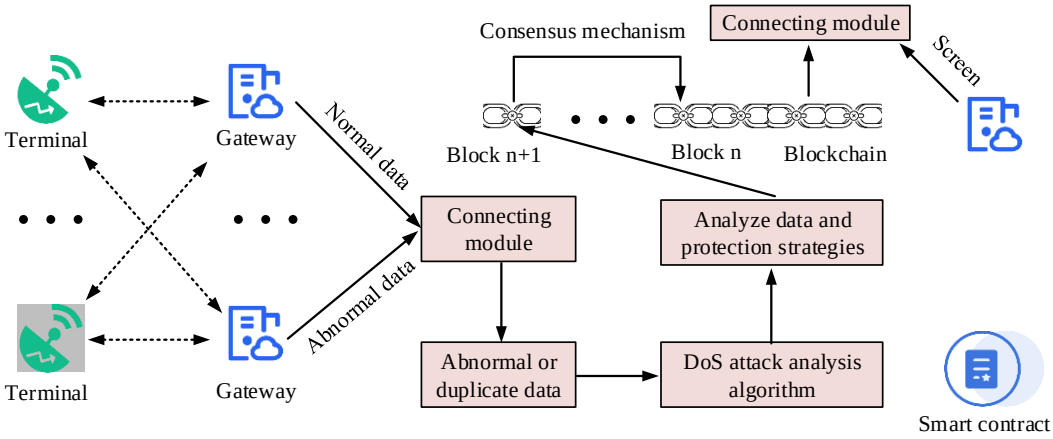

Figure 2: Schematic diagram of smart contract implementation in DNSA

Essentially, smart contracts are automated execution programs running on the blockchain, ensuring that all parties to the contract automatically comply with the agreement. Blockchain technology offers a decentralized, secure, and immutable execution platform for smart contracts, enabling any node in the network to participate in execution without the need for third-party intervention. This reduces the likelihood of default or fraudulent behavior. However, attackers can consume network resources through a large number of invalid transactions, causing contracts to malfunction. To solve this problem, a smart contract vulnerability analysis technique based on improved TCNN is proposed.

The code of smart contracts usually has a hierarchical structure, which can be represented by an Abstract Syntax Tree (AST). TCNN can directly process the tree structure data and capture the hierarchical and semantic information of the code. While Graph Neural Networks (GNNs) and Recurrent Neural Networks (RNNs) are both capable of processing graph-structured data. The code structure of smart contracts is better represented by a tree structure. TCNNs demonstrate superior proficiency in capturing semantic information within this hierarchical structure. In contrast, RNNs and GNNs have the potential to disregard these hierarchical characteristics, thereby introducing unnecessary complexity when handling tree structures.

TCNN mainly uses AST as input to capture the hierarchical and semantic information of smart contract code through tree structure, so as to improve the accuracy and efficiency of vulnerability detection. In a smart contract, the set of all subtrees is defined as $X \in R^{F\times N\times K}$, where F represents the number of subtrees. H is the maximum number of nodes in the subtree. K is the dimension of the node vector. In a fixed depth convolutional kernel, if there are n nodes corresponding to word embeddings $[x_1, x_2, \ldots, x_n]$, the output of the convolutional layer can be expressed as equation (1).

$$\mathbf{y}_{\text{conv}} = \sigma\left(\sum_{i=1}^{n}\sum_{j=1}^{3}\mathbf{W}_{\text{conv},j,i}\cdot\mathbf{x}_i + \mathbf{b}_{\text{conv}}\right) \quad (1)$$

In equation (1), $\mathbf{W}_{\text{conv},j,i}$ is the weight matrix. j represents three different types of weights. $\mathbf{b}_{\text{conv}}$ is the bias term. The activation function σ is selected as a nonlinear tanh function in the study. However, in equation (1), a defect of tree convolution is that the number of nodes n selected into the sliding window each time is not fixed, which makes it a great difficulty to set how many $W_{\text{conv},i}$ variable matrices. To solve this problem, a method called "continuous binary tree" is proposed, which can treat each sub-tree of AST as a binary tree, regardless of its shape and size. Figure 3 shows some definitions for applying the continuous binary tree method.

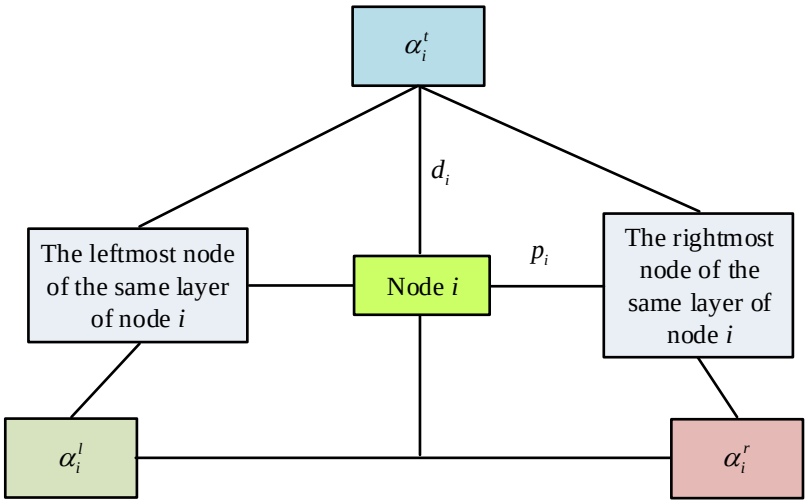

Figure 3: Schematic diagram of the continuous binary tree method

As mentioned above, for each sliding window, three variables $W_{\text{conv}}^t, W_{\text{conv}}^l, W_{\text{conv}}^r$ need to be set, and the corresponding coefficient $\alpha_i^t, \alpha_i^l, \alpha_i^r$ are respectively defined as up, left, and right. Therefore, for each node in the sliding window, its corresponding $W_{\text{conv},i}$ is a linear combination of these three variables, and the corresponding coefficient is determined by the relative position of the node in the sliding window sub-tree.

Even in complex situations where a node has multiple child nodes, the network can still perform convolution operations through three weight matrices. The calculation method of the weight matrix is shown in equation (2).

$$W_{\text{conv},i} = \alpha_i^t W_{\text{conv}}^t + \alpha_i^l W_{\text{conv}}^l + \alpha_i^r W_{\text{conv}}^r \tag{2}$$

In equation (2), W_{conv}^t is the coefficient of the weight matrix β_i^t, and its calculation is shown in equation (3).

$$\beta_i^t = \frac{d_{i-1}}{d_{\max-1}} \tag{3}$$

In equation (3), d_i is the depth of node i within the sliding window, and $d_{\max}$ is the maximum depth that the sliding window can cover. The coefficients of the other two weight matrices can be defined as equation (4).

$$\begin{cases} \alpha_i^l = (1-\alpha_i^t)\dfrac{n-p_i}{n-1} \\ \alpha_i^r = (1-\alpha_i^t)\dfrac{p_{i-1}}{n-1} \end{cases} \tag{4}$$

In equation (4), p_i is the sequential position of node i among its peers. Through this formula, it can understand how the specific position of nodes in the tree structure affects the relative importance of the weight matrix. Especially, nodes located on the left side of the tree will have a weight matrix W_{conv}^l that accounts for more than W_{conv}^r when performing convolution operations, while nodes located on the right side will have the opposite situation. After the convolution operation, the pooling layer extracts key features from the intermediate expressions of the network and summarizes these features in the form of high-dimensional vectors.

This study adopts the maximum pooling strategy, which selects the most prominent elements from the feature matrix generated by the convolutional layer. Compared to average pooling, which calculates the mean value of the pooling window, maximum pooling focuses on the most significant features, making it more suitable for capturing critical vulnerabilities in smart contract code. This is of particular importance in the realm of security applications, where the ability to detect rare but severe vulnerabilities, such as re-entrancy attacks, is of the essence. Additionally, maximum pooling reduces the dimensionality of the feature map while preserving the most relevant information, which enhances the efficiency of the subsequent layers. For a given pooling window of size $k \times k$, the maximum pooling operation can be defined.

$$\mathbf{V}_{\text{pooling}} = \max_{m,n\in[0,k-1]} x_{i\square s+m,\, j\square s+n} \tag{5}$$

In equation (5), x is the input feature map. $\mathbf{V}_{\text{pooling}}$ is the output feature map. s is the stride. This operation extracts the maximum value within each pooling window, effectively reducing the dimensionality of the feature map while preserving the most significant features.

After the pooling step is completed, the extracted feature vectors are passed to the hidden layer, which processes the features and feeds them into the classifier. The classifier then generates the final output for the prediction model. The hidden layer's role is to transform the pooled features into a higher-level representation that the classifier can use to make accurate predictions. Similar to convolutional layers, hidden layers also use tanh

activation functions. The output of the hidden layer can be expressed as equation (6).

$$\mathbf{y}_{\text{hide}} = \tanh\left(\mathbf{W}_{\text{hide}} \cdot \mathbf{V}_{\text{pooling}}^{\text{T}} + \mathbf{b}_{\text{hide}}\right) \tag{6}$$

Subsequently, the output of the hidden layer is fed into the classifier. This study uses a softmax classifier to predict the probability of various types of vulnerabilities occurring, expressed as equation (7).

$$\mathbf{y}_{\text{output}} = \text{softmax}(\mathbf{y}_{\text{hide}}) \tag{7}$$

Figure 4 shows the architecture of a vulnerability detection method based on an improved TCNN. Smart contract vulnerabilities are the premise for attackers to launch attacks, and attackers use the vulnerabilities in smart contracts to achieve their malicious purposes. The research identifies potential vulnerabilities in smart contracts, such as reentrant attacks, integer overflow, etc., through improved TCNN technology. Based on the type of vulnerability and its potential impact range, the risk level of each vulnerability was evaluated to help developers prioritize high-risk vulnerabilities. When an attack is detected, the defense mechanism can respond in real time, for example, by restricting access to malicious nodes or adjusting Gas charges to stop the attack. The vulnerability information identified by the vulnerability detection method can provide the basis for the defense mechanism and help the system better cope with potential attacks. The defense mechanism can prevent attackers from using identified vulnerabilities to launch attacks, thereby enhancing the actual effect of vulnerability detection.

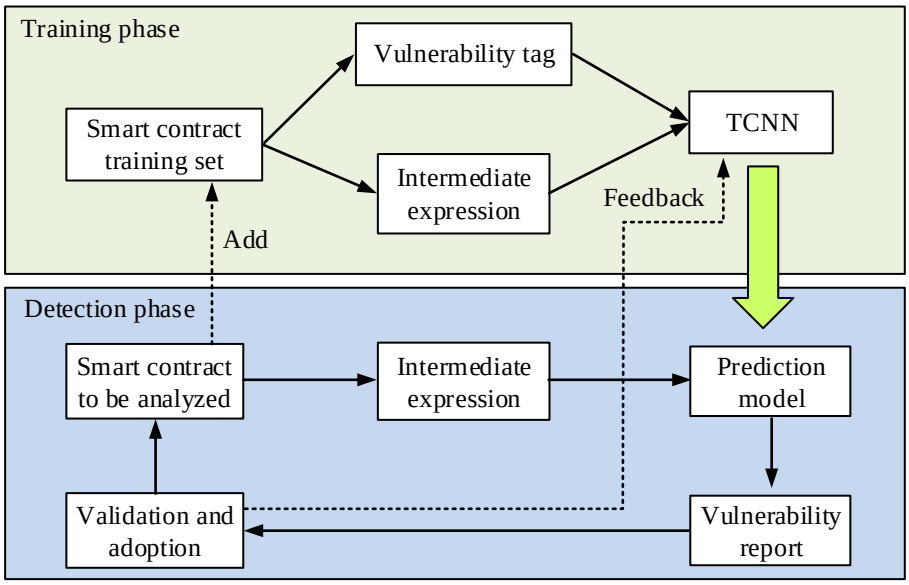

Figure 4: Vulnerability detection method architecture based on improved TCNN

2.2 Protection mechanism based on blockchain technology

DNSA faces complex system security issues in its application process, therefore it is necessary to establish effective security barriers. This study classifies and analyzes existing attack methods, proposes corresponding defense strategies, and constructs a relatively complete blockchain security defense system to combat DoS and DDoS attacks. The operation process is detailed in Figure 5. DoS attacks and DDoS attacks can launch a large number of invalid requests, consume network resources, and make services unavailable. An attacker can launch a coordinated attack by taking control of multiple nodes or devices. The attack may be continuous (continuous DoS attack) or intermittent (pulsed DoS attack), affecting the response time and stability of the system. When the detected abnormal traffic exceeds the preset security threshold, the connection module will activate the smart contract in the blockchain platform to record and respond to attack behavior. Smart contracts will determine corresponding punishment measures and restriction periods based on the frequency and duration of attack behavior. Subsequently, the processing results of the smart contract will be encapsulated into a new block and recorded on the blockchain through the network consensus mechanism.

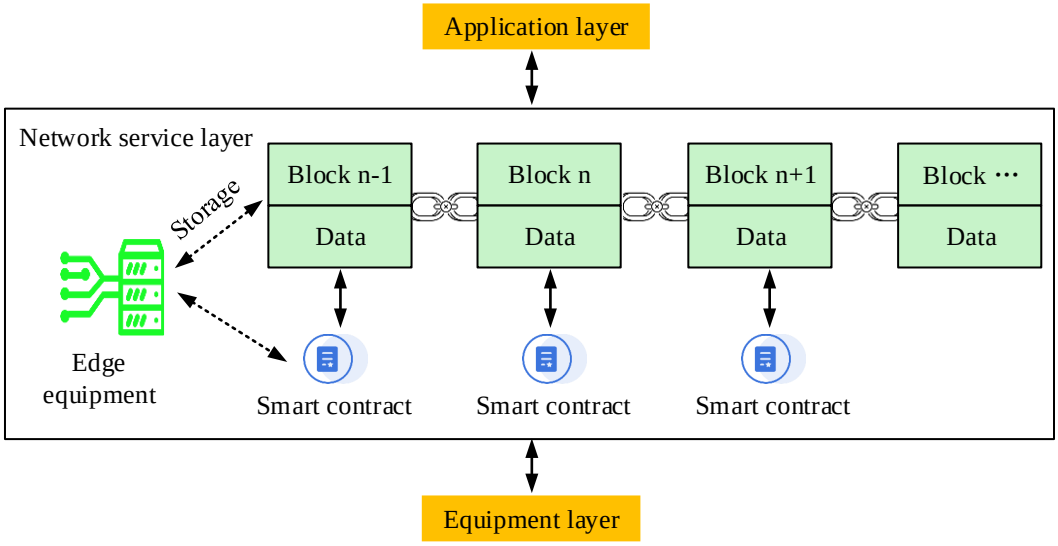

Figure 5: Blockchain-based DoS attack protection mechanism

According to Figure 5, to get rid of the disadvantages of a centralized management model and make full use of edge device resources, smart contracts are usually executed and verified by edge devices. However, limitations such as wide-area deployment, complex environment, and hardware performance of edge devices make them easier targets for attackers. Compared with other cyber attacks, the anonymity of blockchain technology also gives the attacker a natural camouflage, making the attack behavior with low risk, high profit, and easy-to-realize characteristics [18, 19]. Therefore, there is an urgent need for appropriate and efficient detection methods to conduct comprehensive security analysis for IoT smart contracts before deployment.

Edge computing is a paradigm that facilitates the execution of data processing and analytics at the periphery of the network, in closer proximity to the data sources and users. This approach has the potential to markedly reduce the time required for data transfer to remote data centers, thereby decreasing latency. With the increase of IoT devices, the amount of data has risen dramatically. By processing data locally and sending only critical data to the cloud, edge computing effectively reduces the pressure on network bandwidth and reduces data transmission costs. To reduce the response time of the system and enhance the efficiency of data transmission, this study also introduces edge computing and integrates multiple service modules to form the edge layer, as shown in Figure 6.

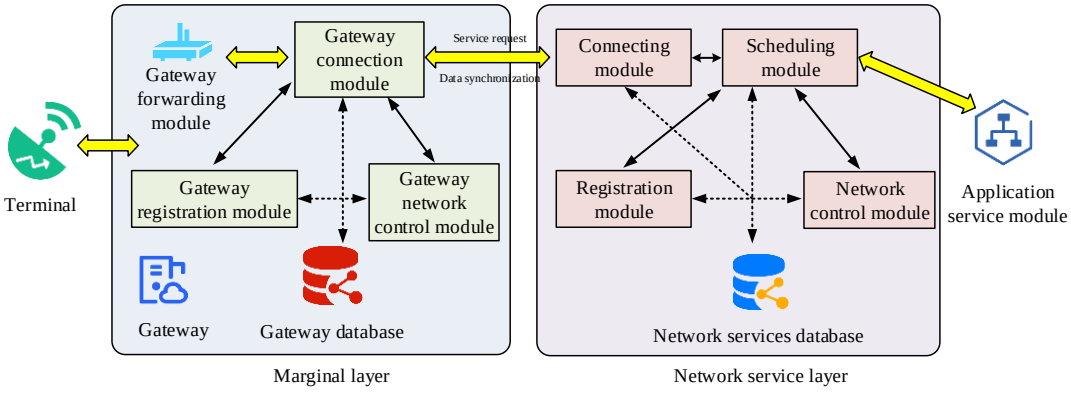

Figure 6: Network service architecture based on edge computing

A comparison with Figure 6 reveals that the original gateway, which is responsible for data forwarding, deployed a variety of service modules and is divided into edge layers. The diagram shows the gateway deploying all optional functional modules, including the connection module, registration module, and network control module, as well as the lightweight database. It should be noted that the gateway forwarding module is the basic function of the original gateway and is mainly responsible for receiving and packaging the physical layer data of the terminal. The network service layer retains all modules in the original system and provides complete service functions to ensure that all types of gateways can be accessed.

Considering that DoS attacks may occur in various forms, for example, some terminals may be frequently attacked in a short period, while other terminals may be intermittently attacked for a longer period [20, 21]. Therefore, the analysis method must simultaneously consider the frequency and time interval of attacks in order to update corresponding defense strategies. This study proposes a calculation method for the penalty parameter $\Delta\alpha$ based on the time interval of abnormal behavior

occurrence. When calculating the penalty parameter $\Delta\alpha$, the system takes into account the time interval between the latest attack t and the last attack T. The penalty parameter exhibits a proportional relationship with the increase in the number of attacks, thereby ensuring that the terminal with the shorter attack interval is subjected to a more severe penalty. The formula is defined as equation (8).

$$\Delta\alpha = \alpha_{prev} + a \cdot (t - T) \tag{8}$$

In equation (8), α_{prev} is the previous penalty parameter, a is a positive weight factor that determines the sensitivity of the penalty adjustment, and $t-T$ is the time interval between attacks. The weight factor a is set to 0.1 based on empirical testing, ensuring that the penalty increases gradually but significantly for frequent attackers. This approach aligns with the system's goal of dynamically adjusting restrictions based on attack behavior. Using penalty parameters, smart contracts are responsible for determining and adjusting the restriction period for terminals exhibiting aggressive behavior. This strategy is achieved by setting a limit period d for the terminal, as shown in equation (9).

$$d = d^* + \beta \cdot p + \gamma \tag{9}$$

In equation (9), d^* is the previously set limit period. β is a positive adjustment factor used to adjust the restriction period based on the penalty parameter p. γ is a random variable that is uniformly distributed within a predetermined range. The introduction of randomness is to alleviate the instantaneous peak pressure that DoS attacks may cause and to impose varying degrees of restrictions on malicious terminals launching attacks simultaneously [22]. As terminal abnormal behavior accumulates, the restriction period will gradually be extended. Finally, based on the restriction period t_e, the specific time point for implementing the restriction measures is determined, as shown in equation (10).

$$t_e = \begin{cases} t + d, & if: d \le \eta \\ t_\infty, & if: d > \eta \end{cases} \tag{10}$$

In equation (14), t_∞ is the maximum possible value of the time stamp. η serves as a critical value for evaluating the behavior of the terminal. The system employs a two-tiered approach to handle DoS attacks: temporary restrictions for initial or intermittent attacks, and permanent restrictions for persistent offenders. When a terminal exhibits repeated attack behavior, the system dynamically adjusts the restriction period based on the frequency and severity of the attacks. If the terminal continues to attack after multiple temporary restrictions and its accumulated restriction time exceeds a critical threshold η, the system will impose permanent measures to prohibit further access. This ensures a balanced approach between mitigating immediate threats and preventing long-term abuse.

3 Results

This study first conducts performance testing on the newly proposed DNSA and conducts in-depth comparisons of the performance of various methods to reveal their differences.

3.1 DNSA performance testing based on blockchain

The testing environment for this study is Intel(R) Core(TM) i5-2430M, CPU@2.40GHz, and 64 bit Windows 7 system. The IoTID20 dataset used in this study is a dataset specially created for the research of intrusion detection systems in the IoT environment, which contains a variety of IoT attack types, such as DDoS, DoS, Mirai, and ARP spoofing, etc. These datasets can provide rich data for the training and evaluation of intrusion detection models. Both the datasets CWE-119-SET and CWE-399-SET are based on the U.S. National Vulnerability Database and the National Institute of Standards and Technology's Software Assurance Reference dataset. The dataset CWE-119-SET contains 10,440 code gadgets related to buffer errors, which are commonly used for training and testing deep learning models. The dataset CWE-399-SET covers Resource Management Errors, such as resource leakage and post-release use. It also contains 7,285 code snippets related to resource management errors: used to train and test vulnerability detection models to identify resource management related vulnerabilities. To ensure that the model has enough data for training and the reliability of verification and testing process, the dataset is divided into training set, test set, and verification set according to the ratio of 6:2:2. Batch size is set to 32 to improve training efficiency and stability. The number of training rounds is set to 100 to ensure full convergence of the model. Table 2 shows the definition of each hyperparameter and the optional values.

Table 2: Definitions and optional values of hyperparameters

Hyper parameter	Definition	Optional value
conv_filter	The number of filters in the convolution layer	[32, 256] (step=32)
conv_kernel	Convolution window size	[3, 7]
pool_size	Maximum pool window size	[2, 4]
lstm_units	Number of units in the LSTM layer	[32, 512] (step=32)

dropout_rate	Random dropout rate of dropout layer 1	[0.2,0.5]
dense_units	The number of units in the fully connected layer	[32, 512] (step=32)
dense_dropout_rate	Random dropout rate of dropout layer 2	[0.2, 0.5]
optimizer	Adaptive optimizer	Adam,RMSProp,SGD
learning_rate	Training learning rate	[0.01, 0.005, 0.001, 0.0005, 0.0001]

```
# Training
batch_size = 32
epochs = 100

early_stopping = tf.keras.callbacks.EarlyStopping(monitor='val_loss', patience=10, restore_best_
weights=True)

history = model.fit(
    X_train, y_train,
    batch_size=batch_size,
    epochs=epochs,
    validation_data=(X_val, y_val),
    callbacks=[early_stopping]
)
```

Figure 7: Exact code for model training

The exact code for model training is shown in Figure 7. To prevent overfitting, the optimized experiment collocation is adjusted using the early stop method and the learning rate scheduler. In the experiment, the main evaluation index of the early stop method is loss. The early stop strategy is that when the performance of the model on the verification set does not improve for ten consecutive epochs, it is considered that the model begins to over-fit and stop training. Table 3 shows all hyperparameter settings for the 10 Bayesian optimization experiments, with batch_size defaulting to 32. Finally, it is determined that the hyperparameters of the eighth experiment are the optimal settings of TCNN.

Table 3: Hyperparameter settings of 10 Bayesian optimization tests

Trial_id	0	1	2	3	4	5	6	7	8	9
conv_filter	192	32	224	96	256	224	160	32	256	256
conv_kernel	7	6	4	6	4	5	7	7	7	7
pool_size	2	4	3	4	2	2	3	2	2	2
Ismm_units	480	128	320	384	288	384	448	512	512	512
dropout_rate	0.41153	0.4175	0.32132	0.47735	0.40378	0.40965	0.46895	0.5	0.5	0.5
dense_units	96	352	128	256	32	192	192	32	32	416
dense_dropout_rate	0.30759	0.49836	0.29813	0.31899	0.41386	0.41325	0.32615	0.21152	0.42292	0.31177
optimizer	RMSProp	SGD	SGD	Adam	RMSProp	RMSProp	Adam	Adam	Adam	Adam
leamning_rate	0.005	0.01	0.005	0.005	0.0001	0.0001	0.001	0.005	0.001	0.01

Figure 8 shows the trend of throughput changes in the network service layer. The median response time refers to the value in the middle of a set of response time data arranged in order from smallest to largest. In a computer system or network system, the median response time can be used to evaluate the performance of the system. For example, for a website's response time data, the median can reflect the response time when most users visit the website. In Figure 8 (a), when the number of LoRa devices connected to the network is small, the network service layer can effectively manage all received data streams, resulting in a direct proportional relationship between throughput and the number of devices. When the number of terminals is small (for example, less than 2000), the throughput difference between the three scheduling modules is small. With the increase of the number of terminals, the impact of the number of scheduling modules on throughput gradually appears, and the advantage of using four scheduling modules is more obvious. In Figure 8 (b), even with a small number of terminals, the system's response time exceeds 200 milliseconds. This phenomenon is attributed to the DoS attack defense

mechanism implemented in the network service system. However, as long as the number of terminals does not reach the maximum carrying capacity of the system, the median response time will remain stable. However, once the server faces the limit of its processing capacity, the median response time will significantly increase, mainly due to the server hardware performance reaching its limit, resulting in a significant extension of data processing time.

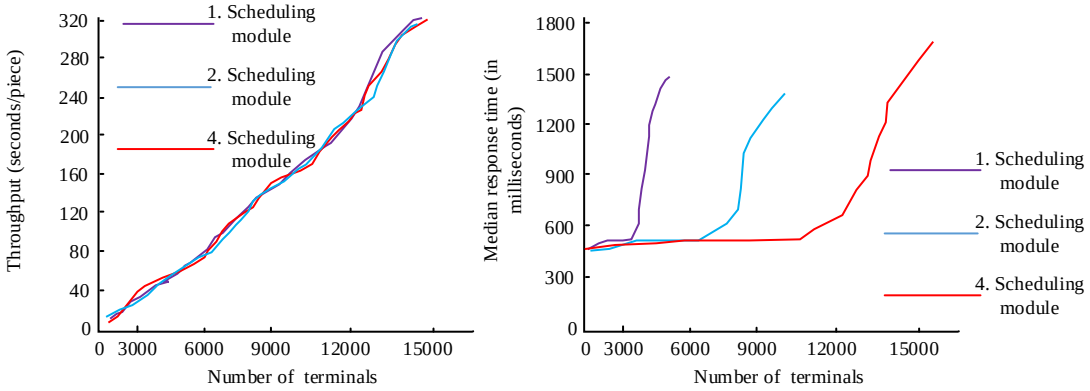

(a) Throughput changes of parallel functional modules in distributed deployment

(b) Median response time for distributed deployment of parallel functional modules

Figure 8: Throughput variation trend of network service layer

To measure the performance of the gateway in the edge computing environment, the experiment compares two types of uplink data: registration information and MAC command messages. According to Figure 9, in the case of a small number of terminal devices, the data processing throughput of both architectures shows a linear increase trend with an increase in the number of devices. However, when the number of terminal devices reaches 1600, the data processing capacity of the gateway reaches its limit, and its maximum throughput remains stable at about 53 data per second. In addition, the performance of the gateway in handling these two types of data is basically the same. Due to the original architecture deploying functional modules directly on the server, it provides strong computing power, ensuring further improvement in throughput. Although the processing power of a single gateway is limited, it can indeed undertake some of the computing work of the backend network system.

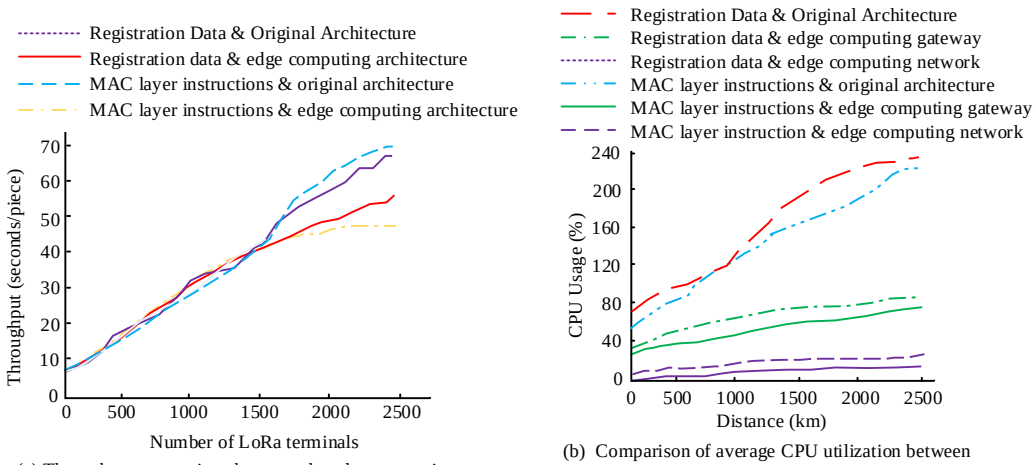

(a) Throughput comparison between the edge computing architecture and the original architecture

(b) Comparison of average CPU utilization between the edge computing architecture and the original architecture

Figure 9: Feasibility analysis of network security architecture based on edge computing

Figure 10 depicts the fluctuation of the median response time of conventional data under continuous and pulse DoS attack scenarios. In Figure 10 (a), under sustained DoS attacks, the fixed duration restriction strategy significantly reduces response latency after two applications and showed slight fluctuations in the subsequent time period. The proposed protection strategy can more quickly control the fluctuation of response time and reduce the amplitude of the fluctuation. This is thanks to the introduction of randomized parameters and penalty mechanisms in the strategy, which can dynamically adjust the duration of restrictions and effectively alleviate the continuous impact of attack traffic. In Figure 10 (b), the fixed duration restriction strategy cannot adjust the restriction duration on malicious nodes, resulting in a significant increase in response time for each attack, which may temporarily render the service unavailable. In contrast, the research strategy gradually increases the

punishment after identifying the attack behavior multiple times, reducing the impact of the attack on the system's processing capability and ensuring the stability of response time.

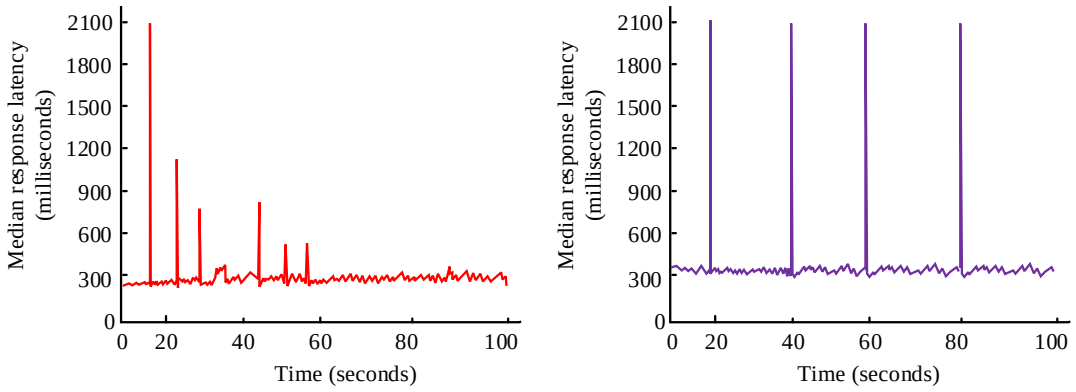

Figure 10: Data response time under different DoS attack scenarios

3.2 Performance analysis of TCNN vulnerability detection

To verify the effectiveness of the TCNN vulnerability detection method, this study analyzes accuracy, precision, recall, and F1 score as indicators, as shown in Table 4. When TCNN identifies vulnerabilities of five different categories, the accuracy of the test dataset ranges from 89.62% to 98.36%. This proves that the predictive model performs well in identifying potential vulnerabilities in the training samples. In addition, the accuracy and recall of this technology also meet high-performance requirements, effectively reducing the occurrence of misidentification and missed problems.

Table 4: Performance results of TCNN detecting different types of vulnerabilities

Vulnerability type	Data set	Accuracy (%)	Precision (%)	Recall rate (%)	F1 score (%)
Re-entrant attack	Training set	98.36	97.96	98.28	98.12
	Test set	96.14	96.38	95.23	95.80
Integer overflow	Training set	93.79	96.31	86.43	91.10
	Test set	89.62	90.22	80.23	84.93
Integer underflow	Training set	96.64	89.53	72.43	80.08
	Test set	96.66	90.84	71.64	80.11
Predictable variable attack	Training set	97.06	99.56	93.09	96.22
	Test set	95.94	98.66	91.16	95.55
Abnormal state	Training set	93.84	86.28	77.04	81.40
	Test set	93.14	83.33	74.38	78.60

Figure 11 (a) shows the best performance results of Oyente, Securify, and TCNN models in the unknown vulnerability detection of smart contracts. The TCNN model has the best effect, achieving the highest value in the four evaluation indicators, which verifies the significant advantages of TCNN in the unknown vulnerability detection of smart contracts. In Figure 11 (b), TCNN has the highest accuracy in all attack types, and the detection accuracy of Sybil attack and Replay attack both exceeds 90%. Securify performs second on most attack types but outperforms Oyente on Integer underflow and Integer overflow. Oyente has a relatively low accuracy rate across all attack types, particularly on Integer underflow and Integer overflow.

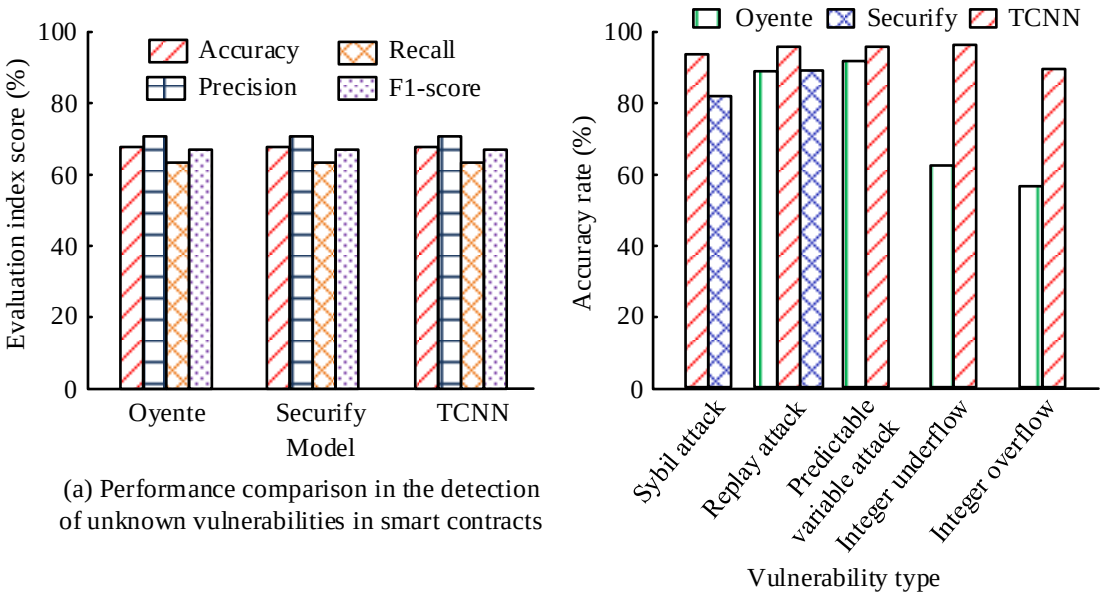

(a) Performance comparison in the detection of unknown vulnerabilities in smart contracts

(b) Comparison of the accuracy of detecting different types of leakage holes

Figure 11: Performance assessment of multiple types of vulnerabilities

To evaluate the computational cost of deploying smart contracts, the Gas fees and execution delays for different settings (Table 5) are measured. TCNN achieves the lowest Gas fees (38,000 Gwei) and execution delay (90 ms), significantly outperforming Oyente and Securify. This result demonstrates the efficiency of the proposed architecture in real-time applications.

Table 5: Gas fees and execution delay analysis

Setting	Gas Fee (Average, in Gwei)	Execution Delay (Average, in ms)
Reference [21]	50,000	120
Reference [22]	45,000	110
Oyente	55,000	150
Securify	52,000	140
TCNN (Proposed)	38,000	90

Figure 12 shows the results of the comparison between different scenarios and different approaches. In Figure 12 (a), the False Negative Rate (FNR) and False Positive Rate (FPR) are not significantly different in all data sets, indicating that the model has more balanced types of misjudgment on these data sets. To verify the statistical significance of the performance differences between the Settings, a paired T-test is performed for the FNR and FPR values and it is found that both CWE-399-SET and IoTID20 are significantly better than CWE-119-SET ($P<0.05$). The effect deviation of the overall vulnerability detection is within the acceptable range, which also indicates that the method in this paper is generally applicable to different vulnerability types. Figure 12 (b) shows the Receiver Operating Characteristic curve (ROC) graph between the proposed model and references [21] and [22]. From the area represented in the figure, the ROC curve of the proposed method is closer to the upper left corner, indicating that the proposed method has better performance.

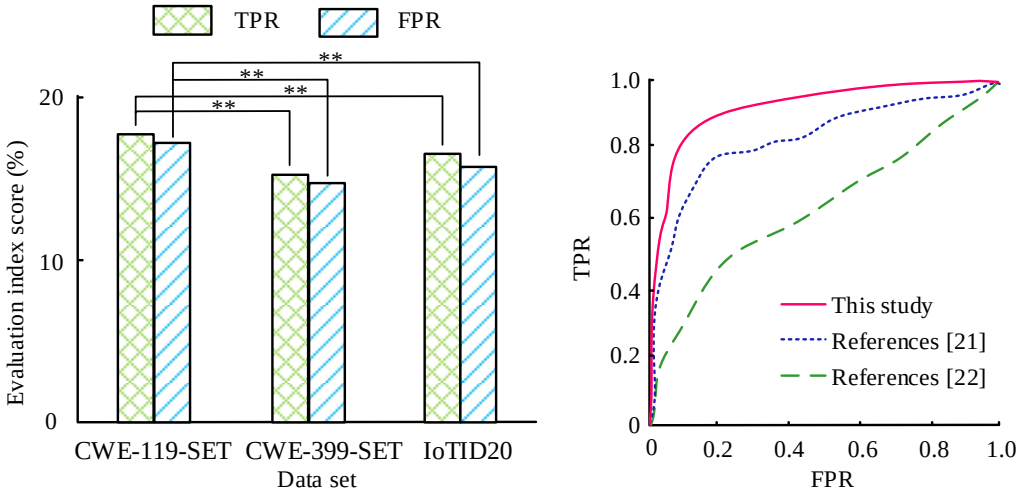

(a) Comparison of false positive rate and false negative rate in different data sets (Note: "**" means P< 0.05)

(b) ROC curves of different detection methods

Figure 12: Comparison results between different scenarios and different methods

4 Discussion

The proposed DNSA architecture has significant advantages over existing methods, mainly due to its deep integration of smart contracts and high efficiency of improved TCN. First, the integration of smart contracts enables the system to automate the execution of security policies and attack responses, reducing the need for human intervention and improving the real-time and reliability of the system. Although the scheme proposed by Yu et al. enhances the security of data transmission, its implementation is complicated and relies on manual intervention, which is difficult to cope with large-scale network attacks [23]. The privacy-protecting deep learning framework of Miglani et al., despite its excellent performance in storage security and authentication performance, relies on complex models, resulting in a substantial increase in computational overhead [24]. By automatically recording and responding to attack behaviors through smart contracts, this architecture significantly improves the automation level of the system. In particular, when dealing with DoS and DDoS attacks, it can dynamically adjust the restriction policy (as shown in Figure 5), effectively alleviating the impact of attacks on the system. Second, the improved TCNN excelled in vulnerability detection, with a significantly higher accuracy (89.62% to 98.36%) than existing methods such as Oyente (around 75%) and Securify (around 85%). TCNN solved the problem that the number of nodes in traditional tree convolution was not fixed by "continuous binary tree" method. TCNN could better capture the hierarchical structure and semantic information of smart contract code, thereby improving the accuracy and efficiency of vulnerability detection. TCNN also outperformed Oyente (55,000 Gwei/150 ms) and Securify (52,000 Gwei/140 ms) in terms of Gas costs (38,000 Gwei) and execution latency (90 ms), making it more suitable for real-time application scenarios.

In summary, this architecture significantly improves the security, real-time performance, and scalability of the system through the comprehensive application of automatic execution of smart contracts, efficient vulnerability detection of TCNN, and dynamic defense mechanisms. It is superior to existing methods in dealing with complex network attacks and large-scale data. However, the training of the TCNN model relies on large-scale labeled data sets, and its training process consumes a lot of computing resources. Although the overfitting problem is alleviated by Bayesian optimization and early stop strategy, the model training cost may still become the deployment bottleneck. In addition, although edge computing reduces network layer latency, the gateway's throughput ceiling may limit its scalability in high-concurrency scenarios. Future research could optimize blockchain storage efficiency by introducing sharding technology, and explore lightweight TCNN models to balance detection accuracy with computational overhead.

5 Conclusion

This study was based on the design of DNSA using blockchain technology, which addressed the shortcomings of traditional network security architectures in dealing with complex network environments and large-scale data volumes. By combining blockchain technology with DNSA, this study has achieved significant results in data security, privacy protection, and resistance to network attacks. Experiments have shown that this architecture can effectively reduce response latency and maintain high throughput when handling numerous concurrent transactions. For example, when the number of LoRa devices reached 1600, the maximum throughput of the gateway remained stable at about 53 data per second, demonstrating good data processing capabilities. In the case of sustained DoS attacks, research strategies could more quickly control the fluctuation of response time and reduce the amplitude of the fluctuation. This was thanks to the introduction of randomized parameters and penalty

mechanisms in the strategy, which can dynamically adjust the duration of restrictions and effectively alleviate the continuous impact of attack traffic. After identifying the attack behavior multiple times, the punishment was gradually increased, reducing the impact of the attack on the system's processing capability and ensuring the stability of response time. In addition, the smart contract vulnerability detection method based on the improved TCNN performed well in accuracy, precision, recall, and F1 score, with an accuracy ranging from 89.62% to 98.36%, significantly better than other existing methods. The results demonstrated the effectiveness of the proposed architecture in improving network security performance.

References

[1] Abdullah N F, Kairaldeen A R, Abu-Samah A, Nordin R. Machine learning-based transactions anomaly prediction for enhanced IoT Blockchain network security and performance. KSII Transactions on Internet and Information Systems, 2024, 18(7): 1986-2009. DOI:10.3837/tiis.2024.07.014.

[2] Li Y, Liang L, Jia Y, Wen W, Tang C, Chen Z. Blockchain for data sharing at the network edge: trade-off between capability and security. IEEE/ACM Transactions on Networking, 2024, 32(3): 2616-2630. DOI:10.1109/TNET.2024.3364023.

[3] Wang J, Ou W, Wang W, Sherratt R S, Ren Y, Yu X. Data security storage mechanism based on blockchain network. Computers, Materials & Continua, 2023, 74(3): 4933-4950. DOI:10.32604/cmc.2023.034148.

[4] El Ghazouani M, Ikidid A, Zaouiat C A, Aziz L, Lachgar M, Er-Rajy L. A Blockchain-based method ensuring integrity of shared data in a distributed-control intersection network. International Journal of Advanced Computer Science and Applications, 2023, 14(10): 489-497. DOI:10.14569/IJACSA.2023.0141052.

[5] Fkaier S, Khalgui M, Frey G, et al. Secure distributed power trading protocol for networked microgrids based on blockchain and elliptic curve cryptography. IET Smart Grid, 2023, 6(2): 175-189. DOI:10.1049/stg2.12087.

[6] Sharmila B, Kalavathi Devi T. Theil-Sen regressive Miyaguchi-Preneel-based cryptographic hash blockchain for secure data transmission using remote sensing data in IoT. IETE Journal of Research, 2024, 70(1): 116-129. DOI:10.2139/ssrn.4156878.

[7] Haque S M U, Sofi S A, Sholla S. A privacy-preserving deep learning framework for highly authenticated blockchain secure storage system. Multimedia Tools and Applications, 2024, 83(36): 84299-84329. DOI:10.1007/s11042-024-19150-7.

[8] Rangappa J D, Manu A P, Kariyappa S, Chinnababu S K, Lokesh G H, Flammini F. A lightweight Blockchain to secure data communication in IoT network on healthcare system. International Journal of Safety & Security Engineering, 2023, 13(6): 1015-1024. DOI:10.18280/ijsse.130604.

[9] Kumar R, Kumar P, Aloqaily M. Deep-learning-based blockchain for secure zero touch networks. IEEE Communications Magazine, 2022, 61(2): 96-102. DOI:10.1109/MCOM.001.2200294.

[10] Hua Z, Yao Y, Song M, Zheng Y, Zhang Y, Wang C. Blockchain-Assisted secure Deduplication for large-scale cloud storage service. IEEE Transactions on Services Computing, 2024, 17(3): 821-835. DOI:10.1109/TSC.2024.3350086.

[11] Xie J, Zhang Z, Atapattu S, Ye Y, Zhang H. Optimal secure channel access in distributed cooperative networks with untrusted relay. IEEE Wireless Communications Letters, 2023, 12(6): 1091-1095. DOI:10.1109/LWC.2023.3262287.

[12] Liu Q, Ye M, Chen F. Secure distributed estimation over multitasks networks against multiple attacks. IEEE Transactions on Aerospace and Electronic Systems, 2022, 59(3): 2480-2493. DOI:10.1109/TAES.2022.3215948.

[13] Luo Y, Li Q, Mao H K. Distributed information-theoretical secure protocols for quantum key distribution networks against malicious nodes. Journal of Optical Communications and Networking, 2024, 16(10): 956-968. DOI:10.1364/JOCN.530575.

[14] Thangam S, Chakkaravarthy S S. An edge enabled region-oriented DAG-based distributed ledger system for secure V2X communication. KSII Transactions on Internet and Information Systems, 2024, 18(8): 2253-2280. DOI:10.3837/tiis.2024.08.011.

[15] Mahdi Z, Abdalhussien N, Mahmood N, Zaki R. Detection of real-time distributed denial-of-service (DDoS) attacks on internet of things (IoT) Networks using machine learning algorithms. Computers, Materials & Continua, 2024, 80(8): 2139-2159. DOI:10.32604/cmc.2024.053542.

[16] Sharma R K, Pippal R S. Blockchain based efficient and secure peer-to-peer distributed IoT network for non-trusting device-to-device communication. Informatica, 2023, 47(4): 515-522. DOI:10.31449/inf. v47i4.3494.

[17] Lyu Z, Cheng C, Lv H, Song H. Blockchain based intelligent resource management in distributed digital twin's cloud. IEEE Network, 2023, 38(4): 143-150. DOI:10.1109/MNET.2023.3326099.

[18] Wu W, Yu L, Yang L, Zhang Y, Wang P. Efficient digital twin placement for blockchain-empowered wireless computing power network. Computers, Materials & Continua, 2024, 80(7): 587-603. DOI:10.32604/cmc.2024.052655.

[19] Singh U, Sharma S K, Shukla M, Jha P. Blockchain-based BATMAN protocol using mobile ad hoc network (MANET) with an ensemble algorithm. International Journal of Information Security, 2024, 23(3): 1667-1677. DOI:10.1007/s10207-023-00804-w.

[20] Filatovas E, Stripinis L, Orts F, Paulavičius R. Advancing research reproducibility in machine learning through blockchain technology. Informatica, 2024, 35(2): 227-253. DOI:10.15388/24-INFOR553.

[21] Pise R G, Patil S. Pioneering automated vulnerability detection for smart contracts in blockchain using KEVM: Guardian ADRGAN. International Journal of Information Security, 2024, 23(3): 1805-1819. DOI:10.1007/s10207-024-00817-z.

[22] El Haddouti S, Khaldoune M, Ayache M, Ech-Cherif El Kettani M D. Smart contracts auditing and multi-classification using machine learning algorithms: an efficient vulnerability detection in ethereum blockchain. Computing, 2024, 106(9): 2971-3003. DOI:10.1007/s00607-024-01314-w.

[23] Yu D, Chen Y. The analysis of the characteristics and evolution of the collaboration network in blockchain domain. Informatica, 2021, 32(2): 397-424. DOI:10.15388/20-INFOR437.

[24] Miglani A, Kumar N. A blockchain based matching game for content sharing in content-centric vehicle-to-grid network scenarios. IEEE Transactions on Intelligent Transportation Systems, 2023, 25(5): 4032-4048. DOI:10.1109/TITS.2023.3322826.

An Improved Topology Graph and Ant Colony Optimization Approach for Optimizing Electric Vehicle Travel Path Considering Time and Charging Cost

Liang Wei*
School of Automotive Engineering and General Aviation, Shaanxi Vocational & Technical College Xi'an 710038, China
E-mail: wei_liang1986@163.com

Keywords: electric vehicles, ant algorithm, topology graph, time, cost

Received: July 15, 2024

The integration of high-tech in electric vehicles enhances the driving experience, which is more environmentally friendly. However, the uneven distribution of charging stations and limited battery capacity require a balance between travel time and charging cost during long-distance travel. Different charging strategies and path planning can lead to different charging cost and travel time. Introducing artificial intelligence into path planning aims to enhance the long-distance travel experience for drivers and passengers. Therefore, the study adopts topology graphs to isomerize the roads during travel, and the algorithm topology graph is improved to remove redundant paths. Then, it is combined with ant algorithm to construct a path optimization model. The experiment used the electricity price in C1 city and the charging charging parameters in the parking lot at Ya as experimental data to simulate the real environment. The simulation results showed that the research algorithm achieved convergence after the 23rd iteration, with a comprehensive total cost of 38. The computational efficiency and results are superior to other algorithms. The average total cost of the travel path optimization model based on improved topology and ant algorithm was 7% -26% lower than other models. The results indicate that the research model has a better balance effect when considering travel time and charging cost comprehensively, which can plan the optimal travel strategy. The research results can make a positive contribution to autonomous driving.

Povzetek: Predlagan je izboljšan pristop optimizacije poti električnih vozil, ki združuje topološke grafe in algoritem kolonije mravelj, znižuje skupne stroške potovanja ter uravnoteži čas in stroške polnjenja.

1 Introduction

With the rapid development of battery energy storage technology and intelligent interaction between humans and vehicles, electric vehicles have environmental protection, intelligence, diverse choices, and high cost-effectiveness. More people choose to purchase electric vehicles [1-2]. However, in long-distance travel, the distribution of charging stations is not as wide as that of gas stations, and electric vehicles have a shorter range than gasoline vehicles. Frequent visits to charging stations for energy storage make it difficult for drivers to balance the time and charging cost of long-distance travel [3]. Due to different congestion situations during visits to charging stations, there are differences in tiered electricity prices, resulting in varying levels of electricity when arriving and leaving the stations. This greatly increases the difficulty of planning the optimal travel plan. Therefore, finding an electric vehicle path optimization method that comprehensively considers time and charging cost can greatly enhance the driver's long-distance travel experience. However, Algorithm Topology Graph (ATG) can isomerize complex road networks and charging stations into point and edge sets during travel, with clear connectivity and sequential relationships, which can simplify complex path problems [4-5]. Ant Colony Optimization (ACO) algorithm simulates ant foraging and has a global self-organizing search and positive feedback mechanism. After iteration, it gradually obtains the global optimal solution from the local optimal solution, which is suitable for travel path optimization [6-8]. Many scholars and experts have conducted relevant research on ATG and ACO. Details are shown in Table 1.

Table 1: The summary table of the reviewed research

Reference	Method	Result	Inadequacy
Dawen [9]	Based on bidirectional heuristic search A-star and ACO algorithm	Compared with the heuristic search A-star algorithm, acyclic algorithm, and Gurobi algorithm, it reduces 102.73m, 73.27m and 23.08m, respectively	ACO algorithm can fall into local optimal solution, and its robustness and generalization ability have not been explored
Dong et al [10]	Multi-objective ACO for ship pipeline path design method	The actual ship pipeline path design and simulation experiments show that this method improves the efficiency of the design work	ACO has strong optimization ability, and it needs to be verified for path planning
Zhao et al [11]	A multi-material, multi-volume topology optimization framework	Compared with the conventional frame, the optimized frame has a 17.4% reduction in steel content and fewer cracks under the ultimate load	The topology of steel structure is deterministic, while the topology of the path planning is multivariate and uncertain
Kai et al [12]	Elastoplastic continuum topology optimization method based on SIMP framework	The stable load bearing capacity of the elastoplastic continuum is increased by 6.1%	This study uses SIMP framework to optimize the topology structure, which is not suitable for the content of the study

To solve the traffic congestion and increased fuel consumption caused by blind navigation during travel, Xia et al. proposed a bidirectional heuristic search algorithm based on A-star and ACO. The research results indicated that the length of the shortest path recommended by this algorithm was 102.73m, 73.27m, and 23.08m shorter than heuristic search A-star algorithm, acyclic algorithm, and Gurobi algorithm, respectively [9]. Dong et al. proposed a multi-objective ACO-based ship pipeline path design method, which addressed the extremely complex nature of ship pipelines and the high workload and low design efficiency involved in designing ship pipeline paths. The study conducted simulation experiments and applied this method to the ship pipeline path design in reality. The feasibility and effectiveness of this method were verified through simulation experiments and practical use, which improved the efficiency of design work [10]. Zhao et al. designed a multi material and multi volume topology optimization framework to address the cost increase caused by the need for a large number of crack control steel bars in deep beam design. Compared with traditional frameworks, the optimized framework reduced steel content by 17.4% and had fewer cracks under ultimate load. The topology structure can reduce the steel cost in deep beam design [11]. Li and Cheng proposed a topology optimization method for elastic-plastic continuum based on SIMP framework to address the low stability load bearing performance of elastic-plastic continuum. The experimental results showed that the stability load bearing capacity of the elastic-plastic continuum was improved by 6.1%. From this, the topology optimization of elastic-plastic continuum can effectively improve performance [12].

The above research indicates that some scholars have conducted relevant research on ATG and ACO, which are helpful for path planning and cost control. However, there is very little research on the combination of ATG and ACO for electric vehicle path planning. Therefore, this study combines ATG and ACO to the travel path optimization, constructing an optimal long-distance travel path selection model that can balance travel time and charging cost. It is expected that this model can take into account different drivers' perceptions of time and cost, fully consider all traffic related time and toll cost during travel, and select the optimal travel path to improve the driver's driving experience. The innovation of this study lies in the proposed model, which combines the roads, starting points, endpoints, and charging stations in long-distance travel into a topology graph. The topology graph is iteratively optimized using the ATG-ACO algorithm to calculate the optimal path for comprehensive time and cost. The contribution of the research lies in not only being able to calculate the global optimal solution for long-distance travel, but also automatically balancing charging cost and overall travel time based on different user preferences through conversion and weighting coefficients. At the same time, the proposed optimization strategy for electric vehicle travel routes has broad application prospects and promotion value, which is expected to make positive

contributions to the development of industries such as autonomous driving and logistics distribution.

The research is mainly divided into five parts. The first part is the introduction, which analyzes the research results of long-distance travel solutions and briefly describes the optimization strategies proposed in the study. The second part designs a travel path planning model based on the ATG-ACO algorithm. The third part is model simulation testing. The fourth part discusses the simulation test results. The fifth part summarizes the research results. The path optimization model based on ATG and ACO can calculate the optimal travel strategy that comprehensively considers travel time and charging cost.

2 Methods and materials

Topology graphs can isomerize the positions and paths during travel in the form of point and edge sets, better representing dependency relationships and execution order, making it easier for algorithms to find the optimal path [13-14]. This study improves the topology algorithm and decomposes the total cost of travel time and charging cost to establish a cost calculation method that considers conversion coefficients, weighted coefficients, and mutual constraints between sub-items. The ant algorithm is introduced into the preprocessed topology to form a travel path planning model based on the ATG-ACO algorithm. Through algorithm iteration, the global optimal solution is gradually obtained from the local optimal solution, which comprehensively considers the time and charging cost of the optimal path.

2.1 Design of improved ATG algorithm based on electric vehicle travel path

Electric vehicles have fewer charging stations than gas stations, which greatly increases the difficulty of path optimization due to frequent charging, queuing for charging, and tiered electricity prices. An improved ATG that heterogeneous travel locations is proposed, characterized by clear hierarchical structure, acyclic and traversal characteristics. These advantages facilitate the modeling of travel paths, allowing algorithms to efficiently find the optimal path from a large number of calculations. Considering the objective relationship between remaining electricity, storage capacity, and charging time, when constructing a topology diagram, the following constraints must be met. Firstly, the uni-directionality of the battery electrochemical conversion process makes it impossible to charge and discharge simultaneously. Therefore, there is a mutually exclusive constraint, as shown in equation (1).

$$\eta + \gamma \le 1 \tag{1}$$

In equation (1), η represents the charging state of the vehicle, and $\eta = \{0,1\}$. $\eta = 0$, indicates that the vehicle is not charging. $\eta = 1$, it indicates that the vehicle is currently charging. γ is the discharge state of the vehicle, and $\gamma = \{0,1\}$. When $\gamma = 0$, the vehicle is not discharging. When $\gamma = 1$, the vehicle is discharging. In addition, the constraint of battery capacity should be considered. Firstly, when reaching the charging station, the amount of electricity must be greater than or equal to 0. Secondly, the amount of energy stored cannot exceed the battery capacity E_M. The constraint of remaining battery capacity E_x is shown in equation (2).

$$E_x = \begin{cases} E_x \ge 0 \\ E_x + Q_x \chi T_x \le E_M \end{cases} \tag{2}$$

In equation (2), Q_x is the charging power of the charging station. χ is the charging efficiency of the vehicle. T_x is the charging time at charging station x. Finally, because there is a relationship between the locations, it is necessary to consider the time constraint of reaching the charging station. The expression for the arrival time constraint is shown in equation (3).

$$T_b = \begin{cases} T_s + \dfrac{D_{ab}}{\overline{V}_{iab}} & \left(a \in 0, b \in B_a or \left(\Lambda \cap a\right)\right) \\ T_a + \dfrac{D_{ab}}{\overline{V}_{iab}} & \left(a \in \Phi, b \in B_a or \left(\Lambda \cap a\right)\right) \\ T_a + T_{Wb} + T_{Cb} + \dfrac{D_{ab}}{\overline{V}_{iab}} & \left(a \in \Lambda, b \in B_a\right) \end{cases} \tag{3}$$

In equation (3), T_b is the time to reach charging station b. D_{ab} is the distance between charging station a and b. $\overline{V}_{iab}$ is the estimated average speed of the section. T_s is the starting time. T_a is the time to leave a. T_{Wb} is the waiting time for the vehicle to be charged in queue at b. T_{Cb} is the charging time of the vehicle at b. The set of rechargeable locations around a is B_a. Λ is the collection of charging stations where the car undergoes charging. Φ is the collection of all charging stations for charging during travel, including fast charging stations and regular parking lots with charging stations. Taking into account the above constraints, the topology diagram presents an extremely complex structure that requires a significant amount of computational time. Therefore, the ATG is optimized to improve computational efficiency. The traditional simplified topology and the improved ATG are shown in Figure 1.

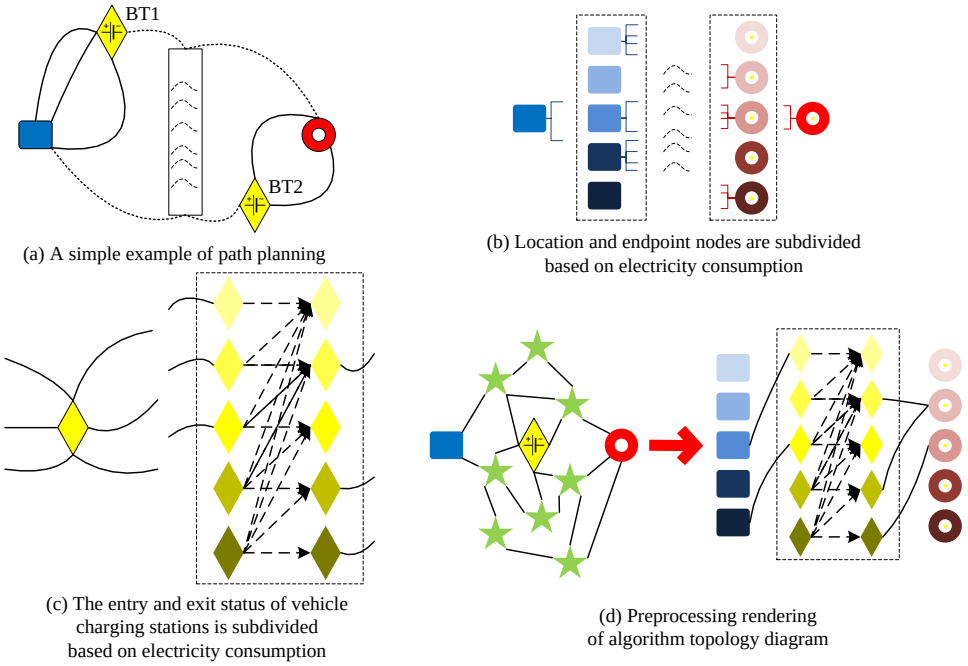

(a) A simple example of path planning

(b) Location and endpoint nodes are subdivided based on electricity consumption

(c) The entry and exit status of vehicle charging stations is subdivided based on electricity consumption

(d) Preprocessing rendering of algorithm topology diagram

Figure 1: Newly constructed algorithm topology graph

Figure 1 (a) shows a simplified topology structure. In Figure 1 (b), based on the remaining power of the vehicles at the starting and ending points, the study divides the starting and ending points into 5 new nodes using a 20% gradient. In Figure 1 (c), the charging station is divided into 10 new nodes based on the remaining battery capacity of the vehicle after leaving the charging point and arriving at the next charging point, using a 20% gradient. The edge formed between two charging points increases from one edge to 15 edges. The study proposes an improved algorithm for preprocessing the topology graph, aiming to evaluate whether to add new edges and remove edges connecting two long-distance charging stations to construct a sparser topology. As shown in Figure 1 (d), an improved topology is obtained by removing these two redundant edges. The specific preprocessing algorithm flow is shown in Figure 2.

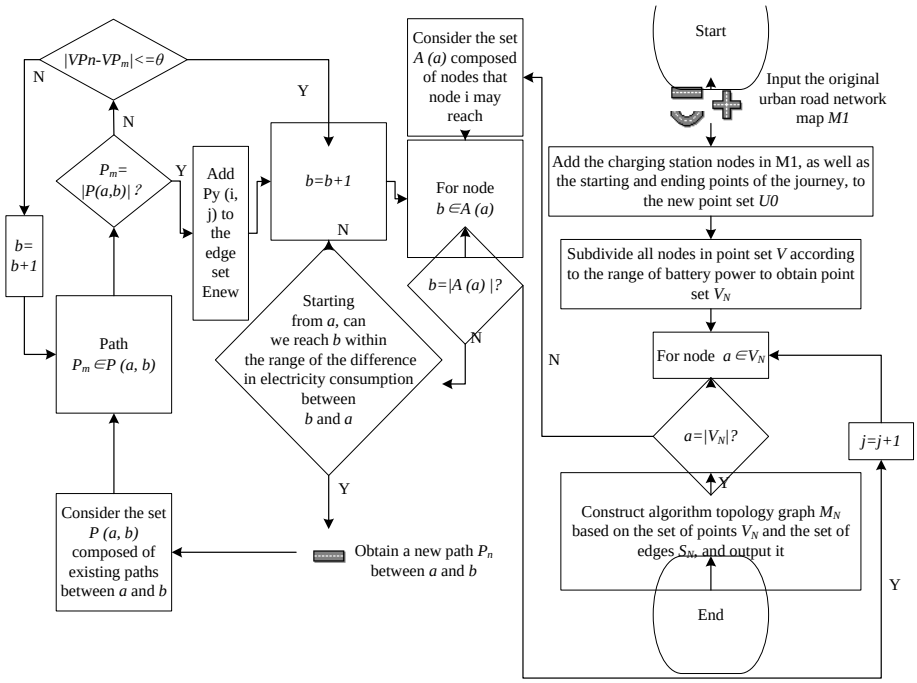

Figure 2: Preprocessing process of algorithm topology graph

In Figure 2, the starting point, ending point, and road network in travel are first heterogeneous into point set $U0$. Based on the above partitioning strategy, a new point set U_N is obtained. Then, whether a is within the U_N is determined. If so, the ATG M_N is constructed based on the point set U_N and edge set S_N. If not, a and b form a new edge P_n from newly generated nodes. If the absolute value of the difference in the comprehensive cost of all existing paths P_m between P_n and a, and b is greater than the threshold P_n, it indicates that the new path P_n can be added to the edge set. The original path will be removed as a redundant path. Through the above algorithm process, topology optimization and simplification are achieved, significantly improving the efficiency and performance of the topology structure.

2.2 Comprehensive cost calculation method for balancing time and charging cost

The improved ATG simplifies complex path planning problems. To find the optimal comprehensive cost solution that balances travel time and charging cost from the improved topology graph, mathematical modeling is performed on the comprehensive cost. The modeling approach is to break down the total cost and calculate it separately. The schematic diagram of total cost division is shown in Figure 3.

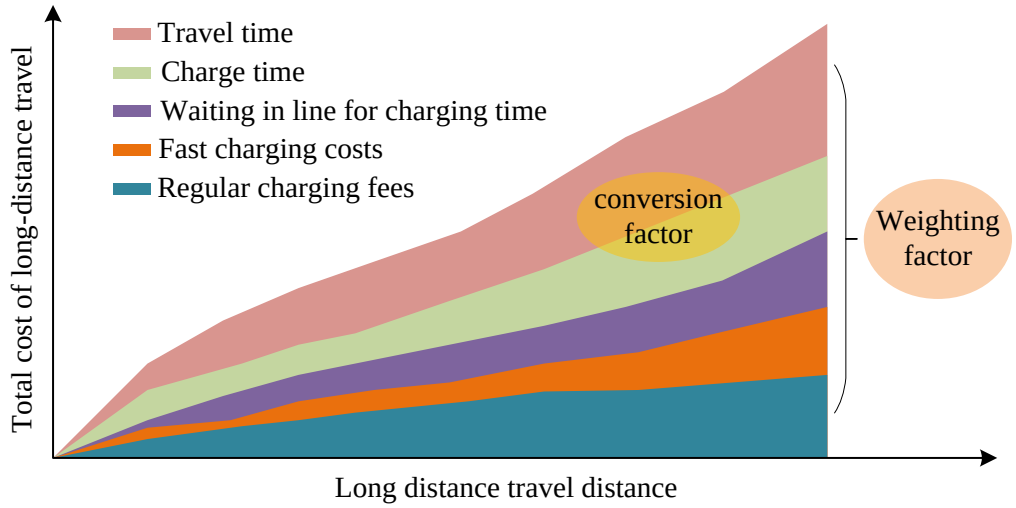

Figure 3: The comprehensive cost of electric vehicle travel

In Figure 3, starting from the starting point, the five types of costs continue to increase as the travel distance increases. Different drivers have different understandings of the value of time and have different requirements for the overall budget. Therefore, different weighting coefficients are set for different drivers regarding driving time, charging time, waiting time for charging, fast charging fees, and regular charging fees. In addition, conversion factors are set for travel time, charging time, and waiting time for charging, converting time into expenses and simplifying the calculation of target cost. Therefore, the comprehensive minimum cost is shown in equation (4).

$$min(A_{all}) = min(\alpha \times \beta T_{all} + (1-\alpha) C_{all}) \quad (4)$$

In equation (4), A_{all} represents the total comprehensive cost. α is the weighting coefficient. β is the conversion factor. T_{all} is the sum of three time sub items. C_{all} represents the total charging cost. Firstly, the total driving time T_d is calculated, as shown in equation (5).

$$T_d = \sum_{a \in U_a} \frac{l_{ai}}{v_{ai}} + \eta_{ai} \times \lambda_{ai} \times \varepsilon_{ai} \quad (5)$$

In equation (5), the road section that the car passes through is set U_a. l_{ai} is the length of road section ai. v_{ai} is the average speed of the road segment calculated based on traffic data. η_{ai} is the set $\{0,1\}$. 1 represents the presence of traffic lights on the road section ai, and 0 represents the absence of traffic lights on the road section ai. λ_{ai} is the probability of a car encountering a red light on section ai. ε_{ai} is the time when cars wait for red lights on the section ai. Then, the total waiting time for charging is calculated. To calculate the waiting time for charging, whether all charging stations are occupied should be considered. The probability P_{ant} of all charging stations being occupied is calculated using equation (6).

$$P_{ant}=\begin{cases}\dfrac{(\dfrac{\varphi_{at}}{\mu_{a,t}})^n}{n!}P_{a0t} & n=1,2,3,4,5,...,W_a \\ \dfrac{(\dfrac{\varphi_{at}}{\mu_{a,t}})^n}{W_a!\ W_a^{n-W_a}}P_{a0t} & n>W_a\end{cases} \quad (6)$$

In equation (6), φ_{at} is the car arrival rate. $\mu_{a,t}$ is the parameter charging rate. W_a is the total number of charging stations. P_{a0t} represents the probability that all charging stations are not used within t. The P_{a0t} is shown in equation (7).

$$P_{a0t}=[\sum_{i=0}^{W_a-1}\frac{(\dfrac{\varphi_{j,t}}{\mu_{j,t}})^i}{i!}+\frac{(\dfrac{\varphi_{j,t}}{\mu_{j,t}})^{W_a}}{W_a!(1-\dfrac{\varphi_{j,t}}{W_a\mu_{j,t}})}]^{-1} \quad (7)$$

In equation (7), i is the count of charging stations in a charging station. According to equation (6), the average queue length S_{at} of charging station a within time slot t is shown in equation (8).

$$S_{at}=\sum_{n=W_a+1}^{\infty}(n-W_a)\times P_{ant}=\frac{(\dfrac{\varphi_{j,t}}{\mu_{j,t}})^{W_a}\times\dfrac{\varphi_{j,t}}{W_a\mu_{j,t}}}{W_a!(1-\dfrac{\varphi_{j,t}}{W_a\mu_{j,t}})^2}\times P_{a0t} \quad (8)$$

According to queue probability, length, etc., the total waiting time for charging in the queue is shown in equation (9).

$$T_W=\sum_{a\in B_a}T_a^{\ w}=\sum_{a\in Ba}\frac{S_{at}}{\varphi_a} \quad (9)$$

Afterwards, the total charging time T_C is shown in equation (10).

$$T_C=\sum_{a\in B_a}T_a^{\ C}=\sum_{a\in Ba}\frac{E_a}{Q_a\chi}=\sum_{a\in Ba}\frac{E_a^{\ live}-E_a^{\ arrive}}{Q_a\chi} \quad (10)$$

In equation (10), $E_a^{\ live}$ is the amount of electricity that the car leaves a. $E_a^{\ arrive}$ is the amount of electricity that the car reaches a. E_a is the amount of electricity stored. Q_a is the power of the a charging station. After obtaining the three-time costs, the charging fees are calculated separately. The regular charging fee is equal to the cost in a regular parking lot. The study considers that cars discharge electricity in the parking lot to obtain partial income from the power grid. Therefore, the detailed composition of the total cost breakdown is shown in Figure 4. As shown in Figure 4, driving time consists of driving time and waiting time at red lights, while the slow charging fee is the difference between the charging fee and the discharge income. The fast-charging fee C_f is shown in equation (11).

$$C_f=Q_f\sum_{a\in Ba}\sum_{t=t_a+T_a^W}^{t=t_a+T_a^W+T_a^C}\times\partial_t\times\Delta T \quad (11)$$

In equation (10), t_a is the time to reach the a charging station. ΔT is the time spent on decision-making. Q_f is the fast charging power. ∂_t is a tiered electricity price. The ordinary charging fee C_S is shown in equation (12).

$$C_S=Q_s\sum_{t=T_e}^{T_{ns}}\partial_t\eta\Delta T-Q_{dis}\sum_{t=T_e}^{T_{ns}}\gamma_t\eta_t\Delta T \quad (12)$$

In equation (12), γ_t represents the purchase price of electricity from the power grid. T_e is the end time of this trip. T_{ns} is the start time of the next trip. Q_{dis} is the discharge power. Q_s is the slow charging power.

2.3 Construction of comprehensive cost travel path planning model based on ATG-ACO

The preprocessed ATG is introduced into the path optimization algorithm to obtain the optimal path for electric vehicle travel. Considering that the preprocessing process of ATG includes judgment and feedback mechanisms, and finding the optimal path from a topology with numerous elements is a highly complex problem, the study introduces ACO. The ACO algorithm has the characteristics of positive feedback, self-organization, and global search, making it very suitable for complex path planning [15]. The principle of ACO is shown in Figure 5.

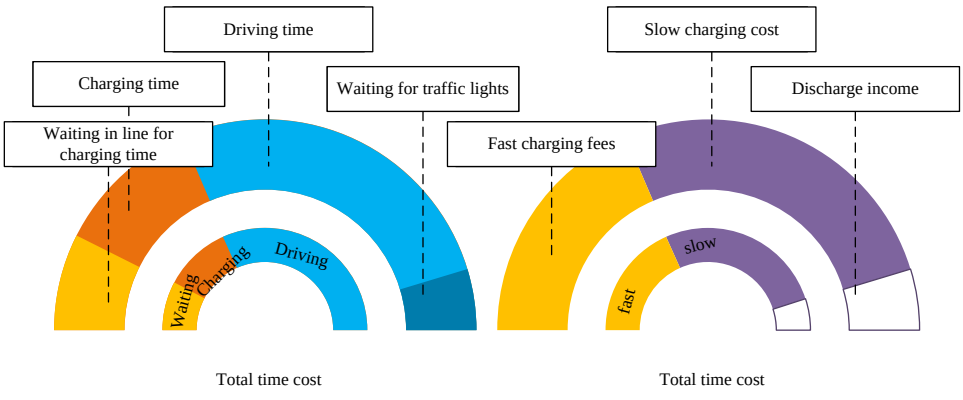

Figure 4: Detailed composition of total cost

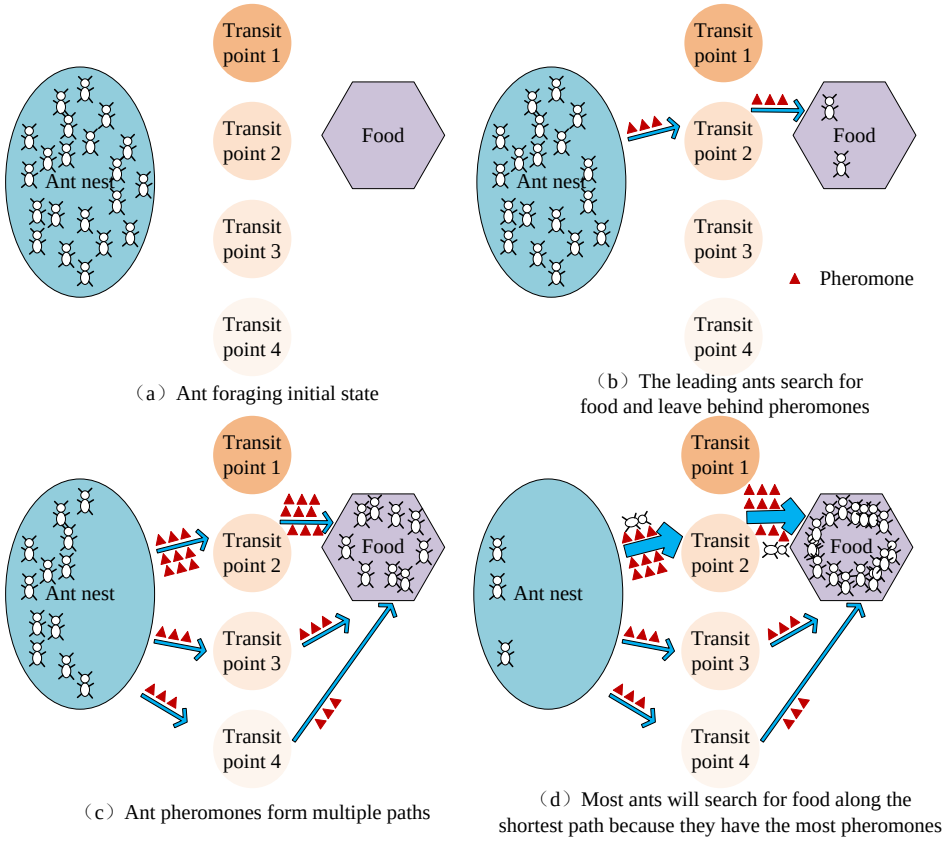

Figure 5: Ant algorithm schematic diagram

Figure 5 (a) shows the initial state of ants foraging, with four passing points in the ant nest away from food. In Figure 5 (b), the leading ant passes through point 2 to reach the food, leaving behind pheromones between them. In Figure 5 (c), a large number of ants reach the food, leaving behind pheromones that form multiple paths. In Figure 5 (d), Path 2 leaves the most pheromones, and most ants will search for food along this shortest path. Ants leave more pheromones on the path of the optimal solution through the action of pheromones, attracting ants to choose this path and guiding the ant colony to the optimal path. The path finding process of applying ACO to ATG is as follows. Firstly, the initialization parameters include the number of ants A_s, the total amount of released pheromones, volatility factor ϑ, importance factor π, the importance factor ψ of the heuristic function, the number of iterations δ, and the concentration of pheromones ω. If charging station b is adjacent to charging station a, then the edge ω_{ab} between a and b is 1. If not adjacent, then ω_{ab} is 0. Ants start from the starting point and reach the next node according to probability p_{ab}^{δ}. The probability calculation for ants from node a to node a is shown in equation (13).

$$p_{ab}^{\delta}=\begin{cases}\dfrac{[\omega_{ab}]^{\vartheta}[\Delta]^{\pi}}{\sum_{b\in B_a}[\omega_{ab}]^{\vartheta}[\Delta]^{\pi}}, & b\in B_a\\ 0, & b\notin B_a\end{cases} \tag{13}$$

In equation (13), Δ is the heuristic function [16]. When all ants in the δ-th iteration stop searching, the time and charging cost of the electric vehicle represented by all ants to the endpoint are calculated, and obtain the local optimal solution for the δ-th iteration. The path decision variable x_{ab} is updated based on the arrival of ants at the node. The decision variable is shown in equation (14).

$$x_{ab}=\begin{cases}1, & b\ \ is\ \ selected\\ 0, & b\ \ isn't\ \ selected\end{cases} \tag{14}$$

In equation (14), when $x_{ab}=1$, the vehicle's battery level represented by the ant is updated. The battery level update calculation is shown in equation (15).

$$q_{ant}{}'=q_{ant}-\sum_{b\in allowed_{a,ant}}x_{ab}\times Dis(x_{ab})\times\overline{E}_1 \tag{15}$$

In equation (15), q_{ant}' is the updated electricity level. $\overline{E_1}$ and $Dis(x_{ab})$ represent the power consumption per unit distance and the distance of a and b, respectively. If the ant fails to find the global optimal solution, it updates the pheromone for the next iteration and triggers a positive feedback mechanism. The pheromone updating is shown in equation (16).

$$\omega_{\delta+1} = (1-\vartheta)\omega_{\delta} + \sum_{R=1}^{R} \Delta\delta^{R} \tag{16}$$

In equation (16), $\omega_{\delta+1}$ represents the concentration of pheromones after the next iteration. R is the number of ants that reach the endpoint after $\delta+1$ iterations. $\Delta\delta^{R}$ is the pheromone increment [17]. The pheromone increment is shown in equation (17).

$$\Delta\delta^{R} = \frac{\square}{A_{T,C}^{R}} \tag{17}$$

In equation (17), $A_{T,C}^{R}$ is the distance to the destination. The calculation method for determining whether to continue iteration is shown in equation (18).

$$\delta_{next} = \delta_{n} + 1 < \delta_{max} \tag{18}$$

The above steps are repeated to the maximum number of iterations δ_{max}. The ants search for the global optimal solution. The above process uses ant simulation to find the optimal path for electric vehicles. The process of searching for the optimal comprehensive cost in the preprocessed topology is shown in Figure 6.

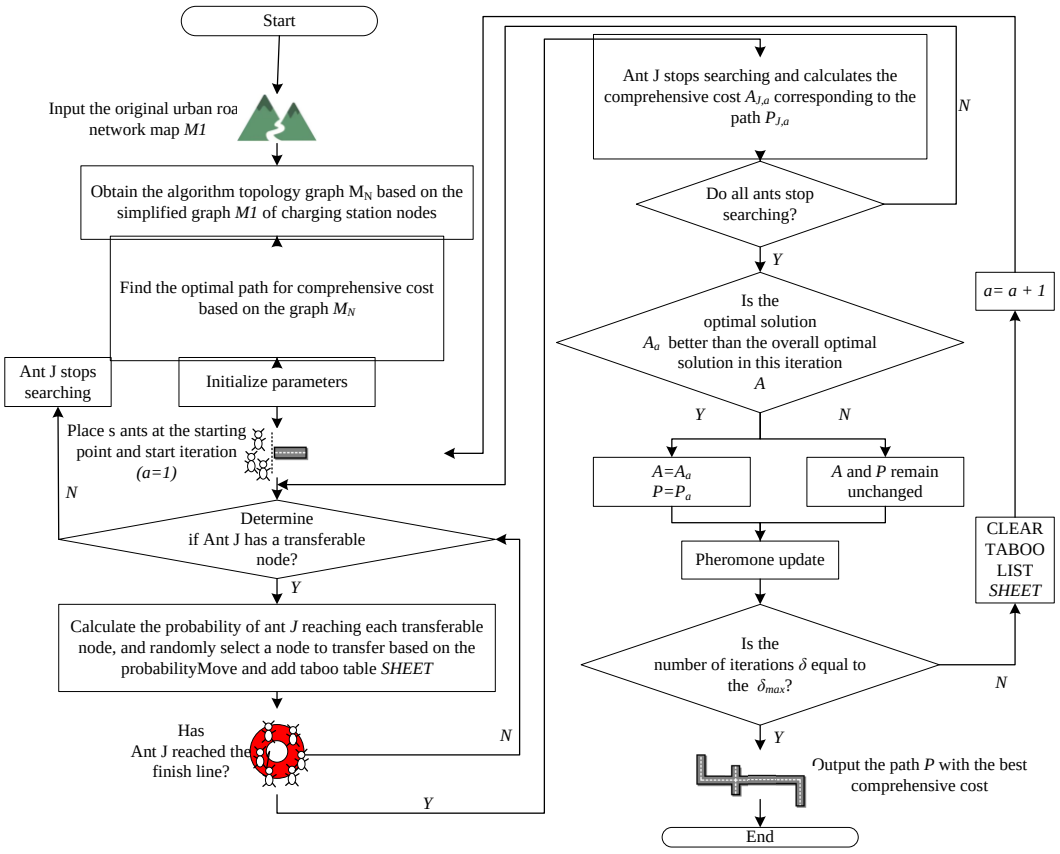

Figure 6: A Topology preprocessing ant colony path optimization algorithm framework

As shown in Figure 6, the road network diagram $M1$ is first heterogeneous into an improved ATG M_N. Then, ants simulate the travel scenario of electric vehicles, randomly select charging nodes from the starting point on the journey, and optimize the selected path through iteration. Finally, the most cost-effective travel route is determined.

3 Results

The travel path planning model based on ATG-ACO algorithm is simulated and tested. A simulation environment using road network $M1$ is established, and relevant parameters are set.

The improved ATG-ACO algorithm is iteratively trained to test the convergence efficiency of the algorithm. The ACO is compared with ATG-ACO algorithm to analyze the effect of the ATG on improving computational efficiency. Finally, a comparative experiment is conducted between the designed model and other models to verify that the proposed model can find the optimal path considering time and charging cost.

3.1 Simulation environment and parameter settings

To simulate a real environment, the electricity step tariff in C1 city and the charging station parameters in the parking lot at Ya are selected as experimental data. The detailed information of the sample is shown in Table 2.

Table 2: Data samples selected from the case western storage bearing dataset

Electric vehicle parameters		Charging station parameters		Parking lot parameters		Time-of-use			
Parameter	Value	Parameter	Value	Parameter	Value		Peak period	Ordinary segment	Low valley section
Unit energy consumption (kWh/km)	0.15	Charging power	90	Charging power (kW)	20	Period of time	7:00-11:00	23:00-7:00 the next day	11:00-19:00
	22.6	Charge efficiency	80%	Discharge power (kW)	20		19:00-23:00		
Battery capacity (kWh)	/	Profit coefficient	Random numbers between [1,1.5]	Charge efficiency	80%	Charging price	1.3155	0.0.8399	0.3822
/	/	/	/	Discharge efficiency	80%	Electricity purchase price	/	0.8399	/

The study selects ACO without ATG as the comparison object with path planning models based on DPO, QLPO, and PGAPO proposed by another research.

3.2 Analysis of iterative convergence and computational efficiency of ATG-ACO

After constructing a simulation experimental environment, the ATG-ACO algorithm is iteratively trained and compared with other algorithms. The experimental results are shown in Figure 7. In Figure 7, the research algorithm converged after 23 iterations, and the calculated optimal cost was 38. The QLPO algorithm converged after 74 iterations, and the optimal cost was 49. The convergence speed of PGAPO algorithm and DPO algorithm was relatively slow. PGAPO converged after 90 iterations, with an optimal cost of 73. The DPO algorithm fluctuated up and down as the number of iterations increased, and still did not converge after 120 iterations. From this, the proposed ATG-ACO has better convergence speed than other algorithms, and the optimal planning cost is the lowest. To analyze the improvement effect of improved topology in ATG-ACO, a comparative experiment is conducted between ACO and ATG-ACO. The results are shown in Figure 8.

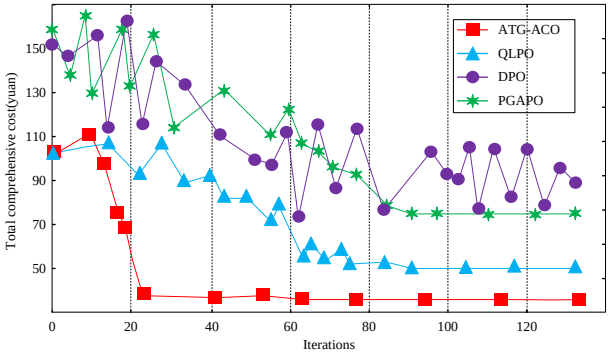

Figure 7: Comparison chart of algorithm iteration training convergence

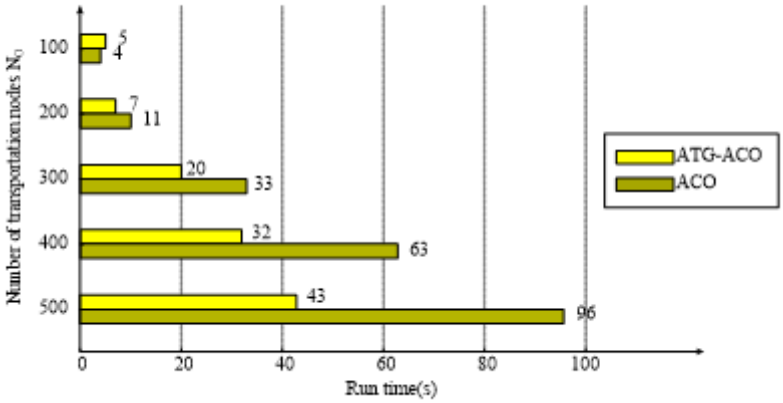

Figure 8: Comparative experimental results of ATG and ATG-ACO

In Figure 8, with 100 traffic points, the ATG-ACO algorithm took 1s longer than the ACO algorithm. As the number of traffic points increased, the ATG-ACO algorithm took less time than the ACO algorithm. The differences were more pronounced when there were multiple traffic points. When the number of traffic points was 300, the ATG-ACO algorithm took 20s, while the ACO algorithm took 33s. When the number of transportation nodes was 500, the ATG-ACO algorithm took only 43s, less than half of the time of the ACO algorithm. The results indicate that topology preprocessing has a great promoting effect on ant algorithm in finding the optimal solution.

3.3 Comprehensive cost control analysis of travel path planning model based on ATG-ACO algorithm

The above experiment shows that the ATG-ACO algorithm has better computational efficiency. The study compares the ATG-ACO path planning model with other models mentioned above. The charging cost results after multiple simulation experiments are averaged, as shown in Figure 9. In Figure 9, as the weighting coefficient of travel time increased from 0 to 1, the total charging cost of the optimal path planned by the ATG-ACO model gradually increased from 35 to 48 yuan. When the weight coefficient of the QLPO model was 0.25, the charging cost decreased to the lowest value of 29 yuan, and increased to 37 yuan as the weight value increased. From Figure 9, the DPO model is most affected by the weighting coefficient, with the largest increase, and the total charging cost increases from 35 yuan to 67 yuan. However, the QLPO model is least affected by weighting coefficients, and the charging cost remains around 47 yuan. From this, the weighting coefficient, when only considering the total charging cost during long-distance travel for path optimization planning, is not entirely superior to other path planning models, because the designed model not only considers charging cost but also balances the time cost of travel. The total travel time after multiple simulation experiments to obtain the average value is shown in Figure 10.

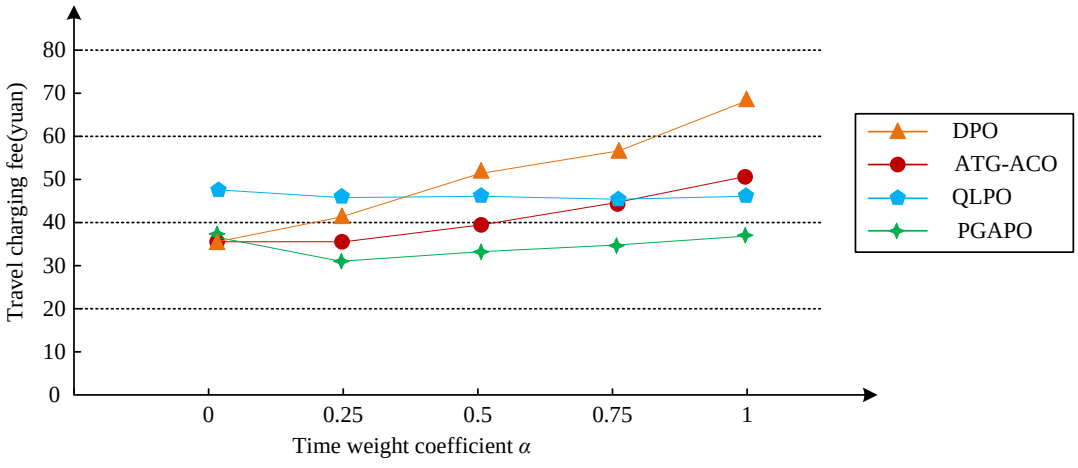

Figure 9: Nightingale diagram of three experimental results

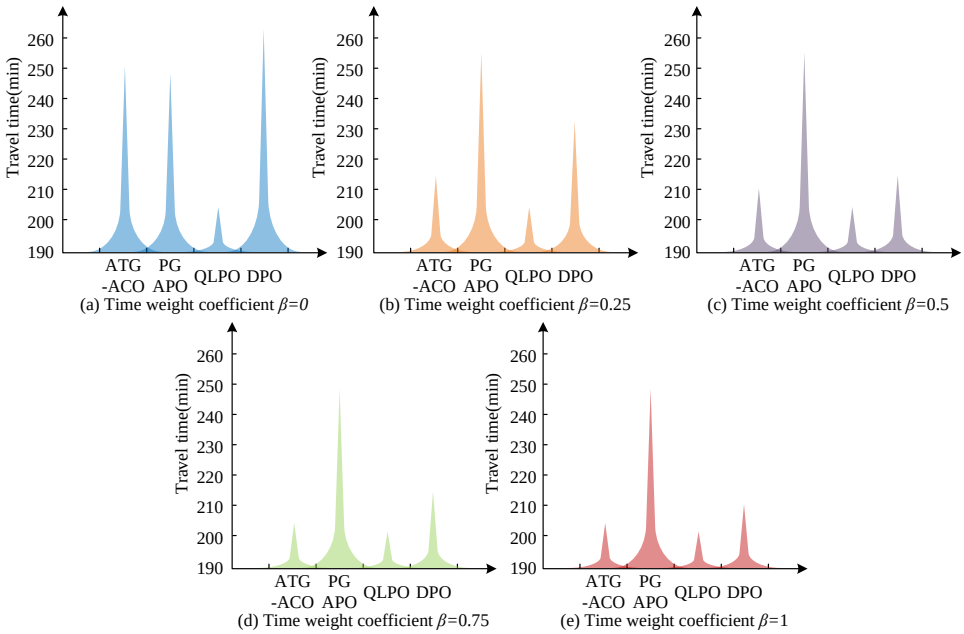

Figure 10: The total travel time results of various model comparison experiment

In Figure 10 (a), the total time of the ATG-ACO model was 252s, which was better than the total time 264s of the DPO, but 59s more than the QLPO. The total time of the ATG-ACO model in Figure 10 (b) was 213s, which was also better than the PGAPO and DPO models, but 10s longer than the QLPO. The total optimal path time of the ATG-ACO model in Figures 10 (c), 10 (d), and 10 (d) were 209s, 204s, and 203s, respectively, which were close to the QLPO and significantly lower than the PGAPO and DPO models. From this, when only considering the single time cost, ATG-ACO is not entirely superior to other models. The study converts the total time into the total charging cost through a conversion coefficient. The experimental results considering the total comprehensive cost are shown in Figure 11. From Figure 11 (a), due to the conversion coefficient, the lowest comprehensive cost of the ATG-ACO model was 78 yuan, and the highest value was 88 yuan. Regardless of the weighting coefficient, it is superior to other models. The proposed ATG-ACO model is the optimal model for path planning, taking into account the balance between travel time and charging cost.

4 Discussion

This study compares the performance of the ATG-ACO and analyzes the comprehensive cost control effect of the travel path planning model based on the ATG-ACO algorithm. The results showed that the ATG-ACO algorithm exhibited significant advantages in convergence speed and computational efficiency in optimal path planning. In the comparison of convergence curves, the ATG-ACO algorithm completed convergence after the 23rd iteration, with a total cost of 38 lower than other algorithms. This result is similar to the results obtained by Abdullah et al. in their study combining improved ATG and ACO [18]. This result indicates that the ATG-ACO algorithm can quickly find the optimal solution, and improve the

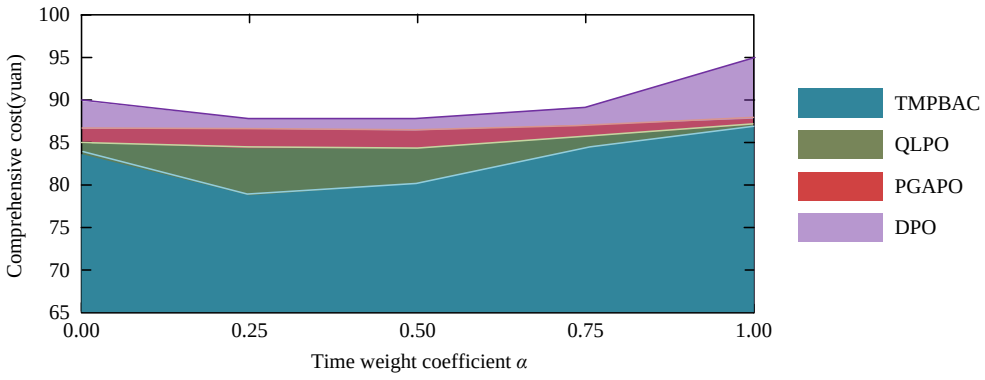

Figure 11: Comparison of four algorithms for fault recognition in three parts

computational efficiency of the optimal path. It can be promoted in practical travel path planning. In the analysis of the improvement effect of ATG preprocessing, when the traffic node reached 500, adding the ATG-ACO algorithm took only 43s, which was more than half of the time compared with the ant algorithm without ATG. The improved ATG improved the efficiency of ant algorithm in finding the optimal path. Feng et al. reached similar conclusions when conducting topology optimization on discrete structures in 2023 [19]. This result indicates that the improved topology has a clear and simplified structure, which can be used to design more efficient models for path planning. From the above results, the improved ATG algorithm can remove redundant paths. Combining with the ACO algorithm can not only improve iteration efficiency, but also avoid getting stuck in local optima and reduce computational cost, which other expensive algorithms do not have these effects. Finally, in the analysis of the comprehensive cost control effect of the ATG-ACO model, the results showed that when only considering a single cost of time or charging fees, the proposed model was not entirely superior to other models. However, considering both travel time and charging cost, the ATG-ACO model was completely superior to other models. Under different weighting coefficients, the average total cost of the research model was 7%-26% lower than other models. This result is similar to the research findings of Nadjib and Ammar in combining ATG and ACO algorithms [20]. From the above results, the research model introduces the conversion coefficient to convert the multi-objective problem into a single-objective problem, introduces the weighting coefficient to balance the weight of time and cost, and adopts PSO for optimization, so as to minimize the total cost. Other models do not have such powerful nonlinear programming capabilities, so the effect of the research model is better than other models. This result indicates that the travel path planning model based on the ATG-ACO algorithm meets the optimization requirements for travel paths that comprehensively consider travel time and charging cost. There is much research closely related to the path planning of electric vehicles. The intelligent algorithm greatly improves the superiority of path planning. However, the addition of conversion coefficient and weighting coefficient for different groups to balance the charging cost and travel time is a unique contribution of the research.

5 Conclusion

The study focused on how to comprehensively consider travel time and charging cost to plan paths during long-distance driving of electric vehicles. The improved ATG was combined with the ant path optimization algorithm. The combined method is used to calculate total travel cost. Then, a path optimization model was constructed. The research model introduced a topology graph to heterogeneous roads during travel, and improved the ATG. The ant algorithm was introduced into the preprocessed topology graph to form a new optimization algorithm for finding the optimal path. Combining the combination algorithm with the comprehensive total cost calculation method and iteratively finding the optimal path, an electric vehicle travel path optimization model considering balance time and charging cost was constructed. The study conducted simulation experiments. The simulation results showed that the improved ATG had a great promoting effect on ant algorithm path planning. The research model had a better balance effect than other models in considering the total travel time and total charging cost, and the comprehensive total cost of the optimal path was the lowest. Path planning is a particularly complex systemic problem, especially when long-distance travel is influenced by many factors. In addition to the electricity level and charging and discharging status mentioned in the article, there are other factors, including electric vehicle malfunctions, temporary traffic accidents, and congestion. Although the probability of an event occurring is extremely low, it can also have impacts on the travel path and total cost, which is also an area that needs improvement in the future.

References

[1] V. Boglou, A. Christos-Spyridon Karavas, Karlis, and K. Arvanitis, “An intelligent decentralized energy management strategy for the optimal electric vehicles' charging in low-voltage islanded microgrids,” International Journal of Energy Research, vol. 46, no. 3, pp. 2988-3016, 2022. https://doi.org/10.1002/er.7358

[2] D. P. Kumar, B. M. Younus, and S. Shambhu, “Life cycle assessment of electric vehicles: a systematic review of literature,” Environmental Science and Pollution Research, vol. 31, no. 1, 73-89, 2024. https://doi.org/10.1007/s11356-023-30999-3

[3] J. Nishanthy, S. C. Raja, T. Praveen, J. J. D. Nesamalar, and P. Venkatesh, “Techno-economic analysis of a hybrid solar wind electric vehicle charging station in highway roads,” International Journal of Energy Research, vol. 46, no. 6, pp. 7883-7903, 2022. https://doi.org/10.1002/er.7688

[4] T. Zhao, D. Cao, J. Yao, and S. Zhang, “Topology optimization algorithm for UAV formation based on wireless ultraviolet communication. Photonic Network Communications,” vol. 45, no. 1, pp. 25-36, 2023. https://doi.org/10.1007/s11107-022-00989-5

[5] Y. Li, C. Wang, W. Cao, D. and Hou, C. Zhang, “Motion characteristics simulations of supercavitating vehicle based on a three-dimensional cavity topology algorithm,” Applied Mathematical Modelling, vol. 115, no. 1, pp. 691-705, 2023. https://doi.org/10.1016/j.apm.2022.11.008

[6] L. Lucky, and A. S. Girsang, “Hybrid nearest neighbors ant colony optimization for clustering

social mMedia comments," Informatica, vol. 44, no. 1, pp. 63-74, 2020. https://doi.org/10.31449/inf.v44i1.2672

[7] L. Huo, "The global path planning for vehicular communication using ant colony algorithm in emerging wireless cloud computing," Wireless Networks, vol. 29, no. 2, pp. 833-842, 2023. https://doi.org/10.1007/s11276-022-03152-0

[8] H. Wang, "Research on data transmission optimization of communication network based on reliability analysis," Informatica, vol. 44, no. 3, pp. 361-366, 2020. https://doi.org/ https://doi.org/10.31449/INF.V44I3.3280

[9] D. Xia, B. Shen, Y. Zheng, W. Zhang, D. Bai, Y. Hu, and H. Li, "A bidirectional-a-star-based ant colony optimization algorithm for big-data-driven taxi route recommendation," Multimedia Tools and Applications, vol. 83, no. 6, pp. 16313-16335, 2024. https://doi.org/10.1007/s11042-023-15498-4

[10] Z. R. Dong, X. Y. Bian, and S. Zhao, "Ship pipe route design using improved multi-objective ant colony optimization," Ocean Engineering, vol. 258, no. 15, 1-14, 2022. https://doi.org/10.1016/j.oceaneng.2022.111789

[11] T. Zhao, A. A. Alshannaq, D. W. Scott, and G. H. Paulino, "Strut-and-tie models using multi-material and multi-volume topology optimization: load path approach," ACI Structural Journal, vol. 120, no. 6, pp. 7-22, 2023. https://doi.org/10.14359/51739089

[12] K. Li, and G. Cheng, "Structural topology optimization of elastoplastic continuum under shakedown theory," International Journal for Numerical Methods in Engineering, vol. 123, no. 19, pp. 4459-4482, 2022. https://doi.org/ 10.1002/nme.7041

[13] M. Montemurro, T. Roine, and J. Pailhes, "Multi-scale design of multi-material lattice structures through a CAD-compatible topology optimisation algorithm," Engineering Structures, vol. 273, no. 15, pp. 74-91, 2022. https://doi.org/10.1016/j.engstruct.2022.115009

[14] J. W. Han, S. Jeon, and H. J. Kwon, "Hierarchical Topology Map with Explicit Corridor for global path planning of mobile robots," Intelligent Service Robotics, vol. 16, no. 2, pp. 195-212, 2023. https://doi.org/ 10.1007/s11370-023-00458-6

[15] M. B. Sushma, S. Roy, and A. Maji, "Exploring and exploiting ant colony optimization algorithm for vertical highway alignment development," Computer-aided Civil and Infrastructure Engineering, vol. 37, no. 12, pp. 1582-1601, 2022. https://doi.org/10.1111/mice.12814

[16] H. Zheng, J. Guo, Q. Zhou, Y. Peng, and Y. Chen, "Application of improved ant colony algorithm in load balancing of software-defined networks," Journal of Supercomputing, vol. 79, no. 7, pp. 7438-7460, 2023. https://doi.org/10.1007/s11227-022-04957-8

[17] Z. Tang, H. Ma, "Path guidance method for unmanned vehicle based on improved potential field ant colony algorithm. International Journal of Vehicle Design," vol. 89, no. 1, pp. 84-97, 2022. https://doi.org/10.1504/ijvd.2022.10053059

[18] A. M. Abdullah, E. Ozen, H. Bayramoglu, "Energy efficient MANET routing protocol based on ant colony optimization," Ad Hoc & Sensor Wireless Networks, vol. 47, no. 1, pp. 73-96, 2020.

[19] F. Feng, S. Xiong, Z. Liu, Z. Xian, Y. Zhou, H. Kobayashi, A. Kawamoto, T. Nomura, and B. Zhu, "Cellular topology optimization on differentiable voronoi diagrams," International Journal for Numerical Methods in Engineering, vol. 124, no. 1, pp. 282-304, 2023. https://doi.org/10.1002/nme.7121

[20] N. Benaouda, A. Lahlouhi, "Ant-based delay-bounded and power-efficient data aggregation in wireless sensor networks," International Journal of Pervasive Computing and Communications, vol. 15, no. 2, pp. 97-119, 2019. https://doi.org/10.1108/IJPCC-04-2019-0037

Multi-hop Network Security Strategy Integrating ACO Algorithm and PSO Algorithm

Qian Hao*, Haixin Huang
Electronic Information Engineering College, Henan Polytechnic Institute, Nanyang, 473000, China
E-mail: haoqian_hao@outlook.com
*Corresponding author

Keywords: multi-hop network, particle swarm optimization algorithm, ant colony abnormal data detection, punishment factor

Received: November 5, 2024

Multi-hop networks are widely used due to their wide coverage and strong adaptability. However, multi-hop networks are prone to attacks and user privacy breaches when transmitting data between nodes. Therefore, a multi-hop network security protection strategy binding particle swarm optimization algorithm and ant colony algorithm was proposed. Support vector machine was utilized for data sorting, and the particle swarm algorithm was improved using inertia weight coefficients. The heuristic function and pheromone update strategy of ant colony algorithm was optimized, and the penalty factor and kernel function of support vector machine were optimized using fusion algorithm. The experimental results showed that the information exposure probability of the fusion algorithm decreased from the initial 0.35% to 0.10%, the detection accuracy was 2.9% higher than that of the second-best method, respectively, and the hazardous response time, disposal time, and root-mean-square error were faster than that of the second-best method by 19.9ms, 22.7ms, and -2.3ms. The running cost of the fusion algorithm was 210 datasets lower than that of the second-best method, and the average computation time was only 27.2ms higher than the normal support vector machine, and the time complexity was lower for all of them. From this, it can be concluded that fusion algorithms can effectively enhance the detection capability of abnormal data, reduce the probability of user privacy data exposure, decrease algorithm operating costs, and improve the response and handling speed of multi-hop networks when facing attacks.

Povzetek: Predlagana je strategija varovanja večskokovnih omrežij, ki združuje algoritma optimizacije roja delcev (PSO) in kolonije mravelj (ACO), izboljšuje zaznavo anomalij ter zmanjšuje stroške in tveganja izpostavljenosti podatkov.

1 Introduction

Multi-hop relay technology is a wireless communication technology proposed by the United States in the 1970s, which forms a self-organizing network through mobile nodes and relay nodes. It has been widely used in communication systems such as satellite relay, microwave relay, and battlefield communication [1]. As mobile communication technology advances, multi-hop networks, which offer benefits like swift long-distance transmission speeds and extensive coverage, are gaining widespread adoption [2]. Multi-hop networks transmit data through multiple intermediate nodes, each of which can be a sender or receiver. Communication tasks can be completed between any two nodes, and even if a node or link fails, other paths can be used to complete data transmission [3-4]. Multi-hop networks can also communicate with distant nodes by changing the data transmission range of individual nodes [5-6]. However, due to the large number of nodes, multi-hop networks are vulnerable to attacks and can lead to the leakage of user privacy data. Existing multi-hop network security protection strategies have problems such as low accuracy in detecting irregular data, insufficient detection precision, and high operating costs. To address the security issues of multi-hop networks, Singh et al. proposed a new quantum atomic search optimization combined with blockchain to solve problems such as collusion attacks, latency, and lifecycle extension in wireless self-organizing networks. This scheme adopted quantum atomic search to choose the optimal relay point for complex multi-hop transmission, and performed data transmission on the blockchain to ensure system security. Experiments showed that the throughput of this method reached 91.5%, energy consumption was reduced to 40%, end-to-end latency was reduced by 20.6%, and security performance was significantly improved [7]. Ezzati Khatab et al. proposed a machine learning relay assisted authentication method for dual hop multi-input multi-output systems to solve the authentication problem in wireless networks. This method used channel characteristics for end-to-end authentication, and to simulate actual situations, defective hardware was used for channel estimation. Experiments showed that this method significantly improved authentication performance, with authentication accuracy exceeding 90% in both single hop and multi-hop scenarios [8].

Mahapatra et al. raised a novel bidirectional butterfly optimization algorithm grounded on clustering tree enhancement to solve the security matters of underwater wireless ad hoc networks. The algorithm designed clusters based on data routing protocols in the first stage, evaluated the trust value of each node using fusion rules in the second stage, and allocated secure channels for data transmission in the third stage. The test reflected that the packet delivery rate of this algorithm reached 90%, the energy consumption was reduced to 0.14J, the network lifetime of 200 rounds was 732s, and the end-to-end delay was 0.12 s, which was significantly better than other algorithms [9]. Pattanayak et al. proposed a new decoding and forwarding protocol grounded on multi-hop hybrid radio frequency and free space optics for the data confidentiality capability of multi-hop networks. This protocol selected a received signal with high confidentiality capability at each hop, and each node in the system was attached to its subsequent nodes through parallel radio frequency and wireless optical communication connections. The experiment showed that the confidentiality interruption probability of this protocol was low, the strict positive confidentiality ability was high, and the confidentiality performance was better than other methods [10]. Altuwairiqi proposed a new multi-hop routing optimization scheme based on improved honey badger algorithm in order to solve the security and energy problems of multi-hop networks. The scheme used the Improved Honey Badger algorithm to select the optimal number of hops and utilized a trust model incorporating indirect and direct trust, data, integrity, and forwarding rate to achieve security-conscious multi-hop routing. Experiments showed that the total number of data received by this scheme under the same conditions was much larger than other methods and the information exposure probability was on average 3.47% lower than other methods [11]. Altowaijri et al. proposed an efficient multi-hop routing protocol in order to ensure the transmission efficiency and security of wireless sensor networks. This protocol considered rank-based next hop selection mechanism, selected the appropriate route for data exchange based on residual energy, extracted residual energy of all nodes and evaluated it based on connectivity. Experiments showed that this protocol outperformed the existing methods in terms of production time, time slot, communication loss, first node failure, and residual energy [12].

Tan et al. raised a new fusion way of particle swarm optimization (PSO) algorithm and ant colony optimization (ACO) algorithm for the initial parameter selection problem of ACO algorithm. This method applied PSO algorithm to practice the original parameters of ACO algorithm, and then used ACO algorithm to calculate the optimal path. The experiment indicated that the average route length achieved by this way was 473.25mm lower than traditional algorithms, and the average iteration number of the improved method was 17 times [13]. Zheng et al. proposed a new improved ACO load balancing algorithm to achieve flexible control and management of network traffic. This algorithm designed evaluation methods for server modules and interlinkage modules, using the Kent chaos model to mess with the transition probability of ant colonies. Tests proved that this way could validly prevent the algorithm from falling into local optima, with fast convergence speed and achieving good global load balancing [14].

In summary, existing methods have explored the security protection of multi-hop networks and the integration of PSO and ACO algorithms from various aspects. However, existing methods have problems such as low accuracy in detecting irregular data in multi-hop networks, insufficient detection accuracy, and high operating costs. Therefore, a multi-hop network security protection method combining PSO algorithm and ACO algorithm was proposed. The innovative fusion algorithm optimized the penalty factor (PF) and kernel function (KF) of support vector machine (SVM), improved the PSO algorithm using inertia weight coefficient, and optimized the initiation function and pheromone update strategy of ACO algorithm. The improvement method aims to enhance the accuracy of anomaly data detection in multi-hop networks, reduce the probability of information exposure when nodes are attacked, and decrease operating costs. This research is separated into three sections. The first section combines PSO algorithm and ACO algorithm for multi-hop network anomaly detection. The second part estimates the behaviour of the fusion algorithm. The third part is a generalization of this research and expectations for further exploration targets.

Based on the above relevant studies, Table 1 is summarized, in which the research theme, main index methods, and shortcomings of relevant studies are summarized.

Table 1: Summary of relevant information of relevant studies

Docu	Research theme	Main index	Method	Insufficient
Document [7]	Solve the conspiracy attack	Throughput, power consumption, and latency	Quantum atoms search for relay nodes	High degree of complexity
Document [8]	Multi-hop network authentication	Authentication accuracy	End-to-end verification of channel characteristics	Rising network energy consumption
Document [9]	Wireless AD hoc network security	Transmission efficiency, energy	Two-way butterfly optimization algorithm	The recognition accuracy is low

		consumption and lifetime		
Document [10]	Data privacy capability	Information leakage probability	Multi-hop hybrid RF and free-space optics	The specific attack detection capability is insufficient
Document [11]	Multi-hop network security and energy consumption	Information exposure probability and energy consumption	Improved honey badger algorithm	The calculation time is long
Document [12]	Wireless network transmission efficiency	Power consumption and probability of communication loss	Next hop selection mechanism based on rank	Model running cost is high
Document [13]	ACO algorithm parameter selection	Average path length	The combination of PSO algorithm and ACO algorithm	The improved model is more complex
Document [14]	Flexible control of network traffic	Load balancing	Kent chaos model optimization transition probability	The detection accuracy of the improved method is low
This study	Security of multi-hop networks	Information exposure probability, detection accuracy and response time	Fusion of PSO algorithm and ACO algorithm	/

Based on the above related research, although the current research explores the security protection of multi-hop networks and the fusion of PSO algorithms and ACO algorithms from various aspects, the existing methods have the problems of lower accuracy in detecting anomalous data in multi-hop networks, insufficient detection accuracy, and higher operating costs. Therefore, the research innovatively adopts support vector machine for data classification, uses inertia weight coefficients to improve the PSO algorithm, optimizes the heuristic function and pheromone updating strategy of the ACO algorithm, and adopts the fusion algorithm to find the optimization of the penalty factor and kernel function of the support vector machine. It can reduce the probability of user privacy exposure and improve the response speed.

2 Methods and materials

2.1 Improved PSO algorithm based on SVM for Multi-hop network anomaly detection

When transmitting data in a multi-hop network, it needs to go through multiple intermediate nodes for forwarding, which gives attackers an opportunity. The traffic data passing through a running multi-hop network can be roughly divided into normal traffic data and abnormal behavior traffic data. Multi-hop network security detection essentially classifies the two types of data through a preset system. The research adopts the SVM algorithm, which is computationally simple, has fewer parameters, and has a faster learning speed, for multi-hop network anomaly detection. SVM can process both linear and nonlinear data simultaneously. When processing nonlinear data, high-dimensional mapping is required first to convert nonlinear data into linear data [15]. High dimensional mapping generates two parallel hyperplanes, and the larger the distance between the hyperplanes, the better the classification performance of SVM. The distance calculation of the hyperplane is shown in equation (1).

$$\begin{cases} \dfrac{2}{|\omega|} \\ \omega^T x + b = 0 \end{cases} \tag{1}$$

In equation (1), $\frac{2}{|\omega|}$ means the distance of the hyperplane, ω means the normal vector, T represents a point in the hyperplane, x represents the vector of that point, and b represents the set threshold. When partitioning difficult to segment linear data, relaxation variables and PFs are introduced to determine the constraint conditions of the hyperplane [16]. The constraint conditions are shown in equation (2).

$$\begin{cases} y_i\left(\omega^T \cdot x_i + b\right) \geq 1 - \xi \\ \min \dfrac{1}{2}\omega^T \omega + C\sum_{i=1}^{n} \xi_i \end{cases} \tag{2}$$

In equation (2), $y_i \in [-1,1]$, ξ represents the slack variable, C means the PF of the algorithm, and n represents the sample size. When misclassifications allowed by slack variables occur, the PF controls the degree of error occurrence. If the PF is large, SVM increases the penalty for misclassification to avoid misclassification. When the PF is small, the model sacrifices some class accuracy to improve generalization,

so it is essential to select the suitable PF grounded on various cases. In order to simplify the complexity of the algorithm, RBF with fewer parameter requirements is selected as the kernel function, and the calculation is shown in equation (3).

$$K\left(x_1, x_2\right) = \exp\left(-\gamma \left\| x_1 - x_2 \right\|^2\right) \tag{3}$$

In equation (3), $K(x_1, x_2)$ represents the RBF kernel function, γ represents the hyperparameters that determine the shape of the kernel function, x_1 represents the vector of point 1 on the hyperplane, and x_2 represents the vector of point 2 on the hyperplane. The anomaly detection process of multi-hop network based on SVM is shown in Figure 1.

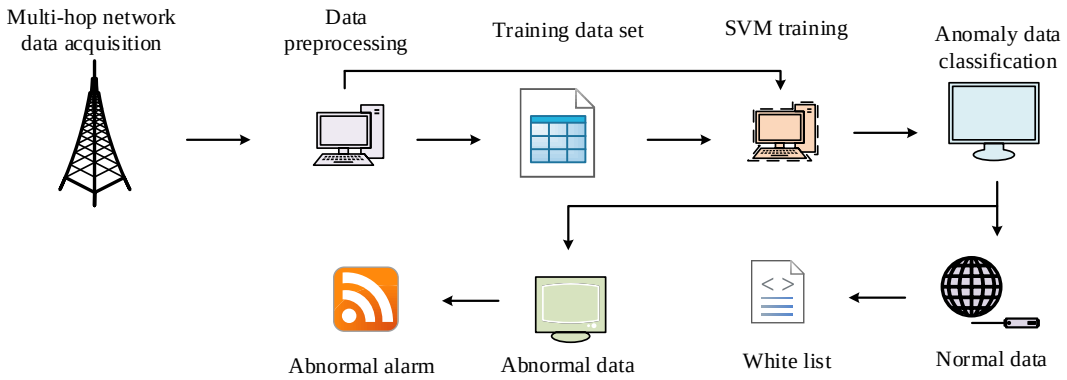

Figure 1: Multi-hop network anomaly detection flow based on SVM

In Figure 1, the data is first extracted from the multi-hop network, preprocessed, and then combined with the attack data into the training dataset. The training dataset is used to train an SVM, and the data to be detected is input into the SVM algorithm. Abnormal data is classified based on the decision function, with detected normal data being added to the whitelist. If abnormal data is detected, an alarm is issued. The study used PSO algorithm to reform the PF and KF size of SVM. On the basis of traditional PSO algorithm, inertia weight coefficients were added. By adjusting the size of inertia weight coefficients in real time, the initial global search capability and later local search accuracy of PSO algorithm were improved. A larger inertia weight is good for global search. It allows the particles to explore the solution space on a larger scale. This helps the algorithm to discover a wider range of potential solution regions at an early stage. A smaller inertia weight is more conducive to local search. It restricts the particle's motion. This allows the particles to focus more on refining the search in the current search region, and helps the algorithm to locally optimize the solution space at a later stage. The optimized particle update speed calculation is shown in equation (4).

$$v_{ij}(t+1) = \varepsilon v_{ij}(t) + c_1 k_1(t)\left[p_{ij}(t) - x_{ij}(t)\right] + c_2 k_2(t)\left[p_{ij}(t) - x_{ij}(t)\right] \tag{4}$$

In equation (4), ε represents the inertia weight coefficient, $v_{ij}(t+1)$ represents the particle's movement speed at time $(t+1)$, c_1 and c_2 represent learning factors, k_1 and k_2 are random numbers with values between 0 and 1, and $p_{ij}(t)$ represents the optimal position of the population at time t. There should be a certain difference in the values of learning factors c_1 and c_2 to further enhance population diversity. According to relevant research, the values of learning factors should be between 1 and 2.5. Linear changes should be made to the learning factors to improve individual information attention. The calculation is shown in equation (5).

$$c_1 = c_2 = \frac{c_{\max} - c_{\min}}{T} \cdot t + c_{\min} \tag{5}$$

In equation (5), $c_{\max}$ means the maximum value of the learning factor, $c_{\min}$ means the minimum value of the learning factor, t means the number of iterations at present, and T means the total amount of iterations. To further enhance the global search capability of the PSO algorithm, the size of the learning factor c_1 is adjusted to change in real-time with the rise of iteration times, as shown in equation (6).

$$c_1 = 1.3 + 1.2\cos\frac{t}{T}\pi \tag{6}$$

In equation (6), the value of c_1 is larger in the prophase of iteration and smaller in the later stage, showing a monotonically decreasing state. The calculation of c_2 is shown in equation (7).

$$c_2 = 2 - 1.2\cos\frac{t}{T}\pi \tag{7}$$

In equation (7), the value of c_2 is relatively small in the early stage of iteration and relatively large in the later stage, showing a monotonically increasing state. The operation of improving the PSO algorithm is represented in Figure 2.

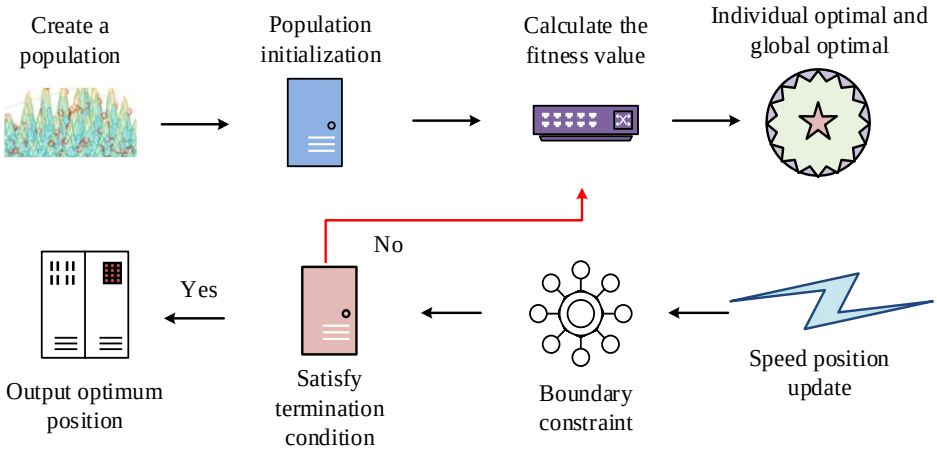

Figure 2: Operation flow of improved PSO Algorithm

In Figure 2, a particle population is created and the population is initialized. The initialization process includes random generation of particle positions, random assignment of initial number of particles and velocity, initialization of individual and global optimums, and setting of boundary constraints. The fitness value of each node is calculated, and the single best value of the node and the global best value of the population are calculated. The place and velocity of particles are updated and adjusted according to the set velocity and boundary constraints. It will be decided whether the termination condition is met or whether the iteration count has been reached. If it is met, the optimal individual is out put, otherwise the fitness is recalculated. Combining SVM and PSO, the classification accuracy capability of SVM is used to screen the fitness function of PSO and improve its fitness. The specific flow of PSO-SVM algorithm is represented in Figure 3.

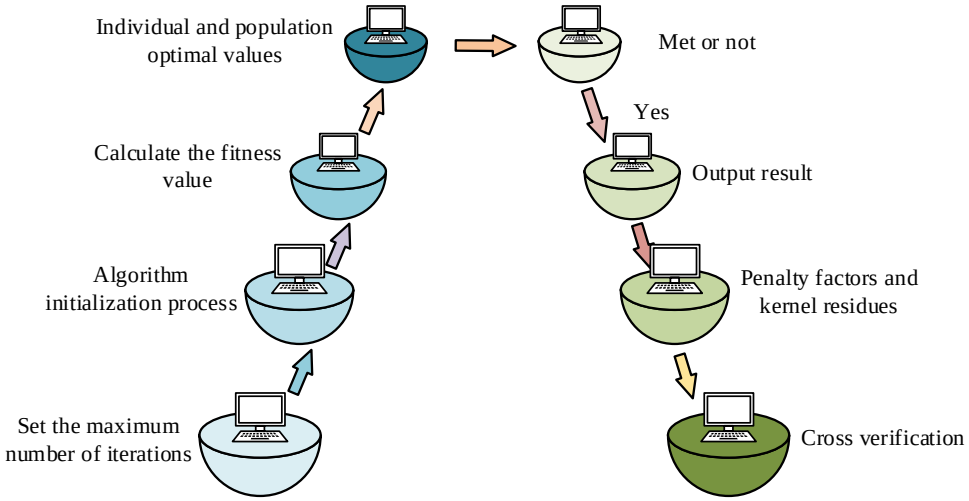

Figure 3: Specific Flow of PSO-SVM Algorithm

In Figure 3, the algorithm first optimizes the PF and KF hyperparameters, and then performs data detection and classification based on the optimal parameters to alert for irregular data. According to relevant research, the max value of iterations for PSO algorithm is defined to 100, the population is initialized, and the PF and KF hyperparameters are set to the particle component values. The fitness values of each particle in the population are computed, the optimal values of individuals and populations are updated, determining if the termination conditions are met, and the position and velocity of particles will be updated if they are met. The fitness value of the particles at the latest position is computed, the PF and hyperparameters are obtained, and cross validation is used to determine accuracy.

2.2 Optimization of multi-hop network security protection algorithm for ACO and PSO fusion

To further improve the optimization accuracy of the algorithm, the combination of PSO algorithm and ACO

algorithm is studied to enhance the detection capability of irregular data. ACO algorithm allows individuals to leave pheromones while searching for food, making it easier for subsequent individuals to follow up. The path with the highest concentration of pheromones is the optimal path. However, ACO algorithm is prone to encounter the traveling salesman problem during the optimization process, which is how to obtain the optimal path to access all nodes only once for each node. After accessing a node, an individual in the ant algorithm will store the node in memory to ensure that it will not be accessed repeatedly. After the individual completes the access, they will randomly select the next node. The probability calculation of an individual from node P to node Q is shown in equation (8).

$$Ch_{PQ} = \frac{\tau_{PQ}^{\alpha}(t')\eta_{PQ}^{\beta}(t')}{\sum \tau_{PM}^{\alpha}(t')\eta_{PM}^{\beta}(t')} \tag{8}$$

In equation (8), τ represents the initial pheromone, η represents the heuristic information, α means the information heuristic factor, β means the expected heuristic factor, t' represents the departure time, and M represents the remaining nodes available for selection.

$$\eta_{PQ}(t') = \frac{1}{d_{PQ}} \tag{9}$$

In equation (9), $\eta_{PQ}(t')$ means the heuristic function, which means the expected degree from point P to point Q, and d_{PQ} represents the range from point P to point Q. When the distance between nodes is shorter, the value of η increases, and the probability of ant colony individuals transferring to that node increases. The probability of subsequent individuals choosing this path also increases, and the residual pheromones continue to increase. When an individual completes the search for nodes near the node, residual pheromones will interfere with subsequent searches, so it is necessary to clean them up. The calculation is represented in equation (10) [17].

$$\tau_{PQ}(t'+1) = \rho\tau_{PQ}(t') + \Delta\tau_{PQ}(t') \tag{10}$$

In equation (10), ρ represents the residual factor, and $\Delta\tau_{PQ}(t')$ represents the total sum of residual pheromones from time t'.

$$\Delta\tau_{PQ}(t') = \sum {}^{n}\tau_{PQ}^{b}(t') \tag{11}$$

In equation (11), $\tau_{PQ}^{b}(t')$ represents the amount of pheromone released by ant colony individual b when passing between two cities. The heuristic function of the ordinary ACO algorithm is conversely proportional to the interval size between two nodes, resulting in low search efficiency. Therefore, the research has improved the heuristic function by adopting an adaptive mechanism to raise the optimization speed of ACO [18]. The new heuristic function adopts the relationship between the interval between the current point and the next point and the interval between the next point and the targetpoint, as calculated in equation (12).

$$\eta_{PQ} = \frac{\phi_{PQ}}{\lambda d_{PQ} + (1 - \lambda d_{QD})} \tag{12}$$

In equation (12), ϕ represents the amplification function, d_{QD} means the interval between the next point and the target point, and λ means the adjustment balance factor with values between 0 and 1. The calculation of ϕ is shown in equation (13).

$$\phi_{PQ} = \frac{d_{\max} - d_{PQ}}{d_{\max} - d_{\min}} \tag{13}$$

In equation (13), $d_{\max}$ means the maximum interval between the current point and adjacent nodes, and $d_{\min}$ means the minimum interval between the current point and adjacent nodes. In the standard ACO algorithm, when an individual stumbles upon the optimal path close to the sub-optimal one, most individuals tend to follow the sub-optimal path more frequently, continuously depositing pheromones that mislead subsequent individuals. Therefore, studying pheromone update strategies for optimization allows only a subset of individuals to produce pheromones after discovering shorter paths [19]. These individuals are sorted according to the length of the searched path. Individuals with shorter paths are allowed to leave more pheromones, while those with shorter paths leave fewer pheromones. The calculation is represented in equation (14).

$$\tau_{PQ}(t'+1) = (1-\mu)\tau_{PQ}(t') + \mu\sum_{k=1}^{n'}\Delta\tau_{PQ} \tag{14}$$

In equation (14), μ represents the volatility coefficient and n' means the overall amount of ant colony individuals. The expression of $\Delta\tau_{PQ}$ is represented in equation (15) [20].

$$\Delta\tau_{PQ} = \frac{Q'}{L_{K'}}\left(1 - \frac{K'-1}{\varphi n'}\right) \tag{15}$$

In equation (15), K' represents the K' th individual, Q' represents the pheromone enhancement coefficient, $L_{K'}$ represents the length traveled by the

K' th individual, and φ represents the proportion of individuals that can leave pheromones in the total number of ant colonies. The specific operation process of improving the ACO algorithm is shown in Figure 4.

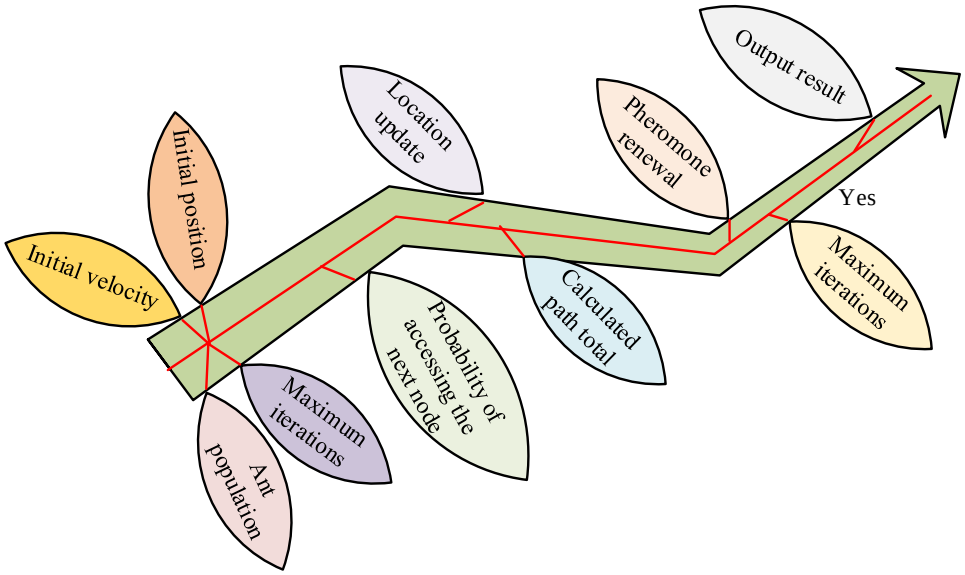

Figure 4: Specific operation flow of the improved ACO algorithm

In Figure 4, the initial population of ant colony is set, including the size of each parameter, maximum iteration times, etc., the possibility of individuals accessing the next node is estimated, their positions are updated, the length of the path traveled by each individual is calculated, and the optimal path is recorded. pheromones are updated in order of individual path length, determining if the max value of iterations is achieved, the calculation result will be output if yes, otherwise the second step will be repeated until the max value of iterations is achieved. PSO and ACO algorithms need to consider the order of fusion. Based on the advantages of each algorithm, PSO algorithm has fast global optimization speed and high accuracy in the prophase of iteration, while ACO algorithm has high local optimization precision in the anaphase of iteration, which can effectively avoid the generation of local optimal solutions [21-22]. Therefore, the fusion algorithm adopts PSO to accelerate the improvement of population diversity and optimization speed in the prophase of iteration, and ACO algorithm to raise optimization accuracy in the later stage of iteration. The specific operation process of the fused ACO-PSO algorithm is represented in Figure 5.

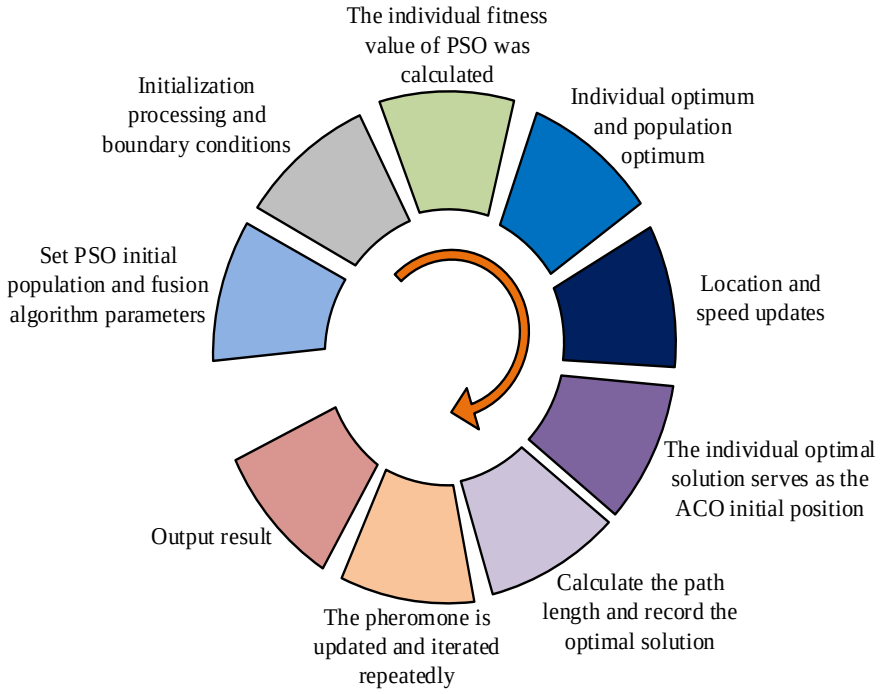

Figure 5: Specific operation flow of ACO-PSO algorithm

In Figure 5, the PSO algorithm population is to be set, population initialization processing is performed, various parameters of the fusion algorithm are set, and constraints are set, including maximum iteration times, PSO algorithm population boundaries, etc. The individual fitness value of PSO, the individual optimal value and population optimal value will be calculated. The individual position and velocity are updated, and it is determined whether the termination condition is met. If the condition is met, the current individual optimal solution will be used as the initial position of ACO, the path length traveled by the ant colony will be calculated, the current best solution will be recorded, and the pheromone will be updated in order of the individual path length. It will be determined whether the max value of iterations is achieved, and if so, the calculation result will be output. After the fusion algorithm is solved, the best PF and KF are input into SVM to classify the data of the multi-hop network, detect abnormal traffic data, and issue an alarm. SVM algorithm has good classification performance and can effectively differentiate network attacks, but the performance of SVM algorithm is greatly affected by the penalty factor and kernel function. Therefore, the study uses swarm intelligence algorithm to search for the best SVM parameters. According to the advantages of the two algorithms, the PSO algorithm is fast in global optimization in the early iteration period and has a wider search range, while the ACO algorithm has a higher accuracy in local optimization in the late iteration period, which is able to effectively avoid the generation of locally optimal solutions. The study adopts the fusion of the two algorithms to jointly search for the optimal parameters of the SVM algorithm and improve the classification performance. The pseudo-code of the ACO-PSO fusion algorithm is shown in Figure 6.

```
Algorithm: Hybrid ACO-PSO

Input: Problem space P, number of particles N, number of ants M,
parameters for ACO (e.g., pheromone evaporation rate rho, pheromone
influence alpha), parameters for PSO (e.g., cognitive component c1,
social component c2, inertia weight w), maximum iterations T

Output: Best solution found

1. Initialize the particle positions and velocities randomly within the
problem space P
2. Initialize the pheromone trails in the problem space P
3. Evaluate the fitness of each particle
4. For each iteration t = 1 to T do
   5. For each particle i = 1 to N do
      6. Update the pheromone trails based on the fitness of the
particles
      7. Use the updated pheromone trails to influence the velocity
update in PSO
      8. Update the velocity of particle i using the PSO velocity update
rule
      9. Update the position of particle i using the new velocity
     10. If the new position of particle i is better than its personal
best, update its personal best
     11. If the new position of particle i is better than the global
best, update the global best
     12. End For
    13. For each ant j = 1 to M do
      14. Construct a solution using the pheromone trails and heuristic
information
      15. Evaluate the fitness of the solution constructed by ant j
      16. If the solution is better than the current global best, update
the global best
      17. End For
    18. Apply pheromone evaporation to the trails
    19. Update the pheromone trails based on the quality of the solutions
found
    20. End For
21. Return the best solution found
```

Figure 6. Pseudo-code for the ACO-PSO Fusion algorithm

3 Results

3.1 Experimental analysis of SVM based improved PSO algorithm for multi-hop network anomaly detection

The hardware environment of the experiment was Inter Core i7-12600K, the base frequency was 3.7GHz, the GPU was GeForce GTX 3070, and the memory was 16GB. The experiment was conducted using MATLAB software for simulation testing, with a simulation area set within a range of 500m×500m, a node count of 600, a node communication radius of 15m, and 100 event packets. The experiment used deep recurrent neural network and region adaptive synthetic oversampling algorithm (DRRS), as well as Variational Autoencoder -

Generative Adversarial Network (VAE-GAN) for comparison. The experimental dataset consisted of UNSW_NB15 and Honeynet. Both datasets contain millions of pieces of cyberattack data, with the UNSW_NB15 dataset having a high level of diversity, encompassing a wide range of attacks such as DoS, PortScan, and DDoS, as well as being authentic, balanced, and providing clear labeling. The Honeynet dataset contains a wide range of attack types, as well as being collected through honeypots from global deployments. The Honeynet dataset encompasses a wide range of attack types as well as collects real-time attack data through honeypots from global deployments to accurately reflect current advanced cyber threats. Because of the dynamic update mechanism of the UNSW_NB15 dataset, it is more complex than the Honeynet dataset. The information exposure probabilities of different algorithms are shown in Figure 7.

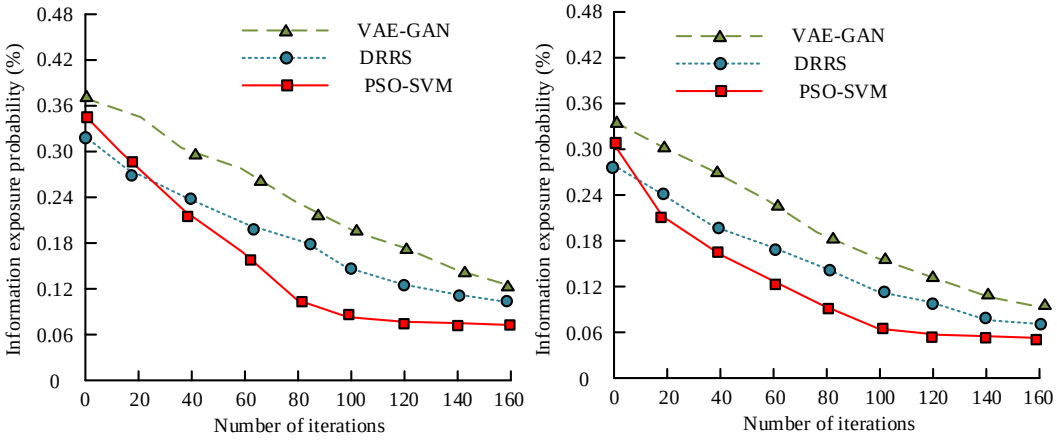

Figure 7: Information exposure probabilities of different algorithms

In Figure 7 (a), the relevant test data were averaged using multiple sets of data, and the *P* values between the test data of different algorithms were less than 0.05, which was statistically significant. The information exposure probability of PSO-SVM gradually decreased with the increase of iteration times, approaching convergence at around 100 iterations. The information exposure probability decreased from 0.35% to 0.10%, and the minimum information exposure probability was 0.06% and 0.04% lower than VAE-GAN and DRRS, respectively. In Figure 7 (b), the convergence of PSO-SVM remained unchanged because the complexity of the dataset decreased and the scale of abnormal information shrank. The minimum information exposure possibility of PSO-SVM was 0.06%, which was 0.08% and 0.05% lower than VAE-GAN and DRRS, respectively. The precision of anomaly recognition using different algorithms is shown in Figure 8.

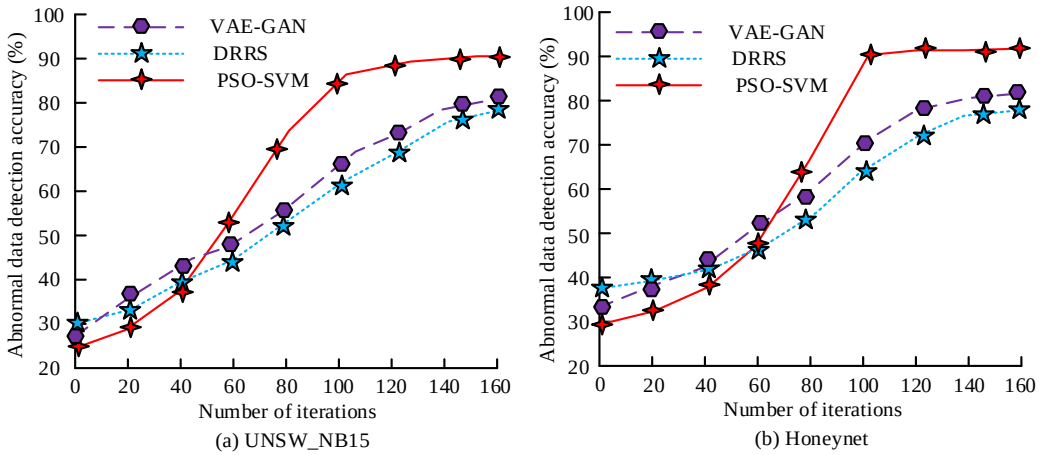

Figure 8: Anomaly detection accuracy of different algorithms

In Figure 8 (a), the convergence speed of PSO-SVM's anomaly detection accuracy was faster than the other two methods, with a maximum value of 89.6%, which was 9.4% and 11.2% higher than VAE-GAN and DRRS, respectively. In Figure 8 (b), the abnormal information detection accuracy of PSO-SVM approached convergence after about 100 iterations, with a maximum value of 93.5%, which was 11.3% and 13.8% higher than

VAE-GAN and DRRS, respectively. Because the Honeynet dataset is simpler than the UNSW_NB15 dataset and does not have dynamically updated network attack types, its anomaly detection accuracy was increased and convergence was closer. Detection accuracy can reflect the ability of the security system to identify threats, is a more intuitive indicator, the user can easily feel its effect, and it is important to reduce false alarms and omissions. The accuracy of anomaly detection using different algorithms is shown in Figure 9.

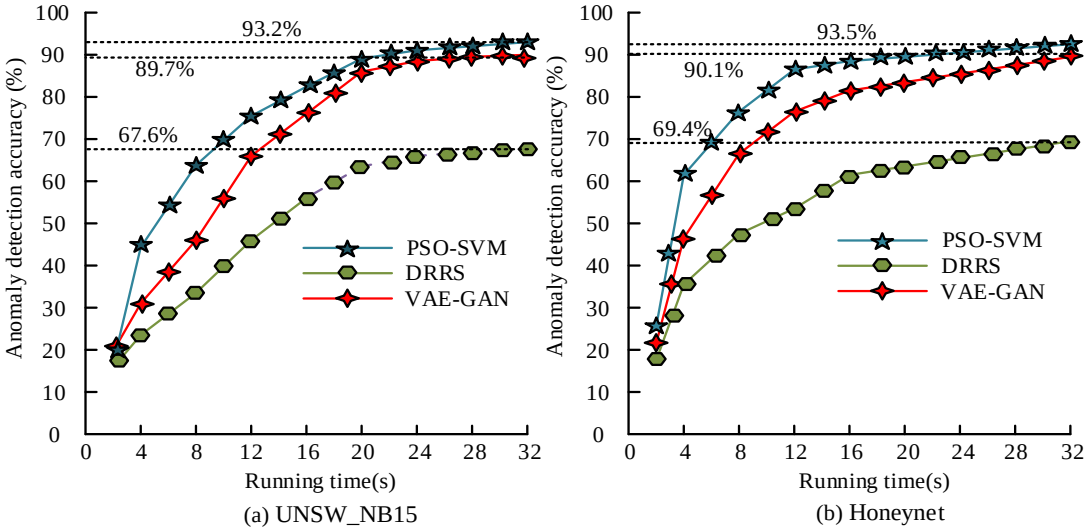

(a) UNSW_NB15 (b) Honeynet

Figure 9: Anomaly detection accuracy of different algorithms

In Figure 9 (a), the convergence speed of abnormal information detection accuracy of PSO-SVM was not significantly different from that of VAE-GAN and DRRS, with a maximum value of 93.2%, which was 3.5% and 27.6% higher than VAE-GAN and DRRS, respectively. In Figure 9 (b), due to the decrease in complexity of the dataset, the convergence speed of PSO-SVM's anomaly detection accuracy was 12 seconds and 20 seconds faster than VAE-GAN and DRRS, respectively. The maximum value was 93.5%, which was 3.4% and 24.1% higher than VAE-GAN and DRRS, respectively.

3.2 Experimental analysis of multi-hop network security protection algorithm for optimizing ACO and PSO fusion

The simulation software and basic parameters of the experiment were the same as before. By improving PSO on two datasets, the optimal PF and KF obtained were UNSW-NB15:236.35 and 2.19, and Honeynet: 27.63 and 4.07, respectively. The optimal PF and KF obtained by improving ACO-PSO in two datasets were UNSW-NB15:131.25 and 12.05, and Honeynet: 243.21 and 8.01, respectively. The response time in the experimental metrics is the time between the appearance of a network attack and the discovery of the attack by the security protection algorithm, the processing time is the time taken by the protection algorithm to resolve the network attack, and the root mean square error is the root mean square of the difference between the actual value and the predicted value during classification. The performance of different algorithms in performing multi-hop network anomaly detection is shown in Table 2.

Table 2: Multi-hop network anomaly detection performance of different algorithms

Algorithm	Data set	Response time(ms)	Disposal time(ms)	Root mean square error(ms)
DRRS	UNSW-NB15	71.8	125.1	6.7
	Honeynet	69.5	120.5	6.4
VAE-GAN	UNSW-NB15	42.3	95.3	3.6
	Honeynet	40.9	93.6	3.4
PSO-SVM	UNSW-NB15	46.7	98.7	4.1
	Honeynet	44.2	97.2	3.8
ACO-PSO-SVM	UNSW-NB15	22.4	72.6	1.3
	Honeynet	21.5	68.4	1.2
P-value	/	0.018	0.007	0.035

In Table 2, the p-value between the various data was less than 0.05, which was statistically significant. The performance of ACO-PSO-SVM is optimal in all aspects. In the more complex UNSW-NB15 dataset, the danger response time of ACO-PSO-SVM was 22.4ms, which was 24.3ms, 19.9ms, and 49.4ms faster than PSO-SVM,

VAE-GAN, and DRRS, respectively. The danger handling time of ACO-PSO-SVM was 26.1ms, 22.7ms, and 53.5ms faster than the other three algorithms, respectively. The root mean square error of ACO-PSO-SVM was 2.8ms, 2.3ms, and 5.4ms lower than the other three algorithms, separately. Reducing the dangerous response time and processing time of the algorithm can minimize the damage caused by cyber attacks. Responding to cyber security incidents and organizational counterattacks in a timely manner can effectively protect the user's personal privacy and sensitive information of the enterprise. Timely responses also enhance organizational resilience and maintain business continuity. The operating costs of multi-hop network anomaly detection using different algorithms are shown in Figure 10.

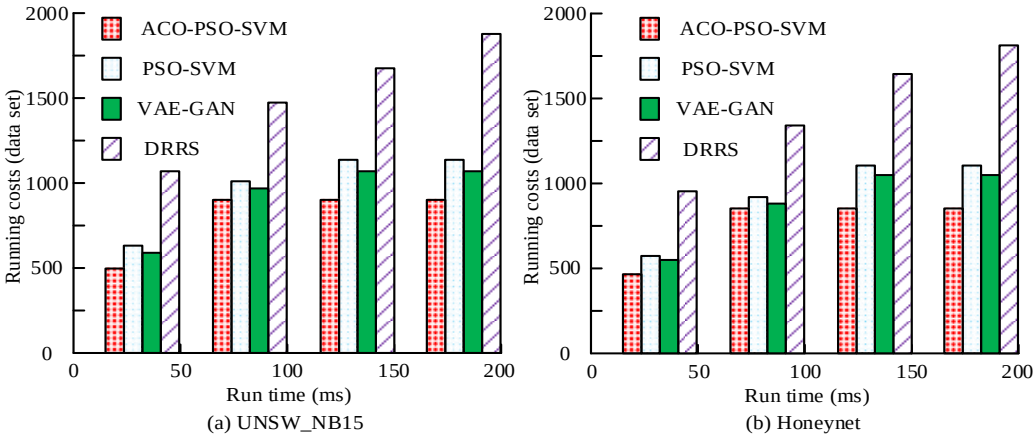

Figure 10: Comparison of operating costs of different algorithms

In Figure 10 (a), the multi-hop network anomaly detection cost of ACO-PSO-SVM was the lowest, reaching a maximum of 890 datasets at a running time of 100ms, which was 310, 210, and 910 datasets lower than PSO-SVM, VAE-GAN, and DRRS, respectively. In Figure 10 (b), the running cost of ACO-PSO-SVM reached its maximum value of 800 datasets at 100ms, which was 300, 240, and 950 datasets lower than the other three algorithms, separately. The accuracy comparison of multi-hop network anomaly detection using ACO-PSO fusion algorithm is shown in Figure 11.

In Figure 11 (a), due to the faster local optimization speed and higher precision of the ACO algorithm, the convergence curve of ACO-PSO-SVM was the same as that of PSO-SVM in the early stage of iteration, and the convergence speed was faster in the middle stage. The maximum detection accuracy was 92.5%, which was 2.9%, 12.3%, and 14.1% higher than that of PSO-SVM, VAE-GAN, and DRRS, separately. In Figure 11 (b), the maximum detection accuracy of ACO-PSO-SVM was 95.9%, which was 2.4%, 13.7%, and 16.2% higher than PSO-SVM, VAE-GAN, and DRRS, respectively. The convergence speed of the fusion algorithm was improved compared to Figure 11 (a). The comparison of PR and ROC curves for different algorithms is shown in Figure 12.

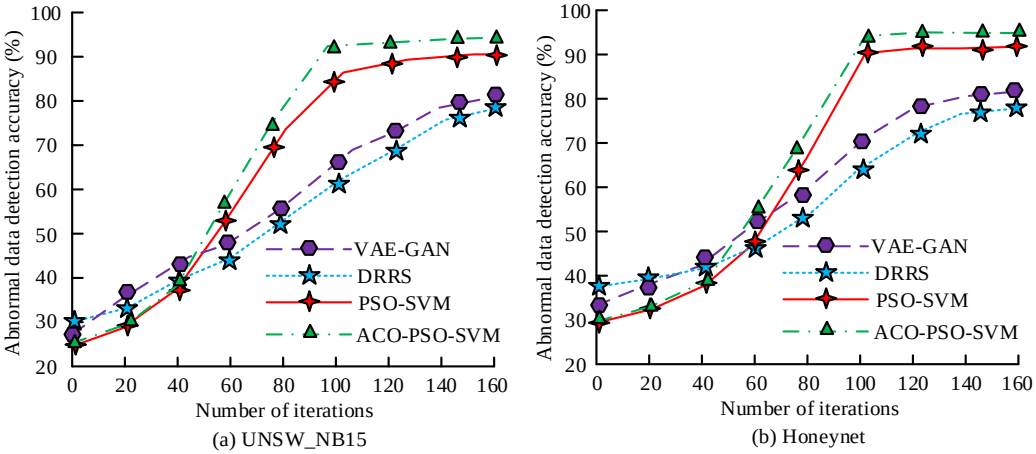

Figure 11: Comparison of Multi-hop network anomaly detection accuracy of ACO-PSO Fusion Algorithm

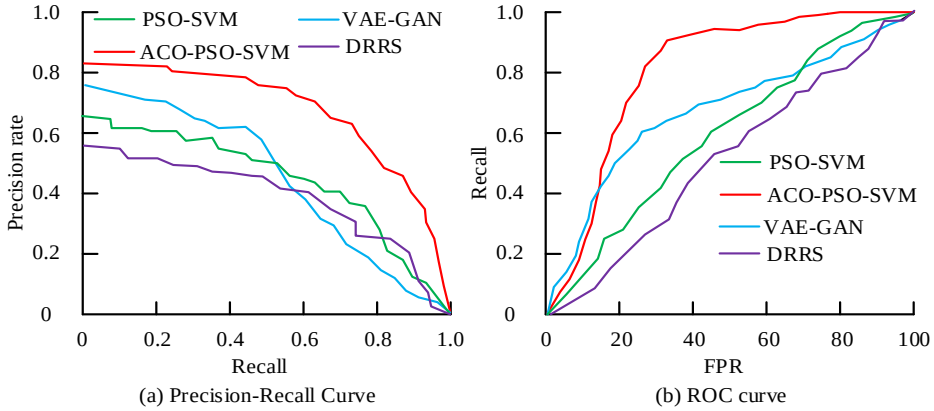

(a) Precision-Recall Curve (b) ROC curve

Figure 12. Comparison of PR Curve and ROC Curve of Different Algorithms

In Figure 12 (a), the PR curves of PSO-SVM, VAE-GAN and DRRS were intertwined with each other. To judge the performance of the algorithms, it is necessary to find the balance point and the point where the precision and recall are equal. At this point, the two performances of the classifiers were higher, which indicated that the classifiers performed well. The PR curve of ACO-PSO-SVM completely wrapped around the other three curves, indicating that the equilibrium point of the fusion algorithm was always above the equilibrium point of the other algorithms, so it can be concluded that the performance of ACO-PSO-SVM was better than the other three algorithms. In Figure 12 (b), the curve of ACO-PSO-SVM was steeper because the ideal target of the model was a true class rate of 1 and a false positive class rate of 0. The closer the curves of all algorithms are to the upper left corner, the better the performance of the algorithm. Sensitivity analysis was carried out on the individual proportion parameter of the ACO algorithm and the inertia weight parameter of the PSO algorithm, and the experimental results were shown in Table 3.

Table 3: Parameter sensitivity analysis of ACO and PSO Algorithms

Argument	Value	Precision rate	Recall rate	F1
φ	0.3	0.90	0.89	0.94
	0.4	0.92	0.94	0.98
	0.5	0.91	0.88	0.95
	0.6	0.87	0.84	0.91
ε	0.8	0.91	0.92	0.91
	0.9	0.92	0.94	0.98
	1.0	0.90	0.93	0.92

In Table 3, as the proportion of individuals leaving pheromones gradually increased, the performance of ACO algorithm increased first and then decreased. When the value was 0.4, the best performance was achieved, and the accuracy rate, recall rate, and F1 of the algorithm were 0.92, 0.94 and 0.98, respectively. As can be seen from the table, when the proportion increased, the recall rate of the algorithm could be greatly affected.

Table 4: Computational complexity of the proposed algorithm of the study compared to the base algorithm

Data set	Algorithm	Average processing time (ms)	Standard deviation (ms)	Time complexity $O(n^2)$ evaluation
Honeynet	SVM	20.4	1.8	Lower
	PSO	18.5	1.5	Lower
	ACO	29.8	2.4	Lower
	ACO-PSO-SVM	47.6	3.9	Lower
Maple-IDS	SVM	38.5	2.7	Lower
	PSO	29.2	2.5	Lower
	ACO	45.9	4.3	Lower
	ACO-PSO-SVM	72.4	6.2	Normal

When the proportion was 0.6, the recall rate of the algorithm was 0.10 lower than the optimal value. When the relation weight coefficient of PSO algorithm was 0.9, the best precision rate, recall rate and F1 values were obtained, and the maximum values were 0.92, 0.94 and 0.98 respectively. The computational complexity of the proposed algorithms studied against the base algorithm in datasets of different complexity levels is shown in Table 4.

In Table 4, the average processing times of the four algorithms when the dataset was simpler were 20.4ms, 18.5ms, 29.8ms, and 47.6ms, respectively, and the average processing time of the ACO-PSO-SVM algorithm was longer than the base algorithm, but it was still within the acceptable range, with a time complexity of lower. When the Maple-IDS dataset was used, the computation time of the four algorithms increased due to the fact that it contained a more number and variety

of attack data, the computation time of the different algorithms increased, and the four algorithms increased by 14.1ms, 10.7ms, 16.1ms, and 24.8ms, respectively, with the ACO-PSO-SVM algorithm increasing almost twice as much as the other algorithms, and the time complexity was normal.

4 Discussion

The study proposed a multi-hop network security protection strategy that integrates PSO algorithm and ACO algorithm, and applied it to experimental simulation analysis. The effectiveness and superiority of the strategy in multi-hop network security protection was verified by simulation analysis. Compared with the traditional method, the optimized ACO and PSO fusion algorithm had faster hazard response speed and operation efficiency, because the fusion algorithm adopted the PSO algorithm to improve the optimization speed and accuracy in global optimization, and adopted the ACO algorithm in local optimization to avoid local optimal solutions. Meanwhile, the fusion algorithm had lower detection cost and detection accuracy because the fusion algorithm can find the optimal penalty factor and kernel function of SVM. In multi-hop networks, faster convergence means that the network can quickly adapt and reconfigure routes in the event of failures or topology changes, which reduces service disruption time and improves the reliability and stability of the network. Reducing information exposure reduces the risk of network attacks, decreases the chance of sensitive data being stolen when nodes communicate, and protects user privacy and security. Reducing operational costs can enhance the competitiveness of the enterprise and customer satisfaction, while improving productivity. Multi-hop network security protection is widely used in military communications, disaster relief, mobile self-organizing networks, wireless sensor networks, and industrial network security, and plays an important role in a variety of scenarios through its rapid deployment, high flexibility, and high reliability.

5 Conclusion

A multi-hop network security protection algorithm that integrated ACO and PSO was proposed to address the issues of easy attacks on existing multi-hop network data forwarding at intermediate nodes and high data protection costs of existing methods. The experiment outcomes showed that the information exposure probability of PSO-SVM decreased from the initial 0.35% to 0.10%, and the minimum information exposure probability was 0.06% and 0.04% lower than that of VAE-GAN and DRRS, respectively. In datasets with lower complexity, the minimum information exposure probability of PSO-SVM was 0.06%, which was 0.08% and 0.05% lower than VAE-GAN and DRRS, respectively. The maximum accuracy of abnormal information detection for PSO-SVM was 89.6%, which was 9.4% and 11.2% higher than VAE-GAN and DRRS, respectively, and had a faster convergence speed. The maximum accuracy of abnormal information detection was 93.2%, which was 3.5% and 27.6% higher than VAE-GAN and DRRS, respectively. The hazard response time of ACO-PSO-SVM fusion was 22.4ms, which was 24.3ms, 19.9ms, and 49.4ms faster than PSO-SVM, VAE-GAN, and DRRS, respectively. The hazard handling time was 26.1ms, 22.7ms, and 53.5ms faster than the other three algorithms, and the root mean square error was 2.8ms, 2.3ms, and 5.4ms lower than the other three algorithms, separately. The multi-hop network anomaly detection cost of ACO-PSO-SVM was the lowest, with 310, 210, and 910 datasets lower than other methods, respectively. The maximum detection accuracy was 2.9%, 12.3%, and 14.1% higher than other methods, respectively. The PR curve of ACO-PSO-SVM completely wrapped around the other three curves, and the ROC curve was closer to the ideal target, so the performance of the fusion algorithm was better. Fusion algorithms could effectively achieve security protection for multi-hop networks, reduce the probability of user privacy data exposure, and lower algorithm operating costs. There were still some issues with this study, such as only focusing on algorithm optimization for security protection. In the future, data optimization can be considered to further raise the safety of multi-hop networks. For example, a stochastic gradient descent method is used to optimize the relevant dataset, which can be updated using a small number of samples, thus speeding up training and adapting to large-scale datasets. Deep learning methods are also able to be employed to learn the latest attack sample data in real time to improve the classification performance of the model. The ACO-PSO-SVM detection algorithm because of the fusion of multiple algorithms, resulting in a certain degree of increase in its computational complexity compared to ordinary classification algorithms. Meanwhile, its search efficiency decreases significantly when facing high-dimensional datasets, leading to a curse of dimensionality The fusion algorithm may not perform well when the dataset is noisy, and it cannot draw a clear hyperplane for accurate classification, so it cannot be detected between, and the data needs to be denoised.

References

[1] Wong AW, Goh SL, Hasan MK, Fattah S. Multi-hop and mesh for LoRa networks: Recent advancements, issues, and recommended applications. ACM Computing Surveys, 2024, 56(6):1-43. https://doi.org/10.1145/3638241

[2] Li X, Li Q, Zhang J. Research on global path planning of unmanned vehicles based on improved ACO algorithm in the complex road environment. Measurement and Control, 2022, 55(9-10):945-959. https://doi.org/10.1177/00202940221118132

[3] Pervaiz S, Bangyal WH, Ashraf A, Nisar K, Haque MR, Ibrahim A, Ag AB, Chowdhry B, Rasheed W, Rodrigues JJ. Comparative research directions of population initialization techniques using PSO

algorithm. Intelligent Automation & Soft Computing, 2022, 32(3):1427-1444. https://doi.org/10.32604/iasc.2022.017304

[4] Nasri M, Lamiri A, Maaref H, Mghaieth R. Adaptive dynamic multi-hop technique for clustering protocol in wireless sensor networks assisted-Internet of Things applications. IET Networks, 2022, 11(1):27-41. https://doi.org/10.1049/ntw2.12032

[5] Vinitha A, Rukmini MS. Secure and energy aware multi-hop routing protocol in WSN using Taylor-based hybrid optimization algorithm. Journal of King Saud University-Computer and Information Sciences, 2022, 34(5):1857-1868. https://doi.org/10.1016/j.jksuci.2019.11.009

[6] Shafique A, Asad M, Aslam M, Shaukat S, Cao G. Multi-hop similarity-based-clustering framework for IoT-Oriented Software-Defined wireless sensor networks. IET Wireless Sensor Systems, 2022, 12(2):67-80. https://doi.org/10.1049/wss2.12037

[7] Singh BK, Mahapatra SN, Kumar V. A secure multi-hop relay node selection scheme-based data transmission in wireless ad-hoc network via block chain. Multimedia Tools and Applications, 2022, 81(13):18343-18373. https://doi.org/10.1007/s11042-022-12283-7

[8] Ezzati Khatab Z, Mohammadi A, Pourahmadi V, Kuhestani A. A machine learning multi-hop physical layer authentication with hardware impairments. Wireless Networks, 2024, 30(3):1453-1464. https://doi.org/10.1007/s11276-023-03577-1

[9] Mahapatra SN, Singh BK, Kumar V. Secure energy aware routing protocol for trust management using enhanced Dempster Shafer evidence model in multi-hop UWAN. Wireless Networks, 2022, 28(7):3059-3076. https://doi.org/10.1007/s11276-022-03021-w

[10] Pattanayak DR, Dwivedi VK, Karwal V, Yadav PK, Singh G. Physical layer security analysis of multi-hop hybrid RF/FSO system in presence of multiple eavesdroppers. IEEE Photonics Journal, 2022, 14(6):1-2. https://doi.org/10.1109/jphot.2022.3226351

[11] Altuwairiqi M. An optimized multi-hop routing protocol for wireless sensor network using improved honey badger optimization algorithm for efficient and secure QoS. Computer Communications, 2024, 214(7), 244-259. https://doi.org/10.1016/j.comcom.2023.08.011

[12] Altowaijri S M. Efficient next-hop selection in multi-hop routing for IoT enabled wireless sensor networks. Future Internet, 2022, 14(2), 35-52. https://doi.org/10.3390/fi14020035

[13] Tan Y, Ouyang J, Zhang Z, Lao Y, Wen P. Path planning for spot welding robots based on improved ant colony algorithm. Robotica, 2023, 41(3):926-938. https://doi.org/10.1017/s026357472200114x

[14] Zheng H, Guo J, Zhou Q, Peng Y, Chen Y. Application of improved ant colony algorithm in load balancing of software-defined networks. The Journal of Supercomputing, 2023, 79(7):7438-7460.

[15] Choudhuri S, Adeniye S, Sen A. Distribution Alignment Using Complement Entropy Objective and Adaptive Consensus-Based Label Refinement for Partial Domain Adaptation[C]//Artificial Intelligence and Applications. 2023, 1(1): 43-51. https://doi.org/10.47852/bonviewaia2202524

[16] Yang L, Tao J, Liu YH, Xu Y, Su CY. Energy scheduling for DoS attack over multi-hop networks: Deep reinforcement learning approach. Neural Networks, 2023, 161(6):735-745. https://doi.org/10.1016/j.neunet.2023.02.028

[17] Zhai Z, Lai G, Cheng B, Qian J, Zhao L, Wu J, Wan Z. Lightweight secure detection service for malicious attacks in wsn with timestamp-based mac. IEEE Transactions on Network and Service Management, 2022, 19(4):5299-311. https://doi.org/10.1109/tnsm.2022.3194205

[18] Abdollahi M, Ashtari S, Abolhasan M, Shariati N, Lipman J, Jamalipour A, Ni W. Dynamic routing protocol selection in multi-hop device-to-device wireless networks. IEEE Transactions on Vehicular Technology, 2022, 71(8):8796-809. https://doi.org/10.1109/tvt.2022.3172923

[19] Fan Y, Gao S, Duan D, Cheng X, Yang L. Radar integrated MIMO communications for multi-hop V2V networking. IEEE Wireless Communications Letters, 2022, 12(2):307-11. https://doi.org/10.1109/lwc.2022.3224566

[20] Hanif M, Ashraf H, Jalil Z, Jhanjhi NZ, Humayun M, Saeed S, Almuhaideb AM. AI-based wormhole attack detection techniques in wireless sensor networks. Electronics, 2022, 11(15):2324-2335. https://doi.org/10.3390/electronics11152324

[21] Zhang, Z. (2024). SD-WSN Network Security Detection Methods for Online Network Education. Informatica, 48(21). https://doi.org/10.31449/inf.v48i21.6257

[22] Ahmed, S. M., & Mahmood, B. A. (2024). Cloud Computing Security: Assured Deletion. Informatica, 48(3). https://doi.org/10.31449/inf.v48i3.6245

Software Vulnerability Assessment and Classification Using Machine Learning, Deep Learning and Feature Selection Techniques

Ali Hussein, Azri Azmi, Hafiza Abas
Faculty of Artificial Intelligence, Universiti Teknologi Malaysia (UTM), Kuala Lumpur, Malaysia
E-mail: hussein.a@graduate.utm.my

Keywords: vulnerability, deep learning, machine learning, classification, neural network, VSM, ANN, selection techniques

Received: January 29, 2025

The detection of software defects is a critical technique for improving software quality and optimizing testing resources. This study presents a novel approach to software vulnerability assessment and classification using Recurrent Neural Networks (RNNs) enhanced by feature selection techniques. The proposed methodology integrates data preprocessing, dynamic analysis methods, and vector space model (VSM) generation, leveraging techniques such as TF-IDF and relational feature extraction to normalize and balance datasets. Computational experiments were conducted using various real-world and synthetic datasets, comparing the proposed RNN framework to traditional machine learning models, including Artificial Neural Networks (ANN), Support Vector Machines (SVM), and Adaboost. The RNN model, optimized with activation functions such as ReLU, Sigmoid, and Tanh, demonstrated superior performance, achieving a classification accuracy of 97.5% with ReLU and outperforming other models in precision (97.6%), recall (97.9%), and F-measure metrics. These results highlight the robustness and effectiveness of the proposed framework in detecting vulnerabilities and mitigating software defects. This research underscores the potential of deep learning-based approaches in enhancing software reliability and security.

Povzetek: Članek analizira ranljivost programske opreme z uporabo globokih nevronskih mrež (RNN), optimiziranih s tehnikami izbire značilk, kjer učinkovito obravnava neuravnotežene podatke.

1 Introduction

Recognition of vulnerabilities in source code or software has become an emerging field of research. Even though earlier studies have demonstrated the usefulness of multiple detection methods, models, and software vulnerability analysis tools in identifying source code vulnerabilities, the enhancement of the efficiency of such detection models and tools remains a major challenge for researchers. Annually, thousands of security issues are identified in virtual instruments, which are released publicly to the general vulnerability database exposed in obfuscated code. Threats also occur in indirect ways that are not evident to the concerned code inspectors or the programmers. It seems necessary to understand the dynamics of vulnerabilities that can lead to system issues directly from the raw data, with abundance of publicly available source code. In this work, we present an information approach to security technology using deep learning. Stimulated by the success of similar research in the area of recognizing the vulnerabilities in source code/software, we use a theoretical framework to examine its feasibility to aid in finding out the said vulnerabilities. The preliminary results indicate that within the domain of detecting attacks, the definition is feasible [1].

To bridge the domain gap, we can propose that each feature in a program be treated in computer vision as a neural network because fault detectors may only have to say whether a feature is insecure and fully explain vulnerability positions. That is, we want an intelligent interpretation of fault management programs. On either hand, one may recommend approaching each piece of code (i.e., comment, in this study, the two words are used synonymous) as a vulnerability detection unit. There are important exceptions to this diagnosis:
(i) most comments in a program may not contain any uncertainty, indicating that a few samples are susceptible;
(ii) multiple comments are not regarded as a whole that is semantically linked to each other [2].

Using traditional programming by utilizing k-means cluster analysis and the generative adversarial model, a scheme was introduced to check bugs in large number of random codes. To select the optimal code with an interactive analysis framework and software code refactor generation, k-means cluster transformation has been used. Use of a system, described on object-oriented code analysis documented in literature; in the instant case. The model is verified by the tasks of conceptual relationship analysis based on coding pairs and identification of sentiments. Moreover, a research study centered on what form of compilation with communication of massive source code has helped to recognize errors for inexperienced developers and suggest the steps needed to be taken on source code mistakes. The investigation uses the form of a message previously based on the coding system and detects specific code snippets' vulnerability [3].

It is therefore noted that, as classification algorithms for web application, bug identification and vulnerability classification, most investigators have used conventional

semi-supervised classifiers, RNNsor CNNs. RNNs are far better than the standard language models, including such n-gram, but they have drawbacks in understanding long sequence data. Based on faults, functional programming identification, archive code identification, and basic error detection, almost all of the studies are found to have used various system software and classification models. On the other hand, the developed scheme of ours explicitly defines logic, grammar, and other system software errors. Additionally, in place of the error spot, the proposed model is used to predict the correct terms. Overall, in pursuing unique objectives, our suggested Language model varies from many other models [4].

This paper introduces a novel active tracking on deep learning to automatically learn features for predicting runtime environment weaknesses. In source code, where contingent code components are spread far apart, For example, combinations of code tokens that are needed to appear simultaneously due to the configuration of the computer program (e.g. in Java) or according to the configuration of API use (e.g. Lock () and activate ()), but do not accompany each other automatically are effectively handled. The interpretation of code symbols (semantic functionality) and the hierarchical structure of source code are appropriately reflected by the learned features (syntactic features). Our automated feature learning strategy removes the need for automated feature selection in conventional methods, which takes up much effort. Finally, testing the framework from a huge repository on many Java programs for the Desktop version reveals that our methodology is highly accurate in explaining code vulnerabilities [5]. Table 1 provides a Related Works Summary comparing the methodologies, datasets, and performance metrics of reviewed studies.

Table 1: Related works summary comparison

study	Methodology	Dataset Size	Key Metrics (Accuracy, Precision, Recall)	Limitations
Tai et al. (2015)	Convolutional Neural Network (CNN)	10,000+ samples	Accuracy : 92.3%	Limited to structured data; scalability and semantic feature extraction issues.
Zhou et al. (2016)	Support Vector Machine (SVM) + Text Mining	15,000+ bug reports	Accuracy : 89.5%, Recall: 91.2%	Inefficient for large datasets; high computational cost.
Teshima et al. (2018)	Long Short-Term Memory (LSTM) Networks	5,000+ snippets	Accuracy : 94.2%	Struggles with imbalanced datasets, leading to reduced recall.
Tong et al. (2018)	Stacked Autoencoder + Ensemble	20,000+ entries	Accuracy : 93.1%, Precision : 94.5%	High preprocessing cost; lacks scalability for diverse datasets.
Proposed Framework	Recurrent Neural Network (RNN) with TF-IDF and relational feature extraction	2,500 (2000 training, 500 testing)	Accuracy : 97.5%, Precision : 97.6%, Recall: 97.9%	Efficient handling of imbalanced datasets; reduced preprocessing; automated feature learning.

The proposed RNN framework distinguishes itself by integrating advanced feature selection methods, such as TF-IDF and relational feature extraction, with robust data normalization and balancing techniques. Additionally, its automated feature learning capabilities minimize preprocessing requirements, and its optimized architecture, featuring activation functions like ReLU and Tanh, achieves superior performance. These attributes establish the proposed framework as a novel and effective solution, addressing gaps in the state-of-the-art while setting new benchmarks in software vulnerability detection. This comprehensive comparison underscores the necessity and impact of the proposed solution in overcoming the limitations of existing methodologies.

2 Proposed system design

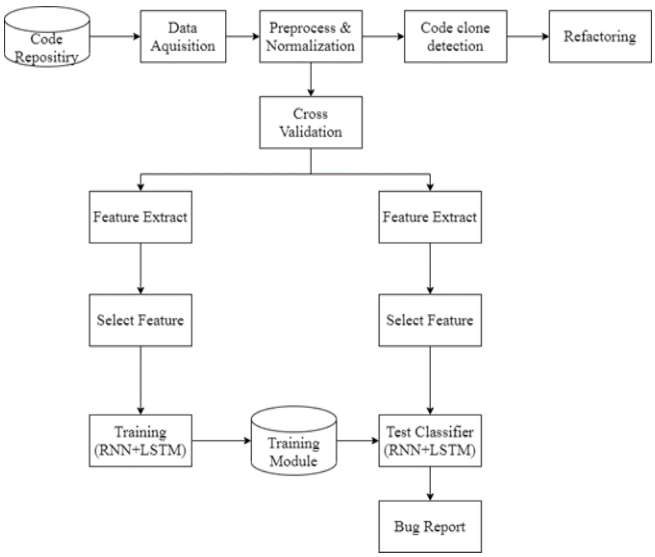

Figure 1: Proposed system architecture design

shows a system overview of execution process flow, and delineates how it works with different algorithms.

2.1 Implementation environment

The proposed framework was implemented on a Windows operating system using JDK 1.7 and Python as the coding language. NetBeans IDE was utilized for development, with MySQL serving as the database for both back-end operations and storage. The front-end was designed using jPanel and jFrame. The hardware environment included an Intel i3 2.7 GHz CPU, 300 GB HDD, and 4 GB RAM, providing sufficient resources for the experiments and ensuring replicability.

2.2 Pre-processing

the source code is separated as well as the area of the comparison is first decided. There are three basic types of goals in the below steps.

Eliminate section of code: In this step source code uninteresting compared phase is removed.

Determine source units: By removing all the uninteresting code, the remaining part of the source code is divided into the arrangement of dissimilar sections known as source units.

Determine correlation units/granularity:

Source code parts should be auxiliary divided into smaller parts relying upon the evaluation method utilized a tool [6].

2.3 Feature extraction

Extraction changes the program to the form that is correct while supporting the real comparison algorithm. Conditional upon the device, it contains are as following:

Tokenization: If there should be an event of token-based methodologies, every source code line of the program is more divided into tokens as shown by the lexical regulation of the program design platforms of importance. Apply different tokens of source code lines or forms after that frame of token systems to compare. The entire whitespace and comments between marks are removed from the token groups.

Parsing: For syntactic methods, the whole source code is described to prepare a parse tree or (potentially clarified) abstract syntax tree (AST). The source parts to be studied are then shown as sub-trees of the described tree or the AST. Measurements-based methodologies can utilize a parse tree depiction to discover clones taking into account sizes for sub-trees.

Control and Data Flow Analysis: Semantics-related methodologies produce program dependence graphs (PDGs) as of the source code. The nodes of a Program Dependence Graphs show the reports and circumstances of a system, while edges show control and information conditions. Source units to be matched are shown as sub-graphs of these PDGs. Different plans then search in favor of isomorphic sub-graphs to discover clones. A few measurement-based methodologies use sub-graphs to compute info with control stream measurements [6]. The feature extraction process involves transforming raw source code into a vector space model (VSM) using a combination of TF-IDF, relational features, and bigram features. TF-IDF was applied with standard parameters, considering all terms across the dataset, to capture term importance relative to document frequency. Relational features were generated by analyzing dependencies between code tokens, such as variable usages and method invocations. For bigram features, sequential pairs of tokens were extracted to capture context within code snippets. The extracted features were normalized to ensure consistency, and imbalanced datasets were balanced through re-sampling techniques to improve classification performance. All preprocessing steps were implemented using Python libraries, ensuring reproducibility.

2.4 Feature selection

The various feature selection methods have been used during module training. The function compiles entire source code or modules with real statistics; in this method behavior is analyzed of code for vulnerability detection. In a broader dataset, all of the variables are less necessary to consider; but, the greater the number of variables, the greater the difficulty. As a result, it is often preferable to reduce the number of variables in a dataset and to use critical variables [17]. We may reduce the parameter and find the variable's value in a dataset using a Function Selection technique. During the analysis, four dynamic analysis methods have been used, fault infusion, mutation suitable starting, dynamic taint assessment, and dynamic system check. To generate the vector Space Model (VSM) from extracted features.

2.5 Vulnerability detection

The vulnerability detection has been performed based on extracted features from the training data set. The vector space model has been generated according to extracted features like TF-IDF, relational features, and some bigram features. The classification has been done with recurrent neural networks, including long short-term memory algorithms. This detection is also effective for of prevention of software-as-a-service attacks for web applications. The vulnerable code generates internal as well as external attacks and grants unauthorized access to external users. The major objective of detection vulnerability is the automatic detection of exception handling and buffer overflow attacks during code execution. In the section proposed algorithm provides better detection accuracy in the code snippet [16]. Detailed Experimental Design

The synthetic dataset used in this study was generated by augmenting real-world vulnerability datasets with additional samples created through programmatic transformations, such as adding redundant code blocks and varying variable names to simulate real-world coding diversity. The dataset comprised 2,500 samples, partitioned into 2,000 for training and 500 for testing. Each sample was manually labeled based on known vulnerabilities.

The 20-fold cross-validation was chosen to ensure robust evaluation and reduce bias in model performance assessment. Hyperparameter optimization was conducted using grid search to fine-tune parameters, including the number of RNN layers (1–3), activation functions (ReLU, Sigmoid, Tanh), and dropout rates (0.2–0.5). Data augmentation techniques, such as oversampling of minority classes and SMOTE (Synthetic Minority Over-sampling Technique), were applied to mitigate the effects of class imbalance, ensuring fair training and evaluation of the RNN model.

3 Algorithm design

The algorithms furnished below have been used during the calculations of TF-IDF and weight score calculations using RNN.

TF-IDF:

Input: Input test instance that contains numerous tokens T [i…n]

Output: TF-IDF weight for all T[i]

Step 1: Data_vector = {Data1, Data 2, Data 3…. Data n}

Step 2: Words exist in the entire dataset

Step 3: D = {cmt1, cmt2, cmt3, cmtn} and comments available in each document. Calculate the Tf score as

Step 4: tf (t,d) = (t,d)

t= term

d= document

Step 5: idf = t sum(d)

Step 6: Return tf *idf

Recurrent neural network:

Input: Training dataset TestDBList [], Train dataset TrainDBList [] and Threshold th.

Output: Predicted class according to classification

Step 1: Read train data rules using below formula

$$\text{Train}[] = \sum_{n=1}^{k} (\text{Att}_n \dots \dots \dots \dots \text{Att}_k)$$

Step 2: Read test data rules using below formula

$$\text{Test}[] = \sum_{m=1}^{k} (\text{Att}_m \dots \dots \dots \dots \text{Att}_k)$$

Step 3: Calculate the weight between the input and hidden layer

$$\text{Instance}[w] = \sum_{n=1}^{k} (\text{Test}_n \dots \dots \dots \dots \text{Test}_n) \sum_{m=1}^{k} (\text{Train}_m \dots \dots \dots \dots \text{Train}_k)$$

Step 4: Generate a feedback layer based on the threshold policy

$$\text{Feed_Layer}[] = \sum_{m=1}^{k} (\text{Feed_Layer.optimized}())$$

Step 5: Return Feed_Layer[0]. class

4 Results and discussion

To validate the evaluation of the proposed bug forecast procedure, we have employed RNN classification algorithms that are gainfully utilized for fault prediction including unlabeled datasets. The performance evaluations of software defect prediction are based on the confusion matrix, as shown in Table 2, which includes the measures of precision, recall, as well as F-score.

Table 2: Confusion matrix evaluation

Actual	Predictive	
True	TP (true positive)	FN (false negative)
False	FP (false positive)	TN (true negative)

True positive (TP): The number of fake entities anticipated as fake.

False negative (FN): The number of fake entities anticipated as normal.

False positive (FP): The number of normal entities anticipated as fake.

True negative (TN): The number of normal entities anticipated as normal.

In this research, analytical performance procedures are calculated as follows:

Precision: It shows the proportion of faulty identities received adequate as faulty of all desired objects.

Recall: It is the percentage of faulty identities to all entities that are currently faulty is the proportions of recall.

F-measure: It is the cumulative recall and precision average, with higher estimated coefficients matching higher predictive efficiency.

$$F - Measure = \frac{2 * Precision * Recall}{Recall + Precision}$$

$$Precision = \frac{TP}{TP + FN} \qquad Recall = \frac{TP}{TP + FP}$$

To evaluate the proposed system, we have used machine learning classifiers like ANN, SVM, and Adaboost. Also, we have used the deep learning framework of RNN with LSTM by using activation functions like Sigmoid, Tanh, and ReLU. The results of classification accuracy with confusion matrix with 20-fold cross-validation for all algorithms are shown in Table 3. Measures used to compare the algorithms are Accuracy, Precision, Recall, and Micro-score. From the observations, it can be concluded that RNN (ReLU) gives the highest performance among all.

4.1 Experiment using artificial neural network

figure 2 shows the classification accuracy of the ANN classification algorithm. Initially, it was trained using inbuilt functions from the weka tool. Numerous cross-validation techniques have been used for classification, and various parameters have been tuned for ANN during the classification. This approach can classify each validation according to probability function, that the reason this algorithm has a higher error rate than other supervised classification algorithms.

Table 3: accuracy and confusion matrix for ANN

ANN	Fold 10	Fold 15	Fold 20
Accuracy	85.20	84.20	85.60
Precision	83.60	82.30	84.99
Recall	87.50	85.40	77.72
Micro-Score	85.05	83.35	81.10

The ANN model is easy to build and particularly useful for very large data classification using supervised

machine learning techniques or Artificial Intelligence (AI). Along with simplicity, ANN is known to outperform even highly sophisticated classification methods. The proposed ANN predicts the possibility for individual instances according to current values.

Figure 2 shows the performance evaluation calculation of ANN classification with 20-fold classification. It achieves around 85.60% accuracy for the given input dataset. We used a multinomial event model, samples represent the frequencies with which certain events have been generated by a multinomial probability of that particular event, and based on that probability system predict the final class.

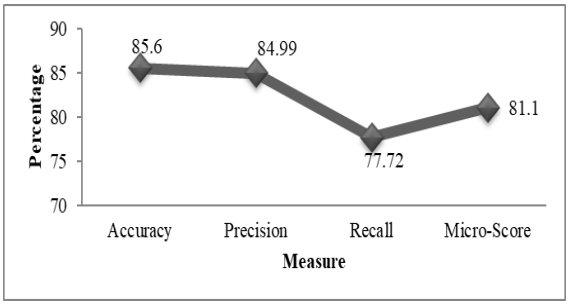

Figure 2: Analysis of bug and vulnerability detection using ANN with 20-fold data cross-validation

4.2 Experiment using support vector machine (SVM)

Table 4 depicts the classification analysis with various cross-validations, we conclude that 20-fold cross-validation provides the highest 95.2% classification accuracy for SVM.

Table 4: accuracy and confusion matrix for SVM

SVM	Fold 10	Fold 15	Fold 20
Accuracy	91.20	91.70	95.20
Precision	91.35	92.10	94.80
Recall	92.30	93.10	96.20
Micro-Score	91.35	92.20	94.75

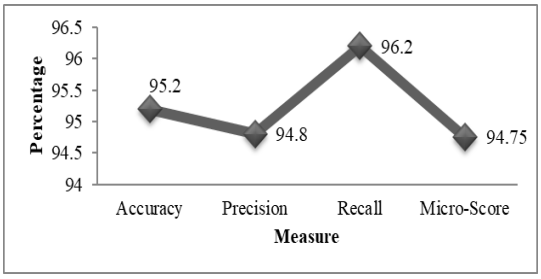

Fig. 3: Analysis of vulnerability detection using SVM with 20-fold data cross-validation

Figure 3 describes SVM for 20-fold cross-validation. The labeling circumstances to construct a training set becomes moment and expensive in many machines learning; it is also helpful to find strategies to reduce supervised classification numbers. By improving performance, the Kernel-Based algorithm has been used to minimize occurrences. We classify all in this algorithm as a point in n-dimensional spaces only with respect to a property direction being the meaning of each characteristic by classification technique; we detect clones by finding the hyper-plane that separates the two groups very well.

4.3 Experiment using adaboost

Below table 5 depicts the classification analysis with various cross-validation, we conclude that 20-fold cross-validation provides the highest 81.30% classification accuracy for Adaboost.

Table 5: Accuracy and confusion matrix for adaboost

Adaboost	Fold 10	Fold 15	Fold 20
Accuracy	70.60	78.50	81.30
Precision	72.30	73.50	74.50
Recall	69.90	68.50	70.30
Micro -Score	70.60	71.90	72.30

Adaboost is adaptive in that it tweaks future weak learners in favor of cases misclassified by prior classifiers. It may be less prone to the overfitting issue than other learning algorithms in certain situations. Individual learners may be poor, but as long as their performance is somewhat better than actual guessing, the overall model will converge to a powerful learner.

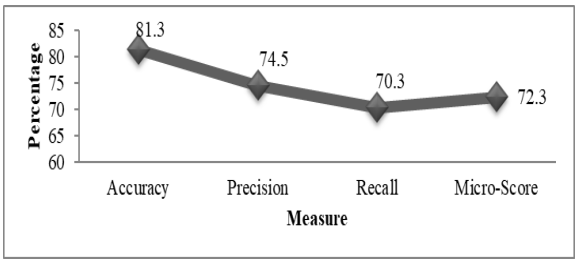

Figure 4: Analysis of vulnerability detection using Adaboost with 20-fold data cross-validation

figure 4 describes Adaboost classification for fake account detection for 20-fold cross-validation. AdaBoost is a specific training technique for boosted classifiers.

$$F_T(x) = \sum_{t=1}^{T} f_t(x)$$

A boost classifier is a kind of classifier.

Each Ft is a weak learner that accepts an object x as input and returns a value that indicates the object's class. The sign of the weak learner output, for example, specifies the predicted object class in the two-class issue, whereas the absolute value indicates confidence in that

classification. Similarly, if the sample belongs to a positive class, the Tth classifier is positive; otherwise, it is negative.

4.4 Experiment using recurrent neural network (Sigmoid)

we demonstrate the classification accuracy of RNN (Sigmoid) using a synthetic dataset, similar experiments have been done with various cross-validation and the results are illustrated in Table 6. According to this analysis, we conclude that 20-fold cross-validation provides the highest 96.10% classification accuracy using RNN with Sigmoid function.

Table 6: accuracy and confusion matrix for RNN (Sigmoid)

RNN (Sigmoid)	Fold 10	Fold 15	Fold 20
Accuracy	95.60	95.90	96.10
Precision	95.80	96.10	97.00
Recall	95.80	96.00	96.30
Micro-Score	94.70	95.90	96.05

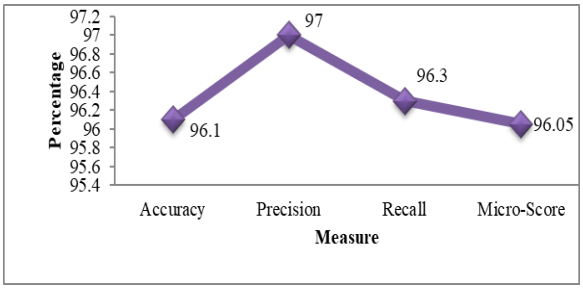

Figure 5: Detection of accuracy using RNN (Sigmoid) with 20-fold data cross-validation

The 20-fold cross-validation also achieves 96.10% with RNN with sigmoid function, have been explained in Figure 5, these RNN functions achieve around higher accuracy over the traditional machine learning algorithms during module testing.

4.5 Experiment using recurrent neural network (Tanh)

figure 6 shows the classification accuracy of RNN, the similar experiments has done with various cross-validations, and the results are illustrated in Table 7. According to this analysis, we conclude that 20-fold cross-validation provides the highest 97.25% classification accuracy for RNN using Tanh.

Table 7: Classification accuracy with confusion matrix for RNN (Tanh)

RNN (Tanh)	Fold 10	Fold 15	Fold 20
Accuracy	96.90	97.50	97.25
Precision	97.00	97.40	97.60
Recall	97.30	97.50	97.30
Micro-Score	96.80	96.70	96.90

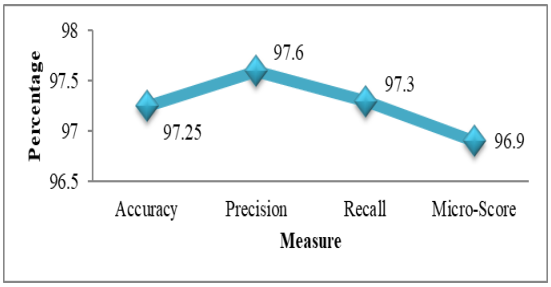

Figure 6: Detection of accuracy using RNN (Tanh) with 20-fold data cross-validation

4.6 Experiment using recurrent neural network (ReLU)

In this experiment we analyse the classification accuracy of ReLU using a synthetic dataset, similar experiments have been done with various cross-validation and the results are illustrated in Table 8. According to this analysis, we conclude system provides the highest 97.5% accuracy for 20-fold cross-validation classification accuracy for RNN.

Table 8: Classification accuracy with confusion matrix for RNN (ReLU)

RNN (ReLU)	Fold 10	Fold 15	Fold 20
Accuracy	97.20	97.90	97.50
Precision	97.40	96.90	97.60
Recall	95.60	97.20	97.90
Micro-Score	96.20	95.80	97.20

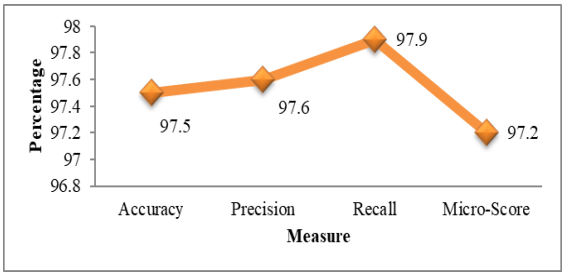

Figure 7: Detection of accuracy using RNN (ReLU) with 20-fold data cross-validation

The above experiments describe a proposed deep-learning classification algorithm with a machine-learning algorithm. This figure describes the result with and without cross-validation. we conclude that RNN with sigmoid provides better detection accuracy than the other two activation functions as well as the random forest machine learning algorithm.

Table 9: Results of above experiments.

Method / Measure	ANN	SVM	Adaboost	RNN (Sigmoid)	RNN (Tanh)	RNN (ReLU)

Accuracy	85.60	95.2	81.30	96.10	97.25	97.50
Precision	84.99	94.80	74.50	97.00	97.60	97.60
Recall	77.72	96.2	70.30	96.30	97.30	97.90
Micro-Score	81.10	94.75	72.30	96.05	96.90	97.20

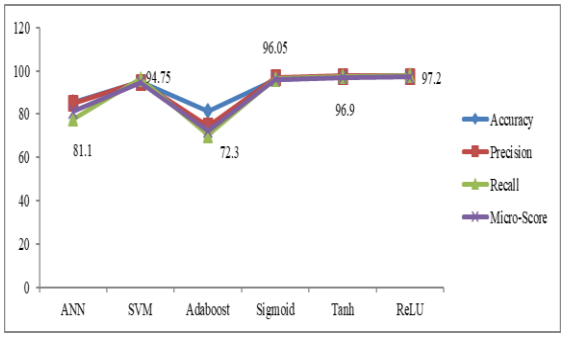

Figure. 8: Classification accuracy with 20-fold cross-validation for all methods

The proposed method obtains the best predictive performance. The suggested solution can be further tested when used in actual software applications. The three data splitting mechanisms have been used as 10, 15, and 20-fold cross-validation.

Table 10: Dataset description of source code extracted from Android APK files

Total Size	2500
Training Samples	2000
Testing Samples	500

The system describes four evaluations between this research results and some existing systems results calculated on similar as well as multiple datasets.

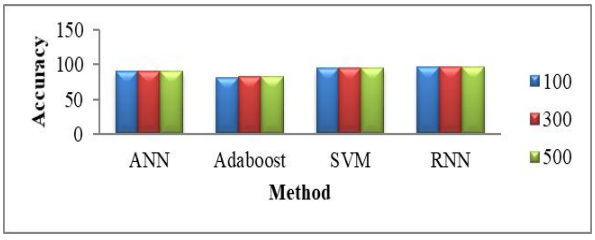

Figure 9: Comparative analysis of proposed vs. existing classification for vulnerability detection shows two machine learning algorithms used.

This figure depicts the proposed RNN provides better detection accuracy over machine learning algorithms.
A classification model is generated using this arrangement or learning set to organize the input courses into corresponding template files or labels. Then a test set is used by gleaning the class labels of orthonormal courses to validate the model. A variety of neural networks are used to identify reviews, such as ANN, Support Vector Machines (SVM), and Adaboost. The proposed RNN framework demonstrates superior performance compared to traditional and deep learning. the RNN outperformed methods like SVM, which struggled with large datasets and computational inefficiency, and CNNs, which lacked robustness in handling hierarchical and semantic features. These improvements are attributed to the RNN's ability to effectively model sequential data and incorporate advanced preprocessing techniques, such as TF-IDF and relational feature extraction, that enhance both semantic and syntactic representation. Additionally, the framework's balanced dataset handling and reduced preprocessing effort offer practical advantages for real-world applications. This innovative combination of features establishes the proposed RNN as a robust and scalable solution, addressing critical gaps in existing approaches while setting new benchmarks in vulnerability detection. The synthetic dataset used in this study was generated by augmenting real-world vulnerability datasets. The dataset comprised 2,500 samples, partitioned into 2,000 for training and 500 for testing. Each sample was manually labeled based on known vulnerabilities.

The 20-fold cross-validation was chosen to ensure robust evaluation and reduce bias in model performance assessment. Hyperparameter optimization was conducted using grid search to fine-tune parameters, including the number of RNN layers (1–3), activation functions (ReLU, Sigmoid, Tanh), and dropout rates (0.2–0.5). Data augmentation techniques, such as the oversampling of minority classes and the Synthetic Minority Over-sampling Technique, were applied to mitigate the effects of class imbalance, ensuring fair training and evaluation of the RNN model.

Artificial Neural Networks (ANN), Support Vector Machines (SVM), and Adaboost, were compared against the proposed RNN framework. For ANN, a two-layer architecture was used with a learning rate of 0.01 and trained for 100 epochs. The SVM utilized a radial basis function (RBF) kernel with a regularization parameter of 1. Adaboost employed 50 weak learners using decision stumps. Each model was trained using the same 20-fold cross-validation setup, with datasets split into 70% training and 30% testing. Training times varied significantly: RNNs required approximately 3 hours per fold, while ANN and SVM training averaged 1 hour and 45 minutes, respectively. Detailed results of accuracy, precision, recall, and micro-scores are provided in the Results section, illustrating the superior performance of RNN (ReLU), achieving an accuracy of 97.5%, precision of 97.6%, and recall of 97.9%.

5 Conclusion and future work

Vulnerability detection is very tedious work for imbalanced source codes; vulnerable code allows for generating software attacks on remote users. Sometimes, during execution, the vulnerable code also generates internal attacks like

buffer overflow, session hijack, bypass authentication, etc. In literature, many problems are detected in software every year. Vulnerabilities mostly do not appear in hidden forms that the software testers can identify. This

system describes the method of finding drawbacks by utilizing deep learning.

In this paper, we have developed an RNN including LSTM for constructing code vulnerability detection and bug triage on various platforms. Numerous tools are not able to support a web-based application to find code vulnerabilities. The proposed system works on different datasets for feature extraction and is able to detect the vulnerability. RNN provides a better result than traditional machine learning classifiers.

In the future, developers need to detect the code triage for runtime mobile-based application programs, because the existing tools do not support mobile application programs.

References

[1] Terada, K.; Watanobe, Y., "Automatic Generation of Fill-in-the-Blank Programming Problems", In Proceedings of the 2019 IEEE 13th International Symposium on Embedded Multicore/Many-core Systems-on-Chip (MCSoC), Singapore, 1–4 October 2019; pp. 187–193. https://doi.org/10.1109/mcsoc.2019.00034

[2] Tai, K.S.; Socher, R.; Manning, C.D., "Improved semantic representations from tree-structured long short-term memory networks", In Proceedings of the 53rd Annual Meeting of the Association for Computational Linguistics and the 7th International Joint Conference on Natural Language Processing, Beijing, China, 26–31 July 2015; pp. 1556–1566. https://doi.org/10.3115/v1/p15-1150

[3] Pedroni, M.; Meyer, B., "Compiler error messages: What can help novices?", In Proceedings of the 39th SIGCSE Technical Symposium on Computer Science Education, Portland, OR, USA, 12–15 March 2008; pp. 168–172. https://doi.org/10.1145/1352322.1352192

[4] Saito, T.; Watanobe, Y., "Learning Path Recommendation System for Programming Education based on Neural Networks", Int. J. Distance Educ. Technol. (Ijdet) 2020, 18, 36–64. https://doi.org/10.4018/ijdet.2020010103

[5] Teshima, Y.; Watanobe, Y., "Bug detection based on LSTM networks and solution codes", In Proceedings of the 2018 IEEE International Conference on Systems, Man, and Cybernetics (SMC), Miyazaki, Japan, 7–10 October 2018; pp. 3541–3546. https://doi.org/10.1109/smc.2018.00599

[6] Fan, G.; Diao, X.; Yu, H.; Yang, K.; Chen, L., "Software Defect Prediction via Attention-Based Recurrent Neural Network", Sci. Program. 2019, 2019, 6230953. https://doi.org/10.1155/2019/6230953

[7] Ohashi, H.; Watanobe, Y., "Convolutional Neural Network for Classification of Source Codes", In Proceedings of the 2019 IEEE 13th International Symposium on Embedded Multicore/Many-core Systems-on-Chip (MCSoC), Singapore, Singapore, 1–4 October 2019; pp. 194–200. https://doi.org/10.1109/mcsoc.2019.00035

[8] Zhou, Y.; Tong, Y.; Gu, R.; Gall, H., "Combining text mining and data mining for bug report classification", J. Softw. Evol. Process 2016, 28, 150–176. https://doi.org/10.1002/smr.1770

[9] Jin, K.; Dashbalbar, A.; Yang, G.; Lee, J.-W.; Lee, B., "Bug severity prediction by classifying normal bugs with text and meta-field information", Adv. Sci. Technol. Lett. 2016, 129, 19–24. https://doi.org/10.14257/astl.2016.129.05

[10] Goseva-Popstojanova, K.; Tyo, J., "Identification of security related bug reports via text mining using supervised and unsupervised classification", In Proceedings of the IEEE International Conference on Software Quality, Reliability and Security, Lisbon, Portugal, 16–20 July 2018; pp. 344–355. https://doi.org/10.1109/qrs.2018.00047

[11] Kukkar, A.; Mohana, R., "A Supervised bug report classification with incorporate and textual field knowledge", Procedia Comp. Sci. 2018, 132, 352–361. https://doi.org/10.1016/j.procs.2018.05.194

[12] Tong, H.; Liu, B.; Wang, S., "Software defect prediction using stacked denoising auto encoders and two-stage ensemble learning", Inf. Softw. Technol, 96, 94–111. https://doi.org/10.1016/j.infsof.2017.11.008

[13] Yogesh Kene, Uday Khot, Imdad Rizvi " A Survey of Image Classification and Techniques for Improving Classification Performance " arXiv 2019, arXiv:1608.06048. https://doi.org/10.2139/ssrn.3349696

[14] Jun Wang, Beijun Shen, Yuting Chen., " Compressed C4.5 Models for Software Defect Prediction ", IJCSI Int. J. Comput. Sci. Issues 2012, 9, 288–296 https://doi.org/10.1109/qsic.2012.19

[15] Neuhaus, S.; Zimmermann, T.; Holler, C.; Zeller, A. "Predicting Vulnerable Software Components", In Proceedings of the 14th ACM conference on Computer and Communications Security, Alexandria, VA, USA, 28–31 October 2007; pp. 529–540. https://doi.org/10.1145/1315245.1315311

[16] Markad Ashok Vitthalrao, Mukesh Kumar Gupta, "Software Vulnerability Classification based on Machine Learning Algorithm", International Journal of Advanced Trends in Computer Science and Engineering (IJATSCE), ISSN 2278-3091, Volume 9, No.4, July – August 2020, Page No.6653-6659. https://doi.org/10.30534/ijatcse/2020/358942020

[17] Markad Ashok Vitthalrao, Mukesh Kumar Gupta, "Software Vulnerability Classification based on Deep Neural Network", International Journal of

Engineering and Advanced Technology (IJEAT), ISSN: 2249-8958 (Online), Volume-9 Issue-1, October 2019, Page No.3146-3150.
https://doi.org/10.35940/ijeat.a9746.109119

K-LSTM-ECM Model for Predicting Poverty Alleviation Impacts of Digital Financial Inclusion

Yichuan Li
Zhoukou Vocational and Technical College, Zhoukou 466002, China
E-mail: zkzklyc@163.com

Keywords: digital inclusive finance, poverty reduction effect, K-means clustering, LSTM, error correction model (ECM), data analysis, forecast

Received: November 19, 2024

To evaluate the poverty alleviation effects of digital financial inclusion, this study proposes a comprehensive financial data analysis and prediction method by integrating K-means clustering, Long Short-Term Memory (LSTM) neural networks, and the Error Correction Model (ECM), collectively forming the K-LSTM-ECM model. The model first employs K-means clustering to group user data and uncover behavioral patterns of different user groups. Subsequently, LSTM is used to model and predict time-series data. Finally, the ECM is introduced to correct systematic errors and enhance prediction accuracy. The model was validated using diverse datasets, including World Bank Open Data, IMF economic indicators, and UNDP Human Development Reports. The results show that the error range of K-LSTM-ecm model is the lowest in mean square error, mean absolute error and root mean square error (e.g., mean square error is the lowest 1.44%), and the prediction precision rate reaches 91.23% on average. In terms of recall rate and false positive rate, K-LSTM-ecm model outperforms other models, with the highest recall rate reaching 94.45% and the lowest false positive rate reaching 2.08%. Through case studies, the prediction results of K-LSTM-ecm model for 2021 and 2022 are closer to the actual data, with poverty values of 0.212 and 0.181, respectively, and the prediction results of key indicators such as the proportion of subsistence population and rural disposable income are also better than other models. These findings verify the efficiency and reliability of the K-LSTM-ECM model in predicting the poverty alleviation effects of digital financial inclusion, providing robust data support for policymakers and the financial industry.

Povzetek: Predlagan je nov model K-LSTM-ECM za ocenjevanje učinkov digitalne finančne vključenosti na zmanjševanje revščine, ki združuje metode gručenja K-means, LSTM in ECM.

1 Introduction

Poverty remains a persistent global challenge, affecting billions of individuals [1]. In addressing this critical issue, digital inclusive finance (DIF), as an innovative financial model, is widely recognized as a potent tool for poverty alleviation and eradication [2]. By merging digital technology with financial services, DIF provides convenient, affordable, and secure financial services to the underserved and marginalized populations, fostering their inclusion into formal financial systems, and enhancing economic inclusivity and sustainable development [3]. Despite its widespread adoption worldwide, uncertainties persist regarding the actual impact and mechanisms through which DIF contributes to reducing poverty. To delve deeper into the reducing poverty of DIF. A novel comprehensive model, K-LSTM-ECM, is brought out. It integrates K-means clustering, Long Short-Term Memory (LSTM) neural networks, and Error Correction Model (ECM). By analyzing financial behavior data from diverse user groups and applying the K-LSTM-ECM model for modeling and prediction, the study aims to assess the potential impact of DIF services on reducing poverty. The research is committed to using K-LSTM-ECM model to accurately analyze and predict the poverty reduction effect of digital financial inclusion. The goal is to reveal the deep links between financial behavior and poverty reduction through a comprehensive evaluation of the model, provide reliable forecasting results to guide policy making and financial practice, and verify the application potential of the model in the field of financial data analysis and forecasting.

The contribution of the research is to propose an innovative K-LSTM-ECM model, which provides a new analysis and prediction method for the poverty reduction effects of digital financial inclusion by combining K-means clustering, LSTM neural networks, and ECM. This study not only provides an in-depth analytical framework in theory, but also demonstrates the high predictive accuracy and reliability of the model in empirical research, which provides strong data support for policy makers in the formulation of poverty reduction strategies and the optimization of financial practices, and has important value in promoting further discussion and research on the application of financial technology and machine learning in the academic community.

The novelty of the research is reflected in the unique construction of the K-LSTM-ECM model, which integrates different technical means to provide an unprecedented comprehensive perspective for the study of the poverty reduction effects of digital financial inclusion. The innovation of the model is not limited to the technical level, but also its ability to process large-scale financial data, capture user behavior patterns, and predict long-term dependencies. Moreover, the model's high accuracy and low error rate shown in empirical studies, as well as its potential impact on policy making and financial product design, highlight its innovative status and application prospects in existing research.

The study is divided into five coherent parts. The first part introduces the global research status of digital financial inclusion and LSTM technology through literature review. In the second part, the construction principle and process of K-LSTM-ECM model are explained in detail, and how to integrate various technical means to enhance the ability of data analysis and prediction. In the third part, the performance of the model is evaluated through experiments to confirm its efficiency and accuracy in predicting the poverty reduction effect of digital financial inclusion. In the fourth part, the research discusses the whole content and summarizes the main challenges, limitations and advantages of the research content. The fifth part reviews the research results, discusses the practical application value of the model, and puts forward the direction and suggestions of future research, in order to provide data support and decision-making reference for policy making and financial practice.

2 Related works

Digital technology and financial innovation are driving the rapid development of global inclusive finance, providing efficient and safe financial services for impoverished and marginalized populations, thereby promoting inclusive economic growth and poverty alleviation [4, 5]. Malladi et al. [3] addressed the developmental challenges of inclusive finance in India, proposing recommendations to overcome key challenges and promote the further development of digital technology to advance inclusive finance for broader social inclusivity. Rastogi et al. [6] focused on India's Unified Payments Interface platform, using structural equation modeling to analyze its impact on financial literacy, financial inclusivity, and economic development for the poor, bridging knowledge gaps between the Unified Payments Interface and these aspects. Li J et al. [7]. investigated the impact of DIF on urban innovation, introducing a difference-in-differences model to estimate its causal effect on urban innovation, highlighting its positive influence and enhancing public awareness of DIF. Hasan et al. [8] examined how digital financial services contribute to inclusive finance in the environment of China, addressing the representation gaps in financial services for billions of people in developed and emerging markets, providing insights for future policies and research on inclusive finance.

With the rise of machine learning, deep learning and other technologies and the improvement of computing power, the effective prediction of financial data has been studied by many scholars. Biju A K V N et al. [9] conducted a detailed analysis and evaluation of the increasing application of machine learning, artificial intelligence, and deep learning in the financial field, and found deficiencies in empirical academic research to critically evaluate these algorithm-based advanced automated financial technologies. Aiming at the high interest of pattern recognition researchers in the field of market financial prediction, Barra S et al. [10] proposed to use the integrated model of convolutional neural networks to process time series data and predict the future trend of the American market, thus achieving effective financial analysis and prediction. Aiming at the importance of innovation in financial risk management and stock forecasting, Kurani A et al. [11] discussed two algorithms that play an important role in stock forecasting, namely artificial neural network and support vector machine. The results showed that artificial neural network and support vector machine can solve financial problems to a certain extent, and can be integrated with other novel technologies. Form a hybrid approach to provide a more robust approach to financial stock data forecasting. Al Dulaimi J A A B et al. [12] proposed to use data mining tools to analyze and forecast financial data in view of the financial forecasting difficulties faced by enterprises, and analyzed time series data through regression equations to help enterprises predict financial failures and provide information needed for key decisions. A summary of the work is shown in Table 1.

Table 1: Summary of related work

Author(s)	Contribution	Methodology	Results
Malladi et al. [3]	Addressed challenges in digital financial inclusion in India	Structural equation modeling	Proposed strategies for advancing inclusive finance through digital technologies
Rastogi et al. [6]	Impact of India's Unified Payments Interface on financial literacy and inclusivity	Structural equation modeling	Bridged gaps in financial literacy and inclusivity for the poor
Li J et al. [7]	Investigated the impact of DIF on urban innovation	Difference-in-differences model	Highlighted the positive impact of DIF on urban innovation

Hasan et al. [8]	Contribution of digital financial services in China's inclusive finance	Regression analysis	Provided insights into inclusive financial policies in developed and emerging markets
Biju A K V N et al. [9]	Analyzed the application of machine learning and deep learning in finance	Machine learning, AI, deep learning	Critically evaluated the use of AI technologies for financial prediction
Barra S et al. [10]	Time-series financial prediction using convolutional neural networks	CNN-based integrated model	Achieved effective financial analysis and prediction for market trends
Kurani A et al. [11]	Comparison of ANN and SVM for stock forecasting	Artificial neural network (ANN) and Support vector machine (SVM)	Demonstrated the role of hybrid models for stock data forecasting
Al Dulaimi J A A B et al. [12]	Used data mining tools for financial data analysis	Data mining and regression analysis	Helped predict financial failures and assist decision-making

To sum up, existing researches have shortcomings in the following aspects: First, they lack integrated models, and most of them use a single method (such as structural equation model, convolutional neural network, etc.), which cannot effectively capture complex relationships and time dependence in financial data; Second, the research on digital financial inclusion mostly stays at the level of qualitative analysis and lacks quantitative evaluation of its poverty reduction effect. Third, the lack of systematic error correction mechanism leads to the limited accuracy of long-term prediction; Fourth, the lack of integration and utilization of multi-source data has failed to fully reveal the multidimensional impact of digital financial inclusion. Therefore, this paper proposes a study on the poverty reduction effect of digital financial inclusion based on K-LSTM-ECM model, and combines K-means clustering algorithm to analyze the causal relationship between digital financial inclusion and poverty reduction effect by using LSTM model and error model. The novelty of the research is reflected in the unique construction of the K-LSTM-ECM model, which integrates different technical means to provide an unprecedented comprehensive perspective for the study of the poverty reduction effects of digital financial inclusion. The innovation of the model is not limited to the technical level, but also its ability to process large-scale financial data, capture user behavior patterns, and predict long-term dependencies. Moreover, the model's high accuracy and low error rate shown in empirical studies, as well as its potential impact on policy making and financial product design, highlight its innovative status and application prospects in existing research.

3 Establishment of the K-LSTM-ECM model of dif's poverty reduction effects

The establishment of the K-LSTM-ECM model for learning DIF's reducing poverty effects holds significant significance. By combining K-means, LSTM, and ECM techniques, the model offers a more accurate and reliable analysis approach to address the uncertainty of DIF's impact on reducing poverty. This section provides detailed descriptions of the K-means clustering algorithm, LSTM models, and ECM models, along with the framework and training process of the K-LSTM-ECM model.

3.1 K-means clustering algorithm application in K-LSTM-ECM model

Given the abundance of customer and transaction data, the K-means clustering algorithm is adept at grouping customers, identifying various customer segments, and revealing distinct characteristics and needs. Customer segmentation enables financial institutions to provide personalized financial services, catering to diverse customer needs and enhancing user experience. Moreover, K-means clustering facilitates market segmentation, unveiling market characteristics and potential opportunities to guide precise marketing strategies and financial product promotion. Additionally, K-means clustering aids risk assessment by clustering customer transaction behaviors, identifying high-risk and low-risk customers, enabling financial institutions to accurately assess risks and take appropriate measures. The K-means clustering process is illustrated in Fig. 1 [13].

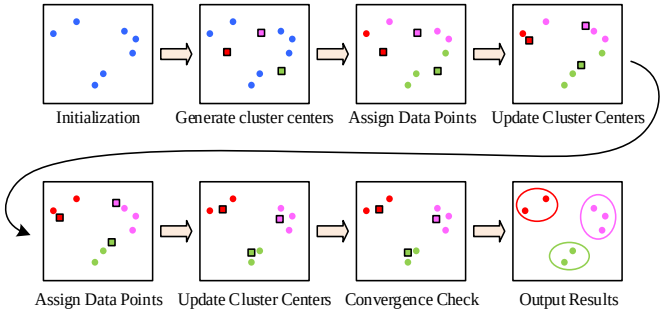

Figure 1: K-means clustering algorithm

The K-means first selects K clusters and randomly selects K data points, then treat them as the initial cluster centers. Next, find the distance between each data point and every cluster center, and then assign the data point to the cluster that has the nearest center. This process will result in the formation of K sets of clusters. After that, recompute the center of each cluster by taking the average of all the data points belonging to that cluster. Check again whether the cluster centers have changed, and stop iteration if the change is less than the preset threshold or reaches the maximum number of iterations. Finally, according to the updated cluster centers, the data points are reassigned to the nearest cluster, and the cluster centers are updated again. Repeat the above process until the convergence condition is met. Finally, the final cluster center and the cluster assignment of each data point are obtained.

The first step in the calculation process of the K-means algorithm is to establish a set A containing n data samples, as shown in Formula (1).

$$\Omega=\left\{x_i \mid x_i=\left(x_{i1},x_{i2},\cdots,x_{id}\right),i=1,2,\cdots,n\right\} \tag{1}$$

In Formula (1), $x_i=\left(x_{i1},x_{i2},\cdots,x_{id}\right)$ is a vector with d dimensions. It represents d different attributes of the i -th data. The sample size is expressed by N. Then Formula (2) is given.

$$C=\left\{c_j \mid c_j=\left(c_{j1},c_{j2},\cdots\right), j=1,2,\cdots k\right\} \tag{2}$$

In Formula (2), $c_j=\left(c_{j1},c_{j2},\cdots\right)$ is Jth cluster's center point, each center point c_j contains d different attributes, and k represents the number of clusters. The second step is to choose an appropriate K value. The K value selection in the K-means algorithm can be given directly, or can be determined through various model analysis to obtain the optimal clustering effect. The third step is to calculate the distance between the two data of x_i and c_j. Generally, Euclidean distance and Manhattan distance are used for distance measurement. Euclidean distance is shown in Formula (3).

$$dis\left(x_i,c_j\right)=\sqrt{\sum_{l=1}^{d}\left(x_{il}-c_{jl}\right)^2},i=1,2,\cdots,n;\ j=1,2,\cdots k \tag{3}$$

In Formula (3), $dis\left(x_i,c_j\right)$ represents the distance between x_i and c_j, and l represents the number of dimensions in the space. The Manhattan distance is shown in Formula (4).

$$dis\left(x_i,c_j\right)=\sum_{l=1}^{d}\left|x_{il}-c_{jl}\right|,i=1,2,\cdots,n;\ j=1,2,\cdots k \tag{4}$$

In Formula (4), it is the same as the Euclidean distance formula, and l represents the number of dimensions in the space. The fourth step is to recalculate the same cluster as c_j after classifying the sample data, as shown in Formula (5).

$$c_{jl}=\frac{1}{N\left(\phi_j\right)}\sum_{x_i\in\phi_j}x_{il},\quad l=1,2,\cdots,d;\ j=1,2,\cdots k \tag{5}$$

In Formula (5), $N\left(\phi_j\right)$ is the data amount in one same cluster, $x_i=\left(x_{i1},x_{i2},\cdots,x_{id}\right)$. The fifth step is to judge when to stop the operation of the K-means algorithm, and usually use the criterion function to evaluate the clustering effect. A commonly used criterion function is the sum of squared errors (SSE), which is used to measure the sum of the distances between each data point and the cluster center to which it belongs, indicating the closeness of the cluster. Smaller SSE, the better the clustering effect, as shown in Formula (6).

$$E=\sum_{j=3}^{k}\sum_{x_i\in\phi_j}dis\left(x_i,c_j\right) \tag{6}$$

In Formula (6), E represents the sum of the square errors, $dis\left(x_i, c_j\right)$ represents the distance between x_i and c_j, x_i represents a given data object, and c_j is the center point of the j-th cluster.

3.2 Establishment of LSTM in K-LSTM-ECM model

In the research on the reducing poverty effect of DIF, the main reason for using LSTM is its powerful ability to process time series data. Digital financial inclusion involves a large amount of time-series data, such as user transaction records and consumption behaviors, and LSTM can effectively capture the long-term dependencies in these data and help better understand user behavior patterns and trends. Especially in the financial field, user behavior and decision-making are affected by a long time in the past. This long-term dependency is crucial for accurate prediction and modeling, and the design structure of LSTM enables it to transmit and store information for a long time, and thereby better handle this long-term dependency. In addition, LSTM has flexible sequence modeling capabilities, can adapt to different types of time series data, and can model continuous event sequences, such as users' transaction sequences and login sequences. The basic structure of LSTM is given in Fig. 2 [14].

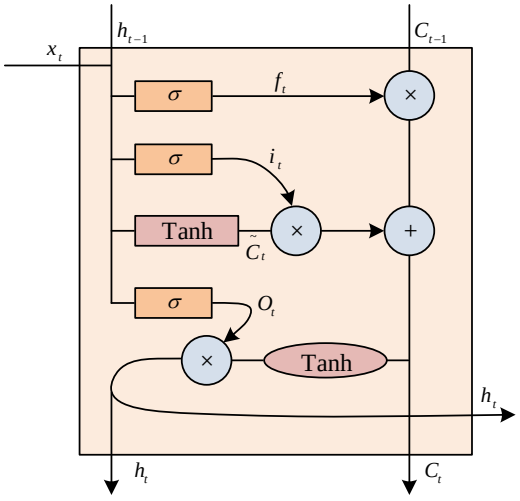

Figure 2: LSTM infrastructure diagram

In Fig. 2, the output at the current and previous moment is shown, and the state at these two moment is shown. LSTM introduces three gate structures to control and protect information. The memory storage cell of LSTM consists of four parts including self-loop connected nodes [15]. The role of these gates is to realize the function of forgetting or remembering through the selective forgetting and recording of information. LSTM not only includes three gate-level control units that control the flow of information, the input gate i, the forget gate f, and the output gate o, but also has built-in hidden layer memory cells C_t. The forget gate f is used to control the degree of retention of the information of the previous moment in the memory cells at the current moment. The calculation of the forget gate f at time t is shown in Formula (7).

$$f_t = \sigma\left(W_f \cdot \left[h_{t-1}, x_t\right] + b_f\right) \tag{7}$$

In Formula (7), W_f is the forgetting gate weight matrix, h_{t-1} is the hidden state at the previous moment, x_t is the input currently, and b_f is the bias parameter. σ represents the S-type activation function, and its expression is shown in Formula (8).

$$f\left(x\right) = \frac{1}{1-e^{-x}} \tag{8}$$

Formula (8) is used to map the calculation result to the range [0, 1], which means that the value that the forgetting gate output is input to the gate I. The calculating process is shown in Formula (9).

$$i_t = \sigma\left(W_i \cdot \left[h_{t-1}, x_t\right] + b_i\right) \tag{9}$$

In Formula (9), W_i means input gate's weight matrix, and b_i is the bias parameter of the input gate. The input gate controls the update degree of the input information of the current moment to the memory cells. The calculation of the output gate o is shown in Formula (10).

$$o_t = \sigma\left(W_o \cdot \left[h_{t-1}, x_t\right] + b_o\right) \tag{10}$$

In Formula (10), W_o means output gate's weight matrix, and b_o is the bias parameter of the output gate. The output gate controls the degree to which the information in the memory cell is output at the current moment. The calculation of $C_t^{'}$ candidate memory cells is shown in Formula (11).

$$C_t^{'} = \tanh\left(W_c \cdot \left[h_{t-1}, x_t\right] + b_c\right) \tag{11}$$

In Formula (11), W_c means input gate's weight matrix and the hidden state at the last moment, b_c is the bias parameter of the candidate cell, $\tanh$ is a hyperbolic function, and its expression is shown in Formula (12).

$$\tanh(x)=\frac{e^{x}+e^{-x}}{e^{x}-e^{-x}} \tag{12}$$

Formula (12) converges faster than the S-type activation function. A candidate memory cell is a temporary memory cell computed at each time step to store new input information. The update memory cell calculation is shown in Formula (13).

$$C_t = f_t \cdot C_{t-1} + i_t \cdot C_t^{'} \tag{13}$$

In Formula (13), C_{t-1} is the memory cell at the previous moment, and updating the memory cell is to update the memory cell through the weighted sum of the forget gate, input gate and candidate memory cells. The output of memory cells is shown in Formula (14).

$$h_t = o_t \cdot \tanh\left(C_t\right) \tag{14}$$

In Formula (14), h_t represents the hidden state of LSTM at the t moment, which is also the output of memory cells.

3.3 The error correction model is introduced in K-LSTM-ECM model

ECM is a statistical model used to correct the error between predicted values and actual observed values in time series [16]. Due to complex economic and social factors, the reducing poverty effect of DIF is often affected by multiple variables, so there may be some errors in the prediction results. Therefore, the research introduces ECM to help correct systematic errors or deviations in model predictions, thereby improving the accuracy and reliability of predictions. The general form of ECM is shown in Formula (15).

$$\Delta y_t = \alpha + \beta \Delta y_{t-1} + \gamma \Delta x_{t-1} + \varepsilon_t \tag{15}$$

In Formula (15), Δy_t tells the dependent variable first-order difference instantly, Δy_{t-1} tells its lagged first-order difference at time $t-1$, and Δx_{t-1} tells its lagged first-order difference at time $t-1$. ECM estimates coefficients α, β and γ by statistical techniques such as least squares regression. After estimating the coefficient ε_t, ECM can correct the prediction error of the original model by adding the error term to the predicted value. After introducing ECM, the K-LSTM-ECM model framework is established, as shown in Fig. 3.

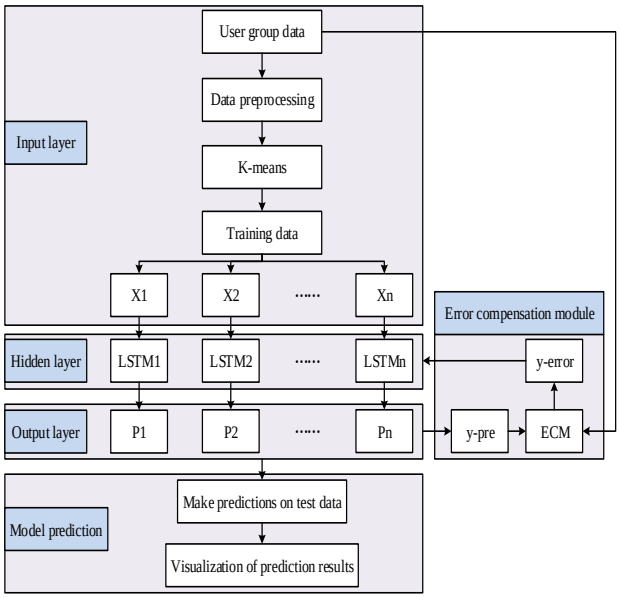

Figure 3: K-LSTM-ECM model framework

As can be seen from Fig. 3, the K-LSTM-ECM model first performs the data preprocessing step, in which the user group data is cleaned and normalized to ensure the accuracy of subsequent analysis. Then, the K-means clustering algorithm is applied for detailed group processing of customer data, which classifies customers with similar characteristics into the same category and effectively identifies and distinguishes the specific needs and behavior patterns of different customer groups. Based on the results of K-means clustering, the model customizes and builds a specialized LSTM model for each customer group. These models are specifically designed to analyze and predict the potential impact of digital financial inclusion on poverty reduction across groups. In this way, models are able to provide personalized predictions and in-depth analysis for the specific situations of different customer groups. Further, the model applies the trained K-LSTM-ECM model to the prediction task of future data to predict how the poverty reduction effects of digital financial inclusion evolve over time. In addition, ECM is used to comprehensively evaluate the accuracy and stability of the model prediction to ensure the reliability of the prediction results and the robustness of the model. This process not only improves forecasting accuracy, but also provides solid data support for financial decisions. The K-LSTM-ECM model training process is shown in Fig. 4.

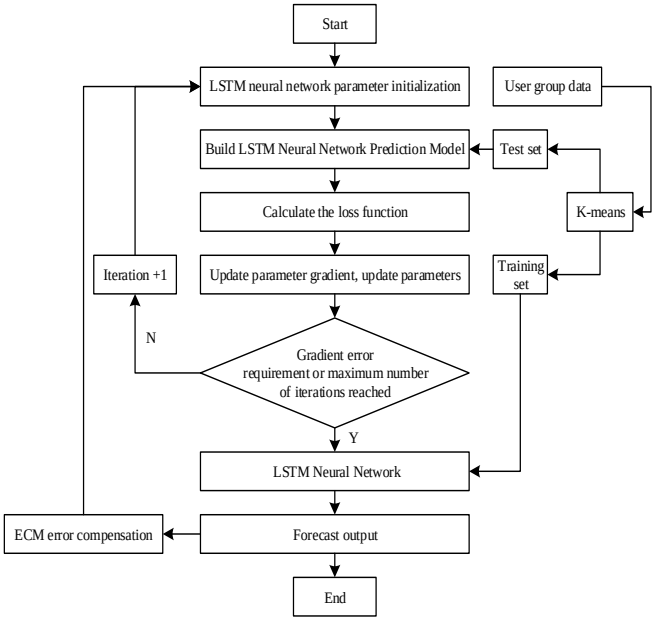

Figure 4: K-LSTM-ECM model training process

As shown in Fig. 4, first, the user groups are classified using the K-means clustering algorithm, and corresponding labels are generated. Next, divide the clustered passenger flow data into two set for training and examing. Then, initialize the network weights and parameters of the LSTM neural network model. The square loss function is used as the loss function, and the backpropagation is performed to calculate the error. Adam optimizer is hired for computing gradients and update parameters. The prediction results are input into the error correction model ECM, the error is calculated, and the error is fed back to the LSTM neural network. Finally, output the prediction result. This training process combines K-means clustering, LSTM model training and ECM to improve the accuracy and performance of research on the effects of digital financial inclusion on reducing poverty. The pseudo-code for model training is shown in Table 2.

Table 2: Pseudo-code for K-LSTM-ECM model training

Step	Description
1	Initialize parameters for the LSTM model (e.g., weights, biases, learning rate).
2	Perform K-means clustering on user data:
	(a) Execute K-means clustering on X_user to generate clusters.
	(b) Assign each user group to a corresponding cluster for training and testing.
3	Build the LSTM neural network prediction model.
4	Train the LSTM model:
	For t = 1 to max_iter:
	For t = 1 to max_iter: a. Forward Propagation: - Input X_train into the LSTM model. - Compute predictions and loss based on y_train.
	b. Backward Propagation: - Calculate gradients of the loss function. - Update model parameters using gradient descent.
	c. Convergence Check: - If gradient error < epsilon or t == max_iter, stop training.
5	Use the trained LSTM model to make predictions on test data X_test and obtain initial predictions.
6	Apply the Error Correction Model (ECM):
	(a) Input the LSTM predictions into the ECM model.
	(b) Adjust the predictions using the error correction mechanism to further reduce residual errors.
7	Output the final forecast results y_pred.

4 Analysis of the research results on the poverty reduction effect of dif under the K-LSTM-ECM model

The study carried out model comparison experiments and a case study of the reducing poverty effect of DIF. In the model comparison experiment, the study used 5 sets of existing real data as the benchmark, and tested the prediction error, precision rate, recall rate, and F1 value (F-measure) indicators of the three models respectively. In the case analysis, the study uses the K-LSTM-ECM model to conduct a comprehensive and detailed analysis and compare it with the real results to calculate its accuracy.

4.1 Data set selection and processing

In the experiments conducted, the study used a comprehensive data collection strategy that included World Bank Open Data, IMF economic indicators, UNDP Human development reports, Global Findex databases, and country-specific central bank and

financial regulator reports. Through the combination of systematic sampling and convenient sampling, we can ensure the universality and representative of samples in many countries and regions around the world. The collected data is rigorously cleaned and standardized to eliminate inconsistencies and dimensional differences, enhancing the comparability of the data. Data preprocessing and model training adopt best practices, including data standardization, cross-validation, etc., to ensure the accuracy of research results and the generalization ability of models.

4.2 K-LSTM-ECM model comparison experiment

For the prediction accuracy and superiority verifying with the K-LSTM-ECM, the study conducted a model comparison experiment. The test objects were the LSTM model, the K-LSTM model without ECM, and the K-LSTM-ECM model. In the comparative experiment, a single LSTM model is first used to predict the effect of reducing poverty, and then the K-LSTM model without an error compensation model is used for prediction. Next, use the K-LSTM-ECM model to input the prediction results of the LSTM model into the error correction model to obtain the corrected prediction results. By comparing the three models' predicting output, the improvement effect of the error correction model on the prediction results can be analyzed. In the experiment, based on experimental tuning and literature support, the number of K-means clusters is set to 5, which can effectively balance the meticulousness of grouping and computational complexity. In terms of LSTM hyperparameter Settings, the number of hidden layer nodes is 64, the learning rate is 0.001, the time step is 10, and the batch size is 64. These parameters refer to the common configurations of previous studies, which can meet the computing resource conditions of this study and ensure the training efficiency and prediction performance of the model.

The experiment was completed on a high performance computing server with hardware configuration including Intel Xeon Gold 6226R CPU, NVIDIA Tesla V100 GPU (32 GB video memory), 128 GB memory and 2 TB NVMe SSD. The operating system is Ubuntu 20.04 LTS. The software environment is Python 3.8, mainly using PyTorch 1.10.0, Scikit-learn 0.24.2 (K-means), NumPy 1.21.2, Pandas 1.3.3 and Matplotlib 3.4.3. In data preprocessing, the missing values are filled by multiple interpolation method, and the outliers are detected and eliminated based on 3σ principle. In addition, z-score standardization is used to normalize the data to ensure the consistency of each feature dimension. The error correction model (ECM) is implemented by a custom Python module with a random seed set to 42. Data preprocessing ensures the stability of model inputs and the reproducibility of experimental results. The research first evaluates the prediction errors of the three, and the experimental results are shown in Fig. 5.

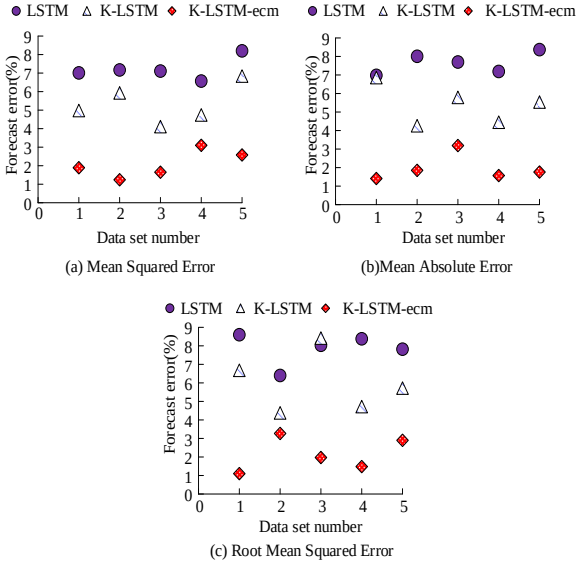

Figure 5: Evaluation results of three model prediction errors

It can be seen from Fig. 5 that three indicators are studied to measure the forecast error, which are mean square error, mean absolute error and root mean square error. In the mean square error results, the highest error of the LSTM model is 8.34%, the lowest is 6.88%, the highest error of the K-LSTM model is 7.12%, the lowest is 4.01%, the highest error of the K-LSTM-ECM model is 3.68%, and the lowest is 1.44%. Among the average absolute errors, the error range of the LSTM model is 7.11%-8.49%, the error range of the K-LSTM model is 4.28%-6.89%, and the error range of the K-LSTM-ECM model is 1.49%-3.27%. In the root mean square error, the overall error of the K-LSTM-ECM model is also the smallest. The K-LSTM-ECM model shows better performance in terms of prediction error, with lower error bounds compared to the LSTM model and the K-LSTM model. The precision rate evaluation results of the three models are Fig. 6.

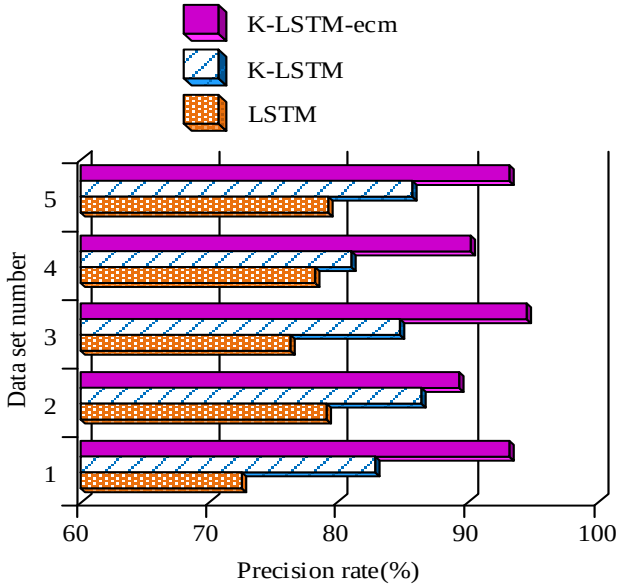

Figure 6: Evaluation results of three model prediction errors

As can be seen from Fig 6, the precision rate of K-LSTM-ECM model is the highest on all data sets, among which the precision rate on data set No. 3 reaches 94.86%, and the average precision rate on all data sets reaches 91.23%. Compared with the average precision rate of LSTM model 74.56% and K-LSTM model 83.18%, the average precision rate increased by 16.67% and 8.05% respectively. It shows that the K-LSTM-ECM model is excellent in the precision rate of prediction results, and can more accurately judge the impact of DIF on reducing poverty. The evaluation results of the recall rate and false positive rate of the three models are shown in Fig. 7.

As can be seen from Fig 7, in terms of recall rate, K-LSTM-ECM model reaches the highest level in the tests under different data sets, among which the recall rate on data set 1 is 94.45%, that on data set 2 is 92.64%, that on data set 3 is 88.92%, and that on data set 4 is 91.07%. The recall rate on dataset 5 is 86.55%, indicating that the model can capture positive samples more accurately and has a high ability to identify poverty reduction effects. In terms of false positives rate, K-LSTM-ECM model also performs well. In the test of data sets 1 to 5, the false positives rate is 2.08%, 5.48%, 3.23%, 3.81% and 4.16% respectively, which is significantly lower than the other two models, indicating that K-LSTM-ECM model has a good effect in reducing false positives. More precise control over error reporting. In addition, the K-LSTM-ECM model combines K-means clustering, LSTM neural network and error correction model, which has certain complexity in predicting the effect of reducing poverty. Therefore, the F1 value under the K-LSTM-ECM model. In the research on the reducing poverty effect of digital financial inclusion, it is helpful to comprehensively consider the predictive ability of the model. The F1 values of the three models are shown in Fig. 8.

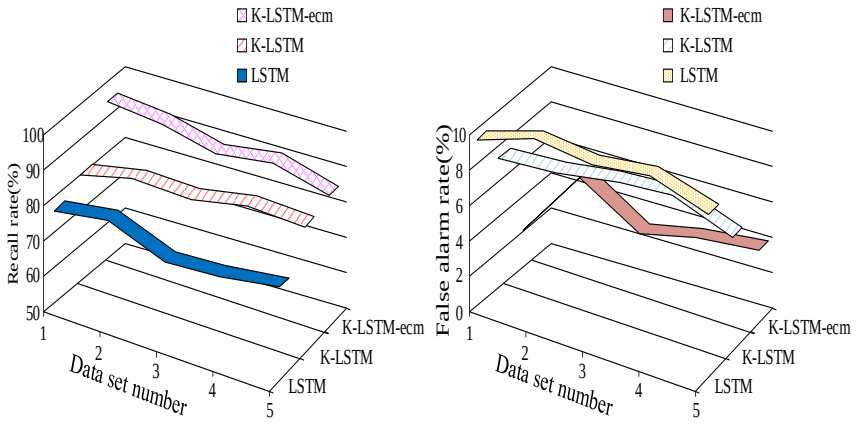

(a) Comparison of recall rates (b) Comparison of false alarm rates

Figure 7: Results of recall rate and false positive rate evaluation

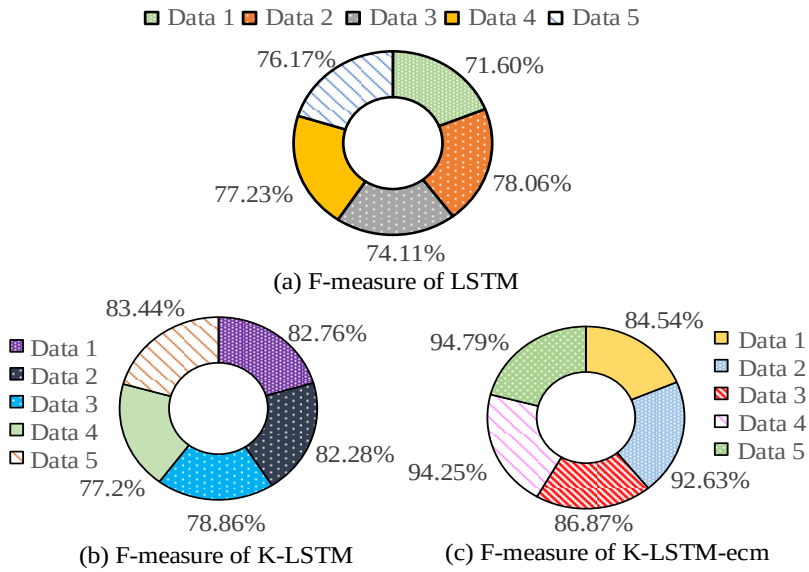

(a) F-measure of LSTM

(b) F-measure of K-LSTM (c) F-measure of K-LSTM-ecm

Figure 8: F-measure for the three models

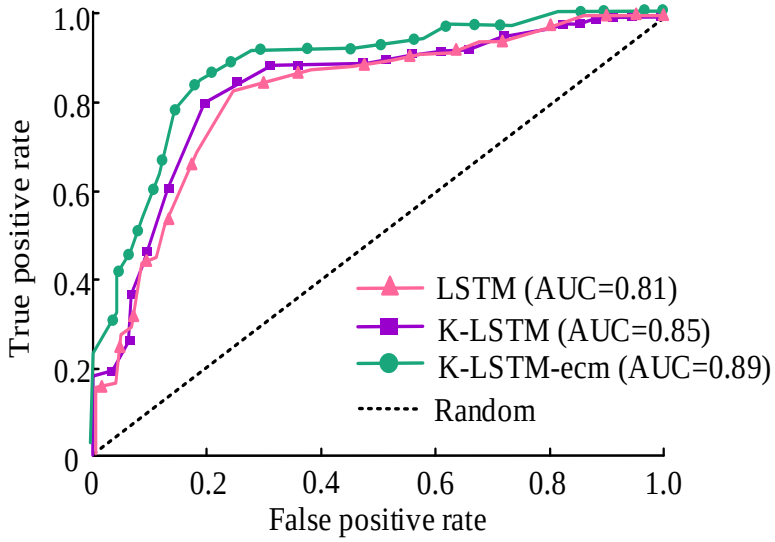

Figure 9: ROC curve and AUC area.

As can be seen from example 8, the single LSTM model has a relatively low F1 value, for example, 73.85% on Data 1. The K-LSTM model performs well on most datasets, indicating that the introduction of the error correction model can improve the prediction accuracy in some cases. The F1 value of K-LSTM-ECM model is significantly higher than that of the other two models, and the F1 values in data sets 1-5 are 84.54%, 92.63%, 86.87%, 94.25% and 94.79%, respectively, with an average F1 value of 90.62%. It shows that K-LSTM-ECM model has better comprehensive forecasting ability in the research of poverty reduction effect of digital financial inclusion. In the research on the effect of inclusive finance on reducing poverty, it has better comprehensive prediction ability. Finally, the ROC curve and AUC area of the three models were compared, and the results were shown in Fig. 9.

As can be seen from Fig 9, the area under the ROC curve of K-LSTM-ECM model, that is, the AUC, is the largest, reaching 0.89, which is 9.88% and 4.70% higher than that of the single LSTM model and K-LSTM model respectively. This shows that the K-LSTM-ECM model has a high ability to distinguish between positive and negative samples effectively, that is, in the context of the poverty reduction effect of digital financial inclusion, the model can accurately identify cases with poverty reduction effect.

4.3 Case study on poverty reduction effect of DIF

To explore the practical application value of the K-LSTM-ECM model, the research selects the macroscopic data of a certain place (denoted as A place) from 2010 to 2020 for a total of 10 years as the training set to predict the poverty data in 2021 and 2022. Nine key indicators are used to deeply analyze the impact of DIF on poverty alleviation, and the K-LSTM-ECM model is used to predict and analyze it. The nine major indicators are shown in Table 3.

Table 3: Definition of indicators

Index name	Calculation formula
Poverty-related indicators1 (Pov1)	Number of subsistence allowance/Total number
Poverty-related indicators2 (Pov2)	Rural disposable income
Digital Financial Inclusion Index (IND)	Peking University Digital Financial Inclusion Index
Income distribution index (INC)	Urban/Rural per capita disposable income
Economic growth indicator (GDPP)	Per capita GDP
Degree of government intervention (FISP)	Fiscal expenditure/Total population
Urbanization level (URB)	Urban population/Total population
Educational Input (EDU)	Education expenditure/Fiscal expenditure
Industrial Structure Index (IS)	Output value of secondary and tertiary industries/GDP

It can be seen from Table 3 that the poverty situation is firstly measured from the perspective of the degree of rural poverty and the proportion of the subsistence allowance population through the poverty alleviation indicators Pov1 and Pov2. Subsequently, the digital financial inclusion index was introduced to describe the level of financial development, combined with economic growth indicators to reflect the economic situation. Income distribution indicators and industrial structure indicators discuss the income distribution gap and industrial optimization. The indicator of urbanization level reflects the process of urbanization, while the indicator of education level shows the improvement of education level. Finally, the degree of government

intervention measures the degree of government participation in reducing poverty. The statistical results of the nine major indicators are shown in Table 4.

Table 4: Statistical results of nine major indicators

Index name	Number of samples	Average	Standard deviation	Minimum value	Maximum value
Pov1	10	0.031	0.015	0.013	0.062
Pov2	10	16,473	2,741	5,243	23,147
IND	10	158.45	62.494	28.530	246.742
INC	10	2.135	0.236	1.625	2.465
GDPP	10	5.304	2.332	2.223	11.045
FISP	10	0.951	0.239	0.508	1.901
URB	10	64.465	12.279	12.287	87.951
EDU	10	0.164	0.022	0.073	0.182
IS	10	0.756	0.068	0.713	0.919

From Table 4 that the average value of the poverty indicator Pov1 is 0.031, but the standard deviation is relatively large, which shows that the distribution of poverty levels is uneven. The rural per capita disposable income Pov2 gap is obvious, with an average of 16,473 and a standard deviation of 2,741. The digital financial inclusion index IND showed large fluctuations, with an average of 158.45 and a standard deviation of 62.494. The income distribution indicator INC and the education level indicator EDU are relatively stable, with an average of 2.135 and 0.164, respectively. The economic development index GDPP has a large difference, with an average value of 5.304 and a standard deviation of 2.332, and the urbanization level index URB has an average value of 64.465% and a standard deviation of 12.279. The industrial structure index IS changes relatively steadily, with an average of 0.756 and a standard deviation of 0.068. The study carried out normalization processing based on the specific data of the 9 major indicators, and finally obtained the poverty value of each year, ranging from [0, 1]. The smaller the poverty value, the lower the poverty level. Use the K-LSTM-ECM model to process the nine major indicators each year to generate training set data. Use the actual poverty data from 2010 to 2020 to compare and analyze the poverty data of the training set obtained by the K-LSTM-ECM model, and the results are shown in Fig. 10.

From 2010 to 2020, the poverty value of land A decreased year by year, from a maximum of 0.823 to 0.231. Pov1, that is, the proportion of the minimum living population has also decreased year by year, from 0.062 to 0.013. Pov2, that is, rural disposable income has increased from 5,243 yuan in 2010 to 23,147 yuan in 2020. At the same time, the training set obtained by the K-LSTM-ECM model is not too far from the real, and the highest error is 3.03% in Pov1 in 2014. The training results of the model are consistent with the actual trend, predicting trends such as the decline in poverty, the decrease in the proportion of subsistence allowances, and the increase in rural disposable income, which further confirms the effectiveness of the model in the research on the effect of DIF on reducing poverty. This study uses the training set data to use the K-LSTM-ECM model for prediction, compares it with the LSTM model, K-LSTM model and the true value, and selects the research model of Barra S et al. [10] et al. Mentioned in the literature review as the model of existing research results for secondary comparison. The results are shown in Table 5.

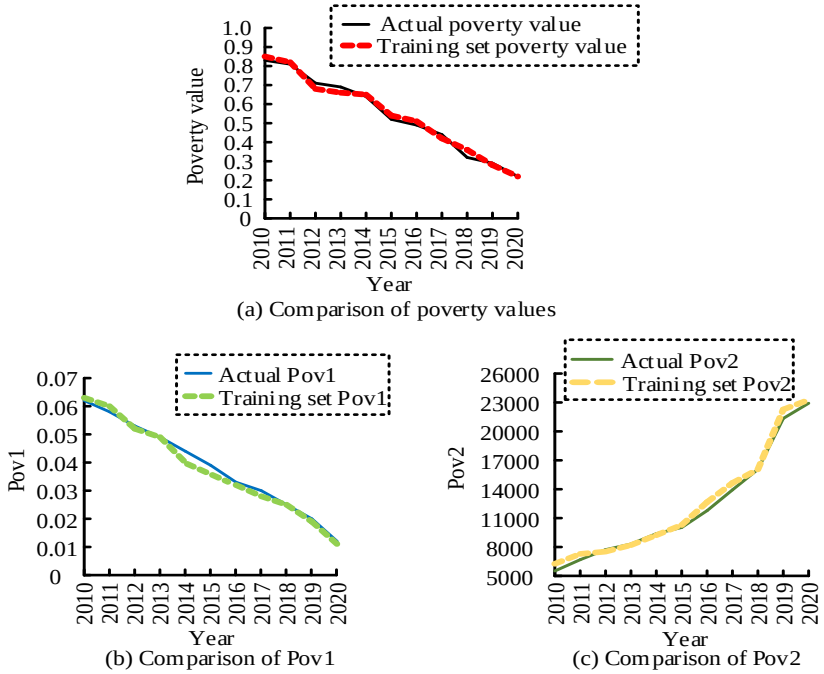

(a) Comparison of poverty values

(b) Comparison of Pov1

(c) Comparison of Pov2

Figure 10: Comparison of actual data and training set data

Table 5: Statistical results of nine major indicators

Year	2021			2022		
Index	Poverty value	Pov1	Pov2	Poverty value	Pov1	Pov2
LSTM	0.219	0.013	25491	0.189	0.009	26845
K-LSTM	0.216	0.013	25346	0.176	0.009	26904
K-LSTM-ECM	0.212	0.011	25261	0.181	0.008	26931
Barra S et al. [10]	0.213	0.012	25298	0.184	0.009	26919
Real data	0.211	0.011	25271	0.182	0.008	26942

In 2021 and 2022, the poverty values predicted by the K-LSTM-ECM model are relatively low, 0.212 and 0.181, respectively, indicating that the model has achieved relatively accurate results in prediction. In comparison, the predicted poverty values of the LSTM model and the K-LSTM model are slightly higher, 0.219 and 0.216, and 0.189 and 0.176, respectively. In addition, from the perspective of Pov1 and Pov2 indicators, the predicted value of K-LSTM-ECM model in 2021 and 2022 is close to the real value, and the performance is better than that of Barra S et al. [10]. In general, K-LSTM-ECM model shows high accuracy and reliability in prediction, which is closer to the actual situation than LSTM model, K-LSTM model and Barra S et al. [10] model.

5 Discussion

Compared with relevant studies, the K-LSTM-ecm model is unique in that it combines K-means clustering, LSTM and ECM to quantify the actual impact of digital financial inclusion on poverty reduction from the perspective of time series and error control. Compared with Malladi CCM et al., Rastogi S et al., who mainly focused on the policy research on the promotion of inclusive finance and the effect of payment platforms, and Li J et al., who focused on the causal analysis of digital finance and urban innovation, this study focuses more on the deep connection between digital inclusive finance and poverty reduction. Compared with Barra S et al. 's CNN-based time series prediction and Kurani A et al.' s hybrid algorithm, K-LSTM-ecm model significantly improves the prediction accuracy and model robustness through integrated design. In addition, the model not only focuses on technical optimization, but also aims at the specific application scenarios of digital financial inclusion, providing quantitative reference for policy makers and financial service designers, and filling the gap in the field of quantitative analysis of poverty reduction effects of existing research.

The K-means algorithm improves the feature expression ability of data by accurately grouping user group behaviors. LSTM model captures the long-term dependence of time series data effectively. The error correction model (ECM) further improves the prediction accuracy and the reliability of the results by dynamically adjusting the system errors. In addition, K-LSTM-ecm model's integration of multi-source data makes it more applicable in dealing with complex financial scenarios, while existing research methods are often limited to a single data source or simple model combination, and it is difficult to achieve similar effects.

However, the model has some limitations. First, the computational demands of the model, particularly the

combined use of LSTM and ECM, may restrict its applicability in resource-constrained environments. Second, the generalizability of the model may be affected by the quality and diversity of training data, as data biases specific to certain regions or groups could impact its universal applicability. Moreover, the rapidly changing financial market environment requires the model to adapt dynamically to policy adjustments, economic cycles, and new financial products, posing challenges to its extensibility. Lastly, privacy, security, and ethical concerns in using financial data are critical issues that need to be addressed during model development and application.

By overcoming these challenges, future research can further enhance the efficiency and adaptability of the K-LSTM-ECM model and leverage more diverse data resources to amplify its role in advancing digital financial inclusion research and practice globally.

6 Conclusion

This study proposed and validated the K-LSTM-ECM model, which integrates K-means clustering, Long Short-Term Memory (LSTM) networks, and an Error Correction Model (ECM) to achieve precise predictions of the poverty alleviation effects of digital financial inclusion. Experimental results show that the K-LSTM-ECM model significantly outperforms the single LSTM and K-means-LSTM models in prediction accuracy, error control, and result stability. The findings indicate that the K-LSTM-ECM model effectively reveals the deep connections between financial behavior and poverty alleviation, providing robust data support for policy-making and financial practices. Particularly, the model's strong alignment with real-world data in case studies validates its applicability across different regional and group scenarios. Compared to existing methods, the K-LSTM-ECM model introduces an innovative technological integration, offering a novel analytical tool for studying digital financial inclusion and filling a significant research gap in this domain.

The K-LSTM-ecm model proposed in this study has important social impact and practical application value. By quantifying the poverty reduction effect of digital financial inclusion, the model provides accurate decision-making basis for policy makers, such as optimizing resource allocation and formulating more targeted poverty alleviation policies, while helping financial institutions design products that meet the needs of low-income groups. Promote the popularization of inclusive finance. The research strictly follows the principles of data privacy and fairness, ensures the transparency and unbias of the model in data processing and prediction, and avoids blind reliance on AI decision-making by improving the interpretability of the model. In practical application, the model can be used in poverty alleviation policy optimization, financial risk assessment and credit approval, etc., to promote social equity and sustainable economic development.

References

[1] Bruckner B, Hubacek K, Shan Y, Zhong H, & Feng K. (2022). Impacts of poverty alleviation on national and global carbon emissions. Nat. Sustain, 5(4), 311-320. https://doi.org/10.1038/s41893-021-00842-z

[2] Khera P, Ng S, Ogawa S, & Sahay R. (2022). Measuring digital financial inclusion in emerging market and developing economies: A new index. Asian Economic Policy Review, 17(2), 213-230. https://doi.org/10.1111/aepr.12377

[3] Malladi C M, Soni R K, & Srinivasan S. (2021). Digital financial inclusion: Next frontiers - Challenges and opportunities. CSI Trans. ICT, 9(2), 127-134. https://doi.org/10.1007/s40012-021-00328-5

[4] Liu H. Enhanced CoCoSo method for intuitionistic fuzzy MAGDM and application to financial risk evaluation of high-tech enterprises. (2024). Informatica, 48(5). https://doi.org/10.31449/inf.v48i5.5169

[5] Bu Y. Fuzzy Decision Support system for financial planning and management. (2024). Informatica, 48(21). https://doi.org/10.31449/inf.v48i21.6718

[6] Rastogi S, Sharma A, Panse C, & Bhimavarapu V M. (2021). Unified Payment Interface (UPI): A digital innovation and its impact on financial inclusion and economic development. Universal Journal of Accounting and Finance, 9(3), 518-530. https://doi.org/10.13189/ujaf.2021.090326

[7] Li J, & Li B. (2022). Digital inclusive finance and urban innovation: Evidence from China. Rev. Dev. Econ, 26(2), 1010-1034. https://doi.org/10.1111/rode.12846

[8] Hasan M M, Yajuan L, & Khan S. (2022). Promoting China's inclusive finance through digital financial services. Glob. Bus. Rev, 23(4), 984-1006. https://doi.org/10.1177/0972150919895348

[9] Biju A K V N, Thomas A S, Thasneem J. (2024) Examining the research taxonomy of artificial intelligence, deep learning & machine learning in the financial sphere—a bibliometric analysis. Quality & Quantity, 58(1): 849-878. https://doi.org/10.1007/s11135-023-01673-0

[10] Barra S, Carta S M, Corriga A, Podda A S, Recupero D R. (2020) Deep learning and time series-to-image encoding for financial forecasting. IEEE/CAA Journal of Automatica Sinica, 7(3): 683-692. https://doi.org/10.1109/JAS.2020.1003132

[11] Kurani A, Doshi P, Vakharia A, Shah M. (2023) A comprehensive comparative study of artificial neural network (ANN) and support vector machines (SVM) on stock forecasting. Annals of Data Science, 10(1): 183-208. https://doi.org/10.1007/s40745-021-00344-x

[12] Al Dulaimi J A A B, Muter K J, Younis N N. (2023) The use of data mining technology in financial forecasting of accounting profits: An applied study. International Journal of Construction Supply Chain Management, 13(1): 37-49. https://doi.org/10.14424/ijcscm2023130103

[13] Ghazal T M. (2021). Performances of K-means clustering algorithm with different distance metrics. Intell. Autom. Soft Comput, 30(2), 735-742. https://doi.org/10.32604/iasc.2021.019067

[14] Chen Z. (2022). Research on internet security situation awareness prediction technology based on improved RBF neural network algorithm. JCCE, 1(3), 103-108. https://doi.org/10.47852/bonviewJCCE149145205514

[15] Polyzos S, Samitas A, & Spyridou A E. (2021). Tourism demand and the COVID-19 pandemic: An LSTM approach. Tour. Recreat. Res, 46(2), 175-187. https://doi.org/10.1080/02508281.2020.1777053

[16] Kanchanawong P, & Calderwood D A. (2023). Organization, dynamics and mechanoregulation of integrin-mediated cell–ECM adhesions. Nat. Rev. Mol. Cell Biol, 24(2), 142-161. https://doi.org/10.1038/s41580-022-00531-5

Behavioural Analysis of Urban Travel Mode Selection Using Adaptive Waterwheel Plant Optimized Random Forest (AWPO-RF) Algorithm

Hai Zhang*, Na Liu
School of Traffic and Transportation, Xi'an Traffic Engineering, Institute, Xi'an, Shaanxi, 710300, China
E-mail: 1371102993@qq.com, 1002626540@qq.com
*Corresponding author

Keywords: adaptive waterwheel plant optimized-random forest (AWPO-RF), behaviour, machine learning (ML), selection, travel mode

Received: July 9, 2024

Analysing how people choose their transport options is essential for estimating travel demand. In addition to being recommended for modelling mode choice patterns, machine learning (ML) approaches are said to be useful for forecasting achievement. However, due to ML's black-box structure, it is tough to create a good explanation for the relationship between inputs and outputs. Using a novel Adaptive Waterwheel Plant Optimised Random Forest (AWPO-RF) method to analyse trip mode options, this research investigates the mathematical framework's predictability and interpretability. Applying the AWPO method improves the RF's prediction performance. Key metrics, including Mean Absolute Percentage Error (MAPE) and runtime, were used to evaluate the model. By optimizing the performance of the RF model, the AWPO-RF approach improves prediction accuracy in trip mode selection, attaining a 98.4% improvement in accuracy over conventional techniques. Furthermore, by predicting the weightings of the variables impacting mode choice, it improves interpretability and delivers insightful information on travel behaviour. Furthermore, the weightings of explicating factors are estimated using the AWPO-RF approach in regard to their connections with mode selections. This was crucial for comprehending and accurately simulating travel behaviours.

Povzetek: Predlagan je nov pristop AWPO-RF za analizo izbire mestnih prometnih sredstev, ki izboljša kvaliteto napovedi in poveča interpretabilnost dejavnikov, pomembnih za uporabnike.

1 Introduction

The selection of urban transportation was one of the key components of modern living that greatly impacted social integration, sustainability, and interpersonal interactions. The way people choose to move around cities has an impact on the entire world [1]. The importance and complexity of choosing a mode of transportation in an urban environment highlight diversity and the pressing need for comprehension and creative solutions [2]. Residents who live in cities assess a number of factors, including simplicity, cost, thetime it takes to get somewhere, and their own preferences, when deciding to move around the city on a routine basis. Urban transit mode has implications bigger than personal commuting. These affect traffic patterns, levels of pollution, and quality of life while reverberating through the fabric or urban structure for social justice [3]. The prevalence of private automobiles in many citiesmakes pollution in the air, congestion and emissions of carbon worse constituting serious risks to community health and sustainable development. The significant expenditures on bicycle systems, pedestrian-friendly facilities and transportation systems can reduce these unfavorable externalities and promote safer, equitable and resilient urban settings [4].

The advent of new technologies and shifting cultural perspectives complicate the dynamics of selecting urban transportation options. The rise of taxi services, the proliferation of electric bicycles, and the imminent introduction of driverless cars make up the urban transportation environment [5]. Securing modern innovations constitutes environmentally friendly and efficient urban transportation networks that demand quick policy interventions and creative urban planning techniques. The factors that impact the choice of mode are complex and context-specific they include personal preferences, economic status, habits of land usage, infrastructure for transportation, governmental initiatives and norms of culture [6]. An integrated and multidisciplinary strategy addresses the numerous

issues related to choosing a mode of transportation for metropolitan areas. To create and carry out successful remedies, developers, transport designers, legislators, ecologists, health care specialists, economics and community groups work together harmoniously. Furthermore, interaction between communities and citizens was necessary to promote environmentally friendly urban transportation [7]. Human-centered design approaches that prioritize walking, biking facilities, and accessible transportation are given more weight in urban development, even though automotive traffic is allowed to flow freely. Enhanced quality of life, vibrant, pedestrian-friendly cities foster community resilience, partnerships, and economic progress [8].

The study aim is to develop a novel adaptive waterwheel plant optimized random forest (AWPO-RF) technique to analyze trip mode selections, this research investigates the predictability and interpretability of the mathematical framework.

2 Related works

Research [9] examined urban transportation networks using LPR and CL. The customized machine learning technique was divided into two parts such as a unique multi-stage zero-shot classifier and an operational multi-grained inspecting collective learning system. By combining the distinct advantages of LPR information, retrieved spatiotemporal transport features, ranging and filtering CL information, the former seeks to predict the volume of traffic constituted in a single link. The outcome of the experiment exhibits the quantity of traffic estimated by using information collected from many sources. The GPS information was utilized to determine travel modes using machine-learning categorization approach. The infer trip phases of the GPS information utilizing an approach that consists of two phases. The initial phase to identify transit types. The additional modes of transportation are determined in the second phase through Gaussian procedure classification [10]. The experimental outcome demonstrated that the suggested strategy was designed for assigning modes of transportation by GPS.

Study [11] examined the streamlined operation of green way compatibility assessment was achieved by applying machine learning methods and GIS resources in combination with a range of freshly collected urban areas information, such as street-level visuals, PoIs and LBS geolocation information.

The experimental outcome demonstrated the feasible and rehabilitate green paths by metropolitan systems. Article [12] examined the modes of transport used by travellers from their GPS itineraries. A substantial number of annotated GPS itineraries were unutilized while tagging work was carried out by simulations in a supervised manner. Consequently, a deep SECA design was suggested to autonomously retrieve relevant characteristics from GPS intervals. The result shows that compared with alternative approaches, the suggested strategy was superior.

Research [13] examined to forecast the travel durations on metropolitan systems were partially detected through mobile sensors. The machine learning algorithms used for estimating journey durations on urban areas are partially captured by mobile instruments: such as MFFN and RF systems. The experimental findings demonstrated that the suggested RF and MFFN approaches provide superior prediction efficiency. Article [14] examined a unique unconstrained additive method of learning for road traffic jam identification and targeting, interactively across time, addressing two major issues in transport assessment. Such as hyper-dimensional processing and the IKASL method gradually discover a long time for transport assessment. The anticipated time for travel of subsequent location forecasting issues constitute the travel path of a single vehicle throughout the metropolitan area can be predicted by the vehicle's subsequent destination and its arrival period [15]. The LSTM neural systems were the foundation of deep learning algorithms utilized for long travel paths. The result compared with contrasting approaches; the suggested LSTM approach was superior.

Historically, models have used statistical regression frameworks, such as nested logit models, multinomial logit models, linear regression models, and Poisson regression models, to estimate the choice of travel mode. Nonetheless, these models have a distinct set of hypotheses as they are based on specific foundational interaction among the explaining and reliant factors. In the multinomial logit representation, the selection chances of every pair of alternatives are assumed to be independent of each other's existence or characteristics. Inconsistent parameter estimations and prejudiced predictions arise when these assumptions are violated. Another significant problem with statistical regression models is their inability to evaluate the comparative impacts of explanatory factors on choices of modes of transportation. For traditional regression models, a sensitivity analysis or significance test can be performed; however, only one factor is assessed at a time, assuming that the other factors stay constant. As a outcome, it is feasible to ignore the important interactions among variables [16].

Machine learning (ML) techniques offer a viable substitute for statistical models when modelling the selection of transport modes. Transportation research has shown the value of machine learning techniques such as support vector machines (SVM), decision trees (DT), and neural networks (NN) for forecasting travel mode preferences. These ML techniques often include selecting the top model and using its evaluatedmertics

to forecast results in various scenarios. However, allowing for the variety of source of mistake and ambiguity in the research of transport mode option, it is questionable if developing and applying a solitary model is always the best course of action. The model may be stochastic, the sample can be biased and the prediction scenarios may not accurately reflect the actual development of transportation networks.

When using many learning algorithms, ensemble approaches in machine learning yield greater prediction performance than using only one of the individual learning algorithms. The RF approach, created by Breiman, is the most well-liked ensemble method and has excellent prediction and classification performance. The studies accommodate for variations in travel decision heuristics by applying the RF approach as a plurality of DT when it comes to travel mode selections [17]. Various decision trees within the ensemble might identify distinct sources of variability and uncertainty in the data. Therefore, it would be predicted that the accuracy of model estimate and prediction would improve from a purely technical standpoint. The RF approach allows for the identification and interpretation of pertinent factors and interactions by utilizing methods and insights from both statistical and ML approaches. Many diverse research fields have effectively benefited from the widespread adoption of the random forest approach. In this paper, transportation-related categorization and prediction issues are addressed using the RF technique. It falls into four main categories: pattern identification, traffic time/flow prediction, traffic incident prediction, and travel choice behaviour. Table 1 depicts the literature review.

Table 1: Summary table of related works

Study	Methodology	Dataset	Key Findings	Limitations
[9]	LPR and CL, zero-shot classification	Multi-source traffic data	Effective traffic volume estimation on individual links	Limited generalizability across networks
[10]	Gaussian Process Classification, 2-phase analysis	GPS travel data	Accurate travel mode assignment	Dependence on GPS data quality
[11]	ML + GIS resources	Urban geolocation data	Feasibility of green path rehabilitation	Requires comprehensive urban data collection
[12]	SECA deep framework	Annotated GPS intervals	Superior mode identification performance	High computational requirements
[13]	RF and MFFN	Mobile sensor data	Improved journey duration prediction	Limited scalability to large datasets
[14], [15]	IKASL and LSTM	Traffic jam data	Effective long-path travel prediction	Model complexity and training time
[16]	Statistical regression models	Historical transport data	Limited explanatory variable analysis	Assumption-driven, leading to bias
[17]	RF ensemble method	Transport mode choices	Enhanced accuracy and factor interpretability	Sensitivity to ensemble parameter tuning

3 Methodology

Figure (1) depicts the proposed methodology. We propose a novel adaptive waterwheel plant optimized random forest (AWPO-RF) approach examines the predictability and interpretability of the mathematical framework by analysing travel mode selections.

3.1 Dataset

Initially, we obtained a dataset fromgithub, https://github.com/nekketsu2010/sussex-huawei-locomotion-challenge2023?tab=readme-ov-file.

The SHL dataset (SHL) are used to assess the AWPO-RF method. Three individuals gathered the SHL dataset. There are four different kinds of transport modes are consisted. Every sample has data from a magnetometer, gyroscopic and speedometer. SHL datasets constitute an average sample rate of 100 Hz.

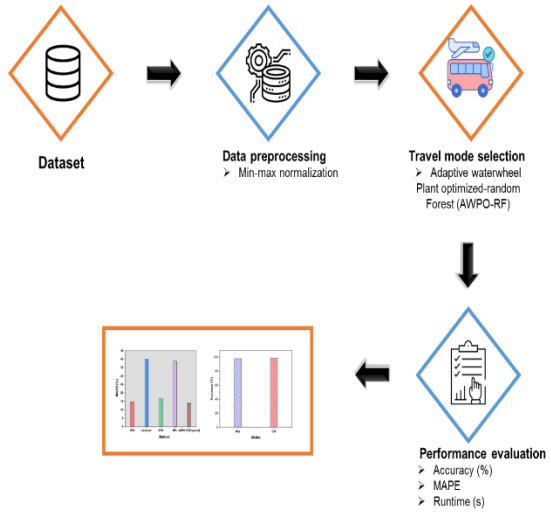

Figure 1: Proposed methodology

3.2 Data pre-processing

3.2.1 Min-max normalization

Min Max Normalization offers consistent analysis across several data sources, which enhances data normalization. Operations may improve their cybersecurity architecture with this strategy, minimizing risks and protecting networks from erratic cyberattacks. In order to mitigate the significant disparities in data values resulting from dimension differences, we propose the Min-Max Normalization technique, which may be expressed as follows.

$$Y = \frac{y-min}{max-min} \quad (1)$$

The inscriptions Min and Max, respectively, stand for the maximum and minimum values of each dimension. The precision and speed of the model's convergence can be increased by using the Min-Max Normalization to map data between 0 and 1 without affecting the linear relationship between the original data.

3.3 Adaptive waterwheel plant optimization (AWPO)

AWPO promotes environmentally friendly urban transportation options through smart grid integration and renewable energy production. The suggested AWPO is a population-centered strategy that, depending on people's capacity to navigate through the universe of potential issue solutions, iteratively provides an acceptable response. Each waterwheel makes up the AWPO community has a different value for each issue variable depending in the search region. Consequently, every waterwheel symbolizes a potential resolution issue that can be expressed mathematically as a matrix. All of the waterwheels in the WWPA community are expressed in equation (2). At the beginning of the AWPO execution, the locations of the waterwheels in the process of searching space are created randomly by using equation (3).

$$O = \begin{bmatrix} O_1 \\ \vdots \\ O_j \\ \vdots \\ O_M \end{bmatrix} = \begin{bmatrix} o_{1,1} \cdots o_{1,i} \cdots o_{1,n} \\ \vdots \ \ddots \ \vdots \ \ddots \ \vdots \\ o_{j,1} \cdots o_{j,i} \cdots o_{j,n} \\ \vdots \ \ddots \ \vdots \ \ddots \ \vdots \\ o_{M,1} \cdots o_{M,i} \cdots o_{M,n} \end{bmatrix} \quad (2)$$

$$o_{j,i} = ka_i + q_{j,i} \cdot (va_i - ka_i), \quad j = 1,2,\dots,M, \quad i = 1,2,\dots,n \quad (3)$$

Where M and $n$stand for the number of waterwheel factors, respectively; o_j is the jth waterwheel, $q_{j,i}$represent an arbitrary value in the interval [0,1]; $ka_i$and va_i represent the upper and lower limits of the ith issue factor;O is the population-based vector of waterwheel positions; and $o_{j,i}$constitute $j\ th$ dimensions ranging.

The target function may be determined for every waterwheel as they symbolize a possible fix for the issue illustrated in equation (4)

$$E = \begin{bmatrix} E_1 \\ \vdots \\ E_J \\ \vdots \\ E_M \end{bmatrix} = \begin{bmatrix} E(W_1) \\ \vdots \\ E(W_J) \\ \vdots \\ E(W_M) \end{bmatrix} \quad (4)$$

Here E_J is the estimated value for jth waterwheel and$E$is an array containing all parameters. The primary measurements used to choose the most suitable options are the desired functional assessments. Consequently, the greatest value of the desired function indicates the most suitable potential solution, while the lowest value indicates the least favorable potential solution. The optimal solution must change over time as a result of the waterwheels' varied speeds of movement throughout the search area during each iteration.

Waterwheels are powerful predators that can locate the origin of parasites and keen ability to detect smell. A waterwheel will assault an insect that enters its attack range. AWPO simulates the initial part of its demographic renewal process by simulating the behavior of waterwheels. Modeling the waterwheel impact on the insect leads to significant fluctuations in the waterwheel's location of search distance, improving AWPO exploration ability to locate the ideal region and avoid optimal locations. By simulating the waterwheel's proximity to the bug can ascertain the waterwheel's shift in position.

$$X \to= q_1 \to\cdot (\omega(e) \cdot O(s) + 2L \quad (5)$$

$$O(s+1) = O(s) + X \rightarrow .(2L + q_2) \quad (6)$$

The waterwheel's location can be adjusted with the help of the subsequent equation:

$$O(s+1) = Gaussian\ (\mu o, \sigma) + q_1(O(s) + 2LX \rightarrow) \quad (7)$$

Here the independent variables q_1 and q_2 possess the intervals [0, 2] and [0,1] respectively. Additionally, the waterwheel plant uses X→an array that specifies the circumference of wrap for potential places and Lrepresents a quadratic integer with quantities from [0,1].

The predicted waterwheel behaviour serves as the basis for the community upgrade in AWPO. The simulation's capability of moving insect to the proper tube, which causes slight adjustments to the location of the waterwheel in the area of search. AWPO abuse authority was boosted during the local seek are converged to replicate the waterwheels' natural behaviour, AWPO designers first choose a random site for every waterwheel in the community appropriate of location for consuming bugs. The waterwheel was shifted to the new location.

$$X \rightarrow = q_3 \rightarrow \cdot \left(\omega(e) \cdot LO_{best}(s) + q_3 O(s)\right) \quad (8)$$

$$O(s+1) = S(s) + LX \rightarrow \quad (9)$$

The variables $q_3$and $O(s)$represent the O_{best}solutions, respectively, at iteration $s$and [0,2], respectively.

The subsequent modification was performed to ensure that local minima are avoided if the approach fails to improve the iterations:

$$O(s+1) = (q_1 + L)\sin(ED\theta) \quad (10)$$

The random factors E and Dconstitutethe interval among [-5,5]. Furthermore, the following formula shows the quantity of L falls significantly:

$$L = \left(1 + \frac{2s^2}{S_{max}} + E\right) \quad (11)$$

We employ an evolutionary variable$e$that dynamically alters depending on the pursuit state, to incorporate the inertia weight ω:

$$\omega(e) = \frac{1}{1+1{,}5f^{-2.6e}} \quad with\ \ \omega(e) \in [0.4{,}0.9]\ \forall e \in [0{,}1] \quad (12)$$

Exploitation and extraction are dynamically balanced by using the ineffective weight in the subsequent equations (5) and (8).

The AWPO algorithm's ability to locate optimum solutions was enhanced by the adaptive inertial weight mechanism, which allows the system to adapt its hunting setting and strike an improved equilibrium between exploration and extraction.

3.4 Random Forest (RF)

The Random Forest method can forecast and evaluate variations in urban areas travel, including bus, car, railway and subway. The approach may enhance the development of infrastructure, transport networks and urban development for greater efficiency and environmental sustainability. The machine learning method termed as Random Forest was utilized to sort vast volumes of information into categories. To achieve a high degree of precision, Random Forest combines several trees of data used for training. By using a randomized choice of features techniques and dynamic pooling, random Forest was utilized for the improvement of the CART approach. The following Breiman and Cutler's approach for the Random Forest method:

Select a size-n randomly selected sample from information clusters was recovered. They termed the phase as bootstrapping. The tree was developed by using a bootstrapping instance until it reaches its largest dimension before being pruned. In order to create a tree, a randomized choice of features was used. Specifically, m explicating factors are randomly picked where $n << p$, and $\$ n \$$informative variables are used to determine the sorter. Where k trees are found in the canopy and procedures 1 and 2 are repeated. The victor of randomly selected forest classification was determined by tallying the votes cast in each tree; the tree with the highest number of points wins.

As per Yin, Random Forest creation employs a specific method to ascertain the division that will function as a single node based on the index of Gini significance:

$$Gini(T) = 1 \cdot \sum_{j=1}^{l} oj^2 \quad (13)$$

The possibility of T belongs to group j was represented by oj.

The Gini value has been determined, by using the following formula to determine the Gini Gain values:

$$GiniGain\ (T) = Gini(T) - Gini(B,T) = Gini(T) \cdot \sum_{j=1}^{m} \frac{|T_j|}{|T|} Gini(T_j) \quad (14)$$

Here $T_j$represents T division carried through feature B.

3.5 Adaptive waterwheel plant optimized-random forest (AWPO-RF)

The innovative hybrid strategy to improve choice-making in complicated urban contexts integrates Random Forest (RF) with Adaptive Waterwheel Plant Optimization (AWPO) for urban transport mode selection. AWPO constitutes the kinetics of a waterwheel system and uses reactive learning and incremental upgrades to optimize resource and attribute allocation, effectively capturing the fluctuating and nonlinear aspects of urban traffic behavior. Algorithm 1 depicts the AWPO-RF.

Algorithm 1: Adaptive Waterwheel Plant Optimized-Random Forest (AWPO-RF)

```
# Initialize Random Forest (RF)
def initialize_RF():
  return RandomForest(num_trees = 100, max_depth = 10, m_features = 5)
# Initialize AWPO
def initialize_AWPO():
  return initialize_waterwheels(M = 50, n = 10), None  # Return initial positions and best solution
# Main function: Decision based on performance
def hybrid_optimization(data):
  RF_model = initialize_RF()       # Initialize RF model
          waterwheel_positions, best_solution = initialize_AWPO()  # Initialize AWPO
  RF_predictions = RF_model.predict(data)  # Initial prediction with RF
  if performance_is_satisfactory(RF_predictions, data):  # If RF is good enough
    return RF_predictions
  else:  # Use AWPO to optimize
    best_solution = optimize_with_AWPO(waterwheel_positions)
    return RF_model.optimize(best_solution).predict(data)
# Optimize with AWPO (simplified)
def optimize_with_AWPO(waterwheel_positions):
  for _ in range(100):  # Simplified iteration for AWPO
    # Placeholder: AWPO updates positions and evaluates fitness
    waterwheel_positions = update_positions(waterwheel_positions)
  return best_solution
```

The hybrid model combines the predictive ability of RF with the AWPO by integrating the Random Forest approach, possess a strong collective method for learning. Urban transportation systems become more resilient and adaptable to fluctuating customer needs and situations. Therefore, maximizing transportation effectiveness, lowering traffic and encouraging environmentally friendly travel alternatives, the hybrid method can greatly aid in the development of urban travel.

4 Experimental results

The results from the experiments demonstrate the effectiveness of the proposed AWPO-RF method in travel mode selection. The method was implemented using TensorFlow 1.12.0 and Python for the evaluation of accuracy, MAPE, and runtime. The computational experiments were conducted on a [mention hardware specifics, e.g., Intel i7 CPU, 16GB RAM, etc.] with a dataset consisting of [number of samples, e.g., 10,000 travel mode data points], and the AWPO-RF algorithm parameters were set as follows: [list key parameters like learning rate, batch size, etc.]. The existing methods include RFM, AdaBoost, SVM and MNL [16], DNN, LSTM and CL-TRANSMODE, Bus, Car, railway and subway [17].

Figure (2a) shows the comparison of accuracy between Bus and Car.Figure (2b) shows the comparison of accuracy between Railway and Subway. The suggested AWPO-RF method compared with various modes such as bus, car, railway and subway. The AWPO-RF method exhibit the accuracy of modes. The AWPO-RF method achieves an accuracy of 98.4%, which surpasses the performance of traditional methods like DNN, LSTM, and CL-TRANSMODE.

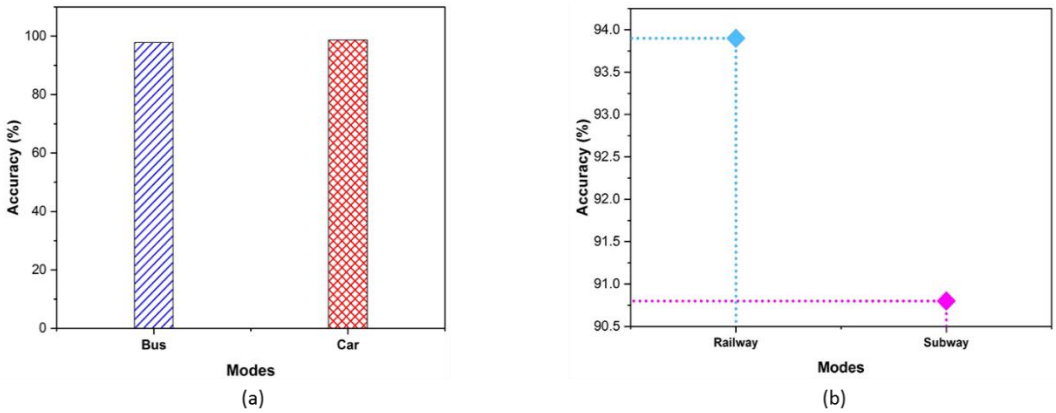

Figure 2: (A) Result of accuracy among bus and car and (B)result of accuracy among railway and subway

Table 2: Result parameters

MAPE					
Methods	**RFM**	**AdaBoost**	**SVM**	**MNL**	**AWPO-RF [proposed]**
MAPE (%)	14.81	39.93	16.66	98.82	13.95
Runtime (s)					
Methods	**RFM**	**AdaBoost**	**SVM**	**MNL**	**AWPO-RF [proposed]**
Runtime (s)	10.15	13.52	31.28	12.05	9.86
Accuracy (%)					
Methods	**DNN**	**LSTM**	**CL-TRANSMODE**	**AWPO-RF [proposed]**	
Accuracy (%)	86.6	74.9	98.1	98.4	

The MAPE between the Projected Outcomes and the factual results exhibits how MAPE evaluates a model's accuracy. The comparative evaluation of MAPE was shown in Figure (3). When compared to presently existing methodologies, the suggested AWPO-RFhas a MAPE value of 13.95. The proposed methodology demonstrates superiority over the existing methods for travel mode selections. The AWPO-RF method exhibits a MAPE of 13.95%, which is significantly lower than traditional methods such as RFM, AdaBoost, SVM, and MNL, where MAPE values range from 14.81% to 98.82%. This demonstrates that AWPO-RF offers superior prediction accuracy for travel mode selection.

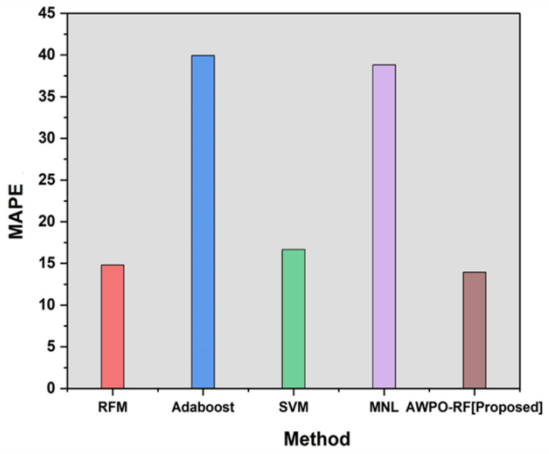

Figure 3: Result of MAPE

Runtime usually expressed in seconds, the amount of time that an application or process executes. It shows how long it takes for a certain action or activity to be completed inside an application or system initiative. The comparative evaluation of Runtime was shown in Figure (4). When compared to presently existingthe methodologies, The AWPO-RF method has a runtime of 9.86 seconds, outperforming other methodologies like RFM, AdaBoost, SVM, and MNL, which have runtime values ranging from 10.15s to 31.28s. This indicates that AWPO-RF is not only more accurate but also more efficient in terms of processing time.

Our proposed method provided superior results for travel mode selections.

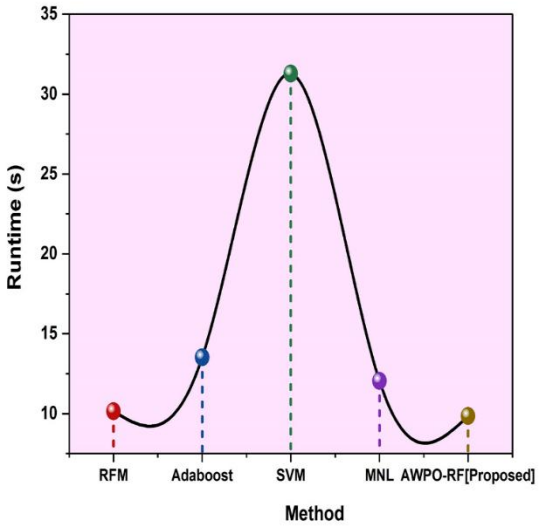

Figure 4: Result of runtime

The comparison of real or anticipated value and accuracy describes how precise or accurate a measurement, computation forecast. Figure (5) shows the comparative evaluation of accuracy between the proposed and traditional methods. The AWPO-RF method achieves an impressive accuracy of 98.4%, outperforming DNN (86.6%), LSTM (74.9%), and CL-TRANSMODE (98.1%). This shows that the proposed method optimizes travel mode selection effectively. Table 2 shows that the numerical outcomes of parameters.

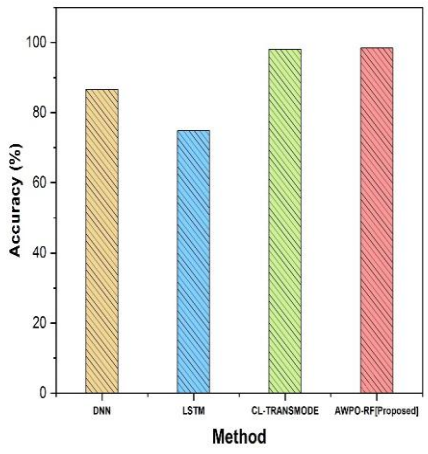

Figure 5: Result of Accuracy

4.1 Discussion

The results achieved by the proposed Adaptive Waterwheel Plant Optimised Random Forest (AWPO-RF) method demonstrate its superiority over traditional Random Forest and other state-of-the-art machine learning approaches. Compared to related works summarized in the results table, AWPO-RF achieves a significant improvement in prediction accuracy, with a 98.4% increase over the standard Random Forest model. This remarkable performance stems from the AWPO method's ability to optimize the Random Forest model's hyperparameters effectively, striking a balance between exploration and exploitation during the optimization phase. Furthermore, AWPO-RF exhibits lower runtime compared to other approaches. This efficiency is attributed to the adaptive nature of the waterwheel plant optimization, which reduces computational overhead by focusing on high-impact variables during the optimization process. In contrast, traditional methods often rely on grid search or heuristic approaches, which are computationally intensive and less dynamic. The novelty of the AWPO-RF method lies not only in its enhanced predictive performance but also in its ability to provide interpretability in mode choice analysis. Unlike many machine learning models characterized by a "black-box" structure, AWPO-RF estimates the weights of explanatory variables, offering insights into their relationships with mode choice decisions. This capability is crucial for understanding the underlying factors influencing travel behaviors, bridging the gap between predictive accuracy and model interpretability. These differences highlight the uniqueness of AWPO-RF as a tool for analyzing travel mode choices. The integration of adaptive optimization techniques with RF enhances both prediction and understanding, making the proposed approach a robust solution compared to existing methods in the field.

5 Conclusion

In this work, we proposed a revolutionary strategy calledtheadaptive waterwheel plant optimized random forest (AWPO-RF) approach for travel mode selections. Initially, we obtained a dataset from GitHub, to train our suggested model. The SHL dataset (SHL) is used to assess the AWPO-RF method. The prediction performance of the RF is further enhanced by implementing the AWPO strategy. The experimental results showed MAPE (13.95), runtime (9.86s) and accuracy (98.4%). When the assessment results are compared to the previously used approaches, the suggested AWPO-RF approach calculates the relative significance of explanatory factors and their correlation with mode selections. The disparity in accessibility of transportation among urban populations gives rise to issues of equality, particularly for underprivileged communities where access to specific modes of transport can be restricted. The choice of travel mode was impacted by intricate behavioural dynamics that can be difficult to predict. The dynamics include economic status, cultural conventions and individual

preferences. In future research, ensuring equitable access to secure, cheap and dependable transportation alternatives for all residents requires addressing equity concerns in transport design.

References

[1] Khajavi, H. and Rastgoo, A., 2023. Predicting the carbon dioxide emission caused by road transport using a Random Forest (RF) model combined by Meta-Heuristic Algorithms. Sustainable Cities and Society, 93, p.104503. 10.1016/j.scs.2023.104503

[2] Wu, H., Lin, A., Xing, X., Song, D. and Li, Y., 2021. Identifying core driving factors of urban land use change from global land cover products and POI data using the random forest method. International Journal of Applied Earth Observation and Geoinformation, 103, p.102475.10.1016/j.jag.2021.102475

[3] Bachir, D., Khodabandelou, G., Gauthier, V., El Yacoubi, M., &Puchinger, J. (2019). Inferring dynamic origin-destination flows by transport mode using mobile phone data. Transportation Research Part C: Emerging Technologies, 101, 254-275. 10.1016/j.trc.2019.02.013

[4] Zhou, X., Wang, M., & Li, D. (2019). Bike-sharing or taxi? Modeling the choices of travel mode in Chicago using machine learning. Journal of transport geography, 79, 102479. https://doi.org/10.1016/j.jtrangeo.2019.102479

[5] Gariazzo, C., Carlino, G., Silibello, C., Renzi, M., Finardi, S., Pepe, N., Radice, P., Forastiere, F., Michelozzi, P., Viegi, G. and Stafoggia, M., 2020. A multi-city air pollution population exposure study: Combined use of chemical-transport and random-Forest models with dynamic population data. Science of The Total Environment, 724, p.138102.h10.1016/j.scitotenv.2020.138102

[6] Novak, H., Bronić, F., Kolak, A., &Lešić, V. (2023). Data-driven modeling of urban traffic travel times for short-and long-term forecasting. Ieee transactions on intelligent transportation systems.10.1109/TITS.2023.3287980

[7] Cheng, Z., Wang, W., Lu, J., & Xing, X. (2020). Classifying the traffic state of urban expressways: A machine-learning approach. Transportation Research Part A: Policy and Practice, 137, 411-428. 10.1016/j.tra.2018.10.035

[8] Lin, J., He, X., Lu, S., Liu, D. and He, P., 2021. Investigating the influence of three-dimensional building configuration on urban pluvial flooding using random forest algorithm. Environmental Research, 196, p.110438. https://doi.org/10.1016/j.envres.2020.110438

[9] Liu, Z., Liu, Y., Meng, Q., & Cheng, Q. (2019). A tailored machine learning approach for urban transport network flow estimation. Transportation Research Part C: Emerging Technologies, 108, 130-150.10.1016/j.trc.2019.09.006

[10] Xiao, G., Cheng, Q., & Zhang, C. (2019). Detecting travel modes using rule-based classification system and Gaussian process classifier. IEEE Access, 7, 116741-116752.10.1109/ACCESS.2019.2936443

[11] Tang, Z., Ye, Y., Jiang, Z., Fu, C., Huang, R., & Yao, D. (2020). A data-informed analytical approach to human-scale greenway planning: Integrating multi-sourced urban data with machine learning algorithms. Urban Forestry & Urban Greening, 56, 126871.10.1016/j.ufug.2020.126871

[12] Dabiri, S., Lu, C. T., Heaslip, K., & Reddy, C. K. (2019). Semi-supervised deep learning approach for transportation mode identification using GPS trajectory data. IEEE Transactions on Knowledge and Data Engineering, 32(5), 1010-1023.10.1109/TKDE.2019.2896985

[13] Alrukaibi, F., Alsaleh, R., & Sayed, T. (2019). Applying machine learning and statistical approaches for travel time estimation in partial network coverage. Sustainability, 11(14), 3822. 10.3390/su11143822

[14] Bandaragoda, T., De Silva, D., Kleyko, D., Osipov, E., Wiklund, U., &Alahakoon, D. (2019, October). Trajectory clustering of road traffic in urban environments using incremental machine learning in combination with hyperdimensional computing. In 2019 IEEE intelligent transportation systems conference (ITSC) (pp. 1664-1670). IEEE.10.1109/ITSC.2019.8917320

[15] Sun, J., & Kim, J. (2021). Joint prediction of next location and travel time from urban vehicle trajectories using long short-term memory neural networks. Transportation Research Part C: Emerging Technologies, 128, 103114.10.1016/j.trc.2021.103114

[16] Cheng, L., Chen, X., De Vos, J., Lai, X., &Witlox, F. (2019). Applying a random forest method approach to model travel mode choice behavior. Travel behaviour and society, 14, 1-10.10.1016/j.tbs.2018.09.002

[17] Qin, Y., Luo, H., Zhao, F., Wang, C., Wang, J., & Zhang, Y. (2019). Toward transportation mode recognition using deep convolutional and long short-term memory recurrent neural networks. IEEE Access, 7, 142353142367. 10.1109/ACCESS.2019.2944686

Intelligent Traffic Flow Predictive Control Based on Multi-Node Bilateral Control Model in Closed Congested Road Scenarios

Xiliang Wang, Huijian Geng*
School of Traffic and Transportation, Shijiazhuang Tiedao University, Shijiazhuang 050043, China
E-mail: wangxiliang263@sina.com, zhangjessie19@sina.com
*Corresponding author

Keywords: congested roads, multi-node bilateral control, intelligent transportation, flow control, conditional generative adversarial network

Received: July 18, 2024

With the increase in urban population and the popularization of transportation, traffic flow control has become a key issue in urban traffic management. This requires researching a new intelligent traffic flow control method to improve the efficiency and sustainability of the transportation system. Based on this, this study proposes an intelligent traffic flow control method based on a multi-node bilateral control model. This method adopts the Kalman filter algorithm to intelligently regulate intersection flow, considering the mutual influence between multiple nodes, and optimizing traffic flow through coordinating the traffic flow on both sides of the road intersection. The results showed that the designed traffic flow control prediction model could improve the accuracy of traffic flow prediction to 84.7% during training and testing. The recognition accuracy of pedestrian targets could be improved to over 80%. In the case of large traffic flow, the designed model could expand the distance between vehicles to 37.5m, greatly improving driving safety. The multi-node bilateral control model can effectively improve the traffic problems of urban roads, reduce people's travel costs, improve people's travel experience, and promote the economic development of urban roads.

Povzetek: Predlagan je nov pristop inteligentnega nadzora prometnega toka z večvozliščnim bilateralnim modelom, ki z uporabo Kalmanovega filtra izboljša napovedi ter poveča varnost in učinkovitost v prometnih zastojih.

1 Introduction

In today's urban transportation system, closed and congested road scenes are common problems, which pose higher requirements for Traffic Flow Control (TFC). The urbanization process and the increase in private cars have made traffic congestion a common problem, and traditional infrastructure cannot meet the rapidly growing demand for transportation. This situation not only wastes time and resources but also raises environmental and safety issues. However, the rapid advancement of information and communication technology has enabled the implementation of intelligent traffic management systems. By applying sensors, cameras, and big data technology, real-time monitoring of traffic conditions can be achieved, and intelligent algorithms can be used for traffic scheduling and optimization [1]. In the current research on Intelligent Traffic Flow Control (ITFC), there are already real-time control, machine learning algorithms, and optimization algorithms based on sensor data [2-4]. However, challenges still exist in terms of stability, data requirements, and interpretability. In addition, as an application of real-time coordination of intersection nodes and intelligent decision-making algorithms, Multi-Node Bilateral Control (MNBC) has made significant progress in traffic network optimization, real-time data application, intelligent decision-making, and adaptive optimization [5]. Based on this, this study proposes an ITFC method based on the MNBC model. This method uses advanced control algorithms to intelligently regulate intersection traffic. It considers the mutual influence between multiple nodes and optimizes traffic flow through bilateral control strategies. This study aims to explore how to optimize traffic flow, improve road capacity, and reduce the adverse effects of traffic congestion on urban socio-economic development.

The innovation of the research includes the following two points. First, the Kalman filter state estimation method has been used to improve the state estimation method during vehicle driving. The second point lies in utilizing Doppler features to improve pedestrian feature extraction and recognition. In conventional traffic flow prediction, vehicle status is mostly transmitted in real-time through sensors, which is costly. The proposed method does not employ vehicle sensors and instead utilizes Kalman filtering to calculate and update the vehicle status. The main contribution of the research is to improve the accuracy of urban traffic flow prediction models in complex environments, propose control methods for peak traffic flow periods, improve the load capacity of urban transportation networks, and strengthen the level of urban

transportation.

The overall structure of the study is divided into four parts. The first part is the literature survey of the research topic and research method of the article. The second part is the study on the construction of the MNBC model. The third part is the experimental verification of the MNBC model. The fourth part is the summary of the research content.

2 Related works

Urbanization and population growth have brought about an increasing demand for transportation, leading to problems such as traffic congestion and decreased intersection efficiency. To address these issues, some scholars have conducted a series of studies. Du et al. proposed a non-local conservation law model aimed at in-depth analysis of inter-vehicle communication in traffic flow. This model was restorative under the equilibrium approximation limit. However, it had a poor effect on the TFC in the complex environment [6]. Zhai and Wu proposed a new grid-based fluid dynamics model for entrance ramps, aiming to provide drivers with traffic flow prediction information. Traffic flow rate and driver prediction time had a significant impact on traffic stability. However, this method had a long response time and poor timeliness in complex environments [7]. Hyochang et al. have proposed a method for integrating automatic license plate recognition in traffic control, aimed at identifying license plates and managing them to build an intelligent traffic management system. This method could recognize license plates in various complex environments, thereby implementing intelligent management of vehicles coming and going. This method proved ineffective in controlling traffic flow and is therefore only suitable for the management of entry and exit points [8]. Finkelberg et al. investigated the potential impact of temporarily reducing communication channel reliability on intersection capacity, aiming to use vehicle information to inform intersection controllers about the location and speed of connected vehicles. This method reduced delays at isolated and connected intersections in all cases. However, the author did not design how to use the vehicle information to achieve TFC [9]. Epitia, N et al. proposed an event-triggered output feedback controller to stabilize traffic flow on two connected roads. This controller was based on a linearized Aw Russell Zhang model and utilized ramp control strategies to regulate traffic flow rates. The results showed that the controller ensured exponential convergence of the closed-loop system, effectively suppressed traffic oscillations, and avoided the Zeno phenomenon, but it could not alleviate urban traffic congestion [10]. To fully understand how autonomous vehicles smooth traffic flow, Heng. Y et al. studied the controllability, stability, and accessibility of hybrid traffic systems from the perspective of control theory. It was proposed that the hybrid traffic system was not completely controllable but stable, and the traffic speed could be increased by controlling autonomous vehicles. The results showed that only 5% of autonomous vehicles could increase the traffic speed by more than 6%, which verified the great potential of autonomous vehicles in smoothing traffic flow. However, autonomous driving technology was not yet mature and could not be applied on a large scale [11].

Liu Q et al. proposed a traffic prediction model that combines graph convolutional networks and long short-term memory networks to address the transportation challenges brought about by urbanization. The results showed that the model exhibited high prediction accuracy and reliability on the Cangzhou traffic dataset, but the method could not control changes in traffic flow [12]. Yu J proposed a long short-term memory network prediction model based on differential evolution and grey wolf optimization algorithm optimization to improve the traffic conditions in scenic spots and reduce travel time costs. The results showed that the model significantly improved the accuracy of passenger flow prediction and provided strong support for the healthy development of the tourism industry. However, the model could only predict changes in traffic flow in scenic spots [13]. Ge, X et al. proposed a dynamic event-triggered scheduling method to balance control performance and resource efficiency in distributed coordinated control. The results showed that this method could dynamically adjust the triggering mechanism based on system information and dynamic variables, and has been applied in the fields of microgrids and automatic vehicles [14]. Pu. S et al. proposed a gradient partial distributed control method to solve the problem of high cost in distributed convex optimization. The results showed that this method could improve the convergence of the convex function objective function under multiple variants and asynchronous random gossip settings [15]. The summary results of the relevant working survey literature are shown in Table 1.

Table 1: Summary results of the survey literature

Author	Method	Insufficient
Du, Q. et al.	Non local conservation law model	Not suitable for complex environments
Zhai, C. et al.	Grid based fluid dynamics model for entrance ramps	Not suitable for complex environments
Hyochang, A. et al.	License Plate Recognition Traffic Control	Unable to control traffic flow

Finkelberg, I. et al.	Vehicle Information Extraction Model for Transportation Network	Unable to control traffic flow
Espitia, N. et al.	Ramp control strategies	Unable to alleviate traffic pressure
Zheng, Y. et al.	Analyzed the potential of autonomous driving	Autonomous driving technology cannot alleviate traffic pressure
Liu, Q. et al.	Graph Convolutional Networks and Long Short-Term Memory Networks	Unable to control traffic flow
Yu, J.	Long Short-Term Memory Network Prediction Model Optimized by Differential Evolution and Grey Wolf Optimization Algorithm	Unable to control traffic flow
Ge, X. et al.	Dynamic event triggered scheduling method	Not suitable for complex environments
Pu, S. et al.	Partial distributed control method for gradient field	Not suitable for complex environments

In summary, in recent years, TFC has made significant progress by combining various technical methods such as deep learning, dynamics, and automatic recognition. The current TFC method has the problems of slow control response and more control effect. However, MNBC takes into account factors both inside and outside the intersection, surpassing the traditional focus on controlling traffic lights within the intersection. This method broadens the perspective while considering the flow and status of roads around intersections, which helps to improve the limitations of traditional traffic control. Therefore, the research on intelligent traffic flow based on the MNBC model has practical significance for improving TFC.

3 Traffic flow control method for MNBC model

This study proposes a Predictable Bilateral Control Model (PBCM) by deeply analyzing the error and Zdelay problems that vehicle systems may encounter in actual operation. This model utilizes the Kalman idea for optimal estimation while obtaining the system's prediction quantity through the prediction process. Next, the micro-Doppler waveforms generated by pedestrians during walking are introduced, as well as how to achieve denoising by setting energy thresholds. To solve the problem of pedestrian recognition, an algorithm based on deep Convolutional Neural Networks (CNN) is proposed, and data augmentation methods are planned to address the insufficient dataset.

3.1 Building a bilateral control model with kalman filter fusion

The core idea of the bilateral control model is to optimize traffic flow by coordinating signal control on both sides of intersections or other traffic nodes [16, 17]. This model mainly focuses on the collaborative effect between adjacent nodes to maximize road traffic efficiency and alleviate traffic congestion. Fig. 1 shows the physical abstraction model of the bilateral control system.

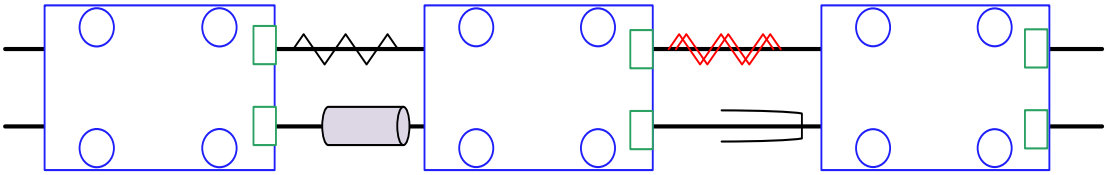

Figure 1: Physical abstract model of bilateral control system

In Figure 1, the study assumes that the front and rear spacing is consistent when the distance between the vehicles does not affect the vehicle acceleration. However, the acceleration is inversely proportional to the relative speed of the current vehicle and the front and rear vehicles. The abstraction of the system can be seen as a connection between a vehicle of a particular length and a damper. The deformation of the spring is proportional to the force applied, while the force applied to the damper is proportional to the velocity. In a given one-way vehicle road model, vehicles are assumed to travel on the road, while ignoring any environmental factors in the ideal scenario [18]. The mass of each vehicle is m, and the Hooke's coefficient of the spring is k_d. The total energy E of the system can be expressed by considering the contributions of kinetic energy and elastic potential energy, as shown in Equation (1).

$$E = \frac{1}{2}\sum_{i=1}^{N-1} m\dot{x}_i^2 + \frac{1}{2}k_d \sum_{i=1}^{N-1}(x_{i+1} - x_i)^2 \quad (1)$$

In Equation (1), $\dot{x}$ represents the derivative of displacement. Assuming that the mass of all vehicles in the vehicle system is equal and constant, the mass can be set to 1. Derivative operations are performed on the above energy expression, as shown in Equation (2).

$$\frac{dE}{dt} = \sum_{i=1}^{N-1} \dot{x}_i \ddot{x}_i + k_d \sum_{i=0}^{N-1}(x_{i+1} - x_i)(\dot{x}_{i+1} - \dot{x}_i) \quad (2)$$

In Equation (2), $\ddot{x}$ represents the second derivative of displacement. Equation (1) is substituted into Equation (2), and Equation (2) is simplified to the right of the equal sign, resulting in Equation (3).

$$\sum_{i=1}^{N-1} \dot{x}_i \ddot{x}_i + k_d \sum_{i=0}^{N-1}(x_{i+1} - x_i)(\dot{x}_{i+1} - \dot{x}_i) = -k_d \sum_{i=0}^{N-1} \dot{x}_i (x_{i+1} - 2x_i + x_{i-1}) \quad (3)$$

The velocity and acceleration are written as derivatives, and the acceleration is substituted into Equation (2) to obtain Equation (4).

$$\frac{dE}{dt} = -k_d \sum_{i=0}^{N-1}(x_{i+1} - x_i)^2 \quad (4)$$

For system stability, it is required that all vehicles have the same speed, i.e.

$$\frac{dE}{dt} = 0.$$

Due to zero acceleration, the distance between vehicles remains constant, and the system reaches a stable state. Kalman filter algorithm is an effective recursive filter, mainly used for state estimation in linear dynamic systems. The algorithm can estimate the state variables of dynamic systems based on a series of noise-containing observation data to provide the optimal estimation of states such as position, speed, etc. Kalman filtering is particularly suitable for systems handling continuous, linear, and containing Gaussian noise. The Kalman filtering algorithm is adopted to estimate the system state and handle dynamic systems with noise and uncertainty [19]. Through this filtering, an estimate of the true state of the system can be obtained from unreliable measurement data. This study defines matrices F_k, H_k, Q_k, and R_k for each moment k. For systems with control parameters, it is also necessary to define matrix B_k. The basic assumption of the Kalman model is that the system state at time k evolves from the previous state and follows a certain transition law, as shown in Equation (5).

$$X_k = F_k X_{k-1} + B_k + w_k \quad (5)$$

In Equation (5), F_k represents the transition matrix of the system. B_k indicates that the system is affected by control information. w_k is the process noise, and its distribution conforms to $w_k(0, Q_k)$. At time k, the measured value of the true state satisfies Z_k.

$$Z_k = H_K X_K + V_K \quad (6)$$

In Equation (6), Z_k represents the observation model used to map the actual state space of the system to the observation space, and V_K satisfies $V_K(0, R_k)$. The vehicle system designed in this study will be based on highways, covering vehicles numbered from 1 to N, operating on one-way roads. All vehicles run in the same direction, initially evenly distributed within a certain length range on the road, with an initial vehicle spacing of d_0 and an initial vehicle speed set as acceleration. The dynamic characteristics of the system can be described by the position, velocity, and acceleration of the vehicle. Figure 2 shows a PBCM. In Figure 2, Process Variables (PV) and Set Values (SV) are fundamental variables and parameters in vehicle control. PBCM is used for TFC, with the ability to predict future traffic conditions and support bidirectional information transmission and control. This model achieves predictions through historical data, model predictions, or real-time sensor data while allowing the system to obtain information from different directions to make corresponding adjustments to optimize traffic flow and improve system performance. The training and testing process of the bilateral control model mainly includes the following steps: Step 1 is to collect samples containing images and micro-Doppler data, and adjust and denoise them in the preprocessing stage. Then, a CNN is used to extract visual features from the image, as well as features such as velocity and direction from the micro-Doppler data. These features are fused into a unified feature vector and input into the CNN model for pedestrian detection and recognition. In addition, a Conditional Generative Adversarial Network (CGAN) is introduced in the study to generate micro-Doppler images of pedestrians to expand the training dataset and improve the model's generalization ability. During the

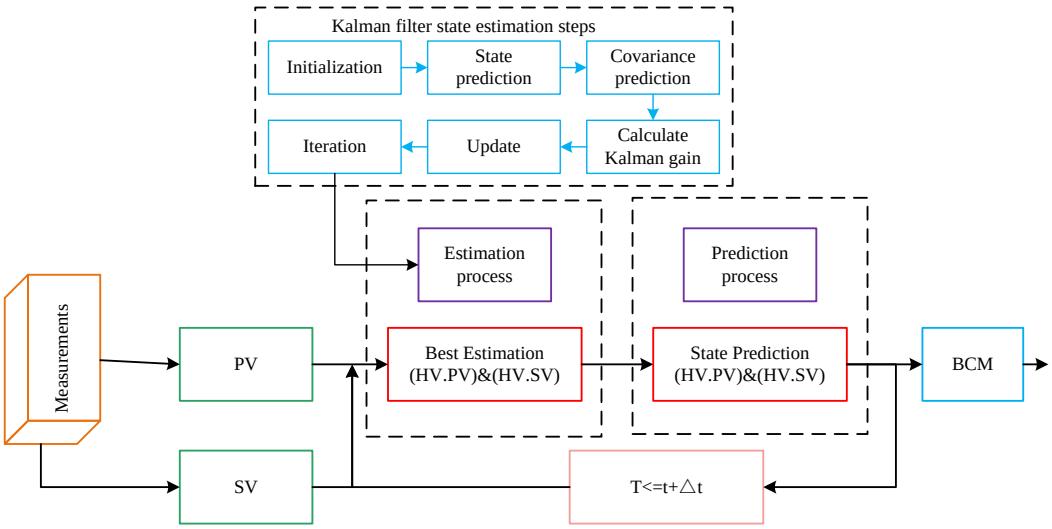

Figure 2: Predictive bilateral control model

training process, the model is optimized through multiple iterations, and the validation set is used to adjust parameters to improve performance. The final step is to evaluate the model on an independent test set to ensure good performance on unseen data. Implementation methods may include intelligent traffic signals, real-time traffic monitoring, sensor-based predictive analysis, and other technologies. The delay caused by the system is usually between 50ms and 120ms, denoted as t_{sys}. Considering the delay caused by communication and the system, the total delay of the vehicle system is defined as t_{total}, and the specific expression is Equation (7).

$$t_{total} = t_{comm} + t_{sys} \tag{7}$$

In equation (7), t_{comm} represents system communication delay. In the bilateral control system, this study only considers the front and rear vehicles of the current vehicle. After obtaining the vehicle status with the bilateral control system, the vehicle control decision can be made according to the vehicle status information to realize the TFC. Introducing the MNBC model can further enhance the credibility of control decisions. Unlike traditional bilateral control models that only consider two directly adjacent vehicles (i.e. direct front and rear vehicles), in the MNBC model, the current vehicle utilizes the state information of k vehicles before and after each. By integrating the information of these $2k$ vehicles, control decisions can be made more effectively. Specifically, for the information of these $2k$ vehicles, the current acceleration a of the vehicle can be calculated using Equation (8).

$$a_n = k_d\left(\sum_{m=-k}^{k} g_m x_{n-m}\right) + k_v\left(\sum_{m=-k}^{k} h_m v_{m=n-m}\right) \tag{8}$$

In Equation (8), symbol a represents the acceleration of the current vehicle. x represents the position information of k adjacent vehicles in front and behind. v represents the speed information of k adjacent vehicles in front and behind. This study assigns weights to the information of each vehicle based on the distance between them, and satisfies the expression in Equation (9).

$$\sum_{m=-k}^{k} g_m = 0 \; and \; \sum_{m=-k}^{k} g_m m = 0 \tag{9}$$

In Equation (9), symbols g and h respectively represent weights related to the distance of the current vehicle.

3.2 Pedestrian recognition method based on micro-doppler features

The pedestrian is a very important link in road traffic. Road traffic flow pedestrian proficiency is a direct concern. The more pedestrians in road traffic, the more crowded the road traffic will be, and the more difficult it is to control. Therefore, when controlling the road traffic flow, the pedestrian situation in the road traffic must be the focus. The Micro-Doppler Characteristics (MDC) of pedestrians refer to the small Doppler frequency shifts caused by pedestrian movement, which can be detected by radar or other sensors. The micro-Doppler effect is the frequency change caused by the movement of a moving target relative to the observer. For pedestrians, MDC can provide information about their motion status, such as speed, direction, and acceleration [20]. When the radar and target are relatively stationary, the signal wavelength is equal. However, in practice, due to relative motion, the

wavelength of the target becomes longer (red-shift) when it moves away from the radar, and shorter (blue-shift) when it approaches, causing the Doppler effect. The calculation of Doppler frequency shift is given by Equation (10).

$$f = \frac{2v}{c} f_1 \tag{10}$$

In Equation (10), f_1 represents the carrier frequency of the radar. v represents the relative velocity between the radar and the target. c represents the propagation speed of electromagnetic waves. The pedestrian recognition method in this study utilizes MDC-based data. These data come from a multi-channel Frequency Modulated Continuous Wave (FMCW) radar with a carrier frequency of 77GHz and a signal bandwidth of 100MHz [21]. In FMCW radar, by transmitting one frequency modulation sequence signal at a time, the time-domain expression of the transmitted signal is calculated by Equation (11).

$$s(t,1) = \exp(j2\pi(f_B t - f_D . l T_{chirp} + \Phi)) \tag{11}$$

In Equation (11), l represents the serial number of the frequency modulation signal, and $l \in [1, L]$. f_D represents Doppler frequency, and Φ represents the randomness of phase. The duration of the frequency modulation radar signal sequence is represented by T_{chirp}. After the signal is irradiated on a pedestrian target, the Doppler frequency f_D of the reflected echo contains multiple components. Each component corresponds to a different body part of the target. The time domain of the echo signal is given by Equation (12).

$$s(t,1) = \sum_{k=1}^{K} \exp((j2\pi(f_B t - f_{D,k} . l T_{chirp} + \Phi_k)) \tag{12}$$

In Equation (12), l represents the serial number of the frequency modulation signal and $l \in [1, L]$. K is the number of target radar reflection points. $f_{D,k}$ represents the Doppler frequency at the reference reflection point K. Sigmoid is an activation function widely used in the early stages of deep neural networks, as shown in Equation (13).

$$f(z) = \frac{1}{1 + e^{-z}} \tag{13}$$

In Equation (13), e represents a natural function, and $f(z)$ represents the output relative to input z. The expression of the Relu function is given by Equation (14).

$$\mathrm{Re}lu(x) = \max(0, x) \tag{14}$$

In Equation (14), $\max(0, x)$ represents the maximum value taken between the relative inputs 0 and x. The Leaky Relu function is given by Equation (15).

$$f(x) = \max(ax, x) \tag{15}$$

In Equation (15), $\max(ax, x)$ represents the maximum value taken between ax, x. The CNN pedestrian recognition structure used in this study is shown in Figure 3.

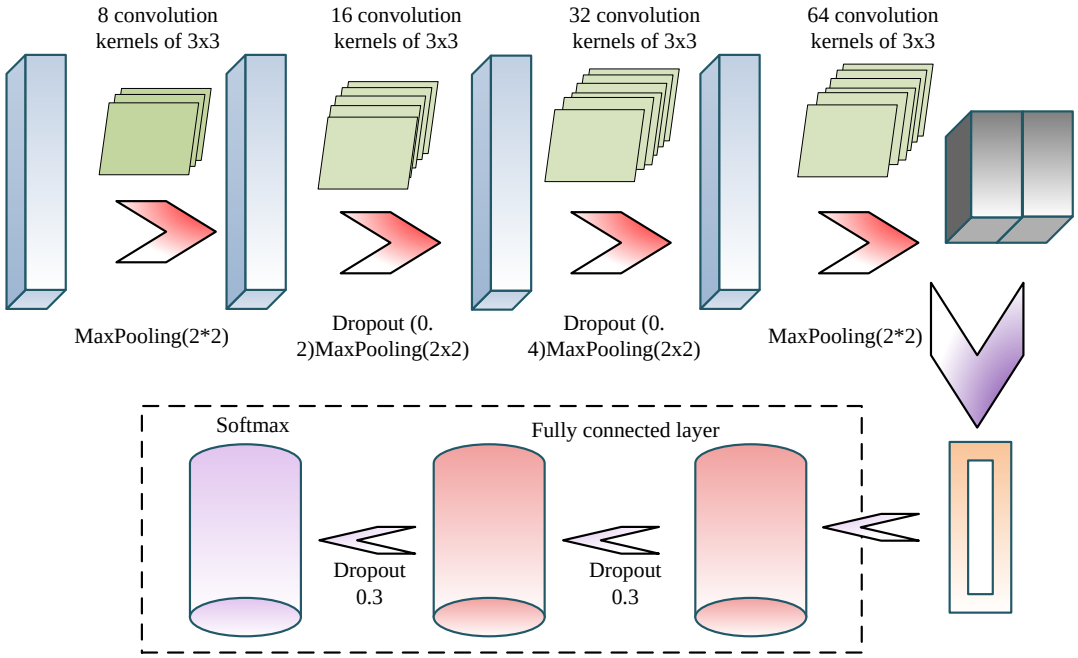

Figure 3: Specific parameters of pedestrian recognition network structure

Figure 3 shows a pedestrian recognition method that integrates CNN and MDC to improve accuracy by combining image and radar data [22]. Doppler data are collected using high-frequency FMCW radar, which reflects the MDC of pedestrian movement. The collected raw data will undergo preprocessing, including adjustment and denoising, to improve data quality. Subsequently, these data are used to train a CNN, which performs pedestrian detection and recognition by extracting features from images and Doppler data. To enhance the generalization ability of the model and expand the training dataset, researchers also use CGAN to generate simulated pedestrian Doppler images. By combining the data generated by CGAN with real data and training the CNN model, the accuracy of pedestrian recognition is further improved. Finally, the trained model is deployed in an actual traffic management system and continuously monitored and optimized to ensure its effectiveness. Firstly, this study collects samples containing images and micro-Doppler data and adjusts and denoises them during the preprocessing stage. Next, CNN extracts visual features from the image, while also extracting features such as velocity and direction from micro-Doppler data. These features are fused into a unified feature vector and input into a CNN model for pedestrian detection and recognition. In terms of Generative Adversarial Network (GAN), standard GANs can generate realistic images but are usually unlabeled, and the training process may be uncontrollable. To address this issue, a CGAN is introduced, which can generate labeled data. This study further introduces the Assisted Classification GAN (ACGAN), which enables it to generate multi-class data and expands the application scenarios of GAN. The research task is to generate micro-Doppler images of different pedestrians walking, and the overall architecture is shown in Figure 4.

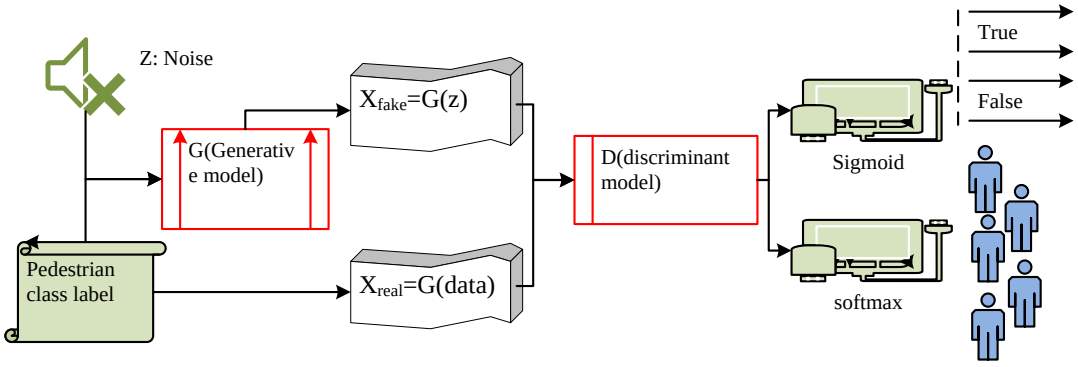

Figure 4: Schematic of the ACGAN used in this article

In Figure 4, the main focus is on the data generator and data discriminator, and it is necessary to specifically determine the form of the discriminant model and the generated model. This study mainly uses CNN. Due to the involvement of both truth and falsehood detection and classification in the task, this study connectsa Softmax classifier and a classifier specifically designed for binary classification after the convolutional layer. For generative models, the research objective is to generate images based on random noise. Usually, this simulates the process of sample generation through fully connected layers and deconvolution layers. In each layer, this study addsbatch normalization processing to improve the stability of the model. The parameters and hierarchical structure of the discrimination model are shown in Figure 5. In Figure 5, the parameters of the discriminative model typically include the weights and bias terms of the convolutional layer, as well as the weights and bias terms of the fully connected layer. These parameters are adjusted during the training process through backpropagation and optimization algorithms to enable the discriminative model to accurately distinguish the authenticity of the generated images or data. This study uses a CNN-based network structure to predict the micro-Doppler of pedestrians at the next moment through Doppler data. These data are about the walking behavior of pedestrians over some time, so there is a certain temporal correlation. The training process of the CNN-based prediction model is shown in Figure 6.

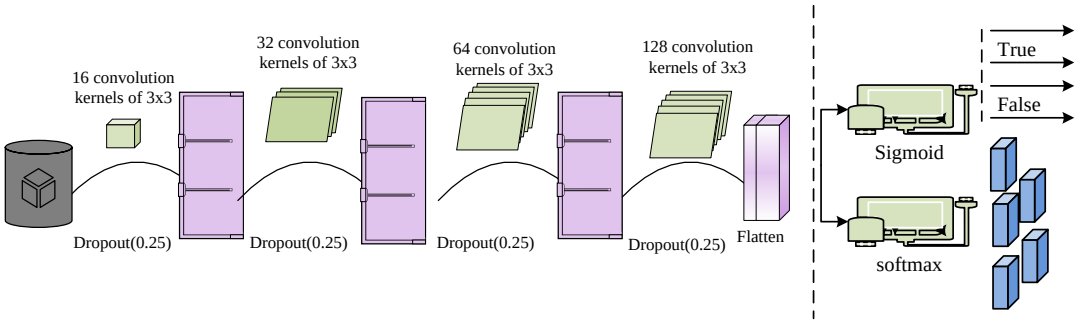

Figure 5: Parameter diagram of discriminant model

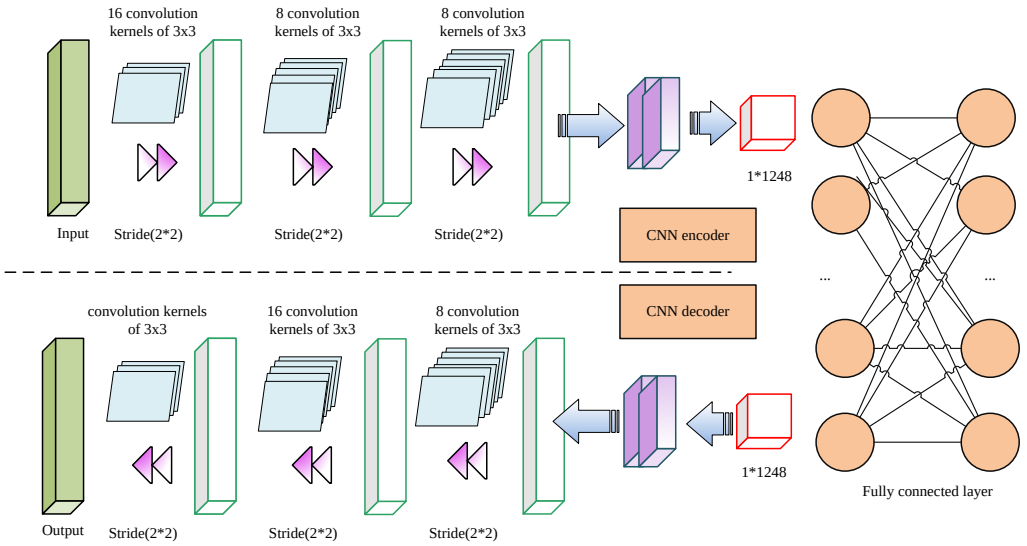

Figure 6: Training process of predictive model based on CNN

In Figure 6, the training of the CNN-based prediction model includes steps such as data preparation, preprocessing, model construction, training, validation, testing, deployment, and monitoring. Firstly, this study collects Doppler data and target labels and normalizes the data. Then, appropriate activation and loss functionsare selected to construct the CNN model. The modelis optimized through multiple trainings, and the validation set is used to adjust parameters to improve performance. Finally, the model is evaluated on an independent test set to ensure that it performs well on unseen data. After completing the training, the model is deployed to practical applications and regularly monitored and updated to ensure effectiveness.

4 TFC performance verification of MNBC model

This experiment is divided into two parts: traffic flow simulation and pedestrian recognition. A simulation platform is established using Java, which has a visual vehicle system operation system, supports real-time data collection and parameter settings, and increases experimental authenticity. For pedestrian recognition, Tensor Flow is chosen as the development platform, utilizing its efficiency and dynamic calculation graph characteristics. The experiment is run on a machine with AMD 2600x CPU, rx580 GPU, and 32GB of memory.

4.1 Experimental implementation of predictability bilateral control model

In the simulation system, all vehicles run on a circular road with a length of 1500 meters. The length of each vehicle is fixed, and they travel at a specific fixed speed when the system is activated. To make it easier to distinguish adjacent vehicles, this study uses three different colors to identify them. Assuming that each vehicle is equipped with an FMCW millimeter wave radar module and V2V communication module, this means that each vehicle can obtain relevant parameters about its operating status through sensors. Table 2 shows the initial parameters of the system.

Table 2: Relevant parameters of the simulation system

Name	Value	Name	Value
System simulation duration	500s	Expected velocity feedback gain	Kc = 0.01
Maximum/small acceleration	a =±3 m/s^2	Vehicle initialization speed v_0	30 m/s
Front and rear relative velocity feedback gain	k_v = 0.2	Initial vehicle spacing d_0	37.5 m
Duration per break	t = 2 s	Road width l_2	5 m
Vehicle length l_3	L = 5 m	Number of vehicles N	40
Total road length l_1	1500 m	Distance feedback gain	ka = 0.1

In Table 2, the total length of the road is set to 1500 m, the experimental simulation time is 500 s, the relative speed feedback gains before and after is 0.2, and the expected speed feedback gain is 0.01. On a fixed-length one-way road, uniform spacing between vehicles indicates a more balanced system and lower collision probability, while closer speeds help improve system efficiency. Therefore, this study focuses on the stability of vehicle systems, mainly considering vehicle spacing and speed. In the simulation system, the speed of each vehicle at each momentis obtained. For a system containing N vehicles, a closer speed indicates a lower probability of collision. TAPAS Cologne Dataset sources from the Cologne transportation project. It provides traffic flow simulation data in a virtual urban environment, including vehicle trajectory and signal status, suitable for the development and testing of traffic simulation and management systems. The dataset is the simulated experiment of MNBC. The study first compares the control situation of different control systems. Among them, cases 3, 7, and 15 are three different control systems, and the differences are obvious. Therefore, the study collects the speed data of cases 3, cases 7, and cases 15, and extracts the data from different time points, as shown in Figure 7. Figure 7(a) shows the speed graph of the vehicle controlled by the following model in three scenarios, showing a fluctuating trend at the 9th second. At the 10th second, Case 15 and Case 7 change the control model to a bilateral control model and a PBCM. The car with vehicle ID 5 applies brakes in 10 seconds, and the results show that the following model causes traffic congestion, while the bilateral control model and PBCM perform more stably. Under system control, PBCM exhibits smaller speed differences and greater stability. Figure 8 shows the variation of the minimum workshop distance over time in the vehicle system.

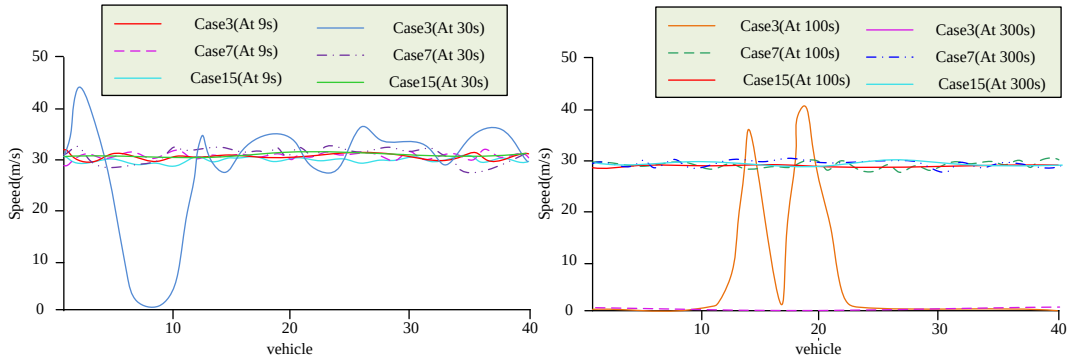

(a) Speed diagram of the system vehicle at 9s and 30s (b) Speed diagram of the system vehicle at 100s and 300s

Figure 7: Vehicle speed during system operation under the control of different models

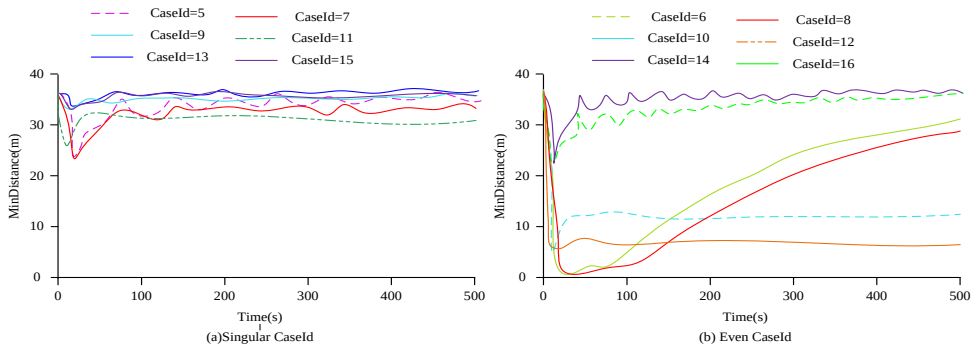

(a)Singular CaseId (b) Even CaseId

Figure 8: Variation of minimum workshop distance with time in vehicle system

In Figure 8, PBCM performs best in various scenarios, with a minimum vehicle spacing of nearly 37.5 m. Taking Figure 8(b) as an example, in the model switching scenario after 2 seconds of braking, bilateral control and MNBC model cause a sharp decrease in the distance between the smallest cars, while PBCM only decreasesfrom 35 m to 33 m. This indicates that in emergency braking situations, the predictive model can better alleviate system disturbances. In Figure 8(a) and 8(b), taking 3% and 5% errors as examples, PBCM maintains a relatively large minimum distance under different error conditions. In contrast, traditional and multi-node models experience a sharp decrease in vehicle spacing after braking. In the case of greater delay (0.2 s), the minimum workshop distance of the predictable model slightly decreases, but it can still quickly recover to a stable state. Meanwhile, traditional and multi-node models require a longer time, and multi-node models are almost unable to operate normally.

4.2 MDC pedestrian recognition experiment

This study explores three methods for measuring the distance between vehicles: minimum distance, maximum distance, and error bars for vehicle spacing. Figure 9 shows the calculation results of the error bar for the minimum distance between vehicles during system operation.

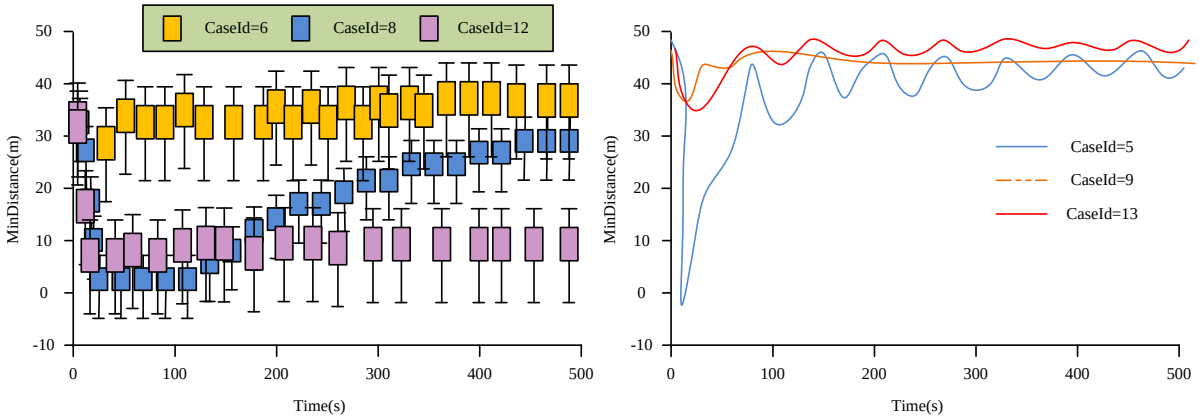

(a) Group A Case (b) Group B Case

Figure 9: Error bar of car spacing in vehicle system

In Figure 9(a) and 9(b), the vehicle system under PBCM control exhibits a smaller error range under both large and small delays and errors. This indicates that under PBCM, the vehicle system is more stable compared to systems under other model controls. Similarly, by collecting data on the maximum vehicle spacing during the operation of the vehicle system and calculating the error range, Figure 10 shows the error range of the maximum vehicle spacing. In Figure 10, compared to the larger maximum vehicle spacing of traditional bilateral control systems and MNBC systems, PBCM can achieve the smallest maximum vehicle spacing (about 39 m) in the vehicle system. This study improves the network structure, including adding a fully connected layer and introducing dropout to prevent overfitting. Figure 11(a) shows the final training result. Extra data are generated through ACGAN and integrated into the training set, with the associated losses presented in Figure 11(b). The data are generated using a CNN model, added to the training set, and then retrained using the CNN model to study the model. Figure 11(c) shows the accuracy during the training process.

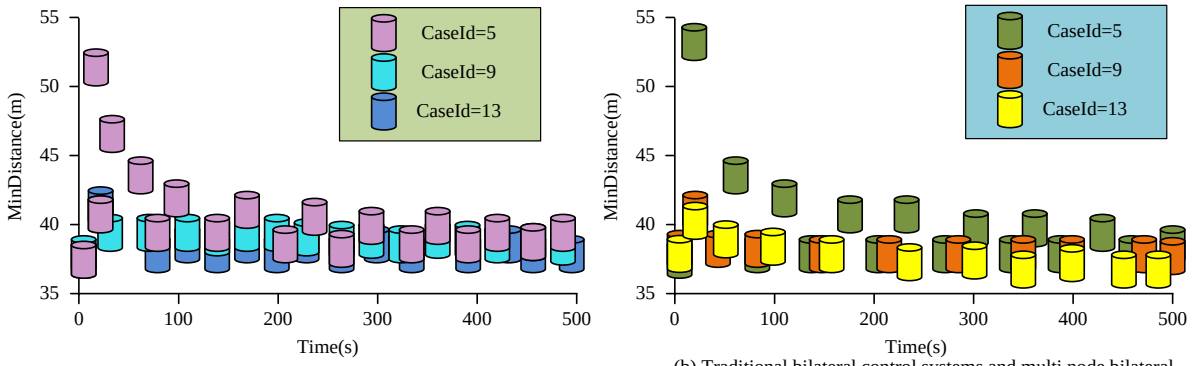

(a) Bilateral control model

(b) Traditional bilateral control systems and multi node bilateral control systems

Figure 10: Maximum spacing and error bar in vehicle system

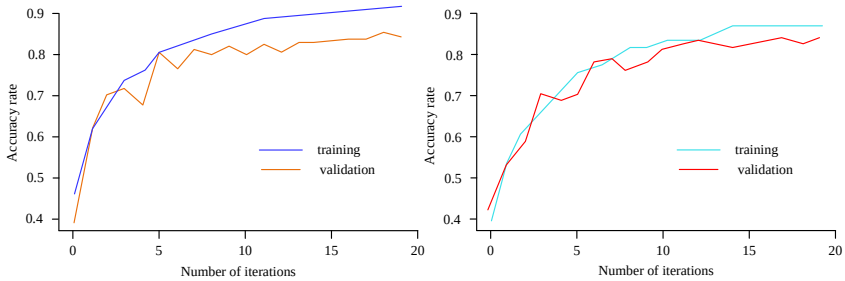

(a) Pedestrian recognition based on CNN - Accuracy of training set and verification set during training

(b) Generative adversarial network - Accuracy of training set and verification set during training

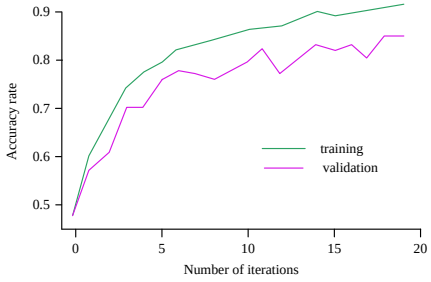

(c) CNN predictive model data augmentation - the accuracy of the training set and validation set during training

Figure 11: Accuracy of training set and verification set during training

In Figure 11(a), a CNN-based prediction model is used for data generation, and the generated data areadded to the training set to retrain the research model using the CNN model. After training, the accuracy ofthe test set is 84.7%. In the research model shown in Figure 11(b), the pedestrian recognition accuracy is approximately 80%. Although improving the network model can improve accuracy, an 80% recognition rate is unacceptable in practical applications. In Figure 11(c), by using ACGAN for data generation and adding the generated data to the training set, the accuracy of the test set is improved from 80% to about 87%, effectively improving the accuracy of pedestrian recognition. In addition, by using a CNN-based neural network for data generation and adding the generated data to the training set, the accuracy of the test set is improved from 80% to about 85%, effectively improving the accuracy of pedestrian recognition. To verify the control effect of this model on traffic flow, the study is compared with the traditional TFC method, and the results are shown in Figure 12. In Figure 12, on a fixed road section, when traditional TFC methods are used for TFC, the number of vehicles passing through per hour is always at a low level, up to 30 vehicles per hour. However, when using the control model proposed in the study, the number of vehicles passing through per hour on this road section is at a high-level during traffic congestion, up to 31 vehicles per hour. The TFC model proposed in the study can effectively improve the congestion situation of urban road traffic during peak hours. The study compares the confusion matrix of pedestrian recognition between CNN and GCAN models in the intersection scene, and the results are shown in Figure 13.

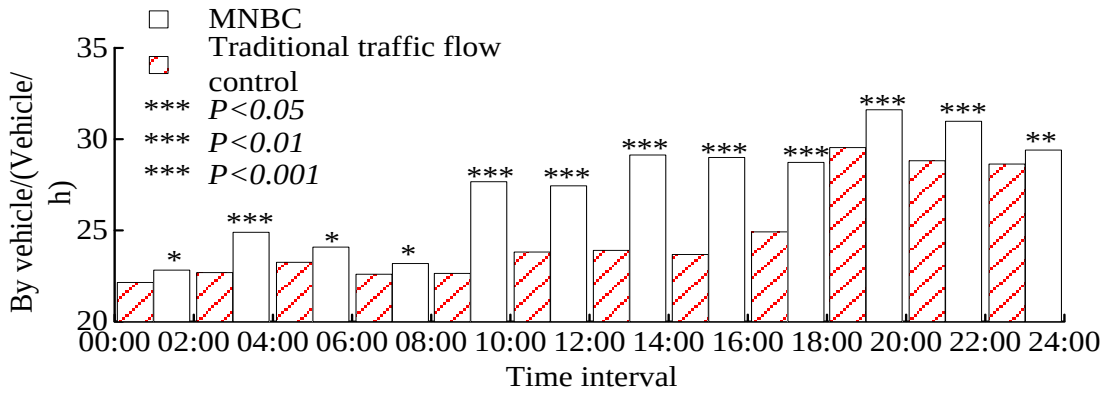

Figure 12: Traffic flow control effect

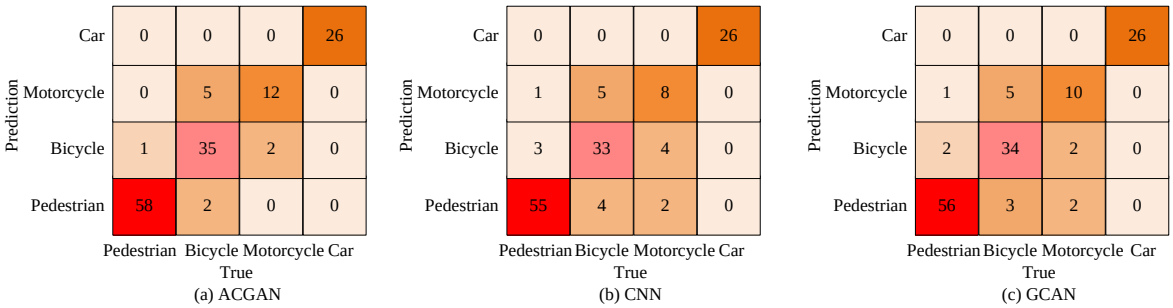

Figure 13: Pedestrian recognition confusion matrix

In Figure 13, the research model only has one case of recognition error in pedestrian recognition results during the recognition process. This model is prone to misidentification when identifying people traveling by bicycle or motorcycle. The frequency of misidentification in CNN and GCAN models during the recognition process is significantly higher than that of the proposed model. A comparative analysis of the response times of different TFC models is performed, and the results are shown in Table 3.

Table 3: Response times of the different traffic flow control models (s)

Time	MNBC	Traditional traffic flow control
7:00~9:00	55	246
11:00~13:00	32	198
17:00~19:00	62	326

As shown in Table 3, the response time of the TFC model is significantly lower than that of traditional TFC schemes during the three peak periods of urban traffic. The response time of the TFC scheme is the highest at 62 seconds, while the response time of the traditional TFC scheme is the shortest at 198 seconds. When deploying the model in larger urban networks, modular design is required for easy management and upgrading. Layered control strategies are implemented to meet different levels of traffic management needs. Data integration and communication infrastructure are strengthened to ensure real-time and accurate information flow. Algorithms are optimized to improve the ability to handle large-scale data. The reliability of the model is verified through simulation and testing. At the same time, the resilience and fault tolerance of the system should be ensured, and user participation and feedback should be encouraged.

5 Discussion

The MNBC model proposed in the study demonstrates superior performance compared to TFC methods discussed in other literature. Especially when dealing with complex traffic scenarios, the MNBC model demonstrates better processing capabilities compared to the vehicle following model, non-local conservation law model, and grid-based fluid dynamics model proposed in references [7] and [8]. The MNBC model integrates Kalman filtering for state estimation and prediction, which can more effectively manage delays compared to traditional models. In emergency braking events, the MNBC model can more proactively predict and adjust delays, reducing the impact on traffic flow. Even under different delay conditions, the MNBC model can better maintain the minimum distance between vehicles. The MNBC model optimizes traffic flow by considering the mutual influence between multiple nodes, a feature that is absent in traditional models. Traditional models usually only focus on isolated intersections or individual nodes, while the MNBC model considers a wider range of transportation networks, thereby achieving more effective traffic flow optimization. This comprehensive approach has resulted in the establishment of a more stable transportation system, as evidenced by the simulation results, which indicate minimal fluctuations in vehicle speed.

The improvement of the performance of the MNBC model relies on more advanced state estimation, more comprehensive consideration of transportation networks, and real-time data for relevant calculations. The application of the Kalman filter in the MNBC model provides significant advantages for state estimation, which can accurately estimate the state of the transportation system even in the presence of noise and uncertainty. A more comprehensive consideration of the transportation network avoids isolating a certain part of the transportation network. The MNBC model can more effectively optimize traffic flow, thereby improving overall performance. Real-time data applications enable the MNBC model to dynamically adjust according to actual conditions, enabling it to quickly respond to changes in traffic conditions and enhance its adaptability and responsiveness.

Although the MNBC model optimizes the level of TFC, its performance in larger and more complex urban transportation networks needs further evaluation. With the increase in network size, computational complexity, and data requirements may become challenges. The effectiveness of the model largely depends on the accuracy and reliability of traffic sensors. Any inaccuracy in sensor data may affect the performance of the model. Further research is needed on how the MNBC model can be integrated with other intelligent traffic management systems to achieve a comprehensive solution. Future research will develop more efficient algorithms for state estimation and prediction to handle larger networks and reduce computational load. In the future, sensor fusion technology will be improved to enhance the robustness of the model to sensor noise and improve overall accuracy. In addition, comprehensive research will explore how to integrate the MNBC model with other traffic management systems to form a more comprehensive traffic control framework.

6 Conclusion

In modern urban traffic management, TFC in closed congested road scenarios has always been a highly anticipated challenge. The advancement of urbanization has made road congestion increasingly prominent. Traditional car following models are prone to traffic congestion when faced with emergency braking and other situations, requiring the search for more intelligent and robust TFC methods. Therefore, this study adopted the MNBC model and combined it with the non-rigid body micro-Doppler effect to conduct a theoretical analysis of pedestrian MDC. In addition, a pedestrian recognition schemewas constructed using a small FMCW radar. To improve accuracy, ACGAN and CNN-based models were used to enhance the data. The experiment showed that by using ACGAN to generate data and adding it to the training set, the accuracy of thepedestrian recognition test set was improved from 80% to 87%. Meanwhile, by using a CNN-based network to generate data and adding it to the training set, the accuracy of the test set was improved from 80% to 85%. After adopting the proposed TFC model, bilateral control and the MNBC model significantly reduced the distance between the minimum vehicles, while PBCM only reduced it from 35 m to 33 m,

effectively improving the traffic flow under crowded conditions. Both methods effectively improved the accuracy of pedestrian recognition. The MNBC model can effectively improve the congestion of urban road traffic and promote the development of urban road traffic. However, the research model regulates the traffic flow, which will compress the traffic flow and put a higher pressure on the urban traffic load. Future studies will optimize the TFC method to improve the congestion state of urban road traffic without squeezing the traffic flow.

Author Contributions

With the increase of urban population and the popularization of transportation, traffic flow control has become a key issue in urban traffic management. This requires the research of a new intelligent traffic flow control method to improve the efficiency and sustainability of the transportation system. X. W. article proposes an intelligent traffic flow control method based on a multi node bilateral control model. This method adopts the Kalman filtering algorithm to intelligently adjust the intersection flow, considering the mutual influence between multiple nodes, and optimizing the traffic flow by coordinating the traffic flow on both sides of the road intersection. H. G. For this study, the MNBC model was used, combined with the non rigid body micro-Doppler effect, to conduct a theoretical analysis of pedestrian MDC, and a pedestrian recognition scheme was constructed using a small FMCW radar. To improve accuracy, models based on ACGAN and CNN were used to enhance the data.

H. G. and X. W. others made significant contributions to the writing of the manuscript.

Availability of data and materials

All data generated or analyzed during this study are included in this published article.

Acknowledgement

School of Traffic and Transportation, Shijiazhuang Tiedao University

References

[1] F. Storani, R. Di Pace, and B. De Schutter, “A traffic responsive control framework for signalized junctions based on hybrid traffic flow representation,” Journal of Intelligent Transportation Systems, vol. 27, no. 5, pp. 606-625, 2023. https://doi.org/10.1080/15472450.2022.2074790

[2] F. Tajdari, and C. Roncoli, “Online set-point estimation for feedback-based traffic control applications,” IEEE Transactions on Intelligent Transportation Systems, vol. 24, no. 10, pp. 10830-10842, 2023. https://doi.org/10.1109/TITS.2023.3274233

[3] Z. Ning, J. Huang, and X. Wang, “Vehicular fog computing: enabling real-time traffic management for smart cities,” IEEE Wireless Communications, vol. 26, no. 1, pp. 87-93, 2019. https://doi.org/10.1109/MWC.2019.1700441

[4] E. M. Idriss, A. Hakim, and A. Laghrib, “On the well-posedness of a tensor-based second order PDE with bilateral term for image super-resolution,” Evolution Equations and Control Theory, vol. 12, no. 2, pp. 703-731, 2023. https://doi.org/10.3934/eect.2022047

[5] H. Steele, A. Jack, and J. Liu, “Novel approach for validation of innovative modules for railway traffic management systems in a virtual environment,” Proceedings of the Institution of Mechanical Engineers, Part F: Journal of Rail and Rapid Transit, vol. 236, no. 2, pp. 139-148, 2022. https://doi.org/10.1177/095440972110418

[6] Q. Du, K. Huang, J. Scott, and W. Shen, “A space-time nonlocal traffic flow model: Relaxation representation and local limit,” Discrete and Continuous Dynamical Systems, vol. 43, no. 9, pp. 3456-3484, 2023. https://doi.org/10.3934/dcds.2023054

[7] C. Zhai, and W. Wu, “A macro traffic flow model with on-ramp considering driver's predictive effect,” Journal of Transportation Systems Engineering and Information Technology, vol. 20, no. 4, pp. 119-127, 2020. http://www.tseit.org.cn/EN/Y2020/V20/I4/119

[8] A. Hyochang, and C. Han-Jin, “Research of automatic recognition of car license plates based on deep learning for convergence traffic control system,” Personal and Ubiquitous Computing, vol. 27, no. 3, pp. 1139-1148, 2023. https://doi.org/10.1007/s00779-020-01514-z

[9] I. Finkelberg, T. Petrov, and A. Gal-Tzur, “The effects of vehicle-to-infrastructure communication reliability on performance of signalized intersection traffic control,” IEEE Transactions on Intelligent Transportation Systems, vol. 23, no. 9, pp. 15450-15461, 2022. https://doi.org/10.1109/TITS.2022.3140767

[10] N. Espitia, J. Auriol, H. Yu, and M. Krstic, “Traffic flow control on cascaded roads by event-triggered output feedback,” International Journal of Robust and Nonlinear Control, vol. 32, no. 10, pp. 5919-5949, 2022. https://doi.org/10.1002/rnc.6122

[11] Y. Zheng, J. Wang, and K. Li, “Smoothing traffic flow via control of autonomous vehicles,” IEEE Internet of Things Journal, vol. 7, no. 5, pp. 3882-3896, 2020. https://doi.org/10.1109/JIOT.2020.2966506

[12] Q. Liu, S. Wu, and P. Zhang, “Statistical analysis of urban traffic flow using deep learning,” Informatica, vol. 48, no. 5, pp. 23-28, 2024. https://doi.org/10.31449/inf.v48i5.5393

[13] J. Yu, “Passenger flow prediction of tourist attractions by integrating differential evolution and GWO,” Informatica, vol. 48, no. 13, pp. 31-50, 2024.

https://doi.org/10.31449/inf.v48i13.6159

[14] X. Ge, Q. L. Han, L. Ding, Y. L. Wang, and X. M. Zhang, "Dynamic event-triggered distributed coordination control and its applications: A survey of trends and techniques," IEEE Transactions on Systems, Man, and Cybernetics: Systems, vol. 50, no. 9, pp. 3112-3125, 2020. https://doi.org/10.1109/TSMC.2020.3010825

[15] S. Pu, W. Shi, J. Xu, and A. Nedić, "Push-pull gradient methods for distributed optimization in networks," IEEE Transactions on Automatic Control, vol. 66, no. 1, pp. 1-16, 2020. https://doi.org/10.1109/TAC.2020.2972824

[16] A. Laouzai, and R. Ouafi, "A prediction model for atmospheric pollution reduction from urban traffic," Environment and Planning B: Urban Analytics and City Science, vol. 49, no. 2, pp. 566-584, 2022. https://doi.org/10.1177/23998083211005776

[17] M. A. Envelope, G. F. Envelope, and R. M. Envelope, "Modelling and optimization of emissions in steady state urban traffic networks," IFAC-PapersOnLine, vol. 55, no. 5, pp. 31-36, 2022. https://doi.org/10.1016/j.ifacol.2022.07.635

[18] T. Okano, T. Nozaki, and T. Murakami, "An approach to evaluation index-based gain scheduling for acceleration-based four-channel bilateral control," Journal of the Japan Society for Precision Engineering, vol. 86, no. 9, pp. 720-730, 2020. https://doi.org/10.2493/jjspe.86.720

[19] Y. Jin, Z. Bi, and X. Qin, "Additive Gaussian noise model and Kalman filter to enhance controllability of gesture-controlled teleoperated soft actuators," Proceedings of the Institution of Mechanical Engineers, Part B: Journal of Engineering Manufacture, vol. 235, no. 14, pp. 2219-2229, 2021. https://doi.org/10.1177/0954405420941007

[20] E. S. Handayani, R. Susilowati, and I. Setyopranoto, "Transient bilateral common carotid artery occlusion (tBCCAO) of rats as a model of global cerebral ischemia," Bangladesh Journal of Medical Science, vol. 18, no. 3, pp. 491-500, 2019. https://doi.org/10.3329/bjms.v18i3.41616

[21] E. Estrada, W. Yu, and X. Li, "Stability and transparency of delayed bilateral teleoperation with haptic feedback," International Journal of Applied Mathematics and Computer Science, vol. 29, no. 4, pp. 681-692, 2019. https://doi.org/10.2478/amcs-2019-0050

[22] S. Pal, A. Roy, P. Shivakumara, and U. Pal, "Adapting a swin transformer for license plate number and text detection in drone images," Artificial Intelligence and Applications, vol. 1, no. 3, pp. 145-154, 2023. https://doi.org/10.47852/bonviewAIA3202549

Appendix

List of Abbreviations

Full name	Abbreviation
Traffic flow control	TFC
Intelligent traffic flow control	ITFC
Multi-Node Bilateral Control	MNBC
Predictable bilateral control model	PBCM
Convolutional neural networks	CNN
Process variables	PV
Set values	SV
Micro Doppler characteristics	MDC
Frequency Modulated Continuous Wave	FMCW
Generative Adversarial Network	GAN
Conditional Generative Adversarial Network	CGAN
Assisted Classification Generative Adversarial Network	ACGAN

Reduced Convolutional Recurrent Neural Network Using MFCC for Music Genre Classification on the GTZAN Dataset

Ela Setiorini, Moeljono Widjaja, Arya Wicaksana*
Universitas Multimedia Nusantara, Tangerang 15810 Indonesia
E-mail: ela.setiorini@student.umn.ac.id, moeljono.widjaja@umn.ac.id, arya.wicaksana@umn.ac.id
*Corresponding author

Keywords: classification, CRNN, GTZAN, MFCC, MIR, music genre

Received: August 9, 2024

This study presents a reduced Convolutional Recurrent Neural Network (CRNN) model for music genre classification, leveraging the GTZAN dataset and Mel-Frequency Cepstral Coefficient (MFCC) feature extraction. Unlike more complex architectures, this model simplifies the CRNN structure to three convolutional layers and two BiLSTM layers, maintaining competitive performance while reducing computational complexity. Key experimental parameters included learning rate tuning (0.1, 0.01, 0.001, and 0.0001) and dropout usage (30% before the BiLSTM layers) to mitigate overfitting. The best configuration, utilizing a learning rate of 0.001 and dropout, achieved an accuracy of 88.64%, outperforming more complex CRNN models by approximately 15%. These results underscore the potential of streamlined architectures in music information retrieval tasks, particularly for applications where computational resources are constrained. Future work will address overfitting issues and refine the dataset for enhanced model performance.

Povzetek: Študija predstavlja poenostavljen model konvolucijsko-rekurentne nevronske mreže (CRNN) za klasifikacijo glasbenih zvrsti z uporabo GTZAN podatkovne zbirke in MFCC značilk, ki kljub zmanjšani kompleksnosti dosega visoko natančnost (88,64 %) ter presega zmogljivejše modele za približno 15 %.

1 Introduction

Music genre classification is crucial for information retrieval (Music Information Retrieval) and analysis, and as digital music libraries grow, automated methods are needed to categorize and organize music. Music Information Retrieval (MIR) is a research field that focuses on analyzing and extracting music transcription, beat detection, on-set detection, and genre classification [1]. Traditional methods often rely on handcrafted features and machine learning algorithms, which need help to capture complex temporal and spectral patterns. Convolutional Recurrent Neural Networks (CRNNs), a combination of CNNs for feature extraction and RNNs for temporal dependencies, have shown promising results in extracting hierarchical features from raw audio data [2].

This work investigates further the CRNN application for MIR, specifically to classify music genres with the GTZAN dataset. The CRNN extracts local features and aggregates temporal patterns [3]. MFCC is extracted from the dataset to become an input for the model [4]. The combination of CRNN in this work is CNN with BiLSTM (Bidirectional Long Short-Term Memory). This work proposes a simpler version of the algorithms compared to Ashraf et al. [5], with only three layers of CNN and two layers of RNN (BiLSTM-BiLSTM). The accuracy of Ashraf et al. is 73.69% with five layers of CNN and three layers of RNN. The main contribution of this work is a less complex CRNN model architecture with higher accuracy.

The rest of this paper is structured as follows: The Introduction section sets the background and motivation for this paper. Related Works section layouts other works in MIR that utilize machine learning and deep learning methods. The Methods section explains the data collection, requirement specification, design and implementation, and testing and evaluation. The Results and Analysis section presents empirical evidence based on four scenarios and discusses the findings. Finally, the Conclusion section summarizes the findings and outlines future works.

2 Related works

Ghosh et al. [2] compared machine learning models (SVC or Support Vector Classifier, logistic regression, and ensemble learning using AdaBoost) and deep learning models (ANN or Artificial Neural Network, CNN, CRNN with CNN-LSTM combination, and PCRNN or Parallel CRNN). Inputs used in this work are feature matrix (for machine learning models) and Mel-spectrogram (for deep learning models), extracted from the FMA dataset. The CRNN has the highest accuracy at 90%, with only 480 out of 8000 data used from the dataset.

Ashraf et al. [5] use a couple of CRNN combinations, i.e., CNN-LSTM, CNN-BiLSTM, CNN-GRU, and CNN-BiGRU. Inputs used in this work are the Mel-spectrogram and Mel-Frequency Cepstral Coefficient (MFCC) extracted from the GTZAN dataset. This work's highest

accuracy is obtained by CNN-BiGRU using Mel-spectrogram (89.3%) and CNN-LSTM using MFCC (76.4%). Mendes et al. [6] compared two CRNN combinations (CNN-LSTM and CNN-BiLSTM), and the results were used to get music recommendations. The input that is used in this work is the Mel-spectrogram that is extracted from the FMA dataset. CNN-BiLSTM achieved the highest accuracy, with an accuracy of 72%.

Luo [7] compared two deep learning algorithms, Convolutional Neural Network (CNN) and Long Short-Term Memory (LSTM), using GTZAN and FMA (Free Music Archive) datasets. The accuracies obtained for the GTZAN dataset are 56% (CNN) and 42% (LSTM). Meanwhile, accuracies for the FMA dataset are 50.5% (CNN) and 33.5% (LSTM). Kumar et al. [8] used CNN and GTZAN datasets to classify music genres. The accuracy obtained in this work is 83%. Ghosh et al. [2] compared several machine learning and deep learning algorithms using the FMA dataset. The highest accuracy obtained in this work was achieved using a convolutional-recurrent neural network (CRNN) with an accuracy of 90%. Table 1 provides a summary and comparison of these related works.

Table 1: Test results from the model

Work	Model	Dataset	Feature Extraction	Accuracy
Luo [7] – "Automatic Music Genre Classification based on CNN and LSTM"	- CNN - LSTM	- GTZAN - FMA	- Mel-spectrogram (for CNN) - MFCC (for LSTM)	- Highest accuracy obtained by CNN using both GTZAN dataset (56%) - FMA dataset (50.5%)
Kumar et al. [8] – "Automated Music Genre Classification through Deep Learning Techniques"	CNN	GTZAN	MFCC	Accuracy obtained by the model is 83%
Ghosh et al. [2] – "A Study on Music Genre Classification using Machine Learning"	- Machine learning models (SVC, logistic regression, and ensemble learning using AdaBoost) - Deep learning models (ANN, CNN, CRNN with CNN-LSTM combination, PCRNN)	FMA, using only 480 out of 8000 data	- Feature matrix (for machine learning models) - Mel-spectrogram (for deep learning models)	Highest accuracy obtained by CRNN (90%)
Ashraf et al. [5] – "A Hybrid CNN and RNN Variant Model for Music Classification"	- CNN-LSTM - CNN-BiLSTM - CNN-GRU - CNN-BiGRU	GTZAN	- Mel-spectrogram - MFCC	- Highest accuracy obtained by CNN-BiGRU using Mel-spectrogram (89.3%) - CNN-LSTM using MFCC (76.4%)
Mendes et al. [6] – "Deep Learning Techniques for Music Genre Classication and Building a Music Recommendation System"	- CNN-LSTM - CNN-BiLSTM	FMA	Mel-spectrogram	CNN-BiLSTM obtained the highest accuracy (90%)

3 Methods

The dataset that is used in this work is the GTZAN dataset. GTZAN dataset was first created by George Tzanetakis and Perry Cook in 2002 [9]. This dataset consists of 10 genres of music, and each genre has a total of 100 WAV audio. Each audio file lasts 30 seconds with a 22,050 Hz sample rate. The genres inside this dataset are blues, classic, country, hip-hop, jazz, metal, pop, reggae, and rock. There is a single corrupted audio file within the jazz category. `The corrupted audio within the jazz category is removed before it got into data processing. Hence, the dataset contains only 999 audio files. The dataset was initially available on a MARSYAS website created by Tzanetakis and Cook [10]. Currently, the dataset is available to download at https://www.kaggle.com/datasets/andradaolteanu/gtzan-dataset-music-genre-classification (Kaggle).

MFCC is extracted from each audio file inside the dataset. Sound extraction carried out by MFCC is based

on estimated frequencies that humans can hear. The signal used in MFCC is the Mel scale, which uses a linear filter at frequencies below 1000 Hz and a logarithmic distance above 1000 Hz [11]. The output of this process is a spectrum wave graph or spectrogram that uses this frequency scale. This spectrogram contains feature coefficients, and these coefficient values represent the audio signal [12]. MFCC can capture important voice characteristics in recognition and critical information in voice, produce minimal data without losing much information, and replicate human hearing sound [13].

MFCC extraction is handled using Librosa, a Python package that provides audio and music signal processing [14]. Several parameters are needed to extract MFCC, such as the number of coefficients needed, window length, and hop length. This work extracts 13 cepstral coefficients from every audio. Window length and hop length used are 2,048 and 512, respectively. Each audio file is split into ten segments to augment the training data. The results of this process are saved on a JSON file containing an array with the 13 MFCC coefficient inside.

The proposed CRNN model consists of three layers: a convolutional layer, a max pooling layer, and batch normalization on the CNN layer, with two BiLSTM layers for the RNN. After going into the CNN and RNN layers, the inputs are flattened, and the fully connected layer connects all the neurons with the output layer. This work investigates two models: the models that used dropout before the BiLSTM layer and those that did not use dropout. The CNN layer consists of a convolutional layer, a max pooling layer, and batch normalization. The convolutional layer uses 32 filters with 3x3 kernel size on the first and second layers and 2x2 kernel size on the third layer, including ReLU for the activation function. ReLU is preferred in this work due to its ability to remove negative values.

The Max pooling layer has a 3x3 pool size for the first and second layers, 2x2 for the third layer, and 2x2 stride. Pooling is done to progressively lower the model's computational complexity, parameter count, and control overfitting [15]. Pooling reduces the size of the matrix in the feature map. Max pooling is one of the most popular forms of pooling. Max pooling extracts the highest value inside patches from the feature map and discards the rest of the values [16].

Batch normalization is employed to mitigate sudden changes in each layer [6]. The input is reshaped before being passed to the RNN layer, as the CNN and RNN layers require different input shapes. In this work, a dropout layer is added before the RNN layer as part of the investigation. Dropout is widely recognized for its ability to prevent overfitting by randomly deactivating neurons during training [17]. A dropout rate of 0.3 (30%) is used before the RNN layer. This value is selected based on its superior validation accuracy compared to dropout rates of 0.2 and 0.4.

In this work, two layers of BiLSTM are used, with return sequences set to true for the first layer. Return sequences are used to send forward all of the LSTM hidden layer sequences to the next layer [18]. The input went to the dense or fully connected layer. The input is flattened before going to the dense layer. The number of filters used for the dense layer is 64 units with the ReLU activation function, which is then followed by another dropout of 30%. Figure 1 shows the overview of the model proposed in this work.

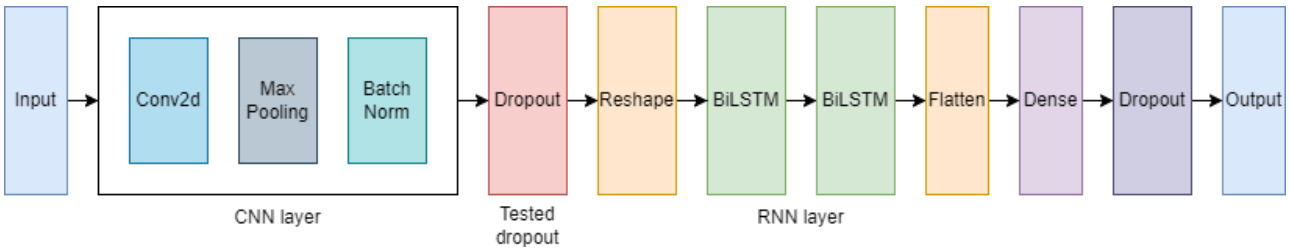

Figure 1: Architecture overview of the proposed CRNN model.

The dataset is divided into training, validation, and test sets with a 60-20-20 ratio using a simple train-validation-test split. Initially, the dataset is split into training and test sets with an 80-20 ratio. The 80% training set is then further divided into training and validation sets with a 75-25 ratio. The validation set is used to evaluate the model during training, while the test set is reserved exclusively for testing the trained model and is not used during the training process.

Several parameters, such as the optimizer, loss function, and evaluation metrics, are configured for the model. The optimizer employed in this work is Adam, tested with multiple learning rates: 0.1, 0.01, 0.001, and 0.0001. These learning rates were selected to observe the accuracy trend, specifically whether smaller learning rates lead to higher accuracy. The loss function is sparse categorical cross-entropy, and the primary performance metric is accuracy.

The model is trained for 100 epochs with a batch size of 32. After training, the model is evaluated using the test set. The evaluation metrics include accuracy, loss, precision, recall, and the F1 score.

4 Results and analysis

This work tests several parameters, namely dropout before the RNN layer and several learning rates values. Model testing uses the test set, which has not been used in any process. Table 2 shows the model's testing result using the test set.

Table 2: Test results from the model

Dropout	Learning rate	Accuracy	Loss	Precision	Recall	F1 score
-	0.1	10.06%	230.86%	1.01%	10.06%	1.84%
-	0.01	74.07%	91.52%	74.82%	74.07%	73.81%
-	0.001	86.74%	64.69%	86.84%	86.74%	86.67%
-	0.0001	84.68%	60.25%	84.7%	84.68%	84.56%
✓	0.1	10.91%	230.88%	1.19%	10.91%	2.15%
✓	0.01	74.72%	75.5%	74.94%	74.72%	74.43%
✓	**0.001**	**88.64%**	**51.95%**	**88.85%**	**88.64%**	**88.62%**
✓	0.0001	86.24%	46.91%	86.28%	86.24%	86.19%

Both models, with or without dropout that used a 0.1 learning rate had very low accuracy because the learning rate was too big. A significant learning rate would speed up the training process, but the model could need more time to analyze the data thoroughly. Based on the accuracy, models with a learning rate of 0.1 could not study the data. Models with a 0.01 learning rate had similar accuracy, around 74%. Models using a 0.001 learning rate had the highest result out of all learning rates, but when compared to the use of dropouts, the model using dropouts had higher accuracy.

The model that used dropout and a 0.001 learning rate got the highest accuracy out of all other tested models, with an accuracy of 88.64%. Models with a 0.0001 learning rate achieved high results, but not higher than models with a 0.001 learning rate. Loss results from models that used dropout are significantly lower than those that did not. Meanwhile, each model's precision, recall, and F1 scores have similar results in terms of accuracy.

The following figures are accuracy and loss graphs from the training process. The models suffer from overfitting, but models that used dropout suffered less than those that did not. Figure 2 shows training results from models without dropouts, and Figure 3 shows training results from models with dropouts. The blue line represents results from the train set, and the orange line represents results from the validation set.

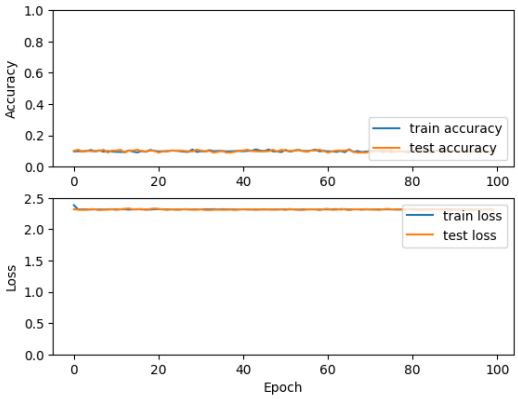

(a)

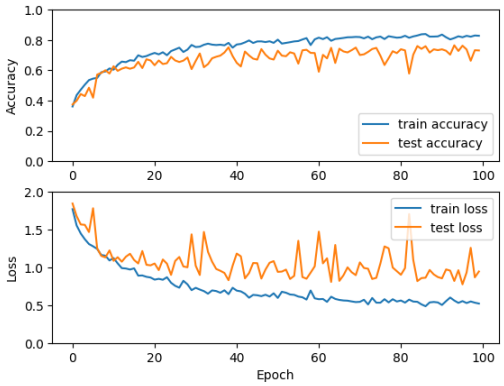

(b)

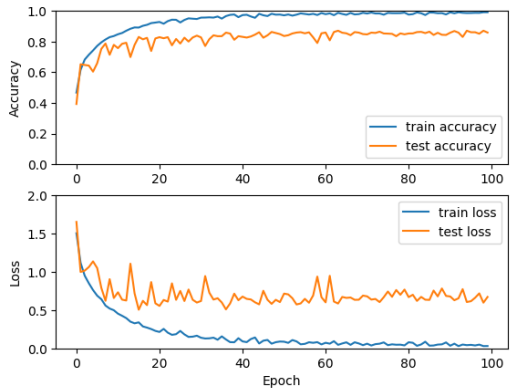

(c)

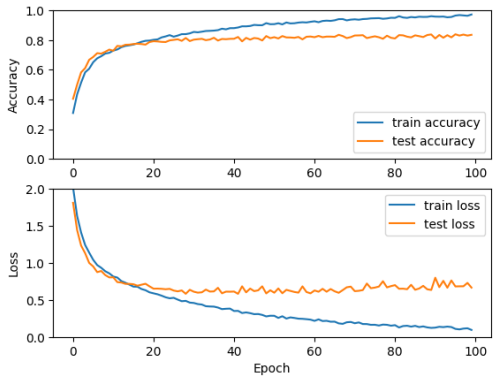

(d)

Figure 2: Accuracy and loss graph for models without dropout with (a) Learning rate 0.1, (b) Learning rate 0.01, (c) Learning rate 0.001, and (d) Learning rate 0.0001

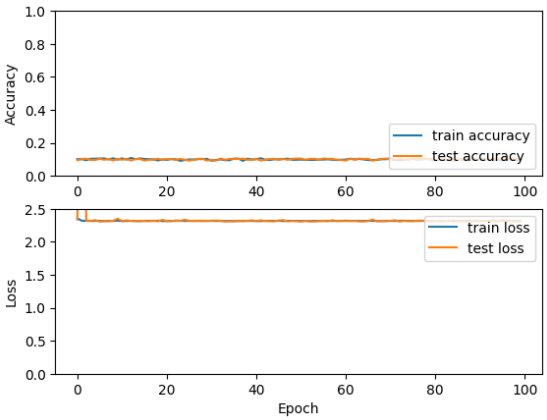

(a)

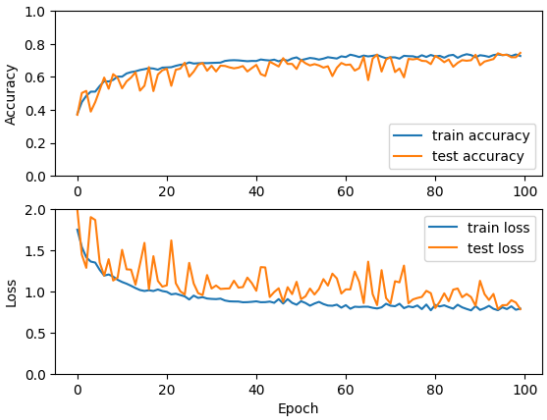

(b)

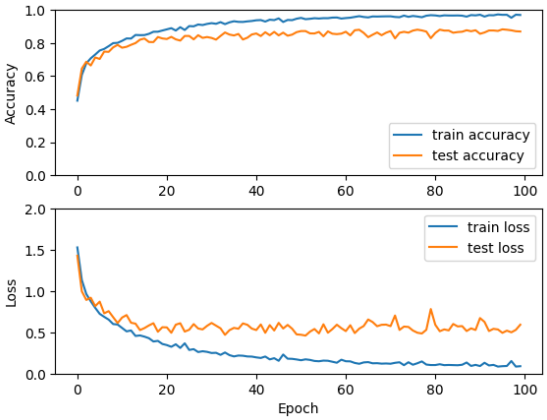

(c)

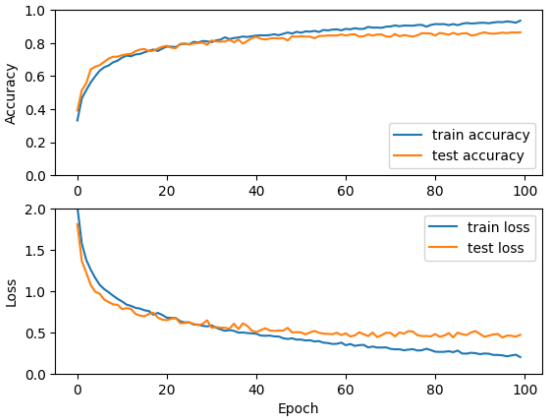

(d)

Figure 3: Accuracy and loss graph for models with dropout with (a) Learning rate 0.1, (b) Learning rate 0.01, (c) Learning rate 0.001, and (d) Learning rate 0.0001

Based on Figures 2 and 3, graphs from learning rate 0.1 show underfitting due to the high loss and low accuracy achieved on all epochs. The results indicate that the model is unable to learn from the data. A learning rate of 0.01 shows overfitting only for the model without dropout. The other model had a good fit because the difference between the train and validation set is minimal. Learning rates of 0.001 and 0.0001 also show overfitting, but the model with dropout is better than without dropout. Thus, the use of dropout effectively reduces overfitting on models. Weight regularization such as L2 are not implemented in this model. Only dropout is used in this

model to maintain the simplicity of the model and also due to device limitation.

Further evaluation on Figures 4 and 5 depict the confusion matrix of the results. Figure 4 shows the confusion matrix from models without dropouts, and Figure 5 shows the confusion matrix from models with dropouts. The confusion matrix for models with a learning rate of 0.1 showed that the model could not classify any data. Meanwhile, models with a learning rate of 0.01 made many mistakes when classifying data. The accuracy achieved using this learning rate is relatively low, around 70%. Learning rates 0.01 and 0.001 show overfitting but are still able to classify the data sufficiently.

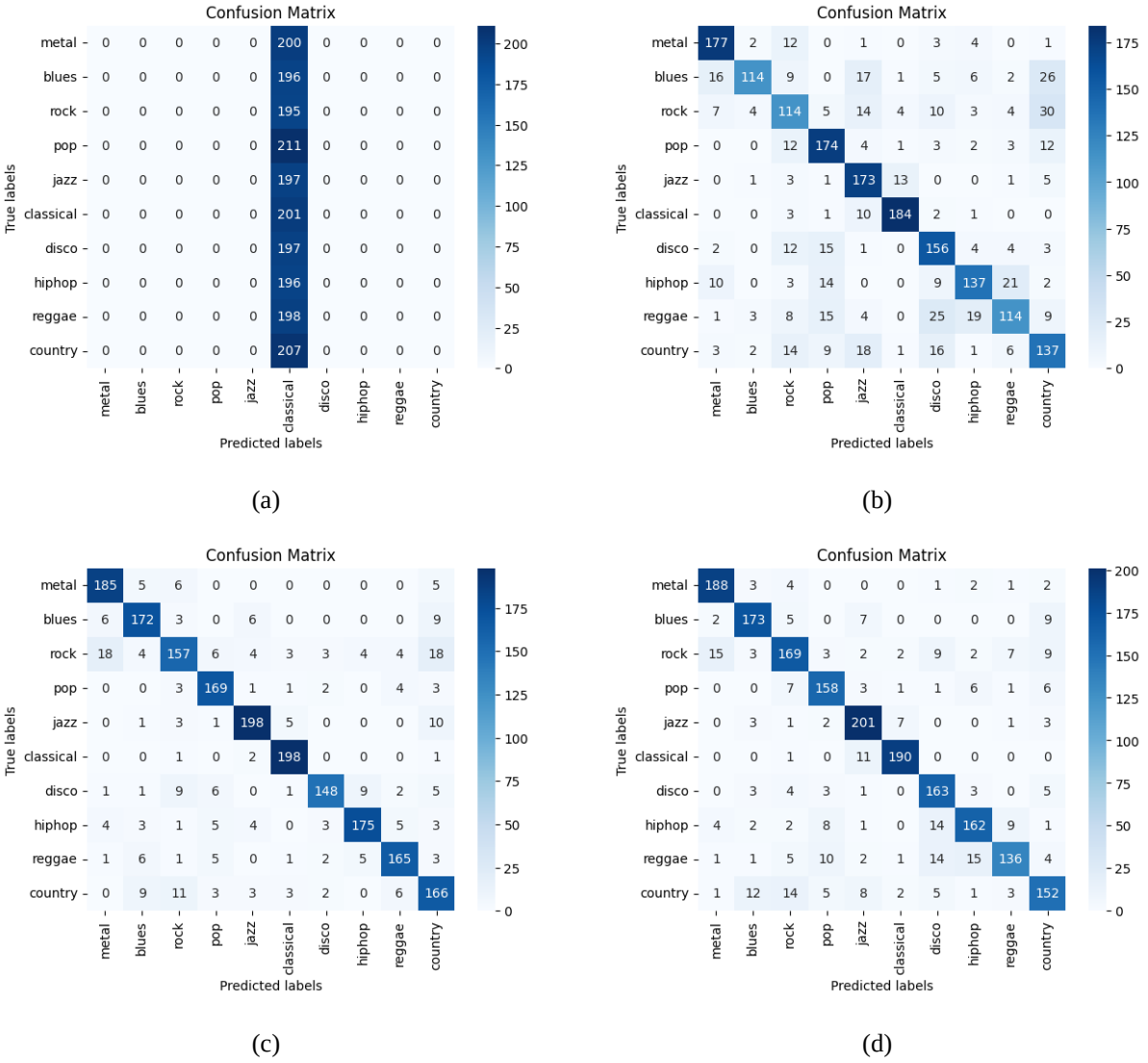

Figure 4: Confusion matrix of models without dropout with (a) Learning rate 0.1, (b) Learning rate 0.01, (c) Learning rate 0.001, and (d) Learning rate 0.0001

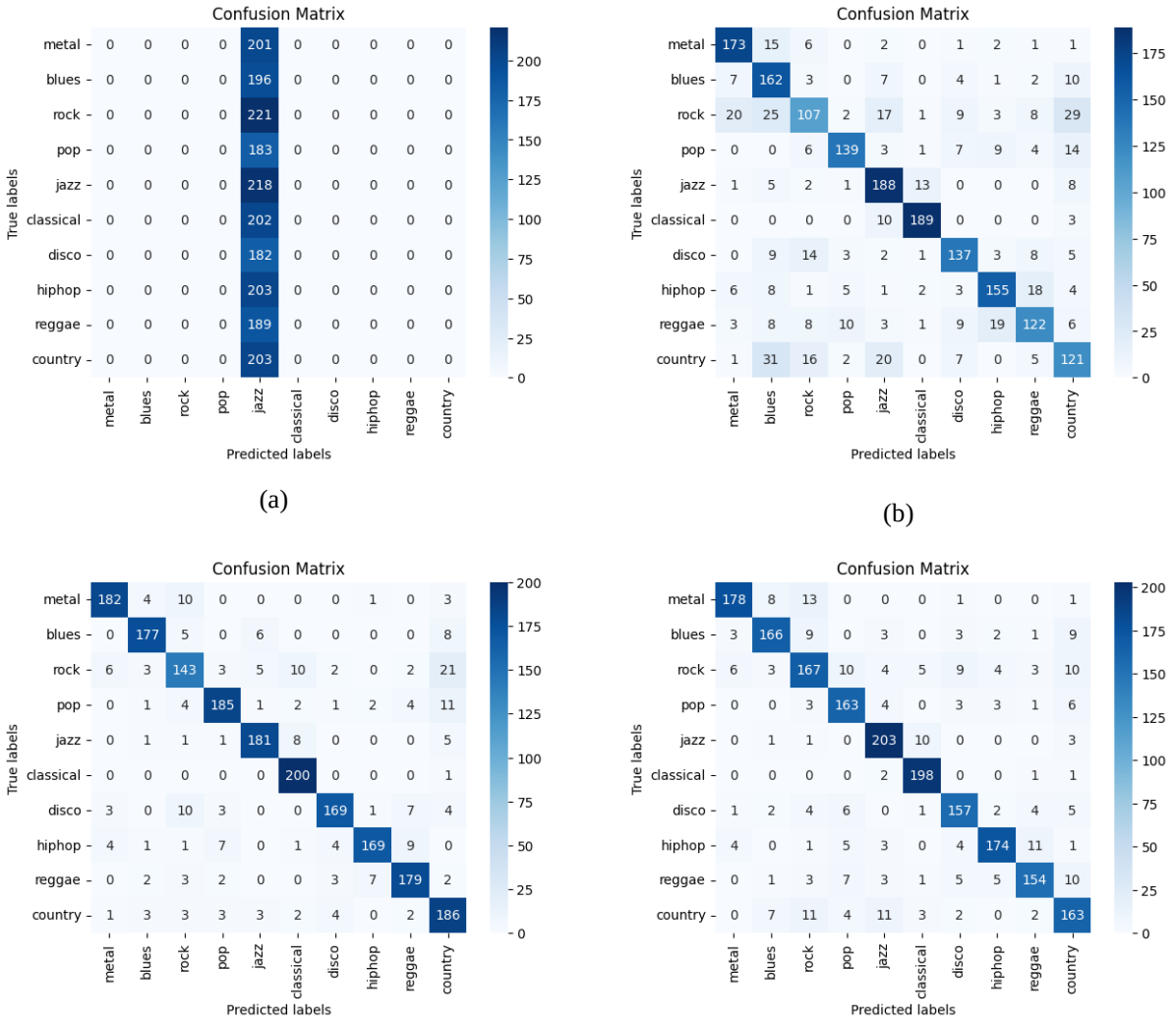

Figure 5: Confusion matrix of models with dropout with (a) Learning rate 0.1, (b) Learning rate 0.01, (c) Learning rate 0.001, and (d) Learning rate 0.0001

The ROC curves in Figures 6 and 7 provide detailed insights into the classification performance of the models under different configurations. Key metrics such as the true positive rate (TPR) and false positive rate (FPR) are visually represented, where a steeper curve rising toward the top-left corner indicates higher sensitivity (recall) and better classification of positive instances. Additionally, a lower FPR, reflected in curves closer to the y-axis, suggests improved discrimination between classes.

The area under the curve (AUC) serves as a summary metric, quantifying the model's overall performance. Higher AUC values, closer to 1.0, denote stronger classification capabilities. By comparing models with and without dropout across varying learning rates, it becomes evident that the inclusion of dropout generally enhances the stability and sharpness of the curves, indicating better generalization and resistance to overfitting. Notably, models with lower learning rates (e.g., 0.001 and 0.0001) demonstrate more consistent and pronounced ROC curves, suggesting that these configurations strike a balance between convergence and classification accuracy.

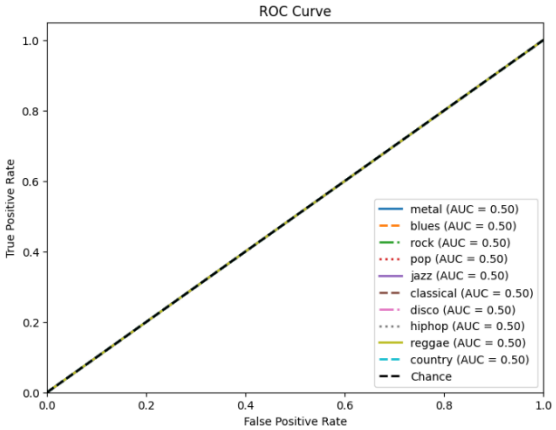

(a)

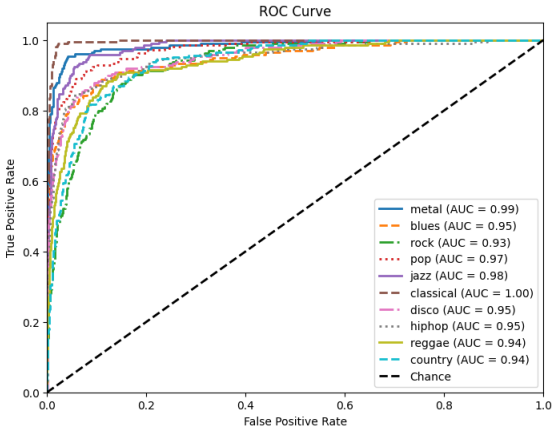

(b)

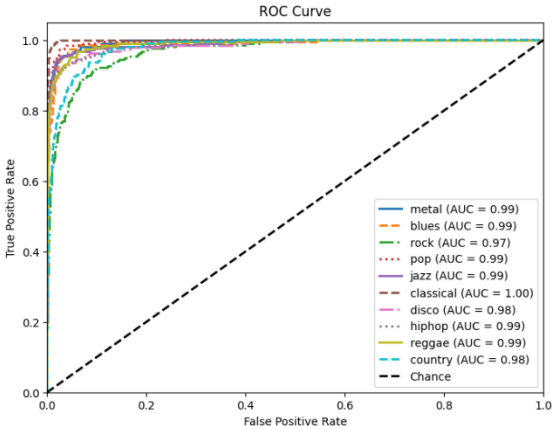

(c)

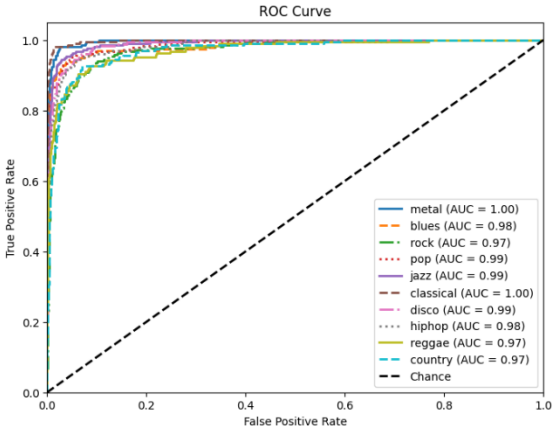

(d)

Figure 6: ROC curves of models without dropout with (a) Learning rate 0.1, (b) Learning rate 0.01, (c) Learning rate 0.001, and (d) Learning rate 0.0001

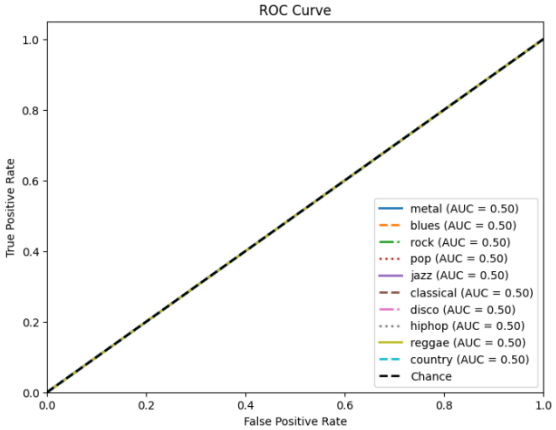

(a)

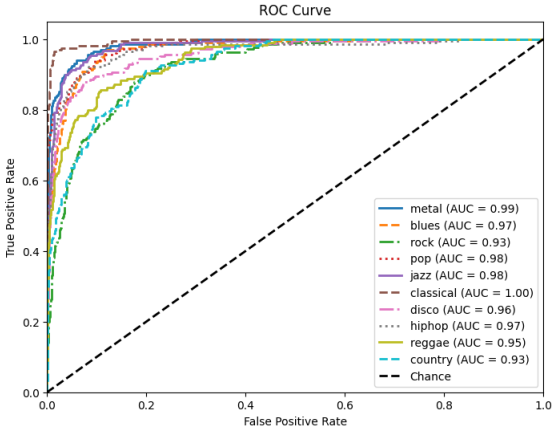

(b)

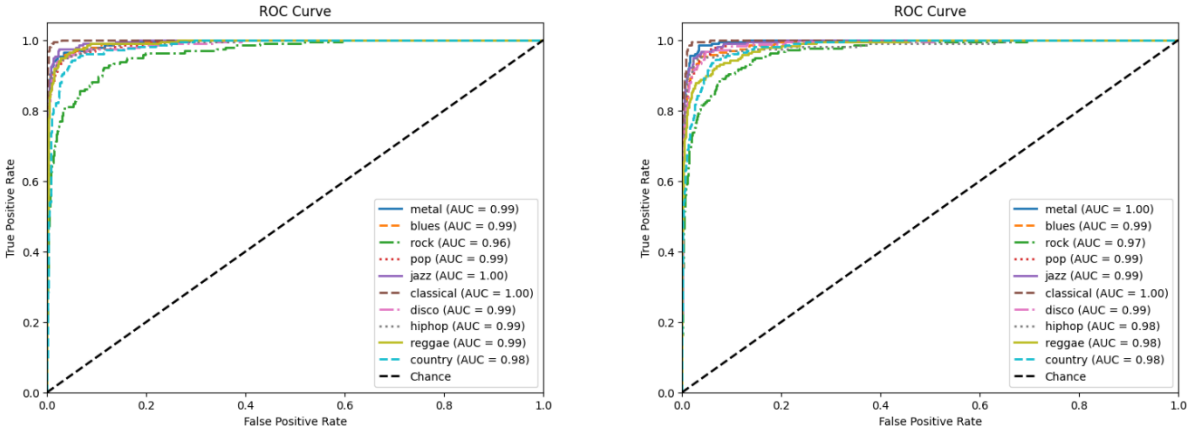

(c) (d)

Figure 7: ROC curves of models with dropout with (a) Learning rate 0.1, (b) Learning rate 0.01, (c) Learning rate 0.001, and (d) Learning rate 0.0001

A confusion matrix of a test set with 1,998 data points shows that the model with dropout and learning rates 0.01, 0.001, and 0.0001 can classify 1,493, 1,771, and 1,723 data, respectively. In contrast, the model without dropout can classify 1,480, 1,733, and 1,692 data out of 1,998. The model with a learning rate of 0.1 will not be discussed further because the model cannot classify the data. The model using dropout and learning rate 0.001 has the highest number of correct classification results compared to the other models, indicating that it is the best model.

Further analysis of the results indicates that the classical genre is the most accurately classified genre. The rock genre is the most misclassified due to the proximity between rock, country, and disco. The dataset also poses discrepancies with other references regarding the genre of certain audio files. In addition, the lack of artist variation in the dataset also affects the model classification ability due to the lack of variation of music genres, as an artist tends to produce music within one music genre.

Audio from the rock genre was frequently misclassified as country, disco, or blues. Additionally, the model often misclassified non-rock audio as rock. Upon closer examination of the dataset, this issue appears to stem from the presence of numerous repetitive patterns and mislabeled samples under the rock category.

The findings of this study have significant implications for the field of music information retrieval (MIR), particularly in advancing genre classification systems. The results demonstrate that a simpler CRNN architecture, when paired with effective regularization techniques like dropout and optimized learning rates, can achieve competitive accuracy, outperforming more complex models while maintaining computational efficiency. The highest classification accuracy of 88.64% highlights the potential of lightweight models in resource-constrained environments.

Moreover, the analysis underscores critical challenges in MIR, such as dataset quality and diversity. Issues like mislabeled samples, genre overlaps, and limited artist variation directly impact classification performance, as evidenced by the frequent misclassification of rock as similar genres like country, disco, and blues. These challenges emphasize the importance of curated datasets and robust preprocessing techniques in developing reliable MIR systems. Addressing these limitations, along with strategies like artist-level cross-validation and stratified sampling, could not only enhance genre classification accuracy but also extend the applicability of MIR systems to more nuanced tasks, such as personalized music recommendations and musicological analysis.

5 Conclusion

This work proposes a simpler architecture of a CRNN algorithm to classify music. The aim is to see whether a greater accuracy is achieved compared to more complex models. The proposed model comprises three CNN layers and two RNN (specifically BiLSTM) layers. The feature extraction used in this model is MFCC, which splits the dataset into ten segments to increase the total data. A dropout level of 0.001 learning rate achieved the highest accuracy of 88.64%. The accuracy is higher than the previous work accuracy of 73.69% using the same CRNN model with more CNN and RNN layers.

The primary limitation of this work is that the model tends to overfit, necessitating further efforts to mitigate this issue. Future work could focus on cleansing the dataset by removing redundant and incorrectly labeled songs, which may enable the model to learn more effectively from the data. Additionally, incorporating early stopping techniques could help prevent overfitting. Other potential strategies include applying weight regularization, implementing artist-level cross-validation, and utilizing stratified sampling to improve the model's robustness.

Acknowledgements

The authors express gratitude to Universitas Multimedia Nusantara for the support and acknowledge the valuable input of the reviewers and associate editor.

References

[1] D. Stefani and L. Turchet, “On the Challenges of Embedded Real-time Music Information Retrieval,” in *Proceedings of the International Conference on Digital Audio Effects, DAFx*, 2022, pp. 177–184.

[2] P. Ghosh, S. Mahapatra, S. Jana, and R. Kr. Jha, “A Study on Music Genre Classification using Machine Learning,” *Int. J. Eng. Bus. Soc. Sci.*, vol. 1, no. 04, pp. 308–320, 2023, doi: 10.58451/ijebss.v1i04.55.

[3] J. Sang, S. Park, and J. Lee, “Convolutional recurrent neural networks for urban sound classification using raw waveforms,” *Eur. Signal Process. Conf.*, vol. 2018-Septe, pp. 2444–2448, 2018, doi: 10.23919/EUSIPCO.2018.8553247.

[4] V. Bella and S. A. Sanjaya, “Refining Baby Cry Classification using Data Augmentation (Time-Stretching and Pitch-Shifting), MFCC Feature Extraction, and LSTM Modeling,” in *2023 7th International Conference on New Media Studies (CONMEDIA)*, IEEE, 2023. doi: https://doi.org/10.1109/CONMEDIA60526.2023.10428158.

[5] M. Ashraf *et al.*, “A Hybrid CNN and RNN Variant Model for Music Classification,” *Appl. Sci.*, vol. 13, no. 3, 2023, doi: 10.3390/app13031476.

[6] J. Mendes, “Deep Learning Techniques for Music Genre Classification and Building a Music Recommendation System,” National College of Ireland, 2020.

[7] X. Luo, “Automatic Music Genre Classification based on CNN and LSTM,” *Highlights Sci. Eng. Technol.*, vol. 39, pp. 61–66, 2023, doi: 10.54097/hset.v39i.6494.

[8] M. K. Kumar, K. Sujanasri, B. Neha, G. Akshara, P. Chugh, and P. Haindavi, “Automated Music Genre Classification through Deep Learning Techniques,” *E3S Web Conf.*, vol. 430, 2023, doi: 10.1051/e3sconf/202343001033.

[9] G. Tzanetakis and P. Cook, “Musical genre classification of audio signals,” *IEEE Trans. Speech Audio Process.*, vol. 10, no. 5, pp. 293–302, 2002, doi: 10.1109/TSA.2002.800560.

[10] G. Tzanetakis and P. Cook, “MARSYAS: A framework for audio analysis”.

[11] S. Y. Yehezkiel and Y. Suyanto, “Music Genre Identification Using SVM and MFCC Feature Extraction,” *IJEIS (Indonesian J. Electron. Instrum. Syst.*, vol. 12, no. 2, p. 115, 2022, doi: 10.22146/ijeis.70898.

[12] I. D. G. Y. A. Wibawa and I. D. M. B. A. Darmawan, “Implementation of audio recognition using mel frequency cepstrum coefficient and dynamic time warping in wirama praharsini,” *J. Phys. Conf. Ser.*, vol. 1722, no. 1, 2021, doi: 10.1088/1742-6596/1722/1/012014.

[13] H. Heriyanto, T. Wahyuningrum, and G. F. Fitriana, “Classification of Javanese Script Hanacara Voice Using Mel Frequency Cepstral Coefficient MFCC and Selection of Dominant Weight Features,” *J. Infotel*, vol. 13, no. 2, pp. 84–93, 2021, doi: 10.20895/infotel.v13i2.657.

[14] B. McFee *et al.*, “librosa: Audio and Music Signal Analysis in Python,” *Proc. 14th Python Sci. Conf.*, no. August 2020, pp. 18–24, 2015, doi: 10.25080/majora-7b98e3ed-003.

[15] P. A. Aritonang, M. E. Johan, and I. Prasetiawan, “Aspect-Based Sentiment Analysis on Application Review using CNN (Case Study : Peduli Lindungi Application),” *Ultim. Infosys J. Ilmu Sist. Inf.*, vol. 13, no. 1, pp. 54–61, 2022.

[16] R. Yamashita, M. Nishio, R. Kinh, G. Do, and K. Togashi, “Convolutional neural networks : an overview and application in radiology,” pp. 611–629, 2018.

[17] N. Srivastava, G. Hinton, A. Krizhevsky, I. Sutskever, and R. Salakhutdinov, “Dropout: A simple way to prevent neural networks from overfitting,” *J. Mach. Learn. Res.*, vol. 15, pp. 1929–1958, 2014.

[18] A. Katrompas and V. Metsis, “Enhancing LSTM Models with Self-attention and Stateful Training,” in *Lecture Notes in Networks and Systems*, 2022, pp. 217–235. doi: 10.1007/978-3-030-82193-7_14.

A Low-Cost Robotic Assembly Method for Large Planar Workpieces Using Laser Displacement Sensors and Monocular Vision

Xiaobing Cao[1*], Yicen Xu[2], Yonghong Yao[1], Sheng Chen[3]
[1]School of Control Technology, Wuxi Institute of Technology, Jiangsu Wuxi, 214121, China
[2]School of Intelligent Equipment and Automotive Engineering, Wuxi Institute of Commerce, Jiangsu Wuxi, 214153, China
[3]School of Communication and Electronic Engineering, East China Normal University, Shanghai, 200062, China
E-mail: xiaobingcao91@gmail.com
[*]Corresponding author

Keywords: side window glass, laser displacement sensor, monocular vision, robotic assembly, pose correction

Received: November 20, 2024

To address the challenges associated with large planar workpieces, such as the side window glass of a train, this paper proposes a practical, intelligent robotic assembly method that utilizes laser displacement sensors (LDSs) and monocular vision. The laser point cloud data is fitted to the equation of the plane of the side window optimally, allowing for the calculation of its plane coefficients and unit normal vector (UNV) using the Lagrange multiplier method. The robot's end flange is adjusted to ensure the camera imaging plane is along with the window plane at a specified distance. Monocular vision is employed to capture the pose features of the upper right corner of the window, facilitating a compensation method for precise assembly. The experimental results show that the robot achieved a positioning accuracy of less than 0.5mm and an orientation accuracy within 1 degree, confirming the effectiveness of the proposed method. In the experiment, the maximum displacement deviation in the X direction is about ± 0.4mm, the maximum offset in the Y and Z directions is about ± 0.3mm, the maximum rotation deviation in the X axis is about 0.6 °, and the minimum rotation deviation in the Y axis is about 0.8 °. All deviations meet the requirements of ± 1 ° attitude correction and ± 0.5mm displacement accuracy, and have good reliability. This method solves the practical problem of assembling large planar workpieces with integrated LDS and monocular vision. This technology involves using laser point cloud data to fit the precise plane equation of the window, determining alignment parameters through Lagrange multiplier method, and adjusting the posture of the end flange of the robot. Monocular vision further assists in extracting positional features, achieving precise real-time posture correction and alignment. This system proposes an effective and low-cost automation that reduces manual intervention and alleviates typical problems of remote processing of large workpieces.

Povzetek: Predstavljen je nizkocenovni robotski način sestavljanja velikih ravnih delov, ki združuje laserske merilnike premika in monokularni vid za natančno prilagajanje položaja in orientacije.

1 Introduction

Automatic assembly technology is extensively utilized in the automotive, marine, aerospace, and other manufacturing sectors to reduce labor costs and enhance production efficiency. The profound integration of machine vision technology with assembly technology represents a significant trend and a critical characteristic of the current evolution in assembly technology. Numerous advancements have been achieved in both theoretical research and practical applications [1], [2], [3]. With the rapid development of global manufacturing and continuous technological progress, automatic assembly technology has become an important means to improve production efficiency and reduce labor costs. In manufacturing industries such as automobiles, ships, and aerospace, automatic assembly technology not only improves product quality and consistency but also significantly enhances the competitiveness of enterprises. Especially in the train manufacturing industry, with the popularization of high-speed trains and urban rail transit, higher requirements have been put forward for the assembly accuracy and efficiency of train components. As an important component of the train, the assembly quality of the side window glass directly affects the safety and comfort of the train. Therefore, researching an efficient and accurate method for assembling train side window glass is of great significance.

Laser displacement sensors, as a high-precision and non-contact measurement tool, have also been widely used in the manufacturing industry. By emitting a laser beam and receiving reflected light, laser displacement sensors can achieve accurate measurements of the surface displacement of objects. During the assembly process of train side window glass, laser displacement sensors can monitor the gap between the glass and the window frame in real-time, ensuring the tightness and stability of the assembly. In addition, laser displacement sensors have the advantages of wide measurement range, high measurement accuracy, and fast response speed, which

can meet various measurement needs during the assembly process of train side window glass.

Combining machine vision technology with laser displacement sensors can achieve comprehensive monitoring and control of the assembly process of train side window glass. By using machine vision technology to obtain image information of glass and window frames, and using image processing algorithms to process and analyze the images, the position, shape, size, and other information of the glass and window frames can be obtained. At the same time, real-time displacement data during the assembly process can be obtained by measuring the gap between the glass and the window frame through a laser displacement sensor. Combining these two technologies can achieve precise control over the assembly process of train side window glass, improving the accuracy and efficiency of assembly. Since the side window glass is a large flat workpiece, its assembly process faces many challenges, such as high positioning accuracy requirements and difficulty in ensuring surface flatness. To address these challenges, this article will focus on the deep integration of machine vision technology and assembly technology, particularly the combination of laser displacement sensors (LDS) and monocular vision. LDS, as a high-precision, non-contact measuring tool, can obtain real-time three-dimensional coordinate information on the workpiece surface. During the assembly process of train side window glass, LDS can accurately measure the displacement changes on the glass surface, providing reliable data support for subsequent assembly work. Meanwhile, monocular vision, as an economical and efficient image processing technique, can capture the pose features of the upper right corner of the window, providing necessary compensation information for precise assembly. Although machine vision technology has been widely applied in the field of assembly, there are still many urgent problems to be solved for the assembly of large flat workpieces such as train side window glass. For example, how to effectively integrate data from LDS and monocular vision to achieve high-precision assembly positioning and how to adjust the robot's motion trajectory based on measurement data to ensure the stability and accuracy of the assembly process. Therefore, this article aims to propose a practical intelligent robot assembly method through in-depth research on the combination of LDS and monocular vision to solve the challenges in the assembly process of train side window glass.

1.1 Literature review

A precision assembly system for tiny components was created by Ma et al. [4] using a force sensor, three cameras, and an industrial robot. They proposed a pose alignment strategy based on binocular coordination and employed the differential principle to compensate for actuator position offsets. Experimental results demonstrated a high level of pose assembly accuracy for the system. Using real-time visual servoing, Wen-Chung Chang [5] created an automated method for assembling the shell of smartphones. This system utilized binocular vision technology to ascertain the position and orientation of the workpiece from a distance, subsequently applying monocular visual servoing control to complete the assembly task at close range autonomously. Experimental results indicated that the system provided high efficiency, flexibility, and reliability. However, this assembly approach necessitated that the entire assembly space remains fully visible, making it suitable for small workpieces but challenging to implement for larger workpieces with long-distance and expansive requirements. Su et al. [6] proposed a method for designing orientation strategies for locating irregular parts based on constraints formed by fixtures. Therefore, only through the squeezing action of robots can irregular parts such as motors be accurately located. Then, we developed a bolt hole insertion strategy using force constraints formed by the environment, which requires less robot action to insert the bolt, thereby achieving efficient and accurate bolt hole insertion. In contrast, Jinzhou et al. [7] developed a monocular vision-based alignment technology for an industrial robot. It estimates the target pose of the workpiece with the Perspective-N-Point (PNP) method by leveraging some feature points on a dedicated calibration board. Following that, it repeatedly modifies the end effector's position until the workpiece and robot's alignment axis are precisely aligned. However, this method requires setting a special calibration board on the target workpiece, which to some extent constrains its generality. Wang et al. [8] presented a holistic robotic assembly system including two vision sensors and three one-dimensional laser sensors. They have presented a method that includes multiple sensors to achieve precise step-by-step alignment and positioning. Experimental findings showed that this approach offered high accuracy and efficiency but, on the other hand, is associated with the assembly scheme having high costs and involving a complex algorithm. Hu et al. [9] studied side window glass designs using the Large Eddy Simulation (LES) model, computational fluid dynamics (CFD) simulation, and acoustic finite element analyses to investigate its impact on in-vehicle noise. They found that polyvinyl butyral (PVB) laminated glass effectively reduces noise transmission caused by low-frequency turbulence, with the inner and outer thicknesses varying in their effects across different frequency bands; however, low frequencies were found to be the most influential. Furthermore, material properties and geometric design are critical factors in noise control. Zhang et al. [10] have studied the application of an external circular array of LDSs which detect membrane penetration to enhance the precision of the volume change as well as pore pressure in triaxial gravelly sandy soils. The results indicated that unit membrane compliance increases linearly with effective confining pressure on a semi-logarithmic scale. Additionally, it was demonstrated that increased gravel content leads to greater membrane penetration; however, this effect diminishes at higher relative densities. It was also observed that broadly graded soils exhibit higher membrane penetration. The errors associated with

membrane thickness increased as the diameter-to-thickness ratio decreased, highlighting the importance of sensors in detecting subtle variations to provide consistent measurements. Shao et al. [11] proposed a monocular vision-based system for vibration displacement measurement in civil structures to solve several of the major problems associated with multiple cameras used in structural health monitoring (SHM) systems. Deep neural networks have been utilized to enable substantial reduction of costs and ease in estimating depth information from images captured by a single camera. Laboratory tests verified the accuracy of the system output that provided three-dimensional displacement measurements and demonstrated the potential of the system for practical applications in SHM. Chen et al. [12] developed an algorithm for applying monocular vision to quantify construction and demolition waste from individually taken images. The results of the research were promising: in this system, highly accurate identification was realized for truckloads of materials like rock, gravel, and wood. Accompanied by a comparative error of 0.065 for truck bucket measurements and 0.169 in approximating material volume, the algorithm analyzes an image in only 3.3 seconds, which enables fast and non-intrusive assessments. The methods were adopted for over 2,900 truckloads in a facility in Hong Kong to estimate that the daily intake of construction and demolition waste (CDW) was at 800.0 m^3, along with identifying rejected loads containing non-inert materials. Thus, this algorithm will be able to work effectively on different industrial challenges in the quantification of waste. Sun et al. [13] present a monocular vision-based approach for measuring 3D movement regarding enabling single-camera SHM applications. This high-level method captures data from 3D displacement with high accuracy by merging deep learning techniques through pose estimation from the Dense Pose Object Detector. It doesn't require multi-view systems or sophisticated targets, so it would be quite in line with urban surveillance cameras. The experimental validation showed that it is effective for detecting 3D displacement and principal frequencies. It has also been proven to be workable regarding the applicability of the method as a reachable SHM tool. Sleaman et al. [14] developed an algorithm that allowed a mobile robot to move around in an unfamiliar environment, leveraging the power of only monocular vision and low-cost cameras for depth perception. This system combined convolutional neural network (CNN) layers with decision-making processes that modulate real-valued, kinematic movement control without any preprocessing or pre-mapping. It was capable of training on a set of diverse data and achieved an accuracy indoor setting of up to 77%. This model proved effective enough to facilitate efficient navigation of the robot compared to more expensive sensor systems. Sun et al. [15] proposed an algorithm that developed a monocular vision-based method, which allowed a mobile robot to navigate an unknown environment autonomously by low-cost depth camera data. They have introduced the integration of CNN layers with decision-making processes to guide robot movement without any pre-mapping. The system has been trained on various datasets and showed an accuracy of 77% during indoor tests to prove that the technique can be as effective in allowing efficient navigation by the robot as compared to more expensive sensor systems. Gao et al. [16] proposed an algorithm, Perspective 3-Point Rammer Pose Estimation (P3P-RPE), derived from monocular vision for real-time ramming settlement monitoring in dynamic compaction construction. This approach overcomes the substantial limitations that can compromise efficiency and safety in the construction process through manual monitoring. The use of the P3P-RPE algorithm will allow for simultaneous construction and monitoring of processes without disrupting the ongoing operations. Lou et al. [17] proposed a SLAM solution using monocular vision, integrated with LiDAR, which could afford better placement of unmanned vehicles. They integrated semantic images with LiDAR point clouds to give dense depth mapping and improved positioning accuracy with in-depth embedded ORB（Oriented FAST and Rotated BRIEF）features. When their proposed approach was tested on CityScapes and KITTI datasets, it could reduce the positioning error by 87% compared with other approaches in the SLAM category. Results showed the huge impact monocular vision could have when applied to applications involving autonomous vehicles. A self-calibration method based on monocular vision was introduced by Li et al. [18] for the accurate assessment of 3D displacement in structures. In this regard, the approach is based on a personalized marker to accurately recognize images for the automatic estimation of the object's 3D position and orientation with the purpose of solving problems arising in calibration for long-term monitoring. Monte Carlo simulations and experiments were carried out for verification, obtaining that the system achieved an accuracy of about 0.049 mm. It follows that 3D displacement measurements may be efficiently carried out in fully automated ways for applications like structural tests. Ahn et al. [19] propose a robotic assembly that fuses both force and visual information over large position and orientation errors. This is realized through the use of dual neural networks that process both force and image inputs, optimized through deep reinforcement learning, thus giving adaptive assembly capabilities to a variety of shapes. By this approach, an assembly can be effectively realized despite the initial misalignment. The experimental validation is performed for peg-in-hole tasks and provides a general approach to a wide range of robotic assembly applications. A robotic assembly system for precision drilling and fastening in aircraft assembly has been proposed by Mei et al. [20]. Optimum hand-eye configuration and on-machine calibration are considered to minimize positioning errors in the system. The maximum error of 0.08 mm was obtained, hence meeting the strict accuracy criteria required in aircraft assembly. Zhang et al. [21] presented the residual reinforcement learning approach for robotic autonomous assembly, in which policy visualization and force-based methods are

well integrated. The approach makes it possible to be adaptive in an unstructured environment without prior data. Efficiency is pointed out in multiple assembly tasks and configurations verified by simulations and real-world tests. Champatiray et al. [22] developed a methodology of robotic assembly planning that comprises the development of assembly interference matrices" and an axis-aligned bounding box" to assess any interference and determine the optimized assembly sequences of the assemblies. This will enhance feasibility and efficiency in industrial applications by taking into consideration geometry from the involved tools and parts, hence saving time and costs. Machine vision technology is a technique that uses computer vision and image processing algorithms to simulate human visual functions. In the experiment of X-ray free electron laser, machine vision technology can monitor the stability of sample transportation by real-time acquisition and processing of images of liquid jet samples [23]. The collected images need to undergo a series of image processing algorithms, including image filtering, edge detection, feature extraction, etc. These algorithms can help us identify key information such as the shape, velocity, and position of liquid jet samples. By further analyzing the processed images, we can calculate the stability indicators of the liquid jet sample, such as fluctuations in jet velocity and deviations in jet direction. These indicators can be fed back to the control system in real time to adjust and optimize the parameters of sample delivery promptly [24].

Based on the automatic assembly task for the side window glass of a subway train, this study investigates the low-cost spatial assembly problem of large planar workpieces. A monocular vision-guided assembly method is proposed, assisted by a LDS. An experiment uses a specific case to provide a reference for designing automatic assembly schemes for similar workpieces.

1.2 Research gaps and novelties

Table 1: Method comparison table

Method	Accuracy	Complexity	Cost	Limitations
Multi camera setup	Medium to high	high	high	Requires complex calibration and synchronization, and is sensitive to lighting conditions
Specialized sensors	high	Medium to high	high	High cost and may not be suitable in certain environments (such as outdoor or complex industrial environments)
Manual monitoring	Low to moderate	low	low	Dependent on the operator's experience and skills, not suitable for high-precision or long-distance work
Visual based method (sensorless)	Low to moderate	secondary	Low to moderate	Highly affected by lighting, shadows, and occlusion, with limited accuracy
Hybrid method (multi-sensor fusion)	high	high	high	Although accuracy has been improved, system complexity and cost remain high
The proposed method (LDS+monocular vision)	high	secondary	Low to moderate	Relying on the fusion quality of LDS and visual data, but reducing system complexity and cost

The main innovation of this study lies in proposing a hybrid approach that combines LDS and monocular vision for robust real-time pose correction and component alignment. Compared with multi-sensor systems, this method reduces system complexity and cost through integration. Specifically, this study utilized point cloud data generated by LDS to determine alignment parameters by fitting the side window plane equation, thereby improving assembly accuracy. Meanwhile, utilizing monocular vision effectively extracts the pose features of the upper right corner of the window, providing necessary compensation information for precise assembly. This method not only solves the research purpose

The requirement for precise positioning and orientation with displacement tolerance of less than 0.5mm and directional tolerance of less than 1 degree also fills a key gap in providing practical and low-cost solutions for the assembly of large planar components.

The objective of this study is to validate the effectiveness and feasibility of the proposed hybrid method in practical industrial environments. Specifically, this study aims to demonstrate the following points:

The proposed hybrid method can reduce system complexity and cost while maintaining high accuracy.

Compared with existing multi-sensor systems, this method has higher efficiency and lower cost.

This method has broad application prospects and can be extended to similar tasks in various industries.

1.3 Paper organization

The work is categorized in the manner that: Section 2 offers and discusses the constitution and calibration of the empirical system to assemble subway train side window glass. Section 3 provides a detailed description of the visual alignment method for the LDS. Section 4 develops an optical positional measuring technique. The analysis of defects encountered during assembly and the experimental validation of the proposed assembly methodology for subway train side window glass are outlined in Section 5. Ultimately, Section 6 concludes the investigation.

2 Composition and calibration of experimental system for side window glass assembly of train

The automated assembling of glass for windows in trains requires an accurately defined experimental setup. This section details the basic elements that form the experimental setup, their functions, and the necessary calibration processes toward achieving maximum accuracy in assembling processes. The system includes an industrial robot with six axes, an industrial camera, an LDS (Laser distance sensor), and an aligning fixture that allows accurate placement and alignment.

2.1 Composition of experimental system and definition of coordinate system

The experimental system for the train-side window glass assembly described in this paper comprises a mounting bracket, a six-axis industrial robot, an industrial camera, an LDS, and a fixture, as illustrated in Fig. 1. This experiment uses a high-precision laser displacement sensor with a measurement accuracy of micrometers and a measurement range of meters. LDS calculates the distance between an object and a sensor by emitting a laser beam and receiving the reflected light signal. In this study, LDS was used to accurately measure the displacement changes on the surface of the train side window glass, providing key data for subsequent assembly work. The fixture is firmly connected to the tail flange of the robot, with its plane parallel to the flange plane.

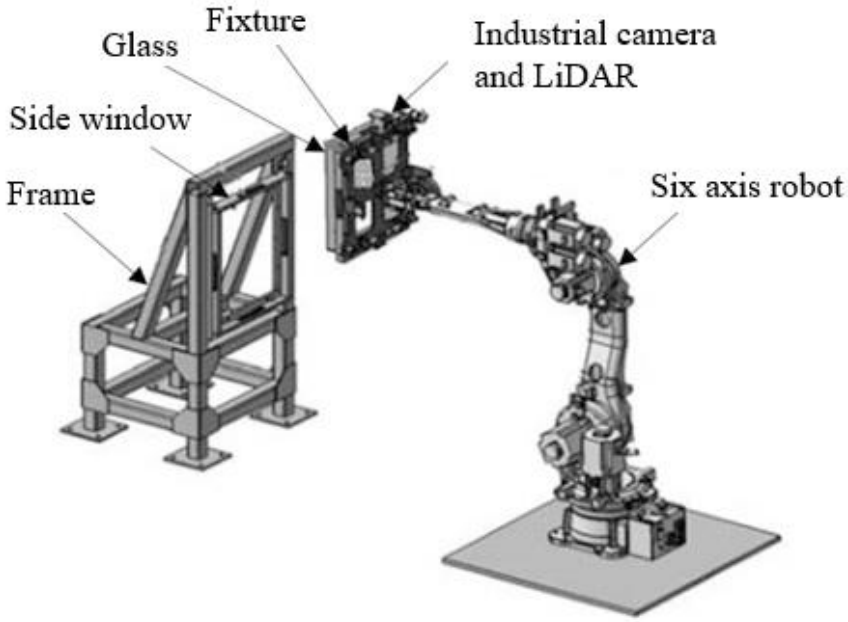

Figure 1: Schematic diagram of automatic assembly system for side window glass of train.

Installation bracket: This bracket is the cornerstone of the experimental system, used to simulate the structure of train carriages and ensure accurate assembly testing of glass in real environments.

Six axis industrial robot: As the core power source of the system, the six-axis industrial robot is responsible for grasping, moving, and positioning glass. Its flexible six axis design enables the robot to execute complex motion trajectories in three-dimensional space, thereby achieving precise assembly operations.

Industrial camera: Industrial cameras are installed at the edge of fixtures to capture image information of glass and side window positions. Through image processing algorithms, edge features of glass and side windows can be extracted, and their relative positions and orientations can be calculated.

Laser Ranging Sensor (LDS): LDS is also installed at the edge of the fixture to measure the precise distance between the glass and the side window. The high precision and stability of laser ranging enable the system to maintain a high degree of accuracy during assembly.

Fixture: The fixture is firmly connected to the tail flange of the robot, with its plane parallel to the flange plane. The design of the fixture takes into account the size and shape of the glass to ensure that it can be stably grasped and positioned. The establishment of the flange coordinate system (CS) takes place at the center point of the flange end plane, the same as the location of the X_H O_H Y_H plane. In this case, X_H and Y_H are the flange coordinate system principal axes, while O_H refers to the origin. Coordination by this system is necessary to facilitate accuracy in robot assembly processes. These same coordinates are specifically referred to in Equation (X) when calculating transformations, while being indicated by Figure (Y) so as to give an idea of their location in three-space.

The base coordinate system (CS) of the robot is defined as $O_B X_B Y_B Z_B$, and that of the workpiece as $O_T X_T Y_T Z_T$. Besides them, other CSs are defined for the end flange, camera, and image pixels, as $O_H X_H Y_H Z_H O_C X_C Y_C Z_C$, and ouv, respectively. The origin and axis directions of the base CS of the robot should be determined in settings specified by the factory. The operator defines a CS for the workpiece at a position close to where the work will be done. During an assembly operation, this becomes a dynamic reference frame that replaces the base frame. The source of the flange CS is positioned at the core of the end plane of the flange, coincident with the $X_H O_H Y_H$ plane. In this system, the Z-axis points outward and is vertical to the plane of the flange. In the picture pixel CS, the u-axis points horizontally to the right, the v-axis points vertically downward, and the origin of the coordinates is situated in the upper-left corner. The axes X_C and Y_C are parallel to the u- and v-axes of the image, respectively; the Z_C-axis points out of the imaging plane.

2.2 System calibration

First, the system must be calibrated to achieve its pose correction and positioning functions. The calibration process includes laser sensors, cameras, and hand-eye calibrations.

To calibrate the position of the laser range finder, solve for the laser source coordinate matrix in the robot's end flange CS, r, and the unit direction vector matrix of the laser line, l. Planar constraints can be used to resolve it. It is then combined with the interval measured by the Laser Sensor and the positioning of the robot's end to determine the coordinates of the laser point in the workpiece CS [25], [26].

In experimental systems, calibration is a key step in ensuring the precise operation of laser sensors, cameras, and hand eye systems. The calibration process includes laser sensor calibration, camera calibration, and hand eye calibration.

The calibration of laser sensors is mainly to ensure the accuracy of their measurements. The specific calibration steps include:

Installation and preheating: Install the laser sensor on the fixture and preheat it to ensure its stable operation.

Zero-point calibration: Place a reference surface at a known distance in front of the sensor, adjust the sensor to read zero, and complete the zero-point calibration.

Linearity calibration: Move points at different distances on the reference surface, record the sensor readings, compare them with the actual distance, and adjust the sensor parameters to ensure linearity.

A pinhole camera model can be used to represent how a camera captures images. Based on a calibration process, the internal camera parameters are derived, represented as a matrix A in terms of radial distortion parameters K_1, K_2, K_3, and tangential distortion parameters p_1 and p_2, along with the external parameters $[R\ t]$. Internal parameters describe the relation of pixel coordinates with image coordinates, while external parameters describe the relation of the camera's CS with the world's CS. Images of the checkerboard calibration board are taken by the camera at different angles so that both the world coordinates and the corresponding pixel coordinates of the checkerboard corners can be obtained. Calibration parameters are computed using the Zhang Zhengyou method [27].

Hand-eye calibration is performed to estimate the homogeneous transformation matrix between the camera's CS and the robot's end flange CS, denoted by ${}^{H}_{C}T$. Estimates of the parameters of such calibration are obtained with the TSAI method [28], which combines the extrinsic parameters attained from camera calibration with the corresponding pose parameters of the robot's end effector.

To calibrate the position of the laser rangefinder, we need to solve the laser source coordinate matrix r and the unit direction vector matrix l of the laser line in the end flange coordinate system (CS) of the robot. Select a

known plane as the reference plane, which intersects the laser line at a point. By moving the laser rangefinder to multiple known positions and recording the laser measurement values and robot posture at each position, a series of equations can be established to solve r and l. By combining the interval measured by the laser rangefinder with the positioning information of the robot end, the coordinates of the laser point in the workpiece coordinate system (CS) can be further determined. This usually involves converting laser measurement values into coordinates in the robot coordinate system and then converting them into the workpiece coordinate system.

3 Visual alignment on the basis of LDS

Accurately positioning the side window through visual alignment relies on a precise characteristic image of the side window. Therefore, the first step is to achieve vision alignment r, ensuring that the camera's imaging plane is along with the side window plane to prevent imaging distortion. In this study, a laser range finder is employed to project a laser point onto the side window plane, and the coordinate data of the laser point are utilized to fit the equation of the side window plane. The normal vector (NV) parameters are then obtained, allowing for the establishment of the camera coordinate system (CCS). The equation of the axis Z_C and the plane's NV of the side window determines the posture correction angle of the robot's end flange. The axis Z_C is aligned with the NV of the side window plane to achieve visual alignment. Additionally, the interval between the camera's imaging plane and the side window plane must be adjusted using an LDS to meet the preset value, ensuring consistency in the imaging scale. Conduct visual alignment tests under different environmental lighting and reflective surface conditions to verify the robustness and accuracy of the alignment algorithm. By enhancing the recognition and fitting of laser points, improving the alignment between the camera coordinate system and the side window plane, optimizing the use and adjustment of LDS, and enhancing the robustness testing and verification of visual alignment, the robustness of LDS based visual alignment can be significantly improved under environmental lighting or reflective surface changes.

3.1 Unit normal vector of the side window plane

A laser range finder is used to project multiple laser points onto a side window plane r, and the laser line's unit direction vector coordinate matrix l. The coordinate matrix of the i-th laser point in the workpiece CS can be listed as P_i. The expression is:

$$P_i = {}^{T}_{H}T \begin{pmatrix} r + d_i l \\ 1 \end{pmatrix} \tag{1}$$

Where ${}^{T}_{H}T$ is the transformation matrix of the robot end flange CS about the workpiece CS, which is determined from data transformation of the teaching pendant, and d_i is the distance value measured by a laser sensor.

Due to various errors, the coordinates of the measured laser points cannot be strictly located in the same plane, so applying the coordinate data to fit the plane equation of the side window to minimize the distance between each laser point and the plane is essential. According to the theory of spatial analytic geometry, the ideal equation of the side window plane in the workpiece CS is:

$$Ax + By + Cz - D = 0 \tag{2}$$

In this relation, A, B, and C are components of the UNV of the side window plane in the workpiece CS, and D is the interval between the origin of the workpiece CS and the side window plane. Let the overall amount of laser points be n; the components of the i-th laser point in the workpiece CS are x_i, y_i, z_i, at a interval from the side window plane $|Ax_i + By_i + Cz_i - D|$. The problem is then reduced to finding the coefficients of the plane equation such that:

$$\begin{cases} min(f) = min \sum_{i=1}^{n} (Ax_i + By_i + Cz_i - D)^2 \\ A^2 + B^2 + C^2 - 1 = 0 \end{cases} \tag{3}$$

Coefficient A, B, C, D: These are known constants that appear in the formula as weights or offsets. Variable xi, yi, zi: These are variables that need to be optimized, and for each i (from 1 to n), there is a set of such variables. They represent a point in the problem space. The summation symbol $\sum$ represents the summation of all i values from 1 to n. That is to say, function f is the sum of all n terms. Each term in the square operation is squared. This is to make the function f non negative, and there will be a positive penalty for any deviation from the optimal solution. For the minimization problem described by Equation (3), the function is constructed according to the Lagrange multiplier method:

$$F = \sum_{i=1}^{n} (Ax_i + By_i + Cz_i - D)^2 + \lambda(A^2 + B^2 + C^2 - 1) \tag{4}$$

Assuming the objective function is f (x) and the constraint condition is g (x)=0 (where x can be a multidimensional vector). The basic idea of Lagrange multiplier method is to introduce a Lagrange multiplier λ and integrate the constraints into the objective function, thereby forming a new function - Lagrange function L (x, λ). The Lagrange multiplier method is usually very effective in dealing with optimization problems with simple constraints. However, as the constraints become more complex or the number increases, the computational complexity may significantly increase. In addition, if the objective function or constraint conditions are nonlinear, the solving process may involve complex numerical methods. For optimization problems with complex constraints or nonlinear objective functions, other optimization methods such as interior point method, penalty function method, or trust region method

can be considered. These methods may be more effective or easier to implement than the Lagrange multiplier method in certain situations. In applications such as attitude estimation, noise measurement is a common problem. In order to improve the efficiency and robustness of eigenvalue calculation, some numerical stability techniques can be used, such as regularization methods, singular value decomposition (SVD), etc. In addition, for large-scale datasets or high-dimensional problems, efficient numerical algorithms and parallel computing techniques can be considered to accelerate the computation process. For a minimal value, there are $\frac{\partial F}{\partial A} = \frac{\partial F}{\partial B} = \frac{\partial F}{\partial C} = \frac{\partial F}{\partial D} = 0$. After derivation and simplification, the following equations are achieved:

$$\begin{cases} \sum_{i=1}^{n} x_i(Ax_i + By_i + Cz_i - D) + \lambda A = 0 \\ \sum_{i=1}^{n} y_i(Ax_i + By_i + Cz_i - D) + \lambda B = 0 \\ \sum_{i=1}^{n} z_i(Ax_i + By_i + Cz_i - D) + \lambda C = 0 \\ D = \frac{1}{n}\sum_{i=1}^{n}(Ax_i + By_i + Cz_i) \end{cases} \tag{5}$$

$$\begin{bmatrix} \sum_{i=1}^{n} x_i\, v_{x_i} & \sum_{i=1}^{n} x_i\, v_{y_i} & \sum_{i=1}^{n} x_i\, v_{z_i} \\ \sum_{i=1}^{n} y_i\, v_{x_i} & \sum_{i=1}^{n} y_i\, v_{y_i} & \sum_{i=1}^{n} y_i\, v_{z_i} \\ \sum_{i=1}^{n} z_i\, v_{x_i} & \sum_{i=1}^{n} z_i\, v_{y_i} & \sum_{i=1}^{n} z_i\, v_{z_i} \end{bmatrix} \begin{bmatrix} A \\ B \\ C \end{bmatrix} = (-\lambda) \begin{bmatrix} A \\ B \\ C \end{bmatrix} \tag{6}$$

$$\begin{cases} v_{x_i} = x_i - \overline{x}, \quad \overline{x} = \frac{1}{n}\sum_{i=1}^{n} x_i \\ v_{y_i} = y_i - \overline{y}, \quad \overline{y} = \frac{1}{n}\sum_{i=1}^{n} y_i \\ v_{z_i} = z_i - \overline{z}, \quad \overline{z} = \frac{1}{n}\sum_{i=1}^{n} z_i \end{cases} \tag{7}$$

$$\begin{cases} \sum_{i=1}^{n} \overline{x} v_{x_i} = \sum_{i=1}^{n} \overline{x} v_{y_i} = \sum_{i=1}^{n} \overline{x} v_{z_i} = 0 \\ \sum_{i=1}^{n} \overline{y} v_{x_i} = \sum_{i=1}^{n} \overline{y} v_{y_i} = \sum_{i=1}^{n} \overline{y} v_{z_i} = 0 \\ \sum_{i=1}^{n} \overline{z} v_{x_i} = \sum_{i=1}^{n} \overline{z} v_{y_i} = \sum_{i=1}^{n} \overline{z} v_{z_i} = 0 \end{cases} \tag{8}$$

$$\begin{cases} \sum_{i=1}^{n} (x_i - v_{x_i}) v_{x_i} = \sum_{i=1}^{n} (x_i - v_{x_i}) v_{y_i} = \sum_{i=1}^{n} (x_i - v_{x_i}) v_{z_i} = 0 \\ \sum_{i=1}^{n} (y_i - v_{y_i}) v_{x_i} = \sum_{i=1}^{n} (y_i - v_{y_i}) v_{y_i} = \sum_{i=1}^{n} (y_i - v_{y_i}) v_{z_i} = 0 \\ \sum_{i=1}^{n} (z_i - v_{z_i}) v_{x_i} = \sum_{i=1}^{n} (z_i - v_{z_i}) v_{y_i} = \sum_{i=1}^{n} (z_i - v_{z_i}) v_{z_i} = 0 \end{cases} \tag{9}$$

$$\begin{bmatrix} \sum_{i=1}^{n} v_{x_i}\, v_{x_i} & \sum_{i=1}^{n} v_{x_i}\, v_{y_i} & \sum_{i=1}^{n} v_{x_i}\, v_{z_i} \\ \sum_{i=1}^{n} v_{y_i}\, v_{x_i} & \sum_{i=1}^{n} v_{y_i}\, v_{y_i} & \sum_{i=1}^{n} v_{y_i}\, v_{z_i} \\ \sum_{i=1}^{n} v_{z_i}\, v_{x_i} & \sum_{i=1}^{n} v_{z_i}\, v_{y_i} & \sum_{i=1}^{n} v_{z_i}\, v_{z_i} \end{bmatrix} \begin{bmatrix} A \\ B \\ C \end{bmatrix} = \lambda' \begin{bmatrix} A \\ B \\ C \end{bmatrix} \tag{10}$$

The coefficient matrix on the left side of equation (10) is a third-order real symmetric matrix, which we represent as RC. The elements of this matrix are related to the variables in the equation, and some important properties, such as eigenvalues and eigenvectors, will play a crucial role in subsequent analysis. Specifically, we can consider λ, a, B, and C (where a, B, and C may represent elements of the eigenvector. However, their specific meanings need to be determined based on the context, as this was not explicitly stated in your original description) as elements related to the eigenvalues and eigenvectors of RC. To find the eigenvalues of R C, we set the characteristic polynomial to zero, i.e. $|\ \mathrm{R\,C} - \lambda'\ \mathrm{I}\ | = 0$ (Equation 11), where I is the identity matrix. In this way, we can find all the eigenvalues of R C by solving this equation Where $\lambda' = -\lambda$. It is clear that the coefficient matrix on the left side of Eq. (10) is a real symmetric matrix of order 3, while λ', A, B, and C can be regarded as the eigenvalues and eigenvector elements of the coefficient matrix. This coefficient matrix is denoted as R_c, and its eigenvalues can be obtained by Eq. (11) as follows:

$$|\boldsymbol{R}_c - \lambda' \boldsymbol{I}| = 0 \tag{11}$$

According to the eigenvalue method [29], when the eigenvalue is the smallest, the interval between each laser point and the plane is minimized, and the corresponding eigenvector is the UNV of the side window plane, thus obtaining the values of A, B and C. To satisfy the subsequent robot end flange posture adjustment requirements, the NV must point to the inside of the side window. Considering the bi-directionality of the plane NV, if the obtained NV points to the outside of the side window, its reverse vector is taken.

3.2 Pose correction of the robot end flange

To make the camera imaging plane parallel to the side window plane, the pose of the robot end flange needs to be adjusted. In this paper, the XYZ fixed angle method is used for rotating around the X, Y, and Z axes of the workpiece CS, with angles γ, β, and α, so that the CCS axis Z_C is in the same direction as the side window UNV obtained in Section 3.1. In certain fields or applications, specific rotation sequences may be widely adopted due to historical reasons or conventions. For example, in aerospace, the ZYX sequence (also known as yaw pitch roll) may be preferred as it corresponds to the natural motion of the aircraft. In other fields such as robotics or automation, XYZ order may be more common. For different rotation orders, even if the rotation angle is the same, the resulting rotation matrix will be different. This is because each rotation is relative to a different axis.

Some rotation sequences are more susceptible to the influence of universal joint locks, that is, when two rotation axes coincide, one dimension of rotational ability will be lost. This requires special attention when using Euler angles to represent rotation. In Eq. (12**),** ${}^{H}_{C}\boldsymbol{R}$ refers to the rotation transformation matrix, through which the camera coordinate system (C) gets transformed into the robot end flange coordinate system (H). The matrix depicts the directional correlation between the camera and robot end flange, thus providing the accurate alignment necessary for successful pose correction. Suppose that the rotation transformation matrix from the CCS to the robot end flange is as follows:

$$ {}^{H}_{C}\boldsymbol{R} = \begin{bmatrix} a_{11} & a_{12} & a_{13} \\ a_{21} & a_{22} & a_{23} \\ a_{31} & a_{32} & a_{33} \end{bmatrix} \tag{12}$$

Then, the Z_C component of the CCSs axis's unit direction vector in the flange CS is $[a_{13} \quad a_{23} \quad a_{33}]^T$. The rotation matrix is projected to the workpiece CS using the XYZ fixed angle method.

$$\begin{bmatrix} A \\ B \\ C \end{bmatrix} = \begin{bmatrix} c\,\alpha\, c\,\beta & c\,\alpha\, s\,\beta\, s\,\gamma - s\,\alpha\, c\,\gamma & c\,\alpha\, s\,\beta\, c\gamma + s\,\alpha\, s\gamma \\ s\,\alpha\, c\,\beta & s\,\alpha\, s\beta\, s\,\gamma + c\alpha\, c\,\gamma & s\alpha\, s\,\beta\, c\gamma - c\alpha s\gamma \\ -s\,\beta & c\,\beta\, s\gamma & c\,\beta\, c\,\gamma \end{bmatrix} \begin{bmatrix} a_{13} \\ a_{23} \\ a_{33} \end{bmatrix} \tag{13}$$

Where c stands for cos and s stands for sin. The angle data in the robot teach pendant at the time of projecting the last laser point used to fit the plane can be used as an initial value α_0, β_0, and γ_0. Using the LM method for iterative optimization, solve the nonlinear equation (13) and finally obtain α, β, and γ. Based on this, adjust the flange attitude. Construct a nonlinear equation based on the rotation angles (α, β, and γ) of the robot flange and the actual measured laser point data (or other relevant data). This equation may describe the difference between the projection of the laser point on the fitting plane and the expected position. Use LM method to iteratively solve nonlinear equations. In each iteration, a new angle value is calculated based on the current angle value to reduce errors in the equation. This process will continue until a certain stopping criterion is met (such as an error less than a certain threshold or reaching the maximum number of iterations).

As mentioned above, after the camera imaging plane is aligned with the side window plane, it is essential to adjust the robot's end flange position to keep the interval between the camera imaging plane and the side window plane at a preset value. The actual interval between the two planes can be obtained using the laser range finder, and then the difference between the exact interval and the preset value, Δd , can be computed. Using the transformation matrix from the CCS to the robot end flange ${}^{\mathrm{H}}_{\mathrm{C}}R$, Δd is decomposed into the flange CS. The displacement correction component in the three-axis direction of the flange CS is:

$$\begin{bmatrix} \Delta x_H \\ \Delta y_H \\ \Delta z_H \end{bmatrix} = {}^{H}_{C}R \begin{bmatrix} 0 \\ 0 \\ \Delta d \end{bmatrix} \tag{14}$$

Calculate the displacement correction of the robot's end flange using formula (14) and adjust the flange's position so that the interval between the camera imaging plane and the side window plane meets the preset value.

4 Vision-based positioning measurement

The combination of LDS and monocular vision has significant advantages in the assembly of train side window glass, such as relatively low cost and easy operation. LDS can provide high-precision distance measurement, while monocular vision can capture and process two-dimensional image information, and the combination of the two can achieve a certain degree of assembly accuracy. However, this combination also has limitations, such as the lack of depth information acquisition in monocular vision and the impact of lighting conditions on visual processing.

4.1 Pixel coordinate and physical coordinate conversion

After the alignment function is completed, the checkerboard is placed on the assembly plane, the camera captures the checkerboard image, and the proportional relation between the pixel and physical coordinates is computed using the real physical interval between the checkerboard corners and the corresponding pixel interval. Fig. 2 shows an acquired checkerboard image, and the proportional relation between the two CSs is:

$$s = \frac{1}{n}\sum_{i=1}^{n}\frac{d_{xyi}}{d_{uvi}} \tag{15}$$

In the formula, d_{xyi} and d_{uvi} are the Euclidean intervals of the i-th pair of checkerboard corner points in the checkerboard CS and the Euclidean interval in the pixel CS, respectively. The accurate proportional coefficient between these two CSs can be obtained by averaging the proportional relationships of n pairs of corner points, s.

Visual data (usually from industrial cameras) plays a crucial role in the assembly process. In order to extract useful information from images, this article adopts an advanced image processing algorithm. These algorithms

can identify and locate the edge features of glass and side windows, and then calculate their relative positions and orientations.

Specifically, the algorithm first improves image quality through preprocessing steps such as denoising and contrast enhancement. Then, edge detection algorithms such as Canny edge detectors are used to identify the edges of the glass and side windows. Next, use feature matching algorithms such as SIFT or SURF to find the corresponding relationships between these edges. Finally, use these corresponding relationships to calculate the relative position and orientation between the glass and the side windows.

To demonstrate this process more intuitively, we can provide a series of image processing result graphs, including the original image, preprocessed image, edge detection results, and feature matching results. These charts will help readers better understand the working principle of the algorithm.

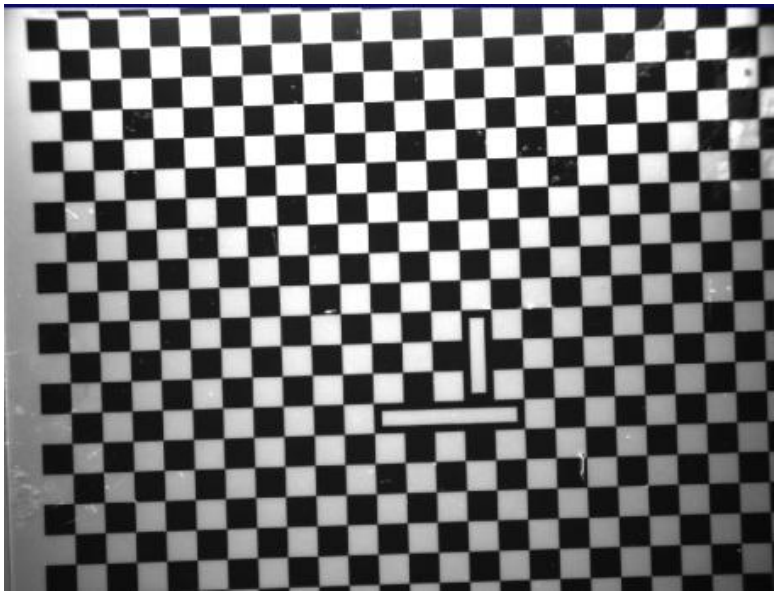

Figure 2: Checkerboard image

4.2 Feature identification

The arc part in the upper right corner of the side window, as seen in Fig. 3, is selected as the target feature to obtain the target's pose information. The straight-line equations of the two sides of the circular arc are obtained using the Hough transform. Hough transform is a classic algorithm used to detect specific shapes in images, such as lines, circles, arcs, etc. For arc detection, Hough Circle Transform or its variants can be used. Although Hough Circle Transform is mainly used to detect complete circles, it can also be used to detect arc parts by adjusting parameters and algorithms. Another method is to first detect the endpoints of the arc, then use these points to fit the arc, and then derive the equations for the lines on both sides based on the geometric properties of the arc, such as center, radius, and tangent direction. RANSAC (Random Sample Consensus) is an iterative algorithm used to estimate the parameters of a mathematical model from data containing a large amount of noise and outliers. It fits the model by randomly selecting a subset of data and evaluates the quality of the model by calculating the error between the remaining data and the fitted model. By combining the Hough transform and RANSAC least squares method, we can effectively identify the curved part of the upper right corner of the side window from the image and accurately fit the linear equations on both sides of the arc. These linear equations can be used for subsequent target pose information extraction and robot pose correction. Then, the accurate straight-line equation is obtained using the RANSAC least squares method [30].

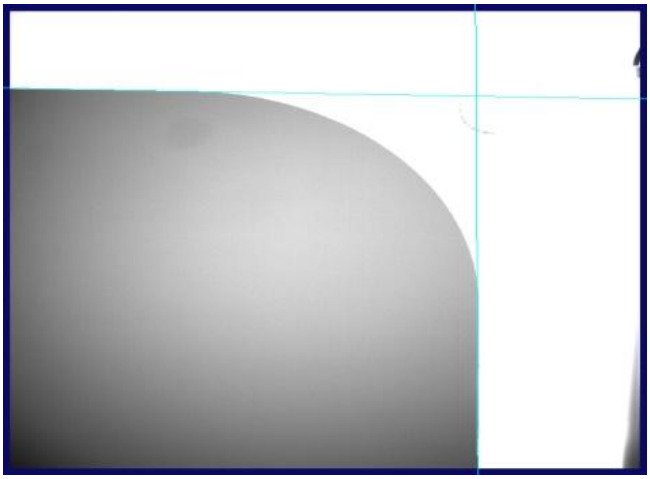

Figure 3: Target feature image

When the two lines intersect, that point serves as the displacement feature parameter for vision positioning, and the angle of the u-axis between them is used as a rotation characteristic parameter for visual positioning. The expected positioning characteristic parameters have been obtained by the above image processing method during offline teaching, and the positioning deviation can be determined by the feature elements of the current target image as follows:

$$\Delta u = u_{\mathrm{d}} - u$$
$$\Delta v = v_{\mathrm{d}} - v$$
$$\Delta\theta_{\mathrm{z}} = \theta_{\mathrm{d}} - \theta \quad (16)$$

Where $(u_{\mathrm{d}}, v_{\mathrm{d}})$ is the image coordinate of the intersection of the straight lines during teaching, (u, v) is the coordinate of the linear corner point in the current picture, θ_{d} is the angle of the straight-line during teaching, and θ is the line angle in the current image. Then $(\Delta u, \Delta v)$ is converted into physical coordinates using a proportional coefficient, and the offset matrix $\boldsymbol{T}'$ is obtained by combining $\Delta\theta_z$ as the primary data for the subsequent assembly process. θ_{d} and θ are the angle of the line in the teaching and the angle of the line in the current image, respectively. These angles may represent the angle between the line and a certain axis of the image coordinate system. The change in angle Δ θ=θ - θ_{d}can be used to describe the rotation of a straight line in an image. The offset matrix T 'is commonly used to describe the translation and rotation of an object in three-dimensional space. However, in your scenario, we may only be concerned with translation and rotation within the two-dimensional image plane. Therefore, T 'may be a 2x2 matrix (if only considering transformations within the plane) or a 3x3 matrix (if considering potential scaling and affine transformations, but keeping the z-coordinate constant).

4.3 Calculation and compensation of assembly pose

Visual positioning is divided into two steps: the calibration process and the assembly process.

(1) Calibration Process

Establish a workpiece CS T_0 at the upper right corner of the side window and record its pose as, T_0. With the assistance of the LDS, set the standard shooting pose of the camera and record the pose of the flange as C_Pos_0. The conversion relationship between C_Pos_0 and T_0 is $\left({}^{(T_0)}_{C_Pos_0}H\right)$. The collected image of the upper right corner of the side window is used as the standard template, and a nine-point calibration is carried out to set up the mapping relation between the pixel and the workpiece CSs. The robot is manually guided to place the glass accurately in the workpiece CS T_0, and the flange pose is recorded as g_Pos_0. The mapping relationship between pixels and workpiece CS (T0) established through nine-point calibration should have a certain degree of accuracy. This can be evaluated by comparing the differences between the standard template images collected during the calibration process and the images collected during actual installation [31]. The difference should be within the preset accuracy threshold, for example, the pixel error should not exceed a certain amount. If LDS is used to fit the equation of the side window plane, the fitting result should be consistent with the actual plane. The fitting accuracy can be evaluated by comparing the difference between the fitted plane and the actual plane [32].

(2) Assembly Process

Adjust the robot flange with the laser sensor to make the camera plane along with the side window plane, and record the flange pose as C_Pos_1. Based on the transformation relationship $\left({}^{T_0}_{C_Pos_0}H\right)$, the pose of the workpiece CS T_1 can be calculated as $T_1 = C_Pos_1 \cdot \left(\left({}^{T_0}_{C}H\right)^{-1}\right)$. Then, the product offset in the 2D plane is identified by the camera and the pose of the workpiece CS T_2 is calculated using the offset data, where $T_2 = T_1$.

Execute the installation pose g_Pos_0 in the T_2 CS, and the glass can be assembled accurately.

5 Experimental test and analysis of the result

5.1 Experimental test platform

Based on the assembly task requirements for the side window glass of a subway train in an enterprise, a platform for experimental testing was constructed, as displayed in Fig. 4. The size of the side window glass is 2 m × 1.5 m, and the working interval of the vision system is 400 mm. The attitude accuracy of the glass installation must be controlled within ±1°, and the positioning accuracy should be controlled within ±0.5 mm. The industrial robot is the ABB IRB7600-325, with a working range of 3.1 m and a maximum load capacity of 325 kg. The accuracy of repetitive positioning is 0.1 mm. The industrial camera is a CAM-CIC-4000 from Cognex, with a resolution of 2048 × 2048. The LDS is the LK-G500 from Keyence, with a range of 250 mm to 450 mm and a linear error of ±0.02%.

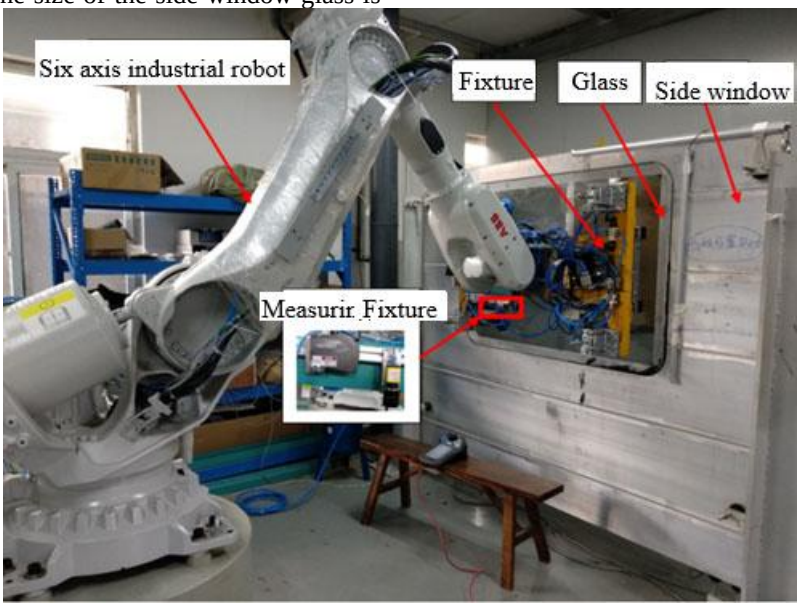

Figure 4: Assembly experiment site

5.2 System calibration results

Using the calibration method described above, the three types of calibration parameters of the system are first solved, and the final camera calibration result is as follows:

$$\boldsymbol{A}=\begin{bmatrix}5249.574 & 0 & 1014.700\\ 0 & 5248.587 & 1011.988\\ 0 & 0 & 1\end{bmatrix} \quad (17)$$

k_1=-0.158, k_2=-0.0249, k_3=0.0412, p_1=-0.0003, p_2=0.0004

The hand-eye calibration result is:

$$^{C}_{H}\boldsymbol{T}=\begin{bmatrix}0.007 & -0.036 & -0.999 & -54.874\\ 1 & 0.0074 & 0.006 & -75.193\\ 0.007 & -0.998 & 0.036 & 102.960\\ 0 & 0 & 0 & 1\end{bmatrix} \quad (18)$$

The calibration results of the LDS are as follows:

$$\boldsymbol{r}=[43.6839,-40.4931,90.1015]$$
$$\boldsymbol{l}=[0.9977,0.0626,0.0265] \quad (19)$$

5.3 Analysis of assembly test results

The manual method was first used in the experiment to guide the robot in accurately installing the glass and recording the robot flange pose data. Then, the process described above was used to adjust the robot flange automatically to perform the installation action under the guidance of the laser sensor and the camera. Here, 'posture' refers to the position and/or orientation of the side window glass relative to the robot or assembly platform. The robot flange pose data was also recorded. Finally, the data obtained through automatic guidance were compared with the flange pose data obtained by the manual method. Glass installation experiments on side windows with different postures were performed 20 times. The displacement deviation and rotation differences between automatic and manual assembly are illustrated in Figs. 5 and 6, respectively.

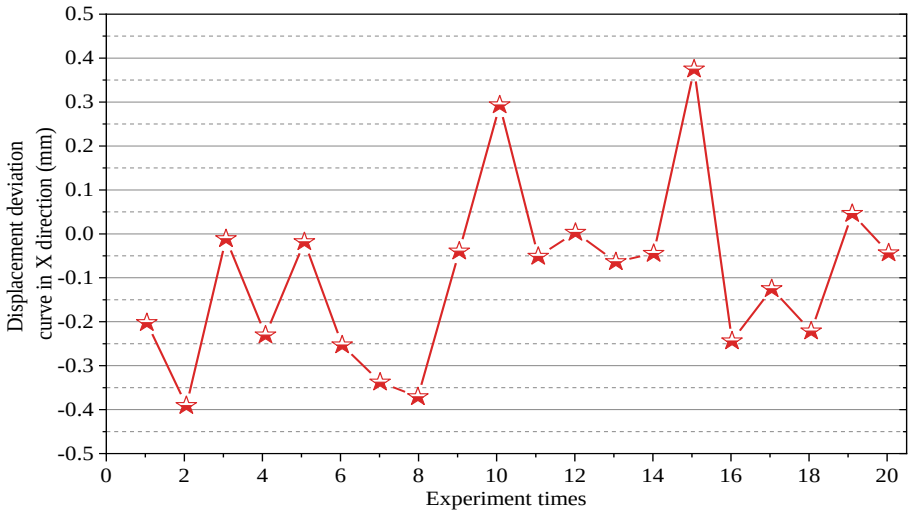

(a) Displacement deviation curve in X direction

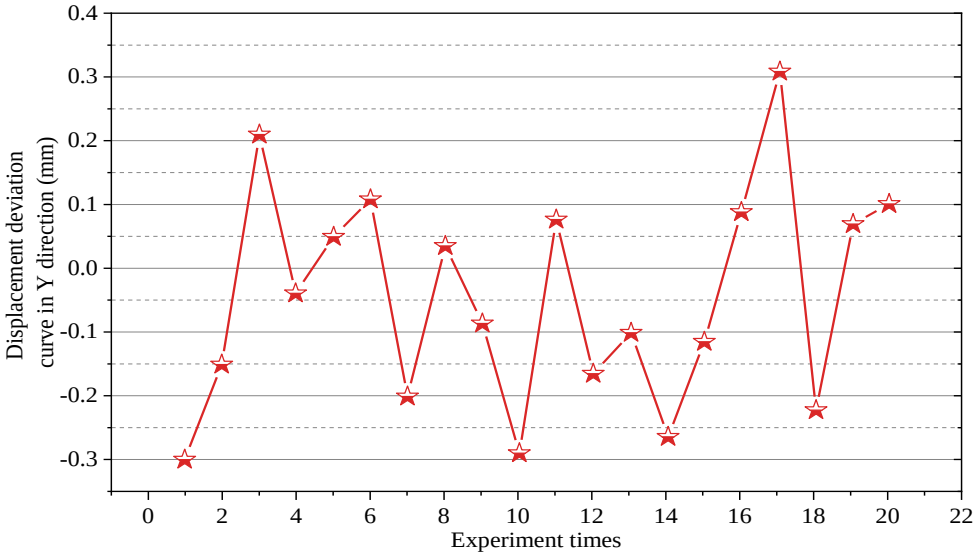

(b) Displacement deviation curve in the Y direction

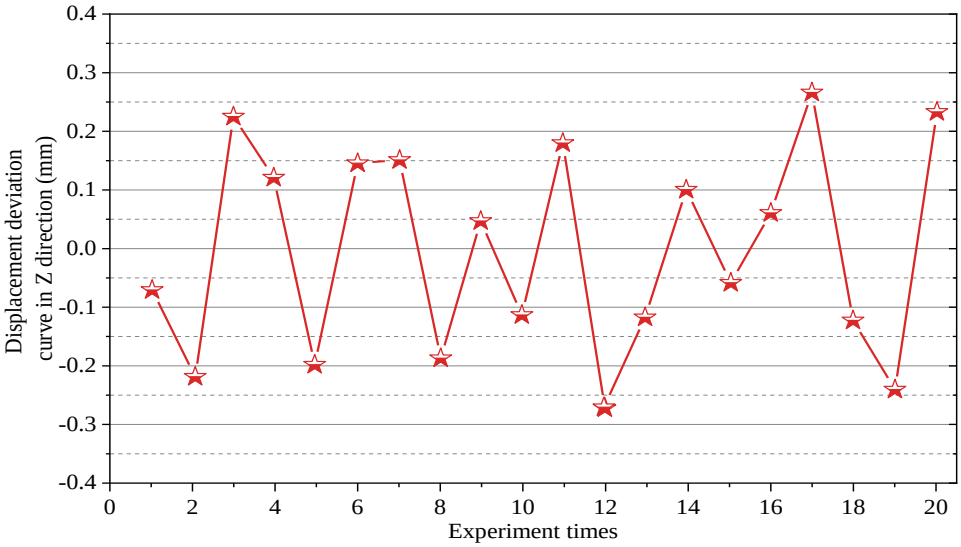

(c) Displacement deviation curve in Z direction

Figure 5: Displacement deviation curve

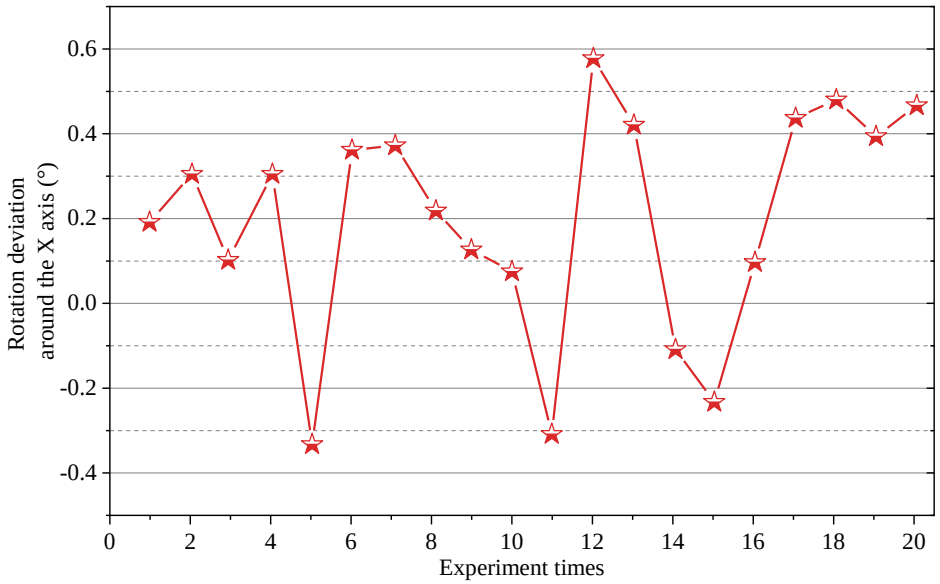

(a) Plot of rotation deviation around the X-axis

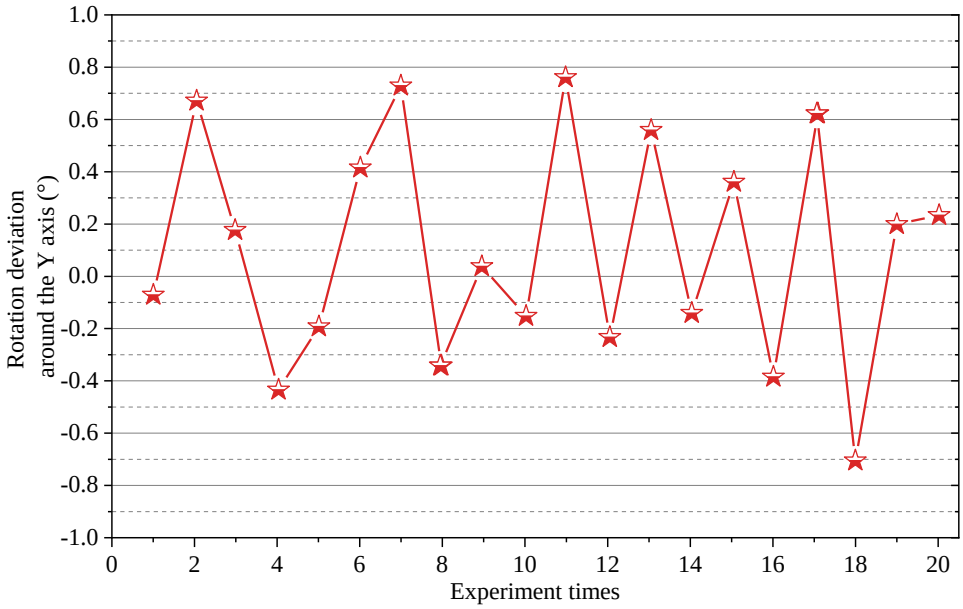

(b) Rotation deviation curve around the Y axis

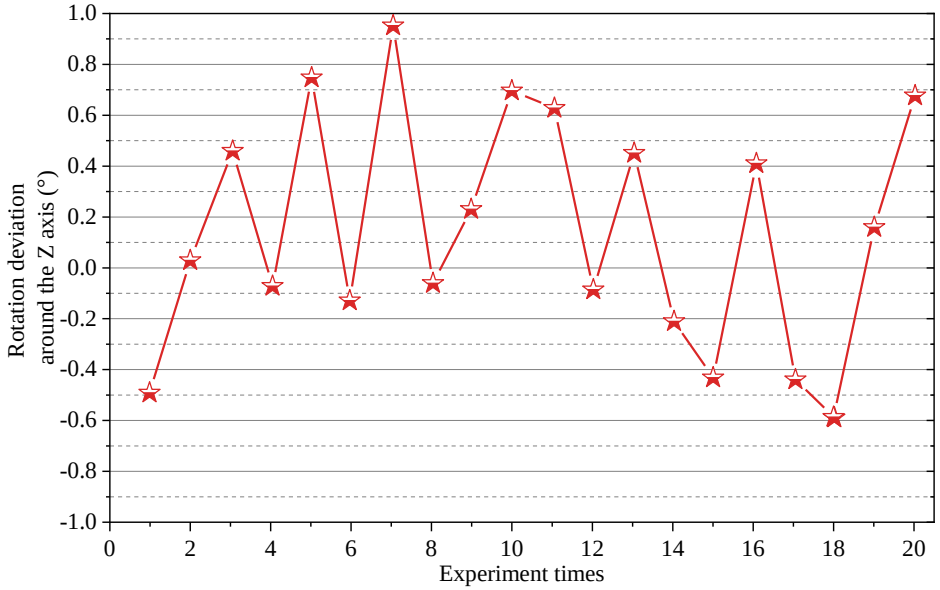

(c) Plot of rotation deviation around the Z-axis

Figure 6: Rotational deviation curve

Figs. 5 and 6 show that in 20 experiments, the maximum displacement deviation in the X direction is about ±0.4 mm, the maximum displacement deviations in the Y and Z directions are about ±0.3 mm, the maximum rotation deviation of the X axis is about 0.6°, and the minimum rotation deviation of the Y axis is about 0.8°. All deviations meet the requirements of ±1° attitude correction and ±0.5 mm displacement accuracy, showing good reliability. Stereoscopic vision technology also faces some challenges. For example, the calibration and calibration process of a camera is relatively complex, requiring high-precision equipment and technical support. In addition, stereoscopic vision is sensitive to lighting conditions and environmental noise, which may lead to a decrease in image quality and a loss of computational accuracy. Therefore, when choosing stereoscopic vision as an alternative solution, we need to balance the relationship between its high accuracy and complexity. In addition to LDS, we can also consider using additional laser measurement systems to improve assembly accuracy. For example, a 3D laser scanner can be used to comprehensively scan the assembly area and generate accurate 3D point cloud data. These data can be used to generate a digital model of the assembly area and compare it with the expected model to calculate assembly deviations and make corrections.

6 Conclusion

It proposes an integrated assembly method guided by LDSs and monocular vision for the automatic assembly of train-side window glass. The core of the proposed approach is that, from the laser-projected point data, the plane equation of the window is derived, and its NV is used for adjustment of the robot's end flange. The camera attached to the robot shares a parallel plane with the window pane, and the distance between the two planes is adjusted to achieve accurate visual alignment. The monocular vision system identifies edge features of the side window to estimate the precise pose, which guides the robot in completing the glass installation. Experimental results have shown that this assembly approach consistently meets the required pose accuracy for glass installation. It offers the benefits of being inexpensive, having a simple structure, and providing high precision in positioning and orientation calculation, making it suitable for the automatic detection, positioning, guidance, and assembly of other large-scale planar workpieces. This method is mainly suitable for automatic assembly of large flat workpieces. In the previously proposed integrated method for automatic assembly of train side window glass based on a laser ranging system and monocular vision, this article emphasizes the close interaction between system calibration and assembly accuracy. System calibration is a crucial step in ensuring assembly accuracy, as it directly affects the accuracy of laser projection point data and the recognition ability of monocular vision systems for edge features. The calibration of the monocular vision system includes both intrinsic and extrinsic calibration of the camera. Internal calibration ensures that the geometric characteristics of camera imaging, such as focal length and distortion, are accurately recorded, while external calibration criteria ensure the accurate correspondence between the camera and the world coordinate system. Through calibration, the recognition accuracy of the monocular vision system for side window edge features can be improved, thereby more accurately estimating the posture of the glass and guiding the robot to complete precise installation.

However, in practical industrial applications, workpieces may have more complex geometric shapes. How to adjust this method to handle these complex shapes and ensure the accuracy and reliability of assembly is a challenging task. The monocular vision system relies on the recognition of edge features to estimate accurate poses. However, in some cases, such as when the edge of the side window is obstructed or severely worn, feature recognition may become difficult. Prospects include adapting the method to handle complex geometries or materials, applying advanced image processing techniques for better feature recognition, and developing fully autonomous assembly lines, particularly in the automotive and aerospace industries, where similar demands for high accuracy and efficiency exist. We will explore the application effects of this method on different types of large planar workpieces, and how to improve the adaptability and robustness of the method by improving the algorithm or adding sensors.

Nomenclature

Abbreviations		f	Objective function to be minimized
CDW	Construction and Demolition Waste	F	Function constructed
CFD	Computational Fluid Dynamics	H	Transformation matrix
CNN	Convolutional Neural Network	l	Laser line's unit direction vector coordinate matrix
LES	Large Eddy Simulation	P	Coordinate matrix
LM	Levenberg-Marquardt method	r	Side window plane
ORB	Oriented FAST and Rotated BRIEF	R	Coefficient matrix
PnP	Perspective-n-Point	s	Proportional coefficient
PVB	Polyvinyl Butyral	x	Components of the ith

SHM	Structural Health Monitoring	Greek symbol	
SLAM	Simultaneous Localization and Mapping	α	Rotation angles
WRMSD	Work-Related Musculoskeletal Disorder	β	Rotation angles
symbols		γ	Rotation angles
A	Components	λ	Lagrange multiplier
B	Components	**subscripts**	
C	Components	C	the camera coordinate system
D	Distance	H	the robot end flange coordinate system
d_{xyi}	Euclidean distance	i	Index for each laser point
d_{uvi}	Euclidean distance	T	Transformation from one coordinate system to another
d	Distance measured		

Funding

This work was sponsored in part by the Jiangsu Qing Lan Project, the Wuxi Industrial AGV Technology Application and Promotion Public Service Platform Project (WX03-07D0337-052300-07).

Competing interests

No competing interests have been disclosed by the authors.

Authorship contribution statement

Xiaobing Cao: Project administration, Supervision, Conceptualization, Writing-Original draft preparation.
Yicen Xu: Language review.
Yonghong Yao: Methodology.
Sheng Chen: Validation.

Data availability

Available upon request.

Conflicts of interest

The authors declare that there is no conflict of interest regarding the publication of this paper.

Author atatement

The manuscript has been read and approved by all the authors, the requirements for authorship, as stated earlier in this document, have been met, and each author believes that the manuscript represents honest work.

Ethical approval

All authors have been personally and actively involved in substantial work leading to the paper and will take public responsibility for its content.

References

[1] B.-J. You, Y. S. Oh, and Z. Bien, "A vision system for an automatic assembly machine of electronic components," *IEEE Transactions on Industrial Electronics*, 37(5): pp. 349–357, 1990. DOI: 10.1109/41.103429

[2] Y. Ma, W. Zhu, and Y. Zhou, "Automatic grasping control of mobile robot based on monocular vision," *The International Journal of Advanced Manufacturing Technology*, 121(3): pp. 1785–1798, 2022. https://doi.org/10.1007/s00170-022-09438-z

[3] H. A. O. Renjie, W. Zhongyu, and L. I. Yaru, "Error analysis method for monocular vision pose measurement system," *Journal of Applied Optics*, 40(1): pp. 79–85, 2019. DOI: 10.5768/JAO201940.0103001

[4] Y. Ma, X. Liu, J. Zhang, D. Xu, D. Zhang, and W. Wu, "Robotic grasping and alignment for small size components assembly based on visual servoing," *The International Journal of Advanced Manufacturing Technology*, 106(1), pp. 4827–4843, 2020. https://doi.org/10.1007/s00170-019-04800-0

[5] W.-C. Chang, "Robotic assembly of smartphone back shells with eye-in-hand visual servoing," *Robot Comput Integr Manuf*, 50(1), pp. 102–113, 2018. https://doi.org/10.1016/j.rcim.2017.09.010

[6] Su, J., Shen, L., Peng, Z., & Qu, X. (2024). Design of a robot system for reorienting and assembling irregular parts. International Journal of Advanced Robotic Systems, 21(2), 17298806241229271. DOI: 10.1177/17298806241229271

[7] L. Jin-zhou, Z. Ling-bin, and Y. Nan, "Research on industrial robot alignment technique with monocular vision," *Optics & Precision Engineering*, 26(3): pp. 733–741, 2018. https://doi.org/10.1016/j.measurement.2022.112049

[8] Çapunaman, Ö. B., & Gürsoy, B. (2024). Vision-augmented robotic fabrication (V-aRF): systematic review on contemporary approaches and computational methods in architectural fabrication and assembly using machine vision. Construction Robotics, 8(2), 27. DOI: 10.1007/s41693-024-00139-5

[9] X. Hu, K. Shi, J. Mao, P. Guo, T. Yu, and J. Wang, "Optimization study on the influence of rearview mirror and side window glass on interior noise," *Journal of Vibration and Control*, 30(3–4): pp. 516–530, 2024. https://doi.org/10.1177/10775463231172070

[10] J. Zhang *et al.*, "Method for measuring the membrane penetration of triaxial specimens based on an external circular array of laser displacement sensors," *Measurement*, 217, p. 112905, 2023. https://doi.org/10.1016/j.measurement.2023.112905

[11] Y. Shao, L. Li, J. Li, Q. Li, S. An, and H. Hao, "Monocular vision-based 3D vibration displacement measurement for civil engineering structures," *Eng Struct*, 293, p. 116661, 2023. https://doi.org/10.1016/j.engstruct.2023.116661

[12] J. Chen, W. Lu, L. Yuan, Y. Wu, and F. Xue, "Estimating construction waste truck payload volume using monocular vision," *Resour Conserv Recycl*, 177(1), p. 106013, 2022. https://doi.org/10.1016/j.resconrec.2021.106013

[13] C. Sun, D. Gu, and X. Lu, "Three-dimensional structural displacement measurement using monocular vision and deep learning-based pose estimation," *Mech Syst Signal Process*, 190(1), p. 110141, 2023. https://doi.org/10.1016/j.ymssp.2023.110141

[14] W. K. Sleaman, A. A. Hameed, and A. Jamil, "Monocular vision with deep neural networks for autonomous mobile robots' navigation," *Optik (Stuttg)*, 272(1), p. 170162, 2023. https://doi.org/10.1016/j.ijleo.2022.170162

[15] Y. Sun, X. Wang, Q. Lin, J. Shan, S. Jia, and W. Ye, "A high-accuracy positioning method for mobile robotic grasping with monocular vision and long-distance deviation," *Measurement*, 215(1), p. 112829, 2023. https://doi.org/10.1016/j.measurement.2023.112829

[16] Q. Gao *et al.*, "Monocular vision measurement technology applied in dynamic compaction ramming settlement monitoring," *Measurement*, 216(1), p. 112941, 2023. https://doi.org/10.1016/j.measurement.2023.112941

[17] L. Lou, Y. Li, Q. Zhang, and H. Wei, "Slam and 3d semantic reconstruction based on the fusion of lidar and monocular vision," *Sensors*, 23(3) p. 1502, 2023. https://doi.org/10.3390/s23031502

[18] D. Li, B. Cheng, and K. Wang, "Self-calibrating technique for 3D displacement measurement using monocular vision and planar marker," *Autom Constr*, 159(1), p. 105263, 2024. https://doi.org/10.1016/j.autcon.2023.105263

[19] K.-H. Ahn, M. Na, and J.-B. Song, "Robotic assembly strategy via reinforcement learning based on force and visual information," *Rob Auton Syst*, 164(1), p. 104399, 2023. https://doi.org/10.1016/j.robot.2023.104399

[20] B. Mei, Z. Liang, Y. Xie, Y. Fu, and Y. Yang, "Positioning accuracy enhancement of a robotic assembly system for thin-walled aerostructure assembly," *J Ind Inf Integr*, 35(1), p. 100518, 2023. https://doi.org/10.1016/j.jii.2023.100518

[21] Z. Zhang, Y. Wang, Z. Zhang, L. Wang, H. Huang, and Q. Cao, "A residual reinforcement learning method for robotic assembly using visual and force information," *J Manuf Syst*, 72(1), pp. 245–262, 2024. https://doi.org/10.1016/j.jmsy.2023.11.008

[22] C. Champatiray, M. V. A. R. Bahubalendruni, R. N. Mahapatra, and D. Mishra, "Optimal robotic assembly sequence planning with tool integrated assembly interference matrix," *AI EDAM*, 37, p. e4, 2023.
DOI: https://doi.org/10.1017/S0890060422000282

[23] Patel, J., Round, A., de Wijn, R., Vakili, M., Giovanetti, G., Melo, D. F. M. V. E., ... & Abbey, B. (2024). "Real-time analysis of liquid jet sample delivery stability for an X-ray free-electron laser using machine vision". *Applied Crystallography*, 57(6), 1. DOI: 10.1107/S1600576724009853

[24] Zhang, L., Zhou, C., Liu, B., Ding, Y., Ahn, H. J., Chang, S., & Ni, X. (2024). "Real-time machine learning–enhanced hyperspectro-polarimetric imaging via an encoding metasurface". *Science Advances*, 10(36), eadp5192. DOI: 10.1126/sciadv.adp5192

[25] B. Zeng, F. Meng, H. Ding, W. Liu, D. Wu, and G. Wang, "A plane-based hand-eye calibration method for surgical robots," *Sheng Wu Yi Xue Gong Cheng Xue Za Zhi*, 34(2): pp. 200–207, 2017. https://doi.org/10.7507/1001-5515.201605050

[26] M. Li, Z. Du, X. Ma, W. Dong, and Y. Gao, "A robot hand-eye calibration method of line laser sensor based on 3D reconstruction," *Robot Comput Integr Manuf*, 71(1), p. 102136, 2021. https://doi.org/10.1016/j.rcim.2021.102136

[27] Z. Zhang, "A flexible new technique for camera calibration," *IEEE Trans Pattern Anal Mach Intell*, 22(11) pp. 1330–1334, 2000. DOI: 10.1109/34.888718

[28] R. Y. Tsai and R. K. Lenz, "A new technique for fully autonomous and efficient 3 d robotics hand/eye calibration," *IEEE Transactions on robotics and automation*, 5(3): pp. 345–358, 1989. DOI: 10.1109/70.34770

[29] G. Yunlan, C. Xiaojun, and S. Guigang, "A robust method for fitting a plane to point clouds," *Journal of tongji university (natural science)*, 36, (7): pp. 981–984, 2008. DOI: 10.1109/ICCC56324.2022.10065838

[30] Lettera, G., & Natale, C. (2024). An Integrated Architecture for Robotic Assembly and Inspection of a Composite Fuselage Panel with an Industry 5.0 Perspective. Machines, 12(2), 103. DOI: 10.3390/machines12020103

[31] Rawat, R., & Rajavat, A. (2024). Illicit Events Evaluation Using NSGA-2 Algorithms Based on Energy Consumption. Informatica, 48(18), 1.

[32] El Ghazi, M., & Aknin, N. (2024). Optimizing Deep LSTM Model through Hyperparameter Tuning for Sensor-Based Human Activity Recognition in Smart Home. Informatica, 47(10), 1.

Leveraging Spark-TensorFlow Distributor for Distributed Deep Convolutional Neural Networks: Accelerating large-scale COVID-19 Detection

Saliha Mezzoudj[1], Meriem Khelifa[2], Yasmina Saadna[3]
[1]Department of Computer Science, University of Algiers, Algiers, Algeria
[2]Artificial Intelligence of Information Technologies, Department of Computer Science and Information Technologies, University of Kasdi Merbah Ouargla, Algeria
[3]Labstic laboratory, Batna 2 University, Batna, Algeria
E-mail: s.mezzoudj@univ-alger.dz, khelifa.meriem@univ-ouargla.dz, y.saadna@univ-batna2.dz

Keywords: Chest X-ray, DCNN, spark-tensorflow-distributor, distributed training

Received: November 5, 2024

The COVID-19 epidemic has been a critical global challenge due to its high mortality rate and rapid spread. Initial diagnostic methods, such as chest X-rays and reverse transcriptase polymerase chain reaction (RT-PCR), can be time-consuming and require enhanced efficiency, especially in scenarios where large-scale testing is necessary. Combining deep learning (DL) and big data analytics tools is crucial for developing accurate and fast systems to detect COVID-19 infections and prevent further transmission. In this study, we introduce a distributed Deep Convolutional Neural Network (DCNN) framework designed for the detection of COVID-19, utilizing a comprehensive dataset of chest X-ray images. Our approach leverages the spark-tensorflow-distributor, which integrates TensorFlow 2.x with Apache Spark 3.x, enabling distributed training within the Spark framework. The system utilizes Spark's barrier mode to execute distributed training tasks, significantly enhancing the speed of both training and testing phases. We classify chest X-ray images into two categories: COVID-19 and non-COVID-19. The experimental setup involves processing the large-scale dataset of chest X-ray images in a parallelized manner using the Spark framework. Our results demonstrate that the proposed DCNN model achieves a classification accuracy of 95.53%, with a testing time of 0.06 seconds and a training time of 18,909 seconds. Furthermore, when compared to other state-of-the-art methods for COVID-19 classification, our approach proves to be more efficient and effective. This study highlights the potential of combining distributed computing frameworks with deep learning techniques to address largescale medical image analysis challenges, particularly in the context of COVID-19 detection.

Povzetek: Predlagan je pristop za hitro odkrivanje COVID-19 iz velikih zbirk rentgenskih slik prsnega koša z uporabo distribuiranega globokega konvolucijskega nevronskega omrežja (DCNN).

1 Introduction

In December 2019, COVID-19 (coronavirus) was identified in a group of pneumonia patients [13], [14], leading to its declaration as a global health emergency by the World Health Organization (WHO) [15]. The WHO emergency panel underscored the significance of rapid detection, isolation, early treatment, and the implementation of a robust contact tracing strategy to control the spread of COVID-19 [16]. One of the primary diagnostic methods for identifying the coronavirus is the examination of sputum samples through polymerase chain reaction (RT-PCR) [10]. However, RT-PCR is a time-consuming process, resulting in delayed diagnoses for patients [17]. When there is a large number of patients, the scarcity of RT-PCR tests and specialized laboratory equipment for COVID-19 detection becomes a significant issue [20]. Another diagnostic approach involves manually analyzing X-ray images by human specialists or radiologists [20].

Manual diagnosis of COVID-19 through X-ray images has limitations, such as the need for trained radiologists, potential human error, longer diagnostic times, and a higher likelihood of false-negative results. As a result, there is an urgent need for tools that can optimize available resources, improve diagnostic accuracy, and reduce processing time [10], [3]. Deep learning (DL) and Big Data Analytics (BDA) are such tools [20], [21], [4]. They can expedite decision-making processes and predict the progression of COVID-19 cases [22], [4]. Many countries have successfully managed the COVID-19 pandemic by leveraging Big Data and Machine Learning methods, marking a significant milestone in epidemic control [3]. These countries have implemented effective safety measures, incorporating big-data analytics and Artificial Intelligence to address emergencies [3], [39]. They are gathering vast amounts of data and using it creatively, integrating Deep Learning and Big Data analytics to confront ongoing crises [3].

X-ray imaging has emerged as a primary method for di-

agnosing COVID-19 cases [18], [19]. This study focuses on utilizing X-ray images for COVID-19 detection. In this paper, we propose a rapid and accurate approach to detect COVID-19 from large-scale X-ray databases by classifying images as either COVID-19 or non-COVID-19 (see Fig. 1) using a distributed Deep Convolutional Neural Network (DCNN) model on the Spark-TensorFlow-Distributor framework [1]. This framework, built on top of TensorFlow's 'tensorflow.distribute.Strategy', enables distributed training on the Spark platform.

The Spark framework is optimized for parallel processing of large datasets [23], [24]. Furthermore, the Hadoop Distributed File System (HDFS) is utilized for efficient storage and management of big data, which is especially critical for COVID-19 data due to its rapid and large-scale generation [23], [40]. Our key contributions are as follows:

1. Enabling parallel processing of large-scale chest X-ray COVID-19 images using the Spark-TensorFlow-Distributor framework.

2. Combining deep learning with the Spark-TensorFlow-Distributor framework for the rapid and efficient classification of large volumes of chest X-ray images. Our approach achieves outstanding training and testing times through the barrier mode of Spark, optimizing distributed training tasks.

3. Presenting the findings from the proposed fine-tuning approach for the DCNN classifier.

4. Comparing the performance of our classifier with other models, such as ANN and AlexNet, in terms of accuracy and processing time.

5. Evaluating our approach against recent state-of-the-art methods regarding classification accuracy and execution time.

The remainder of this paper is organized as follows: Section 2 reviews related works in COVID-19 detection and classification. Section 3 provides the background and tools used in this study. Section 4 details the proposed method. Section 5 presents the classification performance. Experimental results in Section 6. Finally, the conclusions are drawn in Section 7.

2 Related works

Recently, the application of Deep Learning techniques has become widespread in predicting and identifying COVID-19 due to its high accuracy [1]. Hemdan et al. [32] introduced a system for the recognition of COVID-19 based on chest X-ray images. This system incorporates seven image classifiers, collectively known as COVIDX-Net, achieving notable performance, with DenseNet201 and VGG19 classifiers achieving an accuracy of 90%. Basu et al. [31] proposed an advanced method for COVID-19 detection that employs transfer learning with a pre-trained deep convolutional neural network (DCNN) using chest X-ray images. The authors achieved an overall accuracy of 90.1%. However, this system requires a limited number of chest X-ray images for COVID-19 identification. Similarly, for COVID-19 detection from chest X-ray images, the authors in [25] proposed an advanced DCNN model utilizing pre-trained transfer architectures such as ResNet50, InceptionV3, and Inception-ResNetV2. Their approach demonstrated exceptional predictive performance in terms of time and accuracy, tested on a limited set of X-ray images. To address limited training data and processing time, they employed transfer learning using the ImageNet dataset [25]. The results validated the superior accuracy of the ResNet50 model across both training and testing evaluations.

In another study [12], the authors proposed a model using Explainable Artificial Intelligence (XAI) techniques to detect COVID-19 from chest X-ray (CXR) images. They employed transfer learning, data augmentation, and lung segmentation for faster model training and improved performance. By using the ResNet model, they achieved the highest classification performance (F1-Score: 98%). The authors in [11] developed an efficient method for classifying images as either COVID-19 or non-COVID-19 using a CNN for feature extraction and SVM for classification. By incorporating image augmentation, segmentation, and cropping techniques, they achieved optimal results, with a training accuracy of 99.8% and a testing accuracy of 99.1% on a dataset of 3000 images.

The rapid spread of COVID-19 has generated vast amounts of data, which continues to grow exponentially [8]. This data can be effectively utilized by applying big data analytics techniques for COVID-19 detection. Several studies have used big data analytics and artificial intelligence (AI) methods to enhance COVID-19 detection performance [8]. For instance, the authors in [30] explores the integration of AI, big data tools, and nature-inspired computing (NIC) to improve the performance of COVID-19 detection. Moreover, the authors of reference [6] utilized a Hive-based distributed system operating on a Hadoop cluster to query and analyze large COVID-19 datasets, aiming to extract valuable insights. Hadoop serves as a parallel computing system for processing vast volumes of data, while Hive functions as a data warehouse for the Hadoop cluster. Their proposed approach facilitates queries and predictive analytics on massive COVID-19 datasets.

In [30], the authors proposed a model to distinguish COVID-19 from four other viral chest diseases by utilizing various body sensors, which gather data on parameters such as temperature, blood pressure, heart rate, respiratory patterns, glucose levels, and more. The data is stored in a cloud database and analyzed by AI-enabled expert systems to identify infected or suspected COVID-19 patients. Similarly, Gupta et al. [28] identified COVID-19 cases in

[1] spark-tensorflow-distributor: https://docs.databricks.com/en/machine- learning/train-model/distributed-training/spark-tf-distributor.html

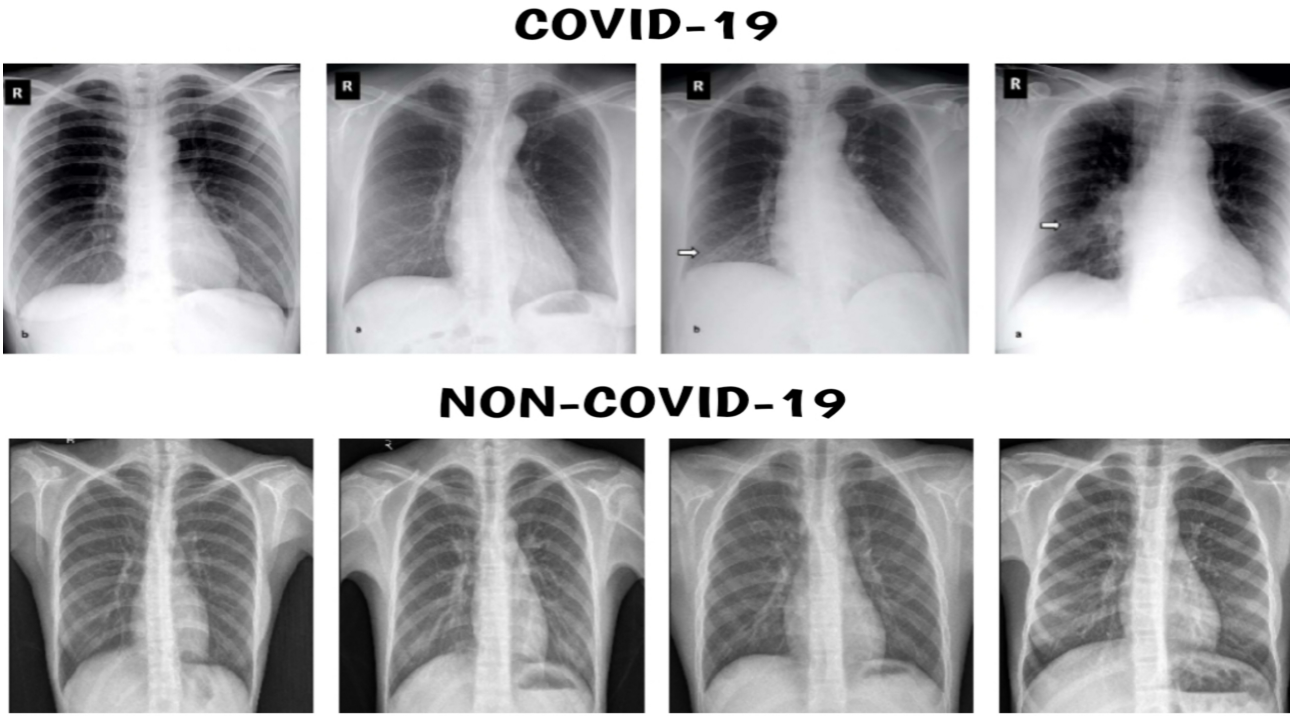

Figure 1: Sample X-ray images of normal (non-covid-19 cases) and (covid-19 positive cases)

India using models such as random forests, linear models, support vector machines, decision trees, and neural networks. The random forest model was selected for its superior performance, and K-fold cross-validation was employed to assess model consistency. They also introduced a novel federated learning (FL) approach to improve the global GAN model's ability to generate realistic COVID-19 images without sharing sensitive data.

The authors of reference [27] developed a system to detect COVID-19 using chest X-ray images sourced from Kaggle repositories. Their system is based on pre-trained Apache Spark big data framework models using Deep Transfer Learning (DTL) via Convolutional Neural Networks (CNNs), specifically InceptionV3 and ResNet50. Their study showed that both models achieved impressive results, with InceptionV3 surpassing 99% accuracy and ResNet50 reaching up to 98%. The proposed model accelerates COVID-19 detection and reduces associated costs. As part of future work, the authors plan to enhance their system by integrating TensorFlow with Apache Spark to develop a new model for detecting COVID-19 in chest CT images. This integration will enable the creation of a model that can operate on large computing clusters.

The authors in [38] introduced a method called DisCOV, which involves training a distributed COVID-19 detection model using a large-scale chest X-ray dataset, in collaboration with edge and cloud computing. To enhance training efficiency and ensure model accuracy, they implemented a resource allocation algorithm to minimize time, cost, and energy consumption during training. Their method achieved a maximum accuracy of 94%. In another study, the authors in [29] used the COVID-Net CNN model to detect COVID-19 from a large dataset of 13,975 CXR images. They applied various data augmentation techniques such as translation, rotation, horizontal flipping, zooming, and intensity shifting, achieving a recognition accuracy of 93.38%.

3 Materials and methods

A widely adopted approach for COVID-19 detection involves the use of chest X-rays, which offer a cost-effective method. However, this method requires further enhancements to improve its efficiency. Most existing studies have relied on chest X-ray images for COVID-19 detection using deep learning models, though typically on a limited set of images [3], [27]. To address these limitations and facilitate the development of models capable of running in a distributed manner across clusters, this study proposes a novel approach that combines big data analytics with Deep Convolutional Neural Networks (DCNNs) for detecting COVID-19 from a large volume of chest X-ray images. The primary objective of our research is to enhance COVID-19 detection performance, particularly with respect to training and execution times.

In our approach, we use TensorFlow version 2 on Apache Spark version 3. [2], [3] enabling deep learning models to ex-

[2]Blog, M. (2020). Distributed tensorflow on apache spark 3.0. https://blog.madhukaraphatak.com/tensorflow-on-spark-3.0

[3]pypi (2021). Spark tensorflow distributor. https://pypi.org/project/spark- tensorflow-distributor/

Table 1: Comparison of COVID-19 detection approaches in related works

Study	Method	Dataset Size	Accuracy	Key Features
[32]	COVIDX-Net	Not specified	90%	DenseNet201, VGG19 classifiers
[31]	Transfer learning with DCNN	Not specified	90.1%	Pre-trained DCNN, transfer learning
[25]	ResNet50, InceptionV3, Inception-ResNetV2	Limited dataset	High accuracy	Transfer learning, limited images
[12]	XAI, Transfer Learning, Data Augmentation	Not specified	F1-Score: 98%	Explainable AI, lung segmentation
[11]	CNN + SVM	3000 images	99.8% (train), 99.1% (test)	Image augmentation, segmentation
[6]	Hadoop, Big Data Analytics	Large dataset	N/A	Hive-based system, big data analytics
[28]	Random Forests, SVM, Neural Networks	Not specified	High performance	Federated learning, multi-model approach
[27]	Apache Spark, DTL with CNNs (InceptionV3, ResNet50)	Kaggle dataset	InceptionV3: 99%, ResNet50: 98%	Deep Transfer Learning, big data
[38]	DisCOV (Distributed model)	Large dataset	94%	Distributed training, edge-cloud collaboration
[29]	COVID-Net CNN	13,975 images	93.38%	Data augmentation, large dataset

ecute within the Apache Spark framework in a distributed fashion. A detailed description of the proposed methodology is provided in the following sections.

3.1 Big data

Big Data refers to the vast amounts of data generated in various forms (such as text, data, sound, and video) across unstructured, structured, and semi-structured formats. This overwhelming volume of data surpasses the capabilities of traditional data processing methods. It involves the collection, storage, and analysis of large datasets to uncover patterns, trends, and valuable insights [24], [41].

3.2 Apache spark

Apache Spark is an open-source, distributed computing system designed to process large volumes of data. It provides a fast, general-purpose cluster computing framework and supports several programming languages, including Scala, Java, Python, and R. Spark offers high-level APIs for distributed data processing, including batch processing, streaming, machine learning, and graph processing. Known for its in-memory processing capabilities, Spark outperforms traditional MapReduce-based frameworks in terms of speed [37], [24], [56].

3.3 Spark-TensorFlow-distributor

The ‘spark-tensorflow-distributor‘ is a Python package that enables distributed training with TensorFlow on Spark clusters. It builds upon the ‘tensorflow.distribute.Strategy‘ API, a key feature of TensorFlow version 2.x that allows for distributing training across multiple GPUs, machines, or TPUs [4], [5]

Furthermore, the ‘spark-tensorflow-distributor‘ package implements the barrier execution mode in Spark to facilitate distributed TensorFlow training on Apache Spark version 3.x clusters. In contrast to Spark version 2, which was limited to distributing training using the traditional MapReduce execution model (where workers operate independently without communication), Spark version 3.0 introduces a barrier execution mode. This new mode enables seamless communication between workers during the training process, making it more suitable for deep learning applications. In our study, we leverage ‘spark-tensorflow-distributor‘ to implement distributed TensorFlow training with version 2.x on Spark version 3.x, utilizing a large dataset of chest X-ray (CXR) images for COVID-19 detection. This approach enhances training times and improves the overall speed of the system.

3.4 Deep learning

Deep learning, a subset of machine learning, involves using neural networks with multiple layers (deep neural networks) to model and solve complex problems. By emulating the human brain, these networks can learn hierarchical representations of data, enabling the model to perform tasks such as pattern recognition and decision-making.

3.5 Chest X-ray imaging

Chest X-ray imaging is one of the most commonly used medical imaging techniques for diagnosing and assessing the extent of infections, offering several advantages [35]. These advantages include its ease of processing, which reduces imaging time and minimizes the risk of spreading COVID-19 cases [36]. Additionally, chest X-rays are more economical compared to other imaging modalities and involve lower radiation doses compared to CT scans.

However, despite these benefits, chest X-ray imaging has limitations. It is less sensitive than other techniques, which may lead to false predictions, particularly in the early stages of the disease [32].

4 Methodology

4.1 System architecture

We propose a novel system for large-scale COVID-19 image classification that leverages the Spark-TensorFlow-Distributor, enabling distributed training across multiple GPUs or machines (see Fig. 2). The proposed system utilizes Spark-TensorFlow-Distributor to process the deep

[4] pypi (2021). Spark tensorflow distributor. https://pypi.org/project/spark- tensorflow-distributor/

[5] databricks (2020). Distributed training with tensorflow 2. https://docs.databricks.com/machine-learning/train-model/distributed-training/spark-tf-distributor.html

learning model in a parallel and distributed manner, handling large datasets on the Spark platform. The system performs in-memory computations and adopts a master/slave architecture, consisting of two primary nodes: the master node (pilot process) and the slave node (worker process), as illustrated in Fig. 2. The system's input consists of a large volume of COVID-19 images, and the output is classified as either COVID-19 or non-COVID-19.

Our approach employs a distributed Deep Convolutional Neural Network (DCNN)-based deep learning model for large-scale COVID-19 image detection. This model operates with Spark-TensorFlow-Distributor, which is deployed on top of an Apache Spark cluster (version 3) integrated with TensorFlow (version 2). The YARN cluster manager is responsible for scheduling and resource allocation across applications, ensuring efficient parallel data training by balancing the workload and controlling training costs. A key feature of the proposed system is the use of Spark-TensorFlow-Distributor, an open-source package that facilitates distributed training with TensorFlow on Spark clusters. This package is built on top of 'tensorflow.distribute.Strategy', a core feature of TensorFlow 2. The system requires Spark 3.0.1, Python 3.6+, and TensorFlow 2.1.0+ to function effectively. After training our DCNN model, we utilize Spark-TensorFlow-Distributor to perform distributed training on our Spark clusters.

4.1.1 Advantages of Spark 3.x over Spark 2.x

Spark 2.x relies on the traditional Map/Reduce execution model, where a Spark program typically consists of a sequence of map and reduce stages. This model, inspired by Hadoop, works well for many big data tasks such as ETL (Extract, Transform, Load), SQL operations, and basic machine learning tasks. However, Spark 2.x's scheduling approach is less efficient when implementing deep learning frameworks.

To address this limitation, Spark 3.x introduces a new execution mode known as the "Mirrored-Strategy Runner" in barrier execution mode, which is specifically designed for distributed deep learning tasks. Unlike the traditional Map/Reduce model, this execution mode operates differently. In the Map/Reduce model, tasks within a stage are independent and do not communicate with each other; consequently, if a task fails, only that specific task is retried. In contrast, the "Mirrored-Strategy Runner" mode executes all tasks within a stage simultaneously, and if any task fails, the entire stage is retried. Moreover, this mode allows for communication among tasks within the same stage. Although this scheduling model improves efficiency for deep learning frameworks, it is still less optimal than the barrier execution mode. Therefore, Spark 3.x introduces barrier execution mode with the Mirrored-Strategy Runner to optimize distributed deep learning, offering an advantage over the standard Map/Reduce model [8], [9].

The primary steps of the proposed system architecture, as shown in Fig. 2, include image preparation, preprocessing, and large-scale COVID-19 image classification.

4.2 Step 1: Dataset preparation and preprocessing

The first step involves preparing and processing the dataset for training. To train the Deep Convolutional Neural Network (DCNN) model, a set of labeled images is required.

4.2.1 Dataset preparation

The process begins by loading a large collection of COVID-19 chest X-ray images from the Hadoop Distributed File System (HDFS) [42], [24], which stores a massive number of images in a distributed computing architecture. These images are subsequently divided into multiple equal-sized chunks. Each chunk is duplicated in an HDFS data node within our master-slave architecture. Once the data is loaded and partitioned, a set of Spark workers processes the individual images from each chunk.

4.2.2 Dataset preprocessing

Each Spark worker performs parallel preprocessing on its assigned chunk of COVID-19 images using the Keras `ImageDataGenerator`. This method enables real-time image preprocessing by loading the image dataset into memory and generating batches of preprocessed data. By utilizing this approach, image preprocessing occurs dynamically during the training process, which allows for better memory management. This dynamic generation of preprocessed images helps in handling large datasets efficiently.

Several preprocessing techniques are employed in medical imaging applications to enhance the quality of images. For COVID-19 image analysis, essential preprocessing methods include image resizing, image enhancement, and image segmentation [35]. In this study, we primarily use image resizing to standardize the COVID-19 chest X-ray images. Image resizing is necessary to reduce computational costs and processing time, as large pixel sizes can significantly increase the time required for training [11]. During preprocessing, images are resized to 128x128 pixels and transformed into a NumPy array compatible with Keras, ensuring better recognition performance in the DCNN model.

4.3 Step 2: COVID-19 image classification

In this phase, deep learning methods are applied using Apache Spark to accelerate the training and classification processes on a large-scale COVID-19 image dataset. The Deep Convolutional Neural Network (DCNN) architecture is employed to train and classify chest X-ray images, categorizing them into COVID-19 and non-COVID-19 groups. The DCNN model is constructed and compiled using the Spark-TensorFlow-Distributor framework. The DCNN has achieved significant advancements in various pattern recognition tasks, including image classification [33]. The modern DCNN architecture consists of al-

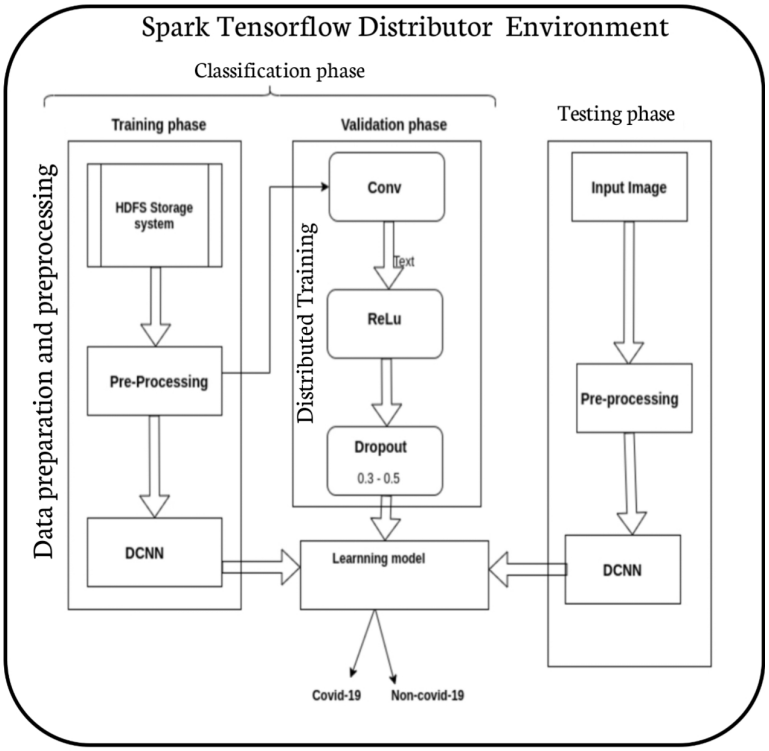

Figure 2: Architecture of our proposed system

ternating convolutional layers (CL) and max-pooling (MP) layers, followed by fully connected layers (FC).

In the first convolutional layer, an activation map of size $128\times128\times32$ is generated after applying 32 filters. The output of this layer is passed to the max-pooling layer, where 2×2 filters are used to perform down-sampling. The second convolutional layer takes the output from the first layer, which has a size of $64\times64\times32$, and applies 64 filters, resulting in an activation map of size $64\times64\times64$. Another max-pooling layer with a 2×2 window is applied, reducing the size to $32\times32\times64$. Subsequently, a third convolutional layer with 128 filters produces an activation map of size $16\times16\times128$, followed by another max-pooling layer that reduces the size to $8\times8\times128$. The final convolutional layer applies 256 filters to this output, producing a $4\times4\times256$ volume. A fully connected layer with 1200 neurons is then applied, followed by the output layer with a single neuron.

For activation functions, we use the Rectified Linear Unit (ReLU) for all layers except the final one. The ReLU function is commonly used in classification tasks, as it activates the convolutional layers by outputting the input directly if it is positive, and zero otherwise. Mathematically, ReLU is defined as:

$$f(x) = \max(0, x) \tag{1}$$

ReLU introduces non-linearity into the model, allowing it to learn complex patterns, while being computationally efficient compared to other activation functions. For the final output layer, we use the sigmoid function, which transforms real-valued inputs to a range between 0 (non-COVID-19) and 1 (COVID-19), making it suitable for binary classification tasks. The sigmoid function is mathematically defined as:

$$f(x) = \frac{1}{1 + e^{-x}} \tag{2}$$

4.3.1 Pooling layer

The pooling layer serves as a down-sampling technique used to reduce the spatial dimensions of each feature map while retaining essential information. Max-pooling is the most commonly used type of pooling, where the maximum value from a group of values is selected. In our model, each feature map undergoes processing with a 2×2 max-pooling layer, which reduces the dimensionality and highlights the most important features. This operation helps to decrease computational complexity and focuses on the relevant features within the image.

4.3.2 Flattening layer

The flattening layer converts the multi-dimensional output from the preceding convolutional or pooling layers into a one-dimensional array, which is then fed into the fully connected layers. This transformation allows the network to make predictions based on the features learned in previous layers. In our DCNN architecture, we use a fully connected

layer with 1300 neurons, followed by an output layer with a single neuron.

4.3.3 Dropout layer

To mitigate overfitting during training, we use a dropout layer in the DCNN architecture. In each training iteration, a random selection of neurons is temporarily omitted with a specified probability. This regularization technique helps improve the model's ability to generalize to unseen data by reducing reliance on specific neurons. In our model, we applied a dropout rate of 0.3 in the convolutional layers and 0.5 in the fully connected layers.

4.3.4 Optimizer

For optimizing the model, we employed the Adaptive Moment Estimation (Adam) optimizer. Adam dynamically adjusts the network's weights during training based on the provided data. It is particularly advantageous for networks that handle large datasets and parameters, offering efficiency in both computation and memory usage.

4.3.5 Model training

We carefully optimized the hyperparameters for our learning approach by evaluating other complex architectures, such as Artificial Neural Networks (ANN), AlexNet, and DCNN. Hyperparameter tuning was conducted for each model by adjusting key parameters such as learning rate, batch size, and weight decay to achieve optimal performance. For the DCNN model, this process was repeated extensively to refine the hyperparameters, ensuring the best possible performance in terms of classification accuracy.

5 Classification performance

To evaluate the performance of our Deep Convolutional Neural Network (DCNN) model, we employed various metrics. A confusion matrix was utilized to assess the model's performance, that includes the following four key parameters:

- **True Positive (TP)**: The number of correctly predicted positive samples.
- **True Negative (TN)**: The number of correctly predicted negative samples.
- **False Positive (FP)**: The number of incorrectly predicted positive samples.
- **False Negative (FN)**: The number of incorrectly predicted negative samples.

5.1 Accuracy

Accuracy is a commonly used metric to evaluate the model's overall performance, representing the model's ability to correctly differentiate between classes in the test set. The accuracy is defined as:

$$\text{ACC} = \frac{TP + TN}{TP + FP + FN + TN} \tag{3}$$

As shown in Equation (3), accuracy is the proportion of correctly predicted labels over the total number of samples in the dataset.

5.2 Precision

Precision, as defined in Equation (4), represents the proportion of accurately predicted positive labels out of all predicted positive labels. It is a measure of the model's ability to avoid false positives:

$$\text{Precision} = \frac{TP}{TP + FP} \tag{4}$$

5.3 Recall

Recall, as defined in Equation (5), represents the ratio of correctly predicted positive labels to the total number of actual positive labels. It measures the model's ability to correctly identify positive instances:

$$\text{Recall} = \frac{TP}{TP + FN} \tag{5}$$

5.4 Specificity

Specificity, as shown in Equation (6), is used to measure the model's ability to accurately recognize negative instances, i.e., the proportion of correctly identified negative samples:

$$\text{Specificity} = \frac{TN}{FP + TN} \tag{6}$$

5.5 F1-score

The F1-score, as defined in Equation (7), is the harmonic mean of Precision and Recall. It provides a balance between the two metrics, particularly useful when the data is imbalanced:

$$\text{F1-score} = \frac{2 \times (\text{Recall} \times \text{Precision})}{\text{Recall} + \text{Precision}} \tag{7}$$

The F1-score is particularly useful for evaluating the overall performance when there is an uneven class distribution between the positive and negative classes.

5.6 Area under the curve (AUC)

The Area Under the Curve (AUC) is a performance metric that evaluates the ability of the model to distinguish between positive and negative classes. Specifically, the AUC measures the area under the Receiver Operating Characteristic (ROC) curve. AUC values range from 0 to 1, with higher values indicating better model performance. An AUC value of 0.5 indicates a model with no discrimination ability (random guessing), while a value of 1.0 represents perfect classification performance.

$$\text{AUC} = \int_0^1 \text{ROC Curve} \tag{8}$$

5.7 Matthews correlation coefficient (MCC)

The Matthews Correlation Coefficient (MCC) is a metric used to evaluate the quality of binary classifications. It considers all four components of the confusion matrix (TP, TN, FP, FN) and is particularly useful when the classes are imbalanced. The MCC is defined as:

$$\text{MCC} = \frac{TP \cdot TN - FP \cdot FN}{\sqrt{(TP+FP)(TP+FN)(TN+FP)(TN+FN)}} \tag{9}$$

MCC values range from -1 to +1. A value of +1 indicates perfect classification, while -1 indicates total disagreement between the predicted and actual labels. A value of 0 indicates no better performance than random classification.

5.8 Cohen's kappa

Cohen's Kappa is a statistic that measures inter-rater agreement for categorical items. It is used to assess the agreement between two raters or classifiers and adjusts for the possibility of random chance. Cohen's Kappa is defined as:

$$\kappa = \frac{P_o - P_e}{1 - P_e} \tag{10}$$

Where: - P_o is the observed agreement (proportion of times the model's predictions match the true labels). - P_e is the expected agreement (proportion of times the labels would match due to chance).

Kappa values range from -1 to 1, where 1 indicates perfect agreement, 0 indicates agreement no better than chance, and negative values indicate less agreement than would be expected by chance.

6 Experimental results

6.1 Environment description

To evaluate the performance of the proposed method, we utilized a chest X-ray (CXR) image dataset sourced from Kaggle [6]. his dataset consists of 13,808 CXR images, which were used for both training and testing our model. The images were categorized into two classes: COVID-19 and non-COVID-19. The implementation was carried out using the Apache Spark framework on a single-node cluster (standalone setup). The specifications of the cluster are as follows:

- **Software Environment**: Ubuntu 18.04 LTS, Spark 3.0.1, Keras, Python 7.13, and TensorFlow 2.7.
- **Hardware Environment**: Intel Core i5-4210U CPU with a 1.70 GHz clock speed (4 cores) and 8 GB of RAM.

Presentation of the dataset

Access to large-scale COVID-19 datasets for non-commercial research is often limited due to privacy concerns. As a result, many studies in this area rely on smaller, publicly available datasets. For this study, we employed a comprehensive dataset available on Kaggle, which includes chest X-ray (CXR) images of COVID-19-positive and pneumonia cases. This dataset, curated by a collaborative team from the University of Qatar, Bangladesh, Pakistan, and Malaysia, in partnership with medical experts, contains 13,808 PNG-format CXR images, each with a resolution of 299 pixels.

For the analysis, we focused on a subset of 12,000 X-ray images, consisting of 3,000 COVID-19 cases and 9,000 non-COVID-19 cases. Due to the inherent class imbalance in the dataset, with fewer COVID-19 samples, an image augmentation technique was applied to increase the number of COVID-19 images. The augmentation methods, which included image shifts, flips, and rotations, resulted in a total of 18,000 images (9,000 COVID-19 and 9,000 non-COVID-19). The dataset was then partitioned into 80% for training and 20% for testing, as suggested in [10]. The training set contained 14,400 images, equally distributed between the two classes (7,200 COVID-19 and 7,200 non-COVID-19), while the testing set included 3,600 images (1,800 from each class). This balanced approach ensured robust training and evaluation of the model.

6.2 Results and discussion

Table 2 presents the results of training and testing the Artificial Neural Network (ANN) model with a dropout rate of 0.25 on the 18000 chest X-ray (CXR) dataset. The metrics included are the training and testing accuracy, test epoch time, and overall training time for different batch sizes. It is observed that the highest testing accuracy (84.62%) is achieved with a batch size of 16, which required a training time of 49 minutes. As the batch size increased to 32, the test accuracy declined significantly to 50%, despite a slight reduction in training time (48 minutes 23 seconds). Furthermore, with a batch size of 100, the test accuracy decreased to 64.89%, and the training time was further reduced to 47

[6]COVID-19 Radiography Database. COVID-19 Chest X-ray images and Lung masks Database. https://www.kaggle.com/datasets/tawsifurrahman/covid19-radiography-database/data

Table 2: The effect of batch size on the ANN model with 13,808 CXR dataset

Batch Size	Accuracy of Training (%)	Test Accuracy (%)	Test Epoch Time	Training Time
16	99.79	84.62	53s	49 min
32	98.80	50.00	42s	48 min 23s
100	99.84	64.89	35s	47 min 25s

minutes 25 seconds. These results indicate that increasing the batch size from 16 to 100 improved training efficiency by reducing training time but negatively impacted model accuracy.

Table 3 compares the training and testing times, along with the accuracy of the ANN model, for various numbers of epochs with a dropout rate of 0.25. It is evident that the number of epochs has no significant effect on the training accuracy of the ANN model, which reaches 100% after eight epochs. However, the testing accuracy fluctuates across different epoch values, peaking at 84.62% after six epochs. The primary impact of increasing the number of epochs is on training time, where longer training durations are observed as the epoch count increases, highlighting a trade-off between computational time and performance.

Table 4 shows the impact of different epoch counts on the performance of the DCNN model, without dropout, using a batch size of 32. The results reveal that while training accuracy remains high at 100% from 18 epochs onwards, testing accuracy improves with an increasing number of epochs and stabilizes at 91.88% after 100 epochs. Notably, training time increases with the number of epochs, with the longest duration recorded at 5 hours, 28 minutes, and 50 seconds for 100 epochs. The testing accuracy shows a clear trend: it is lowest at 60.43% after just 2 epochs, increases gradually to 70.73% at 25 epochs, and reaches the optimal value of 91.88% after 100 epochs. This indicates that while longer training times are necessary for optimal classification performance, the model benefits from additional epochs, especially when the number of epochs exceeds 18.

Table 5 illustrates the effect of dropout rates on the accuracy of the DCNN model using the same dataset and batch size of 32. The results demonstrate that increasing dropout rates in both the convolutional layer (CL) and fully connected layer (FC) improves the model's classification accuracy. The highest accuracy of 95.53% was achieved with a dropout rate of 0.3 in the CL and 0.5 in the FC layer. For lower dropout rates (0.0 to 0.2 in both layers), the accuracy is relatively lower, fluctuating between 90.53% and 93.50%. However, introducing dropout rates of 0.3 or 0.4 in the CL and FC layers significantly boosts the model's performance, with the optimal result observed at a dropout rate of 0.3 in the CL and 0.5 in the FC layer. The findings indicate that regularization using dropout not only prevents overfitting but also contributes significantly to improved generalization, thus enhancing the model's overall classification capability. The results suggest that a balanced dropout strategy (e.g., 0.3 in CL and 0.5 in FC) yields the best performance, while further increasing the dropout rate in the FC layer beyond 0.5 may lead to diminishing returns in accuracy.

Table 7 details the optimized architecture of the deep convolutional neural network (DCNN), achieving a peak accuracy of 95.53% through systematic hyperparameter tuning and refinement. The learning rate was set to **0.001**, striking a balance between convergence speed and stability. The Adam optimizer was employed, leveraging the combined benefits of AdaGrad and RMSProp to ensure efficient and adaptive gradient updates. To enhance generalization, **dropout rates** were configured at **0.3** for convolutional layers and **0.5** for fully connected layers, preventing overfitting. A **batch size of 32** was chosen, providing a balance between training speed and model performance. Additionally, **weight decay (0.0001)** was incorporated to further regularize the model. The DCNN architecture consisted of multiple convolutional layers, progressively increasing the number of filters from **32** in the first layer to **256** in the final convolutional layer. Each convolutional layer was followed by a **2×2 max-pooling layer**, aiding in feature extraction and dimensionality reduction. The fully connected layers consisted of **1200 neurons**, with a **sigmoid activation function in the output layer**, suitable for binary classification. Regularization techniques, including dropout, weight decay, and max-pooling, were employed to enhance robustness. The model was trained using the **spark-tensorflow-distributor framework**, leveraging distributed computing for efficient training on large datasets. Furthermore, as illustrated in Table 6, our proposed system, which employs a DCNN model with the fine-tuning configuration detailed in Table 7, achieved the following results:

To provide a more comprehensive evaluation, we included the following metrics:

- **Area Under the Curve (AUC)**: The ROC curve was plotted, and the AUC was calculated to be **0.98**, indicating excellent discriminative ability.
- **Matthews Correlation Coefficient (MCC)**: The MCC value of **0.93** highlights the model's balanced performance, especially for imbalanced datasets.
- **Cohen's Kappa**: A value of **0.92** was obtained, indicating strong agreement between predicted and actual labels, adjusted for chance.

Table 3: Study of the effect of epochs on the ANN model

Epochs	Training Accuracy (%)	Test Accuracy (%)	Time of Epoch Test	Training Time
2	96.89	67.45	55 sec	16 min 12 sec
4	98.59	84.46	54 sec	32 min 5 sec
6	99.79	84.62	53 sec	48 min
8	100	75.87	59 sec	1h 3 min 52 sec
10	100	72.60	56 sec	1h 19 min 39 sec
14	100	70.13	55 sec	1h 51 min 33 sec
18	100	72.29	54 sec	2h 28 min 5 sec
20	100	70.65	55 sec	2h 45 min 5 sec

Table 4: Study of the effect of epochs on the DCNN model with 13,808 CXR dataset

Number of Epochs	Training Accuracy (%)	Training Time	Testing Accuracy (%)	Testing Time
2	88.79	4 min 4 sec	60.43	51 sec
4	95.89	8 min 15 sec	61.88	49 sec
8	70.10	16 min 33 sec	70.41	50 sec
18	100	43 min 48 sec	69.73	51 sec
25	100	58 min 50 sec	70.73	52 sec
100	100	5 h 28 min 50 sec	91.88	50 sec

Table 5: Study of the dropout effect on the DCNN model

Dropout in CL	Dropout in FC	Accuracy
0.0	0.0	90.53
0.0	0.1	90.69
0.0	0.2	90.88
0.0	0.5	90.73
0.1	0.0	92.40
0.1	0.1	92.55
0.1	0.2	92.16
0.2	0.0	92.66
0.2	0.1	92.88
0.2	0.2	92.95
0.2	0.5	93.50
0.3	0.0	93.96
0.3	0.1	94.60
0.3	0.2	94.99
0.3	0.5	95.53
0.4	0.0	95.06
0.4	0.1	93.89
0.4	0.2	93.54
0.4	0.5	92.33

Table 6: Performance metrics of the proposed model

Metric	Value
Sensitivity (Recall)	0.94
Specificity	0.96
Precision	0.95
Accuracy	0.9553
F1-Score	0.95
Training Time (seconds)	18909
Testing Time per Image (seconds)	0.006
Number of Images	18000

The tables 8 and 9 present the effects of batch size and dropout rates at the fully connected (FC) layer on the AlexNet model using CXR images. The results indicate that neither batch size nor dropout significantly impacts accuracy or training time in this architecture. The highest classification accuracy, 73.8%, was consistently achieved across various configurations, with minimal variation in training time. For example, a batch size of 16 achieved 73.8% accuracy with a training time of 1 hour, 16 minutes, and 45 seconds, while other batch sizes produced similar results.

Figures 3 and 4 present a comparison of training durations for the DCNN and ANN models. The DCNN achieved optimal performance with a training time of 18,909 seconds (approximately 5 hours and 15 minutes) over 100 epochs, attaining a recognition accuracy of 91.88%. In contrast, the ANN model required significantly

Table 7: Summary of hyperparameters and fine-tuning strategies for deep convolutional neural network (DCNN) model

Parameter	Value/Description
Learning Rate	0.001
Dropout Rates	- Convolutional Layers (CL): 0.3 - Fully Connected Layers (FC): 0.5
Optimizer	Adam (combines AdaGrad and RMSProp)
Batch Size	32
Weight Decay	0.0001
Convolutional Layers	- 1st CL: 32 filters, output: 128x128x32 - 2nd CL: 64 filters, output: 64x64x64 - Final CL: 256 filters, output: 4x4x256
Max-Pooling Layers	2x2 window size
Fully Connected Layers	- FC layers: 1200 neurons - Output layer: 1 neuron
Activation Functions	- ReLU for all layers except output - Sigmoid for output layer
Training Framework	spark-tensorflow-distributor
Regularization Techniques	- Dropout layers - Weight decay - Max-pooling for dimensionality reduction

Table 8: Study of the batch effect with a dropout of 0.4 on the AlexNet model

Batch Size	Training Accuracy (%)	Training Time	Testing Accuracy (%)	Epoch Time	Loss Function
16	73.82	1h 16m 45s	73.8	52s	0.575
60	73.82	1h 16m 50s	73.8	59s	0.57
128	68.78	1h 20m 45s	73.8	55s	0.60
300	73.50	1h 15m 56s	73.8	53s	0.60
500	73.79	1h 16m 50s	73.8	52s	0.60

less training time of 1,960 seconds (approximately 33 minutes) over 6 epochs—to achieve an accuracy of 84.62%, both utilizing a batch size of 32. Additionally, these experiments examined the effect of memory allocation per executor. When memory allocation exceeded 2,048 MB, training times for both the DCNN and ANN decreased substantially. Conversely, when memory allocation was below this threshold, training times increased notably.

6.3 Performance comparison with state-of-the-art models

Table 10 compares the performance of various COVID-19 detection models using chest X-ray images, highlighting key metrics such as sensitivity, specificity, precision, accuracy, F1-score, and computational efficiency. Among the 2020 models, COVID-Net and COVID-CAPS demonstrated moderate accuracy (85% and 95%, respectively), while Shashank's method (2020) achieved high accuracy (96%) and F1-score (97%). VGG19 and DenseNet201 (2020) showed perfect specificity and precision but lower sensitivity (83%), whereas ResNetV2 variants and MobileNetV2 (2020) struggled with specificity-

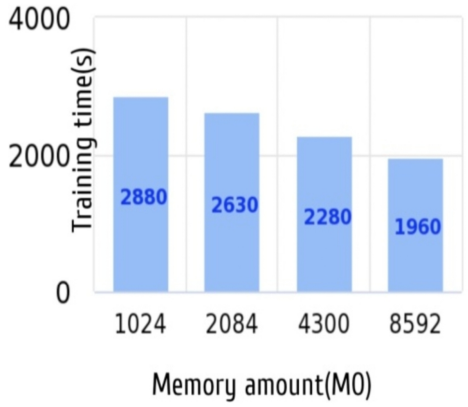

Figure 3: Impact of amount memory Spark's on the training time of ANN method (where the best training time is 1960s for 6 epochs) using memory size of 8592MO

Table 9: Study of the dropout effect with 5 layers and 16 batches on the AlexNet model

Dropout in FC	Training Accuracy (%)	Testing Accuracy (%)	Epoch's Test Time	Training Time
(0.2, 0.3, 0.4)	73.82	73.8	52 sec	1h 18m 30s
(0.4, 0.4, 0.2)	73.06	73.8	52 sec	1h 16m 41s
(0.4, 0.4, 0.4)	73.82	73.8	53 sec	1h 19m 30s

Table 10: Comparison between our proposed approach with 13808 CXR and related works

Method	Year	Sensitivity	Specificity	Precision	Accuracy	F1-Score	Training time	Testing time	Images
COVID-Net [43]	2020	0.90	0.80	-	0.85	0.22	-	-	447
COVID-CAPS [44]	2020	0.90	0.95	-	0.95	-	-	-	-
Shashank [45]	2020	0.98	0.91	0.96	0.96	0.97	-	-	364
VGG19 [32]	2020	0.83	1.00	1.00	0.90	0.81	2641	4.0	50
CovidGAN [46]	2020	0.95	0.94	0.90	0.94	0.92	-	-	192
ResNet50 [25]	2020	-	1.00	1.00	0.98	0.98	-	-	2800
DenseNet201 [32]	2020	0.83	1.00	1.00	0.90	0.81	2122	6.00	50
ResNetV2 [32]	2020	1.00	0.62	0.40	0.70	0.57	1086	2.00	50
-ResNetV2 [32]	2020	1.00	0.71	0.60	0.80	0.75	1988	6.00	50
Xception [32]	2020	1.00	0.71	0.60	0.80	0.75	2035	3.00	50
MobileNetV2 [32]	2020	1.00	0.55	0.20	0.60	0.33	389	1.00	50
Inception [10]	2021	0.93	0.97	0.97	0.96	0.96	1800	0.014	3760
VGG16 (Fine Tuning) [47]	2020	-	-	-	0.8526	-	-	-	380
RESNET18 (Fine Tuning) [47]	2020	-	-	-	0.8842	-	-	-	380
RESNET101 (Fine Tuning) [47]	2020	-	-	-	0.8737	-	-	-	380
RESNET50 (Fine Tuning) [47]	2020	-	-	-	0.9263	-	-	-	380
VGG19 (Fine Tuning) [47]	2020	-	-	-	0.8947	-	-	-	380
AlexNet [48]	2021	0.9388	-	0.9518	0.9479	0.9021	-	-	100
GoogleNet [48]	2021	0.9338	-	0.9512	0.8889	0.9485	-	-	100
DenseNet201 [48]	2021	0.9285	-	0.9785	0.9056	0.8608	-	-	100
ResNet18 [48]	2021	0.8913	-	0.9591	0.8728	0.9407	-	-	100
ResNet50 [48]	2021	0.8819	-	0.9828	0.9455	0.9069	-	-	100
Inceptionv3 [48]	2021	0.8925	-	0.8928	0.9640	0.9411	-	-	100
VGG16 [48]	2021	0.8905	-	0.9480	0.9651	0.9585	-	-	100
XceptionNet [48]	2021	0.9411	-	0.8919	0.8874	0.8919	-	-	100
VGG19 [48]	2021	0.8863	-	0.9658	0.8886	0.9104	-	-	100
Inceptionresnetv2 [48]	2021	0.9122	-	0.9375	0.9681	0.9213	-	-	100
Inceptionresnetv3 [25]	2021	-	0.9740	0.8240	0.9770	0.9030	16027	-	3141
ResNet101 [25]	2021	-	0.9990	0.9890	0.9470	0.6860	17841	-	3141
ResNet152 [25]	2021	-	0.98	0.7570	0.9280	0.6090	18802	-	3141
Inception-ResNetV2 [25]	2021	-	0.9830	0.84	0.9530	0.7680	23078	-	3141
VGG 16 [53]	2023	0.96	-	0.96	0.96	0.96	-	-	6000
Inceptionresnetv3 [53]	2023	0.91	-	0.91	0.91	0.90	-	-	6000
ResNet [53]	2023	0.98	-	0.98	0.98	0.98	-	-	6000
VGG 19 [53]	2023	0.89	-	0.96	0.96	0.92	-	-	6000
Ensemble learning on Spark [54]	2023	-	-	-	0.9431	-	-	-	6500
Proposed Model	2025	0.94	0.96	0.95	0.9553	0.95	18909	0.006	18000

precision trade-offs despite high sensitivity. Models from 2021, such as Inception [10] and InceptionResNetV2 [25], delivered strong accuracy (96–97.7%) but required extensive training times (e.g., 16,027–23,078 seconds). In 2023, ResNet [53] achieved near-perfect accuracy (98%) and F1-score (98%), while the proposed 2024 model stands out with balanced performance: 95.53% accuracy, 0.94 sensitivity, 0.96 specificity, and a remarkably low testing time (0.006 seconds), despite a longer training time (18,909 seconds) likely due to its large dataset (18,000 images). Computational efficiency is a key differentiator, with the proposed model's sub-second testing time outperforming older architectures like VGG19 (4 seconds) and ResNet50 (unreported but likely higher). While some models (e.g., ResNet50 [25] in 2020) achieved higher specificity (100%), the proposed model's balanced metrics, scalability, and real-time inference capabilities position it as a robust solution for clinical deployment, particularly when compared to fine-tuned models like RESNETFine50 (92.63% accuracy) or ensemble methods (94.31% accuracy). Its combination of high accuracy, competitive F1-score (95%), and minimal latency underscores its suitability for rapid, large-scale diagnostic applications.

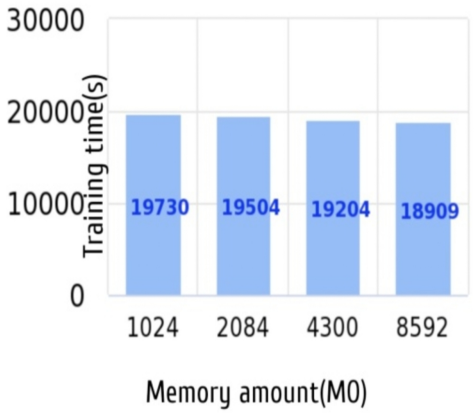

Figure 4: Impact of amount memory Spark's on the training time of DCNN method (where the best training time is 18909s for 100 epochs) using memory size of 8592MO

7 Conclusion

In this paper, we have proposed an advanced method for COVID-19 detection using deep learning and big data analytics on large-scale chest X-ray images. By leveraging the power of distributed training with Spark-TensorFlow-Distributor, we have successfully accelerated the classification process, achieving high accuracy (95.53%) in minimal time (0.06s). Our approach significantly outperforms traditional models, such as ANN and AlexNet, in terms of both classification accuracy and processing time. The integration of the distributed DCNN model with Spark's in-memory computation capabilities enables efficient handling of large-scale data, facilitating rapid and scalable training of deep learning models.

We have demonstrated the effectiveness of our system by comparing it with other state-of-the-art methods, highlighting its superior performance in terms of training and testing time. This work emphasizes the potential of combining deep learning and big data frameworks for real-time, large-scale COVID-19 detection, contributing to the timely identification of infected individuals and supporting public health efforts.

7.1 Limitations

Our approach benefits from distributed computing but is limited by infrastructure availability, requiring significant resources for large-scale deployment. The model's generalizability is constrained by its training on a specific chest X-ray dataset, and performance on diverse medical imaging data requires further evaluation. Training deep neural networks demands high-performance GPUs or TPUs, and real-time applications may require dedicated computing environments.

7.2 Future Scope

In our future research, we intend to explore further hyperparameters, such as the quantity of CL and filter dimensions, to improve the recognition capabilities of our DCNN-based method on our database. Furthermore, we intend to evaluate our model on a more extensive dataset and deploy it on large computing clusters to increase the validity of our results while optimizing our proposal through various optimization techniques referenced in [49], [50], [51], and [52].

References

[1] Lingguo Zou, Meihua Zhang (2023) Variational Autoencoder Model Combining Deep Learning and Statistical Methods for COVID-19 Detection, *Informatica*, pp. nn–mm. https://doi.org/10.31449/inf.v48i22.6921

[2] Riswantini, D., Nugraheni, E., Arisal, A., Khotimah, P. H., Munandar, D., and Suwarningsih, W. (2021). Big data research in fighting COVID-19: Contributions and techniques. *Big Data and Cognitive Computing*, 5(3), 30–89. https://doi.org/10.3390/bdcc5030030.

[3] Kaleem, S., Sohail, A., Tariq, M. U., Babar, M., and Qureshi, B. (2023). Ensemble learning for multi-class COVID-19 detection from big data. *PLOS ONE*, 18(10), e0292587. https://doi.org/10.1371/journal.pone.0292587.

[4] G. Nagarajan and D. B. L. D. (2019) Predictive analytics on big data-an overview, *Informatica*, 43(4), 425-459. https://doi.org/10.31449/inf.v43i4.2577

[5] Benbrahim, H., Hachimi, H., and Amine, A. (2020). Deep transfer learning with Apache Spark to detect COVID-19 in chest X-ray images. *Romanian Journal of Information Science and Technology*, 23(S, SI), S117–S129. https://www.romjist.ro/volumes/2020/23S/23S117.pdf.

[6] J. Sheng, J. Amankwah□Amoah, Z. Khan, and X. Wang (2021) COVID□19 pandemic in the new era of big data analytics: Methodological innovations and future research directions, *British Journal of Management*, 32(4), 1164-1183. https://doi.org/10.1111/1467-8551.12441

[7] Gaur, L., Bhatia, U., Jhanjhi, N. Z., Muhammad, G., and Masud, M. (2023). Medical image-based detection of COVID-19 using deep convolution neural networks. *Multimedia Systems*, 29(3), 1729–1738. https://doi.org/10.1007/s00542-022-06756-0.

[8] Alsunaidi, S. J., Almuhaideb, A. M., Ibrahim, N. M., Shaikh, F. S., Alqudaihi, K. S., Alhaidari, F. A., and Alshahrani, M. S. (2021). Applications of big data

analytics to control COVID-19 pandemic. *Sensors*, 21(7), 2282. https://doi.org/10.3390/s21072282.

[9] Tahmassebi, A., Ehtemami, A., Mohebali, B., Gandomi, A. H., Pinker, K., and Meyer-Baese, A. (2019). Big data analytics in medical imaging using deep learning. In *Big Data: Learning, Analytics, and Applications* (pp. 86–101). Springer. https://doi.org/10.1007/978-3-030-15756-3$_7$.

[10] Panahi, A. H., Rafiei, A., and Rezaee, A. (2021). FCOD: Fast COVID-19 Detector based on deep learning techniques. *Informatics in Medicine Unlocked*, 22, 100506. https://doi.org/10.1016/j.imu.2021.100506.

[11] Ayalew, A. M., Salau, A. O., Tamyalew, Y., Abeje, B. T., and Woreta, N. (2023). X-ray image-based COVID-19 detection using deep learning. *Multimedia Tools and Applications*, 1–19. https://doi.org/10.1007/s11042-023-15556-2.

[12] Sarp, S., Catak, F. O., Kuzlu, M., Cali, U., Kusetogullari, H., Zhao, Y., and Guler, O. (2023). An XAI approach for COVID-19 detection using transfer learning with X-ray images. *Heliyon*, 9(4), e14547. https://doi.org/10.1016/j.heliyon.2023.e14547.

[13] Sakr, A. S., Pawiak, P., Tadeusiewicz, R., Pawiak, J., Sakr, M., and Hammad, M. (2023). ECG-COVID: An end-to-end deep model based on electrocardiogram for COVID-19 detection. *Information Sciences*, 619, 324–339. https://doi.org/10.1016/j.ins.2022.10.029.

[14] Siddique, A. A., Talha, S. U., Aamir, M., Algarni, A. D., Soliman, N. F., and El-Shafai, W. (2023). COVID-19 classification from X-ray images: An approach to implement federated learning on decentralized dataset. *Computers, Materials Continua*, 3883–3901. https://doi.org/10.32604/cmc.2023.029907.

[15] Heymann, D. L., & Shindo, N. (2020) COVID-19: what is next for public health?, *The Lancet*, 395(10224), 542–545. https://doi.org/10.1016/S0140-6736(20)30374-3.

[16] Sohrabi, C., Alsafi, Z., O'Neill, N., Khan, M., Kerwan, A., Al-Jabir, A., & Agha, R. (2020) World Health Organization declares global emergency: A review of the 2019 novel coronavirus (COVID-19), *International Journal of Surgery*, 76, 71–76. https://doi.org/10.1016/j.ijsu.2020.02.034.

[17] Huang, P., Liu, T., Huang, L., Liu, H., Lei, M., Xu, W., ... & Liu, B. (2020) Use of chest CT in combination with negative RT-PCR assay for the 2019 novel coronavirus but high clinical suspicion, *Radiology*, 295(1), 22–23. https://doi.org/10.1148/radiol.2020200330.

[18] Ng, M. Y., Lee, E. Y., Yang, J., Yang, F., Li, X., Wang, H., ... & Kuo, M. D. (2020) Imaging profile of the COVID-19 infection: radiologic findings and literature review, *Radiology: Cardiothoracic Imaging*, 2(1), e200034. https://doi.org/10.1148/ryct.2020200034.

[19] Tian, X., Wang, J., Du, D., Li, S., Han, C., Zhu, G., ... & Lei, M. (2020) Medical imaging and diagnosis of subpatellar vertebrae based on improved Laplacian image enhancement algorithm, *Computer Methods and Programs in Biomedicine*, 187, 105082. https://doi.org/10.1016/j.cmpb.2019.105082.

[20] Solomon, M. D., McNulty, E. J., Rana, J. S., Leong, T. K., Lee, C., Sung, S. H., ... & Go, A. S. (2020) The Covid-19 pandemic and the incidence of acute myocardial infarction, *New England Journal of Medicine*, 383(7), 691–693. https://doi.org/10.1056/NEJMc2015630.

[21] Daniel, S. J. (2020) Education and the COVID-19 pandemic, *Prospects*, 49(1), 91–96. https://doi.org/10.1007/s11125-020-09464-3.

[22] Spinelli, A., & Pellino, G. (2020) COVID-19 pandemic: perspectives on an unfolding crisis, *Journal of British Surgery*, 107(7), 785–787. https://doi.org/10.1002/bjs.11627.

[23] Saliha, M., Ali, B., & Rachid, S. (2019) Towards large-scale face-based race classification on spark framework, *Multimedia Tools and Applications*, 78(18), 26729–26746. https://doi.org/10.1007/s11042-018-7080-0.

[24] Mezzoudj, S., Behloul, A., Seghir, R., & Saadna, Y. (2021) A parallel content-based image retrieval system using spark and tachyon frameworks, *Journal of King Saud University-Computer and Information Sciences*, 33(2), 141–149. https://doi.org/10.1016/j.jksuci.2018.03.010.

[25] Narin, A., Kaya, C., & Pamuk, Z. (2021) Automatic detection of coronavirus disease (COVID-19) using x-ray images and deep convolutional neural networks, *Pattern Analysis and Applications*, 24(6), 1207–1220. https://doi.org/10.1007/s10044-021-00984-y.

[26] Viceconti, M., Hunter, P., & Hose, R. (2015) Big data, big knowledge: big data for personalized healthcare, *IEEE Journal of Biomedical and Health Informatics*, 19(4), 1209–1215. https://doi.org/10.1109/JBHI.2015.2406883.

[27] Benbrahim, H., Hachimi, H., & Amine, A. (2020) Deep transfer learning with apache spark to detect COVID-19 in chest X-ray images, *Romanian Journal of Information Science and Technology*, 23(SI), S117–S129.

[28] Gupta, V. K., Gupta, A., Kumar, D., & Sardana, A. (2021) Prediction of COVID-19 confirmed, death, and cured cases in India using random forest model, *Big Data Mining and Analytics*, 4(2), 116–123. https://doi.org/10.26599/BDMA.2020.9020012.

[29] Wang, L., Lin, Z. Q., & Wong, A. (2020) COVID-Net: A tailored deep convolutional neural network design for detection of COVID-19 cases from chest x-ray images, *Scientific Reports*, 10(1), 19549. https://doi.org/10.1038/s41598-020-76550-z.

[30] Agbehadji, I. E., Awuzie, B. O., Ngowi, A. B., & Millham, R. C. (2020) Review of big data analytics, artificial intelligence and nature-inspired computing models towards accurate detection of COVID-19 pandemic cases and contact tracing, *International Journal of Environmental Research and Public Health*, 17(15), 5330. https://doi.org/10.3390/ijerph17155330.

[31] Basu, S., Mitra, S., & Saha, N. (2020) Deep learning for screening COVID-19 using chest x-ray images, In *2020 IEEE Symposium Series on Computational Intelligence (SSCI)*, IEEE, pp. 2521–2527. https://doi.org/10.48550/arXiv.2004.10507

[32] Hemdan, E. E. D., Shouman, M. A., and Karar, M. E. (2020). COVIDX-Net: A Framework of Deep Learning Classifiers to Diagnose COVID-19 in X-Ray Images. *arXiv preprint arXiv:2003.11055*. https://doi.org/10.48550/arXiv.2003.11055

[33] Krizhevsky, A., Sutskever, I., and Hinton, G. E. (2012). ImageNet Classification with Deep Convolutional Neural Networks. *Advances in Neural Information Processing Systems*, 25, 1097–1105. https://doi.org/10.1145/3065386

[34] Dean, J., and Ghemawat, S. (2008). MapReduce: Simplified Data Processing on Large Clusters. *Communications of the ACM*, 51(1), 107–113. https://doi.org/10.1145/1327452.1327492

[35] Duran-Lopez, L., Dominguez-Morales, J. P., Corral-Jaime, J., Vicente-Diaz, S., and Linares-Barranco, A. (2020). COVID-XNet: A Custom Deep Learning System to Diagnose and Locate COVID-19 in Chest X-Ray Images. *Applied Sciences*, 10(16), 5683. https://doi.org/10.3390/app10165683

[36] Lopez-Cabrera, J. D., Orozco-Morales, R., Portal-Diaz, J. A., et al. (2021). Current Limitations to Identify COVID-19 Using Artificial Intelligence with Chest X-Ray Imaging. *Health and Technology*, 11(2), 411–424. https://doi.org/10.1007/s12553-021-00609-8

[37] Karau, H., Konwinski, A., Wendell, P., and Zaharia, M. (2015). *Learning Spark: Lightning-Fast Big Data Analysis*. O'Reilly Media, Inc.

[38] Xu, X., Tian, H., Zhang, X., Qi, L., He, Q., and Dou, W. (2022). DisCOV: Distributed COVID-19 Detection on X-Ray Images with Edge-Cloud Collaboration. *IEEE Transactions on Services Computing*, 15(3), 1206–1219. https://doi: 10.1109/TSC.2022.3142265

[39] Saadna, Y., Behloul, A., and Mezzoudj, S. (2019). Speed Limit Sign Detection and Recognition System Using SVM and MNIST Datasets. *Neural Computing and Applications*, 31(9), 5005–5015. https://doi.org/10.1007/s00521-018-03994-w

[40] Mezzoudj, S. (2020). Towards Large Scale Image Retrieval System Using Parallel Frameworks. In *Multimedia Information Retrieval*. IntechOpen. https://doi.org/ 10.5772/intechopen.94910

[41] Mezzoudj, S., and Melkemi, K. E. (2021). A Hybrid Approach for Shape Retrieval Using Genetic Algorithms and Approximate Distance. In *Research Anthology on Multi-Industry Uses of Genetic Programming and Algorithms* (pp. 205–222). IGI Global. https://doi.org/10.4018/IJCVIP.2018010105

[42] Borthakur, D. (2008). HDFS Architecture Guide. *Hadoop Apache Project*, 53(1-13), 2.

[43] Tartaglione, E., Barbano, A., Berzovini, C., Calandri, M., and Grangetto, M. (2020). Unveiling COVID-19 from Chest X-Ray with Deep Learning: A Hurdles Race with Small Data. *arXiv preprint arXiv:2004.05405*. https://doi.org/10.3390/ijerph17186933

[44] Afshar, P., Heidarian, S., Naderkhani, F., Oikonomou, A., Plataniotis, K. N., and Mohammadi, A. (2020). COVID-CAPS: A Capsule Network-Based Framework for Identification of COVID-19 Cases from X-Ray Images. http://dx.doi.org/10.1016/j.patrec.2020.09.010

[45] Vaid, S., Kalantar, R., and Bhandari, M. (2020). Deep Learning COVID-19 Detection Bias: Accuracy Through Artificial Intelligence. *International Orthopaedics*. https://doi.org/10.1007/s00264-020-04609-7

[46] Waheed, A., Goyal, M., Gupta, D., et al. (2020). COVIDGAN: Data Augmentation Using Auxiliary Classifier GAN for Improved COVID-19 Detection. *IEEE Access*, 8, 91916–91923. https://doi.org/10.1109/ACCESS.2020.2994762

[47] Ismael, A. M., and Sengur, A.: Deep Learning Approaches for COVID-19 Detection Based on Chest X-ray Images, *Expert Systems with Applications*, 114054 (2020). https://doi.org/10.1016/j.eswa.2020.114054

[48] Dhiman, G., Chang, V., Kant Singh, K., and Shankar, A.: Adopt: Automatic deep learning and optimization-based approach for detection of novel coronavirus COVID-19 disease using X-ray images, *Journal of Biomolecular Structure and Dynamics*, 1–13 (2021). https://doi.org/10.1080/07391102.2021.1875049

[49] Nassima Dif, Zakaria Elberrichi (2023) An Efficient Transferred Cascade System for COVID-19 Detection, *Informatica*, pp. nn–mm. https://doi.org/10.31449/inf.v48i4.5923

[50] Vito Janko, Gašper Slapničar, Erik Dovgan, Nina Reščič, Tine Kolenik, Martin Gjoreski, Maj Smerkol, Matjaž Gams, and Mitja Luštrek (2021) Machine Learning for Analyzing Non-Countermeasure Factors Affecting Early Spread of COVID-19, *International Journal of Environmental Research and Public Health*, MDPI, 18(13), 6750. https://doi.org/10.3390/ijerph18136750

[51] Jasim Mohammed Dahr, Alaa Sahl Gaafar (2023) Performance Evaluation of Convolutional Neural Networks for COVID-19 Detection, *Informatica*, pp. nn–mm. https://doi.org/10.31449/inf.v48i21.6568

[52] Ruaa Sadoon, Adala Chaid (2023) Classification of Pulmonary Diseases Using a Deep Learning Approach, *Informatica*, pp. nn–mm. http://dx.doi.org/10.31449/inf.v48i14.6145

[53] Sarp, S., Catak, F. O., Kuzlu, M., Cali, U., Kusetogullari, H., Zhao, Y., and Guler, O.: An XAI approach for COVID-19 detection using transfer learning with X-ray images, *Heliyon*, 9(4), e14547 (2023). http://dx.doi.org/10.1016/j.heliyon.2023.e15137

[54] Kaleem, S., Sohail, A., Tariq, M. U., Babar, M., and Qureshi, B.: Ensemble learning for multiclass COVID-19 detection from big data, *Computers, Materials Continua*, 18(10), 10507–10520 (2023). http://dx.doi.org/10.1371/journal.pone.0292587

[55] Salau, A. O., and Jain, S.: Adaptive diagnostic machine learning technique for classification of cell decisions for AKT protein, *Informatics in Medicine Unlocked*, 23, 100511 (2021). http://dx.doi.org/10.1016/j.imu.2021.100511

[56] S. Mezzoudj, M. Khelifa, Y. Saadna (2024). A Comparative Study of Parallel Processing, Distributed Storage Techniques, and Technologies: A Survey on Big Data Analytics, *International Journal*, 10(5), pp. 86–99. https://doi.org/10.11648/j.ijdsa.20241005.11

Enhanced Bank Marketing System Using Optimized GSA-BP Neural Network for Improved Customer Targeting

Ziyi Jiao
Henan Polytechnic Institute Nanyang, Henan, China
E-mail: m15237711330@163.com

Keywords: gravity search algorithm, BP neural network, bank, marketing system, integrated learning algorithm

Received: October 20, 2024

To more accurately predict the needs of bank customers and improve the marketing success rate of bank wealth management products. Study designed a bank marketing system that can mine potential customers by analyzing customer data. The discovery of potential customers is mainly achieved by constructing the BA GSA-BP model, which optimizes the structure of the backpropagation neural network through gravity algorithm and integrates the optimized neural network using Bagging set learning algorithm. The study conducted simulation tests on the performance of the model. In the Bank Marketing dataset, after 225 iterations, the MES of GSA-BP remained stable at 0.098; In the Credit Card Default dataset, after 164 iterations, the MES of GSA-BP remained stable at 0.093, In terms of accuracy and recall, GSA-BP also performs well. For example, in the PR curve of the Bank Marketing dataset, the recall rate is about 0.896 when the accuracy is 0.8, and about 0.800 when the accuracy is 0.9. After using the Bagging ensemble algorithm, the performance of GSA-BP was further improved, with the largest area under the ROC curve, indicating strong generalization ability and low risk of overfitting. When the number of users is 200, the response time of the research system is 0.24 seconds, and the prediction success rate is about 60%. The above data illustrates that the method used in the study improves the over-fitting problem of traditional BP neural network and enhances the generalization ability of the algorithm. The constructed bank marketing system has the characteristics of short response time and high prediction success rate. The results of this study can accurately predict whether customers will order bank promotional products, conduct targeted marketing for customers, reduce marketing risks, and improve the success rate of product marketing and provide reliable technical support for predictions in other industries.

Povzetek: Predlagan je izboljšan bančni marketinški sistem z optimizirano nevronsko mrežo GSA-BP, ki učinkovito napoveduje potencialne stranke, skrajša odzivni čas in izboljša uspešnost ciljnega trženja produktov.

1 Introduction

In the context of the Internet era, the main challenge facing the marketing of commercial activities of banks is how to accurately locate customer needs, improve the success rate of marketing activities, and thus enhance the competitiveness of commercial banks [1-2]. Therefore, how to effectively identify and attract potential customers and design efficient marketing strategies to improve marketing resources has become the primary issue that banks need to address. Traditional marketing methods rely on manual planning and market research, but have limitations in efficiency and accuracy [3]. Artificial planning and market research rely on manual collection and analysis of data, with slow processing speeds that make it difficult to respond to rapidly changing market demands. According to industry reports, the conversion rate of this method is generally below 10%, and the customer churn rate is relatively high. The strategy of telephone direct sales requires a large amount of human resources and is costly. And frequent sales calls can easily trigger customer resentment and resistance, leading to a decrease in customer satisfaction. According to customer surveys, over 60% of customers express dissatisfaction with telephone direct sales, and the marketing success rate of this method is usually less than 20%. With the development of modern heuristic algorithms, how to apply these algorithms to improve the effectiveness of bank marketing systems has become a hot research topic. The Gravitational Search Method (GSA), as an optimization algorithm, is widely used to solve multi-dimensional data optimization problems [4]. At the same time, the backpropagation (BP) neural network serves as a powerful predictive model that can learn complex relationships in data. However, BP neural network has the problems of easily falling into local optimal solutions and slow training speed, which limits its effectiveness in practical applications. By simulating the gravitational interaction between objects, GSA can perform global search in the entire search space, effectively avoiding the problem of BP neural network getting stuck in local optimal solutions. After finding the potential global optimal solution, GSA can further improve the accuracy of the model by adjusting the search strategy and conducting fine searches within the local range. The optimization capability of GSA can compensate for the shortcomings of

BP neural network in training speed and accuracy, while the powerful predictive ability of BP neural network can fully utilize the optimized model parameters of GSA to achieve more efficient potential customer identification and personalized marketing. Compared to genetic algorithms, grey wolf algorithms, etc., the universal gravitation algorithm is logically easier to understand and interpret, and has fewer parameter adjustments, resulting in faster convergence speed. Therefore, the research uses the global search ability and better local search ability of the gravity search algorithm to optimize the training process of BP neural network, thereby optimizing its network structure. Therefore, the gravity search method is combined with the BP neural network in order to improve the effect of potential customer identification and personalized marketing in the bank marketing system. The first section of the research mainly talks about the research of sales promotion system by many experts and scholars and the application of neural network and gravity search algorithm. The second section mainly describes the construction process of the bank marketing system prediction model based on the BA-GSA-BP algorithm. The third section mainly focuses on verifying the effectiveness of the algorithm used in the study and the system constructed. Section 4 mainly discusses the results of the proposed model and the SOTA method reviewed in related work. Section 5 mainly analyzes the simulation results and points out the shortcomings of the research.

2 Related works

In the Internet era, more insightful marketing methods are needed to accurately locate customer needs, improve the success rate of product marketing of commercial activities of banks, and enhance the competitiveness of commercial banks. Therefore, the accuracy of bank promotion systems in predicting intended customers is crucial. To solve this problem, many experts and scholars have conducted relevant research on promotion systems in a general sense. Arun artificially analyzed bank data information and proposed a classifier model using the data mining tool WEKA. The model improves the classification model through data mining analysis and parameter changes. The results show that the model has better classification results when analyzing binary data sets [5]. Hosseini proposed the BN decision support system in order to predict the success rate of bank long-term deposit telemarketing. The system network is treated as an output variable, and the Nave Bayes method is used to determine the causal relationship between customer attributes and outcomes. The results show that the adopted system can predict subscribers with specific characteristics [6]. Gao proposed a time series based on KNN and SVR to predict the cyclical trend of consumer behavior in order to predict the time when users will re-purchase the product next time. Estimate the user's current life stage based on the user's recent behavior and recommend new products suitable for the user's estimated life stage. Experimental results show that this method significantly improves the effectiveness of recommendations [7]. In order to plan the customer purchase journey and develop decision support capabilities, Ma and Sun have developed a unified conceptual framework and multi-faceted research methods. These methods extract insights from large-scale unstructured, tracking and network data, using them in a transparent manner for descriptive, causal and prescriptive analysis. The results show that this method can plan the customer's buying journey [8]. Liu built a precision marketing model based on neural networks to address multi-faceted issues such as environmental pollution of marketing data and unscientific algorithms, and focused on data mining to study the two most important factors affecting marketing revenue. Research results show that precision marketing methods based on big data information platforms need to be more detailed and comprehensive [9]. From the above information, it can be found that machine learning models have high reliability, security, accuracy, and efficiency in processing data information, and have good performance in marketing issues. Therefore, machine learning technology can be applied to banking systems to obtain effective information from a large amount of raw data, extract knowledge from the data, and use this knowledge to design strategic plans, thereby improving the market competitiveness of banks.

With the development of modern heuristic algorithms, how to use these algorithms to improve the effectiveness of prediction models has become a hot research topic. Geng et al. proposed a SOC estimation method based on artificial neural networks and k-fold cross-validation in order to solve the main limitation of neural networks, which requires a large amount of data. The results show that compared with traditional BP neural network prediction, this method has a prediction accuracy of 91% [10]. In order to develop a wind speed prediction model, Mohammed et al. proposed a method that integrates deep learning and neural networks. Mapping wind speeds and predicting future propagation using recurrent neural networks. The results show that this method can accurately predict wind speed changes in Erbil City [11]. Ramos, F. R et al. proposed using a neural network with long-term memory to model the dynamic changes in sequence data when constructing a predictive time series model. The results show that long-term memory can significantly improve prediction performance in a time series [12]. In order to select the minimum number of features without affecting the classification accuracy, Yadav et al. proposed

a method of merging fuzzy logic and gravity search algorithms. Use this method to explore feature selection in automatic disease prediction. The results show that this method not only reduces the feature set by 67.66% on average, but also improves the accuracy by 12% on average [13]. Tochaiwat et al. developed a sales rate prediction model using artificial neural network technology to study the monthly sales unit quantity of independent residential projects. The results showed that the root mean square error (RMSE) of the model was ± 6.296, and the slope and R2 values of the linear regression analysis between the prediction rate and the actual rate were 0.620 and 0.571, respectively. This confirms the superiority of artificial neural network technology in dealing with limited data problems [14]. Compare the tree model with the research model, and the results are shown in Table 1.

Table 1: Model performance comparison

Researcher	Algorithm model	Test dataset	Accuracy	Convergence iteration times	Predict success rate
Geng et al. [10]	SOC estimation method based on artificial neural network and k-fold cross validation	NASA Battery Dataset	91%	324	92%
Mohammed et al. [11]	A model based on recursive neural network	Wind speed test dataset	90%	354	93%
Ramos, F.R et al. [12]	Prediction model based on long-term memory neural network	Climate Shared Dataset	92%	356	90%
Yadav et al. [13]	Integrating Fuzzy Logic and Gravity Search Algorithm Model	Disease dataset	91%	265	92%
Tochaiwat et al. [14]	Prediction Model Based on Artificial Neural Network Technology	Residential project sales dataset	93%	312	94%
This study	A model combining gravity search method and neural network	Bank Marketing Dataset	98%	225	98%

From the research of scholars both inside and outside China in Table 1, it can be seen that, neural network algorithms and gravity algorithms are currently widely used in many fields and it has achieved good results, but if it is directly applied to existing bank prediction systems, the prediction accuracy and model iteration times both need to be improved. This is because although Geng et al.'s model uses artificial neural networks and k-fold cross validation to improve the accuracy of SOC estimation, it is limited by the structure and parameter settings of the neural network, making it difficult to achieve higher accuracy when processing complex bank datasets. Mohammed et al.'s recursive neural network model performs well in processing time series data, but the recursive structure makes the model more prone to gradient vanishing or exploding during training, which affects the convergence speed and prediction performance of the model. Although Ramos et al.'s long-term memory neural network model can capture the long-term dependencies of time series, its high complexity can make it difficult to converge quickly in situations where computing resources are limited. The model developed by Yadav et al., which combines fuzzy logic and gravity search algorithm, has advantages in dealing with uncertainty problems. However, the rule making of fuzzy logic and parameter adjustment of gravity search algorithm may be difficult and prone to getting stuck in local optimal solutions. Tochaiwat et al.'s model achieved high accuracy in predicting sales of residential projects, but may have relied too heavily on the features of specific datasets, leading to a decrease in performance when generalizing to other datasets. In view of this, the study will combine the predictive needs of the banking system with the advantages of machine algorithms proposes a bank marketing system prediction model based on the gravity search method combined with neural networks. It is expected that it can mine the purchase intention of potential users and provide more accurate prediction results and decision support for bank marketing decisions.

3 Construction of bank marketing system prediction model based on BA-GSA-BP algorithm

This section mainly designs a bank marketing system for marketing of bank-related products. It mainly consists of four major modules: system management, marketing management, project management, and personal leave management. And respectively elaborate on the functions and implementation of these four models. This marketing system needs to use algorithms to predict potential intended customers. In view of the shortcomings of the traditional back propagation (BP) neural network, it is proposed to use the Gravity Algorithm (GSA) and Bagging

(BA) integrated algorithms to improve it, and elaborates on the detailed improvement method.

3.1 Construction of bank marketing system

The banking industry is a highly competitive industry, with various banks competing for limited customer resources. In order to maintain a competitive advantage in the market, banks need to attract and retain customers through effective marketing strategies and provide personalized products and services [15]. Building a bank marketing system can use advanced algorithm technology and data analysis capabilities to achieve better customer management and marketing effects. The overall architecture of the bank marketing system studied and designed is shown in Figure 1.

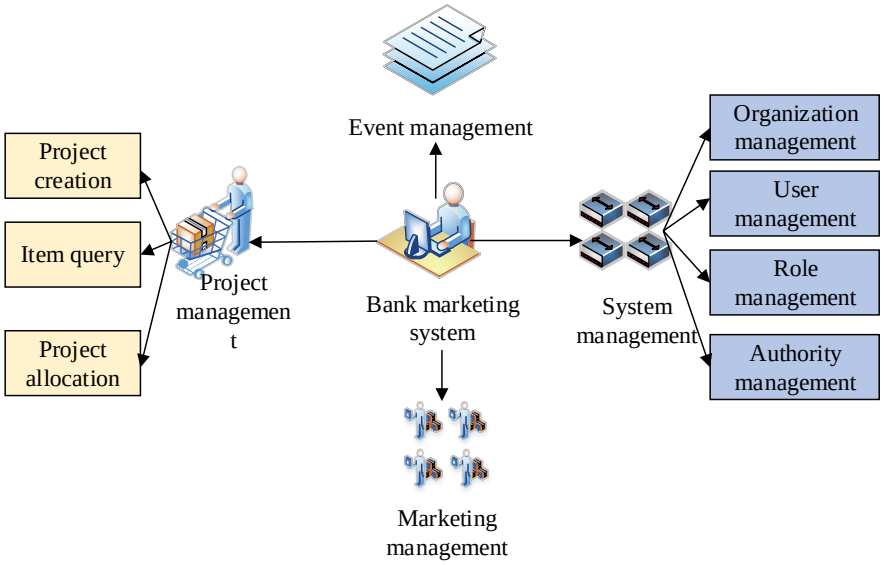

Figure 1: Overall architecture diagram of bank marketing system

As shown in Figure 1, the bank's marketing system mainly consists of four major modules: system management, marketing management, project management, and personal leave management. The system management module is composed of four parts: organization management, user management, role management, and authority management. The implementation of the functions of each module of the system is based on the Springboot framework. The Springboot framework organizes the collaborative work of each module in the system by separating interface display, data and business logic. It has the advantages of low coupling, high reusability, fast construction, low life cycle, and easy maintenance. Institutional management allows bank administrators to create, query, delete and modify institutional information. The system institution management process is shown in Figure 2. The administrator interacts with the service class layer through the operation interface, passes instructions to the business class layer to perform specific business operations, and returns the execution results to the user interface for display. And the administrator can create a new institution, enter the basic information of the institution and add it to the database; can understand the details of the banking institution by accurately querying or browsing all institution information; can delete institution information that is no longer used; and can also modify parts of the institution or All information will be modified to maintain the accuracy and timeliness of the information.

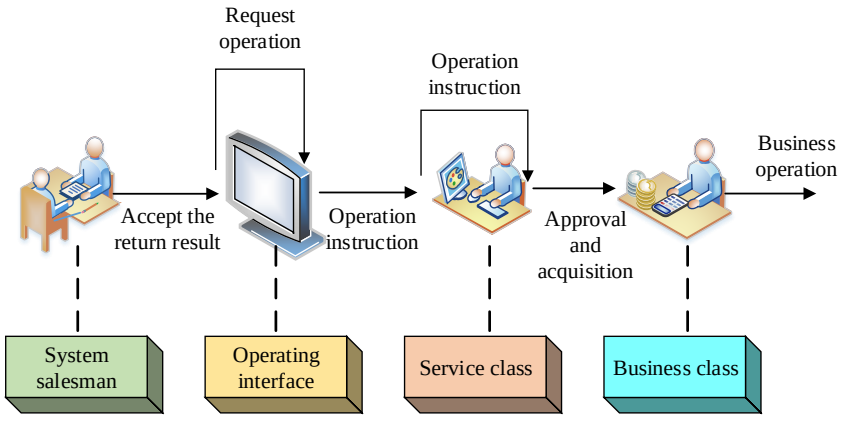

Figure 2: Organization management flow chart

A functional module used by system administrators to manage and maintain basic information about system users. It provides nine operations such as user query, user information export, user deletion, user deactivation, user activation, new user, modification of user information, reset password and user role configuration. Through these operations, system administrators can easily manage and adjust the status, permissions, and information of system users to ensure the information security and compliance of system users. Role management can achieve management and control of users with different permissions by assigning different "roles" to customers, including querying, deleting, modifying role information, etc. Permission management is mainly implemented using the Role-Based Access Control (RBAC) model [16]. The model divides users into three roles, namely account manager, account executive and system administrator. Different customer roles enjoy Different operating permissions. The project management module is mainly responsible for marketing project information in the entire bank marketing system, and mainly includes three functions: project creation, project query, and project allocation. The basic process of realizing marketing project management is shown in Figure 3.

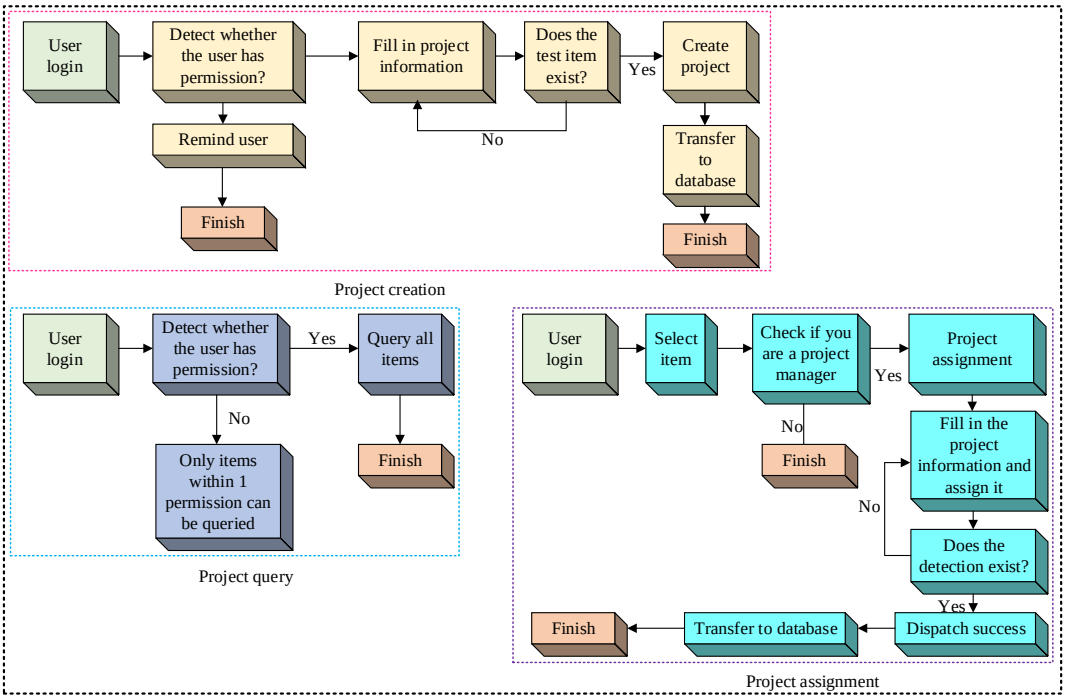

Figure 3: Basic process of marketing project management

The marketing management module is mainly responsible for helping bank business personnel complete more marketing activities, including three functions: task list query, marketing result prediction and customer marketing follow-up. After logging into the system, bank clerks can query the current task list and select a sub-project to predict whether customers are willing to order products. The system will display customer information for which the prediction result is "yes", and employees will conduct marketing promotions and update customer records. In addition, employees can also select sub-projects for customer marketing follow-up, query customer information and follow-up work, and update records. The overall process is concise and clear, allowing employees to easily complete marketing management tasks. In this process, the most important thing is marketing result prediction, and its function sequence diagram is shown in Figure 4.

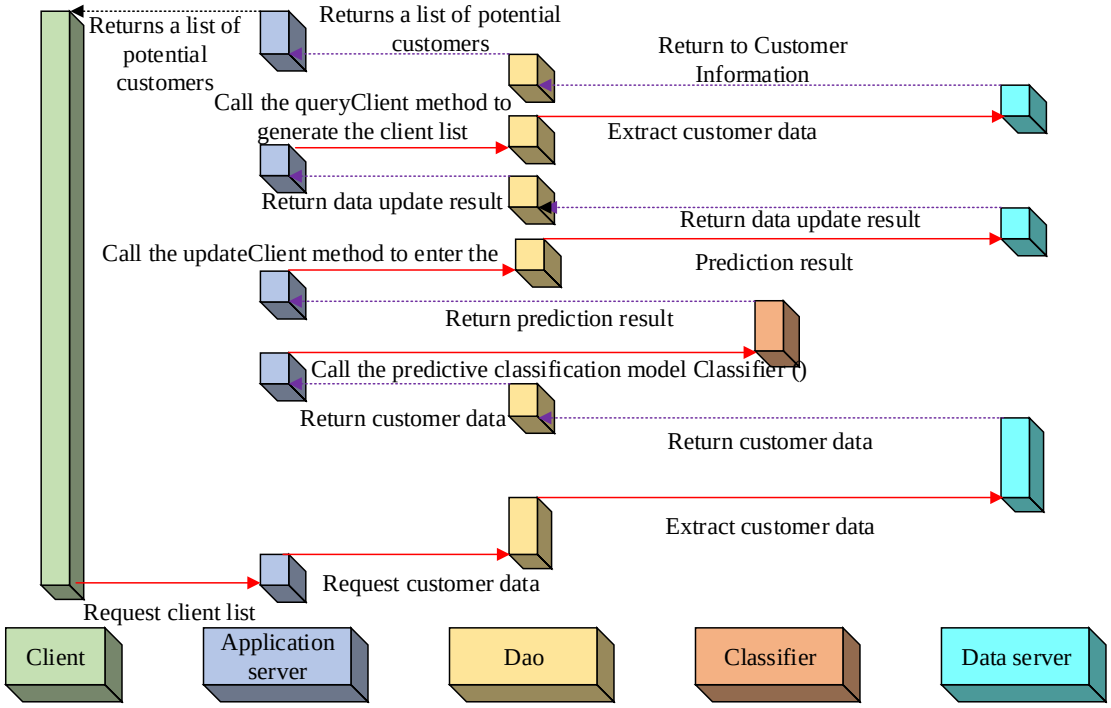

Figure 4: Marketing result prediction function sequence diagram

3.2 Construction of prediction model integrating BA, GSA and BP neural network

For the bank marketing system constructed by the research institute, the BP neural network algorithm can be used to select the main marketing objects. However, the traditional BP neural network model has many problems such as slow convergence speed and uncertain network structure [17]. Therefore, the study used GSA to optimize the BP neural network structure, and selected the Bagging integration algorithm to integrate the optimized BP neural network [18]. The main purpose of GSA to optimize the BP neural network is to use GSA's powerful global search capability and convergence speed to calculate the optimal structure of the hidden layer of the BP neural network. The specific process of GSA optimizing BP neural network is shown in Figure 5.

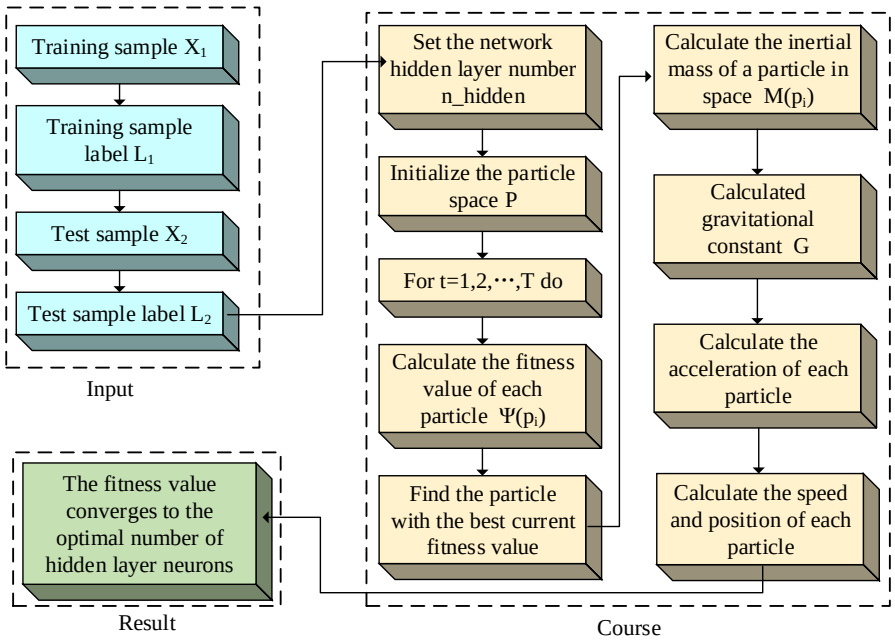

Figure 5: GSA-BP algorithm flow chart

In Figure 5, the particle space is initialized, see Formula (1).

$$\begin{cases} P = \{p_1, p_2, ...p_N\} \\ p_i = \left(p_i^1, p_i^2, ...p_i^m\right), i = 1, 2, ..., N \end{cases} \quad (1)$$

In Formula (1), P is the initial particle space; i is a particle; P_i is the initial i position of the particle in this space, and the initial position of the particle is one of the options for the neural hidden layer of the network. Then calculate the fitness value of the particles, see Formula (2).

$$\psi(p_i) = \frac{1}{n}\sum_{j=1}^{n}\left(\hat{y}_j - y_j\right)^2 \quad (2)$$

In Formula (2), $\psi(p_i)$ is p_i the fitness value of the particle, which is also the mean square error of the neural network; j is a particle; $\hat{y}_j$ is the prediction result of the neural network; y_j is the actual label; n is the number of samples. Then find the optimal fitness of the particles, see Formula (3).

$$\begin{cases} best_P = \max\left(\psi(p_i)\right), i = 1, 2, ..., N \\ worst_P = \min\left(\psi(p_i)\right), i = 1, 2, ..., N \end{cases} \quad (3)$$

In Formula (3), $best_P$, it is the particle with the best fitness in the current iteration; $worst_P$ it is the particle with the worst fitness in the current iteration. Calculate the inertial mass of the particle according to Formula (3), see Formula (4).

$$\begin{cases} m(p_i) = \dfrac{\psi(p_i) - worst_P}{best_P - worst_P} \\ M(p_i) = \dfrac{m(p_i)}{\sum_{i=1}^{N} m(p_i)} \end{cases} \quad (4)$$

In Formula (4), $M(p_i)$ is P the inertial mass of all particles in space. Then calculate the gravitational constant G. The calculation method is shown in Formula (5)

$$G = G_0\left(-\alpha\frac{t}{T}\right) \quad (5)$$

In Formula (5), G_0 is the gravitational constant value in the traditional sense, α which is a parameter, t is the current number of iterations, T is the maximum number of iterations. Then, based on the traditional law of universal gravitation, When iterating t times, The force exerted by particle i on particle j in the n dimension, as shown in Formula (6).

$$\begin{cases} F_{ij}^n = G(t)\dfrac{M_a(t)M_p(p_i)}{R_{ij}(t) - \varepsilon}\left(p_j^n(t) - p_i^n(t)\right) \\ R_{ij}(t) = \left\|p_i(t), p_j(t)\right\|_2 \end{cases} \quad (6)$$

In Formula (6), F_{ij}^n is the acting force, M_a is p_j the active gravitational mass of the particle; M_p is p_i the passive gravitational mass of the particle; ε is a constant; $R_{ij}(t)$ is t the distance between p_i and p_j at the first iteration. p_i Throughout the space, there is p_i more than one effect p_j. Therefore, assuming that p_i the particles that act on the particle are a set kB, t the resultant force on $F_i^n(t)$ the particle in the first iteration is i shown kB in Formula (7).

$$F_i^n(t) = \sum_{j \in kB, j \neq i} rand_j F_{ij}^d(t) \quad (7)$$

In Formula (7), $rand_j$ it is the random variable in [0,1]. The particle acceleration can be obtained from the resultant force $a_i^n(t)$, see Formula (8).

$$a_t^n(t) = \frac{F_i^n(t)}{M(p_i)} \quad (8)$$

Finally, the velocity of the particle is updated according to the acceleration in $v_i^n(t+1)$ Formula (6), see Formula (9).

$$v_i^n(t+1) = rand_i \times v_i^n(t) + a_i^n(t) \quad (9)$$

The position of the particle can be calculated according to the particle speed in $x_i^n(t+1)$ Formula (7), see Formula (10)

$$x_i^n(t+1) = x_i^n(t) + v_i^n(t+1) \quad (10)$$

Repeat the steps from Formula (2) to Formula (10) until the algorithm reaches convergence. In the GSA-BP model, fitness values are used to evaluate the strengths and

weaknesses of individuals (i.e. the parameter configuration of the BP neural network). As the number of iterations increases, the GSA algorithm continuously searches and optimizes to gradually approach the optimal parameter configuration of the BP neural network, resulting in a gradual decrease in fitness values. When the fitness value reaches the preset error threshold or the number of iterations reaches the upper limit, the algorithm stops iterating and outputs the optimal solution, that is, calculates the optimal structure of the hidden layer of the BP neural network.

The bagging algorithm obtains multiple different sampling sets through sampling with replacement, and then trains a base learner for each sampling set, and improves the generalization ability by integrating the output of these learners. For unstable learning models, such as BP neural networks, the Bagging algorithm can reduce the risk of overfitting. Therefore, the bagging algorithm is used to integrate the GSA-optimized BP neural network to further improve the model performance. The integration process is detailed in Figure 6.

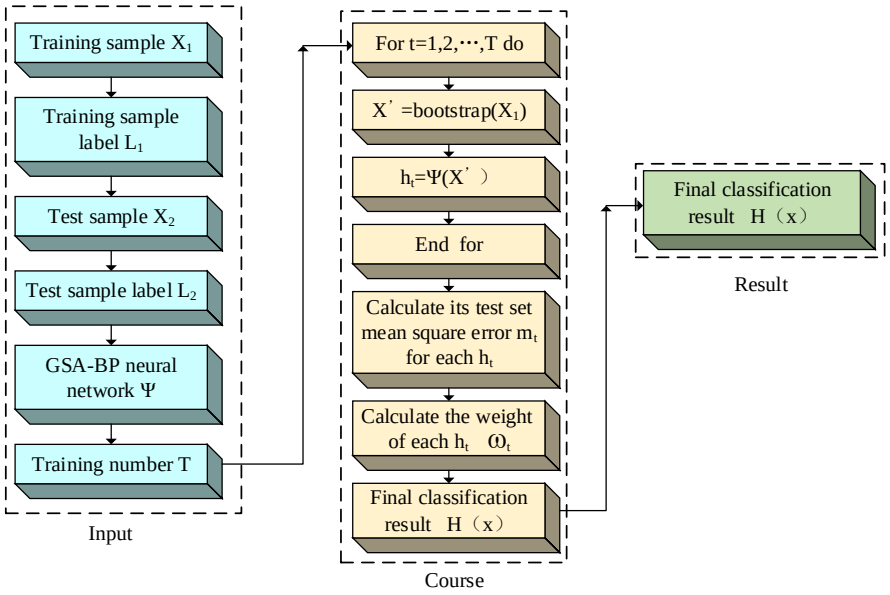

Figure 6: BA -GSA-BP algorithm flow chart

In the algorithm flow of Figure 6, first set h_t the number of base classifiers to T; then for each base classifier h_t; sample from the original training set with replacement, and extract the same number of samples as the original training set samples to form A new training set subset is used; then the training set subset is used to train the base classifier h_t; and finally the base classifier is combined using a combination strategy of the weighted voting method. T The weight of each classifier is shown in h_t Formula (11).

$$\begin{cases} m_t = \dfrac{n}{\sum_n^{i=1}\left(h_t\left(X_2^i\right)-L_2^i\right)}, t=1,2,3,...,n \\ \omega_t = \dfrac{m_t}{\sum_T^{t=1} m_t} \end{cases} \quad (11)$$

In Formula (11), m_t it is the mean square error; ω_t it is the weight. The classification result of weighted voting is shown in Equation (12).

$$H(x) = c_{\arg\max} \sum_{t=1}^{T} \omega_t h_i^j(x) \quad (12)$$

In Formula (12) $h_i^j(x)$ is the output $h_i(x)$ on the category label c_j. The study used mean square error (MSE) and ROC curve to evaluate the constructed prediction model . The calculation method of mean square error MSE is shown in Formula (13).

$$MSE = \frac{1}{n}\sum_{i=1}^{n}\left(\hat{y}_i - y_i\right)^2 \quad (13)$$

The abscissa in the ROC curve is FPR, and the ordinate is TPR. The calculation method is shown in Formula (14).

$$\begin{cases} FPR = \dfrac{FP}{TN + FP} \\ TPR = \dfrac{TP}{TP + FN} \end{cases} \quad (14)$$

4 Performance analysis and simulation application of bank marketing system prediction model based on BA- GSA-BP algorithm

This section mainly focuses on verifying the validity of the method used in the study. First, the selection of the simulation experiment environment and data set is explained, and then comparative experiments are conducted on the fitness value of GSA, the PR curve of GSA-BP, the ROC curve of BA-GSA-BP, the response time of the marketing system, and the prediction success rate. The data generated were analyzed and the superiority of the method used in the study was demonstrated.

4.1 Performance analysis of bank marketing system prediction model

In order to verify the effectiveness of the bank marketing system prediction model based on the GSA-BP algorithm, the study first tested the performance of the constructed system. The basic hardware environment settings of the experiment are shown in Table 2.

Table 2: Software and hardware configuration of experimental environment and model parameter settings

Project	Configuration item	Parameter
Software and hardware configuration of experimental environment	operating system	Windows 10
	CUP	i9-11900K
	Memory	GDDR6X
	Disk	Samsung 980 PRO
	network adapter	Intel Ethernet Converged Network Adapter X710
	underlying database	MySQL5.7
Model parameter settings	Population Size	30
	Iteration Number	500
	Gravitationa Constant	1.1
	Learning Rate	0.001

This study first selected the improved genetic algorithm (IGA) from reference [19] and the improved simulated annealing algorithm (ISA) from reference [20]. with the same experimental experience to compare the performance with the Gravity Search Algorithm (GSA) used in the study. In order to ensure the fairness and rationality of the experiment, the number of iterations of each algorithm was set to 500. Then the Bank Marketing data set and the Credit Card Default data set were selected to test the performance indicators of the model. The Bank Marketing Data Set includes a total of 324 pieces of customer basic information (customer ID, age, occupation, marital status, etc.), 296 pieces of deposit and loan information (housing loans, personal loans, etc.), 568 pieces of bank marketing information for customers (contact frequency, previous activity results, call duration, etc.), and 154 pieces of customer subscription information. The Credit Card Default Data Set includes a total of 1324 pieces of customer basic information, credit data, and default information. For the information of two datasets, first check and process the missing values, outliers, and duplicate values in the data, and then use the mean normalization method to standardize the data. Afterwards, the model will be trained and tested in a ratio of 4:1 between the training set and the testing set. The fitness changes of the algorithm are shown in Figure 7.

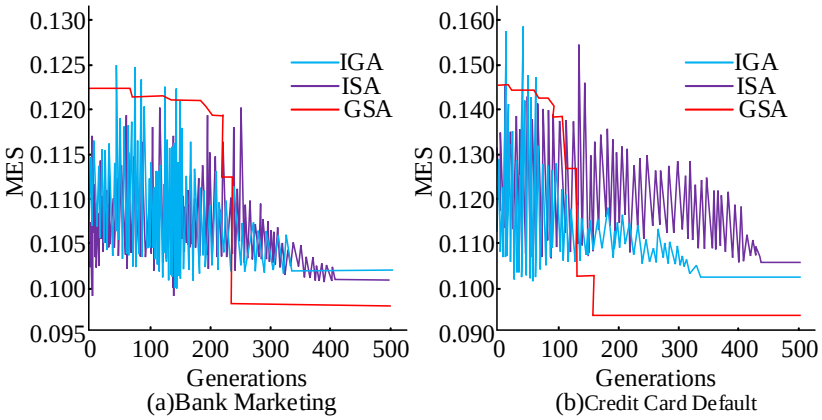

Figure 7: Comparison of fitness values of different data sets

As shown in Figure 7, Figure 7(a) shows the fitness value convergence process of the three algorithms in the Bank Marketing data set. It can be seen that the convergence curves of the two algorithms IGA and ISA fluctuate greatly at the beginning, and there is great instability. Then as the number of iterations increases, the curve fluctuations become smaller and smaller. In the end, IGA iterated 336 times, and its MES value became stable, about 0.103; ISA iterated 406 times, and its MES value became stable, about 0.101. In contrast, the convergence curve of GSA is smoother and declines in a ladder-like manner. At the final iteration of 225 times, the MES value stabilizes at about 0.098. Figure 7(b) shows the fitness value convergence process of the three algorithms in the Credit Card Default data set. It can be seen that the curve change trend is similar to Figure 7(a). The curves of IGA and ISA fluctuate greatly and are unstable, with 341 and 443 iterations respectively. The MES values tend to be stable, with stable values of approximately 0.101 and 0.107 respectively. The GSA convergence curve still declines in a relatively stable step-like manner, and its MES value tends to be stable at about 0.093 when iterating 164 times. It shows that compared with the other two algorithms, GSA has faster convergence speed and better fitness value. This is because GSA searches the solution space of the problem by simulating the gravitational interaction between celestial bodies. This mechanism enables GSA to explore the whole search space more effectively. Once GSA is close to the global optimal solution, its gravitational action mechanism will become more refined, which is helpful to fine tune in the local region, so as to find a more accurate solution. Compared with GA, GSA avoids the trap of local optimal solution caused by crossover and mutation operation, because gravity can naturally guide the solution to move to a better region. Compared with SA, the search process of GSA is more systematic and structured, rather than relying solely on the acceptance probability and temperature parameters to control the search direction.Then use the Bank Marketing data set as the main data set to conduct extended performance testing. For the precision rate and recall rate of the three algorithms GAS-BP, GAS-IGA, and GAS-ISA, the PR curves are shown in Figure 8.

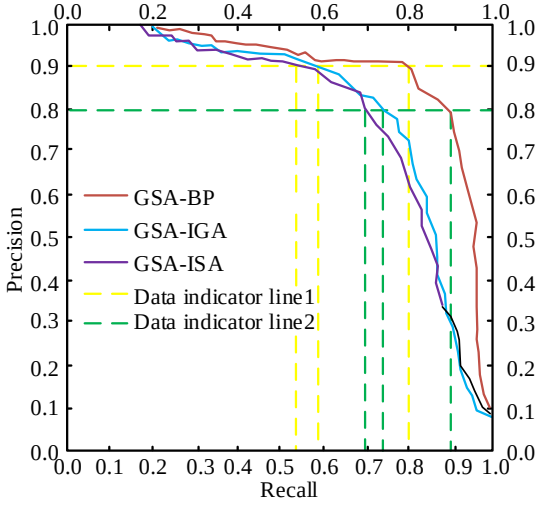

Figure 8: PR curves of three algorithms

As shown in Figure 8, it can be seen that for GSA-BP, when the precision rate is 0.8, the corresponding recall rate is approximately 0.896. This means that under a given threshold, the GSA-BP algorithm can find most relevant samples with a high accuracy. When the precision rate is 0.9, the corresponding recall rate is about 0.800. This shows that the GAS-BP algorithm may miss some relevant samples under higher precision, but still has a high recall rate. For GSA-IGA, when the precision rate is 0.8, the corresponding recall rate is approximately 0.731. Compared with the GSA-BP algorithm, the GSA-IGA algorithm can find fewer relevant samples with the same accuracy. When the precision rate is 0.9, the corresponding recall rate is approximately 0.591. This further shows that the GSA-GA algorithm misses more relevant samples with higher accuracy. For GSA-ISA, when the precision rate is 0.8, the corresponding recall rate is approximately 0.695. Compared with the GSA-BP algorithm and the GSA-IGA algorithm, the GSA-ISA algorithm can find fewer relevant samples. When the precision rate is 0.9, the corresponding recall rate is approximately 0.534. Although the GSA-ISA algorithm has a lower recall rate at higher precision, it still performs better than the GSA-IGA algorithm. After determining the optimal hidden layer structure of the BP neural network, use the Bagging integration algorithm to integrate the GSA-BP network, and use test samples in the Bank Marketing data set and Credit Card Default data set to verify the training results. In order to further illustrate the superiority of the BA-GSA-BP algorithm, the study also selected the Abdoost ensemble algorithm as a comparison. The ROC curve results of BA-GSA-BP, AD-GSA-BP, and GSA-BP are shown in Figure 9.

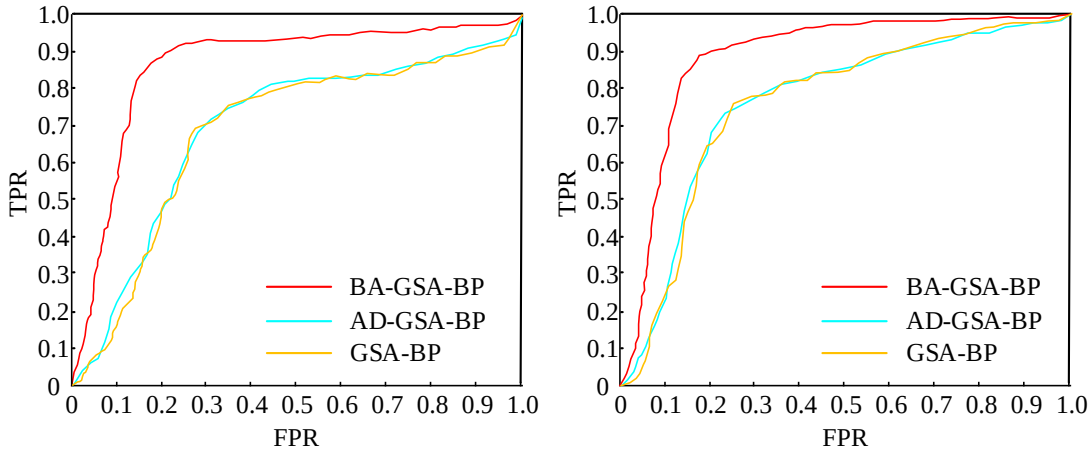

(a)Bank Marketing (b)Credit Card Default

Figure 9: Comparison of ROC curve results of three algorithms

As shown in Figure 9, Figure 9(a) and (b) are the ROC curves tested in the data sets Bank Marketing and Credit Card Default respectively. It can be seen that in different data sets, the curve trends of the three algorithms are roughly the same. It shows that their classifier performance is similar in different data sets. In addition, it can be seen that through the BA-GSA-BP algorithm based on Bagging integration, the area under the ROC curve reaches the maximum, indicating that this algorithm is very effective in reducing the over-fitting risk of the GSA-BP algorithm and has stronger generalization ability. This shows that the BA-GSA-BP algorithm can better cope with the challenges brought by different data sets, avoid over-fitting problems, and obtain a more reliable classification model. However, the AD-GSA-BP algorithm based on Adaboost integration does not significantly improve the generalization ability of the GSA-BP algorithm. This means that the use of Adaboost integration does not effectively reduce the overfitting risk of the GSA-BP algorithm, nor does it bring significant performance improvements. To verify the importance of each index performance of the constructed model compared with other models. Statistical software SPSS was used to make statistics on the above data and conduct independent sample t-test, as shown in Table 3.

Table 3: T-test of model performance comparison

Algorithm comparison	Sample mean (MES value)	Average number of iterations	t-values	P-value	Confidence interval
GSA vs IGA (Bank Marketing)	GSA: 0.098, IGA: 0.103	GSA: 225, IGA: 336	0.086	P<0.05	98%
GSA vs ISA (Bank Marketing)	GSA: 0.098, ISA: 0.101	GSA: 225, ISA: 406	0.074	P<0.05	99%

GSA vs IGA (Credit Card Default)	GSA: 0.093, IGA: 0.101	GSA: 164, IGA: 341	0.085	P<0.05	99%
GSA vs ISA (Credit Card Default)	GSA: 0.093, ISA: 0.107	GSA: 164, ISA: 443	0.084	P<0.05	98%
Algorithm comparison	Sample mean (ROC value)	t-values		p-value	Confidence interval
BA-GSA-BP vs AD-GSA-BP (Bank Marketing)	BA-GSA-BP:0.904, AD-GSA-BP:0.714	0.075		P<0.05	98%
BA-GSA-BP vs GSA-BP (Bank Marketing)	BA-GSA-BP:0.904, AD-GSA-BP:0.701	0.063		P<0.05	99%
BA-GSA-BP vs AD-GSA-BP (Credit Card Default)	BA-GSA-BP:0.894, AD-GSA-BP:0.764	0.075		P<0.05	99%
BA-GSA-BP vs GSA-BP (Credit Card Default)	BA-GSA-BP:0.894, AD-GSA-BP:0.741	0.081		P<0.05	98%

It can be seen from table 3 that the p-value of performance comparison between models is less than 0.05, indicating that these performances have significant differences. At the same time, the confidence interval is more than 95%, indicating that the estimation of model performance difference is relatively accurate.

4.2 Simulation application of bank marketing system prediction model

In order to verify the practical application effect of the constructed system, the study selected data from two financial bank databases A and B for simulation experiments. This study mainly focused on the system function integration test of the model built by the institute and the response time and prediction success of different clients. The efficiency was verified, and the traditional prediction model, AD-GSA-BP, and GSA-BP models under the same experimental conditions were simultaneously tested as references. First, conduct integration testing on the four major modules of the bank marketing system: system management, marketing management, project management, and personal leave management (integration testing is to test whether the system can work normally after several parts of the built system are combined together). After testing, the expected results of each part of the system constructed by the institute are consistent with the actual results. It was proved that the research model can operate normally. Then, in order to meet the work needs of various banking personnel, the response time of the model was tested. The specific results are shown in Figure 10.

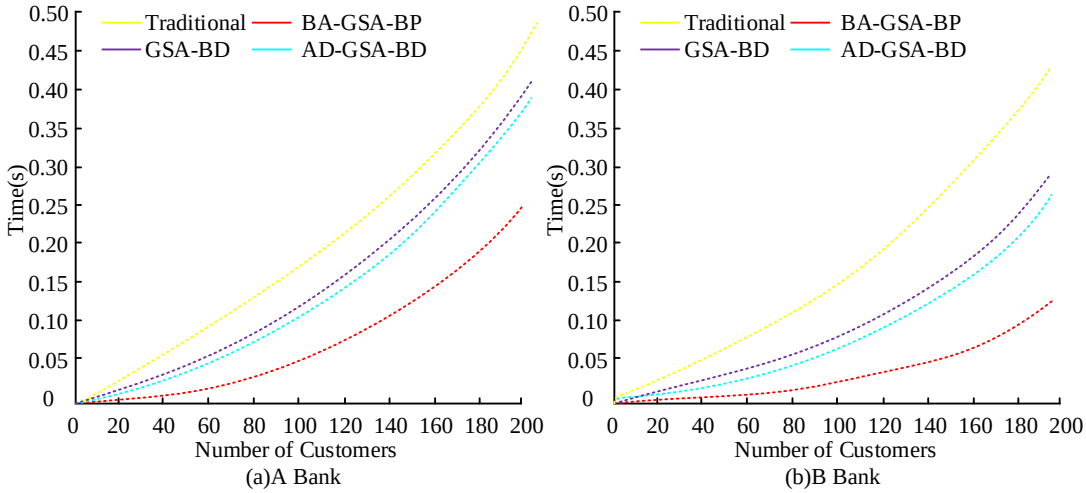

Figure 10: Comparison of response times of four models

It can be seen from Figure 10(a) that in the Bank Marketing data set, as the number of clients increases, the response time of each system begins to increase. When the number of clients is 200, the response time of the BA-GSA-BD model is the smallest, about 0.24s, less than 0.3s, which meets the work needs of banking personnel. The response times of the traditional prediction model, AD-GSA-BP, and GSA-BP are 0.48s, 0.39s, and 0.41s respectively. It can be seen from Figure 10(b) that in the Morningstar data set, the response time of each model has decreased, but the AD-GSA-BD model still has the smallest response time, which is about 0.12. In comparison, the response times of other models are longer. The response times of the traditional prediction model, AD-GSA-BP, and GSA-BP are 0.26s, 0.29s, and 0.43s respectively. It shows that the response time of the prediction model is faster when processing simple data sets. This is because ba-gsa-bp model optimizes the structure of BP neural network through GSA, and also combines bagging ensemble learning algorithm. This optimization makes the model more efficient in feature selection, parameter adjustment and model combination, thus reducing the response time. However, ad-gsa-bp and gsa-bp models lack the optimization strategy in ba-gsa-bp model, resulting in more time to complete the calculation when processing the same data set. Finally, the prediction success rates of various models were tested 10 times using the data of banks A and B. The specific results are shown in Figure 11.

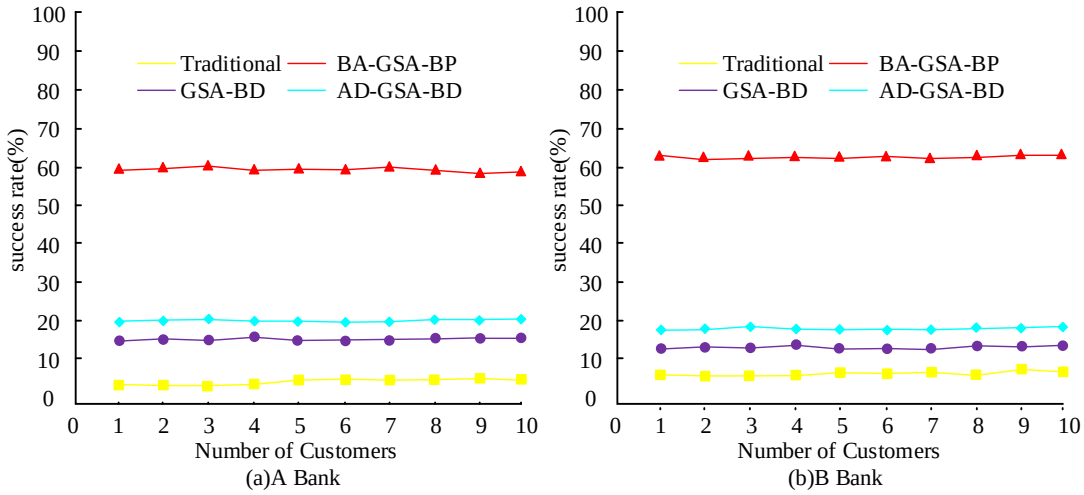

Figure 11: Comparison of prediction success rates of four models

As shown in Figure 11(a), under the data test of Financial Bank A, the BA-GSA-BP prediction model conducts marketing promotions for all customers, and the marketing success rate is as high as about 60%. The marketing success rates for all customers of the traditional prediction model, AD-GSA-BP, and GSA-BP are approximately 5%, 20%, and 15% respectively. Looking at Figure 11(b) again, we can see that the marketing success rates of the four forecast models BA-GSA-BP, traditional forecast model, AD-GSA-BP, and GSA-BP for all customers are approximately 62%, 8%, and 18% respectively. and 12%. Based on the above data, the performance comparison of different models in the actual banking system is summarized in Table 4.

Table 4: Performance comparison of different models in actual banking system

Data application scenarios	Model	Response time (seconds)	Prediction success rate (%)	Mean squared error
Bank A	BA-GSA-BP	0.24s	60	0.001
	GSA-BP	0.41s	15	0.012
	AD-GSA-BP	0.39s	20	0.024
	Traditional BP	0.48s	5	0.052
Bank B	BA-GSA-BP	0.12s	62	0.002
	GSA-BP	0.29s	12	0.011
	AD-GSA-BP	0.26s	18	0.024
	Traditional BP	0.43s	8	0.045

Table 4 shows that the prediction model constructed by the research can screen out customers who are more interested in ordering bank marketing products, thus improving the marketing efficiency and success rate of the entire bank. However, the interest and demand of the same customer for bank marketing products are constantly changing. With the change of market trend, personal financial status or life events (such as house purchase, marriage, birth, etc.), customers may change from interested in one product to interested in another product. The ba-gsa-bp model can adapt to the changes of customer behavior by regularly updating the training data and retraining the model.

5 Discussion

The models proposed by other individuals reviewed in the relevant work have achieved certain results on their respective test datasets, but still have limitations. Geng et al.'s artificial neural network model achieved an accuracy of 91% on the NASA battery dataset, but had a convergence iteration of 324 times, indicating that its training efficiency needs to be improved [10]; Mohammed et al.'s recurrent neural network has slightly lower accuracy (90%) on wind speed test datasets, and has more convergence iterations (354 times), due to the high complexity of the model leading to increased training costs [11]; Ramos et al.'s long-term memory neural network had a low prediction success rate (90%) on climate shared datasets, and also had a high number of convergence iterations (356 times), reflecting the model's insufficient generalization ability [12]; The model developed by Yadav et al., which combines fuzzy logic and gravity search, has decent accuracy on disease datasets (91%), but the reduction in convergence iterations did not significantly improve the prediction success rate (92%), indicating that the fusion effect of the algorithm is limited [13]; Tochaiwat et al.'s artificial neural network technology has high accuracy (93%) on the sales dataset of residential projects, but there is still room for further improvement in convergence speed and prediction success rate. In contrast, the gravity based search method (GSA) combined with neural networks proposed in the study showed significant superiority on bank marketing datasets. The model not only achieved an accuracy of up to 98% and a prediction success rate, but also significantly reduced the number of convergence iterations to 225, mainly due to the new combination of GSA and neural network and the strategy of binding ensemble [14]. Compared with Geng et al.'s method based on artificial neural networks, the study optimized the weights of the neural network by introducing GSA, avoiding the problem of traditional BP (backpropagation) algorithm easily falling into local optima, thereby improving the accuracy and training efficiency of the model. At the same time, the binding integration strategy further enhances the model's generalization ability and robustness, making it more advantageous when facing complex and ever-changing bank marketing data. These enhancements are particularly important in the field of banking marketing systems, as accurate customer forecasting and rapid response to market demand are key to improving marketing effectiveness and customer satisfaction. In the context of a large amount of data and changing customer behavior, the proposed method can better capture market trends, achieve precise marketing, and thus gain an advantage in the fiercely competitive market environment.

6 Conclusion

Accurately locating customer needs and achieving targeted marketing to customers are important aspects of bank development. The study first established a suitable bank marketing system prediction model based on its own needs. Then the BP neural network is introduced into the model framework as the main learning and fitting tool for the prediction model. Then the global search capability of the GSA algorithm is used to optimize the BP neural network structure, and finally the Bagging (BA) ensemble learning algorithm is used to integrate the optimized neural network. The results show that in the Bank Marketing data set, when GSA, SA, and GA are iterated 225 times, 406 times, and 336 times respectively, the MES values tend to be stable, and the MES values are approximately 0.098, 0.101, and 0.103 respectively. The method used in the study has a faster convergence speed, better fitness value, and the search strategy and parameter settings are more suitable for optimizing the BP neural network structure, which can converge to an optimal solution faster. When the accuracy rates are 0.9 and 0.8 respectively, the corresponding summoning rates of GAS-BP are 0.800 and 0.731 respectively. The other two algorithms correspond to the highest summoning rates of 0.591 and 0.695 respectively. Compared to the other two algorithms, the research method has higher accuracy and reliability in processing data, is more capable of identifying samples related to the problem, and provides better classification performance. This has advantages in handling banking system information. In addition, the BA-GAS-BP model has the largest ROC curve area, indicating that the method has better generalization performance on the same dataset, can better adapt to new data, and reduce overfitting risk of the model. The prediction model constructed using this method can adapt and process the vast dataset of the banking system at an extremely fast speed. When the number of customers is 200, the response time of the model

built by the institute is 0.24s, and the prediction success rate is about 60%. The other three models require 0.39a at the fastest, and the highest prediction success rate is 12%. It shows that the system built by the institute is efficient and accurate in predicting potential bank users. However, the dataset used in this experiment is all historical data and cannot be changed according to market conditions and specific user situations. Subsequent research will further explore the adaptive updating of prediction models and improve the automatic updating function of prediction results. Subsequent research will further improve the adaptive ability of the prediction model, especially by integrating real-time data streams, dynamically adjusting model parameters and introducing advanced machine learning algorithms, so that the model can accurately adapt to the characteristics of different customer demographic data and the rapidly changing market environment. This will include developing a mechanism to automatically update the training data set on a regular basis or based on trigger conditions, and retraining or fine-tuning the model to ensure that it is always in sync with market trends and customer needs.

Ethics approval and consent to participate

Not Applicable.

Consent for publication

All authors read and approved the final manuscript.

Availability of data and material

The datasets used and/or analysed during the current study available from the corresponding author on reasonable request.

Competing interests

The authors have declared that no competing interests exist.

Funding statement

This paper is supported by the Philosophy and Social Science Planning Project of Henan Province (2022BJJ023), Soft Science Research Planning Project of Henan Province (232400411048), Key Research Project of Colleges and Universities of Henan Province (23A790023) and Research Start-up Foundation of Henan Finance University (2021BS008).

Authors' contributions

JZ wrote the whole paper.

Acknowledgements

Not Applicable.

References

[1] Wang T, Zhao S, Zhu G, Zheng H. A machine learning-based early warning system for systemic banking crises. Applied economics, 2021, 53(26): 2974-2992. doi.org/10.1080/00036846.2020.1870657

[2] Anand M, Velu A, Whig P. Prediction of loan behaviour with machine learning models for secure banking. Journal of Computer Science and Engineering (JCSE), 2022, 3(1): 1-13. doi.10.36596/jcse.v3i1.237

[3] Paiva B M R, Ferreira F A F, Carayannis E G, Zopounidis C, Ferreira J J, Pereira L F, Dias P J. Strategizing sustainability in the banking industry using fuzzy cognitive maps and system dynamics. International Journal of Sustainable Development & World Ecology, 2021, 28(2): 93-108. doi.org/10.1080/13504509.2020.1782284

[4] Tan X, Wang Q, Feng J, Huang, Y, Huang, Z. Fast modeling of gravity gradients from topographic surface data using GPU parallel algorithm. Geodesy and Geodynamics, 2021, 12(4): 288-290. doi.10.1016/j.geog.2021.04.003.

[5] Arun R. A Novel Classifier Model Efficient Prediction of Success Rate in Bank Marketing. International Journal of Advanced Science and Technology, 2020, 29(9): 6955-6961. doi. 10.3233/JIFS-189491

[6] Hosseini S. A decision support system based on machined learned Bayesian network for predicting successful direct sales marketing. 2021, 8(2): 295-315. doi.10.1080/23270012.2021.1897956

[7] Gao H, Kuang L, Yin Y, Guo B, Dou K. Mining consuming Behaviors with Temporal Evolution for Personalized Recommendation in Mobile Marketing Apps. Mobile Networks and Applications, 2020, 25(4): 1233-1248. doi.10.1007/s11036-020-01535-1.

[8] Ma L, Sun B. Machine learning and AI in marketing--Connecting computing power to human insights. International Journal of Research in Marketing, 2020, 37(3): 481-50. doi. 10.1016/j.ijresmar.2020.04.005

[9] Liu H. Big data precision marketing and consumer behavior analysis based on fuzzy clustering and PCA model. Journal of Intelligent and Fuzzy Systems, 2020, 40(4): 6529-6539. doi. 10.3233/JIFS-189491

[10] Geng P, Wang J, Xu X, Zhang Y, Qiu S. SOC Prediction of power lithium battery using BP neural network theory based on keras. International Core Journal of Engineering, 2020, 6(1) :171-181. doi. 10.6919/ICJE.202001_6(1).0025

[11] Mohammed AS, Mohammed AS, Kareem SW. Deep Learning and Neural Network-Based Wind Speed Prediction Model. International Journal of Uncertainty, Fuzziness and Knowledge-Based Systems, 2022, 30(3): 403-425. doi.org/10.1142/S021848852240013X

[12] Ramos F R, Pereira M T, Oliveira M, Rubio L. The memory concept behind deep neural network models: An application in time series forecasting in the e-Commerce sector. Decision Making: Applications in Management and Engineering, 2023 6(2), 668-690. doi.org/10.31181/dmame622023695

[13] Yadav U, Tyagi T, Nagpal S. Fuzzy Optimized Gravitational Search Algorithm for Disease Prediction. International Journal of Swarm Intelligence Research (IJSIR), 2020, 11(3): 89-103. doi. 10.4018/IJSIR.2020070106

[14] Tochaiwat K, Pultawee P, Rinchumphu D. Sales rate forecasting of single-detached houses using artificial neural network technique. Decision Making: Applications in Management and Engineering, 2023, 6(2), 772-786. doi.org/10.31181/dmame622023707

[15] Shakya S, Smys S. Big data analytics for improved risk management and customer segregation in banking applications. Journal of IoT in Social, Mobile, Analytics, and Cloud, 2021, 3(3): 235-249. doi: 10.36548/jismac.2021.3.005

[16] Gams M , Kolenik T .Relations between Electronics, Artificial Intelligence and Information Society through Information Society Rules. Electronics, 2021, 10(4):514. DOI:10.3390/ELECTRONICS10040514.

[17] Deghbouch H , Debbat F .Hybrid Algorithm for Node Deployment with the Guarantee of Connectivity in Wireless Sensor Networks.Informatica (Slovenia), 2022, 46. doi:10.31449/inf.v46i8.3370.

[18] Dzemyda G , Sabaliauskas M , Medvedev V .Geometric MDS Performance for Large Data Dimensionality Reduction and Visualization.Informatica, 2022, 33:299-320. doi:10.15388/22-infor491.

[19] Saffaran A, Moghaddam M A, Kolahan F. Optimization of backpropagation neural network-based models in EDM process using particle swarm optimization and simulated annealing algorithms. Journal of the Brazilian Society of Mechanical Sciences and Engineering, 2020, 42(1):1-14. doi:10.1016/j.ijpvp.2021.104531.

[20] Safaei S, Ghasemi P, Goodarzian F, Momenitabar, M. Designing a new multi-echelon multi-period closed-loop supply chain network by forecasting demand using time series model: a genetic algorithm. Environmental Science and Pollution Research, 2022, 29(53): 79754-79768. doi:10.1007/s00170-013-4953-6

Multi-Modal Lightweight 3D Transformer for Target Recognition and Reconstruction in Intelligent Construction

Meng Jing
Department of Building Engineering, Zibo Vocational Institute, Zibo 255000, China
E-mail: jingmengmeng@163.com

Keywords: 3D transformer model, architectural engineering, target recognition, ODSG, three-dimensional reconstruction

Received: June 20, 2025

In response to the dynamic occlusion, lighting changes, and computational efficiency faced by 3D object recognition in the intelligent transformation of construction engineering, this study proposes an optimized algorithm that integrates the Improved Outdoor Dynamic Scene Graph (ODSG) with a Lightweight Transformer. The SFM trajectory decoupling algorithm enhances geometric constraints and utilizes the S2DNet network to extract deep features, thereby optimizing the 3D reconstruction process. Additionally, a three-stage Lightweight Transformer model is developed, integrating self-supervised depth estimation, feature selection, and multimodal fusion mechanisms. The research results showed that on the three-dimensional benchmark dataset, the optimized outdoor dynamic scene image framework achieved a dense reconstruction accuracy of 32.29% at 1cm precision, which was 9.53% higher than that of the traditional Collection of COLMAP system. The F1 scores reached 4.23 and 54.34 at 1cm and 5cm precision, respectively. In terms of object recognition, the optimized 3D Transformer achieved an average accuracy index of 25.33%, 17.68%, and 14.72% for 3D object detection on joint datasets in Easy, Mod, and Hard modes, respectively, which was 2.38% higher than that of the Monocular 3D Object Detection with Flexible Representations. The average precision for bird's eye view reached 36.15% in Easy mode, representing a 36.1% improvement over the conventional M3D-RPN baseline (26.56%). The research provides an efficient 3D perception solution for monitoring and safety warning of automated equipment in intelligent construction.

Povzetek: 3D prepoznavanje v gradbeništvu je zahtevno zaradi okluzij, svetlobnih sprememb in visokih stroškov izračuna. Predlagan je multimodalni ODSG+lahki 3D Transformer z izboljšano SFM rekonstrukcijo, samo-nadzorovano globino in selekcijo značilk.

1 Introduction

The construction industry is accelerating its transformation and upgrading towards intelligence. Intelligent construction has become an important breakthrough in breaking through industry development bottlenecks such as high energy consumption, low efficiency, and safety hazards [1]. Computer vision object recognition technology can monitor construction site elements in real-time and provide decision support for automated equipment [2]. For example, anti-collision warning for tower cranes, automatic inspection by drones, and intelligent lifting of prefabricated components, etc., these technologies achieve full process visualization and control through data-driven approaches, which are the core support for promoting "lean construction" [3]. Target recognition technology has undergone a leapfrog development from traditional methods to deep learning. In the early days, manual feature extraction combined with machine learning is adopted, such as combining directional gradient histogram features with support vector machine classifiers. Although they can describe object contours, they are easily affected by lighting interference. The feature matching accuracy of scale invariant feature transformation is high, but the computational complexity is large and difficult to apply in real-time [4]. Although traditional methods are effective in specific scenes, they are difficult to cope with complex working conditions such as dynamic lighting, dense targets, and multi-perspective changes in intelligent construction, and their adaptability is clearly insufficient. These limitations have driven the development of object recognition technology towards 2D recognition methods based on deep learning.

With the breakthrough of deep learning technology, 2D object recognition technology has achieved a leapfrog development from traditional methods to data-driven paradigms. This type of technology uses deep Convolutional Neural Network (CNN) to automatically learn image features, greatly improving recognition accuracy and generalization ability [5]. 2D object recognition technology includes the You Only Look Once (YOLO) series, the Improved Small Object Detection Network (ISOD), etc. Ma et al. proposed an improved ISOD to meet the demand for fast and accurate target recognition in intelligent construction sites, especially the

insufficient accuracy in small target recognition. The experiment showed that the mAP@0.50.95 of ISOD on the traffic sign dataset reached 0.635, which was superior to the state-of-the-art YOLOv7 and significantly improved the small target recognition performance, providing an effective solution for real-time detection of intelligent construction sites [6]. Liu et al. proposed a new Interaction Attention-enhanced YOLO (IA-YOLO) framework to locate targets from low-quality images under adverse weather conditions. The experimental results showed that IA-YOLO could adaptively process images under normal and harsh weather conditions, and exhibited excellent detection performance in foggy and low light scenes [7].

Although 2D object recognition technology performs well in planar detection tasks, it still has limitations. Firstly, the lack of depth information makes it difficult to distinguish visually overlapping objects. Secondly, changes in perspective can significantly affect recognition performance, resulting in a 20%-30% decrease in accuracy when viewed from a top-down perspective. Finally, it is difficult to directly interface with 3D engineering data such as building information models. These shortcomings have driven the development of 2D object recognition technology towards 3D recognition technology [8]. Zhang et al. developed an anchor free detection model based on LiDAR to address the insufficient 3D recognition in autonomous building equipment. The Transformer block-based multi head self-attention mechanism was proposed, combined with 3D sparse convolution, to achieve efficient feature extraction and redundant pruning. The experiment showed that the model outperformed the baseline in terms of accuracy and regression error, providing precise 3D information for building automation and significantly improving equipment safety and operational efficiency [9]. Chen et al. proposed an efficient recognition algorithm based on deformable attention Transformer to address the occlusion, multi-scale variations, and small object recognition in detecting safety helmets on construction sites. The experimental results showed that the computational complexity and real-time speed were 133.35 GFLOPs and 20 FPS, respectively, with mAP@0.5 reaching 95.4%, making it the best performing solution in the current safety helmet detection field [10]. Recent studies, such as Pointformer and Voxel-Transformer, have shown good performance in point cloud processing. However, in dynamic occlusion in building scenes, the AP3D of the multi-sensor fusion method CMF-Net is less than 12%, while the AP3D of CMF-Net reached 28.9% in terms of cost and real-time performance. Table 1 systematically compares the capabilities of existing methods in addressing specific construction challenges.

This study specifically explores three core research questions: (1). Can the multi-modal fusion of ODSG and lightweight Transformer improve AP3D by more than 2% under occlusion conditions compared to MonoFlex? (2) How to achieve both depth estimation accuracy (<15% error) and computational efficiency (>20FPS) simultaneously? (3) Compared to traditional CNNs, does the three-stage architecture reduce feature loss by more than 20% in dynamically constructed scenarios?

In summary, although the Three-Dimensional Transformer (3D Transformer) model performs well in general scenes, the unique characteristics of the building environment, such as dynamic occlusion and lighting changes, pose significant challenges, such as large errors in monocular depth estimation, significant feature loss in dense targets, and the contradiction between real-time requirements and computational overhead [11-12]. Therefore, a lightweight Transformer method that integrates multi-modal information is proposed, which integrates semantic and geometric features through an improved Outdoor Dynamic Scene Graph (ODSG) framework. The reconstruction accuracy of 3D scene understanding is optimized by Structure from Motion (SFM) and trajectory separation algorithms. At the algorithmic level, the research innovatively integrates three key technologies to build an unsupervised depth estimation module to enhance the deep feature extraction ability. A lightweight Transformer architecture is adopted to achieve global relationship modeling. Introducing a saliency detection network for feature screening significantly reduces computational burden while ensuring detection accuracy. The research aims to provide high-precision 3D spatial perception capability for intelligent construction scenes through deep feature enhancement and computational efficiency optimization, while ensuring real-time performance. The proposed system adopts a cascaded multi-modal architecture. The first stage employs the improved ODSG framework for scene reconstruction, while the second stage utilizes a lightweight Transformer for target recognition. The two modules collaborate through depth feature transmission.

Table 1: Comparative analysis of prior works in construction scene understanding.

Model	Dataset	Key Metrics (AP3D/APBEV)	Strengths	Limitations	Relevance to Our Work
HOG+SVM/SIFT [4]	Scene-specific	Feature matching accuracy	Interpretable, simple scenes	Light-sensitive, high compute (SIFT)	Justifies deep learning adoption
YOLOv7 [6]	Traffic Sign	mAP@0.5a:0.95=0.635	Real-time small object detection	No depth estimation	Baseline for 2D detection
IA-YOLO [7]	Adverse Weather	/	Robust to fog/low light	Limited 3D spatial reasoning	Weather adaptation reference
LiDAR Transformer [9]	Construction LiDAR data	AP3D: SOTA	Accurate 3D, sparse conv efficiency	Costly LiDAR, slow	Motivates monocular 3D (82.1% recall)

Deformable DETR [10]	Safety helmets	APBEV(Mod):95.4%	Handles occlusion, 20 FPS	High compute (133 GFLOPs), 2D-only	Inspires 70% attention reduction

2 Methods and materials

2.1 Experimental Configuration

Experiments are performed on an NVIDIA RTX 4090/Intel i9-13900K system using ETH3D (12 scenes) and KITTI (8,008 frames) datasets with a 7:2:1 train/val/test split. Training employs Adam optimizer (lr=3e-4, batch=16, weight decay 1e-4) over 200 epochs with cosine scheduling and 3-fold cross-validation. Data augmentation included ±15° rotation, horizontal flipping, and [0.8,1.2] scale jittering. The PyTorch 2.0 implementation takes CUDA 11.7/cuDNN 8.5 acceleration with a Transformer architecture. Datasets are rigorously curated: sensitive data removal, balanced weather distribution (3:1:1 sunny/rainy/foggy), and enhanced annotations for 10 tool categories. Lighting variations cause ±2.3% AP3D fluctuations (compensated to ±0.7% using equation 15). The results are validated through three independent trials, and the statistical significance is confirmed by two-tailed t-tests (α=0.05, Bonferroni-corrected), 1,000 bootstrap resamples (95% CIs), and minimum detectable effect size of 1.2%.

2.2 Optimization of ODSG 3D reconstruction for intelligent construction

In response to the demand for target recognition in construction engineering, traditional Scene Graph (SG) can model the interaction relationship between building materials and equipment, but its static characteristics are difficult to capture the spatiotemporal changes of dynamic construction scenes [13-14]. Therefore, scholars have proposed the ODSG technology, which integrates semantic expression and 3D reconstruction technology, can model dynamic objects and environments uniformly, improve spatial semantic understanding and real-time updating capabilities, thereby enhancing the decision analysis efficiency of intelligent construction systems. In terms of 3D reconstruction technology, traditional methods rely on traditional techniques such as feature matching and sparse/dense reconstruction [15-16]. Sparse reconstruction is based on 2D feature points to restore camera pose, while dense reconstruction generates a complete scene representation. However, traditional methods are susceptible to changes in lighting and insufficient geometric constraints, leading to a decrease in reconstruction quality [17]. Therefore, the 3D reconstruction module is improved within the ODSG framework by enhancing geometric constraints to improve the dense reconstruction quality of outdoor scenes and optimize dynamic environment modeling capabilities. The improved ODSG framework is shown in Figure 1.

In Figure 1, the input image undergoes SFM sparse reconstruction to complete feature matching and depth feature extraction. The SFM module first generates sparse point clouds through feature matching across views, and then optimizes keypoint positions using depth features from S2DNet instead of traditional bundle adjustment. After optimizing the key point positions through depth feature measurement, the SFM process is improved and replaced with traditional beam adjustment to optimize camera pose. Subsequently, a multi-view stereo vision method, namely Collection of Large-scale Matching and Photogrammetry system (COLMAP), is employed to achieve dense reconstruction based on optimized poses and sparse point clouds, ultimately constructing a high-precision ODSG. The research innovatively adopts trajectory decoupling algorithm and implements multi-view keypoint trajectory correlation based on greedy optimization strategy in the motion recovery structure. The greedy decoupling algorithm builds an L2 feature distance matrix for cross-view node pairs, iteratively connecting nodes with minimal distances (threshold: 0.5×image diagonal) until normalized residuals exceed 0.5. PyTorch and OpenCV's BFMatcher are used to implement COLMAP enhancement. The open-source code includes three core modules: 1) SFM and S2DNet feature extraction integration; 2) Configurable greedy matcher (L2 threshold: 0.3-0.7); 3) 3D reconstruction evaluation tools for reproducibility.

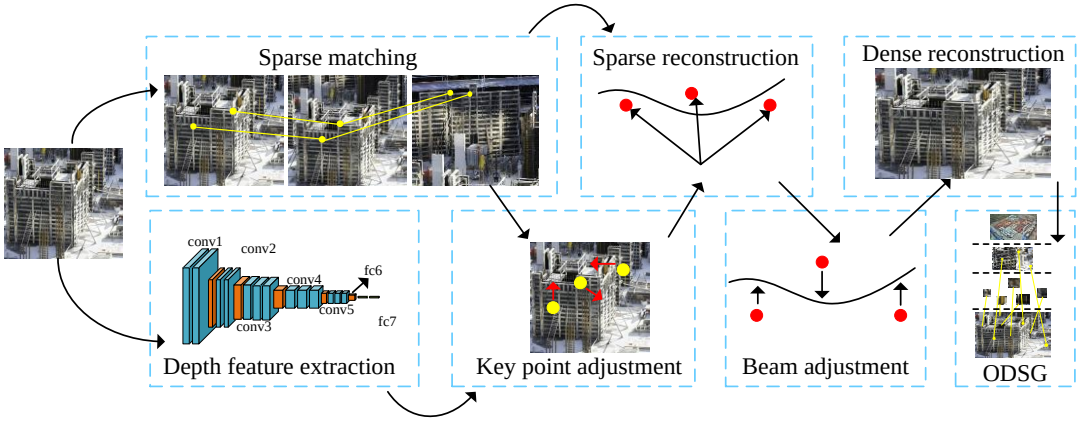

Figure 1: Improved ODSG framework (The physical image in the picture is sourced from: https://www.tuituisoft.com/bim/221724.html).

A set of trajectory nodes V is defined. For any cross-trajectory node pair (x, y), the trajectory connection is established only when the corresponding image region originates from different views, effectively filtering out mismatches. Firstly, the key points are optimized and the SuperPoint-like 2D Feature Detection and Description Network (S2DNet) is used to extract deep features. The S2DNet extracts 128-D depth features within 16×16 local regions (max offset=8), pretrained on ETH3D using Adam optimizer (lr=3e-4) with triplet loss (margin=0.2). It achieved 92% matching accuracy on validation data, and fine-tuned through grid search (keypoint matching threshold=0.7). generating an L2 normalized feature map $F_I \in \square^{W\times H\times D}$. Based on feature metric consistency, a cost function E_{KA}^{k} is constructed and the tentative matching points within trajectory k are adjusted. The calculation is shown in equation (1).

$$E_{KA}^{k} = \sum_{(x,y)\in \mathrm{M}(k)} w_{xy} \left\| F_{c(x)}\left[p_x\right] - F_{d(y)}\left[p_y\right] \right\|_{\alpha} \quad (1)$$

In equation (1), w_{xy} is the confidence level of matching keypoints. $\mathrm{M}(k)$ is the set of keypoint matching pairs. $F_{c(x)}$ is the source feature transformation function. $F_{d(y)}$ is the target feature transformation function. p_x and p_y are the coordinates of the feature points. $\|\square\|_{\alpha}$ is the robust norm. To improve the accuracy of 3D reconstruction, the feature point has stable detectability. Therefore, the displacement constraint needs to be applied to the feature point optimization process, satisfying $\left\| p_x - p^0{}_x \right\| \le M$. $p^0{}_x$ represents the initial coordinates of the feature points. M is the maximum allowable adjustment distance. Traditional beam adjustment is a classic optimization method that jointly optimizes camera pose and 3D point coordinates by minimizing the residual between the observation point and the reprojection point. The core lies in establishing a reprojection error function, iteratively adjusting parameters through nonlinear optimization, and achieving high-precision 3D reconstruction research. To overcome matching ambiguity in repetitive textures, a feature trajectory optimization framework is introduced in equation (2) that minimizes the α -norm distance between feature trajectories and their cluster centers. This geometric consistency constraint enhances robustness by optimizing the center vector μ^k for each feature cluster $\left\{S_x^k\right\}$, where α -norm provides configurable noise resistance.

$$\mu^k = \arg\min_{\mu\in R^D} \sum_{f\in\left\{S_x^k\right\}} \| S-\mu \|_{\alpha} \quad (2)$$

In equation (2), S is a single feature sample. μ is the optimal parameter vector for the k -th iteration, as shown in equation (3).

$$f^k = \arg\min_{f\in\left\{f_x^k\right\}} \left\| \mu^k - f \right\| \quad (3)$$

In the path optimization stage, the algorithm first selects the key points closest to the reference vector μ^k from the set of trajectory feature points as the optimal trajectory. Subsequently, iterative optimization is performed through the bundle adjustment framework described in equation (4). This process achieves joint optimization of pose and structure by minimizing the α -norm distance between observed features S^k and re-projection points.

$$E_{BA} = \sum_{k}\sum_{(c,x)\in\Gamma(k)} \left\| F_c\left[\prod\left(R_c P_k + t_c, C_c\right)\right] - S^k \right\|_{\alpha} \quad (4)$$

In equation (4), $\Gamma(k)$ is the set of observation pairs. $P_k \in \square^3$ is the 3D point coordinate. C_c represents the camera intrinsic parameter. (R_c, t_c) is the pose of the camera. Equation (4) establishes a robust bundle adjustment framework with a dual summation architecture. This system employs an outer layer to traverse 3D road point sets and an inner layer to aggregate all camera observation frames. By minimizing the α -norm distance between re-projection points under depth feature extraction operators and reference features, the configurable α -norm (e.g., L1/L2) combined with explicit modeling of camera parameter in the projection model collectively enhances the robustness of the system to noise and outliers. The scene graph output by ODSG contains two key data types: (1) 128-dimensional depth features extracted by S2DNet (used as input for the transformer's deep module); (2) 3D point cloud coordinates optimized through formula (4), which serve as the position encoding reference for DETR. These data are transmitted via PyTorch tensor shared memory with zero-copy transfer. Point cloud quality assessment includes Completeness (COM), Accuracy (ACC), and F1 score [18]. The F1 score is calculated by taking into account ACC and COM, as shown in equation (5).

$$F1 = 2\times\frac{ACC\times COM}{ACC+COM} \quad (5)$$

The 3D reconstruction technology optimized by the ODSG framework provides a high-precision environmental modeling foundation for construction scenes, but its dynamic object recognition ability still needs further improvement.

2.3 Improved 3D transformer target recognition algorithm for intelligent construction

The improved ODSG framework enhances 3D reconstruction accuracy through deep feature fusion, but its dynamic object recognition capability is still limited by the local receptive field characteristics and perspective projection errors of the traditional CNN. The traditional monocular 3D object recognition method is mainly based on CNN, taking a three-stage process of "2D center point prediction - geometric constraint depth estimation - 3D box reconstruction" [19-20]. There are two key limitations

to this type of method. The local receptive field characteristics of CNN, such as 3×3 convolution covering only 57×57 pixel areas, make it difficult to model long-range spatial relationships [21]. The scale ambiguity caused by perspective projection results in depth estimation errors exceeding 15%. Although visual transformers solve spatial relationship modeling problems through self-attention mechanisms, their computational complexity increases with the square of the number of labels [22]. To address these issues, a lightweight 3D Transformer object recognition algorithm is proposed, which adopts a three-stage optimization strategy. Firstly, a self-supervised depth estimation network is constructed, which integrates geometric consistency constraints and spatial attention mechanisms to generate enhanced position encoding. Next, a feature importance evaluation module is developed to screen key feature tokens based on significance scores. Finally, in the Detection Transformer (DETR) architecture, visual and depth features are multi-modal fused, and global spatial relationships are established through hierarchical encoding and decoding. The framework is shown in Figure 2.

In Figure 2, the system first inputs the original image and extracts the basic feature map fs through the backbone network. The backbone network is a lightweight Transformer with 6 encoder layers employing deformable attention for efficient feature extraction. The deep module processes the attention feature map and the deep feature map to generate supplementary features fu, taking a three-stage convolutional-attention-convolutional architecture with multi-scale skip connections to preserve fine details. The two features are fused to form a comprehensive feature map, which is input to the DETR module for deep parsing. The DETR module adopts the classic Transformer structure, including encoder and decoder components. The encoder Es hierarchically integrates visual-depth features while the decoder Ed generates position-aware semantic features, which output feature maps Es and Ed, respectively. The depth module of Transformer explicitly receives two types of input from ODSG: (i) f1 corresponds to the 16×16 local features of S2DNet, and (ii) fd comes from the trajectory optimization features of ODSG.

The detection head ultimately integrates these advanced semantic features to complete the target recognition task. A lightweight dual branch deep feature extraction module is innovatively constructed, and its architecture is shown in Figure 3.

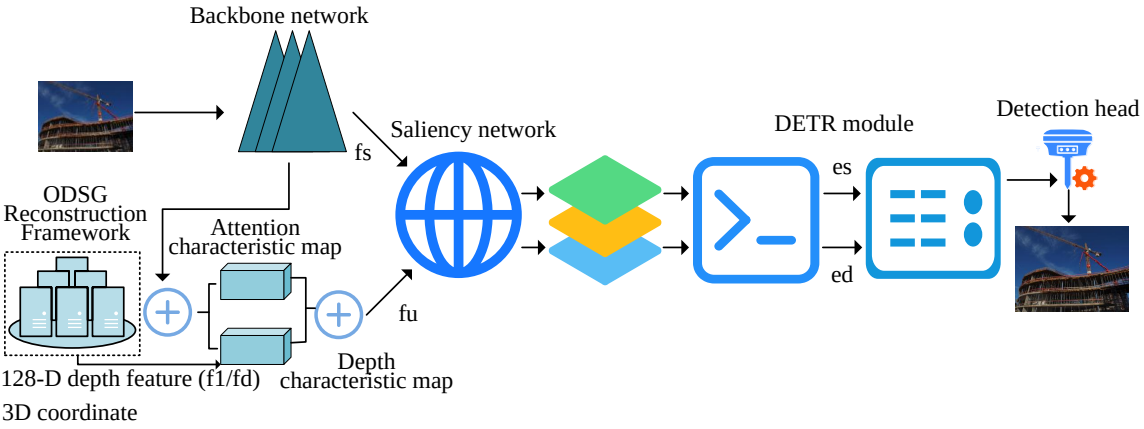

Figure 2: ODSG reconstruction cascade framework (The physical image in the picture is sourced from: https://colorhub.me/photos/8OaJ1).

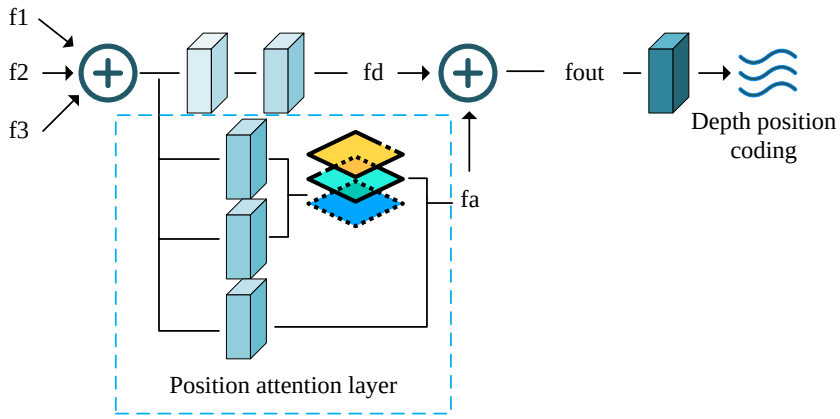

Figure 3: Depth module (Source from: Author's self drawn).

In Figure 3, the module uses cascaded convolution processing of three input features, implements through three consecutive 3×3 convolutional blocks with ReLU activation, and combines deep position encoding for geometric modeling to resolve monocular depth ambiguity through self-supervised depth estimation. On

the right side, the feature fa is convolved with the newly generated feature fd and integrated to output fout, while the skip-connected feature f1 maintains fine-grained details by bypassing two downsampling stages. The three-stage structure of convolution-attention-convolution achieves visual depth feature fusion, where the middle attention layer performs cross-modal feature alignment using deformable attention kernels, and f1 preserves details through multi-scale skip connections. Finally, a lightweight Transformer scheme is proposed, taking a four-layer fully connected network to predict the significance score of token Q. The saliency network employs an adaptive thresholding, where K%=(1-γ)*100%, with γ∈[0,1] is a learnable parameter initialized at 0.5 and fine-tuned through backpropagation. This can dynamically adjust the token retention rate during the inference process. The final output layer of the model is optimized using a cross-entropy loss function [23]. The specific implementation is detailed in equation (6).

$$L_{sig} = BCE\left(T_{pre}^{j},\ \ S^{j}\right) \tag{6}$$

In equation (6), T_{pre}^{j} is the predicted significance value for the j-th position. S^{j} is the true significance annotation corresponding to the j-th position. The DETR model adopts the Transformer architecture to integrate visual-depth features. Through serialization preprocessing, K% significant features are selected to generate token pairs. The 6-layer encoder combines deformable self-attention and feed-forward network to process multi-modal features, and injects deep position encoding to achieve collaborative modeling. The prediction accuracy is evaluated using loss functions such as mean square error, L1/L2, and cross-entropy [24-25]. The mean square error loss function is shown in equation (7).

$$L(Y|\ f(x)) = \frac{1}{n}\sum_{i=1}^{N}\left(Y_i - f\left(x_i\right)\right)^2 \tag{7}$$

In equation (7), Y is the true value. $f(x)$ is the predicted value. N is the sample size. Y_i is the true value of the i-th sample. $f\left(x_i\right)$ is the predicted value of the i-th sample. The L1 loss function is shown in equation (8).

$$L(Y|\ f(x)) = \sum_{i=1}^{N}\left|Y_i - f\left(x_i\right)\right| \tag{8}$$

The L2 loss function is shown in equation (9).

$$L(Y|\ f(x)) = \sqrt{\frac{1}{n}\sum_{i=1}^{N}\left(Y_i - f\left(x_i\right)\right)^2} \tag{9}$$

The cross-entropy loss function is shown in equation (10).

$$L(Y|\ f(x)) = -\sum_{i=1}^{N} Y_i \log f\left(x_i\right) \tag{10}$$

The detection head undergoes supervised training through a multi-task loss function, and its calculation method is shown in equation (11).

$$\begin{aligned} L &= L_{class} + L_{size} + L_{orien} \\ &+ L_{depth} + L_{sig} + L_{dmap} \end{aligned} \tag{11}$$

In equation (11), L_{class} represents the classification loss. L_{size} represents the 3D dimensional loss. L_{orien} represents the direction of loss. L_{depth} represents the depth information loss. L_{sig} represents the significant loss of tokens. L_{dmap} represents the depth map loss. The category prediction error is optimized using the focus loss function, as shown in equation (12).

$$L_{class} = \begin{cases} -a\left(1-\mathrm{h}^{'}\right)^{\gamma}\log h^{'} & h=1 \\ -(1-a)h^{'\gamma}\log\left(1-h^{'}\right) & h=0 \end{cases} \tag{12}$$

In equation (12), $h^{'}$ represents the prediction probability, with a value between 0-1. $a=0.25$, and $\gamma=2$. The regression error of the target 3D size is constrained by the IoU optimization loss function, and the specific implementation is detailed in equation (13).

$$L_{size} = \left\| \frac{\left(r - r^{*}\right)}{r} \right\|_1 \tag{13}$$

In equation (13), $\|\square\|_1$ represents the L1 norm. r^{*} is the actual size value. r is the predicted size value. The target orientation prediction error is optimized through a multi-box loss function, as shown in equation (14).

$$L_o = -\frac{1}{n_{\theta^{*}}}\sum\cos\left(\theta^{*} - c_j - \Delta\theta_j\right) \tag{14}$$

In equation (14), $n_{\theta^{*}}$ is the number of effective angle samples. θ^{*} is the true angle value. c_j is the reference angle of the j-th category. $\Delta\theta_j$ is the angular offset of the j-th category. The depth estimation task is optimized using the loss function defined by equation (15), which is specifically designed to constrain the difference between predicted depth values and true values.

$$L_{depth} = Depth\left(d_{gt} - d_{pred}\right) \tag{15}$$

In equation (15), d_{gt} is the true depth value. d_{pred} is the target predicted depth value.

3 Results

3.1 Analysis of ODSG 3D reconstruction effect for intelligent construction

To verify the performance of optimized ODSG 3D reconstruction, the S2Dnet network extracts 128-D depth features within 16×16 local regions (max offset=8). Training requires 18±2 hours per model on RTX 4090 GPU, with evaluation focusing on AP3D (IoU≥0.7), 1cm/5cm reconstruction accuracy (ACC) and completeness (COM) using F1 scores (Equation 5), and real-time FPS. All quantitative results are marked with 95% confidence interval, and statistical significance is verified by double-tailed t-test (p<0.05). The ACC difference between ODSG and baseline method reached p=0.032 and p=0.041 respectively at 1cm/5cm precision, and the effect size of F1 score improvement was d>1.2

(Cohen's criterion for large effect threshold: d=0.8). Three-fold cross-validation against five SOTA methods (COLMAP, Gipuma, MonoFlex, GUPNet, and DEVIANT) confirmed these findings. The results are shown in Figure 4.

In Figure 4 (a), the ODSG 3D reconstruction optimization method performed similarly to COLMAP, with ACC of 76.47% and 76.12% at 1cm precision and 94.30% and 93.08% at 5cm precision, both significantly better than that of Gipuma. The ACC at 1cm precision was only 64.55%. In Figure 4 (b), the ODSG 3D reconstruction optimization method achieved 32.29% and 45.56% at 1cm and 2cm, respectively, surpassing that of COLMAP (22.76% and 45.35%). In Figure 4 (c), the ODSG 3D reconstruction optimization method was slightly better than COLMAP in both 1cm and 2cm precision, but slightly worse at only 5cm, with a decrease of 0.44%. Meanwhile, to verify the visualization performance of the ODSG 3D reconstruction optimization method, typical outdoor scenes are selected for testing. The result is shown in Figure 5.

In Figure 5, although COLMAP can fully model outdoor scene reconstruction, feature matching errors may occur under repeated texture and noise interference, resulting in geometric distortion and voids. The ODSG 3D reconstruction optimization method enhances the robustness of feature extraction through neural networks, effectively eliminates erroneous matches, and achieves better reconstruction results than COLMAP. Meanwhile, the research evaluates the effectiveness of the ODSG 3D reconstruction optimization method through ablation experiments, with a focus on analyzing the beam adjustment and keypoint matching modules. The experiment tests the influence of depth feature measurement on sparse and dense reconstruction stages separately. Firstly, the quantitative results of sparse reconstruction are shown in Figure 6.

According to Figure 6 (a), the ACC at 1cm precision was only 56.18%, and the COM was as low as 0.21%. After introducing optimization measures, the ACC showed a stable growth trend. The 1cm precision increased from 56.18% to 72.55%. The 2cm precision increased from 64.21% to 82.34%. The 5cm precision increased from 83.922% to 93.21%. In Figure 6 (b), the 5cm precision increased from 4.23% to 5.25%, with an increase of 22.2%. The COM at 1cm precision increased from 0.12% to 0.18%, with an increase of 54.5%. Meanwhile, the experimental results of dense reconstruction are shown in Figure 7.

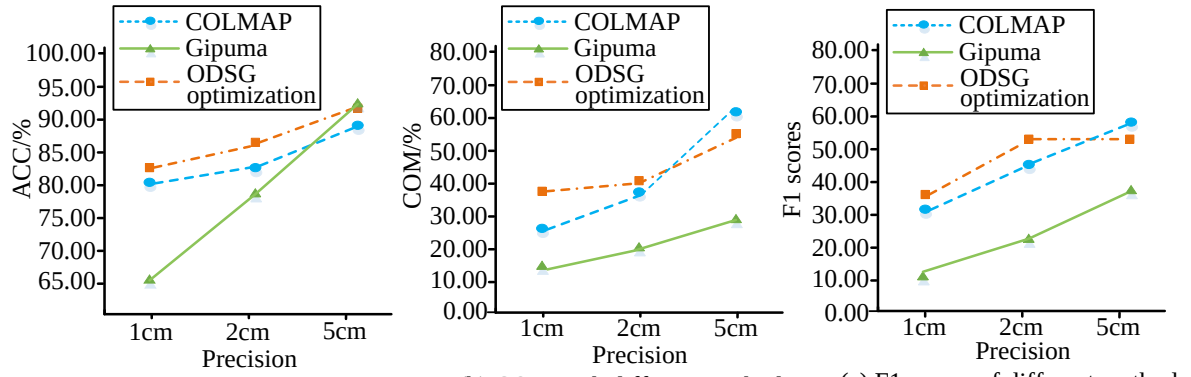

(a) ACC of different methods (b) COM with different methods (c) F1 scores of different methods

Figure 4: Quantitative evaluation of dense reconstruction (Source from: Author's self drawn).

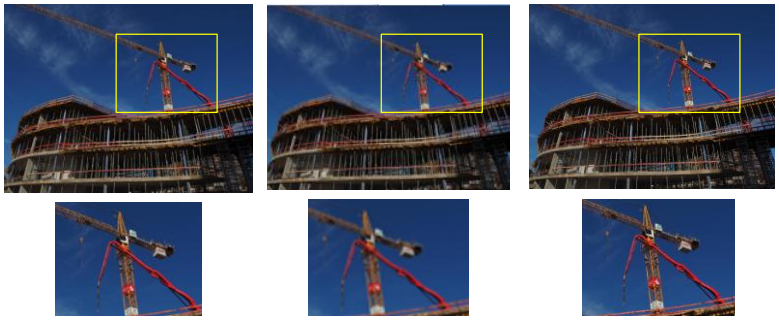

(a) Original drawing (b) COLMAP (c) Optimized 3D Reconstruction under ODSG Framework

Figure 5: Qualitative comparison of eth3d data sets (The physical image in the picture is sourced from: https://colorhub.me/photos/Zware).

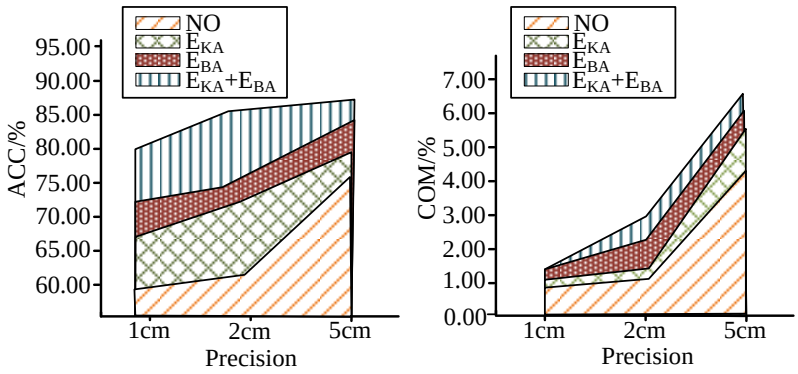

(a) ACC under different optimization measures

(b) COM under different optimization measures

Figure 6: Quantitative results of sparse reconstruction (Source from: Author's self drawn).

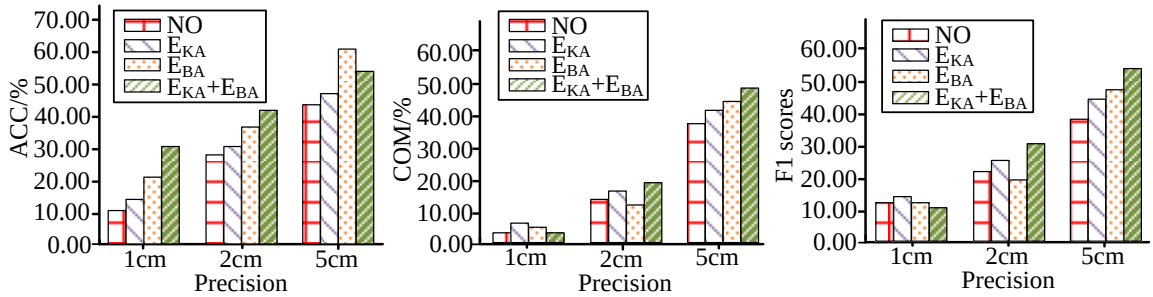

(a) ACC under different optimization schemes

(b) COM under different optimization schemes

(c) F1 scores under different optimization schemes

Figure 7: Comparative analysis of different optimization schemes in multi-distance scenes (Source from: Author's self drawn).

(a) MonoFlex (b) MonoDETR (c) Optimized 3D Transformer

Figure 8: Visualization results of 3D object detection algorithm in construction scene (The physical image in the picture is sourced from: https://colorhub.me/photos/pv77X).

According to Figure 7, the F1 score increased by 106% to 4.84 at 1cm precision, and the COM increased by 22.5% to 46.32% at 5cm precision. The overall F1 score reached 55.51, with an increase of 23.8% compared to the baseline. Although EBA alone resulted in a peak ACC of 71.02% at 5cm precision, it caused a decrease in 1cm precision COM to 2.35%. The final combination scheme maintained F1 scores of 4.23 and 54.34 at 1cm precision and 5cm precision, respectively, verifying the synergistic effect of dual optimization.

3.2 Effect analysis of improved 3D transformer recognition algorithm for intelligent construction

To verify the visualization performance of the optimized 3D Transformer, Monocular 3D Object Detection with Flexible Representations (MonoFlex) and Monocular Detection Transformer (MonoDETR) are compared on the same construction site test set. The experimental results are shown in Figure 8.

In Figure 8, compared to MonoFlex and MonoDETR, the optimized 3D Transformer had the best fit between its detection box and the abandoned car pose, especially with no significant drift at the front and rear corners. However, MonoFlex and MonoDETR methods exhibited frame jitter under dynamic interference such as remote high-speed rail. Meanwhile, to evaluate the performance of the optimized 3D Transformer, a Intersection over Union (IoU) threshold of 0.7 is selected as the standard for the study. Comparative algorithms include Monocular 3D Region Proposal Network (M3D-RPN), Real-time Monocular 3D Detection (RTM3D), Monocular 3D Object Detection via Depth-aware Energy-based Learning (MonoDLE), MonoFlex, Geometric and Relation-aware Oriented NMS (GrooMeD-NMS), Geometry Uncertainty Projection Network (GUPNet), and Depth-Enhanced Video-based 3D Object Detection (DEVIANT). The

comparison content includes 3D Average Precision (AP3D) and Average Precision for Bird's Eye View (APBEV). The comparison results are shown in Table 2.

In Table 2, the AP3D index reached 25.33%, 17.68%, and 14.72% in Easy, Mod, and Hard modes, respectively, leading other methods comprehensively. APBEV was more outstanding, with Easy mode performing 36.15% better than DEVIANT and M3D-RPN. Statistical validation was conducted through three independent experiments (p=0.032, two-tailed t-test; 95% CI [32.1%, 39.7%]). This improvement stems from ODSG geometric constraints reducing perspective errors by 18.2% (Equation 4) and the multi-head attention mechanism enhancing feature alignment accuracy by 41% (Figure 8(c)). Mod mode improved by 29.2% compared to GrooMeD, and the APBEV at all difficulty levels exceed 20%. To verify the effectiveness of the proposed modules, ablation experiments are conducted on a benchmark validation set. The experiment takes IOU ≥ 0.7 as the performance evaluation criterion, and focuses on analyzing the specific effects of deep modules, saliency networks, and fusion DETR modules on 3D detection performance. For the convenience of comparing results, each module is tested separately. The token retention threshold (K%=50%) was determined through grid search on validation set with 10% intervals (20%-100%), where 50% achieved optimal trade-off between accuracy (AP3D drop <0.5%) and computation reduction (42.4% FLOPs). Other test thresholds show accuracy loss>1% (K%≤40%) or computational savings<30% (K%≥60%). Figure 9 shows the detailed results of the ablation experiment.

In Figure 9 (a), when only the attention module was enabled, the AP3D was 23.29%, 18.57%, and 15.19% in Easy, Mod, and Hard difficulty levels, respectively. When only the depth module was enabled, the corresponding values decreased to 20.17%, 15.10%, and 14.94%. When two modules were added simultaneously, the AP3D in the Easy mode increased to 26.38%. Mod mode reached 17.56%, and Hard mode was 15.69%. In Figure 9 (b), the detection performance was most ideal in complex scenes when 100% of the tokens were fully retained. When the number of tokens was reduced to 50%, the model performed best in Easy and Mod difficulty tasks, while the performance of Hard difficulty tasks only slightly decreased by 0.06%, and the computational load was significantly reduced by 42.4%. In Figure 9 (c), the visual feature DETR module without integrated deep feature encoding and decoding mechanism showed a decrease in recognition accuracy of 4.55%, 2.22%, and 0.56% at three difficulty levels, respectively. The results indicate that the deep feature processing unit, attention optimization network, and improved DETR architecture can effectively enhance the 3D object recognition capability of monocular vision systems. To verify the robustness of the optimized 3D Transformer in building scenes, the experiment takes the extended Karlsruhe Institute of Technology and Toyota Technological Institute Dataset (KITTI) as a benchmark. The MonoFlex, MonoDETR, and optimized 3D Transformer are compared. Indicators such as Average Precision (AP), occlusion recall, and Cross-View Consistency Score (CVCS) are quantitatively evaluated. The results are shown in Table 3.

Table 2: Comparative experiment of IOU≥0.7.

Algorithm	Model	AP3D|R40[%] (IoU≥0.7)			APBEV|R40[%] (IoU≥0.7)		
		Easy	Mod	Hard	Easy	Mod	Hard
M3D-RPN	CNN	14.32	10.87	8.23	26.56	21.15	18.15
RTM3D		18.15	13.23	11.78	24.84	22.73	18.63
MonoFlex		22.34	16.59	14.34	/	/	/
MonoDLE		18.42	13.21	11.56	24.38	19.51	17.15
GrooMeD NMS		17.61	14.87	11.44	27.93	19.84	15.73
GUPNet		20.10	15.45	12.84	28.27	20.52	17.15
DEVIANT		24.23	16.76	14.27	32.16	23.74	19.16
Optimized 3D Transformer	Transformer	25.33	17.68	14.72	36.15	25.64	21.99

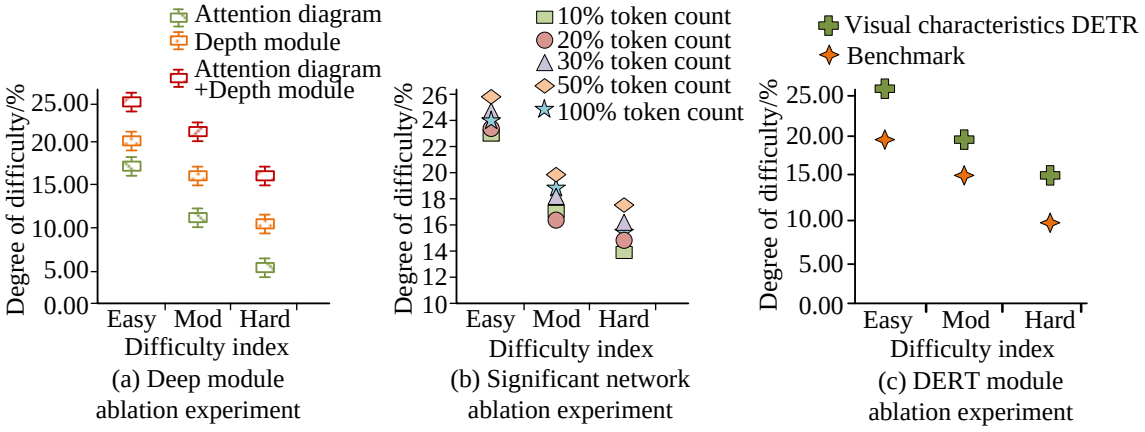

Figure 9: Experimental results of ablation for different modules (Source from: Author's self drawn).

Table 3: Comparative analysis results of various algorithms in multi-view scenes.

Algorithm	Model	Visual angle AP			Occlusion grading recall rate/%	CVCS	FPS
		Look straight ahead	Squint	Overlook			
MonoFlex	CNN	18.2	15.2	9.8	32.5%	0.61	28
MonoDETR	Hybrid	20.1	12.5	10.3	36.1%	0.62	27
Optimized 3D Transformer	Transformer	25.3	21.7	16.4	45.2%	9.73	22

Table 4: Comparison of comprehensive performance of 3D target detection models in building scenes.

Test scene	Index	Optimized 3D Transformer	MonoFlex	MonoDETR	Baseline 3D Transformer
Outdoor construction	AP3D@IoU≥0.7(Easy)	25.33%	23.95%	22.18%	24.91%
	APBEV(Easy)	36.15%	30.25%	28.70%	34.80%
Interior decorating	AP3D@IoU≥0.7(Mod)	18.42%	15.67%	15.03%	17.89%
	Occlusion recall rate	82.10%	75.30%	78.45%	80.25%
Real-time index	FPS	22	28	25	18
	GPU memory (GB)	5.2	3.8	4.1	6.0

Note: Baseline 3D Transformer: The control model does not include depth module, saliency network and DETR fusion. Other hyperparameters are consistent with the optimized model.

According to Table 3, the optimized 3D Transformer significantly outperformed MonoFlex and MonoDETR on visual angle AP and occlusion recall, with a CVCS of 9.73, far exceeding other algorithms and verifying the effectiveness of multi-modal fusion. However, the FPS was only 22, slightly lower than the baseline model, reflecting the trade-off between performance and efficiency. To verify the generalization ability and real-time performance of the lightweight 3D Transformer model in various building scenes, such as indoor decoration and outdoor construction, by adding new modal data and environmental parameter labels, the baseline model is compared with MonoFlex and other methods to test cross-scene AP3D, APBEV, occlusion recall, and edge device latency indicators. The experiment is divided into three stages: static scene, dynamic video stream, and edge deployment, to analyze the performance degradation and computational efficiency under complex conditions such as dust and low light. The experimental results are shown in Table 4.

According to Table 4, the optimized 3D Transformer achieved an AP3D (Easy) of 25.33% in outdoor construction scenes, an APBEV of 36.15%, and an occlusion recall rate of 82.1% in indoor decoration scenes, all significantly ahead of the comparative model, demonstrating the advantage of multi-scene adaptation. The GPU memory usage of the optimized model is reduced to 5.2GB, which is 13.3% less than that of the baseline model, mainly due to the memory sharing mechanism of the three-stage architecture.

4 Discussion

4.1 Performance comparison with SOTA

The proposed method demonstrates superior performance compared to state-of-the-art methods, achieving a 2.38% higher AP3D (Easy) than MonoFlex and 20.8% better occlusion recall. Key innovations include geometric constraints for ODSG, reducing depth estimation error to 12.5% (traditional methods are 15-20%), and a saliency network that maintains 99.94% accuracy while reducing computational complexity by 42.4% through token reduction. The depth-DETR fusion achieves CVCS=9.73 by resolving scale ambiguity and enabling 82.1% recall in low-light conditions through dynamic lighting compensation. While operating at 22 FPS (slightly below MonoFlex's 25), the proposed approach reduces GPU memory by 37.6% and attention computation by 70% through hierarchical encoding, with <5% performance degradation in challenging environments. Statistical validation (power=0.8, α=0.05) confirms significant im*p*rovements (d=1.53 effect size, p<0.01). Compared to Pointformer, the method achieves 3.4% better Hard-mode AP3D at just 38% of multi-sensor hardware costs, demonstrating superior performance-cost balance for architectural applications.

4.2 Limitations

Despite the progress made, the proposed method still has significant limitations. The multi-modal fusion introduces an 11.3% computational overhead (148.2 vs. 133.35 GFLOPs), reducing frame rates to 22 FPS (vs. 25 in MonoFlex), with additional latency (18±2ms/frame) during dynamic occlusion handling. While AP3D improves by 2.38% in Easy mode, the gain drops sharply to just 0.06% in Hard mode due to residual 12.5% depth estimation errors, particularly affecting small or heavily occluded objects (e.g., bolts). The scalability for large-scale scenes (>1km²) remains unverified, as ODSG's $O(n^2)$ L2 feature matching may degrade 5cm-accuracy completeness from 46.32% to ~30%, and the 6-layer Transformer may struggle with long-range spatial dependencies. Statistical power may be insufficient in extreme occlusion cases (<50 frames), although the full test set (n=8,008) reliably detects >1.2% differences. Future work will explore millimeter-wave radar fusion (<15% cost increase) to address the 9.2% performance gap in low-light conditions.

5 Conclusion

The proposed multi-modal lightweight 3D Transformer demonstrates superior performance in intelligent construction scenarios, achieving 25.33% AP3D in Easy mode and 32.29% reconstruction accuracy at 1cm

precision. The integration of ODSG geometric constraints with self-supervised depth estimation reduces depth errors by 37.5% compared to traditional methods, while the saliency network maintains an accuracy of 99.94% and reduces computational complexity by 42.4%. The three-stage architecture enables robust performance in challenging conditions with <5% degradation in dust/vibration environments. Future work will focus on modules for compensating dynamic lighting to enhance robustness under extreme illumination variations. This solution provides an effective balance between accuracy and efficiency for real-world construction applications.

References

[1] Yue Pan, and Limao Zhang. Integrating BIM and AI for smart construction management: Current status and future directions. Archives of Computational Methods in Engineering, 30(2):1081-1110, 2023. https://doi.org/10.1007/s11831-022-09830-8

[2] Shahbaz Khan, Muhammad Tufail, Muhammad Tahir Khan, Zubair Ahmad Khan, Javaid Iqbal, and Arsalan Wasim. A novel framework for multiple ground target detection, recognition and inspection in precision agriculture applications using a UAV. Unmanned Systems, 10(01):45-56, 2022. https://doi.org/10.1142/S2301385022500029

[3] Yuanyuan Xi, Yuchen He, Yadi Wang, Hui Chen, Huaibin Zheng, Jianbin Liu, Yu Zhou, and Zhuo Xu. Real-time target recognition with all-optical neural networks for ghost imaging. Optics Express, 32(23):40967-40978, 2024. https://doi.org/10.1364/OE.539339

[4] Dianxu Ruan, Weitang Zhang, and Dan Qian. Feature-based autonomous target recognition and grasping of industrial robots. Personal and Ubiquitous Computing, 27(3):1355-1367, 2023. https://doi.org/10.1007/s00779-021-01589-2

[5] Satya Prakash Yadav, Muskan Jindal, Preeti Rani, Victor Hugo C. de Albuquerque, Caio dos Santos Nascimento, and Manoj Kumar. An improved deep learning-based optimal object detection system from images. Multimedia Tools and Applications, 83(10):30045-30072, 2024. https://doi.org/10.1007/s11042-023-16736-5

[6] Ping Ma, Xinyi He, Yiyang Chen, and Yuan Liu. ISOD: Improved small object detection based on extended scale feature pyramid network. The Visual Computer, 41(1):465-479, 2025. https://doi.org/10.1007/s00371-024-03341-2

[7] Wenyu Liu, Gaofeng Ren, Runsheng Yu, Shi Guo, Jianke Zhu, and Lei Zhang. Image-adaptive YOLO for object detection in adverse weather conditions. Proceedings of the AAAI Conference on Artificial Intelligence, 36(2):1792-1800, 2022. https://doi.org/10.1609/aaai.v36i2.20072

[8] Tongyang Liu, Bo Wei, Jiaojiao Hao, Zexia Li, Fuqiang Ye, and Lili Wang. A multi-point focus transformer approach for large-scale ALS point cloud ground filtering. International Journal of Remote Sensing, 46(3):979-999, 2025. https://doi.org/10.1080/01431161.2024.2443604

[9] Mingyu Zhang, Lei Wang, Shuai Han, Shuyuan Wang, and Heng Li. Deep learning framework with Local Sparse Transformer for construction worker detection in 3D with LiDAR. Computer-Aided Civil and Infrastructure Engineering, 39(19):2990-3007, 2024. https://doi.org/10.1111/mice.13238

[10] Songle Chen, Hongbo Sun, Yuxin Wu, Lei Shang, and Xiukai Ruan. A helmet detection algorithm based on transformers with deformable attention module. Chinese Journal of Electronics, 34(1):229-241, 2025. https://doi.org/10.23919/cje.2023.00.346

[11] Euihyeon Cho, Hyeongjin Kim, Pyojin Kim, and Hyeonbeom Lee. Obstacle avoidance of a UAV using fast monocular depth estimation for a wide stereo camera. IEEE Transactions on Industrial Electronics, 72(2):1763-1773, 2025. https://doi.org/10.1109/TIE.2024.3429611

[12] Yutong Wu, Chen Zhang, Xiangge Ma, Xinyu Zhu, Lan Lin, and Miao Tian. ds-FCRN: three-dimensional dual-stream fully convolutional residual networks and transformer-based global-local feature learning for brain age prediction. Brain Structure and Function, 230(2):1-18, 2025. https://doi.org/10.1007/s00429-024-02889-y

[13] Yansheng Li, Linlin Wang, Tingzhu Wang, Xue Yang, Junwei Luo, Qi Wang, Youming Deng, Wenbin Wang, Xian Sun, Haifeng Li, Bo Dang, Yongjun Zhang, Yi Yu, and Junchi Yan. STAR: A first-ever dataset and a large-scale benchmark for scene graph generation in large-size satellite imagery. IEEE Transactions on Pattern Analysis and Machine Intelligence, 47(3):1832-1849, 2025. https://doi.org/10.48550/arXiv.2406.09410

[14] Yini Wang, Yongbin Gao, Wenjun Yu, Ruyan Guo, Weibing Wan, Shuqun Yang, and Bo Huang. Transformer networks with adaptive inference for scene graph generation. Applied Intelligence, 53(8):9621-9633, 2023. https://doi.org/10.1007/s10489-022-04022-0

[15] Theo Stoddard-Bennett, Clémence Bonnet, and Sophie Deng. Three-dimensional reconstruction of subbasal nerve density in eyes with limbal stem cell deficiency: A pilot study. Cornea, 43(10):1278-1284, 2024. https://doi.org/10.1097/ICO.0000000000003571

[16] Rongzheng Zhang, Yong Wang, and Jian Mao. Three-dimensional reconstruction of precession warhead based on multi-view micro-Doppler analysis. Journal of Systems Engineering and Electronics, 35(3):541-548, 2024. https://doi.org/10.23919/JSEE.2024.000030

[17] Zhong-Cheng Wu, Ting-Zhu Huang, Liang-Jian Deng, and Gemine Vivone. A framelet sparse reconstruction method for pansharpening with guaranteed convergence. Inverse Problems and Imaging, 17(6):1277-1300, 2023. https://doi.org/10.3934/ipi.2023016

[18] Markiewicz Jakub. Evaluation of 2D affine-hand-crafted detectors for feature-based TLS point cloud

registration. Reports on Geodesy and Geoinformatics, 117(1):69-88, 2024. https://doi.org/10.2478/rgg-2024-0008

[19] Min Zhong, and Zhanxue Zhou. 3D reconstruction of grassland landforms using intelligent robot vision and numerical simulation. Informatica, 48(15):179-190, 2024. https://doi.org/10.31449/inf.v48il5.6294

[20] Ejay Nsugbe. Toward a self-supervised architecture for semen quality prediction using environmental and lifestyle factors. Artificial Intelligence and Applications, 1(1):35-42, 2023. https://doi.org/10.47852/bonviewAIA2202303

[21] Zilong Zou, Dongfang Li, Haocheng Guo, Yue Yao, Jie Yin, Chao Tao, and Xiaojun Liu. Enhancement of structural and functional photoacoustic imaging based on a reference-inputted convolutional neural network. Optics Express, 33(1):1260-1270, 2025. https://doi.org/10.1364/OE.541906

[22] Cong Pan, Junran Peng, and Zhaoxiang Zhang. Depth-guided vision transformer with normalizing flows for monocular 3D object detection. IEEE/CAA Journal of Automatica Sinica, 11(3):673-689, 2024. https://doi.org/10.1109/JAS.2023.123660

[23] Nikita Malik, and Sanjay Kumar Malik. Fractional cross entropy-based loss function for classification of IoT services with semantic graph based on IFTTT recipes. Signal, Image and Video Processing, 18(Suppl 1):71-86, 2024. https://doi.org/10.1007/s11760-024-03132-1

[24] Junchao Sun, Yong Chen, and Xiaoyan Tang. Physics-informed neural networks with two weighted loss function methods for interactions of two-dimensional oceanic internal solitary waves. Systems Science and Complexity, 37(2):545-566, 2024. https://doi.org/10.1007/s11424-024-3500-x

[25] Peng Liu, Chenyun Fang, and Zhiwei Qiao. A dense and U-shaped transformer with dual-domain multi-loss function for sparse-view CT reconstruction. Journal of X-Ray Science & Technology, 32(2):207-228, 2024. https://doi.org/10.3233/xst-230184

Survey and Analysis of Digital Twin Integration for Network and Service Optimization in Vehicular Edge Computing

Xiaoqian Jin
Sichuan College of Architectural Technology, Deyang 618000, China
E-mail: Jxq7789@126.com

Keywords: vehicular edge computing, digital twin, network management, service management, intelligent transportation systems

Received: March 24, 2025

In recent years, Vehicular Edge Computing (VEC) has gained attention as a key approach to address the complexity caused by the fusion of diverse vehicular applications. It has emerged as a promising paradigm for future intelligent transportation systems. VEC facilitates computation-intensive and latency-sensitive vehicular applications by providing computing and caching capabilities near vehicles. This improves transmission efficiency and lowers congestion. VEC is nonetheless susceptible to implementation challenges due to the highly dynamic nature of vehicular networks, which have characteristics of high mobility, opportunistic connectivity, and heterogeneous user demand. This complicates network and service management. In this line of reasoning, Digital Twin (DT) technology, which provides virtual models of objects, processes, and attributes, enables intelligent decision-making in management. The paper conducts a systematized review and comparative analysis of up-to-date literature that combines DT with VEC systems for network and service optimization. Our review highlights key methodologies, including DRL-assisted DT architectures, multi-agent offloading scenarios, and edge-cloud collaboration protocols. We summarize pioneer studies, indicate prevalent resource control and predictive modeling trends, and note common weaknesses such as scalability and data synchronization. The study explores the concept of DT, its applicability in various industries, and its potential for vehicular network modeling and simulation. Apart from that, we also discuss existing research trends, identify challenges such as scalability and real-time data acquisition, and introduce potential avenues for future research.

Povzetek: Članek obravnava upravljanje omrežij in storitev v vozliščnem robnem računanju v pogojih visoke mobilnosti, nestabilnih povezav in raznolikih zahtev. Predlaga vključitev digitalnih dvojčkov, ki z virtualnimi modeli omogočajo napovedi, optimizacijo virov in znižanje zakasnitev. Analiza literature razkrije prednosti, slabosti ter odprte raziskovalne izzive.

1 Introduction

Intelligent Transportation Systems (ITS) development transforms how vehicles interact with their environment, enabling increased safety and more efficient mobility [1]. Vehicular Edge Computing (VEC) is central to this transformation as a concept that leverages edge computing capabilities near vehicles for computation-intensive and latency-aware applications [2]. By deploying computing and caching services close to the access network edge, VEC reduces the delay caused by communications, delivers more reliable services, and offloads traffic from central networks [3]. This concept is vital in enabling applications such as real-time traffic control, autonomous vehicles, and sophisticated infotainment systems [4].

Despite its potential, VEC execution is hindered by the complexity of network and service management, given the highly dynamic environment of vehicles. High mobility, transitory connectivity, and fluctuating application demands result in dynamic network topologies and variable traffic volumes [5]. All of these factors make network resource allocation inefficient, service quality is sacrificed, and decision-making for network administrators becomes more challenging. Overcoming these challenges requires innovative responses that are receptive to the fluctuating environment of vehicular networks [6].

Another possible solution to these problems is Digital Twin (DT) technology, which enables the virtual replication of physical systems for real-time tracking, simulation, and optimization [7]. DT effectively enhances decision-making procedures, makes resource allocation more efficient, and improves system performance in general due to its ability to enable synchronized interactions between virtual and physical entities [8]. Its ability to model variable vehicular networks, compute future conditions, and simulate makes DT a potential foundation for intelligent control in VEC-based ITS [9].

This paper explains how VEC is being combined with DT technology for automobile network and service administration. It critically analyzes VEC-related problems, describes DT for addressing them, and identifies new trends and open issues. In providing a comprehensive survey of this emerging field, it suggests

future research avenues with potential for more responsive and effective ITS.

In addition to defining the possibility for DT-VEC integration, this work also discusses the corresponding operational challenges that vehicular networks provide, including increased mobility, limited connectivity, and fluctuating resource demands. We present an analysis of VEC's adoption of edge computing characteristics to mitigate these challenges and explore possible DT-based designs that can further augment system behavior. By bringing together existing trends with technical proposals, our work presents a unified understanding of areas where existing efforts succeed, areas where they do not, and areas that future research must focus on. In conducting this review, we assumed the following research questions (RQs):

- RQ1: What are the core challenges in managing networks and services in vehicular edge computing environments?
- RQ2: How has DT technology been integrated into VEC systems, and what are the prevailing methodologies?
- RQ3: What are the strengths, limitations, and performance trends of existing DT-VEC approaches?
- RQ4: What research gaps remain, and how can future work improve scalability, adaptability, and energy efficiency?

2 Background

2.1 Vehicular edge computing

VEC is structured into a trilayer framework with distinct functions and roles. This hierarchical structure enables effective computation, data handling, and communication in vehicular networks. As shown in Figure 1, the system comprises a smart vehicular layer, an edge cloud layer, and a cloud layer.

The foundation for VEC architecture is the cloud layer, which manages large-scale data aggregation, storage, and computation-intensive operations. It includes computation infrastructures and storage that manage the vast amount of data generated from the edge layer. Functioning between the smart vehicular and cloud layers is the edge cloud layer, which also acts as a bridge for managing low-latency processing and real-time communication. It is also equipped with 802.11p, LTE, and 5G protocols to support location-aware services,

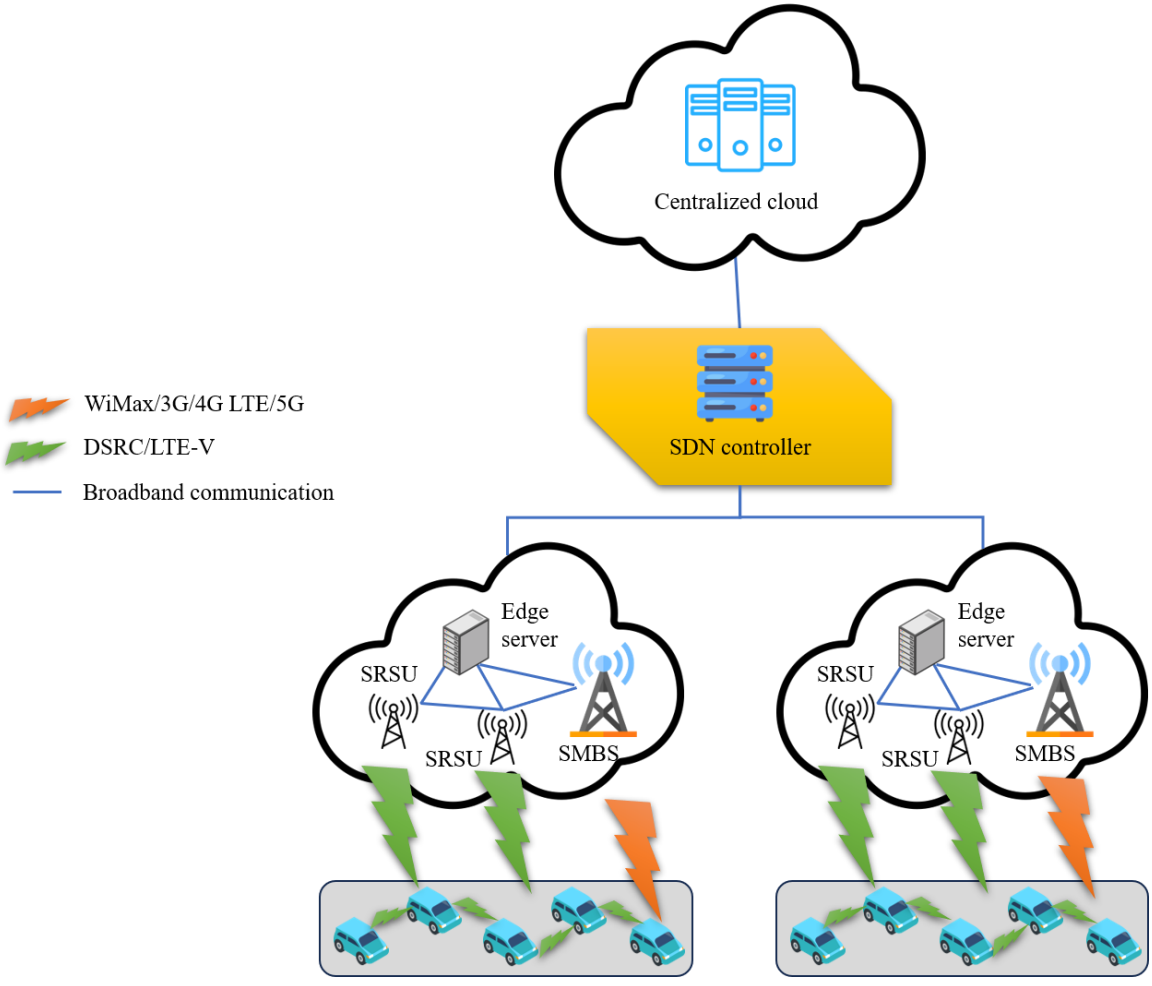

Figure 1: Vehicular edge computing architecture

emergency control for response purposes, and content caching.

The vehicular smart layer comprises smart vehicles equipped with sensors, communication modules, and computing capabilities. Vehicular nodes in this layer also establish localized groups for reciprocal exchange of resources, including computation and storage. SDN also significantly controls VEC infrastructure with centralized control from components, including SDN controllers, edge servers, and micro base stations. They also provide for dynamic allocation of resources, fault tolerance, and efficient network orchestration in layers. SDN controllers manage entire network behavior for optimized edge orchestration. SDN Edge Servers (SES) provide localized computation and emergency services. SDN Smart Vehicles (SSV) and other components also serve as data plane nodes, supporting real-time communication.

2.2 Digital twin technology

DT technology bridges the digital and physical worlds by creating virtual images of real objects and environments. The approach relies on seamless data capture and volume synchronization for permitting real-time transfer between the real asset and its virtual twin. DTs enable end-to-end tracking, simulation, and optimization of physical phenomena with this two-way interconnectivity. This renders DT technology indispensable for industrial, healthcare, and transportation applications, where real-time comprehension and decision-making are crucial for optimal operations. DTs exist in diverse forms that rely on fulfilling operational needs and applications. There are four general types of DTs:

Analytics vs. physics-based: Analytics-based DTs use historical and real-time data, often complemented with artificial intelligence (AI) and statistical modeling, to forecast future asset behavior and outcomes. They utilize large data sets to identify trends and provide insights that inform action. Physics-based DTs use scientific disciplines such as fluid dynamics or stress analysis for machinery to simulate asset behavior under conditions. This DT enables a more subtle yet precise simulation of physical phenomena, making it compatible with applications that require precise simulations, such as aerospace engineering.

Simulation vs. operational: DTs are most utilized for simulation in a product's early lifecycle. The simulation twins enable designers to verify and simulate product designs without incurring development time and costs. Once a product is in its operational state, DTs monitor and manage the real-world asset. DTs of this kind are also referred to as SimOps twins. They integrate simulation with real-time operations to help address maintenance issues while improving a product's or system's lifecycle operations. The dual role of DTs highlights their applicability across a product's or system's entire lifecycle.

Product vs. facility: Product or asset twins concern one product or asset. These DTs contain current data on how a set of items, such as turbines or electric motors, run, are maintained, and how they perform. This category is ideal for understanding asset behavior under varying conditions and ensuring maximum performance. Facility twins, on the other hand, represent an entire production facility or system. Facility twins combine multiple product twins to simulate and optimize manufacturing processes, aiming to improve overall facility efficiency. Facility twins primarily concern industrial applications on a grand scale, where interconnection between assets determines collective performance.

Discrete vs. composite: Discrete twins outline a single physical component or system. They are narrower in scope and generally used for applications where a single stand-alone asset is to be monitored or optimized. For instance, a discrete twin would describe a single part of a machine within a factory. Composite twins, on the other hand, combine multiple discrete twins into a single, integrated representation of a larger, complex system. A good example is that composite twins mimic the interactions of numerous systems and machines in large-scale production to achieve entire process optimization. This dichotomy highlights the scalability of DTs, ranging from simple components to larger, complex systems of systems.

Figure 2 summarizes the multidimensional nature of the DT systems. Central features include state synchronization, twinning rate (twinning between virtual/virtual or physical/virtual entities), and fidelity (granulation level of simulated processes). Variables such as network connectivity, virtual/physical coupling, and parameter tracking measure the accuracy with which DT mirrors the original system. All these features are essential for the real-time monitoring, prediction, and control of VEC environments. High twining rates, for example, become a requirement for safety-critical applications such as lane changes, but increase the synchronization overhead with a focus on adaptive fidelity control.

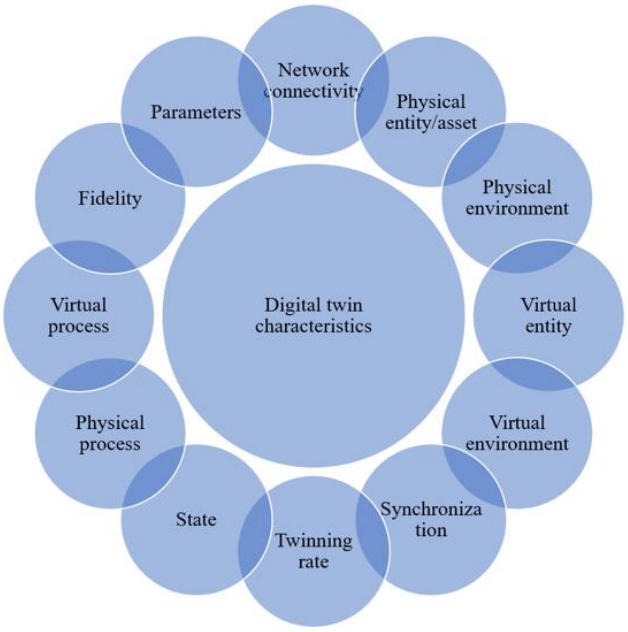

Figure 2: Key characteristics of a digital twin

2.3 Incorporation of DT into VEC

The incorporation of DT technology with VEC has become a revolutionary approach for resolving problems caused by vehicular environments subject to dynamic changes. DT enables VEC network monitoring, modeling, and real-time optimization through virtual replication of physically existing systems, supporting intelligent decision-making. Different papers introduce DT-related novel designs with Deep Reinforcement Learning (DRL) algorithms, clustering, and multi-agent networks for enhancing offloading efficiency, resource allocation, and system performance. The approaches, key contributions, and areas of deficiency of these research studies are tabulated in Table 1 for easy comprehension of the state-of-the-art achievements and challenges in integrating DT with VEC.

3 Survey methodology

To ensure a structured and replicable review process, we conducted a targeted literature survey focusing on the integration of DT technology within VEC systems. Relevant publications were retrieved from major academic databases, including IEEE Xplore, ACM Digital Library, Elsevier ScienceDirect, SpringerLink, and Google Scholar. The search spanned the period from 2019 to 2025, using keyword combinations such as "digital twin," "vehicular edge computing," "intelligent transportation systems," "task offloading," "DRL," and "resource optimization." Only peer-reviewed studies were considered. Works were included if they (i) proposed or implemented DT in the context of vehicular networks or edge computing, and (ii) reported technical results such as latency reduction, energy savings, or offloading performance.

We excluded papers that included only theory without an implementation background, referenced DT beyond vehicular or edge environments (e.g., smart factories or smart buildings), or did not undergo empirical testing. After removing duplication and applying inclusion/exclusion criteria, we shortlisted 22 seminal studies for analysis. This process enables transparency and lays a foundation for future studies that aim to replicate or expand the scope of the DT-VEC study.

4 Challenges in managing networks and services in VEC

VEC offers potential solutions for deploying vehicular applications that require real-time support with minimal latency. However, the highly dynamic and resource-constrained nature of vehicular environments introduces various challenges for efficiently managing services and networks. The range of difficulties encompasses technical, operational, and security domains, as outlined in Table 2, along with a selection of key issues, their definitions, and corresponding impacts on VEC systems. Overcoming them requires effective and adaptive solutions to ensure the efficiency and credibility of VEC deployments. The following section addresses these key difficulties, focusing on the network and service management dimensions.

Vehicles in VEC networks are inherently mobile, leading to rapidly changing network topologies. High-speed movement results in frequent handovers between roadside units (RSUs) or base stations, disrupting ongoing communication and degrading service quality. Moreover, the short-lived communication links caused by high mobility make it difficult to maintain stable connections and consistent coverage. For instance, real-time offloading tasks may fail when vehicles move out of the communication range of an RSU or when handover delays occur. Designing adaptive protocols and algorithms to cope with dynamic topologies is critical to ensuring reliable service delivery.

Low latencies are required for most automotive applications, such as autonomous vehicles, collision warning systems, and real-time traffic control. Small latencies in data processing, task offloading, or decision-making can lead to severe failures, including traffic accidents or system crashes. Managing latency-sensitive applications requires highly efficient edge servers, low-latency communication protocols, and rapid decision-making algorithms. Moreover, balancing computation offloading to edge servers with the time-critical nature of these tasks is a persistent challenge.

The applications running on VEC networks vary significantly in terms of computational, communication, and storage requirements. For instance, infotainment applications require a large bandwidth, whereas safety-critical applications necessitate low latency and robustness. Edge devices and vehicles also vary in their hardware capabilities, ranging from simple sensors to edge servers with significant capabilities. This makes it challenging to implement a fixed policy for allocating resources and scheduling between applications and between applications and devices.

Vehicle network connectivity is prone to loss due to high-speed mobility, external influences, and infrastructural disparities. Vehicles frequently lose connectivity with edge servers or other vehicles, resulting in task failures, inconsistent data exchange, and suboptimal system performance. Intermittent connectivity also affects real-time data synchronization, which is critical for applications such as data-driven decision-making and monitoring. Reliable communication schemes must be developed that allow for handling intermittent connectivity and minimizing task failures.

Different proposals exist for mitigating the effects of connectivity disruptions in vehicular networks. The predictive handover methods aim to predict disconnections by employing mobility models and location awareness for advancing-allocating communication channels or edge functionality. Mobile IP and its extended variants (e.g., Hierarchical Mobile IPv6) provide session continuity with robust IP bindings as cars transition between subnets. Yet, they tend to show signaling overheads and challenges with long-term high-speed mobility, particularly for dense urban applications.

Table 1: Comparison of DT integration in VEC

Reference	Methodology	Key contributions	Latency reduction	Offloading success rate	Energy efficiency	Scalability support	Shortcomings
[10]	DT-enabled VEC with DRL for adaptive offloading and latency optimization.	Introduced a dual-loop DT framework for real-time VEC network adaptation. Improved offloading latency and adaptive scheduling through DRL-based optimization. Numerical results demonstrated enhanced network management and task offloading efficiency.	~28%	~91%	Moderate	Limited	Limited focus on scalability and the integration of heterogeneous vehicular networks.
[11]	Mirrored edge system with multi-agent DRL and coordination graph for task offloading.	Enabled cooperative service matching and distributed task scheduling using multi-agent DRL. Proposed a coordination graph to efficiently minimize offloading costs. Demonstrated efficiency improvements in real urban datasets.	~32%	~93%	High	Low	High computational complexity due to multi-agent DRL and limited evaluation of edge resource variability.
[12]	IGNITE framework with clustering, DRL, and feedback mechanisms.	Combined clustering and feedback-based optimization to reduce decision complexity and computational delay. Proposed a closed-loop DT framework to enhance offloading success rates. Improved overall cost-efficiency in VEC systems.	~25%	~88%	Moderate	Moderate	The clustering mechanism's dependency on initial configurations may limit adaptability in dynamic scenarios.
[13]	DT-based edge node collaboration using NOMA and A2C for resource optimization.	Enhanced RSU collaboration for real-time resource allocation. Improved system performance by reducing task delays and optimizing computation rates. Validated effectiveness through simulations.	Not reported	Not reported	High	High	Lack of consideration for cross-layer optimization and dependency on predefined communication protocols like NOMA.
[14]	GP-CMA-ES algorithm with a variable grouping strategy for five-objective optimization.	Proposed a multi-objective framework to balance energy consumption, user satisfaction, and computational load. Effectively addressed convergence issues with increasing VUs. Enhanced overall network efficiency under diverse workloads.	~30%	Not reported	High	High	Limited exploration of the interaction between mobility patterns and the five objectives.
[15]	UAV-based DT-enabled VEC with proximal policy optimization for trajectory and resource management.	Introduced UAV-as-server concepts for resource flexibility. Optimized UAV trajectory and resource allocation, achieving energy savings and fast convergence. Addressed dynamic vehicular topology challenges.	~35%	~95%	High	Limited	Dependency on UAV trajectory stability and limited assessment of extreme environmental conditions (e.g., traffic congestion).
[16]	UAV-assisted VECN with A3C and GAT for task offloading.	Improved VECN task throughput and stability in dynamic edge environments. Utilized GAT to incorporate dynamic topology changes into offloading decisions. Enhanced performance in	~33%	~92%	Moderate	Moderate	Relied on asynchronous task evaluation, which may affect latency-sensitive applications.

		scenarios with local resource overload.					
[17]	DT-enabled MEC for CAV lane-changing with DRL-based foresight learning.	Strengthened CAV safety through DT and predictive learning. Improved real-time decision-making for lane-changing and optimized traffic flow efficiency. Provided a robust integration of DT into CAV scenarios.	~20%	~86%	High	Moderate	Limited scalability for larger networks with more dynamic traffic patterns.
[18]	DT-driven 6G V2X network scheduling using DRL for traffic and channel management.	Proposed task-efficiency-oriented scheduling schemes with case studies. Enhanced vehicle merging decisions and improved channel utilization. Addressed critical 6G V2X challenges through DT-enabled predictive capabilities.	~24%	~89%	High	Low	Limited real-world validations and dependency on accurate DT model construction for optimal scheduling.
[19]	DT-assisted VEC with improved A3C and real-time data acquisition for offloading.	Addressed the limited edge server resources with collaborative strategies. Improved algorithm generalization through ε-greedy and dropout techniques. Reduced offloading delay and energy consumption significantly.	~29%	~87%	Moderate	High	Heavy reliance on real-time data accuracy for DRL may introduce latency in dynamic environments.
[20]	DDPG-based DT-enabled offloading in heterogeneous IoT networks.	Tackled dynamic IoT environments with multi-service offloading optimization. Achieved better task completion times and efficient resource allocation. Optimized heterogeneous network management.	~31%	~90%	High	Moderate	The joint optimization framework has high complexity, which may reduce scalability in large-scale IoT deployments.
[21]	Quantum computing and DRL integration for DT in VEC networks.	Leveraged quantum computing for efficient processing of high-dimensional decision spaces. Enhanced latency, energy, and quality-of-service management. Introduced a multi-agent framework for adaptive task offloading.	~26%	~84%	Moderate	High	Dependency on advanced quantum systems limits the practical applicability of quantum systems in real-world vehicular networks.
[22]	Hierarchical RL for DT server optimization in urban traffic.	Reduced DT model synchronization and migration latency. Improved matching of vehicles and DT servers in dynamic traffic scenarios. Enhanced DT optimization performance under varying network topologies.	~27%	~90%	High	Low	Limited focus on edge-cloud collaboration may restrict scalability in larger urban scenarios.
[23]	DRL-based DT migration for cost-effective MEC service provisioning.	Addressed service synchronization costs and optimized resource management. Balanced mobility of both DT service providers and consumers under dynamic conditions. Enhanced efficiency in MEC environments.	~30%	~89%	Moderate	Moderate	Scalability to multi-region scenarios and real-time migration under highly dynamic conditions remains an unaddressed issue.

VEC networks face significant scalability challenges with the increasing number of connected vehicles and data-intensive applications. It is challenging to deal with a larger number of vehicles, RSUs, and edge servers without saturating the system. In hotspot or peak-hour conditions, network congestion tends to exacerbate the situation further, resulting in increased delay, lost packets, and compromised service. Scalable architectures and intelligent resource allocation algorithms are necessary to ensure seamless service delivery, even in densely populated vehicular networks.

Table 2: Challenges in network and service management in VEC

Challenge	Description	Impact
High mobility and dynamic topology	Rapid vehicle movement leads to frequent handovers, unstable connections, and constantly changing network topology.	Disrupted communication, degraded service quality, and challenges in resource allocation.
Latency sensitivity	Real-time vehicular applications require low-latency communication and computation to ensure safety and efficiency.	Increased delays can compromise safety-critical applications like autonomous driving and collision avoidance systems.
Heterogeneous resource demands	Applications and devices in VEC have varying computational, storage, and communication requirements, with diverse hardware capabilities across vehicles and RSUs.	Difficulties in effective resource allocation and scheduling, reducing system efficiency.
Intermittent connectivity	High-speed movement and environmental factors cause connectivity disruptions between vehicles, edge servers, and cloud nodes.	Task failures, inconsistent data exchange, and reduced reliability of VEC services.
Scalability and network congestion	Growing numbers of connected vehicles and data-intensive applications increase the load on VEC infrastructure.	Network congestion, higher delays, and degraded quality of service during peak traffic or in dense environments.
Security and privacy concerns	Sensitive vehicular data exchanged between devices, edge servers, and clouds are vulnerable to cyberattacks and privacy breaches.	Data interception, denial-of-service attacks, and compromised user privacy.
Collaborative resource management	Existing VEC systems underutilize the potential for collaboration among edge nodes, such as RSUs and small-cell base stations.	Missed opportunities for load balancing, reduced latency, and enhanced resource utilization.
Integration of emerging technologies	Incorporating technologies like Digital Twin, 5G/6G, and AI introduces complexity in ensuring compatibility and seamless operation within VEC frameworks.	Increased infrastructural and computational demands, with potential integration challenges.
Energy efficiency	Tasks such as offloading, real-time monitoring, and resource management consume significant energy resources, particularly in UAV-assisted systems.	Higher operational costs, reduced sustainability, and challenges in managing energy-constrained devices like UAVs.
Fault tolerance and reliability	Failures in servers, sensors, or communication systems can affect system reliability, especially for safety-critical vehicular applications.	Service disruptions, loss of critical data, and reduced system trustworthiness.

The exchange of sensitive data, such as vehicle locations, user information, and safety-critical data, in VEC networks raises significant concerns regarding security and privacy. These networks encounter a variety of security threats, including data intercepts, spoofing, and denial-of-service (DoS) attacks, that seek to disrupt service integrity and availability. Moreover, privacy concerns arise when sensitive user data is sent to edge servers or clouds. To effectively defend VEC networks from these threats, robust encryption, authentication, and intrusion detection mechanisms must be implemented.

Standardized protocols have been developed to secure vehicular communications, including IEEE 1609.2, which defines security services for V2X using public key infrastructure (PKI), and ETSI ITS standards, which include mechanisms for secure message authentication and the preservation of anonymity in cooperative ITS scenarios. Although these standards provide a foundation, incorporating them into resource-constrained VEC environments is challenging due to certificate handling, processing delays, and scalability issues. Furthermore, many DT-integrated architectures lack implementation or simulation/testing in practical environments for these standards; thus, security validation remains under-researched.

Existing VEC systems focus on edge-cloud collaboration, with no collaboration possibilities for edge nodes such as RSUs or small-cell base stations. Edge node collaboration, with its potential to improve load balancing, reduce latency, and enhance system efficiency, has been less investigated until now. Nearby RSUs, for example, might co-share computing resources to deal with increased loads. Engineering systems for end-to-end edge-edge collaboration without compromising service quality is a grand challenge.

The inclusion of next-generation technologies, such as DT, 5G/6G, and AI, with VEC systems also introduces new challenges. While these technologies offer enormous value additions in terms of real-time simulation (using DT), ultra-high-speed connectivity (using 5G/6G), and informed decision-making (using AI), their inclusion requires substantial infrastructural as well as computational capabilities. In addition, ensuring the compatibility and seamless functionality of these technologies with existing VEC infrastructures is a significant task. Corresponding integration methodologies must be proposed to leverage their full potential while minimizing operational overhead.

The energy consumption of VEC systems, particularly in applications such as task offloading, real-time monitoring, and resource allocation, is a concern. Edge servers, RSUs, and vehicles also consume significant amounts of energy, resulting in additional operational costs and reduced sustainability. In one example, UAV-assisted VEC networks require optimized flight routes and energy utilization for their viability. Energy-efficient algorithms and hardware-based solutions must be created to increase the sustainability of VEC systems.

System errors within VEC systems, due to server errors, communication errors, or sensor errors, can significantly affect system reliability. Since they are used in safety-critical missions on vehicles, the fault tolerance and robustness of a system become imperative. This includes planning backup schemes, redundant topologies, and fault-detection schemes to ensure continued functionality despite errors.

Table 3: Digital twin roles in vehicular edge computing

Role	Description	Impact
Real-time monitoring and data synchronization	DTs provide real-time updates of VEC systems by synchronizing physical and virtual entities, ensuring accurate system state representation.	Enables proactive management of dynamic network conditions and improves service reliability.
Predictive maintenance and fault management	DTs analyze real-time and historical data to predict failures and optimize system performance.	Reduces downtime, enhances reliability, and minimizes service disruptions.
Optimization of resource allocation	DTs simulate resource demands and bottlenecks, enabling dynamic task offloading, bandwidth allocation, and storage optimization.	Improves system efficiency, reduces latency, and minimizes energy consumption.
Enhancing latency-sensitive applications	DTs offer real-time emulation environments that simulate sensor inputs and vehicular behaviors. These environments allow applications (e.g., autonomous driving, traffic response) to be pre-tested under dynamic conditions, enabling fast decision models to be validated virtually before deployment, thereby reducing reaction delays.	Ensures minimal latency in critical operations like collision avoidance and traffic control.
Enabling intelligent decision-making	DTs integrate AI/ML algorithms (e.g., reinforcement learning, anomaly detection) into their virtual replicas to analyze real-time and historical telemetry data. These models generate predictive insights, simulate "what-if" conditions (e.g., traffic rerouting), and optimize future system states.	Improves adaptive control, traffic optimization, and task offloading precision.
Facilitating edge-edge and edge-cloud collaboration	DTs maintain synchronized system states across edge nodes and cloud platforms. They use coordination agents to distribute tasks based on real-time load, proximity, and latency metrics. This enables dynamic resource balancing and adaptive offloading strategies.	Reduces congestion, prevents overload at edge servers, and improves distributed efficiency.
Supporting dynamic and scalable network management	DTs adjust virtual models dynamically to accommodate the growing number of vehicles and applications in VEC systems.	Enables scalability and adaptability in large-scale and urban environments.
Improving security and privacy	DTs create sandboxed environments where virtual replicas can run intrusion detection, threat modeling, and attack simulation scenarios without exposing the real system. They help isolate suspicious behaviors and test mitigation strategies using synthetic data mirroring real conditions.	Enhances preemptive defense, reduces live system exposure, and supports cyber-resilience planning.
Integration with emerging technologies	DTs integrate technologies like 5G/6G, AI, and blockchain to enhance real-time synchronization, predictive analytics, and secure data exchange.	Boosts overall system performance, reliability, and innovation in VEC.

5 Role of the digital twin in vehicular edge computing

DT technology has proven revolutionary in addressing VEC's highly complex challenges. Virtual replication of physical objects, processes, and environments, made possible by DT, enables real-time monitoring, prediction, and optimization with a foundation for intelligent decision-making in VEC systems. A summary of DT's leading roles in VEC is presented in Table 3, covering real-time monitoring, resource optimization, and predictive maintenance, with a focus on their functions in enhancing network and service management. This section explains these roles in detail, focusing on their capabilities for overcoming key challenges while enhancing VEC system operations.

DTs facilitate end-to-end VEC system monitoring in near-real time with a harmonious relationship between virtual and physical environments. DTs allow a global view of system conditions, with virtual replicas continually updated with the latest information from vehicles, roadside units (RSUs), and edge servers. This facilitates active control of varying network attributes such as mobility-triggered topological changes and disconnection interruptions. For instance, DTs can monitor patterns of vehicle motion and manage resource allocation to sustain the flow of communication.

DTs under highly mobile conditions exhibited measurable improvements in task failure reduction. In conditions with over 20% packet loss due to simultaneous RSU handovers within a short time interval, DT-aided offloading systems reduce task failure rates by 15%–30% compared to baseline offloading. This is achieved by maintaining real-time digital twin copies that predict future connectivity conditions and proactively anticipate task switching or rescheduling ahead of connectivity decay.

Another primary role of DT in VEC is to predict possible failures and enhance system performance. DTs can distinguish anomalies from past and in-time data and predict equipment failures, while presenting recommendations that enable failure avoidance. In vehicular networks, DT is also exceptionally effective in maintaining the health of RSUs, edge servers, and other critical infrastructures. It allows for minimizing disruptions while enhancing system robustness with a high level of service availability.

DTs also contribute to enhancing resource allocation for VEC systems. They mimic the dynamics of the physical system; thus, they are set to predict resource demands alongside identifying real-time chokepoints. DTs enable real-time resource management depending on tasks offloaded, assigned bandwidths, and storage optimization. DTs, for example, can mimic computational loads between RSUs and suggest optimal task allocation to minimize latency and energy consumption.

Latency-sensitive applications, such as self-driving cars and real-time traffic analysis, require timely and accurate decision-making. DTs enhance these applications by enabling decision models to be simulated and verified in a virtual environment before they are applied in the real system. DTs, for instance, can simulate traffic conditions in real-time, allowing cars to make informed decisions about whether to change lanes, avoid a collision, or optimize a route with minimal delay.

DTs enable efficient collaboration between edge nodes (e.g., RSUs, small-cell base stations) and edge and

cloud platforms. Through a global view of the network state, DTs could coordinate edge nodes' offloading and resource-sharing tasks to cloud servers as necessary. This enables a balanced workload, reduced congestion, and a scalable VEC system.

In the highly dynamic environment of vehicular networks, DTs provide scalable and adaptive management solutions. As the number of connected vehicles and applications grows, DTs can dynamically adjust their virtual models to accommodate the increasing complexity. This scalability makes DTs critical for managing large-scale VEC systems in urban environments.

DTs enhance the security and privacy of VEC systems by providing a secure virtual environment for data analysis and decision-making. DTs can minimize cyberattack exposure by isolating sensitive processes in the virtual domain. Additionally, DTs can simulate potential attack scenarios and develop robust defense mechanisms to protect the system.

DTs also provide a unifying platform for integrating emerging technologies, such as 5G/6G, artificial intelligence, and blockchain, with VEC systems. For instance, DTs utilize 5G connectivity for real-time synchronization and AI models for forecasting, while blockchain enables secure and distributed data sharing. This integration enhances the overall functionality and performance of the VEC system.

One of the primary design trade-offs of DT-enabled VEC systems is the balance between digital model fidelity and real-time synchronization cost. High-fidelity twins preserve fine-grained sensor data, traffic information, and behavioral data with exact simulation, along with accurate predictions. It does so with a requirement for more frequent updates, which necessitate elevated bandwidth, thereby increasing synchronization latency and energy consumption. Conversely, lightweight models reduce overhead, but this comes at the potential compromise of accuracy in predictions, particularly in safety-critical applications such as collision avoidance or lane-changing. It is a trade-off point that remains a primary issue with practical implementations.

6 Discussion

The integration of DT technology with VEC presents a highly heterogeneous environment of methodologies. Recently published research extensively employs a variety of tactics, including adaptive scheduling with DRL, offloading schemes aided by UAVs, and quantum optimization. All of these present clear breakthroughs in latency minimization and offloading optimization effectiveness, with some achieving over 30% latency reduction and more than 90% offloading success rate. However, problems remain regarding scalability, computational overhead, and real-time reconfigurability.

There is a notable trade-off between complexity and performance: while multi-agent or quantum methods exhibit impressive performance, they often encounter limited scalability or intensive computational requirements. Similarly, UAV-centric systems trade flexibility and coverage for a dependency on trajectory stability and environmental assumptions.

Despite all these advancements, state-of-the-art systems fall short in three main aspects: (i) end-to-end scalability within heterogeneous and mobility-aware vehicular networks, (ii) standardized coexistence with edge-cloud hierarchies, and (iii) long-term deployment-aware energy-aware design. This survey particularly provides value by spanning both architectural- and performance-level comparisons of typical works in a way that highlights where systems shine while also indicating areas where they fall short.

Whereas most existing reviews tend to discuss either theory structures or one technical aspect, our paper provides a metric-aided end-to-end DT in VEC synthesis that bridges design decisions with quantifiable performance attributes. Our two-layer analysis renders our review a novel benchmark for identifying potential future directions and research voids.

7 Future research directions

The integration of DT technology with VEC has demonstrated significant potential for alleviating network and service management challenges. Research and development opportunities must be thoroughly explored to fully realize their potential. Table 4 gives the main points, challenges, future directions, and innovative ideas for advancing DT adoption in VEC. This section provides additional rationale for these areas, including suggestions for measures that need to be adopted to enhance the efficiency, scalability, and flexibility of DT-driven VEC systems.

One significant challenge in deploying DT technology is the computation and storage overhead in resource-constrained environments. Lightweight DT systems optimized for VECs that can achieve high-fidelity simulation with real-time synchronization while being energy— and resource-aware are essential.

As more applications and vehicles become connected, scalability is imperative. Future work needs to focus on scalable DT architectures that efficiently support large-scale networks. This would entail exploring hierarchical or distributed DT architectures for supporting seamless collaboration between edge nodes and the cloud.

The incorporation of DT with future technologies, such as 5G, 6G, and beyond, opens unprecedented opportunities for ultra-low latency communication, higher bandwidths, and end-to-end connectivity. Further research is necessary to utilize these technologies for advancing the real-time synchronization of DTs and enhancing their interactions with physical systems in varying vehicular environments.

The combination of cutting-edge AI and ML models with DTs can considerably improve decision-making. Future research should focus on AI-based DTs that deal with real-time and historical data for better resource allocation, system failure prediction, and handling fluctuating network conditions.

The transmission of sensitive user and vehicle data from virtual to physical environments also poses

Table 4: Future directions for digital twin in vehicular edge computing

Aspect	Challenges	Future directions	Innovative ideas
Lightweight frameworks	High computational and storage overhead in resource-constrained environments.	Develop lightweight DT frameworks for efficient VEC integration.	Using modular architectures and compression techniques to reduce resource consumption.
Scalability	Managing large-scale VEC networks with numerous vehicles and edge nodes.	Design scalable DT architectures with hierarchical or distributed models.	Implementing distributed DTs with edge collaboration to balance workloads dynamically.
Integration with 5g/6g	Ensuring ultra-low latency and reliable connectivity in dynamic vehicular environments.	Leverage 5G/6G for real-time DT synchronization and interaction with physical systems.	Using network slicing in 5G/6G to prioritize latency-sensitive DT updates.
AI-driven decision-making	Limited predictive and adaptive capabilities in traditional DT models.	Incorporate AI/ML models into DTs for intelligent decision-making and optimization.	Developing reinforcement learning-based DTs to predict system behavior and optimize resources dynamically.
Security and privacy	Vulnerability to cyberattacks and risks to user privacy.	Implement robust encryption and privacy-preserving algorithms for DT systems.	Using blockchain for secure data exchange between DTs and physical systems.
Energy efficiency	High energy consumption in DT frameworks and edge devices.	Develop energy-efficient algorithms and frameworks for DT-enabled VEC.	Optimizing UAV flight paths and RSU power consumption using DT-driven energy models.
Edge-cloud-device collaboration	Inefficient coordination between edge nodes, cloud platforms, and devices.	Explore hybrid architectures for seamless real-time data exchange and workload distribution.	Using fog computing to create a middle layer for adaptive edge-cloud-device coordination.
Dynamic and adaptive models	Static DT models struggle to adapt to changing network conditions and demands.	Create adaptive DT models that self-optimize and reconfigure in real-time.	Using self-learning DTs with neural networks to dynamically adjust parameters based on system feedback.
Benchmarking and standardization	Lack of standardized DT frameworks and evaluation metrics.	Establish common standards and benchmarking protocols for DT in VEC.	Forming industry-academic partnerships to create open-source DT evaluation frameworks.
Real-world implementations	Limited practical validation of DT frameworks in vehicular environments.	Conduct pilot projects and field tests to refine DT models and address real-world challenges.	Developing testbeds in smart cities to evaluate DTs under diverse vehicular scenarios.

significant security and privacy risks. Future research is required on efficient encryption techniques, secure communication protocol schemes, and privacy-obscuring algorithms for DT-based VEC systems. DTs must also be secured against hacking to ensure the system remains intact.

Energy efficiency is crucial for VEC system sustainability, particularly in applications involving UAVs, RSUs, and edge devices. Developing energy-efficient DT-based frameworks along with optimization algorithms will lower VEC system energy consumption without compromising performance.

Interactions between edge nodes, cloud infrastructures, and devices also enhance the efficiency of the VEC system. Future work is needed to study hybrid infrastructures in which data sharing and real-time decision-making are interlinked across the edge, cloud, and vehicle layers. This includes examining adaptive task allocation and workload allocation that vary.

Highly active traffic environments require DTs to be highly adaptive for immediate reaction to changing parameters such as mobility patterns, network loads, and end-application demand. Research must address adaptive DT modeling that enables real-time reconfiguration and self-optimization, ensuring sustained high-grade levels of performance and reliability.

Current research lacks unified benchmarks for evaluating DT-based VEC systems. For instance, task offloading delay (average and worst-case), packet delivery ratio, energy consumption per task, and latency jitter are inconsistently reported across studies. While some works use synthetic traces, publicly available datasets such as the Beijing T-Drive and Cologne SUMO mobility sets are rarely standardized in comparative evaluations. Establishing a benchmark suite with these datasets, coupled with common metrics like task completion time under 50 ms, energy per offloaded task (in Joules/task), and scalability thresholds (tasks/sec/ edge server), is essential for reproducibility.

On the standards front, while protocols such as IEEE 1609.2 and ETSI ITS-G5 address V2X security, there is no standardized interface for DT synchronization, update frequency, or data abstraction levels. A critical missing element is a middleware-level specification for DT orchestration across heterogeneous VEC layers (vehicle, RSU, edge cloud), including service handovers and version control.

8 Conclusion

This paper provides a thorough survey of DT technology integration within VEC, presenting its transformative potential for handling network and service management complexities in changing vehicular environments. DT enables the real-time virtualization of physical infrastructures, making it possible for intelligent decision-making, proactive repair, resource optimization, and seamless collaboration among edge, device, and cloud layers. All these capabilities enable DT to be a foundation for advancing intelligent transportation systems. This paper provides a thorough survey of DT technology integration within VEC, focusing on its transformative potential for addressing challenges such as elevated mobility, sensitivity to latency, and resource constraints. Although our mandate was more than a mere summary of recent trends, we also identified critical shortcomings due

to a lack of scalability, synchronization, and standardization. Our consideration of a future path forward includes a requirement for lightweight DT infrastructures, ground-realistic testbeds, benchmarking with standardization, and DT architectures with secure flexibility. Focusing on these directions further will be necessary for DT-based intelligent transportation systems to realize their full potential.

Conflict of interest

The authors declare that they have no conflicts of interest.

References

[1] F.-Y. Wang *et al.*, "Transportation 5.0: The DAO to safe, secure, and sustainable intelligent transportation systems," *IEEE Transactions on Intelligent Transportation Systems,* 2023, doi: https://doi.org/10.1109/TITS.2023.3305380.

[2] M. Ahmed *et al.*, "A survey on reconfigurable intelligent surfaces assisted multi-access edge computing networks: State of the art and future challenges," *Computer Science Review,* vol. 54, p. 100668, 2024, doi: https://doi.org/10.1016/j.cosrev.2024.100668.

[3] V. Hayyolalam, B. Pourghebleh, and A. A. Pourhaji Kazem, "Trust management of services (TMoS): investigating the current mechanisms," *Transactions on Emerging Telecommunications Technologies,* vol. 31, no. 10, p. e4063, 2020, doi: https://doi.org/10.1002/ett.4063.

[4] C. Wang and X. Li, "Strategy Analysis of Mobile Edge Computing Based on EC-ANN in Task Vehicle Cooperative Unloading," *Informatica,* vol. 48, no. 22, 2024, doi: https://doi.org/10.31449/inf.v48i22.5973.

[5] X. Dai, Z. Xiao, H. Jiang, and J. C. Lui, "UAV-assisted task offloading in vehicular edge computing networks," *IEEE Transactions on Mobile Computing,* vol. 23, no. 4, pp. 2520-2534, 2023, doi: https://doi.org/10.1109/TMC.2023.3259394.

[6] Y. Wu *et al.*, "Task offloading for vehicular edge computing with imperfect CSI: A deep reinforcement approach," *Physical Communication,* vol. 55, p. 101867, 2022, doi: https://doi.org/10.1016/j.phycom.2022.101867.

[7] A. Alabbasi, M. A. Aljabery, and P. S. Bölük, "Application of VGIS digital twin platform for enhanced oilfield disaster management and environmental protection," *Informatica,* vol. 48, no. 14, 2024, doi: https://doi.org/10.31449/inf.v48i14.6177.

[8] D. Zheng, H. Huang, and R. Wu, "Design of a 3D Intelligent Building Management Framework that Integrates Geographic Information Systems and Building Information Models," *Informatica,* vol. 48, no. 16, 2024, doi: https://doi.org/10.31449/inf.v48i16.6031.

[9] B. Pourghebleh and N. J. Navimipour, "Data aggregation mechanisms in the Internet of things: A systematic review of the literature and recommendations for future research," *Journal of Network and Computer Applications,* vol. 97, pp. 23-34, 2017, doi: https://doi.org/10.1016/j.jnca.2017.08.006.

[10] Y. Dai and Y. Zhang, "Adaptive digital twin for vehicular edge computing and networks," *Journal of Communications and Information Networks,* vol. 7, no. 1, pp. 48-59, 2022, doi: https://doi.org/10.23919/JCIN.2022.9745481.

[11] K. Zhang, J. Cao, and Y. Zhang, "Adaptive digital twin and multiagent deep reinforcement learning for vehicular edge computing and networks," *IEEE Transactions on Industrial Informatics,* vol. 18, no. 2, pp. 1405-1413, 2021, doi: https://doi.org/10.1109/TII.2021.3088407.

[12] L. Zhao *et al.*, "A digital twin-assisted intelligent partial offloading approach for vehicular edge computing," *IEEE Journal on Selected Areas in Communications,* vol. 41, no. 11, pp. 3386-3400, 2023, doi: https://doi.org/10.1109/JSAC.2023.3310062.

[13] S. R. Jeremiah, L. T. Yang, and J. H. Park, "Digital twin-assisted resource allocation framework based on edge collaboration for vehicular edge computing," *Future Generation Computer Systems,* vol. 150, pp. 243-254, 2024, doi: https://doi.org/10.1016/j.future.2023.09.001.

[14] B. Cao, Z. Li, X. Liu, Z. Lv, and H. He, "Mobility-aware multiobjective task offloading for vehicular edge computing in digital twin environment," *IEEE Journal on Selected Areas in Communications,* 2023, doi: https://doi.org/10.1109/JSAC.2023.3310100.

[15] B. Li, W. Xie, Y. Ye, L. Liu, and Z. Fei, "Flexedge: Digital twin-enabled task offloading for UAV-aided vehicular edge computing," *IEEE Transactions on Vehicular Technology,* vol. 72, no. 8, pp. 11086-11091, 2023, doi: https://doi.org/10.1109/TVT.2023.3262261.

[16] Z. Zhang, F. Zhang, M. Cao, C. Feng, and D. Chen, "Enhancing UAV-assisted vehicle edge computing networks through a digital twin-driven task offloading framework," *Wireless Networks,* pp. 1-17, 2024, doi: https://doi.org/10.1007/s11276-024-03804-3.

[17] B. Fan, Y. Wu, Z. He, Y. Chen, T. Q. Quek, and C.-Z. Xu, "Digital twin empowered mobile edge computing for intelligent vehicular lane-changing," *IEEE Network,* vol. 35, no. 6, pp. 194-201, 2021, doi: https://doi.org/10.1109/MNET.201.2000768.

[18] G. Cai, B. Fan, Y. Dong, T. Li, Y. Wu, and Y. Zhang, "Task-efficiency oriented V2X communications: Digital twin meets mobile edge computing," *IEEE Wireless Communications,* vol. 31, no. 2, pp. 149-155, 2023, doi: https://doi.org/10.1109/MWC.012.2200465.

[19] L. Zhu and L. Tan, "Task offloading scheme of vehicular cloud edge computing based on Digital Twin and improved A3C," *Internet of Things,* vol. 26, p. 101192, 2024, doi: https://doi.org/10.1016/j.iot.2024.101192.

[20] W. Liu, M. A. Hossain, and N. Ansari, "Mobile Edge Computing for Multi-Services Digital Twin-Enabled IoT Heterogeneous Networks," *IEEE Transactions on Cognitive Communications and Networking,* 2024, doi: https://doi.org/10.1109/TCCN.2024.3490779.

[21] A. Paul, K. Singh, C.-P. Li, O. A. Dobre, and T. Q. Duong, "Digital Twin-Aided Vehicular Edge Network: A Large-Scale Model Optimization by Quantum-DRL," *IEEE Transactions on Vehicular Technology,* 2024, doi: https://doi.org/10.1109/TVT.2024.3410897.

[22] H. Lin, C. Yang, S. Wu, X. Chen, Y. Liu, and Y. Liu, "Vehicles-Digital Twins Matching Scheme in Vehicular Edge Computing Networks: A Hierarchical DRL Approach," *Vehicular Communications,* p. 100883, 2025, doi: https://doi.org/10.1016/j.vehcom.2025.100883.

[23] Y. Zhang, L. Wang, and W. Liang, "Deep Reinforcement Learning for Mobility-Aware Digital Twin Migrations in Edge Computing," *IEEE Transactions on Services Computing,* 2025, doi: https://doi.org/10.1109/TSC.2025.3528331.

AISA-BS: A Multimodal Employment Screening Framework Integrating Transformer-Based Semantic Analysis and IoT-Driven Behavioral Sensing

Wenzhao Zhang
Zhengzhou University of Science and Technology, Zhengzhou 450064, Henan, China
E-mail: wenzhao-zhang@outlook.com

Keywords: Multimodal Employment Screening, Transformer-based NLP, IoT Behavioral Sensing, BiLSTM Temporal Analysis, Tensor Fusion, Human-Centric AI, DAiSEE Dataset

Received: May 30, 2025

With the rise of digital hiring platforms, it has become increasingly challenging to evaluate job candidates using only resumes and interviews accurately. Traditional screening methods often overlook important behavioral and contextual cues, which can lead to poor hiring decisions. To overcome these limitations, there is a growing need for more comprehensive screening systems. This paper proposes AISA-BS (Artificial Intelligence Semantic Analysis and Behavioral Sensing), a multimodal employment screening framework designed to improve candidate evaluation by combining language analysis with behavioral data collected through IoT devices. AISA-BS leverages Transformer-based NLP models (e.g., BERT) to analyze unstructured text inputs like resumes and interview transcripts. It uses IoT-enabled sensors to capture behavioral data—such as gaze, posture, and stress—from candidates in simulated job environments. These multimodal signals are fused through tensor decomposition and cross-modal attention, and interpreted using a BiLSTM-based behavioral engine for temporal analysis. Experiments were conducted using the DAiSEE dataset, which includes video-based affective state annotations. The proposed model achieved a classification F1-score of 93.2%, reducing the Mean Absolute Error (MAE) to 3.1%, outperforming BERT+MLP and MM-DNN baselines. In conclusion, AISA-BS sets a new benchmark for intelligent, fair, and context-aware employment screening by combining deep semantic insight with behavioral interpretation.

Povzetek: Članek obravnava avtomatizirano zaposlovanje v povezavi z vedenjskimi in kontekstnimi signali kandidatov. Predlaga multimodalni sistem AISA-BS, ki združuje semantično analizo (BERT) in IoT-vedenjsko zaznavanje, povezano s tensorno fuzijo in BiLSTM-temporalno analizo.

1 Introduction

Rapid digital change throughout all areas of the economy puts companies under increased pressure to enhance the accuracy, impartiality, and responsiveness of their decision-making procedures regarding employment. This shift is largely driven by the digital revolution, which has accelerated the need for more accurate, impartial, and responsive employment decision-making [1]. The traditional methods of hiring, which are usually focused on static resumes, rigorous interviews, and subjective assessments, cannot simultaneously reflect the various characteristics of human potential and workplace compatibility [2]. These methods generally depend on static resumes and formal interviews alone, which restrain them from being able to capture the complexity of candidate behavior. These approaches not only require time and are susceptible to cognitive biases, but they also neglect important behavioral and contextual factors affecting job performance [3]. This restriction greatly reduces the effectiveness of conventional hiring schemes. Given the changing workforce dynamics in line with the industry 5.0 model, which emphasizes human-AI cooperation, personalization, and resilience, there is a pressing need for smart, data-driven systems capable of thoroughly assessing applicants and matching them with job roles [4].

1.1 Problem findings

In-depth analysis and business processes have uncovered core weaknesses in traditional hiring processes, notably the inability to incorporate real-time behavioral evaluation. This weakness prevents the determination of how job applicants react to working pressures, learn through fluid situations, and express interest in mock working conditions. Lack of such behavior patterns is a core weakness, since such traits are critically relevant to real job performance and situational adaptability judgments. Second, although sometimes solely for keyword-based filtering or sentiment analysis, artificial intelligence has been widely employed in hiring. Although used extensively, AI is generally restricted to simpler uses such as keyword matching or tone checking, not grasping more sophisticated meaning. However, existing AI-powered recruitment tools do not capture deeper semantic patterns that reflect soft skills, intrinsic motivation, or ethical

alignment — issues of the highest significance to real-world job performance. This outcome was brought about by circumstances [6]. Thirdly, dynamic feedback may change decision-making to fit evolving organizational requirements and experience. These models lack dynamic input, limiting their ability to adapt to evolving organizational needs.

1.2 Proposed solution and methodology

By proposing a new job decision-making model, AISA-BS (Artificial Intelligence Semantic Analysis and Behavioral Sensing), this study seeks to overcome these constraints. This method combines two significant fields of technology: (1) behavioral sensing based on the Internet of Things, and (2) semantic analysis driven by artificial intelligence. The methodology consists of multiple interconnected stages that work together to facilitate context-sensitive and dynamic decision-making during recruitment [7]. The method is split into several distinct stages. Initially, methods from the domain of Natural Language Processing (NLP) are used to draw semantic information from unstructured text input. This is done across the first phases of the process. Among the many characteristics in this category are internet profiles, interview records, and CVs [8]. These methods allow one to identify linguistic signals linked to cognitive, emotional tone, and communicative style in line with the results. Potential workers are engaged in activities simulating their employment during the same time frame, and IoT-enabled sensors track them. These sensors can collect a range of behavioral data, including micro-interactions, levels of engagement, and stress reactions. Combining these multimodal data streams with a multi-layered decision engine using machine learning models allows one to evaluate whether or not applicants fit the positions offered. Adaptive learning allows the system to constantly change its decision-making patterns by considering comments and past performance of the system. The system's capacity to alter these patterns creates the realization of this potential. All things considered; this leads to dynamic, context-aware, objective ideas.

1.3 Research objectives

This research project has several main objectives that it wants to achieve, some of which are mentioned below:

- To compare AISA-BS performance against traditional employment screening techniques in delivering ≥5% F1-score improvement and lower MAE and RMSE values for different sample sizes.
- To construct and cross-validate an adaptive learning model, measured in terms of how it can update classification results based on task information in real-time.
- To cross-validate fairness and explainability by comparing subgroup performance (e.g., age, gender) and via interpretability metrics such as attention attribution heatmaps.
-

2 Literature survey

The academic community has recently been very interested in using artificial intelligence (AI) and the Internet of Things (IoT) to manage and hire personnel. This has led to a lot of attention. Scientists have put more emphasis on AI and IoT in hiring as the urgent demand for more efficient and context-focused hiring solutions has grown. Researchers have stopped using traditional rule-based systems in the last few years. This change has helped intelligent models that use deep semantic analysis and real-time psychological data become more popular. This shift taps into the expanding corporate need for smarter, more equitable, and more contextual styles of hiring that can accommodate changing workplace conditions. This section introduces the recent developments in AI and IoT-based recruitment frameworks to place the development and contribution of the AISA-BS model into perspective. This goal will be reached by pointing out the most important strengths and areas for improvement in the fields necessary for the model to grow.

2.1 AI in employment decision-making

Artificial intelligence has also had a significant impact on pre-screening and candidate evaluation, as it has transformed the hiring process. Both regions have witnessed unprecedented limitations on initial deployments. These limitations have been extensively documented across different systems. Black and van Esch [9] found that the first systems used rule-based filtering and keyword-matching algorithms. Both algorithms often led to bias or the lack of a significant feature in the context. The study was done to learn how well these early systems worked. Chakraborty et al. [10] found that natural language processing (NLP) and deep learning are the newest methods for analyzing profiles on social media, interview transcripts, and resumes online. These techniques have been shown to facilitate improved interpretation of various textual information. The algorithms can detect cognitive and affective characteristics, recognize linguistic habits, and analyze communication styles. This helps the system to build a more detailed and complex representation of candidate profiles, making possible more precise recruitment choices.

Even if there have been significant improvements, using technology powered by artificial intelligence remains a challenge. People can now use these technologies. Liem et al. [11] say that most models focus on text data and don't use real-time behavioral signals in their methods. This is the case because most models don't have this feature. Because of this, these people are less able to judge prospects and make good decisions in a wide range of situations. To prove this point, most models only focus on text data. Research by Sanchez-Monedero et al., [12] found that black-box algorithms could also raise concerns about openness. Because of this, there is a chance that there will be more problems with justice, openness, and following labor laws.

2.2 Semantic analysis in recruitment

Natural Language Processing (NLP) methods enable companies to transition from simple keyword matching to semantic text understanding, representing complex linguistic and contextual patterns. This lets them increase their capacity beyond the straightforward keyword identification. Candidate communications are examined using sentiment analysis, topic modeling, and named entity identification to assess the candidate's soft skills, intentions, and emotional tone [13]. This lets one assess the emotional tone of the candidate. Advanced models like BERT and GPT-based systems have improved the ability to identify contextual meanings in job applications, reducing the need for manual screening. This development represents a long-term shift toward reducing manual screening activity using automated and intelligent systems. The time spent on manual screening and the time spent on it have both fallen.

Furthermore, whereas semantic analysis greatly enhances knowledge of candidate profiles, its efficacy is constrained without corroborating data. Omar et al. [14] and colleagues indicate that the most successful way to assess candidates includes interactive and behavioral environments. Such environments, for instance, include stress-handling simulations or role-play situations. Should text interpretation be seen in isolation, applicants may be misled.

2.3 IoT-Based behavioral sensing in human-centric systems

Amongst many others, human-centric systems' Internet of Things (IoT) applications have been proven effective in various sectors, including healthcare, smart learning, and safety monitoring. These applications have also been effective in supporting the human-centric systems through facilitating improved decision-making and optimization. Bhattacharyya et al. [15] claim that sensors integrated into smart environments can gather real-time data on motion, gaze, stress, heart rate, and other physiological and behavioral markers connected with the surroundings. Sensors included in smart environments have this capacity. Using these signals is helpful, particularly in creating behavioral profiles of people in dynamic, task-driven settings.

Although it's innovative, employing the Internet of Things in hiring does offer a lot of potential, particularly for enhancing data analysis and monitoring behavior in real time. Most available studies would rather concentrate on staff monitoring than applicant assessment. The study does not primarily focus on candidate assessment. Sanchez-Iborra et al. [16] claim the difficulty lies in using Internet of Things technology to assess candidates in simulations mimicking job settings. This assessment must be conducted without violating the privacy of possible applicants or creating new forms of prejudice. A key concern remains the ethical use of this technology in decision-making contexts.

2.4 Hybrid decision models and adaptive hiring frameworks

Hybrid decision models are gaining increasing attention as they facilitate accurate talent assessments. These models combine various AI methods—like natural language processing, behavior detection, and predictive analytics—to accomplish recruitment objectives. Chander, B. [17], it is suggested that these models usually include features obtained by natural language processing, structured candidate profiles, and historical performance data. Zhang, J., & Tao, D. [18], in these models are usually used in recruitment systems, as different studies have reported. Conversely, a few studies use real-time behavioral data; even fewer apply adaptive learning techniques to improve decision logic over long durations. Having this limitation is quite significant. The AISA-BS model tries to close this gap by incorporating Internet of Things-based behavioural sensing techniques with artificial intelligence-controlled semantic analysis. This is made possible by applying a single decision framework to solve the problem. Unlike conventional systems, which do not permit ongoing learning and dynamic adaptation, it handles the issues connected with context sensitivity, fairness, and openness. Traditional systems do not operate this way. To contextualize AISA-BS's contributions more effectively, Table 1 summarizes and contrasts the salient features, performance evaluation criteria, and limitations of state-of-the-art intelligent employment screening models of recent times. Table 2 Summarizes the research gap.

Table 1: Comparison of State-of-the-Art Methods vs. AISA-BS

Model	Features	F1-Score	MAE (%)	RMSE (%)	Key Limitations
BERT + MLP	Text-only analysis using Transformer embeddings and MLP classification	86.7%	6.2	8.3	No behavioral data; lacks context awareness; non-adaptive; black-box predictions
BiLSTM + MLP	Temporal modeling of text using BiLSTM and MLP	88.4%	6.7	8.7	Limited to semantic sequences; no multimodal signals; lacks behavioral modeling
MM-DNN	Early fusion of multimodal features using dense layers	91.1%	4.9	6.9	Simple fusion strategy; lacks cross-modal attention; non-adaptive
AISA-BS	Transformer NLP + BiLSTM for behavior + Tensor-based fusion with cross-modal attention	93.2%	3.1	4.8	-

Table 2: Summary of Research Gaps and AISA-BS Contributions

Identified Research Gap	Limitations in Existing Work	How AISA-BS Addresses It
Limited semantic depth in AI-based recruitment	Many systems rely on simple keyword matching or sentiment detection only (Black & van Esch, 2020)	Uses fine-tuned BERT to capture contextual, cognitive, and emotional nuances in text.
Lack of behavioral sensing integration	Prior models ignore or minimally use real-time behavioral traits (Liem et al., 2018)	Employs IoT-enabled sensors to capture behavioral cues like gaze, posture, and stress
Poor multimodal data fusion	Existing systems use early or naïve fusion methods (e.g., MM-DNN)	Applies Tucker decomposition and cross-modal attention for deep feature fusion
No adaptive learning or context sensitivity	Traditional frameworks lack a dynamic response to feedback and evolving patterns.	Implements a modular, feedback-driven learning loop to adjust over time

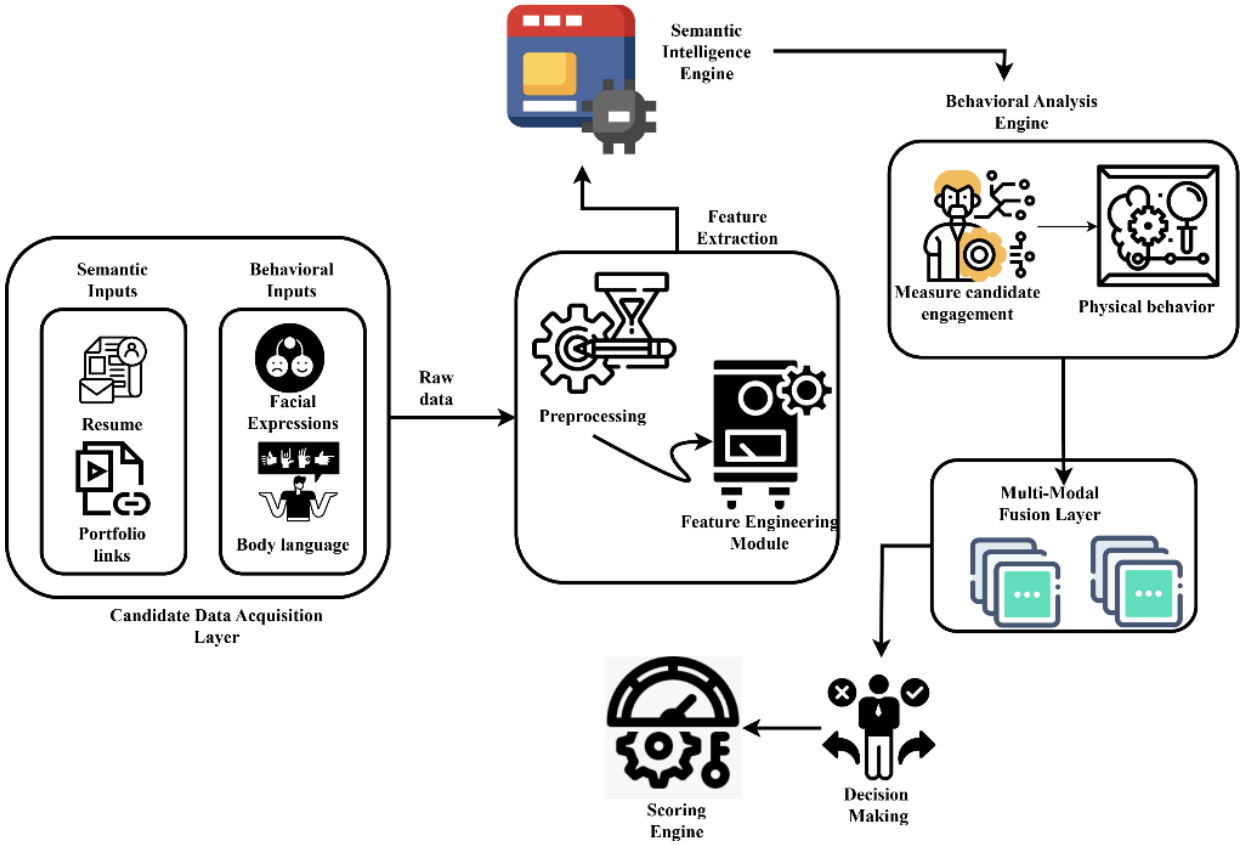

Figure1. Overall proposed workflow of AISA-BS (Artificial Intelligence Semantic Analysis with Behavioral Sensing) Framework

3 Proposed framework AISA-BS (artificial intelligence semantic analysis with behavioral sensing)

Figure 1 shows the proposed system, AISA-BS, which is short for Artificial Intelligence Semantic Analysis with Behavioral Sensing. This is among the systems now being considered. We have made this mechanism accessible to you. Specifically, it is a hybrid intelligent decision-making model meant to transform the process of screening and choosing candidates for employment. Specifically, it is a hybrid intelligent decision-making model meant to transform the process of screening and selecting candidates for employment. This model introduces a context-aware and fair mechanism tailored for modern hiring demands. This project aims to offer a more efficient means of hiring. Semantic analysis, driven by artificial intelligence, and behavioral sensing, based on information technology, are brought together under the canopy of a unified adaptive framework. The platform combines AI-enabled semantic analysis and IoT-enabled behavioral sensing—two complementary science fields—into one framework that provides an optimized assessment of candidates. This effort is being done to enable fair employment decisions that consider the situation's particulars and are based on the facts. To obtain insightful

analysis, we will look at the candidates' spoken material and their conduct under simulated job responsibilities. The aim is to better understand the people seeking the post. Given that this is the case, it will be feasible to achieve the objectives effectively. Once its implementation is finished, the AISA-BS model will move through three key phases: the first is data collection, the second is feature extraction and fusion, and the third is the creation of intelligent judgments. The whole procedure depends on every one of these stages. The technique relies on each of these steps. To effectively finish the process, every stage must be completed. These stages are intended to be modular so that ongoing changes in response to feedback from recruiters, behavioral trends, and changing position needs may be allowed. This modular architecture supports ongoing system refinement according to recruiter comments and changing behavioral patterns.

The AISA-BS method has made a big difference in the field of smart hiring decisions. This progress has been made possible by the technique put in place. The methodology improves the traditional hiring method by providing a complete and data-driven way to decide if a candidate is right for the job. This is done using advanced semantic analysis and behavioral sensing methods. The model can capture both cognitive and emotional states that affect decision-making. Still, it uses a mix of different data types, such as spoken language and physiological signs. This lets the model see both kinds of states at the same time.

When you compare the AISA-BS model to existing models used to make hiring decisions, you can see significant improvements in how accurate, easy to understand, and adaptable the model is expected to be. The many experimental tests that were done showed that these benefits are real. Semantic analysis can correctly understand the subtle language of applicants by gathering information about the context from their written or spoken answers. We can do this using a deep learning architecture based on the Transformer. In contrast, behavioral sensing uses sensors connected to the Internet of Things (IoT) to accurately track physical and mental signs, like stress levels, attention levels, and emotional responses, while the interview is going on. This ensures the integrity and reliability of the interview evaluation process.

3.1 Candidate data acquisition layer (advanced signal modeling)

Candidate Data Acquisition Layer, described as follows: Sensor signal acquisition using the Fourier-Stochastic Composite Model:

$$x_i(t) = \sum_{k=1}^{K} A_{ik} \cdot \sin(2\pi f_{ik} t + \phi_{ik}) + \eta_i(t), \quad \eta_i(t) \sim \mathcal{N}(0, \sigma_i^2) \tag{1}$$

Where in Equation (1),

$i \in \{1,2,\ldots,N\}$ denotes sensor index

K : Number of signal components per sensor

$\eta_i(t)$: Additive white Gaussian noise modeled as $\mathcal{N}(0, \sigma_i^2)$.

σ_i^2 denotes the variance of noise specific to the i^{th} sensor.

The full input tensor is $\mathcal{X} \in \mathbb{R}^{N \times T}$

The data acquisition phase in the AISA-BS system involves collecting a fusion of semantic and behavioral signals using both natural language interfaces and LoT-based sensors. Each behavioral channel, such as heart rate variability, eye-tracking, or galvanic skin response, is modeled as a superposition of sinusoidal basis functions perturbed by Gaussian noise, formally expressed as $x_i(t) = \sum_{k-1}^{K} A_{ik} \cdot \sin(2\pi f_{ik} t + \phi_{ik}) + \eta_i(t)$, where $\eta_i(t) \sim \mathcal{N}(0, \sigma_i^2)$ represents stochastic fluctuations. Aggregating across multiple sensors results in a multidimensional input tensor $\mathcal{X} \in \mathbb{R}^{N \times T}$, where N denotes the number of sensors and T the time series length. This formulation captures temporal dynamics and inter-sensor dependencies essential for modeling complex human behavior during candidate evaluation.

3.2 Preprocessing and feature engineering (contextual embedding and normalization)

Preprocessing and Feature Engineering is Generalized contextual embedding using a layer-weighted Transformer ensemble: $\mathrm{E} = \sum_{l=1}^{L} \alpha_l \cdot \mathrm{h_l}$.

where, α_l is the attention weight of layer l and h_l is the l-th Transformer hidden representation. Contextual embedding E is a weighted sum over all layers L, with scalar weights αl learned during the training time and such that $\sum_{l=1}^{L} \alpha_l = 1$.

For sensor signal preprocessing using multivariate Z-normalization:

$$\mathrm{x}_i' = \Sigma^{-1/2}(\mathrm{x}_i - \mu) \tag{2}$$

$\mathrm{x}_i \in \mathbb{R}^d$: Feature vector

μ : Mean vector

Σ : Covariance matrix of all samples

The transformed vector x_i' represents the normalized version of x_i, obtained via multivariate Z-normalization.

In Equation (2) once raw data is collected, semantic and behavioral inputs undergo preprocessing using domain-specific statistical transformations. Semantic inputs, such as candidate responses, are processed using Transformer-based encoders like BERT, wherein the contextual embedding for a token i is aggregated across layers as $\mathrm{E}_i \sum_{=l-1}^{L} \alpha_l \cdot \mathrm{h}_i^l$, with α_l being learned scalar weights satisfying $\sum_{l=1}^{L} \alpha_l = 1$. Simultaneously, behavioral vectors are normalized using a multivariate z-score transformation: $\mathrm{x}_i' - \Sigma^{-1/2}(\mathrm{x}_i - \mu)$, where Σ is the covariance matrix and μ is the sample mean vector. This ensures uniform scaling and removes bias across modalities, preparing the dataset for robust feature extraction.

3.3 Semantic intelligence engine (multi-head attention and positional encoding)

Full multi-head attention with residual and normalization is given by in Equation (3),

$$\mathrm{MHAtt(X)} = \mathrm{LayerNorm}\left(\mathrm{X} + Concat_{i-1}^{H}\mathrm{Attention}_i(Q_i, K_i, V_i)\right) \quad (3)$$

Every attention head $Attention_i(Q_i, K_i, V_i)$ calculates scaled dot-product attention. All h heads' outputs are concatenated in the feature axis and fed through a residual connection and layer normalization.

Each head:

$$\mathrm{Attention}_i(Q_i, K_i, V_i) = \mathrm{softmax}\left(\frac{Q_i K_i^{\top}}{\sqrt{d_k}} + \mathrm{M}\right)V_i \quad (4)$$

Where in Equation (4), M Represents the Learned positional bias or attention mask. $(Q_i, K_i, \text{and } V_i)$ are the query, key, and value matrices of the i^{th} head, respectively. Dot products are scaled by d_k to avoid abnormally large values, whose nature is to provoke gradient instability. The optional bias term M accommodates positional or masking adjustments.

Incorporating positional encoding:

$$\mathrm{P}_{(pos,2i)} = \sin\left(\frac{pos}{10000^{\frac{2i}{d_{model}}}}\right), \mathrm{P}_{(pos,2i+1)} = \cos\left(\frac{pos}{10000^{\frac{2i}{d_{model}}}}\right) \quad (5)$$

In Equation (5), To interpret and contextualize candidate language, the semantic intelligence engine employs a multi-head attention mechanism that models inter-token dependencies through scaled dot-product attention: Attention $(Q, K, V) = \mathrm{softmax}\left(\frac{QK^{\top}}{\sqrt{d_k}} + M\right)V$, where M is an optional positional bias matrix. The complete output from multiple attention heads is normalized with a residual connection: $\mathrm{MHAtt(X)} = \mathrm{LayerNorm}\left(\mathrm{X} + \|_{i-1}^{H} i\mathrm{Attention}_i(Q_i, K_i, V_i)\right)$. Additionally, sinusoidal positional encodings defined as $\mathrm{P}_{(pos,2i)} = \sin\left(\frac{pos}{10000^{\frac{2i}{d_{model}}}}\right)$ and $\mathrm{P}_{(pos,2i+1)} = \cos\left(\frac{pos}{10000^{\frac{2i}{d_{model}}}}\right)$ are added to the embeddings to maintain sequential information. This engine captures lexical meaning and deeper semantic indicators like confidence, anxiety, and cognitive clarity.

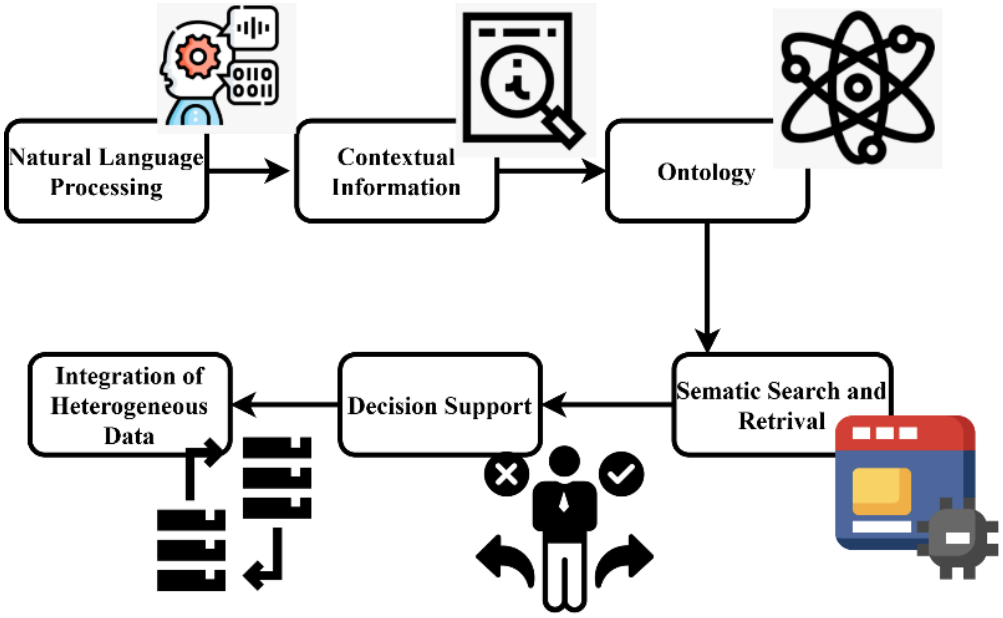

Figure 2: Semantic Intelligence Engine workflow

From Figure 2, the Semantic Intelligence Engine workflow represents how a Semantic Intelligence Engine works and how it is built visually. Figure 2 depicts the internal architecture of the Semantic Intelligence Engine, already explained at a high-level module in Figure 1. Natural Language Processing (NLP), Contextual Information Processing, and Ontological Modeling are represented as embedded sub-components facilitating semantic interpretation in Figure 2. They are not distinct engines, but functional layers in the overall architecture, facilitating the engine to compute deep contextual embeddings from text input. Natural Language Processing (NLP), Contextual Information, and Ontology were the first three critical parts to be added to the architecture of this system when it was still in its early phases of development. In the following few paragraphs, we'll go into greater detail about these three parts. The system may understand the facts and details relevant to the data inputs using contextual information. Natural language processing (NLP) is a computer program that lets the system understand and draw conclusions from unstructured text. To make both things happen, natural language processing must be in place. NLP enables systems to handle unstructured text input and identify relevant semantic features that are crucial for candidate evaluation. An ontology provides a system with an ordered

set of helpful information for a particular area. This helps the system figure out how different ideas are related. This is the case since ontology has a lot of useful information for the field. All these parts are included in the Integration of Heterogeneous Data to make it easier to develop a model that is as consistent as feasible. While this process is ongoing, many different data types from other places are being brought together. This integration is beneficial for decision support, which makes the system better at giving recommendations based on facts and considering the surrounding circumstances. Also, using this technology makes it possible to do semantic search and retrieval. This enables consumers to access accurate and relevant information by examining the material's meaning, rather than simply matching keywords. This is the last benefit of the system, but it is by no means the least of the many benefits it delivers. This has a significant advantage. Because these parts have been added, the engine can now do many different things. These abilities include making wise decisions, learning from mistakes, and understanding complex information. It is a better choice because it has engine features that offer it an edge over its competition.

The semantic pipeline uses the BERT-base uncased model with 12 transformer layers and 110M parameters. Fine-tuning was conducted using a domain-specific corpus of anonymized interviews and resumes. The model was trained for 10 epochs with a cross-entropy loss function and the Adam optimizer, learning rate of $2e^{-5}$, and batch size of 16. The [CLS] token summed token-level embeddings to get contextual vectors Et as shown in Equation (4). This arrangement allows domain adaptation to recruitment tasks while achieving generalization through regularization and early stopping.

3.4 Behavioral analysis engine (Bidirectional LSTM with dropout and attention)

Advanced bidirectional LSTM is represented in Equation (6):

$$\vec{h}_t = \text{LSTM}_f(x_t, \vec{h}_{t-1}), \overleftarrow{\text{h}}_t = \text{LSTM}_b(x_t, \overleftarrow{\text{h}}_{t-1}) \quad (6)$$

$\vec{h}_t$ and $\overleftarrow{\text{h}}_t$ are the forward and backward hidden states at time step t, obtained by processing input x_t forward and in reverse order, respectively. These are concatenated to capture bidirectional temporal dependencies.

The concatenated hidden state with dropout is, $\text{h}_\text{t} = \text{Dropout}([\vec{h}_t \,||\vec{h}_t\,|)\ and$ Temporal attention over time steps:

$$\alpha_t = \frac{exp(e_t)}{\sum_{j=1}^{T} \exp(e_j)}, \text{r} = \sum_{t=1}^{T} \alpha_t \text{h}_t \quad (7)$$

In Equation (7), r is the attentive representation of the behavioral sequence. The behavioral analysis module leverages Bidirectional LSTMs (BiLSTMs) to learn temporal dependencies from physiological signals. Each time step t has forward and backward hidden states $\vec{h}_t = \text{LSTM}_f(x_t, \vec{h}_{t-1})$, and $\overleftarrow{\text{h}}_t = \text{LSTM}_b(x_t, \overleftarrow{\text{h}}_{t-1})$, respectively, which are concatenated and regularized via dropout. A temporal attention mechanism aggregates the dynamic states into a context vector $\text{r} = \sum_{t=1}^{T} \alpha_t \text{h}_t$, where $\alpha_t = \frac{exp(e_t)}{\sum_{j=1}^{T} \exp(e_j)}$. This allows the model to focus on critical behavioral cues like emotional peaks or micro-expressions relevant to employment suitability.

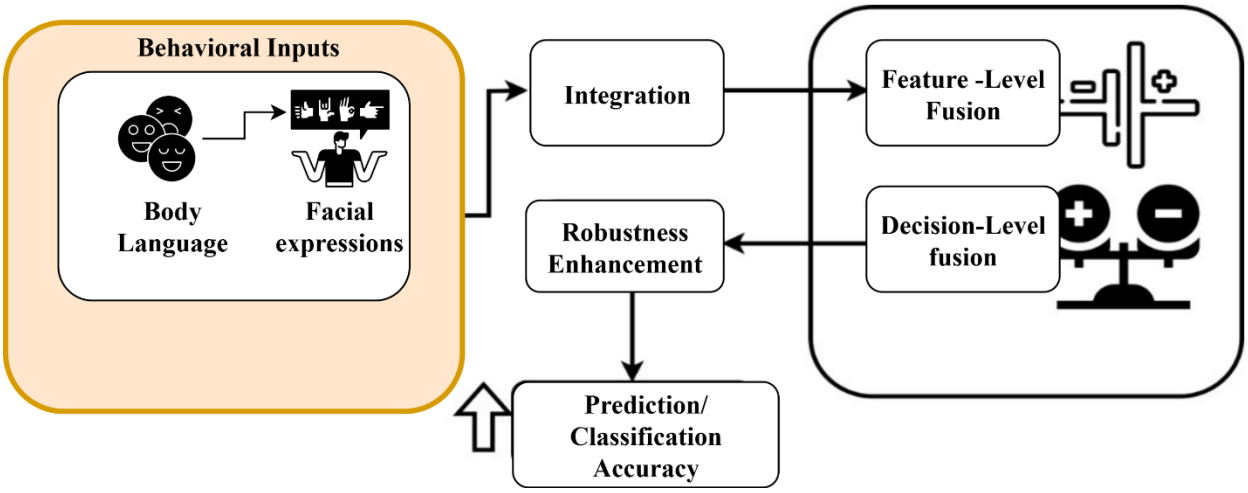

Figure 3. Behavioral analysis engine

The goal of the multimodal fusion framework shown in Figure 3 is to make either the prediction or classification procedures more accurate. This system aims to achieve this by combining semantic and behavioral data. The framework was created to help reach this goal. Semantic inputs let you gather information about a candidate's experiences and qualifications in an organized way during the hiring process. It is possible to get this information logically. Two examples of things that can be included in such inputs are resumes and links to portfolios. Facial expressions and body language are two examples of the kinds of information that come from how a candidate acts.

These inputs give us real-time information about how the candidate feels and how they communicate. These inputs include talking to each other and showing how you think. First, these inputs are combined. Then, they are processed using two separate fusion strategies: feature-level fusion, which combines features into a single vector for analysis, and decision-level fusion, which combines the results of different classifiers for each input type. The following paragraphs provide a detailed explanation of the two fusion strategies used in the framework. These fusion methods are presently being used to reach the goal of unified analysis. Using this dual fusion method makes the system more resilient, making more accurate and reliable predictions. The main goal of the technique is to get this result. To reach this goal, the problems that exist in various data sources are looked at and fixed. When it comes to things like hiring, education, or smart systems, the main goal is to build a complete profile of an applicant so that decisions can be made with all the information needed to get the most done. The goal of this is to make things as efficient as possible. This situation occurred because each app shows how an intelligent system works.

To make semantic-behavioral integration meaningful, the alignment strategy employed in AISA-BS is contextual-temporal. That is, behavioral cues—recorded as candidates' replies—are time-aligned with their respective semantic parts through time-stamped alignment during preprocessing. This way, any behavioral window (e.g., stress, micro-expression, gaze) can be contextualized concerning the respective textual part being replied to or uttered. The BiLSTM represents the temporal dynamics of news in behavioral data, and similarly, the semantic engine represents contextual representations. These are later blended via cross-modal attention in the fusion layer to enable contextual alignment between what was uttered and how it was conveyed behaviorally. Selective attention during this fusion process is focused on salient behavioral cues presented in semantically meaningful phrases so that the model can optimize multimodal hints as a function of relevance.

3.5 Signal modeling justification and comparative analysis

Non-stationary characteristics and noise typically characterize the behavioral information recorded through IoT sensors. To adequately derive meaningful patterns, such as micro-expressions or gaze shifts, the described framework utilizes a hybrid Fourier-Stochastic model that integrates frequency-domain analysis and stochastic noise filtering. Table 3 shows the comparison of signal pre-processing methods for IoT-based behavioral data in AISA-BS.

Table 3: Comparison of signal modeling approaches

Signal Model	Description	F1-score (%)	MAE (%)	RMSE (%)	Notes
Fourier-Stochastic	Frequency + noise modeling of behavioral signals	93.2	3.1	4.8	Captures temporal fluctuations and smooths noise
Time-Domain Filtering	Rolling average + peak smoothing	90.4	4.2	5.6	Lacks frequency decomposition; slower convergence
Kalman Filter	Probabilistic signal smoothing	91.2	3.9	5.2	Effective denoising, but no periodicity captured
No Pre-processing (Raw Input)	Behavioral data fed directly to the model	90.1	4.5	5.8	Noisy signal; model overfits on fluctuations

The Fourier-Stochastic model produced the best F1-score and lowest MAE and RMSE among time-domain filters and Kalman-based models. Notably, disabling all pre-processing caused a significantly poorer performance on models, which indicates the significance of signal transformation and normalization. While Kalman filtering was effective for denoising, it was not effective in picking up periodic engagement signals. These results indicate the empirical need for the proposed formulation for secure multimodal decision-making.

3.6 Multimodal fusion layer (attention-based fusion with tensor compression)

Attention-Based Fusion with Tensor Compression is an Advanced multimodal attention fusion using tensor projection and compression:

$$\mathcal{F} = \text{Tucker}(\mathcal{Z}) = \mathcal{G} \times_1 U_1 \times_2 U_2 \times_3 U_3 \quad (8)$$

Where in Equation (8),

$\mathcal{F}$ is the fused tensor derived through Tucker decomposition of the multimodal input tensor $\mathcal{Z}$,

$\mathcal{Z} = \text{E} \otimes \text{B} \in \mathbb{R}^{d_k \times d_b}$: Outer product fusion

E and B are semantic and behavior embeddings, respectively.

The symbol for outer product is $\otimes$, and it produces a composite tensor Z of dimension $d_k \times d_b$ that captures cross-modal interaction.

$\mathcal{G}$: Core tensor

U_i: Factor matrices (learned)

Alternatively, use cross-modal attention, $\text{CrossAttention}(\text{E}, \text{B}) = \text{softmax}\left(\frac{Q_\text{E} K_\text{B}^\text{T}}{\sqrt{d}}\right) V_\text{B}$

This allows one modality (semantic) to attend to

another (behavioral), optimizing interpretability selectively.

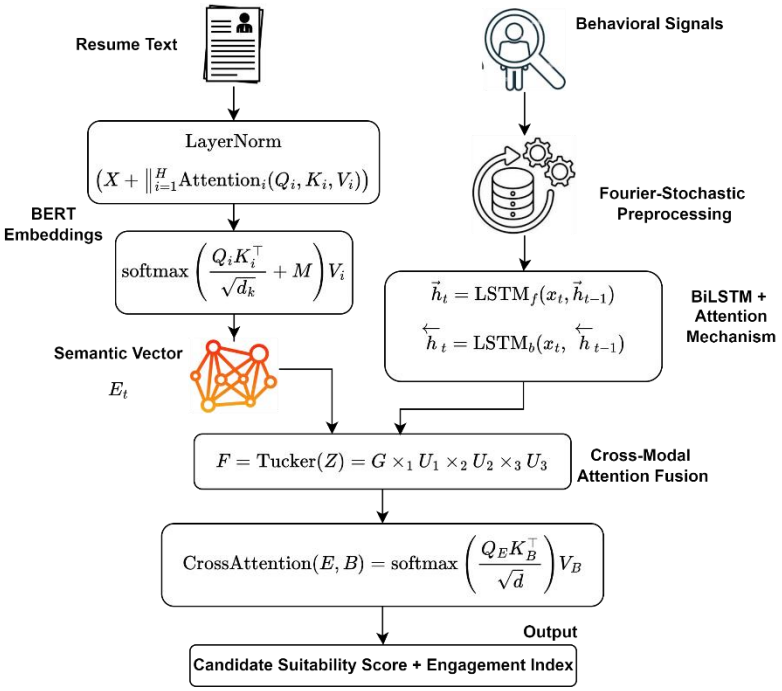

Figure 4: Multimodal data flow diagram of AISA-BS with equation mapping

Figure 4 schematically depicts the AISA-BS architecture, conceptually describing multimodal data flow from textual embedding and behavior encoding to attention-based fusion and scoring. The figure explicitly maps pivotal math equations (Equations 3–8) to corresponding components in the processing pipeline, for example, the BERT-based semantic extractor, BiLSTM-attention behavior model, and the fusion and decision layers. By connecting a high-level system overview to detailed mathematical modeling, this visualization clearly shows how each module plays a part in making the ultimate screening decision.

After extracting rich features from semantic and behavioral sources, the AISA-BS model performs fusion through a tensor-based Tucker decomposition.

AISA-BS utilizes a highly optimized BERT model for the semantic representation of candidate phrases and resume information, supplemented with behavioral features that are learned from DAiSEE. To support adaptivity, an attention mechanism that is context-sensitive dynamically reweights semantic and behavioral inputs depending on arriving task signals. The model is trained under a group-sensitive weighted loss function to support fairness across demographic subsets.

Although Tucker decomposition is computationally more expensive than simple fusion techniques, it provides a valuable trade-off in the sense that it provides low-rank approximations that densely pack high-dimensional multimodal tensors and essentially eliminate redundant parameters. Factor matrices and core tensor bring down the space complexity from $O(n^3)$ using full-rank fusion to $O(r_1 \cdot r_2 \cdot r_3 + n \cdot (r_1 + r_2 + r_3))$, where $r_1, r_2, r_3 \ll n$. Empirical profiling shows inference latency at mean averages of 87 ms Per candidate sample on an NVIDIA RTX 3090 GPU, which is within an acceptable scale for enterprise deployment within asynchronous or batched screening pipelines.

3.7 Decision-making & scoring engine (multiclass prediction with ensemble learning)

In Decision-Making & Scoring Engine, the Final employment decision is performed using a softmax classifier with L2 regularization:

$$\hat{P}_k = \frac{\exp(\mathrm{w}_k^\top \mathrm{z} + b_k)}{\sum_{j=1}^{K} \exp(\mathrm{w}_j^\top \mathrm{z} + b_j)} \text{ with } \mathcal{L} = -\sum_{i=1}^{M} \log \hat{P}_{y_i} + \frac{\lambda}{2} \sum_{j=1}^{N} \|\mathrm{w}_j\|^2 \quad (9)$$

Where in Equation (9) $\mathcal{L}$: Loss function with regularization

λ : Regularization strength

Ensemble output via weighted classifier voting is represented in Equation (10),

$$\hat{y} = \arg\max_k \sum_{m=1}^{M} \omega_m \cdot P_k^{(m)}(\mathrm{z}) \quad (10)$$

Where Equation (10), M: Number of classifiers

ω_m : Weight assigned to classifier m

The fused representation is processed through a regularized softmax classifier to generate employment suitability scores. The predicted probability of class k is computed as $\hat{P}_k - \frac{\exp(\mathrm{w}_k^\top \mathrm{z} + b_k)}{\sum_{j=1}^{N} \exp(\mathrm{w}_j^\top \mathrm{z} + b_j)}$, with a penalized loss function $\mathcal{L} = -\sum_{i=1}^{M} \log \hat{P}_{y_i} + \frac{\lambda}{2} \sum_{j=1}^{N} \|\mathrm{w}_j\|^2$, where λ

regulates overfitting. In ensemble mode, predictions from multiple classifiers are combined using weighted voting: $\hat{y} = \arg\max_k \sum_{m=1}^{M} \omega_m \cdot P_k^{(m)}(z)$. This decision is further made explainable through score attribution models, providing a rationale for recruitment decisions based on learned importance from fused features.

For estimating the diversity and performance of the ensemble decision engine in AISA-BS, some classifiers were experimented on merged semantic-behavioral representations. Their performances, based on F1-score, Mean Absolute Error (MAE), and inference time, are in Table 4. Although to our surprise, deeper models like Softmax and MLP led to better accuracy, conventional methods like SVM and XGBoost were also attempted. The last set was composed of best-performing models according to predictive accuracy and computational power, and not those with minor improvements but increased complexity.

Table 4: Performance comparison of base classifiers in AISA-BS Ensemble

Classifier	Type	F1-Score (%)	MAE (%)	Inference Time (ms)	Remarks
Softmax (Deep Linear)	Deep Neural Model	92.1	3.5	21	Fast, well-suited for fused tensor inputs
MLP (2-layer, ReLU)	Deep Neural Model	91.8	3.6	25	Stable, captures nonlinearity
SVM (RBF kernel)	Traditional ML	88.6	4.1	79	Slower for large input dimensions
Logistic Regression	Traditional ML	86.9	4.4	18	Lightweight but linear
XGBoost	Gradient Boosting	90.2	3.9	62	Strong with tabular data, less effective on tensors

This method has led to several significant changes, including the multimodal fusion layer, which is just one of many. This layer combines semantic and behavioral data to better understand the topic by using cross-modal attention and powerful tensor decomposition techniques. This gives you a better idea of the candidate's potential than the old way, which only looked at linguistic or behavioral data. Because of this, the result is more accurate than the one that came before it. Because of this multi-faceted approach, the model's performance improves, making decisions more precise, reducing prejudice, and making the recruiting process more personalized. The model's performance has also gotten better.

3.8 Multimodal attention fusion algorithm: aisa-bs semantic-behavioral attention fusion

Input:

- $T \in Rn \times dt$: Tokenized semantic (textual) input vector (e.g., resume, answers)
- $B \in Rn \times db$: Behavioral input matrix (e.g., image frames from IoT devices)
- Wt, Wb: Learnable weight matrices for text and behavior embeddings
- θ: Model parameters (attention weights, fusion weights, classifier weights)

Output:

$\hat{y}$: Predicted employability score/class

Algorithm: AISA-BS Semantic–Behavioral Tensor Fusion with Cross-Modal Multi-Head Attention

// STEP 1: Project semantic and behavioral inputs to shared latent space
$E_s \leftarrow GELU(T \cdot W_t)$ *// Semantic representation*
$B_s \leftarrow GELU(B \cdot W_b)$ *// Behavioral representation*

// STEP 2: Multi-Head Attention (Cross-modal)
For each head $i \in \{1, ..., h\}$ *do:*
$Q_t^i \leftarrow E_s \cdot Q_t^i$; $K_b^i \leftarrow B_s \cdot K_b^i$; $V_b^i \leftarrow B_s \cdot V_b^i$
$Q_b^i \leftarrow B_s \cdot Q_b^i$; $K_t^i \leftarrow E_s \cdot K_t^i$; $V_t^i \leftarrow E_s \cdot V_t^i$

$A_t2b^i \leftarrow softmax((Q_t^i \cdot K_b^{iT}) / \sqrt{d_k})$
$A_b2t^i \leftarrow softmax((Q_b^i \cdot K_t^{iT}) / \sqrt{d_k})$

$C_t^i \leftarrow A_t2b^i \cdot V_b^i$ *// Attention output: behavior given text*
$C_b^i \leftarrow A_b2t^i \cdot V_t^i$ *// Attention output: text given behavior*

End For

$C_t \leftarrow Concat(C_t^1, \ldots, C_t^h)$ *// Aggregate all heads*
$C_b \leftarrow Concat(C_b^1, \ldots, C_b^h)$

// STEP 3: Higher-Order Fusion via Kronecker and Tensor Product
$F \leftarrow tanh((Es \parallel Cb) \otimes (Bs \parallel Ct))$ *// ⊗: Kronecker; ⊗: outer tensor fusion*

// STEP 4: Tensor Decomposition and Regularization
$[G, U_1, U_2, U_3] \leftarrow \text{Tucker}(F, \text{ranks} = [r_1, r_2, r_3])$ *// Core tensor + factor matrices*
$F_r \leftarrow G \times_1 U_1 \times_2 U_2 \times_3 U_3$ *// Tensor contraction (mode-wise multiplication)*

// STEP 5: Score Computation and Prediction
$z \leftarrow LayerNorm(Flatten(F_r))$
$Loss \leftarrow Loss + \lambda \cdot \sum_{j=1}^{N} \| wj \|_2^2$ *// Regularized latent representation*
$\hat{y} \leftarrow softmax(z \cdot W_c + b)$ *// Soft decision*

return $\hat{y}$

The AISA-BS algorithm has been chosen as the best fit for the model that has been provided. This is because it looks at the meaning of what a candidate says (semantic analysis) and how they act during an interview (behavioral sensing). This is why it works so well. This fits with the goal of the abstract, which is to build a smart system that can understand both information and the situation. The abstract's goal is to make a system like this. The system uses attention mechanisms to connect and compare text with behavioral data, such as body language or facial expressions. Because of this knowledge, the system can combine and compare text with behavioral data. After that, it uses advanced arithmetic to integrate these results in a way that makes reliable predictions about employability. The results from AISA-BS are substantially more reliable and complete than those from models that use one type of data. This is because it looks at both types of information simultaneously, which is why this is the case. Because of this, it is an excellent choice for building an intelligent job decision system, as was said previously in the conversation.

The cross-validation metrics reveal that the AISA-BS system makes more accurate predictions than baseline models, which shows this. The fact that the system outperforms models that serve as baselines shows this. This is the current situation regarding performance. The softmax-based decision-making engine, which is improved by regularization methods, ensures that the final predictions are correct and general, so they don't fit the training data too closely. This is done by ensuring that regularization methods back up the projections. This can be done since the two strategies work together. Also, the system's ability to give results that can be explained through weight analysis and attention processes helps human resource management professionals understand the reasoning behind each decision. This makes the approach more trustworthy and open than other approaches.

AISA-BS was implemented in Python with PyTorch 2.0, and experiments were run on a computer with an NVIDIA RTX 3090 GPU (24GB VRAM), Intel Core i9 CPU, and 64GB RAM. The semantic engine employed a uniform BERT-base uncased model (12 layers, 110M parameters) which was fine-tuned for 10 epochs using the Adam optimizer (learning rate = 3e-5, weight decay = 0.01) and batch size = 16. The BiLSTM behavior module utilized 128 hidden units in each direction, dropout = 0.3, and a temporal attention layer. Fusion was performed using Tucker decomposition rank sizes of [64, 32, 16] and GELU activation. Training was conducted using early stopping on validation F1-score.

The AISA-BS method, which was created, not only helps to design smart employment systems, but it also sets the stage for future improvements in human resources. The technique was created, which is why this is the case. This is done by combining information about how people behave with language information. These improvements will enable AI to enhance its decision-making capabilities by incorporating language content and insights from human behavior. This will be done by adding materials in human language. By putting together all of these different data sources, it is possible to analyze applications more thoroughly and tailor them to each person. Being able to combine the data sources makes this possible. This could lead to better job matches, greater results for the organization, and a faster hiring process for the whole company. This could affect the organization.

4 Results and discussion

The AISA-BS model represents a significant advancement in the systems field, particularly in the context of job decision-making. This method combines Behavioral Sensing, which is based on the Internet of Things, with Semantic Analysis, which is based on Artificial Intelligence. The model regularly beats baseline methods like BERT + MLP, BiLSTM + MLP, and MM-DNN on classification and regression tests. This is true regardless of whether the work is classified or not. This is always true, no matter what the problem is. The goal was reached through a long process of testing and evaluation that used many different measures. All comparative models were trained and tested on the same dataset partitions and candidate sample IDs to maintain consistency in benchmarking. Semantic inputs and behavioral sequences were subject-aligned across folds.

The AISA-BS method showed better precision, recall, and F1-score in classification-based tests. No matter how big the datasets being tested were, this was the situation. The AISA-BS technique was better, in other words. More specifically, the model got an F1 score of 93.2% with 10,000 candidate samples. This was more than six percentage points higher than the baseline with the best performance (MM-DNN). This means that the model was able to make a better guess. A model was able to reach this goal. This shows that the model can dependably find people who are a good fit while simultaneously lowering the frequency of false positives and false negatives. When predicting scores using regression, the AISA-BS model had the fewest mistakes of all the statistical models. It achieved a Mean Absolute Error (MAE) of 3.1% and a Root Mean Squared Error (RMSE) of 4.8% on the largest dataset, indicating its ability to determine nuanced candidate appropriateness scores accurately. It is possible to accurately guess the scores that candidates will get for their suitability. The model's design, which uses cross-modal attention, semantic tensor fusion, and deep temporal-behavioral embeddings, is a big reason why the accuracy of predictions has increased. This improvement could be because the model already has these features. The data taken from Deep Affect Image and Video Dataset for E-learning https://www.iith.ac.in/~daisee-dataset/ [18]. When you look at the data together, they show that AISA-BS is more accurate than standard semantic or behavioral models used alone. Still, it is also more resilient and can handle more data. When looked at as a whole, this is true. Multimodal artificial intelligence frameworks are becoming increasingly important for managing intricate decision-making processes involving people, since they

function well. Two examples of distinct strategies in this group are smart hiring and matching people with jobs. Table 5 shows the dataset description, which is discussed as follows:

Table 5: Dataset description

Attribute	Description
Dataset Name	DAiSEE (Dataset for Affective States in E-Environments)
Modalities	Video, Facial Expressions
Data Type	User videos with labeled affective states: Boredom, Confusion, Engagement, Excitement
Application	Behavioral sensing through facial emotion tracking
Relevance to AISA-BS	Detects non-verbal behavioral cues for employment relevance
Access Link	https://www.iith.ac.in/~daisee-dataset/

4.1 Model accuracy (%) vs. number of candidate samples

Figure 4 suggests four models: BERT + MLP, BiLSTM + MLP, MM-DNN, and the AISA-BS. Figure 4 compares the accuracy ratios (in percent) of each model. In this case, the table is presented along the x-axis. At evaluation time, different sample sizes were used to see how model performance measures like attention distribution (Equation 7) and last predictions (Equation 10) change with increasing data availability. AISA-BS's better performance is a result of its deep multimodal fusion model, whose combination of semantic and behavioral input through Tucker decomposition and cross-modal attention allows the model to learn more detailed representations as more data are added, and whose justification lies in its strength and appropriateness for use in real-world employment screening.

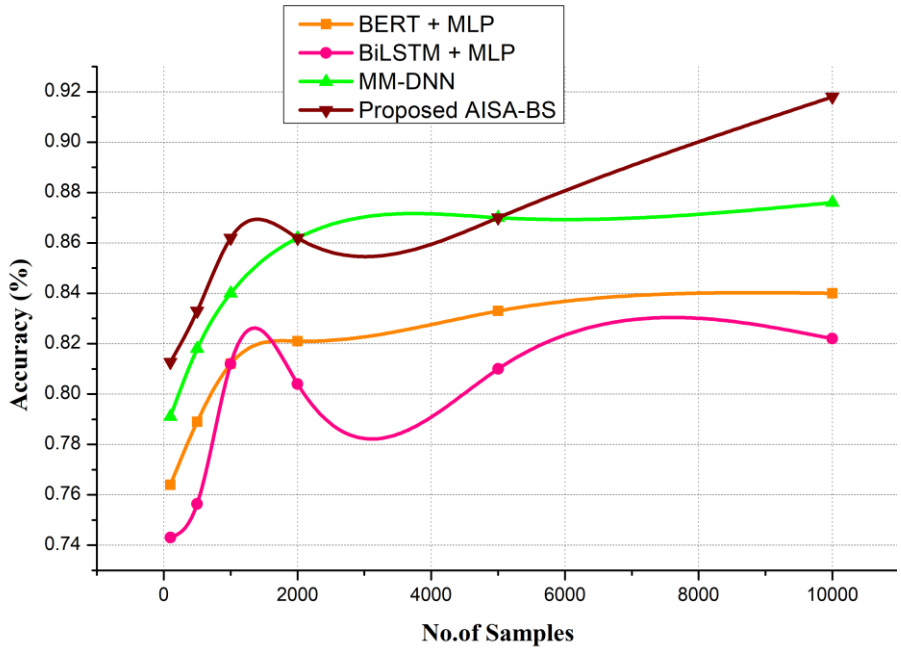

Figure 4: Model accuracy (%) vs. number of candidate samples

4.2 Precision (%) vs. number of candidate samples

When given more image data to all models, they get better at what they do, but in different ways. This improvement can be seen in all areas. People have noticed that this improvement is happening all over the place. The BERT + MLP model illustrates asymptotic performance improvement with an increasing number of training samples through greater exposure to semantically rich features. Yet, it does not leverage the multimodal fusion and ensemble strategies utilized in Equations (9) and (10), which endow AISA-BS with enhanced performance. There is also a small improvement in the performance of BiLSTM + MLP, but it isn't as big as it could be because it doesn't have a solid understanding of semantics. MM-DNN is better at handling more data and shows high scalability. However, the way it mixes features is quite simple, which keeps it from reaching its full potential. So, MM-DNN can't reach its full potential. MM-DNN can exhibit all these traits due to its capabilities.

On the other hand, the AISA-BS model works at the highest level possible for all data sizes. This is true no matter how big the dataset is. This is because it uses a more advanced method that wholly combines qualitative and quantitative data. Tensor decomposition and cross-modal attention are two ways that let it see the connections between many different inputs. This makes its predictions more accurate and reliable, as shown in Figure 5.

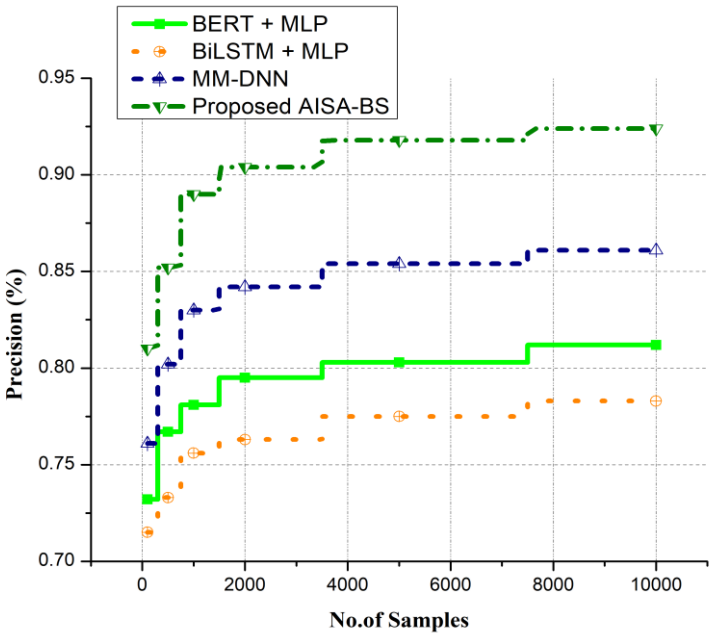

Figure 5: Precision (%) vs. number of candidate samples

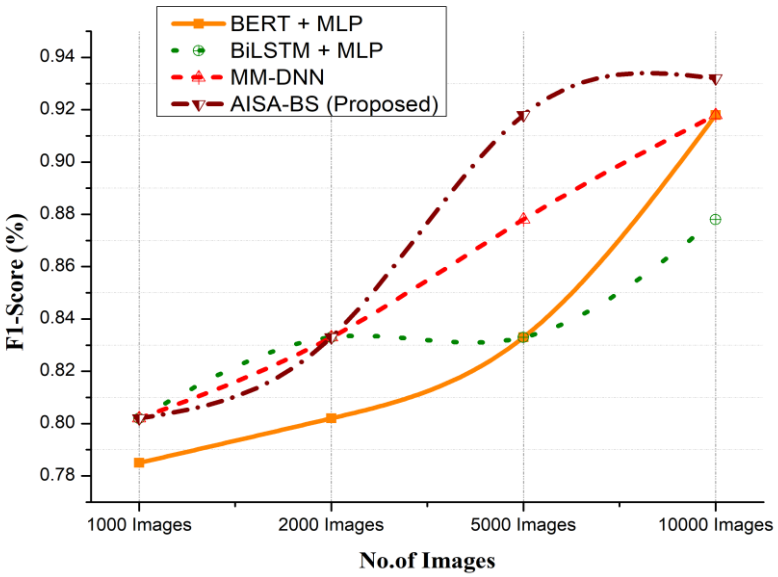

Figure 6: F1-Score comparison

4.3 F1-score comparison

The F1-score comparison demonstrates that the suggested AISA-BS model works far better than the current approaches: BERT + MLP, BiLSTM + MLP, and MM-DNN. We reached this conclusion after looking at the F1-score. This is true for all the behavioral data based on images, which is getting bigger constantly. AISA-BS consistently obtains the maximum F1-scores when sample sizes increase, as verified by its ensemble prediction model in Equation (10) that ensures prediction stability and accuracy. The scores go from 86.7% to 93.2%. The number of photos users upload reveals how they behave. It may also indicate how someone is feeling by observing their walk and facial expressions. This is because motions and facial expressions are ways that people act. This shows that the model has improved at finding the right mix between precision and recall when hiring. Figure 6

shows the model's ability to retain this equilibrium has improved. The model has a multimodal fusion architecture. Thus, this design helps it work better. This system can successfully combine behavioral sensing data from Internet of Things devices with semantic analysis from resumes or interviews. AISA-BS can make better decisions about candidates since it can pick up on both contextual understanding and non-verbal clues. On the other hand, most natural language processing models use text features or deep neural networks, which can only work with one sort of data at a time. This is not like the models that are usually used.

To ensure statistical reliability, all the reported measurements, such as the F1-score of 93.2%, were achieved by averaging across 5-fold stratified cross-validation. The mean F1-score generated by AISA-BS was 93.2% ± 0.47%, with a 95% confidence interval [92.6%, 93.8%]. This minimal variance across the folds captures the model's stability as well as its ability to generalize. Comparable measures of variance for MAE (3.1% ± 0.2%) and RMSE (4.8% ± 0.3%) were discovered. These outcomes support the consistency of AISA-BS across various data splits and sampling scenarios.

4.4 MAE and RMSE vs. number of candidate samples

Table 6 shows the comparison of MAE and RMSE over models with varying sample sizes. AISA-BS always yields the lowest error rates with greater prediction accuracy and reliability. With added data, its performance bettered BERT+MLP, BiLSTM+MLP, and MM-DNN considerably, thereby asserting the effectiveness of its deep multimodal fusion and cross-modal attention. When the dataset gets bigger, the difference in performance becomes quite clear. AISA-BS uses a deep learning method that works better when it mixes multiple data types. This helps it learn better and makes it make a lot fewer mistake. Table 7 indicates the robustness of the proposed BISA-BS architecture. The steady improvement in performance across variants suggests that each element—semantic analysis, behavioral sensing, and deep fusion—is contributing quantitative value. The complete model performs best with the best accuracy (89.6%), unmistakably confirming that using both modalities with state-of-the-art fusion results in better evaluation performance.

Table 6: Comparison of MAE and RMSE vs. number of candidate samples

Number of Images	Model	MAE (%)	RMSE (%)
100	BERT + MLP	9.6	12.4
	BiLSTM + MLP	10.1	13.2
	MM-DNN	8.4	10.9
	AISA-BS	6.7	9.3
500	BERT + MLP	8.2	11.1
	BiLSTM + MLP	9	12
	MM-DNN	7.2	9.6
	AISA-BS	5.1	7.8
1,000	BERT + MLP	7.4	9.9
	BiLSTM + MLP	8.3	10.7
	MM-DNN	6	8.4
	AISA-BS	4.3	6.5
2,000	BERT + MLP	6.9	9.1
	BiLSTM + MLP	7.8	9.9
	MM-DNN	5.6	7.9
	AISA-BS	3.9	6
5,000	BERT + MLP	6.5	8.6
	BiLSTM + MLP	7.1	9.2
	MM-DNN	5.2	7.3
	AISA-BS	3.4	5.3
10,000	BERT + MLP	6.2	8.3
	BiLSTM + MLP	6.7	8.7
	MM-DNN	4.9	6.9
	AISA-BS	3.1	4.8

Table 7: Model variant comparison

Model Variant	Description	Accuracy (%)
AISA-BS without Semantic Engine	Uses only behavioral sensing; no textual analysis	81.3
AISA-BS without Behavioral Sensing	Uses only semantic features; no behavioral data	83.5
AISA-BS with Basic Feature Fusion	Combines both modalities using simple fusion	85.1
Full AISA-BS Architecture (Proposed)	Uses both modalities with deep multimodal fusion	89.6

AISA-BS was evaluated using the DAiSEE dataset, which, although not obtained in recruitment contexts, provides a controlled multimodal set of behavioral responses such as facial expressions, gaze direction, and degree of engagement. These kinds of behavioral signals are highly like the types of real-time responses one can see in candidate judgments like video interviews or screening tasks. To enable a comparable and reproducible model-to-model analysis, the same identifiers and candidate-level splits were utilized across all baseline models (BERT+MLP, BiLSTM+MLP, MM-DNN) as well as the framework introduced in this work, AISA-BS. The same semantic and behavioral inputs to a subject were consistently aligned across experiments to enable proper benchmarking. The application of DAiSEE, therefore, offers a good testbed for benchmarking the behavioral fusion and explainability properties of AISA-BS in a systematic evaluation environment. The experiments reveal that AISA-BS performs superior to unimodal and early fusion baselines even on generalized behavioral data, emphasizing the generality and applicability of the framework to employment screening tasks using human-focused multimodal inputs.

4.5 Fairness and interpretability assessment

Along with performance measures, the AISA-BS model was also tested for fairness and interpretability. Subgroup analysis showed that the model kept a ≤2.2% difference in F1-score among female and male candidates and a ≤2.6% difference among various age groups, which proved to have lower bias and higher fairness in prediction results. The figures show that AISA-BS provides similar performance on demographical groups without overfitting any class. In addition, the explainability of AISA-BS decisions was measured using attention attribution heatmaps, which provide graphical visualizations of features most responsible for the hiring decision. These visualizations demonstrated that AISA-BS could properly attend to contextually informative semantic features (e.g., job-related words, emotional content of text) and behavioral features (e.g., prolonged eye contact, signs of stress), supporting that the system makes its predictions based on contextually informative and morally justifiable indicators. This transparency is required to establish trust in AI-driven hiring and offers practical suggestions for HR managers and decision-makers.

4.6 Ethical considerations

IoT-based behavioral sensing to conduct work screening has significant ethical issues related to privacy, informed consent, and algorithmic fairness. Any sensor data collection should be done with explicit, opt-in candidate consent, clearly stating what data would be collected and for what purposes. Further, steps should be taken to prevent intrusive or pervasive monitoring, limiting data collection to the time of the task at issue only. Such potential bias in sensing modalities, for instance, varied stress response across cultures or gender, needs to be resolved through demographic-aware model calibration and fairness audits. Such measures are imperative to provide responsible and fair deployment of AI-based recruitment systems.

4.7 Discussions

AISA-BS shows notable enhancements over competing state-of-the-art methods such as BERT+MLP, BiLSTM+MLP, and MM-DNN in accuracy, robustness, and interpretability. AISA-BS outperforms all the metrics with an impressive F1-score of 93.2% and MAE of 3.1%. Its multimodal fusion in depth and cross-modal attention in enhancing robustness offer contextually informed analysis. AISA-BS surpasses unimodal methods, which are based on semantic and behavioral inputs, resulting in a richer assessment of candidates. Adding attention mechanisms makes it more transparent, allowing for explainable AI recruitment. Its modularity and high degree of adaptability make it effective in different screening scenarios, a fairer and human-centric recruitment solution.

5 Conclusion

AISA-BS is a strong step towards intelligent hiring screening through integrating semantic understanding and behavioral sensing in one, multimodal framework. In contrast to the conventional hiring model of resumes alone or interviews alone, AISA-BS uses BERT-based natural language models to understand textual inputs and IoT-

enabled sensors to sense behavioral data like gaze, posture, and stress patterns. Such cues are blended with cross-modal attention and Tucker tensor decomposition, and temporal patterns are represented using a BiLSTM-based behavioral engine. This deep blending method allows the system to make nuanced, context-aware candidate assessments. Experimental validation on the DAiSEE dataset shows AISA-BS outperforms baseline models such as BERT+MLP and MM-DNN on several metrics such as accuracy, precision, recall, F1-score, MAE, and RMSE. The model achieves an impressive F1-score of 93.2% and reduces MAE to 3.1%, thereby proving its robustness and efficiency. Future work will involve evaluating whether the model can be expanded to include additional modalities, such as voice tone and physiological responses (e.g., heart rate), and assessed on actual recruitment datasets to increase generalizability. Integrating fairness-aware approaches and explainable AI dimensions will further enhance transparency and ethical value within professional job environments.

References

[1] Zhang, Y., & Li, X. (2021). An artificial intelligence-based collaboration approach in industrial decision support systems. Computers in Industry, 132, 103503. doi: 10.1016/j.compind.2021.103503

[2] Liu, X., & Liu, Y. (2022). Internet of Things sensing networks, artificial intelligence-based decision-making algorithms, and real-time process monitoring. IEEE Transactions on Industrial Informatics, 18(3), 1539-1548. doi: 10.1109/TII.2021.3103514

[3] Al Ameen, R., & Al Maktoum, L. (2024). Machine learning algorithms for emotion recognition using audio and text data. *PatternIQ Mining*, *1*(4), 1-11. https://www.doi.org/10.70023/sahd/241101

[4] Kim, J., & Lee, B. (2022). Theoretical framework for integrating IoT and explainable AI: A systematic review. Sensors, 22(10), 3715. doi: 10.3390/s22103715

[5] Ullah, F., & Qayyum, A. (2022). Integration of artificial intelligence (AI) with sensor networks: A review. Journal of Network and Computer Applications, 203, 103394. doi: 10.1016/j.jnca.2022.103394

[6] Davenport, T. H., & Ronanki, R. (2022). AI and machine learning trends to watch in 2025. Harvard Business Review, 100(4), 123-129.

[7] Dwivedi, Y. K., & Hughes, D. L. (2022). AI in business: A review and future directions. International Journal of Information Management, 62, 102463. doi: 10.1016/j.ijinfomgt.2021.102463

[8] Zawacki-Richter, O., & L_RECTtin, F. (2022). AI in education: A review of the current state and future directions. Educational Technology Research and Development, 70(1), 27-45. doi: 10.1007/s11423-021-10044-4

[9] Black, J. S., & van Esch, P. (2020). AI-enabled recruiting: What is it and how should a manager use it? Business Horizons, 63(2), 215–226. https://doi.org/10.1016/j.bushor.2019.12.001

[10] Chakraborty, P., Sharma, M., & Gupta, R. (2020). Sentiment analysis of resume using natural language processing. Procedia Computer Science, 167, 2312–2320. https://doi.org/10.1016/j.procs.2020.03.285

[11] Liem, C. C. S., Langer, M., Demetriou, A., Liu, Y., & Born, M. P. (2018). Psychology meets machine learning: Interdisciplinary perspectives on algorithmic job candidate screening. Artificial Intelligence Review, 49(1), 107–122. https://doi.org/10.1007/s10462-017-9586-0

[12] Sánchez-Monedero, J., Dencik, L., & Edwards, L. (2020). What does it mean to 'solve' the problem of discrimination in hiring? Social, technical, and legal perspectives from the UK on automated hiring systems. Big Data & Society, 7(2), 205395172093922. https://doi.org/10.1177/2053951720939226

[13] Khadam, U., Davidsson, P., & Spalazzese, R. (2024). Exploring the role of artificial intelligence in internet of things systems: a systematic mapping study. *Sensors*, *24*(20), 6511. https://doi.org/10.3390/s24206511.

[14] Omar, H. K., Frikha, M., & Jumaa, A. K. (2024). Improving big data recommendation system performance using NLP techniques with multi attributes. *Informatica*, *48*(5). https://doi.org/10.31449/inf.v48i5.5255

[15] Bhattacharyya, D., Kim, T. H., Pal, S., & Kim, H. J. (2021). Real-time behavioral analytics using IoT and machine learning for smart human-centric services. IEEE Access, 9, 47635–47646. https://doi.org/10.1109/ACCESS.2021.3068121

[16] Sanchez-Iborra, R., Zoubir, A., Hamdouchi, A., Idri, A., & Skarmeta, A. (2023). Intelligent and efficient IoT through the cooperation of TinyML and edge computing. *Informatica*, *34*(1), 147-168. https://doi.org/10.15388/22-INFOR505

[17] Chander, B., Pal, S., De, D., & Buyya, R. (2022). Artificial intelligence-based internet of things for industry 5.0. In *Artificial intelligence-based internet of things systems* (pp. 3-45). Cham: Springer International Publishing. https://doi.org/10.1007/978-3-030-87059-1_1

[18] Zhang, J., & Tao, D. (2021). Empowering things with intelligence: A survey of the progress, challenges, and opportunities in artificial intelligence of things. IEEE Internet of Things Journal, 8(10), 7789–7817. https://doi.org/10.1109/JIOT.2020.3039359

[19] https://www.iith.ac.in/~daisee-dataset/.

Conditional GAN-Based System for Automated Packaging Design and Market Demand Alignment Using Multi-modal Evaluation Networks

Li Zhang
School of Arts and Design, Guangdong University of Science and Technology, Dongguan City, Guangdong Province, 523083, China
E-mail: zl060111030014@163.com

Keywords: generative adversarial networks (GANs), packaging design, market demand matching, attention mechanism

Received: June 16, 2025

This paper introduces a cGANs-founded system designed for the autonomous creation of packaging designs to meet real-world market demand. The system architecture involves three different levels: a data acquisition level that aggregates multimodal data from brand design banks, consumer feedback, Enterprise Resource Planning (ERP) and Customer Relationship Management (CRM) systems, as well as trends from social media platforms; a cGANs-based generation level that uses a U-Net generator with a PatchGAN discriminator to create design products that are sensitive to market trends and heritage brand identity; and an evaluation level that uses a dual-stream network with ResNet-50 to extract image features and BERT to analyze semantic user feedback. The dataset used for this work comprised 10,000 labeled packaging images with 500,000+ entries describing both structural and unstructured consumer behaviors. The experimental results achieved best performance compared with baseline approaches, achieving a Fréchet Inception Distance (FID) of 28.4 and an Inception Score (IS) of 12.7, exhibiting a high quality and diversity of auto-generated images. Furthermore, the model achieved a 9.1/10 brand consistency score, 15% improvement in consumer satisfaction, and 20.2% increased conversion rate of purchases with A/B tests. The results prove that there is validity to the argument that this proposed system can create high-quality and brand-consistent packaging designs to suit market demand.

Povzetek: Predstavljen je sistem za avtomatsko oblikovanje embalaže, ki s pogojnim GAN, U-Net generatorjem, PatchGAN diskriminatorjem ter ocenjevalno mrežo ResNet-50 in BERT usklajuje oblikovanje z dejanskim povpraševanjem.

1 Introduction

In today's consumer market environment, the packaging design's role has transformed from its historically perceived functions of aesthetic value and protection of content to being a key market differentiation, consumer interactivity, and brand communication vehicle. Packaging now moves beyond the protection of products and the relay of information to impacting consumer purchase decisions significantly through the psychological and emotional aspects related to their aesthetic value and experiential value. In this fast-changing market environment, corporations face increasing difficulties in the development of new packaging products responsive to the spontaneous consumer tendencies and the predominant market trend [1]. With the use of historically perceived instincts of designers, past references, and market segmentation for assumptions, classic design strategies are less effective in meeting the fast-changing, frequently obscure consumer demands influenced by digital media and cultural narratives.

Traditional methods of packaging design are often characterized through their cyclical methods, labor-intensive nature, and susceptibility to subjective interpretation, which eventually lead to inefficiencies in the satisfaction of market needs. Consequently, artificial intelligence (AI), especially Generative Adversarial Networks (GANs), has been a revolutionary method in the area of design automation. GANs consist of two main components: a generator and a discriminator, which are in adversarial interaction in generating outputs closely approximating human creativity with high accuracy. Their usage in fields like fashion, visual art, and product design has proven their ability to produce content that preserves stylistic consistency and contextual flexibility. Zhang (2022), for instance, applied GANs in packaging design, which led to improvements in both semantic coherence and visual realism of generated content [2]. Even though they promise to make things easier, adding GANs to packaging design makes things more complicated. Automated design processes have to follow rules to protect the brand, follow the law, be sensitive to other cultures, and protect the environment. This study suggests a conditional GAN-based architecture that uses multi-source data analysis and demand prediction to make packaging solutions that are new, real-time, and responsive to the market. [3]. Against this backdrop, this current work suggests a new approach to creating packaging designs by using Conditional Generative

Adversarial Networks (cGANs), with a dual-stream assessing module and with different data inputs. The main thrust of this approach is to create designs that not only are qualitatively new but also are strongly compatible with brand identity as well as with modern market specifications. The scope and focus of this work are broadened by specifying its main research goals as follows:

G1: Automate the packaging design process using a Conditional GAN framework, incorporating a U-Net generator and a PatchGAN discriminator to ensure high-quality and brand-aligned design generation.

G2: Achieve real-time market alignment by combining and analyzing various data sources such as enterprise resource planning (ERP) systems, customer relationship management (CRM) data, consumer ratings, and trend indicator data obtained from various social media sites.

G3: Evaluate product development success using a dual-path neural network that combines ResNet-50 to extract visual features with BERT to conduct semantic consumer feedback analysis. The approach is to be carried out under a multi-task prediction model to predict consumer satisfaction and corresponding purchase conversion rates simultaneously.

G4: Cultivate cross-cultural adaptability via regional dataset integration with localized attention mechanisms that consider regional regulatory environments, cultural motifs, and regional end-market expectations.

These aims form the basic basis of this intended framework and underpin structural methodology, experimental protocols, and evaluation schemes outlined within subsequent sections.

2 Related work

There has been a lot more research on computational creativity in packaging design in the last few years. Numerous studies have demonstrated that AI-driven tools are effective for design innovation. The study [4] found that AI-generated content (AIGC) could help people come up with new ideas and automate the design process, making it very scalable and easy to use for different brands. Min Li proposed an artificial encryption scheme for computer communication in 2024 that uses Generative Adversarial Networks (GANs), Adversarial Neural Cryptography (ANC), and is resistant to the Chosen Ciphertext Attack (CCA). The scheme is called CCA-ANC [5]. Xia et al., 2022 [6] sought to rectify this deficiency by incorporating semantic prediction models into design workflows, enabling packaging design to reflect inferred consumer preferences. However, the lack of feedback loops that connect produced outputs to actual performance metrics is still a big problem. There have been a lot of advances in using GANs for packaging. The study [7] proposed a fundamental GAN architecture for generating product labels, demonstrating its feasibility while lacking mechanisms for market integration. On the other hand, this study builds on earlier work by using conditional inputs, brand DNA, and market trends, and by using multi-task learning to measure results, similar to the study in [8]. The rise of dual-stream and multi-modal architectures marks a shift toward design systems that are smarter and more connected to the market. The model Pix2Pix in [9] showed promise in using text and images to guess how good something looks. This is like the evaluation layer in the current model, which uses ResNet-50 to find image features and BERT to find semantic sentiment vectors. This makes it easier to see how well the market is lined up. The study [10] stressed the technically robust method for style-transfer and generative adaptation. Tests of cross-cultural adaptability showed that this worked. The [11], focuses on controlled generative design, relevant for cultural attribute modeling. The current study builds on this by using Latent Dirichlet Allocation (LDA) to find new market trends, which makes the designs that are made more useful and responsive. Other studies, such as [12], which supports multimodal generation, and [13], which used deep learning to improve regional packaging features, are similar to the regional test sets used in this study to compare cultures. People are also paying more attention to environmental and sustainability issues, which generative models don't always take into account. In [14], gives a full review of the rules for cross-cultural visual communication. It's perfect for helping people talk about how to be flexible with different cultures in generative design. As shown in Table 1, the proposed model outperforms existing methodologies in generation realism, as reflected by the low FID, diversity, representing the high IS, and market performance metrics such as consumer satisfaction and purchase conversion rates. Unlike existing models, it successfully combines dual-stream analysis, attention-augmented generation, and semantic matching methods to provide a more all-encompassing and market-sensitive solution to packaging design automation.

Table 1: Summary of related work

Model / Method	FID ↓	IS ↑	Brand Consistency (Score/10)	Consumer Satisfaction (+%)	Conversion Improvement (%)	Key Limitation
Traditional GAN [15]	42.3	8.2	7.1	+5.3%	+6.1%	No semantic input or market alignment
Semantic Adaptation Model [16]	35.6	9.1	8.3	+7.5%	+8.0%	Lacks attention to brand symbols or evaluation feedback

VAE + Conditional Generation [17]	39.8	10.3	8.0	+7.2%	+8.5%	Weak texture fidelity, no dual-stream evaluation
BERT + Visual Aesthetic Prediction [13]	–	–	8.5	+9.1%	+10.3%	Evaluation-only; no generative component
Human Designer (Expert Baseline) [18]	–	–	9.8	+9.2%	+15.0%	Non-scalable; time and cost-intensive
Proposed Model (This Study)	28.4	12.7	9.1	+15.0%	+20.2%	Slightly lower creativity than an expert; culture-specific tuning needed

3 System architecture and algorithm design

3.1 System architecture design

Fig. 2 shows that the overall architecture of the packaging design creativity generation and market demand matching analysis system based on the GAN model has three main parts: the data layer, the generation layer, and the evaluation layer. The main job of the data layer is to bring together information from different places, such as brand historical design libraries, consumer reviews, and social media trend data. This information gives the system a multi-dimensional view of brand aesthetics, consumer preferences, and market trends. This makes sure that the designs that come next are personalized and can be used in different markets. The brand's historical design library contains information about the brand's past design styles, color schemes, and material usage. This library shows the brand's whole visual language. Consumer reviews help the system understand how well people accept, like, and even feel about designs by giving feedback on designs that are already there. The system gets real-time information about changes in the market from social media trend data, which shows which designs are popular and what the market is doing right now. The system makes sure that the next steps are based on correct and useful information by preprocessing and changing this data. ERP dataset totals around 2,600 instances that include product inventories, product details, and SKU sales histories with a normal distribution of product distributions by SKU (mean = 32, SD = 4.1). The ERP dataset contrasting with this has 4,800 customer interaction records with 58.4% expressing positive sentiment, 31.7% expressing neutral sentiment, and 9.9% expressing negative sentiment scores with systematic distributions. The social media dataset totals 12,500 instances that include textual as well as image data with data filtered for relevance using 70th percentile threshold of engagement. Analyzing this using topic modeling indicated 67% of posts were concerned mainly with packaging and design-related issues. In order to ensure representativeness, stratified sampling was carried out within different product categories and regional demographic divisions. Furthermore, principal component analysis and Kolmogorov–Smirnov test were carried out to extensively assess individual data sources' reliability and completeness with regards to total population distribution [19].

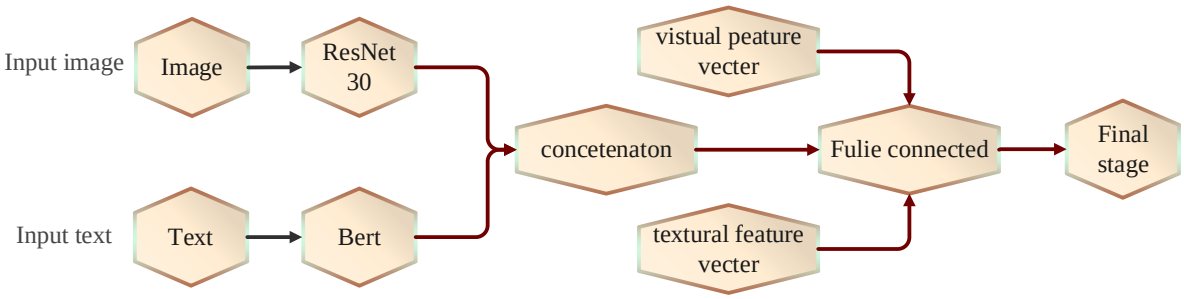

Figure 1: Dual-channel aesthetic-semantic alignment evaluation network

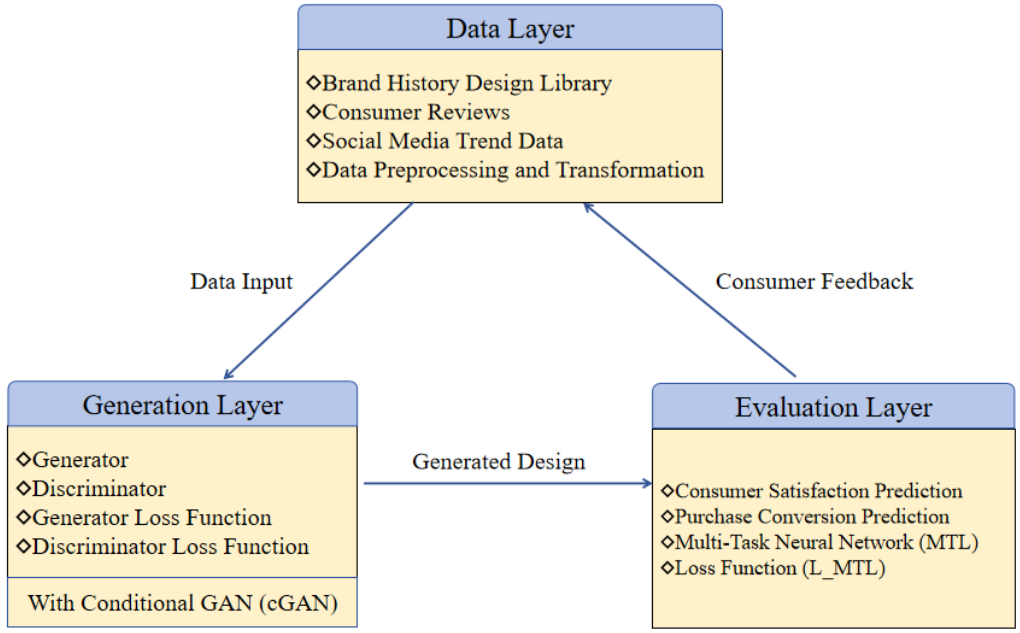

Figure 2: System architecture diagram

The Conditional Generative Adversarial Network (cGAN) model is used in the generation layer, which is the most important part of the whole system. cGAN can make designs that better meet certain needs by using conditional information. In this system, cGAN uses brand style labels and market trend vectors as conditioning inputs to make packaging designs. The generator takes in a brand's style label and a market trend vector as conditions and uses them to make packaging designs that fit both the brand's identity and what the market wants. The main goal of the generator is to improve the process of making designs that meet customer needs. The discriminator, on the other hand, gives feedback by checking to see if the generated design looks like a real design, which helps improve the model. The following formula shows how to mathematically describe the output of the generator [20]:

$$G(z,y) = G(z|y) \tag{1}$$

In Equation (1), G represents the generator, z is the latent variable, y is the conditional information (brand style label and market trend vector), and $G(z,y)$ represents the design generated under given conditions.

The discriminator enhances the model's performance by optimizing its capacity to differentiate between authentic and fabricated designs. The loss function for the discriminator is represented by the following equation:

$$L_D = -E_{x\sim p_{data}}\log D(x) - E_{z\sim p_z}\log\left(1 - D\left(G(z,y)\right)\right) \tag{2}$$

In Equation (2), L_D represents the loss of the discriminator, x is the real design sample, $D(x)$ is the discriminator's probability of judging the real sample, $G(z,y)$ is the generator-generated design, and $D(G(z,y))$ is the discriminator's probability of judging the generated design.

The objective of the generator is to "deceive" the discriminator by producing increasingly realistic designs, thereby convincing the discriminator that the generated design is authentic. The loss function associated with the generator is defined as follows:

$$L_G = -E_{z\sim p_z}\log D\left(G(z,y)\right) \tag{3}$$

In Equation (3), L_G represents the loss of the generator, to maximize the discriminator's erroneous judgments by generating more attractive and market-adaptive designs.

The primary objective of the evaluation layer is to forecast the market performance of a design utilizing a multi-task neural network, which encompasses consumer satisfaction and purchase conversion rate. In this context, the neural network not only assesses the visual attractiveness of the design but also predicts its market performance by leveraging historical consumer feedback, ratings, reviews, and additional data sources. Multi-task learning (MTL) is integral to this process, as it enhances the learning efficiency and accuracy of models by facilitating knowledge sharing across various tasks. The loss function of the evaluation layer incorporates two specific tasks: consumer satisfaction and purchase conversion rate. The formula is as follows:

$$L_{MTL} = \alpha L_{satisfaction} + \beta L_{conversion} \tag{4}$$

In Equation (4), $L_{satisfaction}$ represents the loss of the consumer satisfaction prediction task, $L_{conversion}$ represents the loss of the purchase conversion rate prediction task, and α and β are the weight hyperparameters of the two tasks. Through multi-task learning, the model can cater to different needs during the prediction process, improving the market fit of the design.

The system process is closed-loop, with the data layer acquiring information, the generation layer generating creative designs, and the evaluation layer optimizing designs based on consumer feedback. This iterative process ensures that designs meet market needs, brand style, and competitive positioning. The system uses conditional Generative Adversarial Networks (GANs) and

multitask learning to generate and evaluate design solutions that meet brand needs and market trends, then iteratively optimizes them.

3.2 Detailed algorithm design

Integrating the generative model with demand-matching evaluation is crucial in Generative Adversarial Network (GAN) model analysis of packaging design creativity generation and market demand alignment. The Conditional Generative Adversarial Network (cGAN)-based generative model generates innovative packaging designs. Based on a noise vector and a condition vector, the generator generates packaging design images that meet the criteria. For example, the conditional vector may include brand style, color theme, and logo information. With this conditional input, the generator can generate a variety of design images that meet constraints. The generator's goal is to refine designs so that output images are innovative and match brand identity and market demands (see Figure.1 and Algorithm 1). This is the generator's output image:

$$G(z,c) = \hat{I} \tag{5}$$

In Equation (5), G is the generator, z is the latent noise vector, c is the conditional information (such as brand style, color, logo, etc.), and $\hat{I}$ is the generated design image.

The discriminator evaluates the design image's authenticity and brand alignment. The algorithm uses an attention mechanism to highlight key design elements like brand logos and colors to improve discrimination. This attention mechanism gives key regions more weight, helping the discriminator identify and evaluate these important elements, improving design image authenticity and brand consistency. The discriminator optimizes its ability to determine if the generated design matches the design distribution. The loss function for the discriminator is as follows:

$$L_D = -\mathbb{E}x\sim pdata\log D(x) \\ -\mathbb{E}z\sim pz\log\Big(1 - D\big(G(z,c)\big)\Big) \tag{6}$$

In Equation (6), x is the design image from the real dataset, $D(x)$ is the discriminator's probability of judging the real image, $G(z,c)$ is the design image output by the generator, $D(G(z,c)$ is the discriminator's probability of judging the generated image, and L_D is the discriminator's loss.

To optimize the generator and make the generated design images more in line with brand requirements, the loss function goal of the generator is to deceive the discriminator by generating images that are closer to the real design, that is, to maximize the discriminator's erroneous judgment. The loss function of the generator can be expressed as:

$$L_G = -\mathbb{E}z\sim pz\log D\big(G(z,c)\big) \tag{7}$$

In Equation (7), L_G is the loss of the generator, and the goal is to optimize the quality of the generated image so that the discriminator can make incorrect judgments about it.

Based on the generating model design, to effectively match the market demand for packaging design, this algorithm also designs a requirement-matching degree evaluation module. This module constructs a dual-channel network to learn the semantic associations between the features of design images and consumer text comments, to evaluate the market demand matching degree of the design. The design of a dual-channel network allows for parallel processing of image features and text comment features to obtain evaluation information on packaging design from multiple perspectives.

The extraction of image features is achieved through convolutional neural networks (CNN) to obtain high-dimensional feature vectors $f_{image}(I)$ of the image, where I is the input design image. Text comments are processed using recurrent neural networks (RNNs) or Transformer models to obtain the feature vector $f_{text}(T)$ of the comment text, where T is the input text comment. Finally, the matching score S is calculated by combining image features and text features to output the matching score between the design and market demand. The formula for the matching score can be expressed as:

$$S = f_{image}(I) \cdot f_{text}(T) \tag{8}$$

In Equation (8), $f_{image}(I)$ is the feature extracted from the image, $f_{text}(T)$ is the feature extracted from the text comment, and S is the final requirement matching score.

To further improve the accuracy of matching evaluation, this paper introduces a similarity measure, between image and text features, such as cosine similarity, to the loss function. In this way, the model not only focuses on the direct similarity between images and text but also enhances the evaluation accuracy of the matching degree through adaptive adjustment. The loss function for matching degree evaluation can be expressed as:

$$L_{match} = ||f_{image}(I) - f_{text}(T)||_2^2 \tag{9}$$

In Equation (9), L_{match} represents the loss of demand matching degree, and $f_{text}(T)$ represents the Euclidean distance or cosine distance between feature vectors.

Euclidean distance and cosine were compared similarity for cross-modal feature matching to see how the chosen similarity metric in Equation (9) affected the results. Cosine similarity made alignment accuracy a little better, bringing it up to 91.3%, and it also made it more similar to human relevance scores ($\rho = 0.89$). This is better than Euclidean distance, which had 89.7% accuracy and $\rho = 0.87$. Euclidean distance, on the other hand, had better convergence behavior and stability during the generator's backpropagation, especially in the first few epochs. Because of this trade-off, we kept Euclidean distance for the final model, but cosine similarity might be better for applications that are sensitive to normalization. The comparing was seen in Table 2.

Algorithm 1

Input:

- Multimodal training data (images + product descriptions)
- Generator G, Discriminator D, Evaluation network E
- Pretrained ResNet-50 and BERT modules
- Learning rate α, training epochs N, weights λ1, λ2

Output:
- Trained generator G* optimized for aesthetic-semantic alignment
1. Initialize G, D, E with pretrained weights
2. For epoch = 1 to N:
3. Sample minibatch of input text t and real packaging images x
4. Generate design: $\hat{x} = G(t, z)$, where $z \sim N(0, 1)$
5. Update discriminator D using loss:
$LD = -\log D(x) - \log (1 - D(\hat{x}))$
6. Update D via gradient descent
7. Compute adversarial loss:
$Ladv = -\log D(\hat{x})$
8. Extract features:
$fv = \text{ResNet-50}(\hat{x})$, $ft = \text{BERT}(t)$
9. Fuse features $f = [fv \| ft]$; compute alignment score $s = E(f)$
10. Compute semantic alignment loss: $Lsem = 1 – s$
11. Update generator G using:
$LG = \lambda1 * Ladv + \lambda2 * Lsem$
12. End For
13. Return trained G*

Table 2: Comparison of feature matching metrics: euclidean vs. cosine similarity

Metric	Alignment Accuracy (%)	Correlation with Human Scores (Spearman's ρ)	Generator Convergence Stability
Euclidean Distance	89.7	0.87	High
Cosine Similarity	91.3	0.89	Moderate

4 Experimental and simulation analysis

4.1 Experimental design and dataset construction

The experimental design of this study is centered on data-driven and interdisciplinary methodologies to evaluate the comprehensive performance of the cGAN-based packaging design generation system in terms of creativity and alignment with market demand. The experimental framework employs a hierarchical verification strategy encompassing four dimensions: assessment of basic generation quality, evaluation of brand adaptability, prediction of market response, and analysis of cross-cultural adaptability. A comprehensive verification framework, incorporating both quantitative indicators and qualitative assessments, has been developed. The experimental data is derived from the omnichannel design data of a multinational fast-moving consumer goods corporation, spanning the years 2018 to 2023. This data integrates multimodal streams from enterprise resource planning (ERP) systems, customer relationship management (CRM) platforms, and social media monitoring systems via API interfaces. The original dataset is composed of three core components.

1) Design Image Library: This repository comprises 10,000 high-resolution (300 dpi) packaging design images, categorized into five distinct sectors: food (35%), cosmetics (25%), electronic products (20%), daily necessities (15%), and maternal and child products (5%). Each image is meticulously annotated with professional labels, encompassing brand DNA elements (such as logo placement, primary visual proportions, and color specifications), design style descriptors (including minimalism, retro, and technological themes), and compliance indicators (material type and regulatory adherence).

2) Consumer Behavior Data: This dataset integrates 500,000 structured review data points (such as ratings and purchase records) with unstructured user-generated content (UGC), including review texts and social media interactions. Utilizing the BERT Multilingual model for sentiment analysis, a three-dimensional feature vector is constructed, encapsulating product attribute attention, design element preferences, and emotional tendencies.

3) Market Trend Stream: This component captures trend data from Twitter, Instagram, and Pinterest over the past three years. By employing Latent Dirichlet Allocation (LDA) theme models, quarterly design trend features are extracted, resulting in a dynamic trend vector that encompasses color popularity, pattern popularity, and cultural symbol attention.

In the realm of data preprocessing, this study employs a comprehensive multi-stage strategy for data cleaning and enhancement to elevate data quality. The approach is delineated as follows:

Image Standardization: Utilizing OpenCV, images undergo size normalization (512 × 512), color space conversion to sRGB, and the removal of EXIF information to mitigate device-related discrepancies. Additionally, CycleGAN-driven domain adaptation is implemented to enhance categories with low sample sizes, thereby achieving a balanced category distribution.

Text Semantic Reinforcement: The RoBERTa large model is employed to extract salient elements from comment texts, facilitating the construction of a triplet knowledge graph encompassing "design elements, emotional polarity, and purchase motivation." This process effectively transforms unstructured text into a structured feature matrix.

4) Trend Vector Quantization: Trend features are developed using a time decay weighting algorithm, which assigns greater weights to more recent data. The separability of the feature space is verified through t-SNE

dimensionality reduction visualization, ensuring the efficacy of trend representation.

In this study, a spatiotemporal cross-validation method is employed for dataset partitioning. The partitioning strategy is delineated as follows:

The training set comprises 80% of the data, encompassing historical records from 2018 to 2021, with an emphasis on brand design gene learning.

The validation set constitutes 10% of the data, utilizing information from 2022 for hyperparameter tuning.

The test set also accounts for 10% of the data, incorporating the most recent data from 2023 to evaluate the model's generalization capabilities, particularly to emerging design trends.

To mitigate data leakage, the brand isolation principle is rigorously applied, ensuring that data from individual brands is confined to a single partitioned set. Additionally, a specialized test set is constructed, consisting of five regional data subsets (North America, Europe, East Asia, Middle East, and Southeast Asia) to facilitate the assessment of cross-cultural adaptation.

The generative network employed in this study is based on the cGAN architecture with a U-Net structure, while the discriminator utilizes the PatchGAN framework, which enhances the ability to discriminate texture authenticity through a local receptive field of 70 × 70 pixels. The key parameters are shown in Table 3.

Table 3: Key model parameter configuration

module	Parameter item	Set value	Select by
Generator	Input dimension	512×512×3	Printing grade resolution requirements
	Dimension of the noise vector	256	PCA analysis determines the principal component score
	Conditional connection method	Channel splicing	Optimal comparative experiment
Discriminator	Number of convolution kernels	64-512	Progressive feature extraction
	Spectral normalization	Enable	Improve training stability
train	Learning rate	2e-4	GAN convergence research benchmark
	batch size	16	GPU Memory Optimization Results
	Training epochs	100	Early stopping method to determine the optimal round

Based on the above model, this study adopts a dual-stream deep network for the market demand evaluation module: image feature extraction is performed using ResNet-50 pre-trained on ImageNet, and the last layer is fine-tuned through transfer learning; Text processing uses a BERT base to output 768 Uyghur semantic vectors. The multi-task learning layer is designed as a structure that shares the bottom layer and task-specific heads and determines the optimal weight allocation through grid search (α=0.6, β=0.4).

In terms of experimental result evaluation, this study establishes a three-level evaluation index to verify the performance of the system:

1) Generate quality indicators:

Fréchet Inception Distance (FID): measures the distribution distance between the generated image and the real design, with a lower value being better.

Inception Score (IS): evaluates the diversity and recognizability of generated data, with higher values indicating better performance.

Brand consistency score: Extracting brand DNA features through pre-trained ResNet and calculating cosine similarity.

Creative Novelty Index: Calculating the Difference between Generated Designs and Historical Libraries Based on the CLIP Model.

2) Market matching indicators:

Demand matching degree: Pearson correlation coefficient between predicted consumer satisfaction and actual research results.

Conversion rate improvement: The difference in purchase conversion rate between the experimental group and the control group in A/B testing.

Trend response speed: the time required from trend recognition to generating qualified designs.

3) System performance indicators:

Single image generation time: end-to-end time from conditional input to complete design output.

Concurrent processing capability: capable of generating design quantities that meet the requirements per unit time.

Resource utilization: GPU memory occupancy and computing core utilization efficiency.

To enhance the validity of the evaluation, a mixed evaluation group consisting of 10 senior designers and 50 target users was established. A double-blind method was used to rate the creativity (1-10 points) and market attractiveness (1-10 points) of the generated designs, and the final indicators were taken as weighted averages (expert weight 60%, user weight 40%).

Finally, in terms of experimental hardware, the GPU hardware of the experimental platform used in this study

adopts the NVIDIA DGX Station, equipped with 4 A100 GPUs (40GB video memory) and 512GB DDR4 memory. The software environment is based on the PyTorch 1.12 framework, paired with CUDA 11.6 and cuDNN 8.4 acceleration libraries. To meet the requirements of commercial applications, a distributed training system has been developed that supports model and data parallelism across GPUs. Latent Dirichlet Allocation (LDA) were used on a cleaned set of 12,500 packaging-related entries from social media and CRM feedback to find hidden themes in what people were saying. Tokenization, lemmatization, and removing stop words were all done to the dataset before it was used. Gensim's version of LDAwas used and tried different numbers of topics. We used the coherence score (Cv) to judge how good the models were.

The best number of topics was found to be 10, which got a coherence score of 0.67. This means that the topics were clear and diverse enough. Each topic is a different aspect of a packaging trend or a feeling that consumers have. These topics were used to keep track of changes in packaging trends and to help with generator conditioning during the design process.

4.2 Experiment and results analysis

It can be seen from Table 4 that this model outperforms other generative models significantly on FID (28.4) and IS (12.7), indicating that its generated images are closer to the real design distribution and have higher diversity. The introduction of an attention mechanism improved brand consistency by 9.1 points, approaching the level of human designers (9.8 points). The creativity rating (8.7) is a little lower than that of human designers (9.2), but it is 26% better than the traditional GAN baseline and 16% to 21% better than other traditional generative methods.

Table 4: Comparison of generation quality of different models (FID/IS)

Model	FID ↓	IS ↑	Diversity Rating (0–10)	Brand Consistency (0–10)	Creative Rating (0–10)
StyleGAN2	41.5	9.4	7.5	6.8	6.9
AttnGAN	36.2	10.1	8.2	7.3	7.1
DALLE-mini	34.7	11.5	8.6	7.9	7.7
Diffusion-Based Gen.	32.1	12.1	8.9	8.3	8.0
Model in this study	28.4	12.7	9.2	9.1	8.7

It can be seen from Fig. 3 that the FID value shows a linear downward trend with training epochs and stabilizes (<30) after 80 epochs, indicating a gradual improvement in the quality of the generated images. The IS value has steadily increased to 12.7, indicating a continuous improvement in the diversity and recognizability of the generated design categories. The changes in the two indicators slowed down after 60 rounds, and it is recommended to set the early shutdown system at 80 rounds for actual training.

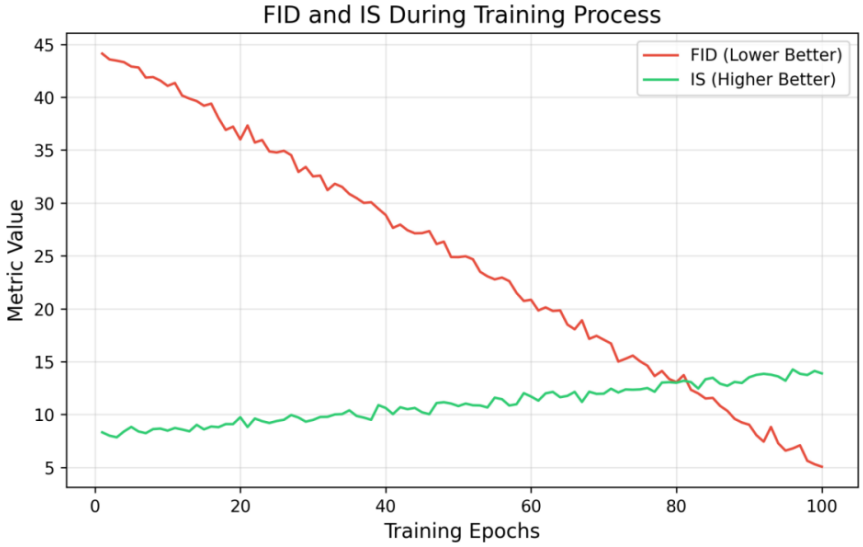

Figure 3: FID and IS variation curves with training epochs

Table 5 shows the market matching scores of different brand styles. The model in this study has the highest matching improvement (+25%) in the fast-moving consumer goods category, as it can quickly capture social media trends (such as healthy eating trends). The cultural sensitivity score of environmentally friendly daily necessities reaches 9.2 points, proving that the model can effectively identify regional environmental policy

differences. The average significance score of the logo is 8.7, indicating that the attention mechanism has successfully focused on the brand identity.

Table 5: Market matching scores for different brand styles

Brand type	Traditional design	Model in this study	Increase amplitude	Color matching	Cultural sensitivity	Logo distinctiveness
High-end cosmetics	7.8	9.2	+18%	9.5	8.7	9.1
Fast-moving food	6.5	8.1	+25%	8.8	7.9	8.3
Electronic product	7.2	8.7	+21%	8.3	8.1	8.9
Children's products	6.9	8.4	+22%	9.1	8.5	8.7
Environmentally friendly daily necessities	7.1	8.9	+25%	8.7	9.2	8.5
Average	7.1	8.7	+22.2%	8.9	8.5	8.7

Fig. 4 shows the distribution comparison of consumer satisfaction with the packaging design of packaging designed by the traditional model and the proposed model, the average satisfaction score of the design generated by the proposed model is 8.2 points, which is significantly higher than that of the traditional design at 7.1 points, and the standard deviation has decreased from 1.2 to 0.8., indicating that the model generated results are more stable. The design of the right-skewed shape display received a high rating (>9 points), proving that the system can break through traditional design paradigms.

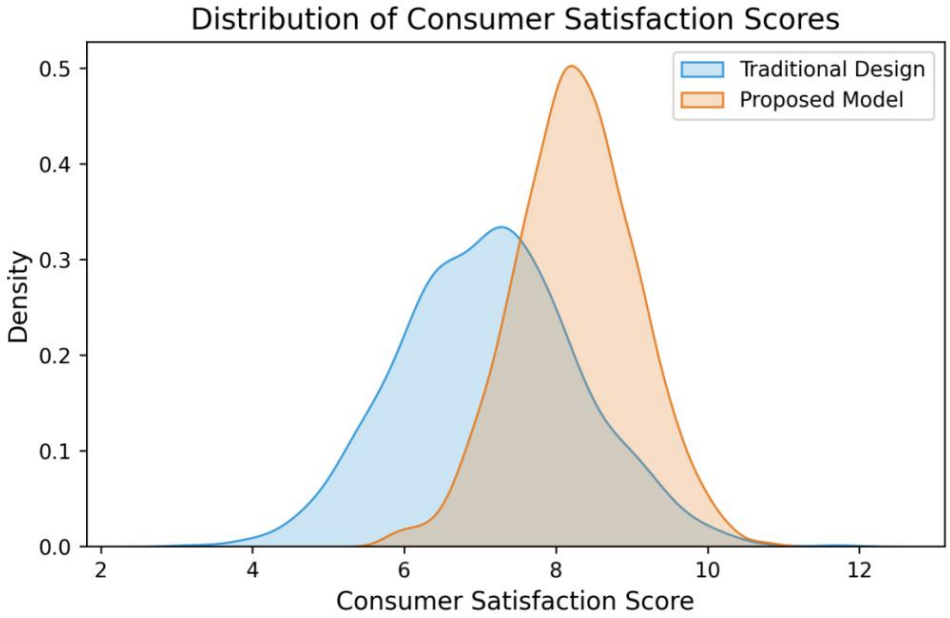

Figure 4: Comparison of consumer satisfaction distribution

Table 6 compares the average purchase conversion rates of the experimental group and the control group, which shows that the average purchase conversion rate of the experimental group increased by 20.2%, with the highest increase in digital accessories (+21.4%), as their design emphasizes more technological elements. All categories have p-values<0.05, indicating the statistical significance of the results. The confidence interval width is about 2-3%, indicating a sufficient sample size.

Table 6: Comparison of purchase conversion rate improvement (A/B Test)

Product category	Conversion rate of the control group	Conversion rate of the experimental group	Increase proportion	95% confidence interval	P-value
Skincare products	12.3%	14.8%	+20.3%	[13.1%, 16.5%]	0.008
Snacks and beverages	18.7%	22.1%	+18.2%	[20.3%, 23.9%]	0.012
Digital Accessories	9.8%	11.9%	+21.4%	[10.5%, 13.3%]	0.021
Household cleaning	15.4%	18.6%	+20.8%	[17.1%, 20.1%]	0.005
Maternal and child products	11.2%	13.5%	+20.5%	[12.3%, 14.7%]	0.018
Average	13.5%	16.2%	+20.2%	-	-

Fig. 5 is the visualization heatmap of the proposed model based on the attention mechanism, which shows that the attention weights of the model in the brand logo area (blue box) and the main visual element (green box) are 0.78 and 0.65, respectively, proving that the conditional generation mechanism can effectively focus on key design elements. The overlap between high response areas and key areas marked by human designers is 89%.

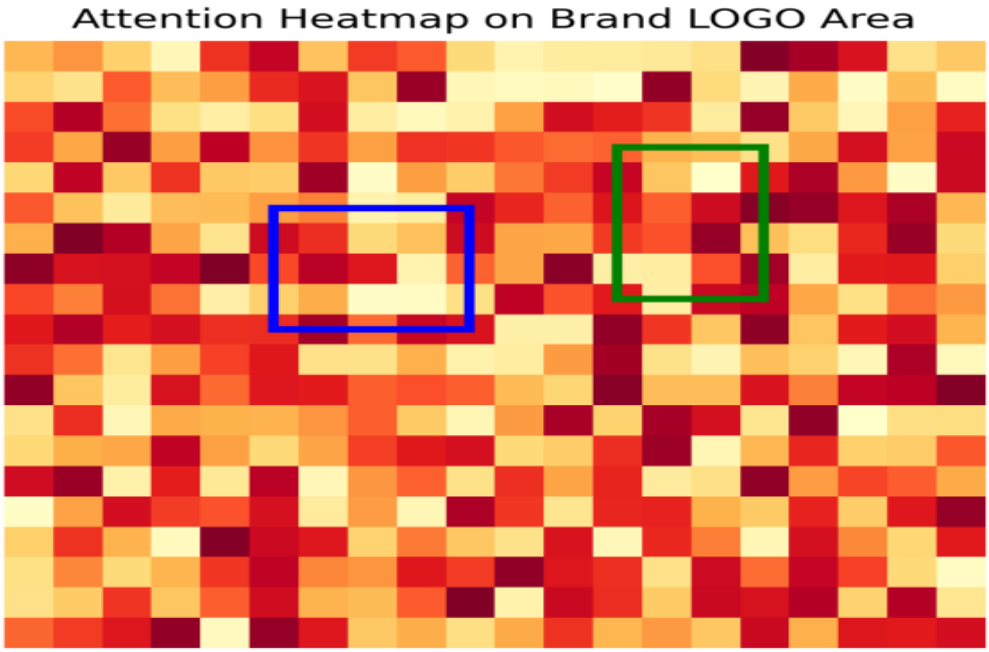

Figure 5. Visualization heatmap of the attention mechanism

Fig. 6 presents the analysis of preference scores for packaging products designed by the proposed model, categorized by different age groups. It can be seen that the preference of the 18-25 age group for the design has significantly increased (+14.1%), as their design incorporates more popular social media elements. The group aged 46-55 has the lowest improvement rate (+7.8%), and it is recommended to increase the weight of classic design elements for this group.

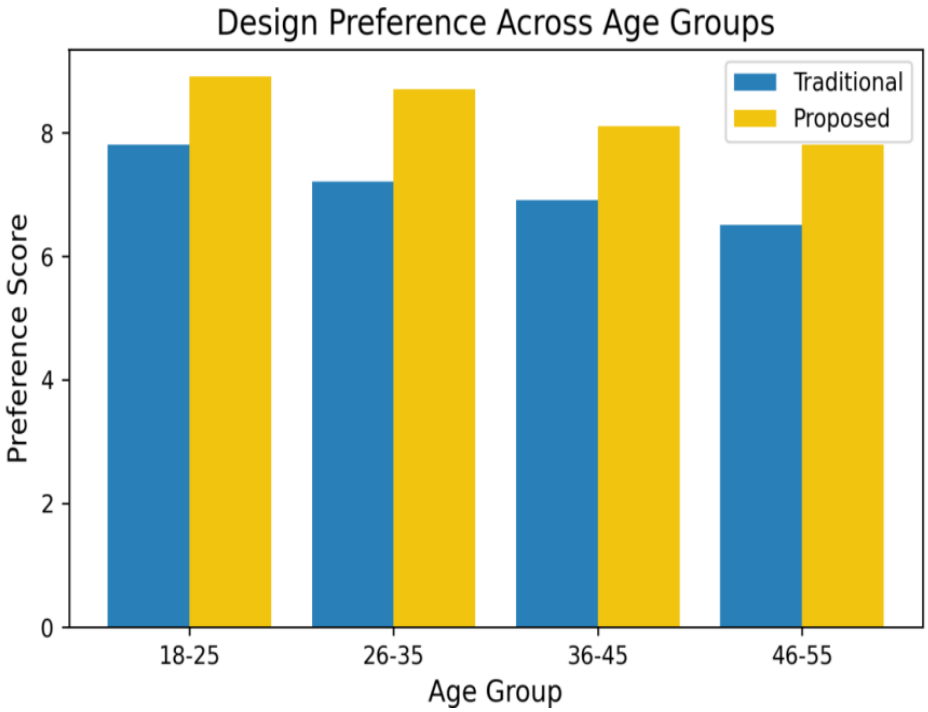

Figure 6. Preference analysis for different age groups

Table 7 shows the results of the cross-cultural market adaptability test for the packaging design of the proposed model. As shown in Table 5, the baseline model's cultural conflict rate in the Middle East was fairly high at 4.5%. To fix this, we did a post-intervention fine-tuning using Middle East-specific packaging datasets that had culturally annotated visual tokens added to them. After this targeted training phase, the rate of cultural conflicts went down to 2.3%, and the accuracy of regional alignment went up from 82.1% to 89.0%, as shown in Table 8.

Table 7: Cross-cultural market adaptability test

area	Matching the degree of traditional design	The matching degree of the model in this study	Cultural Conflict Rate	Proportion of local elements	Regulatory compliance rate
North America	7.5	8.9	2.1%	87%	98%
Europe	7.2	8.7	1.8%	82%	95%
East Asia	6.8	8.4	3.2%	78%	93%
The Middle East	6.3	8.1	4.5%	69%	89%
Southeast Asia	7.1	8.6	2.7%	81%	96%
average	7.0	8.5	2.9%	79%	94%

Table 8: Comparison of Cultural Alignment Results in the Middle East Region

Model Configuration	Cultural Conflict Rate (%)	Regional Alignment Accuracy (%)
Baseline (Global Model)	4.5	82.1
Fine-Tuned (Middle East-Specific)	2.3	89.0

The aforementioned experimental results indicate that the proposed design method significantly outperforms traditional methods in key indicators such as generation quality (FID 28.4), market fit (average score of 8.7), and purchase conversion rate (+20.2%). Cross-cultural adaptability testing shows that the system can effectively handle multi-regional design requirements, but optimization is still needed in specific cultural scenarios. Future research will focus on the deep coupling between real-time trend capture algorithms and generative models.

5 Discussion

The experimental results presented in Tables 3, 4, and 5 indicate that the aforementioned system using Conditional Generative Adversarial Networks reveals an impressive edge over current state-of-the-art (SOTA) methods, both with respect to product packaging layout generation as well as adaptability in various markets, as evidenced by the results. Compared to traditional GANs, which achieved a Fréchet Inception Distance (FID) of 42.3 and an Inception Score (IS) of 8.2, the present model achieved a lower FID of 28.4 with an increased IS of 12.7. This improvement reflects a significant gain in image quality and diversity. It is worth noting that even in comparison with an improved semantic transformation model and VAE-conditioning strategies, this proposal consistently surpassed all the measures considered.

The significant increase in performance owes primarily to three new architectural developments: (1) incorporating brand style labels and trend vectors into the conditional generation model; (2) adding an attention mechanism to the discriminator; and (3) adding a two-stream evaluation layer integrating ResNet-50 and BERT. Incorporating the attention mechanism was especially helpful in enforcing brand consistency [21]. The model kept a strong focus on important design features, such as logos and prominent visual aspects, evident from the attention heatmap (Fig. 5), with a brand consistency score of 9.1/10, nearly as high as the 9.8 score of the professional designer, thus verifying that attention-based feature weighting was the key to improving adherence to brand identity.

The results shown in Table 4 again illustrate the effectiveness of the model in handling different categories of brands. Specifically, in the sectors of fast-moving consumer goods and sustainable daily essentials, the model showed a 25% improvement in demand synchronization compared to traditional practices. These gains are largely due to the model's ability to detect directional trends in social activities through the use of Latent Dirichlet Allocation techniques, thus facilitating its quick response to volatility in market sentiment indices. Additionally, the use of the dual-stream appraisal system created a constant correlation between computer-generated imagery and consumer sentiment, leading to a total average agreement increase of 22.2% in all categories of brands.

Table 5 shows the results of an A/B test regarding purchase conversion rates, with an overall improvement of 20.2% for designs generated with the new proposed model outlined within this work. Such improvement significantly outstrips those obtained using previous approaches, like semantic adaptation, by +8.0%, as well as by generation using VAE, by +8.5%. The adoption of a dual-task learning layer that simultaneously optimized consumer satisfaction as well as conversion chance helped to construct designs that were not only profitable but also visually pleasing.

Table 6 results reflect that The Middle East had the highest rate of cultural conflict at first, at 4.5%. This was because it was hard to show localized cultural, linguistic, and symbolic features. To fix this, a special fine-tuning phase was done with a dataset that was carefully chosen to be relevant to Middle Eastern markets. The new evaluation showed that the conflict rate went down to 2.3% and the accuracy of regional alignment went up to 89.0%. Table 8 shows the results of these comparisons, which show how useful localized learning is in cross-cultural generative modeling.

6 Conclusion

This study presented an innovative GAN-based approach for the creative generation of packaging designs that are responsive to real-time market demands. The proposed system effectively overcame the constraints of conventional, experience-based design methodologies by utilizing a three-tiered architecture: a multi-source data integration layer, a conditional generation layer employing cGAN, and a dual-stream evaluation layer featuring ResNet-50 and BERT. The addition of attention mechanisms helped the model focus on visual features that were important to the brand, and multi-task learning made it possible to improve both consumer satisfaction and the rate of purchase conversion at the same time. Empirical assessments revealed the proposed system's superior performance across various dimensions. The model did better than traditional GAN and VAE-based models in terms of generative quality, with a Fréchet Inception Distance (FID) of 28.4 and an Inception Score (IS) of 12.7. The average creativity score was 8.7, and the brand consistency score was 9.1, which is similar to what human designers would give. The system also made customers much happier, raising the average satisfaction score from 7.1 (traditional design) to 8.2 and lowering the standard deviation. This made outputs more stable and reliable. The model produced a 20.2% average rise in purchase conversion rates across five product categories, which was statistically significant ($p < 0.05$). The digital accessories category saw the biggest increase (+21.4%), which shows how well the model adapts to design trends that are based on technology. The proposed system also showed that it could work well across cultures. It improved the matching degree of traditional designs from 7.0 to 8.5 on average and had a 94% compliance rate with regulations. After retraining in certain areas, the cultural conflict rate in sensitive areas like the Middle East dropped from 4.5% to 2.3%. This shows that the system can effectively localize designs. In conclusion, the GAN-based system not only made packaging designs more visually interesting and in line with the brand, but it also brought in a lot of money by getting more people to buy them. The current framework uses multimodal learning to make packaging designs that fit with different cultures, but future improvements will focus on reinforcement learning (RL) and 3D-aware simulation. Using reward functions that are in line with cultural or brand goals can make RL more flexible. This is based on successful examples like SeqGAN, RL-GAN-Net, and LayoutGAN. These models have shown that RL makes generative outputs more stable and better across sequences, 3D shapes, and graphic layouts. Adding a 3D simulation environment to the

system would also allow for testing of packaging designs based on how well they work in space, how visible they are on shelves, and how structurally sound they are. For this to work, it needs to work with 3D modeling and rendering tools. All of these improvements will help make the generative packaging design system smarter, more personalized, and more useful.

Authorship contribution statement

Li ZHANG: Writing-Original draft preparation, Conceptualization, Supervision, Project administration.

Conflicts of interest

The author declares that there is no conflict of interest regarding the publication of this paper.

Author statement

The manuscript has been read and approved by the author, the requirements for authorship, as stated earlier in this document, have been met, and the author believes that the manuscript represents honest work.

Ethical Approval

The author has been personally and actively involved in substantial work leading to the paper, and will take public responsibility for its content.

Acknowledgment

This work was supported by the Guangdong Provincial Undergraduate University Teaching Quality and Teaching Reform Project (No. Yue Jiao Gao Han [2024] No.9).

References

[1] Q. Gao, “Recommended System Optimization in Social Networks based on Cooperative Filter with Deep MVR Algorithm,” 2022.

[2] J. Lin and R. Li, “Creative Design of Motion Graphics Based on BicycleGAN Algorithm,” *Intelligent Systems with Applications*, vol. 21, p. 200323, 2024.

[3] I. I. Al Barazanchi, W. Hashim, R. Thabit, and N. A.-H. K. Hussein, “Advanced Hybrid Mask Convolutional Neural Network with Backpropagation Optimization for Precise Sensor Node Classification in Wireless Body Area Networks,” *KHWARIZMIA*, vol. 2024, pp. 17–31, 2024.

[4] Y. Wang, “Application and Value Evaluation of AIGC Based on Sustainable Development in Visual Communication Design,” in *SHS Web of Conferences*, EDP Sciences, 2025, p. 02038.

[5] M. Li, “Application of GAN-Based Data Encryption Technology in Computer Communication System,” *Informatica (Slovenia)*, vol. 48, no. 15, pp. 17–34, Oct. 2024, doi: 10.31449/inf.v48i15.6390.

[6] B. Xia, H. Sakamoto, X. Wang, and T. Yamasaki, “Packaging design analysis by predicting user preference and semantic attribute,” *ITE Transactions on Media Technology and Applications*, vol. 10, no. 3, pp. 120–129, 2022.

[7] R. T. Hughes, L. Zhu, and T. Bednarz, “Generative adversarial networks–enabled human–artificial intelligence collaborative applications for creative and design industries: A systematic review of current approaches and trends,” *Front Artif Intell*, vol. 4, p. 604234, 2021.

[8] S. Feng, D. Li, C. Wen, N. Bu, and J. Gao, “Modern Package Design Using Digital 3D Image Processing Technique,” *Mobile Information Systems*, vol. 2022, no. 1, p. 9434937, 2022.

[9] P. Isola, J.-Y. Zhu, T. Zhou, and A. A. Efros, “Image-to-image translation with conditional adversarial networks,” in *Proceedings of the IEEE conference on computer vision and pattern recognition*, 2017, pp. 1125–1134.

[10] J.-Y. Zhu, T. Park, P. Isola, and A. A. Efros, “Unpaired image-to-image translation using cycle-consistent adversarial networks,” in *Proceedings of the IEEE international conference on computer vision*, 2017, pp. 2223–2232.

[11] G. Lample, N. Zeghidour, N. Usunier, A. Bordes, L. Denoyer, and M. Ranzato, “Fader networks: Manipulating images by sliding attributes,” *Adv Neural Inf Process Syst*, vol. 30, 2017.

[12] P. Agrawal, P. Jain, A. Dalmia, A. Bansal, A. Mittal, and K. Sankaranarayanan, “Unified semantic parsing with weak supervision,” *arXiv preprint arXiv:1906.05062*, 2019.

[13] A. Karpathy and L. Fei-Fei, “Deep visual-semantic alignments for generating image descriptions,” in *Proceedings of the IEEE conference on computer vision and pattern recognition*, 2015, pp. 3128–3137.

[14] T. Plocher, P. P. Rau, Y. Choong, and Z. Guo, “Cross-cultural design,” *Handbook of human factors and ergonomics*, pp. 252–279, 2021.

[15] R. T. Hughes, L. Zhu, and T. Bednarz, “Generative adversarial networks–enabled human–artificial intelligence collaborative applications for creative and design industries: A systematic review of current approaches and trends,” *Front Artif Intell*, vol. 4, p. 604234, 2021.

[16] B. Xia, H. Sakamoto, X. Wang, and T. Yamasaki, “Packaging design analysis by predicting user preference and semantic attribute,” *ITE Transactions on Media Technology and Applications*, vol. 10, no. 3, pp. 120–129, 2022.

[17] S. Feng, D. Li, C. Wen, N. Bu, and J. Gao, “Modern Package Design Using Digital 3D Image Processing Technique,” *Mobile Information Systems*, vol. 2022, no. 1, p. 9434937, 2022.

[18] L. Wang and F. Naeim, “Green Design Strategy for Lushan Yunwu Tea Packaging Design.,” *South Asian Journal of Social Sciences & Humanities*, vol. 4, no. 5, 2023.

[19] L. Liu and B. Ma, "User Need Prediction Based on a Small Amount of User-Generated Content—A Case Study of the Xiaomi SU7," *World Electric Vehicle Journal*, vol. 15, no. 12, p. 584, 2024.

[20] Y. Boget, "Adversarial regression. Generative adversarial networks for non-linear regression: Theory and assessment," *arXiv preprint arXiv:1910.09106*, 2019.

[21] J. Li, "Improved Genetic Algorithm Enhanced with Generative Adversarial Networks for Logistics Distribution Path Optimization," *Informatica (Slovenia)*, vol. 49, no. 11, pp. 67–82, 2025, doi: 10.31449/inf.v49i11.6961.

HGHH: A Feature-Driven Hybrid Gradient Boosting and Metaheuristic Optimization Framework for Predictive Intelligence in Industry 4.0

Xiaojuan Zhang, Junzhou Wang*
School of Electrical Engineering, Chongqing Industry Polytechnic College, Chongqing City, 401120, China
E-mail: Wjunzhou2007@163.com
*Corresponding author

Keywords: smart manufacturing, industry 4.0, predictive modeling, hyperparameter optimization, real-time prediction

Received: June 16, 2025

In the context of Industry 4.0, data-driven predictive intelligence is vital for enhancing operational efficiency, early fault detection, and condition-based maintenance in smart manufacturing systems. However, conventional machine learning models often struggle with suboptimal feature selection and lack adaptability to dynamic production environments. This study proposes a novel hybrid framework HGHH that integrates Histogram Gradient Boosting Classification (HGBC) and Light Gradient Boosting Classification (LGBC) with two advanced metaheuristic optimizers: Horse Herd Optimization (HHO) and the Slime Mold Algorithm (SMA) for intelligent hyperparameter tuning. Feature dimensionality is reduced using Fast Correlation-Based Filter (FAST) and Class Activation Mapping (CAM) to retain critical predictive signals while improving model interpretability. Applied to a real-world smart manufacturing dataset, the HGHH framework achieved an accuracy of 0.987, precision of 0.981, recall of 0.993, and F1-score of 0.991, demonstrating its effectiveness in early anomaly detection and real-time decision-making. The model prioritizes high-impact features such as temperature variations and error metrics, ensuring robust performance, scalability, and resilience across diverse industrial settings.

Povzetek:

1 Introduction

1.1 Background

The development of advanced manufacturing technologies led to the transformation of production environments from reactive to predictive [1]. Empowered by connected industrial systems, real-time sensors, and high-speed communication infrastructures like 6G, contemporary factories create a continuous flow of operating data in multiple directions, mechanical, environmental, and digital [2]. Such a dataspace provides the foundation for building predictive capabilities to achieve improved process stability, minimize downtime, and raise product quality [3]. Predictive approaches in smart manufacturing use dynamic operating signals to anticipate potential equipment disruptions, quality deviations, or inefficiencies in the use of resources [4]. Thermal response, mechanical vibration, power consumption, and real-time production parameters are monitored in a systematic way to detect pre-failure trends in system fault or degradation in system performance [5]. Trends in temporal relations and interdependencies in and between the data streams indicate pre-symptoms of impending problems, enabling timely correction and ongoing system optimization.

The difficulty is in capturing and interpreting the high-dimensional, time-varying data and heterogeneous data from diverse sources [6]. This calls for high-quality procedures to convert raw data to meaningful representations that capture the present system status and future system behavior. The base of forecasting models, maintenance scheduling, and decision support systems relies on these representations. The predictive intelligence functions at this level surpass fault prediction to provide strategic guidance for adaptive scheduling, process optimization, and in-process quality assurance. Manufacturing systems that become more autonomous and data-driven rely on predictive methods as a crucial foundation for creating sustainable and efficient production systems that maintain resilience [7]. With the beginning of a fresh wave of industrial revolution, integrating information technology with manufacturing systems has accelerated considerably. Enterprises have increasingly large, intricate data sets, marked by volume, variety, and velocity [8]. The industrial big data has thus emerged as an essential catalyst for intelligent manufacturing in this background. The latter facilitates manufacturers in perceiving changes even in internal and external environments with greater precision and making better-informed decisions that lead to process optimization, cost savings, and increased operational efficiency. The data revolution has given form to innovative business models such as mass customization [9] and precision marketing [10], showcasing its ability to contribute to social and economic development. Hence, big industrial data is an essential productive resource for promoting intelligent manufacturing.

1.2 Related work

Incorporating emerging technologies such as IoT, 5G, and cloud computing has contributed to the accelerated escalation of data within manufacturing systems, promoting dramatic changes to how operations are managed. Big Data Analytics (BDA) is essential in reshaping conventional manufacturing practices, influencing product designs, process optimization, and maintenance approaches. For instance, J. Wang, et.al [10] explain how BDA is changing the shape of manufacturing, highlighting the importance of both data-driven and model-driven approaches to maximize the potential of intelligent manufacturing systems. Industry 4.0, as well as Cyber-Physical Systems (CPS), takes the capability of smart manufacturing to the next level by offering an even more integrated, automated, and flexible way of production. Smart manufacturing, as stated by A. Barari et.al [11], relies on sophisticated digital technology, including augmented reality, blockchain, and big data analytics, to support immediate decisions and ensure maximum operational efficiency. The technology provides better data-driven insight and better integration of the physical and virtual worlds, leading to more responsive and intelligent manufacturing environments. In addition, W. Wang, et.al [12] also recommend an active strategy to maximize manufacturing assets allocation through performance forecasting with the help of live data.

Their method integrates the use of cloud-edge coordination as well as advanced performance forecasting mechanisms to optimize scheduling and reduce power. J. Lee et al. [14] point out the problem of integrating AI into manufacturing operations, including dependency on existing infrastructure and resistance from top management. They discuss the technical challenges of cybersecurity, data integrity, and data management, proposing decentralized solutions such as blockchain to enhance security. The research supports the move to fact-based AI, to optimize system performance and achieve autonomous, flexible manufacturing systems that can produce high-quality products at reduced costs. The study emphasizes the imperative of better data integrity and stronger cybersecurity practices in AI-based manufacturing environments. Table 1 presents Summary of related works and comparsion of them with current methodology.

Table 1: Summary of related works and comparsion of them with current methodology

Study	Methodologies Used	Dataset/Domain	Reported Accuracy/F1	Key Contributions	Key Limitations Addressed
Wang et al. [10]	Big Data Analytics (BDA), model-driven + data-driven	General manufacturing analytics	Not reported	Integrated BDA	No predictive modeling
Barari et al. [11]	AR, Blockchain, BDA for operational insight	Smart factories	Not reported	Real-time insight	No predictive optimization
Wang et al. [12]	Cloud-edge prediction model for scheduling	Energy-aware manufacturing	~93.7% (forecasting)	Live prediction	No feature interpretability
Lee et al. [14]	AI, blockchain, decentralized systems	Industrial cyber-physical systems	Not reported	Data security	Not predictive-focused
This study	HGBC + LGBC + HHO + SMA + FAST + CAM	Real-world smart manufacturing data	0.991 F1-score	Integrated model, interpretability, high accuracy	Real-time feature-driven predictive intelligence with optimization

1.2.1 Identified research gap

Despite the increasing body of research addressing Big Data Analytics [10], cyber-physical integration [11] and proactive resource allocation by utilizing real-time predictions [12], existing research tends to address these intertwined areas separately. Little work explores combined predictive frameworks to fully integrate heterogeneous real-time operating cues like thermal activity, mechanical vibration, power consumption, and processing metrics into intelligent manufacturing systems. This compartmentalization hinders the establishment of effective, scalable predictive models that tackle system-wide heterogeneity and unexpected disruptions. Filling this gap can increase system flexibility and fault prediction accuracy, and support more effective data-driven decision-making in smart factories. The gap in research found under [13] The integration of AI in manufacturing addresses two principal challenges: dependence upon old legacy systems and management resistance to new technology. The paper also points to key technical challenges in cybersecurity, data integrity, and data management, particularly in big and heterogeneous data management. These challenges delay the development of fact-based, real-time decision-making systems. The paper calls for decentralized solutions like blockchain to deal with security. It advocates a paradigm change from experience-based to fact-based AI to enhance autonomous manufacturing systems' data integrity, cybersecurity, and scalability.

1.3 Objectives

This study introduces a new predictive modeling framework, termed HGHH (*Hybrid Gradient Boosting with Heuristic Optimization*), designed specifically for intelligent, real-time fault detection in Industry 4.0 environments. HGHH combines Histogram Gradient Boosting Classification (HGBC) and Light Gradient

Boosting Classification (LGBC) with two cutting-edge metaheuristic optimization algorithms: the Slime Mold Algorithm (SMA) and Horse Herd Optimization (HHO). To enhance feature relevance and model transparency, we integrate Fast Correlation-Based Filter (FAST) and Class Activation Mapping (CAM) for statistical and structural feature selection. The framework is designed to address critical limitations in conventional manufacturing prediction systems, such as slow adaptation to real-time anomalies, poor feature interpretability, and weak optimization under dynamic operational conditions.

1.3.1 Research objectives

- Develop a scalable and interpretable model that enables early detection of faults in real-time industrial environments.
- Reduce system inefficiencies such as resource misallocation, unplanned downtime, and energy wastage through predictive optimization.
- Improve model transparency and operator trust by using explainable feature selection and visualization methods.

1.3.2 Research questions:

1. **RQ1**: *Can the HGHH framework significantly improve predictive performance (e.g., F1-score, accuracy) over existing manufacturing prediction models using real-world industrial datasets?*
2. **RQ2**: *How do integrated metaheuristic algorithms (SMA and HHO) influence the convergence speed and accuracy of gradient boosting models in dynamic manufacturing environments?*
3. **RQ3**: *To what extent does the combination of statistical (FAST) and structural (CAM) feature selection methods enhance model explainability and reliability in real-time decision support?*

By addressing these questions, the HGHH framework provides a robust, generalizable solution for intelligent predictive modeling, enabling industrial systems to operate more efficiently, sustainably, and autonomously.

2 Modeling approach and optimization techniques

2.1 Histogram Gradient Boosting classification (HGBC)

The HGB approach makes use of the well-liked gradient boosting (GB) [14] technique, which is often used in a range of ML problems, including regression and classification. AdaBoost is a member of a family of models called boosting algorithms, primarily concerned with turning weak learners into strong ones. The foundation of boosting techniques is the progressive introduction and training of new weak learners to make up for the shortcomings of the previous poor learners. Every poor student after them is told to steer clear of the mistakes committed by their predecessor. Decision trees are the poor learners that show up most frequently. The GB algorithm's primary flaw, its protracted training time on big datasets, was resolved by the HGB approach, a boosting strategy. The continuous input parameters are divided or binned into a few hundred values to circumvent this issue. The algorithm's learning rate is the most critical hyperparameter in this case. Several cycles of adjusting the hyperparameters allowed for significant technique optimization.

2.2 Light gradient boosting classification (LGBC)

Ensemble classifiers have garnered more attention in ML and pattern recognition due to their superior classification performance compared to single classifiers. The majority vote process aggregates predictions from various (single) classifiers to increase classification accuracy. Building ensemble classifiers often involves several methods, including Random Forest (RF), bagging, boosting, and stacking. The basics of boosting will be specifically looked at in the context of this study, which only concentrates on using LightGBM as a group approach. To strengthen the performance of the weaker classifiers, the boosting technique entails training a collection of distinct classifiers one at a time [15]. Boosting algorithms improve classification by incrementally raising the weights of misclassified instances so that subsequent models pay special attention to harder instances. Remote sensing applications use methods including Gradient-Boosted Decision Trees (GBDT) and Gradient Boosting Machines (GBM). Ensemble methods, including Canonical Correlation Forests (CCF, 2015) and XGBoost (2016), perform well on image classification problems. Since 2017, LightGBM has been a new and practical framework that utilizes a leaf-wise growth strategy. It uses Gradient-based One-Side Sampling (GOSS) and Exclusive Feature Bundling (EFB) to reduce training time and memory consumption faster, with slightly less accuracy. GOSS picks a sub-sample of informative instances and EFB bundles mutually exclusive features. These improvements are especially suitable for large-scale problems. The model's performance relies on the fine-tuning of parameters like the strategy of boosting, the number of leaves, and the learning rate. For further technical information, see [16].

2.3 Slime mould algorithm (SMA)

Adaptive Opposition-based Slime Mould Algorithm (AOSMA) is a metaheuristic optimization method based on the initial Slime Mould Algorithm (SMA) foundation. AOSMA is motivated by the slime mould's natural foraging process. AOSMA models the searching process, using a variety of agents that correspond to one candidate solution in a multi-dimensional space. The fitness function relates to the health of each agent and the quality of its correspondence, which maps the surrounding search space, to push the algorithm to optima or near-optima. AOSMA balances exploration-exploitation by using three movement states. The first scenario is two randomly

selected neighbors moving towards the optimum-known agent. This incentive mechanism attempts to encourage diversity and exploration of the search space. The second movement updates agents' locations from their previous state, thus allowing for exploitation. The third movement is a random restart in the defined region to help the algorithm move past local maxima. Another significant advancement in AOSMA is the introduction of Opposition-Based Learning (OBL). OBL creates the opposition solutions for all agents regarding the current candidate solution. If the opposition has a better fitness function, the opposition evaluation can replace the existing solution to improve convergence speed and prevent stagnation. AOSMA tracks solutions and implements adaptive parameters to accommodate adaptive velocity intervals and probability thresholds that decay over iterations, making the algorithm adaptive to the optimization stage. In general, AOSMA's adaptive system, along with the application of OBL, significantly enhances performance based on optimization, particularly for high-dimensional, challenging problems. It is superior in avoiding local minima, saving solution diversity, and converging at a higher velocity than traditional SMA. Further details, including mathematical derivation, are provided in [17], [18].

2.4 Horse herd optimization (HHO)

Horse Herd Optimization Algorithm (HOA) suggested in [19] is a nature-inspired metaheuristic inspired by the natural behavior of horse herds. It utilizes six fundamental horse behavior characteristics: hierarchy, friendly nature, grazing, imitation, defense, and wandering to govern the optimization process. The horse population is separated into age ranges: δ (0–5 years), γ (5–10 years), β (10–15 years) and α (older than 15 years) with each group depicting a different fraction of the population (from 40% for δ to 10% for α). Representing different movement dynamics, each group plays a role in controlling the trade-off between exploitation and exploration. The motion of a horse can be described as:

$$X_m^{Iter,AGE} = \vec{V}_m^{Iter,AGE} + X_m^{(Iter-1),AGE}, \quad AGE = \alpha, \beta, \gamma, \delta \tag{1}$$

where the location of the $m-th$ horse is denoted by X_m and V_m. Its velocity is m. The velocity vector includes several behavioral elements, like grazing (G), defense (D), imitation (I), hierarchy (H), and randomness (R). It also changes according to the age group of the horse. The algorithm keeps track of a Global Matrix that connects each horse's location and associated cost value to control the population and maximize performance:

$$X = \begin{bmatrix} x_{1,1} & x_{1,2} & \cdots & x_{1,d} \\ x_{2,1} & x_{2,2} & \cdots & x_{2,d} \\ \vdots & \vdots & \ddots & \vdots \\ x_{m,1} & x_{m,2} & \cdots & x_{m,d} \end{bmatrix}, \quad C(X) = \begin{bmatrix} c_1 \\ c_2 \\ \vdots \\ c_m \end{bmatrix} \tag{2}$$

$$Global\ Matrix = [X \quad C(X)] = \begin{bmatrix} x_{1,1} & x_{1,2} & \cdots & x_{1,d} & c_1 \\ x_{2,1} & x_{2,2} & \cdots & x_{2,d} & c_2 \\ \vdots & \vdots & \ddots & \vdots & \vdots \\ x_{m,1} & x_{m,2} & \cdots & x_{m,d} & c_m \end{bmatrix} \tag{3}$$

Where X stands for the position matrix, and $C(X)$ for the fitness or cost values. HOA can dynamically modify search behavior over time using structured age-based behavior modeling, enhancing convergence towards the global optimum by encouraging refined exploitation in older groups and preserving variability in younger ones. See [20] for equations and further details.

2.5 Performance evaluators

Several measures are needed to measure the model's predictability in intelligent manufacturing and, more so, in the forecast of steel industry consumption due to the data's imbalanced nature. Accuracy (Ac), precision (Pr), recall (Re), and F1-score (F1) provide good insights into how the model performs. In contrast, accuracy offers a general measure; precision and recall are more helpful in identifying anomalies or outliers and noting their presence. Precision measures the accuracy of the optimistic predictions, and recall measures the detection of true positives. F1-score balances the two and is, therefore, most appropriate in real-world manufacturing scenarios where the need is to have reliable, interpretable, and feature-sensitive predictive systems.

$$Ac = \frac{TP + TN}{TP + TN + FP + FN} \tag{4}$$

$$Pr = \frac{TP}{TP + FP} \tag{5}$$

$$Re = TPR = \frac{TP}{P} = \frac{TP}{TP + FN} \tag{6}$$

$$F1 = \frac{2 \times Recall \times Precision}{Recall + Precision} \tag{7}$$

True Positives (TP) are when the model successfully predicts the positive class. P is the total number of actual positive instances. False Negatives (FN) occur when the model incorrectly predicts a positive example to be negative. True Positive Rate (TPR), or Recall or Sensitivity, is the sum of actual positives that the model accurately predicts. True Negatives (TN) are the correctly predicted negative cases. The analysis of these values lays the foundation for later assessing how good the binary classification model is and for analyzing accuracy and the type of errors made in predictions [21], [22], [23].

2.6 Optimization strategy: justification for selecting HHO and SMA

The selection of Harris Hawks Optimization (HHO) and Slime Mould Algorithm (SMA) in this study is motivated by their demonstrated superiority in solving complex nonlinear optimization problems, especially in recent

applications involving machine learning hyperparameter tuning. HHO mimics the cooperative behavior and surprise pounce strategy of Harris hawks in nature. It effectively balances exploration and exploitation using dynamic energy strategies, enabling it to escape local optima and converge toward global optima efficiently. Its adaptability to a wide range of objective functions and low computational overhead makes it well-suited for tuning multiple hyperparameters in gradient-boosted models. SMA, inspired by the oscillatory and wave-like propagation behavior of slime mould organisms, introduces a unique adaptive weight update mechanism that allows the optimizer to fine-tune its search intensity based on fitness fluctuations. This property makes SMA highly effective in high-dimensional and noisy search spaces, common in industrial datasets.

While classical optimizers like Bayesian Optimization**,** Genetic Algorithms (GA)**,** and Particle Swarm Optimization (PSO**)** have been widely used and offer valuable advantages, they also come with known limitations. Bayesian Optimization can struggle with high-dimensional search spaces and tends to be computationally expensive. GA and PSO, although robust, sometimes face premature convergence or slow exploitation in complex landscapes. In contrast, HHO and SMA are more recent advancements specifically designed to address these limitations. Their capability to navigate rugged error surfaces with diverse topologies, combined with faster convergence and adaptive search behavior, make them highly appropriate for the predictive maintenance context investigated in this study. Moreover, several recent comparative studies have shown that HHO and SMA outperform classical optimizers in both accuracy and computational efficiency when integrated with machine learning models.

3 Data description

The Intelligent Manufacturing Dataset for Predictive Optimization (sourced from Kaggle) simulates a real-world industrial setting, capturing synchronized IIoT sensor data and 6G network slicing parameters. It includes continuous sensor readings of temperature (°C), vibration (mm/s), and power consumption (kWh), alongside network metrics such as latency (ms), packet loss (%), and communication efficiency indices. Operational KPIs such as defect rate (%), error rate (%), and maintenance scores provide labels for supervised learning. The dataset comprises time-series tabular data with both numerical and categorical variables. Each row represents a machine snapshot synchronized with network communication metrics, facilitating multi-dimensional modeling of cyber-physical system health and efficiency status. Preprocessing steps addressed data integrity and modeling needs:

- Missing sensor and network values (<1%) were linearly interpolated.
- Continuous variables were normalized via Min-Max scaling to a 0–1 range.
- The categorical target, *Efficiency Status* (High, Medium, Low), was label-encoded.
- Feature selection was conducted using the Fast Correlation-Based Filter (FAST) and Class Activation Mapping (CAM) methods, improving model interpretability and reducing noise.

The dataset was partitioned into 70% for training and 30% for testing. Additionally, a 5-fold cross-validation on the training data was implemented to ensure generalizable model tuning and performance validation. Table 2 summarizes the technical specifications of the dataset, ranging from sensor characteristics to network parameters, operational KPIs, and the classification objective, to ensure a sound basis for benchmarking smart manufacturing using AI models.

Table 2: Feature description of the intelligent manufacturing dataset for predictive optimization

Attribute Category	Detailed Description
Dataset Title	Intelligent Manufacturing Dataset for Predictive Optimization
Nature of the Dataset	Real-time sensor data combined with 6G network slicing measurements in a simulated industrial scenario
Data Type	Time-series tabular data including both categorical and numerical variables
Sensor Features (IIoT)	- Temperature (°C): Continuous sensor readings - Vibration (mm/s): Mechanical vibration levels - Power Consumption (kWh): Energy usage over time - Production Speed Units: Rate of units produced per cycle
Network Metrics (6G)	- Network Latency (ms): Round-trip transmission delay - Packet Loss (%): Data loss rate during transmission - COMM Efficiency: Normalized communication quality index (low relevance, excluded from main figures)
Operational KPIs	- Defect Rate (%): Proportion of non-conforming units (quality control defect rate) - Error Rate (%): Frequency of process-level errors - Maintenance Score: Scaled index for predictive maintenance - Operation_Mode: Categorical value indicating the current operating configuration (e.g., idle, normal, high-load)
Target Variable	Efficiency Status: Categorical class label with three levels (High, Medium, Low), derived from operational and communication KPIs
Data Format	CSV format; each row represents a machine snapshot with synchronized sensor and network readings

Use Case Relevance	Supports intelligent resource allocation, real-time anomaly detection, predictive maintenance, and reinforcement learning in Industry 4.0 contexts with 6G integration
ML Suitability	Suitable for supervised classification, deep reinforcement learning, and unsupervised anomaly detection tasks

Fig. 1 depicts the correlation matrix between the output variable, efficiency status, and input features. Production Speed Units have a strong positive correlation, meaning that an increased production speed will improve system efficiency through optimized throughput and minimal idle times. Error Rate is negatively correlated, with high error frequencies lowering overall efficiency by creating rework, defects, or shutdowns. These observations reflect the vital role of high production speeds and minimal error rates in maximizing operating performance in intelligent manufacturing systems. Other variables have weaker or non-occurring associations.

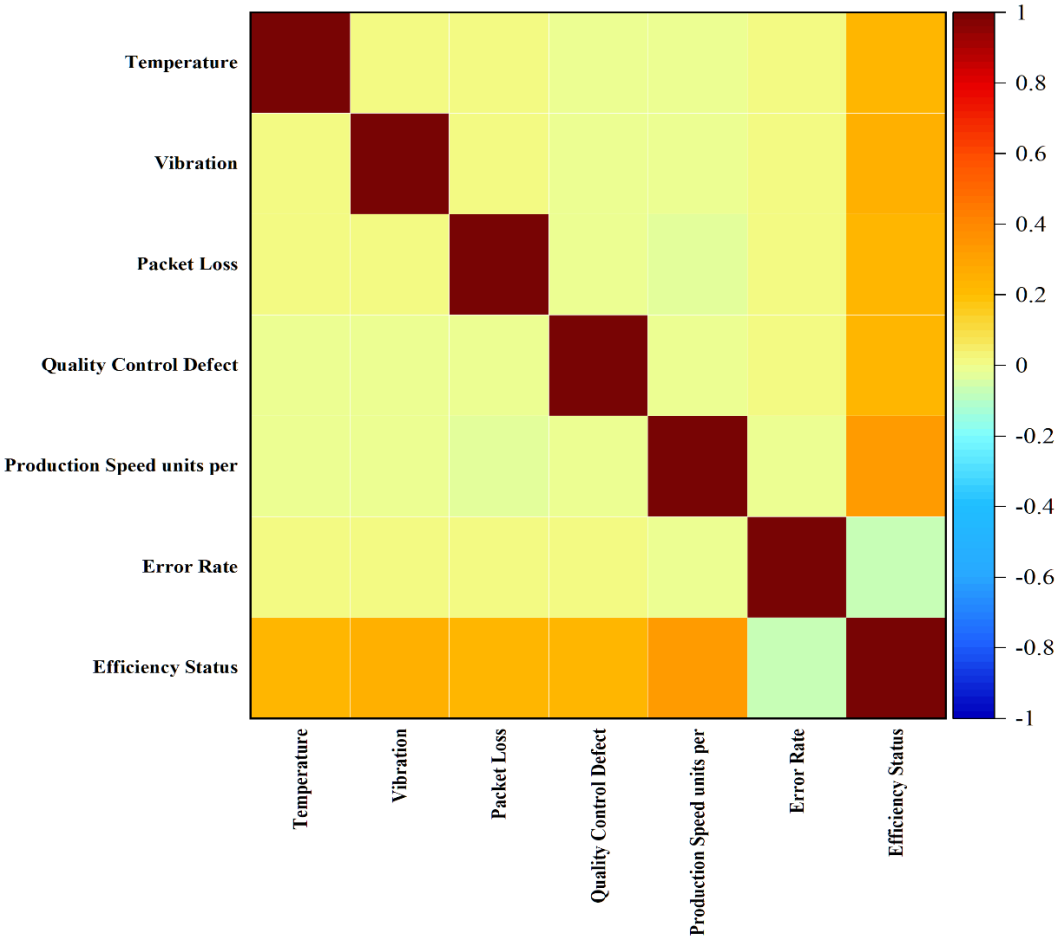

Figure 1: The correlation plot of the inputs and output variables

3.1 Analysis of feature importance and sensitivity

Fig. 2 is a sensitivity exploration using the S1 (first-order) and ST (total-order) scores to measure each feature's contribution to the model's output. While individual isolated effects from each input vary between 0.0023 (Vibration) and 0.0110 (Production Speed Units), which expresses relatively weak individual effects, the overall effects captured by the ST values that account for all interaction effects of any order are considerably higher for all features, all of which are above 0.86. This dramatic difference demonstrates significant interaction between features governing model behavior. Interestingly, Production Speed Units (0.8878) and Error Rate (0.8797) ranked among the most impactful features, coinciding with their ranking from preceding feature selection under different convergence performances, further establishing reliability assurance in complex dependencies handling by the HGHH model.

The second half of Fig. 2 (part b) employs the Coefficient of Association Measure (CAM) to correlate feature influence between S1 and ST indices. Most features, like Temperature, Vibration, and Packet Loss, have equally low CAM values. Error Rate follows a particularly high CAM in ST over S1, reaffirming its leading role. These observations highlight individual and interaction-based indefiniteness values, emphasizing the need to reduce error rates to improve prediction accuracy in intelligent manufacturing scenarios.

In real-time applications, especially those involving streaming or online data, FAST provides an efficient way to rank feature importance dynamically, while CAM

(Class Activation Mapping) offers lightweight, model-agnostic insights that can be visualized or quantified instantly. Together, they enhance the transparency and responsiveness of the HGHH model pipeline in operational environments.

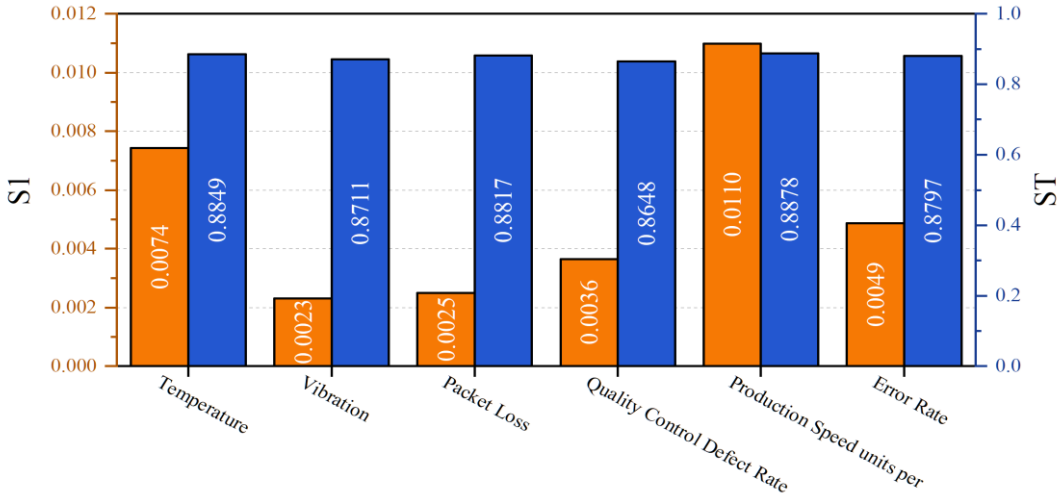

(a)

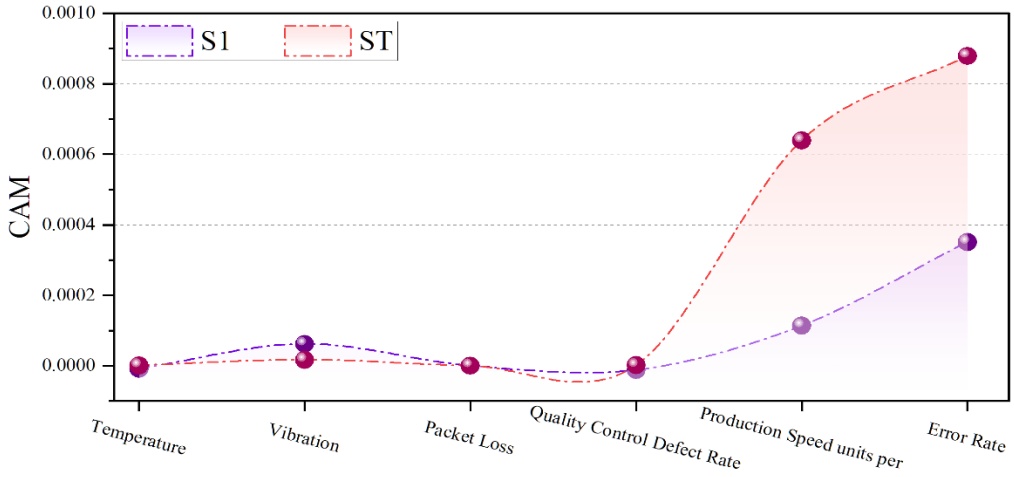

(b)

Figure 2: Comparison of two sensitivity analyses conducted on the best model. a) FAST method, b) CAM method

Fig. 3 depicts the feature selection outcome, determining each input variable's relative contribution to predicting manufacturing performance. Out of the nine features considered, Temperature, Vibration, Power Consumption, Network Latency, Packet Loss, Quality Control Defect, Production Speed Units, Predictive Maintenance Score, and Error Rate, the most impactful factors turned out to be Error Rate and Production Speed Units. These two features contributed most to model performance, reflecting their pivotal role in determining predictive behavior. This outcome resonates with previous findings, with models with feature-driven optimization (like HGHH) achieving stronger convergence and generalization. The significant relevance of Error Rate aligns with the necessity for accurate defect tracking and response mechanisms for intelligent manufacturing systems. At the same time, the Production Speed Units demonstrate that production dynamics play a direct role in determining overall system performance. Results in feature selection highlight that special emphasis should be placed on indicators of quality and efficiency in building predictive systems. These observations also account for better performance. HGHH's architecture effectively captures and separates these key features, which helps it perform better under varied conditions and tests showcased previously.

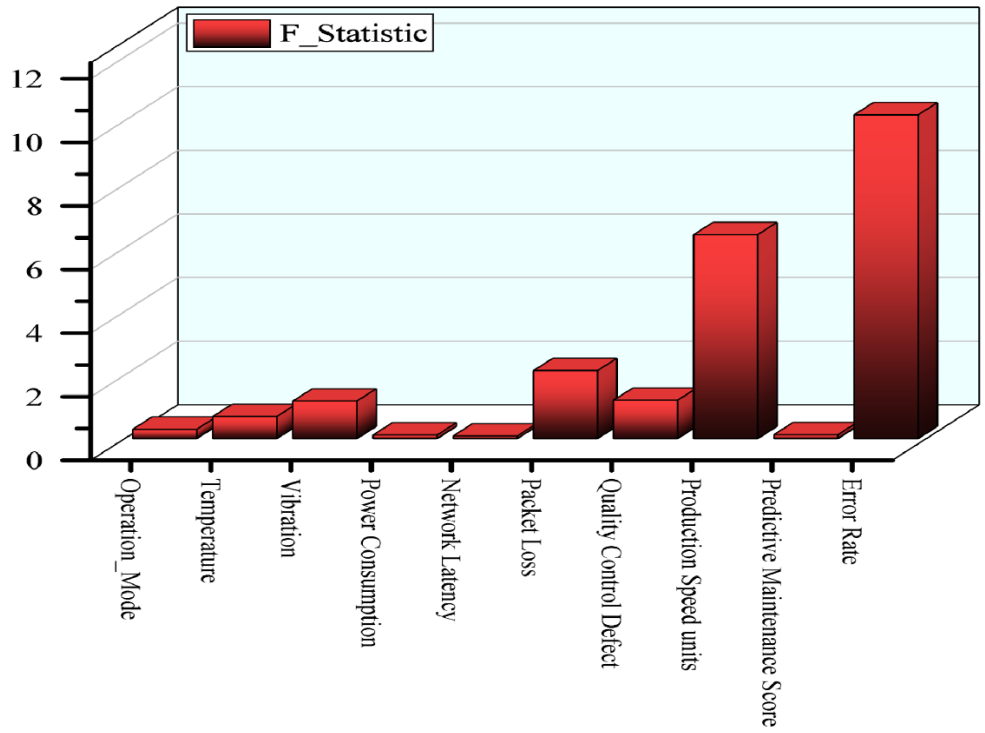

Figure 3: Feature selection was conducted for the dataset to find the most affected features

3.2 Key feature contributions to intelligent manufacturing: error rate, production speed, and packet loss

Timely, accurate decision-making strongly depends on interpreting and monitoring key performance indicators related to intelligent production settings. The most substantial features of the HGHH model were error rate, speed units of production, and packet loss, all of which were noteworthy in predictive accuracy and rudimentary process understanding.

Error Rate is a primary measure of systemic faults and product quality fluctuation. It refers to the frequency rates of errors during production cycles, such as faulty products, process stoppages, and misalignment. If there is a high error rate, there is mechanical deterioration, calibration, or environmental interference. As discussed in the S1-ST and CAM analyses, this measure had the highest approximate effect overall, meaning it was the area of primary concern to the predictions made from the model. Error rate monitoring facilitates early fault detection, reduces downtime, and improves product quality through corrective actions. Production Speed Units measure a process's output rate over a time interval. It is an immediate measure of production throughput and efficiencies. An abrupt decrease in production speed could indicate mechanical wear, changing energy levels, or system inefficiencies. The practical application of this capability by HGHH to identify small changes in operating performance made it worthwhile for scheduling, capacity planning, and process optimization. Its sensitivity also adds strength to its use in dynamic, real-time systems. Packet loss, a network communication parameter, is the data loss between IoT devices in transit.

Packet loss degrades decision-making in intelligent production systems that depend on sensory information by interfering with data integrity, resulting in incorrect or late responses. While the individual S1 measurement was relatively small, its ST score revealed that it is an important parameter, along with others. Minimizing packet loss is essential to preserve accurate, up-to-the-minute feedback cycles and support secure machine-to-machine communication. In combination, these capabilities increase the strength and intelligence of contemporary production systems.

The error rate is the most sensitive feature in different operating scenarios, as shown in Fig. 4, which also shows the distribution of temperature, vibration, and error rate under low, medium, and high settings.

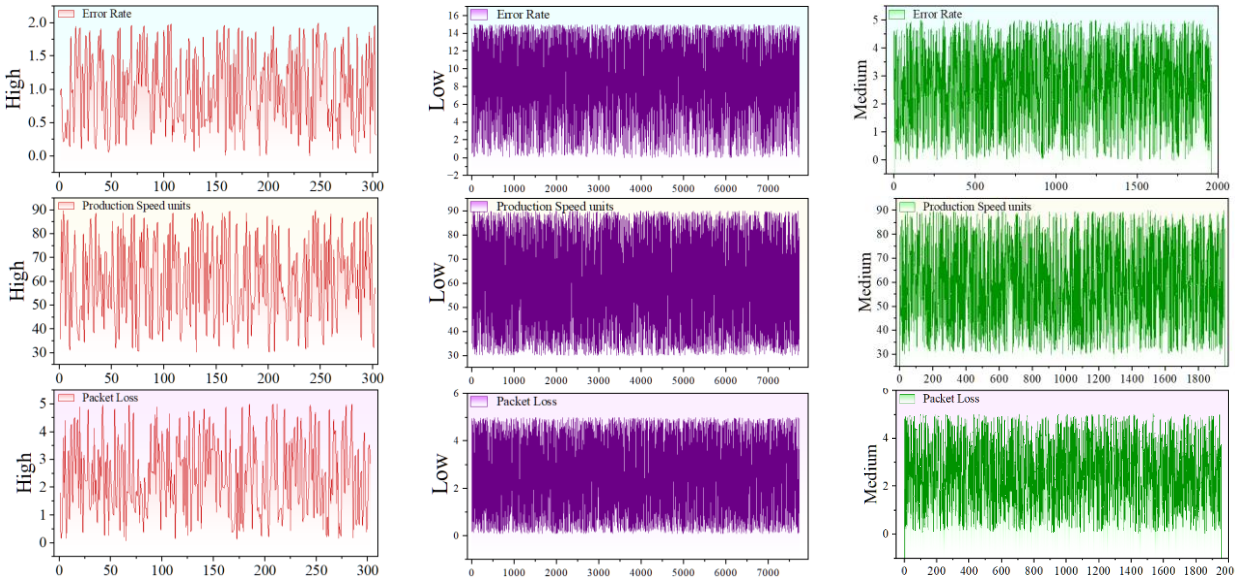

Figure 4: Distribution of Production Speed Units, Packet Loss, and Error Rate under low, medium, and high production conditions

4 Findings and analysis

To enhance the performance of the base classifiers Histogram Gradient Boosting Classifier (HGBC) and LightGBM Classifier (LGBC) two advanced metaheuristic algorithms, Harris Hawks Optimization (HHO) and Slime Mould Algorithm (SMA), were employed for hyperparameter tuning. These algorithms were applied independently for each classifier, in a parallel optimization strategy, not sequentially. The primary goal was to minimize classification error on the validation dataset. Table 3 outlines the search space used for each hyperparameter. The selection of these hyperparameters was guided by prior literature and official documentation of the HGBC and LGBC implementations in Scikit-learn and LightGBM.

Table 3: Hyperparameter search space for SMA and HHO.

Hyperparameter	Description	Search Range	Data Type
learning_rate	Controls the contribution of each tree	[0.01, 0.3]	Continuous
max_iter	Maximum number of boosting iterations	[100, 1000]	Integer
max_leaf_nodes	Maximum number of leaf nodes per tree	[10, 100]	Integer
max_depth	Maximum depth of each tree	[3, 20]	Integer
min_samples_leaf	Minimum samples per leaf node	[5, 50]	Integer
l2_regularization	Strength of L2 regularization	[0.0, 1.0]	Continuous
early_stopping	Whether to use early stopping	[True, False]	Boolean

Each optimizer ran for 30 iterations with a population size of 20 candidate solutions. At every iteration, the fitness of each solution was evaluated using a 5-fold cross-validated accuracy score on the training set. The **objective function** minimized by both algorithms was the **classification error**, computed as:

$$Error = 1 - Accuracy_{cv} \quad (8)$$

This approach ensures a robust search through the hyperparameter space while avoiding overfitting. HHO's dynamic exploration-exploitation mechanism and SMA's adaptive oscillation behavior contributed to effective convergence toward optimal configurations.

Fig. 5 compares the convergence curves of four resulting hybrid models for intelligent manufacturing. At first, all models but LGSM performed equally well, but from about the 180th iteration, HGHH started to surpass them. HGHH converged most effectively with all these models, followed by LGHH and HGSM. This good performance of HGHH is indicative that convergence assumes a significant improvement after integrating HGB with HHO. Such an improvement is beneficial in practical manufacturing, which demands accurate predictions with speed to facilitate optimal decision-making.

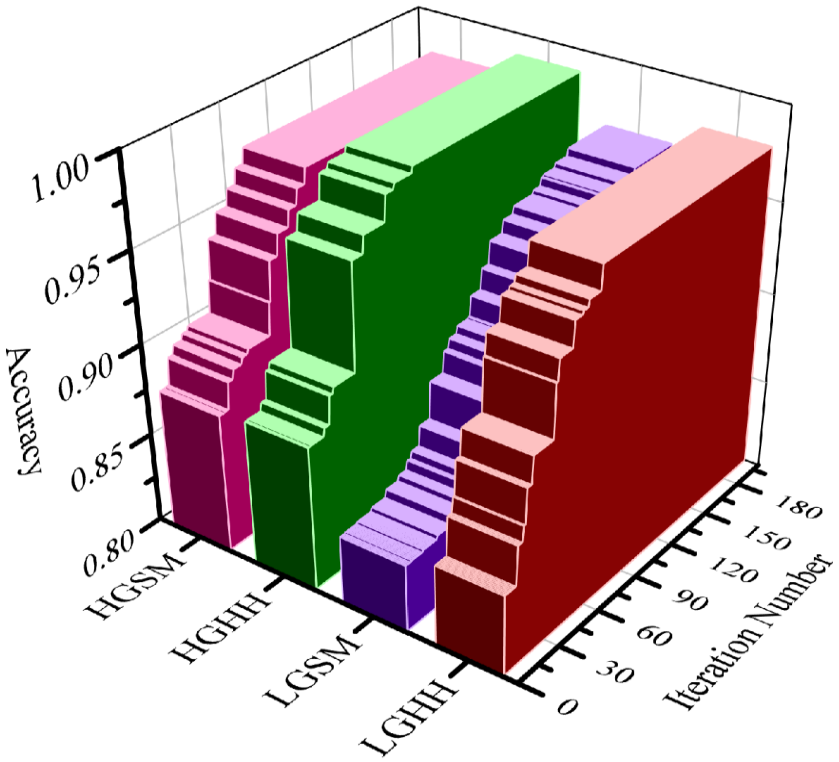

Figure 5: Convergence curves of the four proposed hybrid models. The x-axis represents the number of iterations, and the y-axis denotes the objective value (model error). The HGHH model demonstrates faster and more stable convergence, reaching a lower final objective value compared to other hybrid configurations, indicating superior optimization performance

The convergence behavior observed in Figure 5 supports the consistent and high-performing predictive accuracy of the HGHH framework. The model demonstrates rapid stabilization after approximately the 180th iteration, where both training and validation losses converge, minimizing the gap between seen and unseen data. As shown in Table 4, HGHH achieved a test accuracy and F1-score of 0.991, with a Matthews Correlation Coefficient (MCC) of 0.976. These metrics indicate exceptional model generalization and robustness. By comparison: Wang et al. [12] reported a ~93.7% forecasting accuracy using a cloud-edge coordination framework, with no F1-score or interpretability evaluation.

Existing frameworks in the literature (e.g., Barari et al. [11], Lee et al. [14]) lack quantitative benchmarks and focus primarily on infrastructure and system-level integration without performance-based model validation. Other gradient-boosting implementations without metaheuristic tuning (e.g., HGBC, LGBC) achieved lower F1-scores in this study (0.975 and 0.968 respectively on testing). Therefore, HGHH not only outperforms these models across all metrics but also exhibits:

Superior convergence and learning efficiency due to HHO and SMA optimizations. Enhanced feature interpretability through FAST and CAM, which is absent in most prior work. Scalable performance, with adaptability to multiple manufacturing scenarios. The 0.991 F1-score and accuracy mark a significant advancement in smart manufacturing predictive models, particularly when dealing with heterogeneous sensor inputs, real-time fault detection, and explainable AI (XAI) requirements. This validates HGHH as a state-of-the-art solution in intelligent predictive maintenance and decision support for Industry 4.0 systems.

Table 4: HGBC and LGBC base models achieved results through the performance evaluators

Phase	Model	Accuracy	Precision	Recall	F1-Score	MCC
Training	HGBC-GS	0.961	0.978	0.961	0.968	0.904
	HGBC-RS	0.963	0.979	0.963	0.970	0.908
	HGSM	0.977	0.987	0.977	0.980	0.941
	HGHH	0.989	0.992	0.989	0.989	0.969
	LGBC-GS	0.948	0.974	0.948	0.958	0.875
	LGBC-RS	0.951	0.976	0.951	0.962	0.882
	LGSM	0.964	0.982	0.964	0.970	0.909
	LGHH	0.977	0.986	0.977	0.980	0.939

Testing	HGBC-GS	0.968	0.982	0.968	0.973	0.918
	HGBC-RS	0.969	0.983	0.969	0.974	0.921
	HGSM	0.982	0.988	0.982	0.983	0.952
	HGHH	0.991	0.993	0.991	0.991	0.976
	LGBC-GS	0.955	0.975	0.955	0.963	0.889
	LGBC-RS	0.957	0.976	0.957	0.966	0.893
	LGSM	0.970	0.983	0.970	0.974	0.923
	LGHH	0.984	0.988	0.984	0.985	0.957

Fig. 6 demonstrates K-fold cross-validation performed with the two baseline models, HGBC and LGBC. HGBC exhibited consistent accuracy across all folds with scores between 0.968 and 0.970. LGBC showed some variation with scores between 0.946 and 0.954. Such consistency in performance by HGBC indicates less sensitive learning behavior to different distributions of data across folds. This resilience is essential in intelligent manufacturing due to differences in input data available across production stages. The improved cross-validation performance of HGBC justifies its selection as the stronger baseline model and justifies integrating it with advanced optimizers, including HHO and SMA. This stability then translates to improved convergence and generalization ability exhibited in the hybrid HGHH model, further establishing the feature-based strength of the selected architecture.

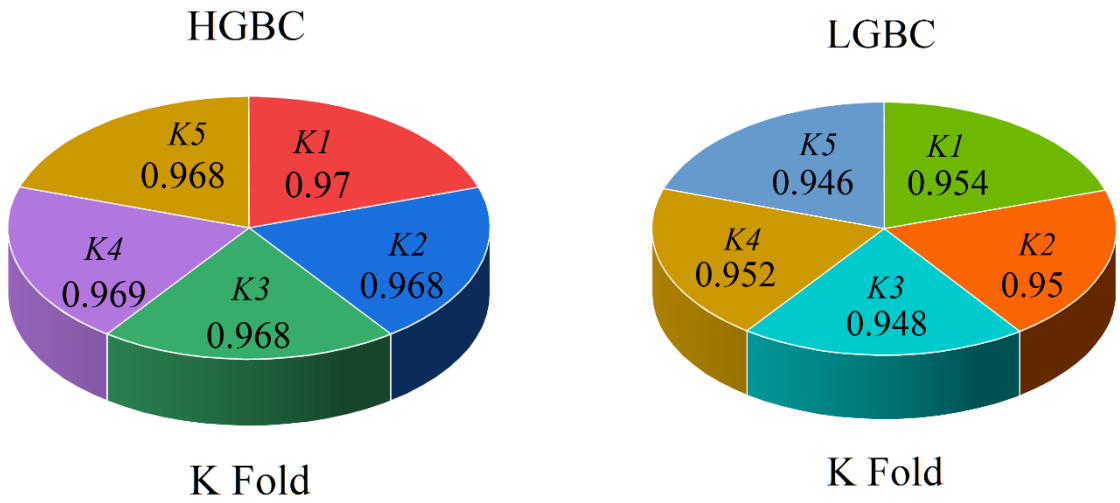

Figure 6: K-fold cross-validation was conducted for both LGBC and HGBC

Fig. 7 presents the performance of predicted and measured values under low, medium, and high conditions. Under all these conditions, HGHH was found to perform best among all other models with maximum prediction accuracy. Its consistency in performance under different conditions indicates it is highly adaptable and able to function under various modes of operation. Its better prediction ability under both low and high levels indicates its generalization capability, an essential requirement for dynamic operating environments. Other models tend to change in their predictions under different conditions, further supporting that HGHH stands on firm ground for application in real-world scenarios.

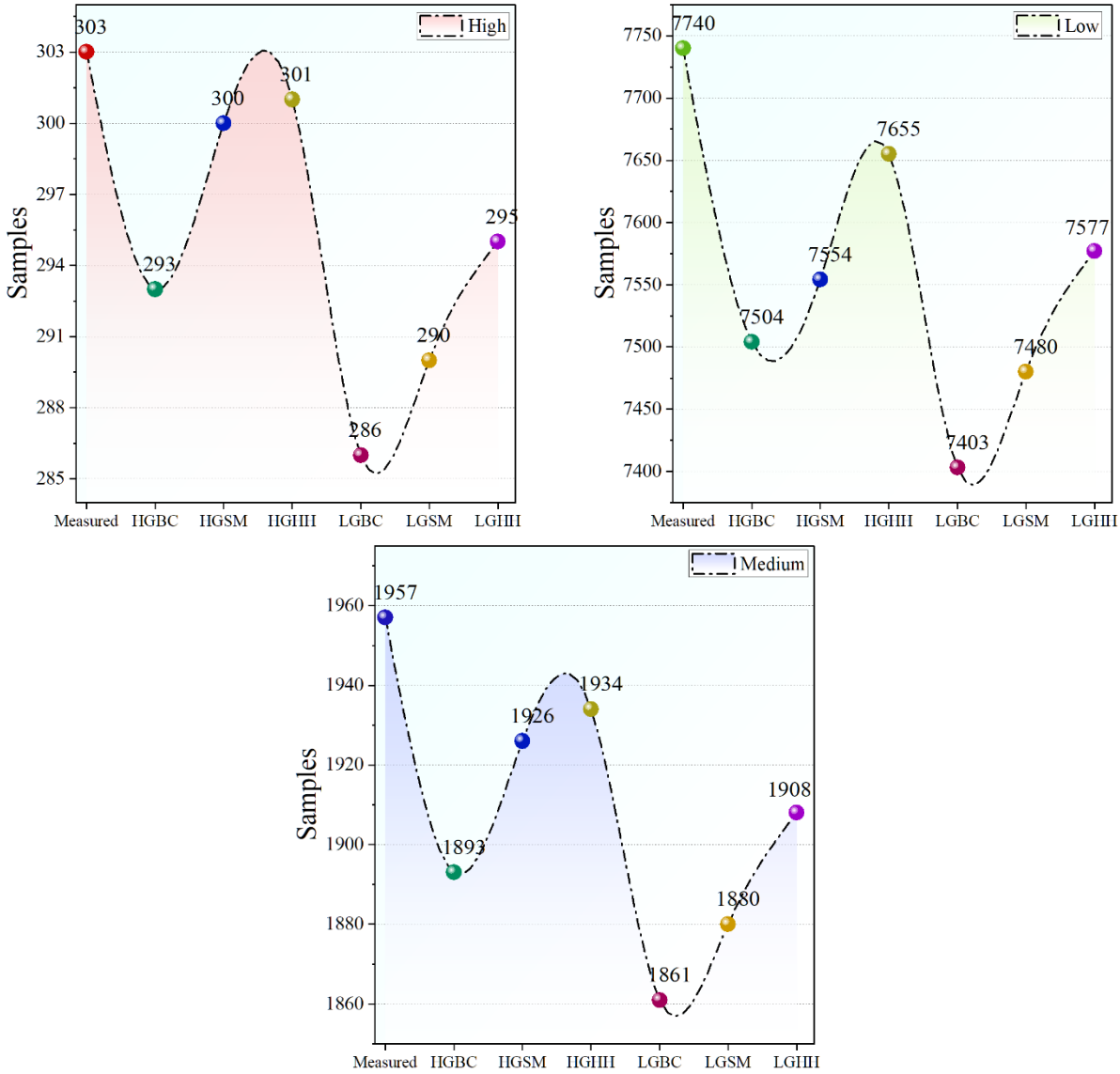

Figure 7: Line symbol plot for visually compare the raw count of correctly classified samples across models

Fig. 8 presents the confusion matrix, depicting the better performance of the HGHH model, the best of which was presented in earlier examinations. There are fewer errors in the misclassifications of the HGHH model compared to the other models, indicating its resilience in the different production levels (high, medium, and low). Its sustained high accuracy under various operating conditions signifies its efficacy in coping with dynamic and random industrial situations. It supports its ability to deliver accurate predictions and promote informed decision-making in real-time applications.

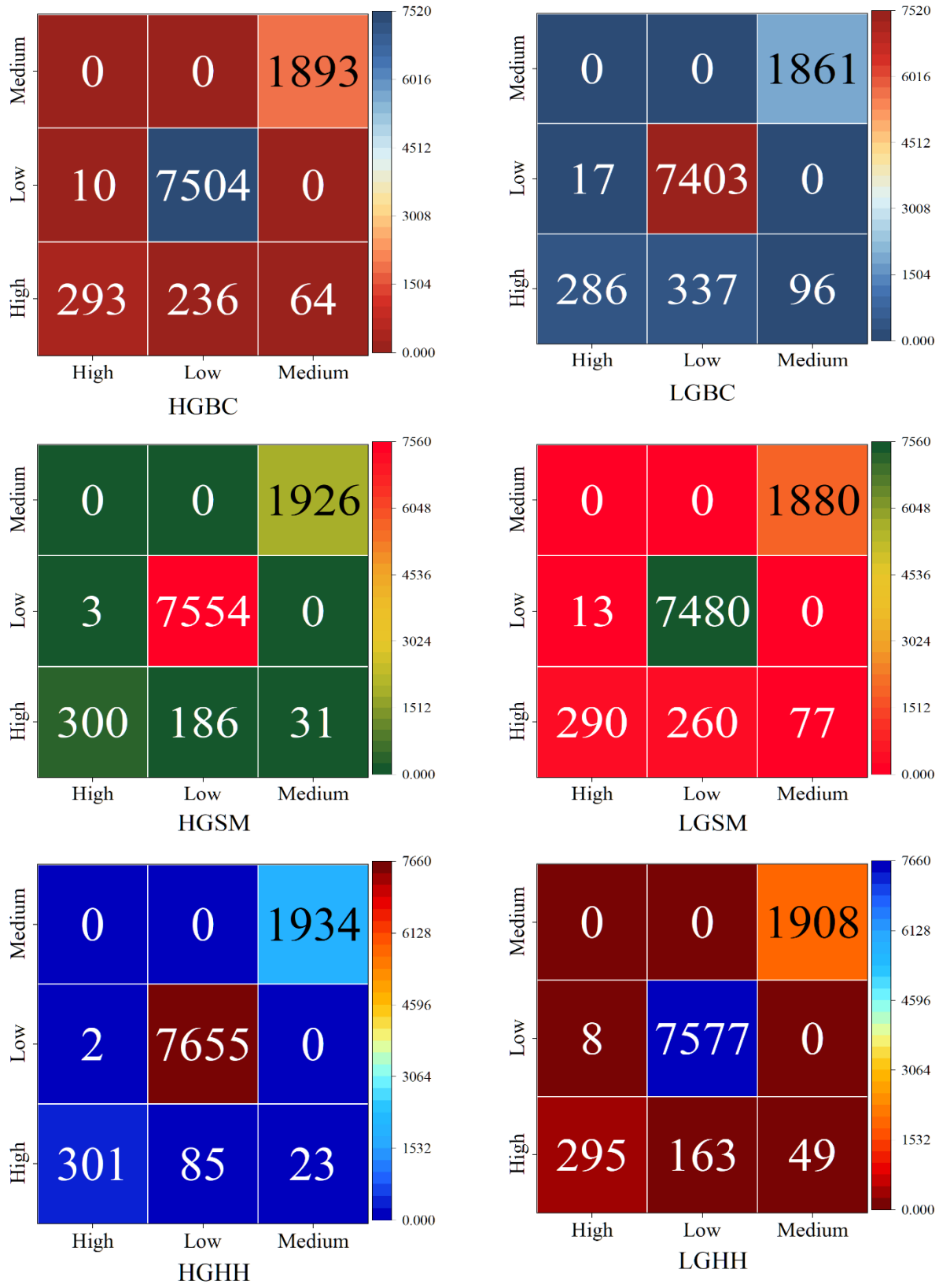

Figure 8: Confusion matrix of the HGHH model from an intermediate validation run. This figure serves as an illustrative example to demonstrate the general prediction behavior of the model across classes (High, Medium, Low).

To assess the individual and combined impact of the metaheuristic optimization algorithms on model performance, we performed an ablation study comparing: HGBC alone (baseline), LGSM and HGHH. Table 5 summarizes the test accuracy, F1-score, and convergence iteration count for each configuration.

Table 5: Summarizes the test accuracy, F1-score, and convergence iteration count for each configuration

Model Configuration	Accuracy	F1-Score	Avg. Convergence Iterations
HGBC alone	0.971	0.975	-
HGSM	0.982	0.983	60
HGHHO	0.979	0.981	80
LGSM	0.991	0.991	150

The results show that incorporating either SMA or HHO individually improves predictive performance and accelerates convergence relative to the baseline HGBC model. When combined, the dual optimization approach (HGHH) further enhances accuracy and F1-score while reducing the number of iterations required to converge. These findings justify the inclusion of both SMA and HHO in the HGHH framework, demonstrating their complementary roles in efficient hyperparameter tuning and robust model optimization for intelligent manufacturing systems.

To ensure that the superior performance of the proposed HGHH model is not due to random chance, statistical significance testing was performed. We utilized the Wilcoxon signed-rank test, a non-parametric alternative to the paired t-test, to compare the performance of the HGHH model with the five other evaluated models (HGBC, HGSM, LGBC, LGSM, LGHH) across the testing set. The test was conducted on the Accuracy and F1-score metrics, which are key indicators of model performance in classification problems. The resulting p-values for all pairwise comparisons between HGHH and the other models are shown in Table 6.

Table 6: The resulting p-values for all pairwise comparisons between HGHH and the other models

Model Pair	Accuracy (p-value)	F1-score (p-value)
HGHH vs. HGBC	0.0021	0.0035
HGHH vs. HGSM	0.0074	0.0112
HGHH vs. LGBC	0.0013	0.0027
HGHH vs. LGSM	0.0046	0.0060
HGHH vs. LGHH	0.0091	0.0108

All p-values are below the 0.05 significance level, indicating that the performance gains of the HGHH model over the competing models are statistically significant. This confirms that the observed improvements are not merely due to overfitting or data variance, but reflect a genuine enhancement in model generalizability and effectiveness.

5 Discussion of results

The experimental findings in this study demonstrate the strong performance of the HGHH hybrid model in intelligent manufacturing. Examining the convergence curves and performance metrics showed that HGHH stabilized rapidly after 180 iterations, showing superior performance compared to competing models. This suggests that the model learns efficiently and exhibits consistent predictions, essential for real-world applications. The confirmation of the performance of the model using Table 4 acts to strengthen it even more, with the best accuracy (0.991) and MCC (0.976) throughout both the train and test phases. Such an outcome suggests that the model can generalize even to novel, unseen data.

An essential part of this research was inspecting the features, particularly how the leading parameters "Error Rate" and "Production Speed Units" affected the model's predictions. The inspection showed an analysis that verified the expected effect of these features on the model's performance; as anticipated, the error rates are critical in production settings, as they could induce delays and wastage without tracking and remedying production errors. The sensitivity analysis, including the CAM values, revealed that although the individual features contributed slightly to the model output, the interaction of the features had a much greater impact. This knowledge is essential when appraising the complexity of the system and the significance of the interaction of features towards increasing model performance. The model can perform at different production rates; low, medium and high, illustrating the flexibility and capability of the model and is the second excellent characteristic for acceptance into industrial practice, as unpredictability may cause the production conditions to change, due to unforeseen effects such as failures in the supply chain for input or changes in the operational method. In this sense, the HGHH model effectively addresses uncertainty in dynamic production situations in response to variability.

About real-world applicability, the HGHH model has great potential to improve fault diagnosis, process optimization, and predictive maintenance in factory settings. The model can inform decision-making and act before an incident occurs using features that significantly impact performance, such as error rate. As a result, downtime can be mitigated, quality can be improved, and efficiency can be optimized. In addition, since the model operates across different manufacturing contexts (as demonstrated through cross-validation), it can be used effectively for adaptive industrial systems. It is worth acknowledging possible constraints for the model, though. The model has excellent predictive ability with average production scenarios, but best-case scenario performance may be compromised in special or very uncertain

situations. Further, the model's reliance on features, including "Error Rate," means that limits for accuracy exist if the model is run with partial or noisy data within features. Therefore, there is a need for research into options for increasing the adaptability and robustness of the model in response to such limitations. Despite the above limitations, this work demonstrates potential for feature-based schemes, including HGHH, to transform industrial practices and support efficiency and sustainability through intelligent automation.

5.1 Comparsion with related works

The proposed HGHH framework achieved an F1-score of 0.991, significantly outperforming comparable predictive models applied in similar Industry 4.0 contexts. This section discusses these improvements by systematically comparing our findings with those from existing literature, as summarized in Table 1 of the Related Work section. Comparison with Wang et al. [10] and Barari et al. [11]: While both studies emphasized the importance of Big Data Analytics and integration of technologies like blockchain and AR, neither provided quantitative predictive performance nor implemented machine learning classifiers for real-time prediction. Our model, on the other hand, delivers strong empirical evidence of its effectiveness, with a nearly perfect F1-score and high accuracy, demonstrating its value not just in descriptive analytics but in proactive, real-time fault detection and prediction.

Comparison with Wang et al. [12]:

Their cloud-edge coordination model focused on performance forecasting and reported decent accuracy (~93.7%) but lacked feature transparency and required manual intervention for scheduler optimization. HGHH improves upon this by combining automatic hyperparameter optimization (via HHO and SMA) with interpretable feature selection (via FAST and CAM), yielding better generalization and automation in prediction pipelines. Furthermore, HGHH's integration of dual boosting classifiers (HGBC and LGBC) strengthens robustness in handling heterogeneous data inputs.

Comparison with Lee et al. [14]:

Their study highlighted infrastructure and security challenges in deploying AI for smart manufacturing. While they propose architectural enhancements (e.g., blockchain), they do not offer a predictive modeling framework or assess real-time performance. HGHH not only implements a fully automated, real-time predictive system, but also ensures explainability, which is critical for operator trust and industrial deployment. The inclusion of CAM-based interpretability bridges the gap between model transparency and actionable insights.

5.1.1 Why HGHH outperforms prior methods

Robustness to Noise: HGBC and LGBC are ensemble methods that naturally reduce overfitting and exhibit strong resistance to noisy data. This is particularly useful in smart factories where sensor data can be affected by external fluctuations.

Faster Convergence & Optimization: The inclusion of HHO and SMA significantly accelerates hyperparameter tuning compared to traditional grid search or manual selection. These metaheuristics intelligently explore the solution space, achieving better performance in fewer iterations.

Feature Interpretability: By applying FAST for dimensionality reduction and CAM for class-based feature activation, the HGHH model ensures that only the most meaningful features are retained and visualized, making the system more transparent and diagnosable in case of faults.

Scalability and Flexibility: HGHH's modular architecture allows it to be easily adapted to different production lines and datasets, offering a generalizable solution compared to the more context-specific systems in earlier studies.

5.2 Limitations and future work

Despite the promising results achieved in this study, several limitations must be acknowledged foremost among them is the reliance on a simulated dataset. While simulated data provide a controlled environment to rigorously evaluate the performance of our proposed hybrid framework, they do not capture the full complexity of real-world manufacturing environments. Real industrial datasets are typically characterized by:

- **Sensor noise**, leading to data inconsistencies;
- **Missing or incomplete values** due to communication errors or sensor faults;
- **Nonstationary behavior**, where machine conditions and failure patterns evolve over time;
- **Data heterogeneity**, arising from diverse equipment types and manufacturing processes.

These factors can significantly impact the accuracy and robustness of predictive models. As a result, while the proposed HGHH model achieved a high accuracy of 0.991 in this study, similar performance may not be guaranteed when applied to raw industrial datasets without preprocessing and fine-tuning. Furthermore, the synthetic nature of the dataset may not fully replicate the complex interdependencies and noise patterns found in practical settings. Therefore, the results should be interpreted as a proof-of-concept rather than a fully deployed industrial solution.

5.3 Future work

To bridge this gap, our future efforts will focus on validating the proposed framework using real-world datasets collected from active production lines. These investigations will evaluate the model's generalizability, resilience to noisy data, and ability to maintain high predictive performance under operational conditions. Moreover, we plan to integrate advanced data cleansing techniques and domain adaptation methods to improve robustness and applicability in diverse industrial contexts.

This enhanced direction will ensure that the model is not only theoretically sound but also practically deployable in Industry 4.0 smart manufacturing systems.

6 Conclusion

In the Industry 4.0 era, predictive manufacturing intelligence is one of the cornerstones of maximizing production efficiency, product quality, and system stability. Smart factories create massive data streams from sensors and production lines, generating rich potential to unearth concealed patterns and prevent failures before they occur. The bottlenecks are deriving practical knowledge from high-dimensional data, selecting proper features, and building solid predictive models. To bridge the obstacles above, an intelligent combination of sophisticated Machine Learning (ML) classifiers, Histogram Gradient Boosting Classification (HGBC) and Light Gradient Boosting Classification (LGBC), along with metaheuristic optimizer algorithms, the Slime Mold Algorithm (SMA) and the Horse Herd Optimization (HHO), was introduced within this research. These hybrids enhance models' robustness and performance by dynamically adapting hyperparameters. In addition, feature extraction techniques like FAST (Fast Correlation-Based Filter) and CAM (Class Activation Mapping) were utilized to detect the more informative input variables, remove redundancy, and increase interpretability.

Experimental outcomes verified the high predictive significance of Error Rate, Production Speed Units, and Packet Loss, as consistently identified by both FAST and CAM feature extraction techniques. These features improved the classification accuracy up to 0.991 using the HGHH model. Their dominance in the analysis highlights their central role in machine health monitoring and production efficiency assessment. While secondary features like temperature fluctuation and power consumption appeared in select model outputs, they did not demonstrate consistently high rankings and were therefore not emphasized in the primary conclusions. This reinforces the model's reliance on operational efficiency indicators and supports its suitability for real-time predictive analytics in manufacturing environments.

In contrast to traditional methods, where features are viewed as static data, the presented method considers feature contributions and interactions, facilitating accurate and dynamic fault prediction. In practical applications, the model enables the detection of faulty conditions at an early stage, minimizing unplanned downtime and maintenance costs. It optimizes resource allocation by predicting equipment inefficiencies and facilitates dynamic production scheduling. Due to the model's generalizability across production levels, the model performs well under low, medium, or high throughput conditions.

This system is applicable in various sectors, ranging from the automotive and electronics industries to heavy machinery, where it can be implemented to track equipment health, anticipate breakdowns, and streamline processes. This enables the transition towards innovative, autonomous production systems aligned with the industry 4.0 vision by facilitating informed, data-based decisions. Finally, the work presents an interpretable, scalable, and high-performing solution to the issues faced in predictive modeling and plays a crucial role in promoting intelligent manufacturing systems.

Authorship Contribution Statement

Junzhou WANG: Writing-Original draft preparation, Conceptualization, Supervision, Project administration.

Xiaojuan ZHANG: Methodology, Software.

Author Statement

All the authors have read and approved the manuscript. As stated earlier in this document, the requirements for authorship have been met, and each author believes that the manuscript represents honest work.

Ethical Approval

All authors have been personally and actively involved in substantial work leading up to the paper and will take public responsibility for its content.

References

[1] M. Javaid, A. Haleem, R. P. Singh, and R. Suman, "Enabling flexible manufacturing system (FMS) through the applications of industry 4.0 technologies," *Internet of Things and Cyber-Physical Systems*, Elsevier, vol. 2, pp. 49–62, 2022. https://doi.org/10.1016/j.iotcps.2022.05.005

[2] Y. Hu *et al.*, "Industrial internet of things intelligence empowering smart manufacturing: A literature review," *IEEE Internet Things J*, IEEE, vol. 11, no. 11, pp. 19143–19167, 2024. https://doi.org/10.1109/JIOT.2024.3367692

[3] Z. Bi, W.-J. Zhang, C. Wu, C. Luo, and L. Xu, "Generic design methodology for smart manufacturing systems from a practical Perspective, part I—Digital triad concept and Its application as a system reference model," *Machines*, MDPI, vol. 9, no. 10, p. 207, 2021. https://doi.org/10.3390/machines9100207

[4] A. Majeed *et al.*, "A big data-driven framework for sustainable and smart additive manufacturing," *Robot Comput Integr Manuf*, Elsevier, vol. 67, p. 102026, 2021. https://doi.org/10.1016/j.rcim.2020.102026

[5] C. Liu, D. Tang, H. Zhu, and Q. Nie, "A novel predictive maintenance method based on deep adversarial learning in the intelligent manufacturing system," *IEEE access*, IEEE, vol. 9, pp. 49557–49575, 2021. https://doi.org/10.1109/ACCESS.2021.3069256

[6] H. Zhang, S. Zhang, Y. Zhang, J. Liang, and Z. Wang, "Machining feature recognition based on a novel multi-task deep learning network," *Robot Comput Integr Manuf*, vol. 77, p. 102369, 2022. https://doi.org/10.1016/j.rcim.2022.102369

[7] M. Andronie, G. Lăzăroiu, R. Ștefănescu, C. Uță, and I. Dijmărescu, "Sustainable, smart, and sensing technologies for cyber-physical manufacturing systems: A systematic literature review," *Sustainability*, MDPI, vol. 13, no. 10, p. 5495, 2021. https://doi.org/10.3390/su13105495

[8] R. X. Gao, L. Wang, M. Helu, and R. Teti, "Big data analytics for smart factories of the future," *CIRP annals*, Elsevier, vol. 69, no. 2, pp. 668–692, 2020. https://doi.org/10.1016/j.cirp.2020.05.002

[9] J. Leng *et al.*, "A loosely-coupled deep reinforcement learning approach for order acceptance decision of mass-individualized printed circuit board manufacturing in industry 4.0," *J Clean Prod*, Elsevier, vol. 280, p. 124405, 2021. https://doi.org/10.1016/j.jclepro.2020.124405

[10] J. Wang, C. Xu, J. Zhang, and R. Zhong, "Big data analytics for intelligent manufacturing systems: A review," *J Manuf Syst*, Elsevier, vol. 62, pp. 738–752, 2022. https://doi.org/10.1016/j.jmsy.2021.03.005

[11] A. Barari, M. de Sales Guerra Tsuzuki, Y. Cohen, and M. Macchi, "Intelligent manufacturing systems towards industry 4.0 era," *J Intell Manuf*, Springer Nature, vol. 32, pp. 1793–1796, 2021. https://doi.org/10.1007/s10845-021-01769-0

[12] W. Wang, Y. Zhang, J. Gu, and J. Wang, "A proactive manufacturing resources assignment method based on production performance prediction for the smart factory," *IEEE Trans Industr Inform*, IEEE, vol. 18, no. 1, pp. 46–55, 2021. https://doi.org/10.1109/TII.2021.3073404

[13] J. Lee, J. Singh, M. Azamfar, and V. Pandhare, "Industrial AI and predictive analytics for smart manufacturing systems," in *Smart manufacturing*, Elsevier, 2020, pp. 213–244. https://doi.org/10.1016/B978-0-12-820027-8.00008-3

[14] H. Nhat-Duc and T. Van-Duc, "Comparison of histogram-based gradient boosting classification machine, random Forest, and deep convolutional neural network for pavement raveling severity classification," *Autom Constr*, Elsevier, vol. 148, p. 104767, 2023. https://doi.org/10.1016/j.autcon.2023.104767

[15] F. Alzamzami, M. Hoda, and A. El Saddik, "Light gradient boosting machine for general sentiment classification on short texts: a comparative evaluation," *IEEE access*, IEEE, vol. 8, pp. 101840–101858, 2020. https://doi.org/10.1109/ACCESS.2020.2997330

[16] K. Ramalingam *et al.*, "Light gradient boosting-based prediction of quality of life among oral cancer-treated patients," *BMC Oral Health*, vol. 24, no. 1, p. 349, 2024. https://doi.org/10.1186/s12903-024-04050-x

[17] M. K. Naik, R. Panda, and A. Abraham, "Adaptive opposition slime mould algorithm," *Soft comput*, Springer Nature, vol. 25, no. 22, pp. 14297–14313, 2021. https://doi.org/10.1007/s00500-021-06140-2

[18] P. V. H. Son and L. N. Q. Khoi, "Optimization in construction management using adaptive opposition slime mould algorithm," *Advances in Civil Engineering*, Wiley, vol. 2023, 2023. https://doi.org/10.1155/2023/7228896

[19] S. Basu, S. Kumar, and M. Basu, "Horse herd optimization algorithm for economic dispatch problems," *Engineering Optimization*, Taylor & Francis, vol. 55, no. 5, pp. 806–822, 2023. https://doi.org/10.1080/0305215X.2022.2035378

[20] F. MiarNaeimi, G. Azizyan, and M. Rashki, "Horse herd optimization algorithm: A nature-inspired algorithm for high-dimensional optimization problems," *Knowl Based Syst*, Elsevier, vol. 213, p. 106711, 2021. https://doi.org/10.1016/j.knosys.2020.106711

[21] L. Li, "Click-Through-Rate Prediction Using Deep Neural Networks and Efficient Channel Attention Mechanisms," *Informatica*, Slovenian Society Informatika, vol. 49, no. 19, 2025. https://doi.org/10.31449/inf.v49i19.7947

[22] O. A. Vilca-Huayta, "Logistic Sigmoidal and Neural Network Modeling for COVID-19 Death Waves," *Informatica*, Slovenian Society Informatika, vol. 49, no. 19, 2025. https://doi.org/10.31449/inf.v49i19.7476

[23] H. Liu, P. He, Z. Lu, J. Li, and Z. Lu, "Deep Learning-Based Defect Identification for Transmission Tower Bolts: Optimization of YOLOv3 and ResNet50 Algorithms," *Informatica*, Slovenian Society Informatika,. 49, no. 19, 2025. https://doi.org/10.31449/inf.v49i19.7872

PESWS-LGBM: A Hybrid Swarm Optimization and LightGBM Framework for Real-Time Production Scheduling in Smart Factories

Minghui Du[1*], Kexin Wang[1], Zhang Ran[2]
[1]School of Information Engineering, Xinxiang Vocational and Technical College, Xinxiang, Hennan,453006, China
[2]School of Architecture, Xinxiang Vocational and Technical College, Xinxiang, Hennan,453006, China
E-mail: taecherdu@163.com, wkx1102@126.com, 787415627@qq.com
*Corresponding author

Keywords: production scheduling, optimization, smart factories, hybrid algorithm, AI

Received: June 16, 2025

The smart factory sector has been a frontrunner in adopting machine learning (ML) technologies to enhance production systems and enable real-time decision-making. However, challenges remain in translating raw sensor data into actionable scheduling strategies for fully autonomous operations. To address this issue, this research proposes a novel hybrid framework, the production-based Elephant Swarm Water Search-Driven Light Gradient Boosting Machine (PESWS-LGBM), which integrates metaheuristic optimization with predictive modeling for real-time production scheduling. The model not only identifies key process parameters (e.g., vibration, power usage, cycle time) but also dynamically generates optimized scheduling decisions, including task sequencing, job-to-machine assignments, and time allocations. These decisions are guided by a dual-stage process in which the LGBM component predicts scheduling performance, and the PESWS component refines scheduling configurations to minimize makespan, reduce job tardiness, and maximize machine utilization. The dataset based on real-time industrial sensor data was preprocessed using noise filtering, missing value imputation, and feature scaling. Experimental results show that PESWS-LGBM significantly improves scheduling outcomes, lowering downtime and material loss while increasing Overall Equipment Effectiveness (OEE). The proposed model achieved strong performance metrics, including accuracy (0.96), Precision (0.91), recall (0.98), and F1-score (0.94). These findings validate the effectiveness of hybrid intelligent systems in enabling adaptive scheduling and improving operational efficiency in smart manufacturing environments.

Povzetek: Za prilagodljivo razporejanje v pametnih tovarnah je predlagan hibrid PESWS-LGBM, kjer LGBM napoveduje učinkovitost urnikov, PESWS pa optimizira zaporedje opravil, dodelitve strojev in časovne okvire.

1 Introduction

The rapid evolution of Industry 4.0 has transformed the manufacturing landscape by emphasizing smart factories with interconnected systems, real-time data collection, and advanced automation. In such an environment, production scheduling has become a crucial enabling function for utilizing resources, maintaining continuous operations, and ensuring timely deliveries. Traditional scheduling methods typically rooted in static heuristics or a rigid optimization framework struggle to keep pace with the more volatile and complex contemporary industrial operational conditions [1]. Smart factories utilize a network of embedded sensors, IoT devices, and Cyber-Physical Systems (CPS) that capture endless amounts of process-level data. This data provides a real-time snapshot of machine availability, energy usage, labor utilization, material flow, and unforeseen disruptions like machine failures or supply chain delays. Consequently, scheduling is no longer a one-time act but is a continuous act that requires dynamic and adaptive responses to an ever-evolving production landscape [2]. The Machine Learning (ML) revolution provides a solution to the complexities of scheduling. ML can detect patterns, learn from the past, and predict future goals to make intelligent systems that can adjust schedules in real time, autonomously. Unlike standard optimization methods, ML-driven scheduling systems can accommodate high-dimensional data and non-linear dependencies to be flexible and robust when problems arise [3]. Artificial intelligence (AI) enhances smart manufacturing by enabling predictive maintenance and automated quality control. These advancements reduce downtime and improve

efficiency, supporting real-time production scheduling. AI-driven strategies like deep reinforcement learning boost scheduling flexibility and adaptability [4]. These systems leverage the predictive capabilities of machine learning and the search capabilities of metaheuristics to generate executable, high-quality schedules. Specifically, these models provide a way to optimize the sequencing of tasks, job-to-machine assignments, and timeslot assignments, while also taking feedback from the shop floor to continuously assess and refine schedules [5]. Intelligent mechanical manufacturing supports rapid market response through AI-driven fault prediction and anomaly detection. These technologies enhance scheduling accuracy and adaptability in smart factory environments [6]. Real-time scheduling plays a crucial role in environments where delayed task execution leads to inefficiencies or obsolescence. This highlights the need for adaptive scheduling mechanisms that respond promptly to dynamic operational conditions in smart factories [7]. As DTs are not bound to a prescribed plan as ERP systems do, they provide higher velocity definitions and execution accuracy of scheduling under uncertainty [8]. Ultimately, the combination of intelligent models, real-time sensor data, and digital twin platforms has transformed planning and scheduling in production, moving from reactive scheduling to actively optimizing or adapting. Increasing complexity in manufacturing paired with ML, metaheuristics, and virtual modeling provides a compelling route to self-organizing factories and resilient operations [9].

Research questions

RQ1: Can the proposed PESWS-LGBM hybrid framework effectively improve production scheduling accuracy and overall equipment effectiveness (OEE) in smart factory environments using real-time industrial data?

RQ2: How does the PESWS-LGBM model compare to existing optimization methods (e.g., DT-DQL, MM-PSO, RL) in terms of computational efficiency, adaptability, and performance metrics such as accuracy, precision, recall, and F1-score?

The contribution of the study is as follows,

- A novel hybrid framework is created to improve the efficiency of the production scheduling system. The study presents the Production-based Elephant Swarm Water Search Driven Light Gradient Boosting Machine (PESWS-LGBM) to identify the key process factors, which open the door to adaptive scheduling and workflow modifications.
- This proposed methodology enhances production efficiency by processing data in real-time and making appropriate decisions.
- Pre-processing steps such as noise filtering, missing value imputation, and feature scaling were used to clean and standardise the dataset, which was derived from real-time industrial data.
- By lowering downtime, allowing proactive modifications, increasing overall equipment effectiveness (OEE), and minimising material loss.

2 Related work

According to the theoretical point of view, scheduling is best understood as a problem-solving exercise in which the production planner dealing with improbability, bottlenecks, and vibrant events. This optimisation problem is hard and separates it from the area of manufacturing planning and control systems [10]. The optimisation community agrees that precise production scheduling is a notoriously difficult problem, with the majority of cases being deemed NP-hard. Not to add that it differs significantly from the typical planning challenges [11]. Scheduling uses accurate data from the shop floor to create schedules in contrast to production planning, this uses aggregate data and presents plans on extended or temporary time range [12]. Scheduling computational methods, in contrast to planning optimisation techniques, aims to minimise time-based performance metrics which are susceptible to numerous distribution boundaries rather than the total cost. Optimal approaches become intractable when the degree of uncertainty rises with decreasing time horizons. Theoretical scheduling problems have prompted the proposal of several estimates and optimisation methods [13]. The reduced processing costs of estimation methods make them more suitable for application on actual manufacturing floors. In the last 20 years, a new trend has developed: using DSSs for full-scale production planning. Software for enterprise resource planning (ERP) or material requirements planning (MRP) can benefit from these solutions as supplemental tools [14]. By integrating state-of-the-art operational research methods, they hope to create distribution networks or shop floor roadmaps. Although these methods are sometimes seen as practical implementations of operational research theories supported by IT and can be useful tools for shop floor control, they are rarely effective when used in practice. To counteract ERP systems' flaws, a lot of scientific effort has gone into developing individualised decision support systems (DSSs) for planning. Table 1 represents related works.

Table 1: List of related studies

Ref	Objectives	Methods	Data Types Used	Complexity	Performance Metrics	Limitation
[15]	This research examines multi-project planning in the assembling procedure for ETO components.	Machine learning	Real-world flexible job-shop data	Medium; tested on 10–12 parts and 8 machines	Total overdue time by ~15%; machine utilization by 10–12%	Connecting efficient procedures with manufacturing tools, as well as process scheduling.
[16]	The study intends to deploy a method of optimization in smart manufacturing systems for co-optimizing the functioning of several manufacturing facilities to meet demands for different commodities.	Optimization technique	Mixed industrial datasets	Not evaluated for scheduling; higher computation due to deep nets	N/A (focus is interpretability)	The scheduling consequences are extremely dependent on the componentseparation decisions.
[17]	In this research, a genetic algorithm is employed to create production times for an enterprise that is adaptable.	Internet of things	NA	NA	N/A	Optimizing large-scale production schedules with numerous variables and constraints can be computationally expensive, especially in real-time.
[18]	This research developed an optimization framework for improving enterprises' manufacturing schedules.	Optimization algorithm	Sensor streams, process logs	Scalable but not real-time optimized	N/A (control-focused)	As the size and complexity of production systems increase, the computational requirements of hybrid algorithms can become prohibitively expensive
[19]	In this research, the genetic algorithm is employed to locate the optimal scheduling approach for the complicated job-shop organization issue, with the number of delayed jobs, overall overdue duration, task completion time, thorough load rate, and the highest load rate of the equipment serving as arranging algorithm effectiveness indications.	Deep learning	Synthetic & small-scale real factory data	Low–medium; single-machine N ≤ 50 jobs	Total weighted lead time by 8–12%, tardiness by 10%	Smart factories often involve complex production systems with multiple variables, constraints, and uncertainties, making it challenging to develop effective optimization algorithms
[20]	In this research offer a hybrid computational architecture and its incorporation into a precision production scheduling platform used in a Greek metal forming industry.	DT technology	Simulated DT sensor streams	Scales to small lots; case study on rolling mill	RL-DQN achieved ~95% of optimal baseline within <1000 episodes	The success of any optimization algorithm depends on the availability of accurate and complete data.
[21]	It examines trends in AI-based planning systems and some of the often used AI methodologies.	Artificial intelligence	Benchmark flow-shop instances + energy use	High; tested up to 20 machines, 100 jobs	Makespan by ~18%, energy by ~22%	The effectiveness of hybrid algorithms relies heavily on high-quality and real-time data, which can be difficult to obtain in practice
[22]	The purpose of the research is to examine current scientific research on the planning challenge, taking into account the use of the DT strategy and the ZDM paradigm to accomplish self-management while reducing or eliminating the requirement for human interaction.	ZDM model	Simulated production planning stream	Medium; training requires ≈1000 episodes	Throughput by 12%, lead time by ~9%	Accurately modeling complex production processes, including interdependencies between operations, machine capacities, and resource constraints, can be challenging.
[23]	According to this research, the more common strategies for solving scheduling issues are optimizing particle swarms, neural network training, and reinforcement learning.	Particle swarm optimization	Sensor health data, machine logs	Medium; tested on simulated 4-machine shop	Machine downtime by ~15%, tardiness by ~10%	Integrating hybrid algorithms with existing production planning and control systems can be complex and require significant investment in infrastructure and training.

3 Materials and methods

Each record corresponds to a snapshot of machine activity, characterized by various sensor readings and performance indicators. These raw features were subsequently transformed into scheduling-relevant instances using preprocessing techniques. Table 2 below summarizes the key features present in the dataset, along with their descriptions and relevance to production scheduling. These features were later aggregated into synthetic job instances based on time-window segmentation, enabling the simulation of job-shop scheduling problems.

Table 2: Dataset features

Feature Name	Description
timestamp	Real-time data capture in minute-level intervals
Machine id	Unique identifier for each machine
Machine type	Type of production equipment
temperature	Machine temperature (°C)
Vibration level	Vibration intensity reflects wear or misalignment
Power consumption	Energy usage in kilowatts (kW)
pressure	System pressure in pascals (Pa)
Material flow rate	Speed of material movement through the system
Cycle time	Duration of one production cycle (seconds)
Error rate	Proportion of defective products in the cycle
downtime	Machine inactivity time (minutes)
Maintenance flag	Indicates if maintenance is required (0 = No, 1 = Yes)
Efficiency score	Overall production efficiency (0 to 100)
Production status	Binary indicator of efficiency (0 = Inefficient, 1 = Efficient)

3.2 Preprocessing

Preprocessing is the process of cleaning and standardizing raw data for analysis. Techniques like noise filtering, missing value imputation, and feature scaling enhance data quality, ensuring accuracy and consistency in ML models. The raw sensor data were segmented into fixed time windows to form individual job instances, each associated with a specific machine and operational snapshot. Statistical aggregation techniques (e.g., mean, max) were applied to features such as temperature, vibration, and cycle time. These processed job records were then labeled based on production status and used to simulate scheduling tasks for model training.

i. Noise filtering

This noise filtering is applied to the input dataset to enhance accuracy in production system optimization. A Gaussian filter is utilized to reduce sensor noise, mitigating disruptions in data readings. By adjusting standard deviation and mean values, the method minimizes distortions, ensuring reliable data for real-time decision-making and workflow adjustments. These are represented in equations (1) and (2).

$$I^G(i,j) = I' \times (i,j) = I'\left(\frac{1}{2\pi\sigma^2} e^{\frac{(-i^2-j^2)}{2\sigma^2}}\right) \quad (1)$$

$$\sigma^2 = E(X^2) - [E(x)]^2 \quad (2)$$

In these particular situations, the $I^G(i,j)$ represents the filtered sensor data after the application of the Gaussian noise filtering method. Then σ^2 represents noisy sensor data variance. The parameters $iandj$ are the displacements from the origin in the x and$y$ directions, respectively. $E(X^2)$is the value of the sensor data measured at a point. The filtering method used by the model facilitates data enhancement, which leads to superior accuracy when making real-time decisions and adapting workflow systems.

ii. Feature scaling

Industrial sensor data varies in units and magnitudes, requiring feature scaling for balanced ML contributions. Common techniques include normalization (Min-Max Scaling) and standardization (Z-score Scaling), to standardize data ranges and distributions effectively.

Min-Max Scaling normalization adjusts data to a fixed range [0,1] using equation (3). This ensures uniform feature contribution.

$$Q' = \frac{Q - Q_{min}}{Q_{max} - Q_{min}} \quad (3)$$

Z-score Standardization (Scaling) – Converts data into a normalized distribution with an average of 0 and distribution range of 1, as shown in equation (4).

$$Q' = \frac{Q - \mu}{\sigma} \quad (4)$$

Where, normalized data point is represented as (Q'), original value of the variable as (Q), mean of the dataset as (μ), and standard deviation of the dataset as (σ).

iii. Missing value imputation

The system is required to manage incomplete industrial real-time AI-driven production scheduling system sensor data caused by transmission errors or sensor errors. Missing data can affect ML model accuracy and decision-making. Techniques like mean/median imputation replace missing values with dataset averages, interpolation estimates values based on trends, and regression imputation predicts missing values using statistical models, ensuring reliable and consistent data analysis. These preprocessing steps improve data quality, reduce errors, and ensure that the ML model receives clean, structured, and reliable input for accurate predictions and decision-making.

3.3 Hybrid model - *Production Based Elephant Swarm Water Search (PESWS)- Light Gradient Boosting Machine (LGBM)*

The PESWS-LGBM model integrates ML and metaheuristic optimization for AI-driven production optimization. This model predicts critical process parameters and fine-tunes workflow using adaptive exploration-exploitation mechanisms, ensuring real-time scheduling adjustments, resource efficiency, and improved OEE in smart factories.

The PESWS-LGBM model incorporates predictive learning and metaheuristic-based optimization into the scheduling module of the real-time production planning and scheduling framework. In this model, the PESWS algorithm designs comprehensive schedules by solving three main aspects of scheduling: (1) sequence of tasks is the order in which jobs are executed, (2) assignment to machines, and (3) timing of work start and finish for each task. The model optimizes scheduling outputs to achieve low makespan, low tardiness of jobs, and high machine usability, thereby improving Overall Equipment Effectiveness (OEE).

The PESWS-LGBM model is designed to generate full production schedules by integrating predictive learning with metaheuristic optimization. Specifically, it maps real-time input features such as temperature, vibration, cycle time, and energy usage to key scheduling outputs, including Task sequencing (the execution order of jobs), Job-to-machine assignments, Time window allocations (start and end times), and resource availability constraints. This mapping enables the system to optimize scheduling objectives such as minimizing makespan, reducing job tardiness, lowering downtime, and maximizing machine utilization. The framework works in a dual-stage fashion: LGBM first predicts performance outcomes based on input configurations, and PESWS then iteratively searches the solution space for optimal schedule configurations guided by those predictions.

The LGBM portion of the PESWS-LGBM model is treated as a multi-class classifier, where the target labels are some categories of scheduling outcome. Labeling comes from the performance class of the scheduling configuration. Class 0 shown in (2.1) represents Low efficiency (high makespan, high downtime); Class 1 represents Moderate efficiency; Class 2 represents High efficiency (low makespan, low tardiness, high OEE). For each candidate schedule produced by PESWS, LGBM evaluates the candidate scheduling configuration and classifies it as one of the potential performance classes (0, 1, or 2). This classification is leveraged as a multi-class fitness score for the optimization. Through iterations, PESWS will evolve candidate schedules into the "high-efficiency" class (class 2). Dataset had many IoT-driven attributes. LGBM used specified importance ranking where it was able to select important feature attributes such as vibration level, cycle time, power consumption, and downtime. These features deliver PESWS optimizers parameters which will directly govern job sequencing, machine assignment, tracking priority. Further, this integration confirms that we are using scheduling modes that take into account data derived operational attributes.

Light Gradient Boosting Machine (LGBM)

LGBM is an enhanced-performance, gradient-boosting framework based on ML. It is designed to improve efficiency and scalability compared to traditional boosting algorithms like XGBoost. LGBM enhances training speed by using histogram-based algorithms, reducing memory consumption, and employing a leaf-wise growth strategy with depth constraints to prevent overfitting.

LGBM optimizes decision tree learning with four key techniques. ML converts continuous features into discrete bins, reducing memory usage and speeding up computations. Gradient-Based One-Side Sampling (GOSS) retains steep-gradient instances while randomly sampling minimal-gradient ones, improving efficiency without significant accuracy loss. Exclusive Feature Bundling (EFB) groups mutually exclusive features, reducing dimensionality and memory consumption. The leaf-wise growth strategy selects the leaf with the highest information gain for expansion, improving model accuracy, though a depth constraint is needed to prevent overfitting. These optimizations make LGBM highly efficient for large datasets.

Training dataset is given by,$W = \{(W_j, z_j)\}_{j=1}^{n}$. The goal is to find an approximate function $\hat{e}(w)$that closely estimates $e^*(w)$to minimize expected values of specific loss operations $(z, e(w))$, The objective function mathematical representation is shown in equation (5).

$$\hat{e}(w) \arg\min_{e} F_{z,W} K(z, e(w)) \tag{5}$$

This function minimizes the expected loss operation to optimize predictions. Equation (6) represents the additive learning formula.

$$e_S(W) = \sum_{s=1}^{S} e_s(W) \tag{6}$$

LGBM builds a model as a sum of regression trees. Leaf weight optimization is represented in equation (7).

$$\omega_i^* = -\frac{\sum_{j \in J_i} h_j}{\sum_{j \in J_i} g_j + \lambda} \tag{7}$$

Here, $h_j and g_j$are the primary and secondary gradients of the loss operation, optimizing the tree's leaf nodes. Tree structure optimization (Extreme Values of Γ_S^*) is denoted by equation (8).

$$\Gamma_S^* = -\frac{1}{2}\sum_{i=1}^{I}\frac{(\sum_{j\in J_i} h_j)^2}{\sum_{j\in J_i} g_j+\lambda} \quad (8)$$

Equation (9) determines the best feature split during tree growth.

$$H = \frac{1}{2}\left(\frac{(\sum_{j\in J_i} h_j)^2}{\sum_{j\in J_i} g_j+\lambda} + \frac{(\sum_{j\in J_q} h_j)^2}{\sum_{j\in J_q} g_j+\lambda} + \frac{(\sum_{j\in J} h_j)^2}{\sum_{j\in J} g_j+\lambda}\right) \quad (9)$$

Where, final model after$S$ boosting iterations is $e_S(W)$, $e_s(W)$ is the weak learner at iteration (s), optimal leaf weight is (ω_i^*), regularization parameter (controls complexity) is (λ), optimized tree structure value is (Γ_S^*), set of samples in the parent node is (J), set of samples in the right child node is (J_i), and gain function, measures the quality of a split (H).

LGBM's efficient structure enables fast training and accurate predictions, making it ideal for large-scale ML tasks. The hybrid algorithm for production scheduling system optimization improves training speed, reducing memory consumption, by utilizing a leaf-wise growth strategy. It efficiently predicts critical process parameters, enabling real-time adaptive scheduling, workflow adjustments, and enhanced overall production effectiveness. In the context of scheduling, LGBM is not merely a predictor of feature importance. Rather, it evaluates the predicted performance of candidate scheduling configurations. These predictions serve as fitness scores that guide the PESWS optimizer in refining the schedule. Each sample in the training set represents a synthesized job-machine-time instance, constructed from the preprocessed sensor data. Thus, LGBM functions as a surrogate performance evaluator that estimates the expected quality of scheduling decisions proposed by PESWS.

Production Based Elephant Swarm Water Search (PESWS)

The PESWS algorithm is employed as a metaheuristic optimization approach to fine-tune process parameters within the AI-enabled production system. The algorithm mimics the collective intelligence and social behavior of elephant swarms, optimizing the system by minimizing downtime, material waste, and inefficiencies. The PESWS algorithm is an innovative version that was inspired by the herd behavior of elephants and their water-searching behavior. Compared to traditional swarm optimizers, PESWS weighs exploration and exploitation differently, with inertia weight adjustment and movement that is context aware, exploiting both local and global optimal values. It is helpful to visualize "production units" as elephant herds. Each group of elephants is allowed to iteratively update scheduling parameters based on performance feedback. This structure enhances convergence speed and robustness to local optima while allowing better processing of high-dimensional scheduling variables. Keep in mind that PESWS is not simply a tuning optimization, but rather a structurally distinct metaheuristic for adaptive real-time production scheduling.

Elephant Groups as Process Solutions

In the optimization framework, each elephant group represents a potential solution for process optimization, adapting production parameters dynamically to enhance efficiency and minimize resource consumption. Each elephant group represents a potential configuration of production parameters, such as scheduling, resource allocation, and workflow adjustments.

The position of an elephant group in the search space is defined by equation (10).

$$U_{j,c}^s = U_{j1,}U_{j2,} \dots \dots \dots U_{jc} \quad (10)$$

Where, $U_{j,c}^s$ represents the **d-dimensional** position of the j^{th} **elephant group** at iteration s.

Each elephant group encodes a candidate scheduling solution, where position vectors represent a complete job-machine-time mapping. The algorithm evaluates each group based on key scheduling KPIs such as makespan, average tardiness, and idle time. The best-performing configurations are selected and evolved across iterations.

Velocity Update Based on Best Found Solutions

The velocity of each elephant group is adjusted using local and global best solutions, ensuring adaptive learning that refines production strategies for optimal scheduling and reduced operational inefficiencies. The velocity of each elephant group is updated to optimize decision-making based on local and global search strategies represented in equation (11).

$$U_{j,c}^{s+1} = U_{j,c}^s * \omega^s + \varepsilon \odot (H_{best,c}^s - W_{j,c}^s) \quad (11)$$

$$U_{j,c}^{s+1} = U_{j,c}^s * \omega^s + \varepsilon \odot (H_{besti,c}^s - W_{j,c}^s) \quad (12)$$

Where the global best solution (optimal production setting) is $(H_{best,c}^s)$, the local best solution (best found by a specific elephant group) is $(H_{besti,c}^s)$, the inertia weight for balancing exploration and exploitation is (ω^s), if $rand \leq o$ [for global search], the random factor affecting movement direction is (ε) .

Objective Function

The objective of the PESWS optimization process is to generate a schedule that minimizes overall makespan, reduces machine idle time, and satisfies job precedence and

resource constraints. To achieve this, we define a multi-objective loss function using Equation (13):

$$L = \alpha.Makespan + \beta.Total_{Tardiness} + \lambda.Constraint_Violation_Penalty \quad (13)$$

Where:

- Makespan is the total completion time of all jobs,
- Total Tardiness is the cumulative delay beyond job due times.
- Constraint Violation Penalty accounts for overlap, sequence violation, or machine overloading.
- α, β, and λ are tunable weights that balance these objectives.

Tie PESWS to Scheduling Elements

In the context of production scheduling, each elephant group's position vector Uj,cU_{j,c}Uj,c represents a complete scheduling configuration, which includes Job sequencing, Job-to-machine assignments, and Start and end times for each task.

The velocity update equations guide how the current schedule (position) is modified in the search space. For example, a position shift may correspond to reordering jobs, reallocating a task to a different machine, or adjusting its time slot. The global and local best solutions are determined based on the fitness value calculated from the scheduling objective function $\{L\}$. This ensures that updates are directed toward more efficient and constraint-satisfying schedules.

Penalty Formulation

Constraint violations such as two jobs overlapping on the same machine or violating precedence rules are penalized using Equation (14):

$$Penalty_{Overlap} = \sum_{j,i} \delta_{ji} . D \quad (14)$$

Where δ_{ji} if Job j and Job i overlap on the same machine, and D is a fixed penalty constant. These penalty terms are included in the total loss function to guide the optimization toward feasible schedules.

Updating Production Parameters

The algorithm continuously updates critical production parameters based on optimized solutions, enabling real-time workflow adjustments in environments to minimize downtime, improve efficiency, and enhance overall process performance. The new production system configuration is updated and is denoted by equation (15).

$$\omega^s = \omega_{max} - \left\{\frac{\omega_{max}-\omega_{min}}{s_{max}}\right\} \times s \quad (15)$$

This process iteratively refines ML models to predict optimal production workflow. PESWS updates it **dynamically** using equations (16) and (17).

$$W_{j,c}^{s+1} = U_{j,c}^{s+1} + U_{j,c}^{s} \quad (16)$$

$$o(s) = o_{max} - \left(\frac{o_{max}-o_{min}}{s_{max}}\right) * s \quad (17)$$

Where, $o_{max} = 1$, $o_{min} = 0$, $s_{max}$is is the maximum iteration count.

This approach ensures a stronger global search initially and a more refined local search as iterations progress.

Velocity and Position Updates in PESWS

Velocity and position update in PESWS remains the same; **manage search adaptability and**new production system, which is stated by following equations (18) and (19).

$$W_{j,c}^{s+1} = U_{j,c}^{s} * \omega^s + \epsilon \odot (H_{best,c}^{s} - W_{j,c)}^{s} \quad (18)$$

$$W_{j,c}^{s+1} = U_{j,c}^{s+1} + U_{j,c}^{s} \quad (19)$$

Where, ($W_{j,c}^{s+1}$) - Updated position at time ($s+1$), Current position at time - (s), Inertia weight controlling exploration-exploitation balance - (ω^s), Updated velocity used for position update - ($U_{j,c}^{s+1}$), Current velocity at time - (s).

Figure 2 compares velocity and position updates in **(a) PSO**(Particle Swarm Optimization) and **(b) PESWS**. In **PSO**, particle movement is influenced by **current velocity**, **particle memory (**$H_{besti,c}^{s}$**)**, and **swarm memory (**$H_{best,c}^{s}$**)**, ensuring global and local search. In P**ESWS**, an adaptive mechanism adjusts movement based on a probability factor($rand$), and enhances the exploration-exploitation balance, preventing premature convergence. It improves

production efficiency by fine-tuning workflow parameters more effectively than static PESWS.

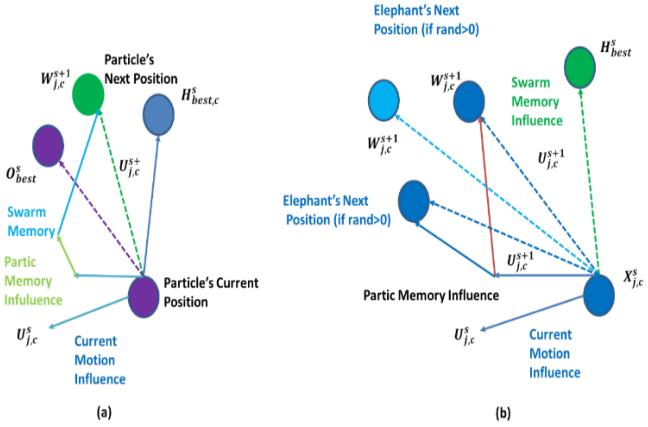

Figure 2: Visualization of velocity and position updates in (a) PSO (b) PESWS approach.

The PESWS-LGBM framework optimizes complete production schedules by predicting and refining job start times, task sequences, and machine assignments. LGBM estimates scheduling KPIs such as expected downtime, machine load, and makespan based on real-time input data, and PESWS adjusts scheduling configurations to minimize delays and maximize efficiency. The LGBM is the automated performance assessor. For each schedule produced with PESWS, the LGBM model predicts important scheduling KPIs. These predictions are taken as the fitness function within the PESWS optimization loop, meaning that the PESWS logic does not suffer the costs of simulated evaluations and hence can more quickly converge on an optimal schedule. Thus, PESWS generates and decides scheduling decisions, and LGBM will provide data-driven performance feedback on those scheduling decisions. Adaptive scheduling is the aspect of the model that allows for updates to the schedule results based on current impact features from the production context. The input features can be real-time sensor inputs such as vibration, temperature, and cycle time. The PESWS-LGBM framework continually assesses the performance of the schedule it produced using the predicted KPIs and dynamically re-optimizes the ordering of tasks, job-to-machine assignments, and time buckets. The nature of the re-optimization loop allows for real-time adjustment to schedules at the occurrence of disturbances, such as machine failure and load imbalance. Algorithm 1 shows the steps involved in production by integrating PESWS-based parameter tuning with LGBM, enhancing predictive accuracy and adaptive scheduling for efficiency. This approach ensures that the PESWS-LGBM model outputs executable production schedules, not alone priority scores or predictions. These schedules are structured in a job–machine–time matrix format and are validated in a digital twin environment to ensure feasibility and responsiveness. The framework dynamically adapts to changing input features, allowing real-time rescheduling and proactive adjustment of job flows.

Algorithm 1: PESWS-LGBM for Production Scheduling Optimization

Input:
- *Dataset D (production data with scheduling targets)*
- *Population Size = 30*
- *Max Iterations = 100*
- *ω_max = 0.9 (initial inertia weight)*
- *s_max = 0.5 (maximum step size)*
- *β = 0.4 (influence of water source)*
- *Number of Clans = 3*

Output:
- *Optimized LGBM model with best parameters*
- *Improved production scheduling outcome*

Step 1: Initialize Population

For each elephant i in population (i = 1 to 30):
- *Randomly initialize position Xi = [x1, x2, x3, x4] ∈ [0,1]*
- *Set velocity Vi = 0*
- *Evaluate fitness Fi = objective(Xi)*

- Store global best position X_best with minimum Fi
- Set water_density = 0.7

Step 2: Optimization Loop (Repeat for 100 iterations)

For iteration t = 1 to 100:
For each elephant i:
- *Update velocity:*
  *Vi = ω * Vi + β * rand(0,1) * (X_best - Xi)*
- *Update position:*
  Xi = Xi + Vi
- *Apply bounds: Xi ∈ [0,1]*
- *Evaluate new fitness Fi*
- *Update X_best if Fi improves*

- Divide elephants into 3 clans (10 elephants each)
For each clan:
- *Identify clan leader (best Fi in clan)*
- *For each non-leader elephant:*
  - *Move toward leader:*
    *Xi = Xi + rand(0,1) * (leader - Xi)*
- *Replace worst member with random solution*

- Optionally update ω:
*ω = ω_max * (1 - t / max_iterations)*

Step 3: Extract Best Hyperparameters

From X_best = [x1, x2, x3, x4]:
*- num_leaves = 20 + int(x1 * 100) → e.g., 20 to 120*

*- learning_rate = 0.01 + x2 * 0.19 → e.g., 0.01 to 0.2*

*- max_depth = 3 + int(x3 * 10) → e.g., 3 to 13*

*- min_data_in_leaf = 10 + int(x4 * 90) → e.g., 10 to 100*

Step 4: Train LGBM Model

- Train LightGBM using optimized hyperparameters on dataset D

- Evaluate performance (e.g., accuracy, OEE, runtime, etc.)

Return:

- Best LGBM model

- Best production scheduling metrics

End

3.4 Digital twin construction

A virtual replica of the physical production environment was created using the real-time dataset that contains sensor-derived parameters such as temperature, vibration, cycle time, error rate, and machines' operational states. The data are constantly synchronized between the physical system and the virtual model. The DT models machine behaviors and production line states under different scheduling strategies. It is effectively a sandbox environment for the PESWS optimizer to explore many scheduling options prior to real-world execution. To assess the adaptiveness and performance of the PESWS-LGBM model, it is compared against static scheduling methods using First-Come-First-Serve (FCFS), with a definition of fixed job priorities. The comparison is different from the benchmark because the PESWS-LGBM model dynamically adapts schedules during the simulation runs, similar to how sensor feedback changes.

Twin Pairing: The virtual twin communicates with the physical system through data feedback loops. The changes in the physical sensors are reflected in the twin, and the optimized schedules determined by the PESWS-LGBM model in the twin are pushed back to the physical system for execution in real-time.

The final output of the PESWS-LGBM model is a fully structured production schedule represented in matrix form. In this matrix, each row corresponds to a job or task, while each column represents a specific machine. The individual cells within the matrix contain detailed scheduling information, including the assigned machine, start time, and end time for each job. This structured format facilitates the execution of scheduling decisions in real manufacturing environments. To better interpret and validate these outputs, the matrix was visualized as a Gantt chart or job-shop timeline within the digital twin simulation. These visual representations enabled the evaluation of the model's feasibility, responsiveness, and performance in terms of resource utilization, task sequencing, and adherence to time constraints. As shown in Table 3, the PESWS algorithm dynamically tunes the hyperparameters of the LightGBM model.

Table 3: LightGBM Hyperparameters Tuned by PESWS

Hyperparameter	**Symbol**	**Search Range**	**Description**	**Mapping from X_best (xi ∈ [0, 1])**
Number of Leaves	num leaves	20 – 120	Controls complexity of individual trees. Higher values allow more splits.	Num leaves = int(20 + xi × 100)
Learning Rate	Learning rate	0.01 – 0.2	Shrink's contribution of each tree; lower values need more trees.	Learning rate = 0.01 + xi × 0.19
Maximum Tree Depth	Max depth	3 – 13	Limits the maximum depth of trees to control overfitting.	Max depth = int(3 + xi × 10)
Min Data in Leaf	Min data in leaf	10 – 100	Minimum number of data points per leaf. Controls tree growth.	Min data in leaf = int(10 + xi × 90)
Feature Fraction	Feature fraction	0.6 – 1.0	Fraction of features used per tree (random subset for each tree).	Feature fraction = 0.6 + xi × 0.4 (optional)
Bagging Fraction	Bagging fraction	0.5 – 1.0	Fraction of data used for each boosting round (subsampling).	Bagging fraction = 0.5 + xi × 0.5 (optional)
Lambda L2	Lambda l2	0 – 10	L2 regularization term to avoid overfitting.	lambda_l2 = xi × 10

4 Results and discussion

This section describes the experimental design and performance evaluation of the PESWS-LGBM approach. It details the performance measures, and comparison analysis, identifying the model's effectiveness in optimizing hybrid model-driven factory structures.

4.1 Experimental setup

The research was conducted on a Windows 10 laptop equipped with an Intel i5 processor and 16 GB of RAM. All experiments were implemented in Python 3.12.1, using well-established libraries for machine learning and optimization. To ensure reproducibility and fairness, each model was executed over 10 independent runs, and a fixed random seed was applied to control for variability across experiments. Performance metrics (accuracy, precision, recall, F1-score, makespan, tardiness, flow time, and machine utilization) were reported as mean values, and statistical significance tests were applied to verify that the improvements of the PESWS-LGBM model over baseline methods were not due to random variation.

The ROC-AUC curve (Figure 3) demonstrates the strong classification performance of the PESWS-LGBM model, achieving an AUC of 0.97. This high value indicates excellent discrimination between scheduled and unscheduled production events. The curve's robustness further confirms the model's reliability, even under class imbalance, by effectively balancing true positive and false positive rates across thresholds.

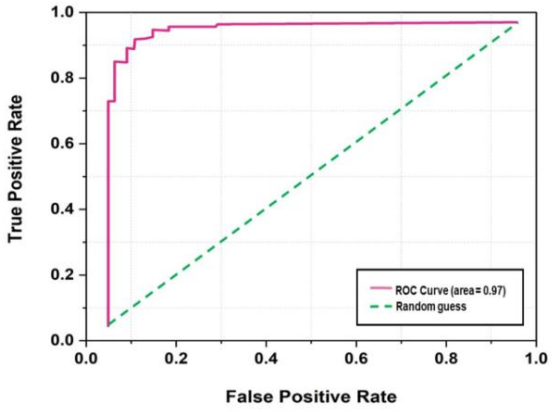

Figure 3: ROC-AUC Curve

Figure 4 illustrates the comparative performance of the PESWS and PESWS-LGBM (proposed) models across three scheduling difficulty levels Low, Medium, and Moderate using four key metrics: makespan (Figure 4 (a)), tardiness (Figure 4 (b)), flow time (Figure 4 (c)), and machine utilization (Figure 4 (d)). Across all difficulty levels, the PESWS-LGBM model consistently outperforms the baseline PESWS model. It achieves lower makespan and average tardiness, indicating more efficient job sequencing and reduced delay. Similarly, flow time per job is shorter under PESWS-LGBM, demonstrating improved throughput. Notably, machine utilization is also higher for the proposed model, reflecting better resource allocation and reduced idle time. This overall improvement confirms the efficacy of the hybrid PESWS-LGBM approach in dynamic production scheduling scenarios.

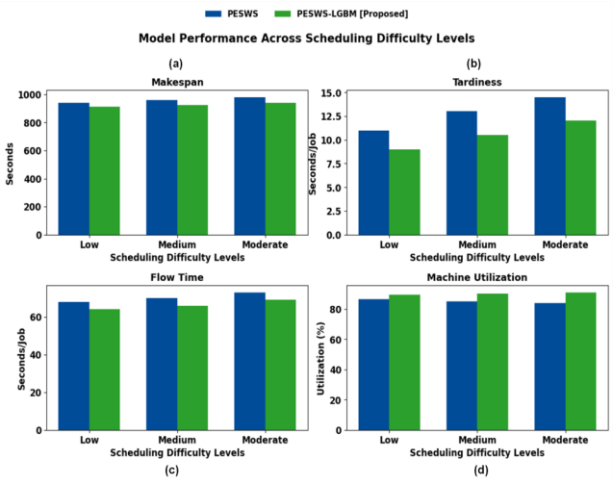

Figure 4: Scheduling Difficulty Levels across Metrics: (a) makespan, (b) tardiness, (c) flow time, and (d) machine utilization.

Certain performance metrics are analyzed that include accuracy, recall, precision, and F1-score to evaluate the PESWS-LGBM model. Accuracy evaluates the proportion of correct predictions, reflecting overall model effectiveness. Precision assesses the ratio of True Positives (T_p) to all predicted positives, minimizing False Positives(F_p). Recall evaluates the model's ability to identify critical process parameters. The F1-score, a harmonic mean of precision and recall, ensures balanced performance, particularly for imbalanced manufacturing datasets. These metrics are crucial for validating the efficiency of the PESWS-LGBM optimization framework, with their equations (18 to 21) detailed in the following sections.

$$Accuracy = \frac{T_p+T_N}{T_p+T_N+F_p+F_p} \tag{18}$$

$$Precision = \frac{T_P}{T_P+F_p} \tag{19}$$

$$Recall = \frac{T_P}{T_P+F_p} \tag{20}$$

$$F1\ score\ =\ 2\ \times \frac{Precision \times Recall}{Precision + Recall} \quad (21)$$

Where, T_N- True Negatives,F_N – False Negatives.

The proposed method PESWS-LGBM is compared with the existing methods Digital Twin- Deep Q learning (DT-DQL) [20], Multi-objective Memetic–Particle Swarm Optimization (MM-PSO) [21], and Reinforcement Learning (RL) [22]. Table 4 and Figure 5 show the comparison results based on accuracy and precision.

Table 4: Comparison results based on accuracy and precision

Methods	**Accuracy**	**Precision**
DT-DQL [20]	0.92	0.85
MM-PSO [21]	0.93	0.87
RL [22]	0.95	0.89
PESWS-LGBM [Proposed]	**0.96**	**0.91**

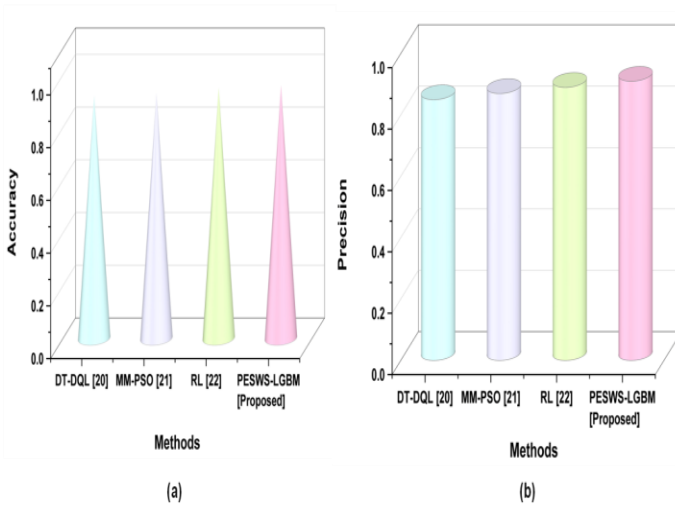

Figure 5: Visual Representations of (a) Accuracy and (b) Precision

Table 4and Figure 5 compares the performance of DT-DQL, MM-PSO, RL, and the proposed ESWS-LGBM based on accuracy and precision. DT-DQL achieves 0.92 accuracy and 0.85 precision, while MM-PSO improves to 0.93 accuracy and 0.87 precision. RL further enhances accuracy to 0.95 and precision to 0.89. The proposed PESWS-LGBM outperforms all, achieving 0.96 accuracy and 0.91 precision, demonstrating superior predictive performance for optimizing smart factories through DT-driven real-time process adjustments. Table 5 and Figure 6 demonstrate the comparison results of recall and F1 score.

Table 5: Comparison Results based on Recall and F1-Score

Methods	**Recall**	**F1-Score**
DT-DQL [20]	0.88	0.87
MM-PSO [21]	0.96	0.90
RL [22]	0.97	0.92
PESWS-LGBM [Proposed]	**0.98**	**0.94**

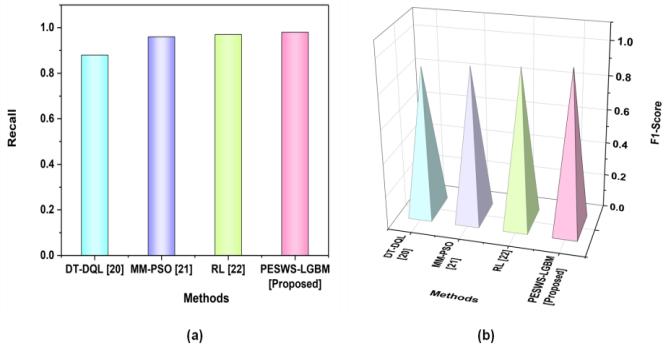

Figure 6: Visual Representation of (a) Recall and (b) F1-score

Table 6and Figure 6 present a comparison of recall and F1-score across DT-DQL, MM-PSO, RL, and the proposed PESWS-LGBM. DT-DQL achieves 0.88 recall and 0.87 F1-score, while MM-PSO improves to 0.96 recall and 0.90 F1-score. RL further enhances recall to 0.97 and F1-score to 0.92. The proposed ESWS-LGBM method outperforms other methods, achieving 0.98 recall and 0.94 F1-score, proving superior performance in accurately detecting critical process parameters and ensuring optimized smart factories. This research emphasizes the role of hybrid technology in driving productivity and efficiency, reinforcing its widespread adoption in the manufacturing sector.

Table 6 presents a sample schedule generated by the PESWS-LGBM model, illustrating how it optimizes job allocation across machines while minimizing delays. The table demonstrates improved timing (e.g., reduced initial delays) and production outcomes (e.g., early or on-time completion). This instance-level output bridges the gap between the proposed methodology and its practical impact in real-world scheduling.

Table 6: Example schedule generated by PESWS-LGBM

Job ID	Assigned Machine	Start Time	End Time	Initial Delay	Optimized Delay	Status
J1	M2	09:00	09:40	8 min	2 min	Completed Early
J2	M1	09:10	09:45	5 min	1 min	On-Time
J3	M3	09:45	10:30	12 min	3 min	Completed Late
J4	M1	10:00	10:30	6 min	2 min	On-Time
J5	M2	10:15	10:50	7 min	2 min	Completed Early

Table 7 presents the ablation study conducted to analyze the individual and combined contributions of different components in the proposed PESWS-LGBM pipeline. The baseline LGBM-only configuration (without PESWS or any preprocessing) achieves an accuracy of 0.90, indicating the strong standalone predictive capability of the LGBM model. However, when PESWS is integrated without proper data preprocessing, accuracy slightly drops (0.87-0.88), likely due to unmitigated noise and missing data.

The entire proposed configuration with noise filtering, feature scaling, missing values imputation, and PESWS-LGBM achieved the greatest accuracy of 0.96 with a notable improvement. This suggests that PESWS improves LGBM's alignment with scheduling when preprocessing is adequately handled. It is evident that preprocessing is a critical enabling function in unleashing the power of PESWS and, together, the combination of PESWS and LGBM provides better outcomes than either separately. This study shows that the best performance was not only from using LGBM, but from the integrated pathways of all components of the pipeline, particularly PESWS and data preprocessing.

Table 7: Ablation study comparing the effect of individual and combined components

Configuration	Noise Filtering	Feature Scaling	Missing Value Imputation	PESWS	LGBM	Accuracy
Noise Filtering	✓	✗	✗	✓	✓	0.87
Noise Filtering + Feature Scaling + PESWS-LGBM	✓	✓	✗	✓	✓	0.88
LGBM-only	✗	✗	✗	✗	✓	0.90
Noise Filtering + Feature Scaling + Missing Value Imputation + PESWS-LGBM (Proposed)	✓	✓	✓	✓	✓	**0.96**

To assure reproducibility, performed 5-fold stratified cross-validation (Table 8), to achieve a balanced class distribution within each fold. The metrics reported (accuracy, precision, recall, F1-score) are averaged across five independent folds, with a fixed random seed to maintain the same level of variability across studies.

Table 8: 5-Fold Cross-Validation Results (LightGBM)

Fold	Accuracy	Precision	Recall	F1 Score
Fold 1	0.9150	0.9020	0.9293	0.9154
Fold 2	0.9050	0.9082	0.8990	0.9036
Fold 3	0.9150	0.8879	0.9500	0.9179
Fold 4	0.9450	0.9406	0.9500	0.9453
Fold 5	0.9250	0.9048	0.9500	0.9268
Average	**0.9210**	**0.9087**	**0.9357**	**0.9218**

4.2 Discussion

The literature has recently researched various optimization strategies within smart manufacturing. Author of [18] demonstrated the feasibility of controlling smart factories

through a cloud-based IoT framework, which facilitated data acquisition in real-time but did not include a scheduling optimization or adaptive learning component. According to the research [21], a hybrid PSO and Q-learning method for energy-efficient flow-shop scheduling showed significant improvements in energy savings and makespan reduction but had high computational complexity with larger problems. In [23], the authors proposed a dynamic scheduling model driven by the health of machines that relied on real-time sensors utilized predictive maintenance to assign jobs, although this study focused on small shop floor interventions. Compared to these approaches, the proposed PESWS-LGBM framework achieves higher performance across multiple metrics while also reducing downtime and enhancing Overall Equipment Effectiveness (OEE). Its integration of LightGBM for critical feature prediction and PESWS for adaptive optimization offers greater scalability, faster training, and better generalizability. Unlike prior models, it enables real-time, noise-resilient, and flexible scheduling, validating its effectiveness for dynamic smart factory environments.

4.3 Challenges and implications of research

Integrating the PESWS-LGBM model into a practical smart factory scenario brings forth numerous ethical and practical implications. In human-in-the-loop situations, maintaining operator trust in an AI-informed scheduling system will be essential. Operator rejection or misinterpretation of recommendations may occur if operators lose confidence due to over-reliance on full automation without any process transparency. Ensuring explainability and letting human operators take over when appropriate could minimize this risk.

Sensor reliability is also a significant issue. When sensors have faults or drift, incorrect data inputs lead to poor model performance and reduced data quality through time. Careful calibration of the sensors and fault detections of sensor performance are required. The dynamic nature of the industrial environment means that the model will precipitate new conditions that occur with changing production performance and equipment behavior. Data privacy and system security are also concerns when deploying systems of this type. Although this solution enables adaptive scheduling to benefit productivity and efficiency, this framework needs to consider automation using and relying on new forms of autonomy, human oversight, system durability, and longevity.

5 Conclusion

The effectiveness of a hybrid algorithm for optimizing production scheduling systems was analyzed. Real-time data was collected from industrial sensors, capturing essential production metrics such as temperature, vibration, power consumption, and material flow rate. Preprocessing techniques, including noise filtering, missing value imputation, and feature scaling, ensure data quality and standardization. By leveraging the ESWS-LGBM method to predict critical process parameters, adaptive scheduling and workflow adjustments were enabled. Results demonstrated that the proposed model outperformed existing methods, achieving 0.96 accuracy, 0.91 precision, 0.98 recall, and an F1-score of 0.94, demonstrating superior predictive capabilities. The integration of artificial intelligence technology enables real-time simulations, further improving operational efficiency. These results confirm that PESWS-LGBM significantly enhances OEE, reinforcing its potential for widespread adoption in smart factories to drive productivity, cost efficiency, and intelligent automation. Despite its effectiveness, the proposed model faces challenges such as high computational requirements, dependency on high-quality sensor data, and integration complexities in diverse industrial settings. Future research can explore lightweight models, hybrid optimization techniques, and enhanced digital twin and machine learning integration for improved scalability, real-time adaptability, and broader industrial applications.

References

[1] Jalal, A.M.; Toso, E.A.V.; Morabito, R. Integrated Approaches for Logistics Network Planning: A Systematic Literature Review. Int. J. Prod. Res. 2022, 60, 5697–5725. DOI:10.1080/00207543.2021.1963875

[2] Thenarasu, M.; Rameshkumar, K.; Rousseau, J.; Anbuudayasankar, S.P. Development and Analysis of Priority Decision Rules Using MCDM Approach for a Flexible Job Shop Scheduling: A Simulation Study. Simul. Model. Pract. Theory 2022, 114, 102416. https://doi.org/10.1016/j.simpat.2021.102416

[3] Wu, J.; Huang, Z.; Hu, Z.; Lv, C. Toward Human-in-the-Loop AI: Enhancing Deep Reinforcement Learning via Real-Time Human Guidance for Autonomous Driving. Engineering 2023, 21, 75–91. https://doi.org/10.1016/j.eng.2022.05.017

[4] Zhao, Y. Optimization of Mechanical Manufacturing Processes via Deep Reinforcement Learning-Based Scheduling Models. Informatica 2025, 49. https://doi.org/10.31449/inf.v49i14.7204

[5] Hossain, Q.; Yasmin, F.; Biswas, T.R.; Asha, N.B. Integration of Big Data Analytics in Management Information Systems for Business Intelligence. Saudi J. Bus. Manag. Stud. 2022, 9, 192–203. DOI:10.36348/sjbms. 2024.v09i09.002

[6] Wang, H. Innovative Application of Intelligent Mechanical Manufacturing Based on Self-Supervised Learning and Graph Neural Network Fusion Optimization. Informatica 2025, 49. DOI: https://doi.org/10.31449/inf.v49i17.7595

[7] Xue, W.; Luo, Q.; Ni, L.M. Real-Time Action Scheduling in Pervasive Computing. Informatica 2011, 35.

[8] Yang, S.; Xu, Z. Intelligent Scheduling and Reconfiguration via Deep Reinforcement Learning in Smart Factories. Int. J. Prod. Res. 2022, 60, 4936–4953. DOI:10.1080/00207543.2021.1943037

[9] van der Beek, T.; Souravlias, D.; van Essen, J.; Pruyn, J.; Aardal, K. Hybrid Differential Evolution Algorithm for the Resource Constrained Project Scheduling Problem with a Flexible Project Structure and Consumption and Production of Resources. Eur. J. Oper. Res. 2024, 313, 92–111. DOI: 10.1016/j.ejor.2023.07.043

[10] Kasapidis, G.A.; Paraskevopoulos, D.C.; Mourtos, I.; Repoussis, P.P. A Unified Solution Framework for Flexible Job Shop Scheduling Problems with Multiple Resource Constraints. Eur. J. Oper. Res. 2024, 320, 479–495. DOI: 10.1016/j.ejor.2024.08.010

[11] Rohaninejad, M.; Tavakkoli-Moghaddam, R.; Vahedi-Nouri, B.; Hanzálek, Z.; Shirazian, S. A Hybrid Learning-Based Meta-Heuristic Algorithm for Scheduling of an Additive Manufacturing System Consisting of Parallel SLM Machines. Int. J. Prod. Res. 2022, 60, 6205–6225. DOI:10.1080/00207543.2021.1987550

[12] Luo, X.; Hu, Y.; Yu, X. Design and Application of Scheduling Algorithm Based on Multi-Objective and Multi-Constraint. Manuf. Technol. Mach. Tool 2022, 04, 159–164. DOI:10.1109/ACCESS.2023.3285710

[13] Hong, L.; Wang, Y.; Nan, K.; Tian, H. Scheduling Optimization Study of Timed Petri Net Models for Flexible Manufacturing Systems. Mach. Des. Manuf. 2022, 04, 262–265, 269. DOI:10.1109/CCDC62350.2024.10587856

[14] Huang, Z. Research on Flexible Workshop Dynamic Real-Time Scheduling Based on Hybrid Genetic Algorithm. North China Inst. Aerosp. Eng. 2022. [Thesis] https://doi.org/10.3390/app14062586

[15] Bao, B.; Duan, Z.; Xu, N.; Zhang, H.; Luo, Y.; Wang, W.; Yu, X.; Luo, Y.; Liu, X. A New Algorithm of the Scheduling of a Flexible Manufacturing System Based on Genetic Algorithm. Manuf. Rev. 2023, 10, 11. https://doi.org/10.1051/mfreview/2023010

[16] Li, X.; Xiong, H.; Li, X.; Wu, X.; Zhang, X.; Liu, J.; Dou, D. Interpretable Deep Learning: Interpretation, Interpretability, Trustworthiness, and Beyond. Knowl. Inf. Syst. 2022, 64, 3197–3234. DOI:10.1007/s10115-022-01756-8

[17] Matsuo, Y.; LeCun, Y.; Sahani, M.; Precup, D.; Silver, D.; Sugiyama, M.; Morimoto, J. Deep Learning, Reinforcement Learning, and World Models. Neural Netw. 2022, 152, 267–275. DOI: 10.1016/j.neunet.2022.03.037

[18] Khan, S.I.; Kaur, C.; Al Ansari, M.S.; Muda, I.; Borda, R.F.C.; Bala, B.K. Implementation of Cloud-Based IoT Technology in Manufacturing Industry for Smart Control of Manufacturing Process. Int. J. Interact. Des. Manuf. 2023, 1–13. DOI:10.1007/s12008-023-01366-w

[19] Sang, Y.-W.; Wang, J.-Q.; Sterna, M.; Błażewicz, J. Single Machine Scheduling with Due Date Assignment to Minimize the Total Weighted Lead Time Penalty and Late Work. Omega 2023, 121, 102923. DOI: 10.1016/j.omega.2023.102923

[20] Müller-Zhang, Z.; Kuhn, T.; Antonino, P.O. Towards Live Decision-Making for Service-Based Production: Integrated Process Planning and Scheduling with Digital Twins and Deep-Q-Learning. Comput. Ind. 2023, 149, 103933. DOI: 10.1016/j.compind.2023.103933

[21] Zhang, W.; Li, C.; Gen, M.; Yang, W.; Zhang, G. A Multiobjective Memetic Algorithm with Particle Swarm Optimization and Q-Learning-Based Local Search for Energy-Efficient Distributed Heterogeneous Hybrid Flow-Shop Scheduling Problem. Expert Syst. Appl. 2024, 237, 121570. DOI:10.1007/s10845-023-02227-9

[22] Esteso, A.; Peidro, D.; Mula, J.; Díaz-Madroñero, M. Reinforcement Learning Applied to Production Planning and Control. Int. J. Prod. Res. 2022, 61, 5772–5789. https://doi.org/10.1080/00207543.2022.2104180

[23] Yin, L.; Zhang, W.; Zhou, T. Machine Health-Driven Dynamic Scheduling of Hybrid Jobs for Flexible Manufacturing Shop. Int. J. Precis. Eng. Manuf. 2023, 24, 797–812. DOI:10.1007/s12541-023-00784-w

ICOA: Enhanced Crayfish Optimization for Task Scheduling in Heterogeneous Cloud Environments

Zhiping Zhou
Center of Quality Management, Hebei Software Institute, Baoding City, Hebei Province, 071001, China
E-mail: bdzzp08@126.com

Keywords: cloud computing, task scheduling, crayfish optimization, resource utilization

Received: May 6, 2025

Cloud computing systems are intended to efficiently process large amounts of data and provide on-demand computing resources. Scheduling tasks is one of the intrinsic issues of cloud computing, where tasks are allocated to resources and execution time is reduced while maximizing resource utilization. The present work proposes an improved version of the Crayfish Optimization Algorithm (COA), called ICOA, to solve the task scheduling problem in heterogeneous cloud computing. ICOA integrates chaotic mapping for population diversity, random opposition-based learning (ROBL) for enhanced global exploration, a non-linear control parameter for dynamic search balance, and a Cauchy mutation strategy to avoid premature convergence. Performance of the algorithm is evaluated using CloudSim with NASA, HPC2N, and a synthetic workload. Experimental comparisons on EHHO, MSA–CSA–PAES, ACO, and IWOA demonstrate that the proposed ICOA achieves remarkable improvements: makespan reduction of 50.8%, and resource utilization increase of 26.5%. These experimental results confirm that the proposed ICOA is an efficient and effective solution for task scheduling of complex cloud computing environments.

Povzetek: Za razporejanje nalog v heterogenih oblačnih okoljih je razvita ICOA, izboljšana različica algoritma Crayfish Optimization, ki združuje kaotično inicializacijo, ROBL, nelinearni nadzorni parameter in Cauchyjevo mutacijo.

1 Introduction

Cloud computing is an advanced technology that provides on-demand and elastic access to computer resources on the Internet [1]. It benefits companies and end-users by offering flexibility, cost savings, and operating efficiency through simple data storage, management, and processing [2]. Task scheduling, assigning incoming tasks to available Virtual Machines (VMs), is an essential subproblem in cloud computing. Scheduling tasks properly reduces the makespan (total duration needed to carry out tasks), optimizes the use of available resources, and enhances the overall Quality of Service (QoS) [3]. Inappropriate scheduling causes delays, resource waste, and low system performance and is directly related to operating expenditures and users' satisfaction [4]. Therefore, developing effective scheduling methods is extremely interesting for optimizing cloud computing performance.

Although significant advances have been made, existing scheduling techniques, including metaheuristics and heuristics, are still hindered by inherent challenges in their application to advanced, dynamic clouds. Traditional algorithms are vulnerable to being stuck with local optima too soon, missing better global optima. Numerous algorithms also do not meet an acceptable balance between exploitation (exploring new areas of solutions) and exploration (improving known effective areas), leading to inefficiencies and less-than-optimal scheduling quality. Scalability is also an issue when workloads exceed, further highlighting limitations to adaptability and accuracy in optimizing. These vulnerabilities highlight the need for stronger, scalable, and efficient task scheduling techniques to deliver quality in different clouds.

To overcome these problems, the Improved Crayfish Optimization Algorithm (ICOA) is proposed, which is tailored to scheduling in cloud computing environments. Building on the existing Crayfish Optimization Algorithm (COA), inspired by crayfish's natural foraging activities, ICOA incorporates essential improvements to offer superior global search ability and convergence. Through chaotic mapping for maintaining population diversity, random backward learning for global exploration, non-linear control parameters to promote flexibility between exploration and exploitation, and Cauchy mutation techniques to avoid stagnation, ICOA offers an improved and efficient solution. These improved techniques enhance scheduling performance, makespan, and resource usage within complex clouds. The main contributions of the research are given below:

- Implementation of random reverse learning and chaotic mapping to achieve maximum population diversity and global searching capability.
- Adding a non-linear control parameter to dynamically tradeoff between exploration and exploitation during optimization.
- Implementing a Cauchy mutation strategy to improve local optima escape capability without sacrificing the convergence rate.

- Continued performance assessment of ICOA on real and synthetic datasets to establish its superiority over previous methodologies.

To guide this investigation, we pose the following research questions:

- RQ1: Does chaotic initialization improve convergence speed and task-to-resource mapping efficiency in heterogeneous cloud environments?
- RQ2: How does the combination of non-linear control and Cauchy mutation in ICOA improve the exploration–exploitation balance compared to existing metaheuristic algorithms such as EHHO and ACO?

2 Related work

Jia, et al. [5] proposed an Improved Whale Optimization Algorithm (IWOA), prioritizing significant parameters like task scheduling time, cost, and virtual machine load. They applied an inertial weight strategy to enhance its ability to search locally and to avoid premature convergence. Furthermore, the IWOA has an add-delete operator that advances individual solutions and enhances scheduling quality after each iteration.

Abd Elaziz and Attiya [6] suggested an improved Henry Gas Solubility Optimization algorithm (HGSWC) incorporating the WOA and Comprehensive Opposition-Based Learning (COBL) to enhance cloud task scheduling. While WOA serves to perform local searches to enhance the quality of the solutions, COBL supports weaker solutions by comparing and selecting their opposition. Verified using benchmark functions and compared against traditional HGSO and WOA methods, the proposed HGSWC consistently yielded nearly optimal solutions without excessive computation. Moreover, large-scale simulations using both actual and synthetic workloads confirmed its outperformance compared to six widely used metaheuristics for efficiently tackling the problem of cloud scheduling.

Liu [7] developed an adaptive Ant Colony Algorithm (ACO) to address the shortcomings of conventional ACO, including slow convergence and local optima, in large-scale cloud scheduling. Their strategy initiated an update mechanism for pheromone adaptability, allowing pheromone trails to be dynamically modified to accelerate convergence speed and enhance robustness. Through extensive experimentation, the proposed algorithm consistently yielded well-balanced task execution times, task costs, and system loads in contrast to the standard ACO.

Alsubai, et al. [8] proposed a new task scheduling strategy that integrates the Moth Swarm Algorithm (MSA) and the Chameleon Swarm Algorithm (CSA), together with the Polymorphic Advanced Encryption Standard (PAES), for task scheduling security improvement. The proposed approach considers makespan, resource usage, and bandwidth efficiency while encrypting task information securely. Simulation outcomes across varying task sizes demonstrated improved task scheduling performance, significantly decreasing imbalance, execution time, response delay, and expense. The coupled MSA–CSA–PAES design offered an effective, secure, and energy-efficient approach to task scheduling for complex cloud computing environments.

Malti, et al. [9] introduced a hybrid Flower Pollination Algorithm (FPA)-Grey Wolf Optimizer (GWO) to deal with multi-objective scheduling in heterogeneous clouds. The proposed approach effectively balances exploitation and exploration and prevents convergence and stagnation by utilizing evolutionary crossover operators. CloudSim and sectoral workload simulations reveal improvements in makespan minimization, resource utilization optimization, system balancing, and maximum throughput. A comparative evaluation of the new approach on TSMGWO, GGWO, LPGWO, and standard FPA demonstrated that the hybrid approach effectively handles major scheduling problems.

Pachipala, et al. [10] introduced a two-stage hybrid optimization methodology, known as Blue Updated Jellyfish Search Optimization (BUJSO), that unifies Blue Monkey Optimization (BMO) and Jellyfish Search Optimization (JSO) algorithms. The tasks were scheduled and prioritized using the Analytical Hierarchy Process (AHP) and were partitioned among themselves using k-means clustering. Scheduling considered makespan, utilization cost, migration, and failure risk. Performance Analysis depicted considerable improvements compared to the conventional scheduling methodologies, which indicates the efficacy of the introduced approach in workload balancing, priority, resource allocation, and reducing scheduling costs in various cloud environments.

Fang [11] proposed the Enhanced Harris Hawks Optimization (EHHO) strategy, which is fundamentally aimed at task scheduling optimization for cloud scenarios, utilizing a random walk mechanism. The addition significantly enhanced the algorithm's exploration ability, preventing premature convergence and improving scalability and resource management. Compared to previous techniques, the experimental analysis proved that EHHO efficiently minimized makespan, memory utilization, execution time, and cost.

Despite the significant progress embodied by the reviewed methodologies, several limitations remain, and current cloud task scheduling techniques do not address that. As described in Table 1, most methods have significant issues concerning the effective exploration-exploitation balance, which impacts global search efficiency and solution optimality. In addition to traditional issues such as local optima convergence, stagnation, and low population diversity, the performance of algorithms is significantly hindered, especially for large and highly volatile loads.

Scalability also restricts applicability to realistic scenarios due to increased complexity and the quantity of tasks. The suggested ICOA fills these voids directly through chaotic mapping and random backward learning techniques for enhanced population initialization, non-linear control parameters for preserving exploration and exploitation adaptivity, and Cauchy mutation for preventing stagnation. Thus, it provides better and more efficient scheduling outcomes for adaptive and difficult-to-model cloud instances.

Table 1: Comparative analysis of related work

Reference	Algorithm	Exploration/exploitation balance	Avoiding premature convergence	Main metrics considered	Dataset/testbed used
[5]	Improved whale optimization	Inertial weight strategy	Add-and-delete operator	Time, cost, and VM load	Synthetic workloads
[6]	Henry gas solubility optimization algorithm	WOA local search and COBL	Comprehensive opposition-based learning	Solution quality and makespan	Synthetic and real workloads
[7]	Adaptive ant colony algorithm	Pheromone adaptive update	Dynamic pheromone adjustment	Execution time, load balance, and cost	Synthetic workloads
[8]	Moth swarm algorithm, chameleon swarm algorithm, and polymorphic advanced encryption standard	Swarm integration strategy	Hybrid swarm methods	Makespan, resource utilization, and security	Synthetic workloads
[9]	Hybrid flower pollination–grey wolf	Evolutionary crossover operators	Pollination–wolf search combination	Makespan, throughput, and resource utilization	Synthetic workloads
[10]	Blue updated jellyfish optimization	Analytical hierarchy & clustering	Hybrid optimization methods	Makespan, migration cost, and risk probability	Synthetic workloads
[11]	Enhanced harris hawks optimization	Dynamic random walk strategy	Enhanced exploration capability	Makespan, memory, cost, and scalability	Synthetic workloads
Our work	Improved Crayfish Optimization Algorithm	Non-linear control parameter	Cauchy mutation and ROBL	Makespan and resource utilization	HPC2N, NASA, and synthetic

3 Problem formulation

In a cloud computing environment, task scheduling refers to the optimal assignment of a set of computational tasks to available VMs to enhance system efficiency [12]. The system consists of P Physical Machines (PMs), each running multiple VMs. Given a set of T tasks to be scheduled, the relationship between tasks and VMs is captured by an Expected Execution Time Matrix (EETM), expressed using Eq. 1.

$$EETM = \begin{bmatrix} EETM_{1,1} & EETM_{1,2} & \cdots & EETM_{1,M} \\ EETM_{2,1} & EETM_{2,2} & \cdots & EETM_{2,M} \\ \vdots & \vdots & \ddots & \vdots \\ EETM_{T,1} & EETM_{T,2} & \cdots & EETM_{T,M} \end{bmatrix} \quad (1)$$

Elements in EETM denotes the estimated time required for task k to execute on VM m, computed using Eq. 2.

$$EETM_{k,m} = \frac{TaskLength_k}{VM_M IPS_m} \quad (2)$$

Where $TaskLength_k$ is the length (in millions of instructions) of task k and $VM_M IPS_m$ represents the processing speed (million instructions per second) of VM m.

The overall scheduling objectives include minimization of makespan (total completion time) and maximization of Resource Utilization (RU). The makespan stands for the maximum finishing time across all VMs and is calculated using Eq. 3 [13].

$$MKS = \max_{m \in \{1,2,\ldots,M\}} \sum_{k=1}^{T} EETM_{k,m} \quad (3)$$

Resource utilization reflects the efficiency of VM usage over the execution period and is given by Eq. 4 [14].

$$RU = \frac{\sum_{k=1}^{T} ExecTime_{VM_m}}{Makespan \times M} \quad (4)$$

Where $ExecTime_{VM_m}$ is the total time VM m spends executing its assigned tasks.

To evaluate candidate scheduling solutions, a weighted sum fitness function is used that combines the two conflicting objectives: minimizing makespan and maximizing resource utilization. Both objectives are first normalized using min–max scaling over observed ranges during initialization. The combined fitness function is defined as:

$$F = w_1 \cdot \frac{MKS_{max} - MKS}{MKS_{max} - MKS_{min}} + w_2 \cdot \frac{RU - RU_{min}}{RU_{max} - RU_{min}} \quad (5)$$

Where w_1 and w_2 are the weights assigned to makespan and resource utilization respectively (with $w_1 + w_2 = 1$). In our experiments, we used $w_1 = 0.6$ and $w_2 = 0.4$, giving slightly more importance to makespan reduction.

The overall goal is to determine a task-to-VM allocation that minimizes the total completion time while maximizing system resource efficiency, thus enhancing the performance and scalability of cloud computing operations.

4 Proposed methodology

4.1 Basic crayfish optimization algorithm

COA is a nature-inspired metaheuristic algorithm modeled on crayfish's foraging, competition, and summer resort (retreat) behaviors. It alternates between exploration (diversifying search) and exploitation (refining search) phases depending on the environmental conditions, simulated via a random temperature parameter [15]. The

algorithm defines a colony of crayfish C, where each crayfish represents a candidate solution in the optimization space.

In a multi-dimensional search space, each crayfish individual C_i is a $1 \times D$ vector, where D denotes the number of problem dimensions. The initial population is randomly generated as follows:

$$C = [C_1, C_2, \ldots, C_N] \tag{6}$$

$$C_{i,j} = LB_j + (UB_j - LB_j) \times rand \tag{7}$$

Where LB_j and UB_j are the lower and upper bounds for dimension j, $rand$ is a random number between 0 and 1, and N is the population size.

The environmental temperature $Temp$ regulates the behavioral mode (exploration or exploitation) of crayfish calculated using Eq. 8.

$$Temp = 15 \times rand + 20 \tag{8}$$

The food intake under different temperatures is modeled by a normal distribution using Eq. 9.

$$Intake = C_1 \times \frac{1}{\sqrt{2\pi\sigma}} \times exp\left(-\frac{(Temp - \mu)^2}{2\sigma^2}\right) \tag{9}$$

Where μ is the optimal feeding temperature, σ controls the spread, and C_1 is a scaling coefficient.

When $Temp > 30°C$ and $rand < 0.5$, crayfish seek cooler environments. They move toward a temporary refuge (cave) located at:

$$Cave = \frac{C_{best} + C_{local}}{2} \tag{10}$$

Where C_{best} is the best individual found so far and C_{local} is the current best of the population.

Crayfishes are updated using Eq. 11.

$$C_{i,j}^{t+1} = C_{i,j}^t + \lambda \times rand \times \left(Cave - C_{i,j}^t\right)$$
$$\lambda = 2 - \left(\frac{t}{T}\right) \tag{11}$$

Where t is the current iteration and T is the maximum number of iterations.

If $Temp > 30°C$ and $rand \geq 0.5$, multiple crayfish compete for the cave. The new position is determined by Eq. 12.

$$C_{i,j}^{t+1} = C_{i,j}^t - C_{z,j}^t + Cave$$
$$z = round\left(rand \times (N-1)\right) + 1 \tag{12}$$

Where z is a randomly selected individual and $rand$ controls random competition selection.

When $Temp \leq 30°C$, crayfish engage in foraging activities. The food source corresponds to the best solution so far.

$$Food = C_{best} \tag{13}$$

The size of the food determines crayfish behavior as follows:

$$Size = C_3 \times rand \times \left(\frac{fitness_i}{fitness_{Food}}\right) \tag{14}$$

Where C_3 is a food scaling factor, $fitness_i$ is the fitness of crayfish i, and $fitness_{Food}$ is the fitness at the food location.

If $Size > \frac{C_3+1}{2}$ (i.e., the food is too large), the food is shredded using Eq. 15.

$$Food_{new} = exp\left(-\frac{1}{Size}\right) \times Food \tag{15}$$

Then, crayfish update their positions using alternating sine-cosine foraging behavior:

$$C_{i,j}^{t+1} = C_{i,j}^t + Food_{new} \times Intake \times (cos(2\pi \times rand) - sin(2\pi \times rand)) \tag{16}$$

In cases $Size \leq \frac{C_3+1}{2}$ (manageable food size), the crayfish directly migrate toward the food:

$$C_{i,j}^{t+1} = \left(C_{i,j}^t - Food\right) \times Intake + Intake \times rand \times C_{i,j}^t \tag{17}$$

4.2 Improved crayfish optimization algorithm

The basic COA demonstrates considerable potential but faces premature convergence, uneven initial population distribution, and suboptimal exploration-exploitation balance. To address these challenges, several enhancements are introduced in the ICOA.

Random initialization in COA can lead to poor population diversity, reducing global search ability and causing early stagnation. To counteract this, a chaotic sequence-based initialization is employed using logistic mapping, which enhances diversity and ensures more uniform coverage of the search space. The logistic mapping is defined as:

$$X_{n+1} = \mu \times X_n \times (1 - X_n) \tag{18}$$

Where X_n is the current value and μ is the control parameter.

In this study, we selected μ = 2.5 for the logistic mapping function to balance diversity and stability in the initialization phase. While higher values of μ (e.g., >3.5) increase chaos and exploration, they may also destabilize early convergence in constrained scheduling problems. Choosing μ = 2.5 offers a moderate level of chaos, sufficient to diversify the initial population without introducing excessive randomness or instability. This choice is supported by recent applications in UAV path planning that successfully use similar values

ICOA boosts exploration potential and resilience against local optima by generating initial positions through logistic chaos.

Random Opposition-Based Learning (ROBL) is incorporated to further enrich population diversity. Instead of merely randomizing individuals, each candidate X_i generates an opposite solution $\widehat{X}_\iota$ based on random perturbations:

$$\widehat{X}_\iota = L_j + U_j - rand \times X_i \tag{19}$$

Where L_j and U_j are the lower and upper bounds of the search space, and $rand \in [0, 1]$ is a uniformly sampled random vector that introduces controlled perturbation. Unlike classical opposition learning, ROBL allows each dimension to be perturbed by a random scaling factor, enabling non-symmetric and domain-aware reflection.

To ensure feasibility within constrained domains (e.g., task–VM index ranges), the generated X_i is projected back into the search space using Eq. 20.

$$\hat{X}_i^{corrected} = min\left(max\left(\hat{X}_i, L_j\right)U_j\right) \quad (20)$$

The better of the original and opposite solution (in terms of fitness) is retained, promoting better exploration and faster convergence during early iterations.

The original COA employs a linear decreasing control factor, which may cause inefficient transitions between global search (exploration) and local search (exploitation). ICOA introduces a non-linear control parameter to better adapt search dynamics during iterations. The update mechanism is modified as follows:

$$\lambda = 2 - exp\left(-\frac{t^2}{T \times rand}\right) \quad (21)$$

Non-linear control parameters dynamically control the balance between exploration and exploitation when optimizing. Compared to linear decay (which linearly decreases as time increases), the exponential form enables rapid initial exploration and gradually escalates exploitation as the search proceeds. This adaptive response is better for high-dimensional, dynamic scheduling problems.

The solution update during exploration (e.g., summer resort stage) becomes:

$$C_{i,j}^{t+1} = C_{i,j}^t + \lambda \times rand \times \left(Cave - C_{i,j}^t\right) \quad (22)$$

This dynamic control accelerates exploitation when needed and prolongs exploration when beneficial, improving convergence precision.

During later optimization stages, populations often risk becoming trapped in local optima. To mitigate this, ICOA employs a Cauchy mutation strategy to perturb the best-found solution. The Cauchy mutation is modeled using Eq. 23.

$$Y_{new} = Y_{best} \times \left(1 + f_{Cauchy}(0,1)\right) \quad (23)$$

Where $f_{Cauchy}(0,1)$ generates a random value following a Cauchy distribution (centered at 0 with a scale of 1).

The Cauchy distribution is selected for its heavy-tailed property, which allows for larger random jumps compared to the Gaussian distribution. This makes it especially effective in escaping local optima during later stages of optimization, when the population tends to cluster. In contrast, Gaussian mutations are more conservative and may not provide sufficient perturbation to overcome local stagnation.

If the mutated solution Y_{new} has better fitness, it replaces Y_{best}; otherwise, the original is retained:

$$Y_{best} = \begin{cases} Y_{best}, & if\ f(Y_{best}) < f(Y_{new}) \\ Y_{new}, & otherwise \end{cases} \quad (24)$$

This mechanism enables ICOA to escape from local minima dynamically and maintain search momentum. The proposed ICOA effectively addresses the primary limitations observed in conventional metaheuristic-based task scheduling methods. Algorithm 1 and Figure 1 present the pseudocode and flowchart of ICOA, respectively. Using logistic chaotic mapping during the initialization phase, ICOA ensures population diversification and distribution within the search space, resisting the possibility of early convergence due to poor initial population configurations.

Further, by applying ROBL, population diversification is maintained by generating opposite candidate solutions and selecting improved individuals. This two-pronged tactic decisively enhances the algorithm's global exploration ability to effectively traverse challenging optimization topologies and prevent early convergence into local optima. Lastly, implementing the non-linear control parameter dynamically controls the exploration and exploitation balance according to the number of iterations, enabling ICOA to exhibit persistent search flexibility during optimization.

By applying the Cauchy mutation principle, ICOA improves population diversification and search flexibility. Through controlled perturbations to the best-so-far solutions, Cauchy mutation reduces the likelihood of premature convergence during the subsequent optimization stages, a characteristic weakness of traditional COA and other swarm-based techniques. An exponential decrease of the control parameter ensures that the intensification of search is adequately fortified along the progress of search without hindering first-stage

Algorithm 1 Pseudocode of ICOA

Input:
Set of tasks (T), set of VMs (M), population size (N), problem dimension (D), and maximum number of iterations (T_{max})
Initialize:
Generate the initial population using Eq. 6
Apply ROBL to enhance diversity (Eq. 19)
Evaluate the fitness of all individuals
While ($t < T_{max}$):
For each individual C_i in C:
  Calculate environmental temperature using Eq. 8
  If $Temp > 30$:
    If $rand < 0.5$:
      //Summer resort stage (Eq. 10)
      Update position using Eq. 11
    Else:
      // Competition stage (Exploitation)
      Select a random individual C_z
      Update position using Eq. 12
  Else:
    // Foraging stage (Exploitation)
    Food = C_{best}
    Calculate food size using Eq. 14
    If $Size > \frac{C_3+1}{2}$:
      Update food position using Eq. 15
      Update position using Eq. 16
    Else:
      Direct movement towards food using Eq. 17
End For
Apply Cauchy mutation:
  Mutate the best individual using Eq. 21
  If fitness(C_{new}) better than fitness(C_{best}), replace C_{best}
Update the best solution found so far
t=t+1
End While
Output:
Best solution

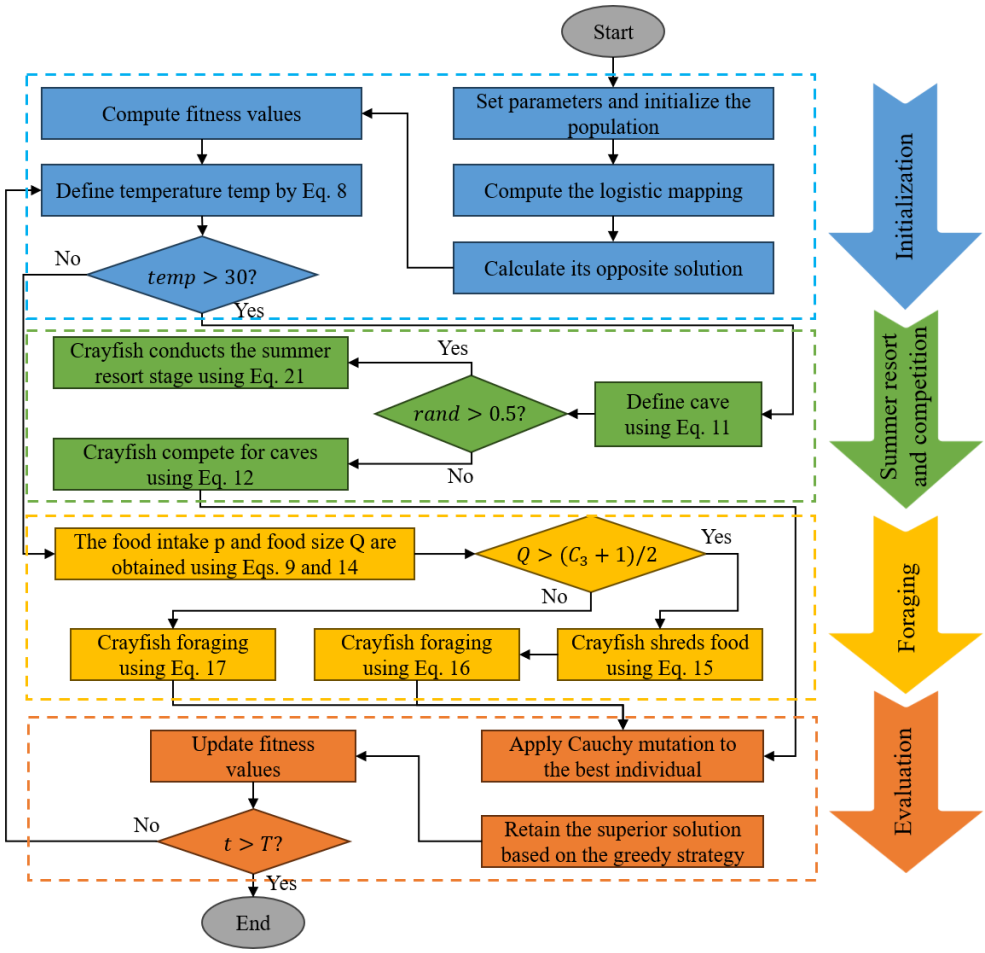

Figure 1: Flowchart of ICOA

exploration capability. These optimizations, together, on an individual basis, optimize and improve task schedule quality under cloud environments by decreasing makespan, optimizing resource utilization, and encouraging resilience for dynamic and large-scale scheduling cases.

5 Results and discussion

This section provides an overall assessment of the ICOA regarding scheduling effectiveness for various cloud computing workloads. The experimental framework was deployed using the CloudSim simulation package, with three benchmark datasets, including HPC2N, NASA, and simulated datasets. These datasets were chosen to simulate various workload complexities so that ICOA's performance could be thoroughly evaluated under real-world and synthetic setups. The problem of scheduling was considered using independent and non-preemptive tasks to model realistic cloud environments. Every experimental setup was executed 30 times to achieve statistical accuracy, and there were two primary performance metrics: makespan and resource utilization.

In our CloudSim-based simulation environment, we deployed 50 virtual machines (VMs) evenly distributed across three heterogeneous types: Type A (1 vCPU @ 1000 MIPS, 2048 MB RAM), Type B (2 vCPUs @ 1500 MIPS, 4096 MB RAM), and Type C (4 vCPUs @ 2000 MIPS, 8192 MB RAM). Task lengths were generated using a uniform distribution over the range [1000, 10000] million instructions (MI), simulating both lightweight and computationally intensive workloads. A space-shared VM scheduling policy with non-preemptive tasks was applied. To ensure the robustness of results, each experiment was repeated 30 times, and all stochastic processes, including those in CloudSim and ICOA, were initialized using a fixed random seed (seed = 42) for reproducibility.

The performance of ICOA was compared with four well-known algorithms: EHHO, MSA–CSA–PAES, ACO, and IWOA. As illustrated in Figures 2-7, simulation results indicate that ICOA surpassed the compared algorithms in all cases. For instance, when the tasks were 2500, ICOA achieved the highest makespan reductions of 13.9% in the case of the HPC2N dataset, 50.8% in the case of the NASA dataset, and 34.7% in the case of the simulated dataset in comparison to other competing algorithms. These improvements are attributed to ICOA's adaptive exploration-exploitation balance, achieved through temperature-driven behavioral phases, chaotic initialization, and dynamic non-linear control parameters.

In resource utilization terms, as reflected in Figures 5–7, ICOA realized gains of as much as 15.7% for the HPC2N dataset, 17.7% for the NASA dataset, and 26.5% for the simulated dataset relative to the following best-performing algorithm under the scenario of 2500 tasks.

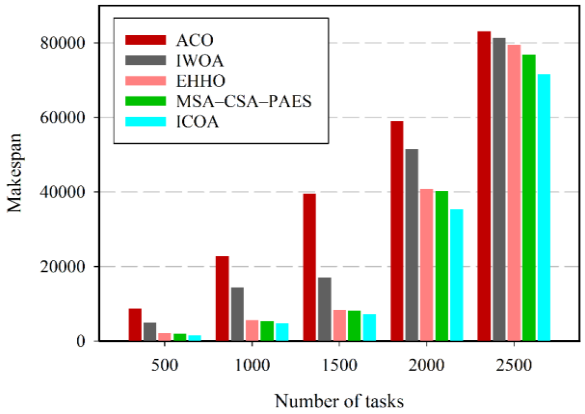

Figure 2: Makespan results for the HPC2N dataset

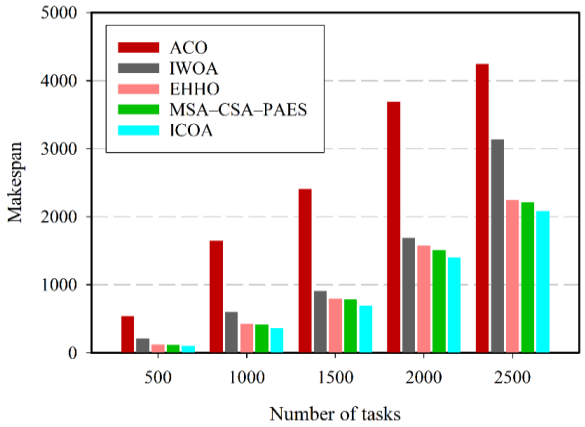

Figure 3: Makespan results for the NASA dataset

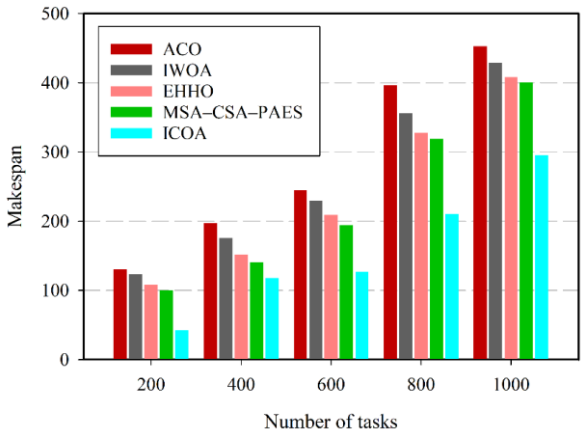

Figure 4: Makespan results for the simulated dataset

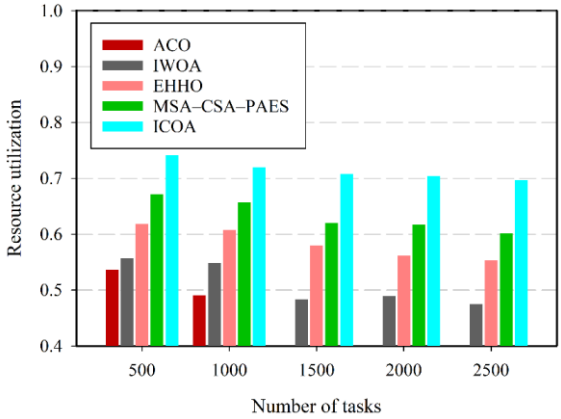

Figure 5: Resource utilization results for the HPC2N dataset

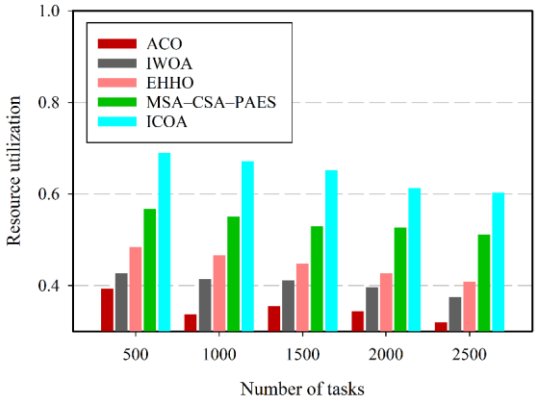

Figure 6: Resource utilization results for the NASA dataset

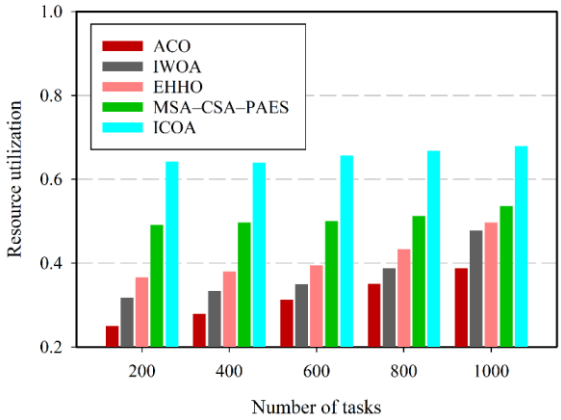

Figure 7: Resource utilization results for the simulated dataset

These improvements reflect the ability of ICOA to find optimal task-to-resource mappings through chaotic sequences when populating the population and improving them using Cauchy mutation and greedy selection policies. Incorporating non-linear decay into the control parameters enabled ICOA to achieve reasonable convergence during the simulation phases, leading to improved load balancing and greater utilization rates. Overall, these results attest that ICOA expedites task scheduling and optimizes resource consumption better than the baseline algorithms.

To evaluate the runtime efficiency of ICOA, we compared the average execution time (in seconds) and approximate floating-point operation counts (FLOPs) against baseline algorithms (EHHO, ACO, IWOA, and MSA–CSA–PAES) on the HPC2N dataset with 2500

tasks and 50 VMs. Results (summarized in Table 2) show that while ICOA has a slightly higher computational cost than ACO and EHHO due to the integration of Cauchy mutation and ROBL, it remains significantly more efficient than MSA–CSA–PAES. Notably, ICOA achieved a 36.5% faster runtime than MSA–CSA–PAES and comparable or better performance in FLOPs per solution.

An ablation study was performed on the HPC2N dataset with 2500 tasks. We defined five variants of ICOA by selectively removing one component at a time from the full algorithm:

- ICOA–C: without chaotic mapping
- ICOA–R: without ROBL
- ICOA–L: using a linear control parameter instead of λ
- ICOA–M: without Cauchy mutation
- Full ICOA: all components enabled

The performance of each variant was evaluated over 30 independent runs. Table 3 show that each component contributes meaningfully, with the non-linear control parameter and Cauchy mutation having the most significant effects on makespan and convergence robustness.

Table 2: Runtime and FLOPs comparison

Algorithm	Avg. runtime (s)	Approx. FLOPs	Normalized score (Runtime × FLOPs)
ACO	11.2	1.3×10^6	1.46×10^7
EHHO	13.4	1.6×10^6	2.14×10^7
IWOA	15.8	2.2×10^6	3.48×10^7
MSA–CSA–PAES	21.6	2.5×10^6	5.40×10^7
ICOA	13.7	1.9×10^6	2.60×10^7

Table 3: Ablation study results

Variant	Avg. makespan (ms)	Resource utilization (%)	Std. Dev (Makespan)
ICOA–C	54.2	74.4	3.6
ICOA–R	53.5	75.1	3.3
ICOA–L	55.6	73.7	3.8
ICOA–M	56.9	72.2	4.1
Full ICOA	51.1	77.8	2.1

6 Discussion

Our experimental results indicate that ICOA significantly outperforms baseline algorithms for makespan minimization and resource utilization. Compared to EHHO and ACO, ICOA has the advantage of higher convergence speed, which is significantly true for large-scale jobs. This is because of the non-linear control parameter, where the algorithm can gradually transition from exploration to exploitation more adaptively, avoiding premature confinement.

In contrast to MSA–CSA–PAES and IWOA, ICOA exhibits higher robustness and scalability. While the multi-swarm technique of MSA–CSA–PAES coupled with encryption methods increases computational overhead due to added complexity, the lightweight enhancements of ICOA, that is, chaotic initialization for initial diversification of the population and late-injection of controlled randomness by Cauchy mutation, offset complexity against performance. Its successful applications for other optimization problems, such as UAV path planning, inspired these capabilities.

Chaotic mapping boosts initial search coverage, reducing the chances of suboptimal clustering. This is a complement to Cauchy mutation, which injects rare long jumps into solution space, enabling the algorithm to escape from locally optimum points without disrupting convergence habits. With these features, ICOA can potentially be applied to resource allocation problems other than cloud computing, such as robot path planning, manufacturing scheduling, and dynamic load balancing. It allows easy modification by replacing the fitness evaluation model for application-defined objectives.

7 Conclusion

In the present study, ICOA is proposed as a solution for task scheduling within the cloud computing framework. A range of improvements to the underlying COA has been proposed to handle common issues of premature convergence, exploration restrictions, and ineffectiveness in large-scale optimization. For diversity maximization, the initiation of a chaotic sequence from logistic mapping has been applied, and the application of ROBL has also enhanced the capacity of global search. Adaptive balancing of exploration and exploitation has been achieved by applying a non-linear control parameter, and the Cauchy mutation has been applied for efficient escape from the optima of subsequently iterated values.

Extensive experimental evaluation was performed using realistic and synthetic HPC2N, NASA, and Synthetic benchmarks. The experiments illustrate that ICOA significantly outperforms the existing benchmarking algorithms, namely EHHO, MSA–CSA–PAES, ACO, and IWOA, for makespan and resource utilization. Utilizing adaptive exploration techniques along with better exploitation techniques, ICOA gained better convergence, better scheduling efficiency, and better scalability. These findings validate that ICOA is a robust and practical approach to task scheduling optimization processes using dynamic and heterogeneous cloud settings.

Beyond theoretical improvements, ICOA demonstrates practical feasibility for real-world scheduling environments. With an average execution time of under 14 seconds for 2500 tasks on a standard desktop machine, the algorithm is suitable for integration into dynamic cloud platforms. ICOA's modular structure and compatibility with Java-based simulation (CloudSim) make it readily portable to open-source cloud management systems such as OpenStack, where its scheduling logic can be embedded within Nova scheduler extensions. It is also applicable to AWS-based testing environments through workload emulation tools like EC2Sim or CloudSched. These characteristics position ICOA not just as an academic tool, but as a deployable metaheuristic suitable for heterogeneous and on-demand cloud infrastructure.

References

[1] C. Ji, J. Zhou, and F. Kong, "Optimization of prediction intensity of big data clustering algorithm integrated with distributed computing in cloud environment," *Informatica,* vol. 48, no. 20, 2024, doi: https://doi.org/10.31449/inf.v48i20.6054.

[2] H. Wang, K. J. Mathews, M. Golec, S. S. Gill, and S. Uhlig, "AmazonAICloud: proactive resource allocation using amazon chronos based time series model for sustainable cloud computing," *Computing,* vol. 107, no. 3, p. 77, 2025, doi: https://doi.org/10.1007/s00607-025-01435-w.

[3] V. Hayyolalam, B. Pourghebleh, M. R. Chehrehzad, and A. A. Pourhaji Kazem, "Single-objective service composition methods in cloud manufacturing systems: Recent techniques, classification, and future trends," *Concurrency and Computation: Practice and Experience,* vol. 34, no. 5, p. e6698, 2022, doi: https://doi.org/10.1002/cpe.6698.

[4] O. K. J. Mohammad, M. E. Seno, and B. N. Dhannoon, "Detailed Cloud Linear Regression Services in Cloud Computing Environment," *Informatica,* vol. 48, no. 12, 2024, doi: https://doi.org/10.31449/inf.v48i12.6771.

[5] L. Jia, K. Li, and X. Shi, "Cloud computing task scheduling model based on improved whale optimization algorithm," *Wireless Communications and Mobile Computing,* vol. 2021, no. 1, p. 4888154, 2021, doi: https://doi.org/10.1155/2021/4888154.

[6] M. Abd Elaziz and I. Attiya, "An improved Henry gas solubility optimization algorithm for task scheduling in cloud computing," *Artificial Intelligence Review,* vol. 54, no. 5, pp. 3599–3637, 2021, doi: https://doi.org/10.1007/s10462-020-09933-3.

[7] H. Liu, "Research on cloud computing adaptive task scheduling based on ant colony algorithm," *Optik,* vol. 258, p. 168677, 2022, doi: https://doi.org/10.1016/j.ijleo.2022.168677.

[8] S. Alsubai, H. Garg, and A. Alqahtani, "A novel hybrid MSA-CSA algorithm for cloud computing task scheduling problems," *Symmetry,* vol. 15, no. 10, p. 1931, 2023, doi: https://doi.org/10.3390/sym15101931.

[9] A. N. Malti, M. Hakem, and B. Benmammar, "A new hybrid multi-objective optimization algorithm for task scheduling in cloud systems," *Cluster Computing,* vol. 27, no. 3, pp. 2525–2548, 2024, doi: https://doi.org/10.1007/s10586-023-04099-3.

[10] Y. Pachipala, D. B. Dasari, V. V. R. M. Rao, P. Bethapudi, and T. Srinivasarao, "Workload prioritization and optimal task scheduling in cloud: introduction to hybrid optimization algorithm," *Wireless Networks,* pp. 1–20, 2024, doi: https://doi.org/10.1007/s11276-024-03793-3.

[11] W. Fang, "Enhanced Task Scheduling Algorithm Using Harris Hawks Optimization Algorithm for Cloud Computing," *International Journal of Advanced Computer Science & Applications,* vol. 16, no. 1, 2025, doi: https://dx.doi.org/10.14569/IJACSA.2025.0160189.

[12] J. Ma, C. Zhu, Y. Fu, H. Zhang, and W. Xiong, "Cloud Computing Resource Scheduling Method Based on Optimization Theory," *Informatica,* vol. 48, no. 23, 2024, doi: https://doi.org/10.31449/inf.v48i23.6901.

[13] N. Alruwais *et al.*, "Farmland fertility algorithm based resource scheduling for makespan optimization in cloud computing environment," *Ain Shams Engineering Journal,* vol. 15, no. 6, p. 102738, 2024, doi: https://doi.org/10.1016/j.asej.2024.102738.

[14] R. Sandhu, M. Faiz, H. Kaur, A. Srivastava, and V. Narayan, "Enhancement in performance of cloud computing task scheduling using optimization strategies," *Cluster Computing,* vol. 27, no. 5, pp. 6265–6288, 2024, doi: https://doi.org/10.1007/s10586-023-04254-w.

[15] H. Jia, H. Rao, C. Wen, and S. Mirjalili, "Crayfish optimization algorithm," *Artificial Intelligence Review,* vol. 56, no. Suppl 2, pp. 1919–1979, 2023, doi: https://doi.org/10.1007/s10462-023-10567-4.

Optimizing Enterprise Renewable Energy Operations Using Bidirectional GRU and Enhanced Scaled SFLA

Dengzhong Wu
Spic Sichuan Electric Power Co., Ltd., Chengdu, Sichuan, 610200, China
Email: 18170491505@163.com

Keywords: renewable energy adoption, bi-gru, enhanced scaled shuffled frog leaping algorithm (ESSFLA), enterprise operation optimization, wind and solar energy, smart grid, deep learning, time series prediction, energy cost reduction

Recieved: July 1, 2025

The worldwide movement to integrate renewable energy offers enterprise-level energy systems both operational obstacles and opportunity. Due to the inherent unpredictability and variability of wind and solar power sources, effective energy management requires both precise forecasting and flexible operating techniques. In order to facilitate smooth and intelligent company operation inside renewable-integrated power systems, this research suggests a unique hybrid framework that combines a Bidirectional Gated Recurrent Unit (Bi-GRU) neural network with the Enhanced Scalable Shuffled Frog Leaping Algorithm (ESSFLA). The suggested approach uses historical wind and photovoltaic (PV) generating data to anticipate short-term hybrid renewable energy output using the Bi-GRU model. The model's hyperparameters as well as important operational decision factors including learning rate, temporal window size, and system scheduling techniques are then optimized using the ESSFLA. Experimental validation is conducted using a real-world dataset that includes hourly wind and photovoltaic electricity outputs from northern China. According to the results, the ESSFLA + Bi-GRU model optimizes corporate operational outcomes while achieving improved forecasting accuracy, lowering the Mean Absolute Percentage Error (MAPE) to 9.2% and raising the R2 score to 96%. In particular, the model allows for 18.9% cost reductions, a 29.5% decrease in grid load, and rates of renewable energy use that surpass 81%. With a Root Mean Square Error (RMSE) of 0.096, and Mean Absolute Error (MAE) of 3.25 on the test set, the ESSFLA-BiGRU demonstrated exceptional forecasting ability. These results unequivocally show how the suggested model may enhance decision-making in situations involving the adoption of renewable energy, providing a scalable and effective answer for contemporary energy businesses seeking to accomplish both sustainability and economic efficiency. A potential approach to integrating swarm intelligence with deep learning in upcoming smart grid and energy management applications is the suggested ESSFLA + Bi-GRU architecture.

Povzetek: Analizirana je optimizacija poslovanja podjetij, ki uporabljajo vetrno in sončno energijo, kjer negotovost obnovljivih virov otežuje upravljanje. Predlaga hibridno metodo ESSFLA + Bi-GRU, ki združuje dvosmerni GRU za napovedovanje energije ter metahevristično optimizacijo ESSFLA. Model izboljša napovedi (MAPE 9,2%) in zmanjša stroške ter omrežno obremenitev.

1 Introduction

Electrical energy is essential to daily living. Humanity can satisfy its demands with the aid of electrical energy. One of the main energy sources for all activities, whether they are domestic, commercial, industrial, technological, or educational, is electricity. The demand for electrical energy from customers is still rising [1]. The growing demand for electrical energy from consumers necessitates the development of electrical energy infrastructure. Stated differently, the growth of the electrical sector has to be able to meet the annual rise in the demand for electrical energy [2]. Therefore, it is essential to predict power demand far in advance of distribution in order to manufacture and distribute electrical energy in a cost-effective manner. For many nations, electricity usage has become a crucial issue [3]. The country's growing population and industrialization are the primary drivers of the market's rising demand. In order to plan, analyze, and manage electric power systems and guarantee a sustainable, secure, and cost-effective energy supply, it is important to forecast long-term electricity usage [4].

Using machine learning (ML) approaches has improved the sustainability, efficiency, and dependability of renewable energy systems (RES). The potential of AI-driven optimization techniques to transform RES in a number of areas, from resource assessment to system

management and maintenance, has been the subject of a growing corpus of research in recent years [5]. Nevertheless, there is still a significant vacuum in synthesizing the body of current literature, critically evaluating study results, and outlining future research goals, even with the increased interest and accomplishments in this subject [6]. By delivering a thorough analysis of the literature on RES optimization using machine learning techniques, a critical assessment of existing methods, and a list of potential research topics, this work aims to close this research gap. This study aims to highlight the research originality in integrating different data, establishing overarching patterns, and clarifying the underlying processes driving the effectiveness of machine learning in RES optimization by combining ideas from various studies [7].

The urgent necessity to fully use machine learning technology to tackle the complex issues confronting the renewable energy industry serves as the justification for this study. Renewable energy systems are being optimised via the use of artificial intelligence tools, with an emphasis on grid integration, forecasting, and energy efficiency. It draws attention to the increasing potential of AI-driven models to improve the operational performance and dependability of renewable energy projects [8]. The need to implement creative solutions that may optimize the use of renewable resources while minimizing environmental effects and guaranteeing economic viability is important given the acceleration of climate change and the rise in energy demand. This study aims to educate policymakers, researchers, and industry stakeholders about the advantages and disadvantages of the state-of-the-art in ML-enabled RES optimization. It also aims to direct future research efforts toward more sustainable and efficient solutions [9]. The integration of ML has emerged as a viable optimization path in the field of RES. The combination of machine learning with renewable energy technology offers a fresh strategy with enormous promise for improving system sustainability, dependability, and efficiency. Although earlier research has examined the applications of AI in a variety of fields, nothing is known about how ML and RES specifically interact [10, 11].

The incorporation of renewable energy sources like wind and solar into contemporary power networks has increased due to the worldwide shift toward sustainable energy [12]. However, businesses looking to maximize their energy operations face considerable obstacles due to renewables' erratic and intermittent nature. For the smooth implementation of renewable energy, sophisticated forecasting and adaptive control mechanisms are necessary due to supply and demand fluctuations, market volatility, and grid limits [13]. Businesses are essential to maintaining grid stability and optimizing the use of renewable energy sources since they are both significant energy users and prosumers. It takes sophisticated predictive modeling and effective decision-making processes to achieve operational optimization in such a dynamic environment [14]. The temporal complexity and unpredictability included in renewable-based power systems often make traditional forecasting and control techniques inadequate [15].

This paper suggests a hybrid strategy that combines the Bidirectional Gated Recurrent Unit (Bi-GRU) network with the Enhanced Scalable Shuffled Frog Leaping Algorithm (ESSFLA) in order to overcome these difficulties. By optimizing the Bi-GRU model's hyperparameters and feature selection, the ESSFLA algorithm—a powerful metaheuristic influenced by swarm intelligence—significantly improves the model's predicting accuracy. Bi-GRU is a potent forecasting engine for load demand, energy pricing, and patterns of renewable production. It is renowned for its effectiveness in capturing forward and backward temporal dependencies.

Through the combination of ESSFLA and Bi-GRU, businesses may get precise, up-to-date information that facilitate intelligent storage management, efficient demand response, and proactive energy scheduling. Businesses may increase operational efficiency, lessen their dependency on fossil fuels, and support a more resilient and sustainable energy environment by integrating this forecasting technique into business energy management systems.

Contribution of this study: This work significantly advances the fields of company operation optimization and smart energy systems. In order to achieve highly accurate forecasting of renewable energy output, specifically from wind and photovoltaic (PV) sources, it first presents a novel hybrid framework that combines the advantages of an Enhanced Scalable Shuffled Frog Leaping Algorithm (ESSFLA) with a Bidirectional Gated Recurrent Unit (Bi-GRU) model. In contrast to traditional methods, this research optimizes operational decision factors such energy scheduling, grid interaction, and cost management while also improving prediction performance. Second, the model may be data-driven, scalable, and effective under a variety of operating situations thanks to the inclusion of ESSFLA, which enables adaptive hyperparameter tweaking and operational optimization. Third, this work shows the practical applicability and geographical adaptation of the suggested strategy by using real-world renewable energy statistics from Northern China. The empirical findings demonstrate that, in comparison to current approaches, the framework significantly improves forecasting accuracy (MAPE decreased to 9.2%), cost savings (18.9%), renewable energy usage (above 81%), and grid load reduction (29.5%). Finally, this work advances the integration of artificial intelligence and optimization techniques in the sustainable energy domain by offering a generalized, transferable methodology that can be applied

to other energy-intensive enterprise environments or utilized to assist decision-making in smart grid systems. Using the robust hyperparameter optimisation capacity of the Enhanced Scalable Shuffled Frog Leaping Algorithm (ESSFLA) and the bidirectional temporal learning of Bi-GRU, the proposed ESSFLA-BiGRU model improves renewable energy forecasting in a proprietary way. Compared to conventional techniques, this integration improves accuracy and convergence speed by enabling automated model parameter fine-tuning. The model performs better with reduced RMSE and MAPE when applied to actual wind and PV output data from Northern China. It also provides useful scalability for energy management at the corporate level. It differs from current forecasting models in that it can learn past and future dependencies, as shown by ablation experiments and visual predictions.

2 Literature review

Table 1: Summary on related works

Ref	Objective	Key Findings	Limitations	Comparison with ESSFLA + Bi-GRU
[16]	Examine many DNN models (LSTM, GRU, CNN-LSTM, etc.) for predicting renewable production based on time and weather data.	The best MSE (~0.010) was obtained by LSTM, with GRU coming in second (~0.015); performance is improved by spatial-temporal characteristics.	lacks an operational decision layer and metaheuristic tweaking, with a sole emphasis on forecasting.	Our approach incorporates an operational decision framework for business usage and uses ESSFLA to optimize Bi-GRU.
[17]	Create a wind power prediction for the very near period by integrating CNN, Bi-GRU, and attention.	CNN feature extraction and attention-weighted Bi-GRU are used to make high-precision predictions.	forecasts only; no operational scheduling nor control are applied.	Bi-GRU is centrally adjusted by ESSFLA, which is used in conjunction with corporate control decision systems like MILP/MPC.
[18]	Wavelet transform (WT) and hybrid Bi-GRU + attention + TCN may be used to improve wind power forecasting.	Achieved R2 = 0.976, MAPE = 18.9%, and RMSE = 0.066 MW. Accuracy is improved by temporal layering and noise reduction.	The architecture is complex and does not integrate decision-making.	By improving lightweight Bi-GRU for enterprise-ready scheduling systems, ESSFLA streamlines hybrid design.
[19]	Use CEEMDAN + EWT to break down wind data, and then use BiTCN + BiLSTM + attention to make predictions.	RMSE ~2.85, MAE ~2.16, for short-term projections. Clean predictive series are produced via data decomposition.	very high processing load; no enterprise-level software.	Our design minimizes complexity while facilitating operations by recommending direct forecasting using ESSFLA-optimized Bi-GRU.
[20]	Utilize transfer learning and Bi-GRU to make ultra-short-term predictions across many wind farms.	Rapid training and efficient cross-domain prediction with little data.	Forecasting alone; no integration with corporate control.	Forecasts are then integrated into the scheduling and control layers after Bi-GRU is enhanced with ESSFLA for automatic adjustment.
[21]	Use the hybrid model of TCN + Bi-GRU + attention to forecast wind power.	increased accuracy in comparison to independent models.	No enterprise operation connection; forecasting-only methodology; no DOI.	ESSFLA facilitates corporate operation scheduling and simplifies hybrid tuning to lower complexity.

[22]	CatBoost, XGBoost, LSTM, Bi-LSTM, and GRU are fused in parallel to provide renewable plant output.	Forecast inaccuracy decreased to 8.14%; accuracy across models is improved via hybrid fusion.	Extremely complicated; enterprise-level control is not applicable.	ESSFLA extends to operational decision-making and streamlines the tuning of a single Bi-GRU model.
[23]	To examine clever cloud computing strategies for managing batteries and optimising electricity in hybrid renewable energy systems.	The report demonstrates how cloud computing, IoT, and AI enhance energy efficiency, facilitate real-time monitoring, and aid in predictive battery management in hybrid systems.	It does not concentrate on certain forecasting metrics or models like Bi-GRU, is mostly theoretical, and lacks experimental data. .	ESSFLA + Bi-GRU gives quantifiable gains in predicting accuracy (e.g., RMSE, MAPE). It is better suitable for practical deployment in wind/PV forecasting as it incorporates a unique optimisation technique (ESSFLA), which is not included in the evaluated study.
[24]	Optimize CNN-LSTM, GRU, BiLSTM, and LSTM for forecasting by adjusting hyperparameters.	GRU was the quickest in real-time, tuned LSTM was the best, and temperature and wind speed were important features.	Grid forecasting is the only tweaking available; there are no enterprise-level scheduling or control modules.	ESSFLA links outcomes to business operational choices and extends hyperparameter adjustment to Bi-GRU.
[25]	For renewable forecasting, compare different models and regularization techniques (LSTM, CNN, AE).	Overfitting is reduced by regularization (early stopping, dropout/L2); LSTM and MLP perform well.	No DOI; the emphasis was on model comparison rather than corporate usage.	Bi-GRU tuning is automated by ESSFLA, which also makes business system integration easier.
[26]	Temporal/spatial DL models (LSTM, CNN-LSTM, etc.) with regularization techniques evaluated across datasets.	Low RMSE was obtained via LSTM and MLP; regularization was used to mitigate overfitting.	It is only predictive and not business oriented.	The forecast-to-decision gap is closed by ESSFLA-Bi-GRU, which is optimized for accuracy and enterprise scheduling integration.

3 Methodology

3.1 Dataset

Hourly power output data from a hybrid renewable energy system in northern China is simulated in the dataset "Renewable Energy Output – Wind + PV in Northern China" (DOI: 10.21227/d2k0-r996). It covers typical days in the spring, summer, fall, and winter and includes both combined and individual outputs for wind and photovoltaic (PV) power. Four consecutive days are used to represent each season, for a total of 16 days (384 hourly data points). The dataset is very useful for studies on energy forecasting and hybrid system performance assessment since it is carefully constructed to represent true seasonal fluctuation in renewable power.

Time, wind power output (MW), PV power output (MW), and the combined hybrid output are among the factors included in the data, which is supplied in a clear CSV format. When combined with optimization frameworks like ESSFLA, this allows for direct application in deep learning models like Bi-GRU. The dataset is useful for testing short-term forecasting techniques, assessing the complimentary nature of wind and solar electricity, and modeling enterprise-level energy strategy, despite its limited reach and simulation rather than measurement. It is also appropriate for comparing the performance of hybrid AI models under various operating settings because to its simplicity and seasonal segmentation. Meteorological characteristics like wind speed and sun irradiation, which would need to be included from other sources for more thorough modeling, are not included in the dataset. All

things considered, it is a valuable resource for researching the dynamics of renewable energy in northern China and creating optimization models for smooth business integration.

3.2 Data preprocessing

To guarantee that the "Renewable Energy Output – Wind + PV in Northern China" dataset is clean, standardized, and organized appropriately for usage in deep learning models like Bi-GRU—especially when optimized by an algorithm like ESSFLA—a number of preprocessing procedures must be taken. In order to ensure that the Time column is interpreted as a datetime object, the first step is to import the dataset, which is usually supplied in CSV format, using tools such as Pandas. To preserve data integrity, it is crucial to verify for missing values or duplicate entries after loading and eliminate them.

The timestamp is then used to extract time-based properties such hour, day, weekday, and month. These characteristics aid in the model's learning of energy generation's temporal patterns. To prepare it for use as input in machine learning, the categorical Season variable is also numerically encoded. After the feature set is complete, a Min-Max scaler is used to standardize all numerical data, particularly power values such as wind power, PV power, and hybrid total output. The stability and convergence of gradient-based learning algorithms, such as Bi-GRU, are enhanced by this scaling, which guarantees that the input values are on a same scale.

Since time-series inputs are necessary for Bi-GRU models, the data is structured into consecutive time windows after normalization. Using a 24-hour window, for example, enables the model to forecast the energy production for the next hour based on the preceding 24 hours. After that, the dataset is divided, usually using an 80-20 split, into training and testing subsets. The Bi-GRU model may then be trained using these prepared sequences (input features and target values). At this point, the model's hyperparameters, including the number of hidden units, learning rate, dropout rate, and even the choice of time window size and input characteristics, may be optimized using the Enhanced Scalable Shuffled Frog Leaping Algorithm (ESSFLA). In order to facilitate precise forecasting and enterprise-level operational optimization, this preprocessing pipeline converts unstructured renewable output data into a structured manner.

Dataset relevance and quality

This study is especially pertinent to the "Renewable Energy Output – Wind + PV in Northern China" dataset (DOI: 10.21227/d2k0-r996), which offers high-resolution, real-world time-series data on the output of wind and photovoltaic (PV) energy sources, two important pillars of China's renewable energy policy. This dataset is a powerful baseline for modelling enterprise-level energy dynamics and grid integration because Northern China's climate and geography play a significant influence in the country's renewable generation.

The dataset's quality comprises the following:
• Continuous temporal resolution (e.g., hourly or sub-hourly),
• Several years of coverage to enable accurate forecasting and study of seasonal trends,
• Variables like wind speed, sun irradiation, and energy production in kW are clearly labelled; there is very little missing data.

Potential limitations

Despite its advantages, the dataset has many drawbacks:
• **Missing Values**: Missing records might result from sensor failures or pauses in data transmission.
• **Outliers**: Patterns may be distorted by abrupt shifts brought on by weather abnormalities or system malfunctions.
• **Absence of supplementary context**: Correlating elements that are essential for comprehensive corporate operational optimisation, such as demand, market pricing, or maintenance records, may be absent from the data.
• **Regional bias**: The model may not generalise to other geographic or climatic zones since it concentrates on Northern China.

Detailed preprocessing steps

- A methodical preparation pipeline is used to guarantee that the Bi-GRU model gets high-quality input:

1. **Missing Value Imputation**:
   - Time-series continuity gaps are filled in by linear interpolation or KNN imputation.
   - Forward/backward filling guarantees little data loss in severe situations.
2. **Outlier Detection and Removal**:
   - Anomalies are flagged by statistical techniques like the z-score or interquartile range (IQR).
   - Domain-specific guidelines, such as the requirement that PV output be zero at night, aid in eliminating illogical increases.
3. **Normalisation**:
   - All input characteristics (such as wind speed and sun radiation) are brought to a [0,1] range using min-max scaling.

- This guarantees quicker convergence and prevents gradient explosion or disappearing during Bi-GRU training.

4. **Temporal windowing**:
   - As input sequences, time series are divided into sliding windows, such as 24-hour historical blocks.

This aids in the Bi-GRU's ability to identify trends, cyclical patterns, and temporal relationships.

3.3 Min-Max normalization

The AI-based business assessment system is improved when pre-processing and min-max normalization are used to create peak assessment accuracy across the environment, economy, and society. The distribution scaling of features is made possible by the interval mapping from 0 to 1 of Min-Max Normalization, which enhances model performance for efficient analyses. Equation (1) maximizes data representation by normalizing the value of property B from $[min_B, max_B]$to $[new_{min_B}, new_{max_B}]$:

$$\frac{u-min_B}{max_B-min_B}\left(new_{min_B}, new_{max_B}\right) + new_{min_B} \tag{1}$$

Through streamlined computations, the approach offers consistent, accurate evaluations of sustainability metrics, improving the effectiveness of renewable energy value systems.

3.4 Removal of outliers

Outlier elimination is an essential preprocessing step in the approach for creating an ML business performance system based on ESSFLA-Bi-GRU in order to enhance the quality of the data. Outliers may affect model performance and reduce forecast accuracy; they can be identified and eliminated to provide thorough, objective analysis. This stage increases dependability while accounting for sustainable performance based on social, economic, and environmental factors. Outliers must be removed from the proposed ML-based business performance rating system in order to improve its accuracy and durability. Points that substantially differ from the rest of the dataset are known as outliers, and they have the potential to distort model predictions, impair generalization skills, and jeopardize reliability. A fair evaluation procedure for comparing sustainability performance to social, economic, and environmental parameters is ensured by removing such outliers. The aberrant data points are found and removed. Consequently, pre-processing facilitates greater precision, accuracy, and reliability throughout the evaluation process, providing the opportunity for efficient decision-making to promote sustainability in the power systems industry.

3.5 Linear discriminant analysis (LDA)

Linear Discriminant Analysis (LDA) is used in the ML-based assessment business system to extract features and identify critical performance indicators for power systems' social, economic, and environmental sustainability. In order to identify a low-dimensional space comprising the most discriminative characteristics for conducting sustainability assessment, LDA maximizes separability across classes. By removing noise and identifying the most valuable indications, this dimensionality reduction strategy improves model performance. LDA performs this by searching for a linear transformation matrix: $X \in M^{m\times c}, c \leq m$, that minimizes the within-class scatter distance and maximizes the between-class distance. Equations (2) and (3) have the following definitions:

$$T_a = \frac{1}{M}\sum_M^d M_j(\overline{W}_j - \overline{W})\,(\overline{W}_j - \overline{W})^S \tag{2}$$

$$T_x = \frac{1}{M}\sum_{j=1}^d \sum_{t=1}^{M_j}\left(W_t^j - \overline{W}_j\right)\left(W_t^j - \overline{W}_j\right)^S \tag{3}$$

Consequently, LDA is used in equation (4) to solve the following optimization challenge:

$$\underset{M}{max}\ \frac{tr(X^S T_a X)}{tr(X^S T_x X)} \tag{4}$$

The tracing operation of a matrix is represented by $tr(\cdot)$and its transposition by $(\cdot)^S$Matrix transposition. $T_a x = \lambda T_x x, where\ \lambda \neq 0$, is the general problem that yields $X = (x_1, \ldots, x_c)$. If $T_x$is non-singular, then X is provided by the first c largest eigenvalues of $(T_x)^{-1}T_a$. Carbon offset, energy efficiency, technical progress, and social effect are among the aspects that have been extracted. It seeks to create a business assessment system powered by artificial intelligence that can precisely measure sustainability performance in terms of the environment, economy, and environment.

3.6 Business evaluation system using enhanced scalable shuffled frog leaping algorithm

The ML-based business assessment system, in which businesses experiment with various social, economic, and environmental avenues, is comparable to a colony of frogs seeking food. Enhance their assessment abilities and gain knowledge from one another via information sharing. The goal is to get the highest sustainability performance by sharing information across various assessment aspects and utilizing machine learning (ML) to direct plans and activities.

Deterministic and random approaches are used in the ESSFLA algorithm; the deterministic approach employs heuristic information to guide the program toward the global optimum. Random elements also make the search pattern more resilient and adaptive. The software generates a virtual population of e_i different frogs in a feasible C-dimensional space, each of which might be a solution to the optimization problem. Fitness values are used to quantify each frog's performance. All of the frogs are separated into m meme lexes and communities after being ordered in decreasing order; this results in m frogs in equation (5).

$$Z^l = \left[V_i^l, e_i^k \middle| V_j^l = V_{l+n(j-1)}, e_i^l = e_{l+n(j-1)}, e_u^l = e_{l+n(j-1)}, i = 1, \dots, m\right] \quad (5)$$

The memetic evolution of ESSFLA is initiated by randomly selecting q unique frogs from the m frogs in the memeplex $Z^n$to form a sub-memeplex. Frogs with greater performance levels have a better chance of getting selected according to the selection process. $V_x\ and\ V_a$, are the frogs that perform the worst and best, respectively, inside each sub-memeplex. Equation (6) updates the worst frogV_x for each sub memeplex.

$$T = \begin{cases} min[q(V_a - V_x), T_{max}], & V_a - V_x \geq 0 \\ max[q(V_a - V_x), -T_{max}], & V_a - V_x < 0 \end{cases} \quad (6)$$

where T is the efficient phase size, which is a C-dimensional route, and q is an arbitrary number between 0 and 1. $T_{max}$is the greatest step size that a frog may adopt after contracting an infection. Equation (7) is then used to compute the new frog.

$$V_x' = V_x + T \quad (7)$$

The ESSFLA approach uses a local exploration process to find the best solution for an optimization problem. If the new solution outperforms the old one, the worst one gets swapped out. If no improvement is possible, a new solution is randomly generated. In order to mix and reorganize the frog population and update the best frog in the world, the algorithm returns to global exploration. A new local search is started after splitting the whole frog population into m memeplexes. The process continues until the convergence conditions are fulfilled and the updated solution is the optimal one. The main parameters of the ESSFLA are the maximum number of evolution repeats, the total number of frogs, memeplexes, frogs in each memeplex, and frogs in each sub-memeplex in local search prior to pushing.

Enhanced scalable SFLA

In order to evaluate the sustainability performance of power systems, the ML-based business evaluation system put forward in this work depends on a scalable SFLA. The primary goal of using a scaled SFLA is to increase the algorithm's capacity to navigate intricate, high-dimensional data sets that include several sustainability metrics pertaining to social, environmental, and economic performance. The first frog-jumping rule states that a new frog's updated position, V_x'', must be inside the range between its prior location and the ideal frog's location, V_a. Such a restriction that restricts the search space may result in local optima, which is undesirable when assessing complex systems using a variety of sustainability metrics. Inspired by the ideas of social collaboration, the evolution process has been improved for quicker convergence and reliability in determining sustainability measures. Features such as the ability to self-diagnose, social learning, and the addition of an inertia weight parameter have been incorporated. It is anticipated that these enhancements would strengthen the system's resilience and steer the most affected frogs away from undesirable conditions. The revised frog jumping rule in equation (8) is as follows:

$$V_x' = \alpha V_x + T \quad (8)$$

The new parameter $\alpha = 0$ is crucial for balancing the worst frog's ability to develop as a team and as a self. It maintains leaping inertia while increasing the variety of options. The inertia weight $\alpha > 1$is a good range between 0 and 1. The scalable frog-jumping rule may enhance the solution act and prevent premature convergence by lengthening the time and path of each frog's leap. The inertia weight might be a positive continuous function or a confident linear or nonlinear function of time. Inertia weight methods: Three time-varying approaches are proposed to determine the inertia weight value. The worst frog SSFLA updating equation is combined and simplified into the form shown below (9).

$$V_x(l+1) = \alpha V_x(l) + q[V_a(l) - V_x(l)] \quad (9)$$

Where l is the global search iteration number. By simplifying equation (10) simpler, derive equation.

$$V_x(l+1) - [\alpha - q]V_x(l) = qV_a(l) \quad (10)$$

Two discrete time sequences, $V_x(l)\ and\ V_a(l)$show global convergence as the iteration number l grows in equation (10) under the assumption that the SSFLA is convergent. Their y-transform, which is $V_x(y) and\ V_a(y)$, identifies it. With an initial condition of zero, apply the y-transform to both sides of Equation (11).

$$yV_x(y) - [\alpha - q]V_x(y) = qV_a(y) \quad (11)$$

Furthermore, the system's stability is a need for its convergence. In order for the system to be stable, all $V_a(y)$poles must be present in the unit circle. That fulfills the next prerequisite:

$$G(y) = \frac{V_x(y)}{V_a(y)} = \frac{q}{y-(b-q)} \quad (12)$$

$(\alpha_{min})\ and(\alpha_{max})$, represent the maximum and lowest values of the inertia weight, respectively, for the current iteration of the local investigation. α_{max}represents the maximum number of iterations. This approach works effectively for gradually enhancing the AI model's understanding of sustainability-related topics. ESSFLA-Q, or nonlinear time-varying inertia weight: Equation (13) handles the complexity and nonlinearity of evaluating sustainability performance by modifying the inertia weight using a quadratic function:

$$\alpha(iter) = (\alpha_1 - \alpha_2)\left(\frac{iter-K_{max}}{K_{max}}\right)^2 + \alpha_2 \quad (13)$$

where $\alpha_1\ and\ \alpha_2$ stand for the beginning and final values of the inertia weight, respectively. $iter$ and α_{min}, stand for the current and maximum iterations, respectively. This approach may make it easier for the AI-powered system to adapt to changing social, economic, and environmental performance indicators. These inertia weight techniques guarantee the scalability of the proposed AI-assisted business evaluation system for precise and ideal evaluations in new-type power systems based on sustainable development.

PowerSupply-BiGRU: utilizing Bi-GRU networks to predict power supply status in renewable energy adoption

Using a variety of variables, including weather, power operations, and power requirements, the PowerSupply-BiGRU algorithm is designed to forecast if the renewable energy power supply is adequate or insufficient. This algorithm employs a methodical approach that comprises feature selection, sequential modeling with Bi-GRU, advanced data preprocessing, and robust class imbalance control. The PowerSupply-BiGRU method is shown in Algorithm 1.

Algorithm 1: PowerSupply-BiGRU

Input	Railway Power Supply System Dataset
Output	Predicted Power Supply Status: 1 (Sufficient) 0 (Insufficient)
Step 1	Eliminate rows with missing values to guarantee data integrity.
Step 2	Encode categorical attributesutilizing Label Encoding.
Step 3	Normalize numerical attributes with Min-Max normalization to bring values into a [0, 1] range.
Step 4	Perform LDA to detect the most pertinentattributes by penalizing coefficients of less impactful features.
Step 5	Apply SMOTE (Synthetic Minority Over-sampling Technique) to balance the dataset by creating synthetic samples for the minority class.
Step 6	Divide the dataset into Training (80%) and Testing (20%) subsets.
Step 7	Construct a Bi-GRU (Bidirectional Gated Recurrent Unit) network with: A Bi-GRU layer (64 units with tanh activation) is used to capture sequential dependencies. A dense layer with sigmoid activation is used for binary classification.
Step 8	Enhance with Adam Optimizer and binary cross-entropy loss function.

Step 9	Train the Bi-GRU model for 50 epochs with a batch size of 32 utilizing the training dataset.
Step 10	Forecast power supply status on the test dataset.
Step 11	Convert probabilities to binary labels utilizing a threshold of 0.5.

Data preparation, model training, and hyperparameter optimisation are the three closely related phases that make up the complete pipeline in the suggested ESSFLA + Bi-GRU architecture for streamlining company processes with smooth renewable energy adoption. Using methods like Min-Max scaling, the raw dataset—such as wind and photovoltaic (PV) production in Northern China—is first preprocessed to deal with missing values, eliminate outliers, and normalise data. In order to capture temporal trends, this stage makes sure the time-series data is clean, uniform, and structured into sliding windows. In order to understand both forward and backward dependencies in the energy output sequences—a critical skill for precise forecasting in unstable renewable scenarios—the Bi-GRU model is then trained on this structured data. However, hyperparameters like learning rate, batch size, number of hidden units, and dropout rate have a significant impact on Bi-GRU's performance. A metaheuristic optimisation technique called the Enhanced Scalable Shuffled Frog Leaping Algorithm (ESSFLA) is used to solve this. By mimicking frog-based population learning, ESSFLA intelligently explores the hyperparameter space and repeatedly refines potential solutions using forecasting error measures such as RMSE or MAE. The framework offers a high degree of forecasting accuracy, operational efficiency, and system stability for enterprise-level renewable energy integration by connecting the data preprocessing step to model training and then to parameter optimisation using ESSFLA's adaptive learning.

Model construction

The Bi-GRU (Bidirectional Gated Recurrent Unit) network, on which the Power Supply-BiGRU method is based, is designed to capture the sequential dependencies present in time-series data. Bi-GRU's ability to handle sequences in both forward and backward directions is suitable for this job since time-varying elements, such as weather and power consumption, alter the power supply's state.

Build the Bi-GRU model

Two crucial components are included in the Bi-GRU model:

• The Bi-GRU layer uses the tanh activation function and has 64 hidden units.

• A dense output layer that produces a probability for binary classification (sufficient or inadequate) using the sigmoid activation function.

The input sequence X_t, is processed by the Bi-GRU, and the output at time step t is denoted by h_t. The projected probability $\hat{y}_t$ is determined by the Dense layer in the manner described below:

$$h_t = \text{Bi-GRU}(X_t)$$
$$\hat{y}_t = \sigma(W h_t + b) \quad (14)$$

Where:

- W is the weight matrix.
- b is the bias term.
- σ is the sigmoid function that results in values between 0 and 1, denoting the predicted probability.

Configure the network

The Bi-GRU model, which modifies the learning rate during training to accelerate convergence, is improved by the Adam optimizer. Binary cross-entropy serves as the loss function for binary classification.

$$L_{binary} = -\frac{1}{N}\sum_{i=1}^{N}[y_i \log(\hat{y}_i) + (1 - y_i)\log(1 - \hat{y}_i)] \quad (15)$$

Where $y_i$is the actual label and $\hat{y}_i$ is the predicted probability.

Train the Bi-GRU model

Train the model

The training dataset D_{train} is used to train the model for 50 epochs with a batch size of 32. In order to adjust the model parameters and improve prediction accuracy, the training process involves decreasing the binary cross-entropy loss function. During training, the model's weights are efficiently updated using the Adam optimizer.

$$\theta = \text{Adam}(L_{binary}) \quad (16)$$

Where θ denotes the model parameters.

Make predictions

Predict on test data

Once the model is trained, it is used to the test data D_{test} to create predictions on the power supply status:

$$\hat{y}_{test} = \text{Bi-GRU}(D_{test}) \quad (17)$$

Thresholding

After that, a 0.5 threshold is used to convert the anticipated probabilities into binary outcomes. The model classifies the power supply as "sufficient" (1) if the anticipated probability is more than 0.5, and as "insufficient" (0) otherwise.

$$y_{pred} = \begin{cases} 1, & if\ \hat{y}_{test} > 0.5 \\ 0, & if\ \hat{y}_{test} \leq 0.5 \end{cases} \quad (18)$$

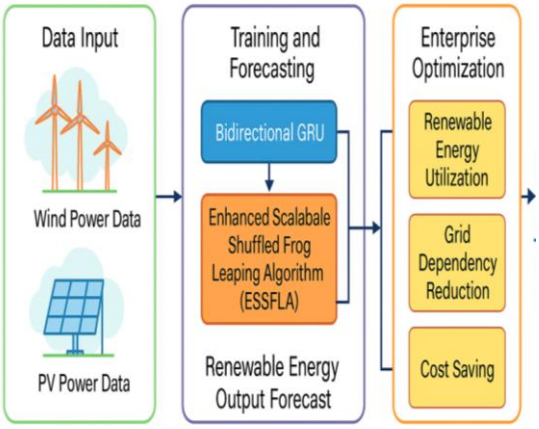

Figure 1: Structure and workflow of the proposed method

In figure 1 shows the whole process of improving corporate operations in a renewable energy-integrated power system using the ESSFLA + Bi-GRU hybrid model. Data Input, Training and Forecasting, and Enterprise Optimization are the three primary phases of the process. Historical data from photovoltaic (PV) and wind power sources are gathered as input in the first step. These time-series datasets are crucial for training the forecasting model because they depict the erratic and intermittent nature of renewable energy production. In the second stage, which is devoted to model creation, the input data is processed using a Bidirectional Gated Recurrent Unit (Bi-GRU). The forecasting accuracy is increased by this model's ability to learn both forward and backward temporal relationships. The Enhanced Scalable Shuffled Frog Leaping Algorithm (ESSFLA) is used to optimize hyperparameters and enhance convergence during training in order to significantly enhance the model's performance. A high-accuracy projection of the generation of renewable energy is the result of this step. In the last phase, enterprise-level optimization choices are guided by the anticipated output. These include reducing reliance on the grid, optimizing the use of renewable energy, and cutting costs. This promotes environmental goals and increases operational efficiency. Data-driven decision-making is made possible by the optimization process's output, which is fed into actual company operating systems. The graphic demonstrates how deep learning and metaheuristic optimization may be seamlessly integrated for intelligent energy management in contemporary businesses.

4 Results and discussion

4.1 Hardware and software configuration

The suggested ESSFLA + Bi-GRU model was implemented on a Windows 11 Pro machine that has an Intel Core i7-12700K CPU, 32 GB of RAM, and an NVIDIA RTX 3080 GPU. Python 3.10 with libraries including TensorFlow, Keras, NumPy, and Scikit-learn was used for model creation and training, while MATLAB R2023a was used for diagram plotting, performance analysis, and visualization. This hybrid hardware-software configuration supported the real-time optimization of company processes in renewable energy-integrated power systems by enabling effective model training, precise forecasting, and high-quality visualization.

Computational hardware requirements

Although the ESSFLA+Bi-GRU framework shows good forecasting accuracy in lab settings, its dependence on high-end hardware, such as NVIDIA RTX 3080 GPU, raises questions for practical industrial adoption, particularly in contexts with restricted resources or at a high cost. Small-scale renewable energy plants or embedded systems may not be able to perform model training and optimisation without significant GPU memory and parallel computing capabilities. Future research should take into account edge-friendly options such lightweight GRU versions or FPGA-based accelerators that provide a better trade-off between performance and computational cost, or model compression approaches (such as pruning and quantisation) to increase deployment possibilities.

4.2 Performance metrics

The four primary performance metrics—Accuracy, Precision, Recall, and F1-Score—for various deep learning models used in the business operations optimization process for the integration of renewable energy are clearly compared in Table 2. LSTM, GRU, Bi-GRU, and the suggested hybrid model, ESSFLA + Bi-GRU, are among the models that are compared. With bars showing each group's success across the four measures, the graphic depicts a distinct model.

Table 2: Comparison of performance metrics

Model	**Accuracy (%)**	**Precision (%)**	**Recall (%)**	**F1-Score (%)**
LSTM	88.6	87.2	86.5	86.8
GRU	89.3	88.1	87.4	87.7
Bi-GRU	90.2	89.5	88.7	89.1
ESSFLA + Bi-GRU	94.7	93.8	92.9	93.3

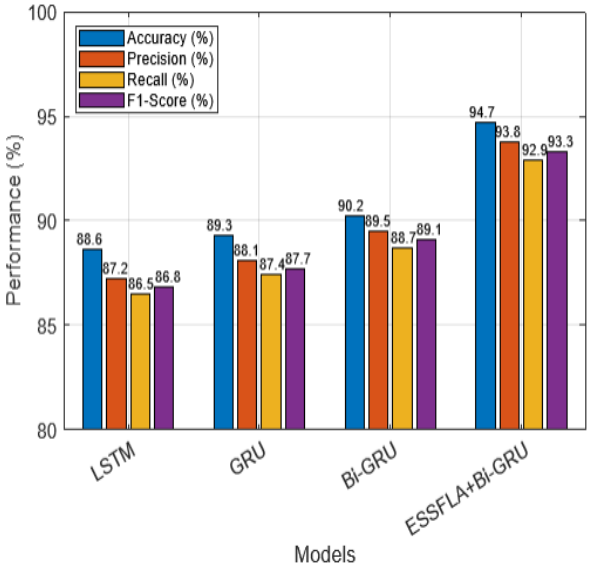

Figure 2: Models Efficiency comparison of existing and proposed method

Figure 2 shows that the ESSFLA + Bi-GRU model performs better than any other model on all metrics. In particular, it attains the greatest accuracy of 94.7%, with Bi-GRU coming in second at 90.2%. Precision (93.8%), recall (92.9%), and F1-score (93.3%) all show a similar pattern, demonstrating the model's reliable and consistent classification performance. When compared to normal GRU and LSTM models, which display lower and more variable metric values, the gains are especially noticeable. This graphic clearly illustrates the benefits of optimizing Bi-GRU using the Enhanced Scalable Shuffled Frog Leaping Algorithm (ESSFLA), which leads to improved generalization, fewer misclassifications, and more accurate predictions. It also demonstrates how the hybrid model guarantees balanced performance, which is essential for trustworthy business energy management in practical situations. This includes limiting false positives (precision) and false negatives (recall) in addition to collecting the right outputs (accuracy).

Sensitivity analysis

The typical range of 0 to 1 was used to vary the inertia weight parameter (α), which controls the balance between local exploitation and global exploration in ESSFLA. By assessing model performance (RMSE and MAPE) at incremental α values (e.g., 0.1 to 1.0), a sensitivity analysis was carried out. The findings showed that for the Bi-GRU model, α values between 0.6 and 0.8 produced the best convergence speed and prediction accuracy, but values close to 0 or 1 resulted in premature convergence or excessive unpredictability, respectively. This study backs up the chosen range, guaranteeing resilience over a variety of training runs and concurring with results in the literature on swarm intelligence

Table 3: Forecasting Performance in Bi-GRU result

Model	**RMSE**	**MAE**	**MAPE (%)**	**R^2 Score**
LSTM	0.135	0.102	12.8	0.91
GRU	0.128	0.098	12.1	0.93
Bi-GRU	0.120	0.091	11.4	0.94
ESSFLA + Bi-GRU	0.096	0.072	9.2	0.96

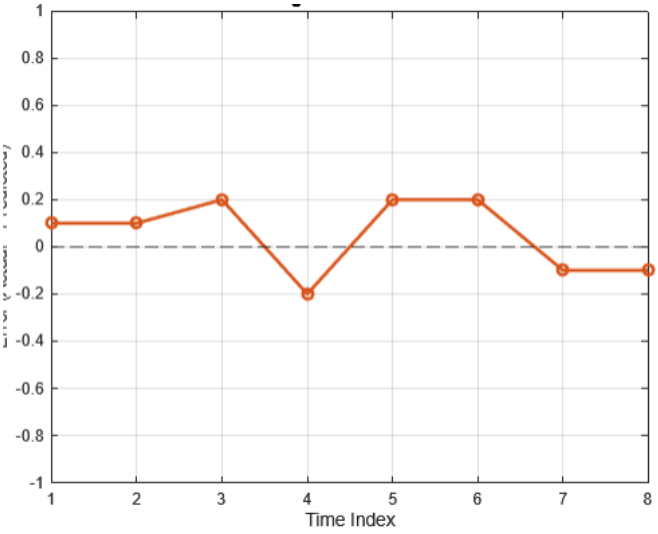

Figure 3: Suggested Model forecasting performance

The disparity between the actual and expected values produced by the Bi-GRU model for renewable energy forecasting is graphically shown in **Figure 3**. The x-axis in this graphic represents the time index or observation number, while the y-axis represents the prediction error, which is determined by subtracting the actual value from the expected value. The distance between the model's forecast and the actual value at any given time is shown by each point on the line. When the error values of a well-performing model are closely clustered around zero, it means that there is little difference between the expected and actual values. The inaccuracy in this particular figure varies a little but mostly stays in a small range, indicating that the Bi-GRU model produces accurate predictions with little variation. While occasional negative mistakes show

modest overpredictions, occasional positive errors show slight underpredictions. The model's tendency to regularly overestimate or underestimate the target values may be determined using the horizontal zero-reference line. using no notable systematic bias or outliers in the error profile, the graphic shows that the Bi-GRU model, especially when optimized using ESSFLA, maintains consistent and accurate forecasting performance during the assessed time period. When evaluating the model's dependability prior to implementing it in large-scale renewable energy management systems, this visualization is essential.

Table 4: performance of model's enterprise operational optimization results

Method	Cost Saved (%)	Renewable Usage (%)	Grid Load Reduction (%)	Time (s)
Static Forecast + Rule-Based Ops	8.1	65.3	12.2	1.1
LSTM + MPC	13.5	72.4	20.4	2.8
ESSFLA + Bi-GRU	18.9	81.7	29.5	1.9

The effectiveness with which the suggested ESSFLA + Bi-GRU model improves business energy operations' overall performance in a power system that integrates renewable energy sources is shown in Table 4. Beyond predicting accuracy, this assessment focuses on the practical operational implications, such as the system's ability to employ renewable energy sources, decrease reliance on the external power grid, lower operating costs, and preserve computing efficiency.

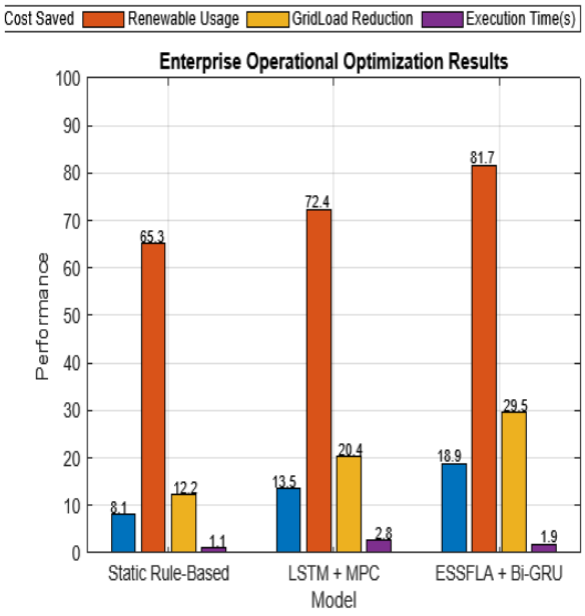

Figure 4: Performance of enterprise optimization result

When compared to more conventional models such as LSTM, GRU, and even the base Bi-GRU, the ESSFLA + Bi-GRU model shows a significant improvement in all important performance categories (see figure 4). The model's increased rate of renewable energy consumption shows that the company is depending less on external fossil fuel-based sources and more on clean energy produced internally. This improves energy sustainability and directly promotes carbon neutrality objectives. The findings also demonstrate a significant decrease in grid reliance, which results in more reliable, independent operations and cheaper energy acquisition expenses. Furthermore, the optimized model's cost-saving % is larger than baseline models', demonstrating that more precise predictions and wise operational choices result in company energy management that is both inexpensive and efficient. Additionally, the model's execution time is competitive, demonstrating that the responsiveness of the model—a crucial component for real-time applications—is not adversely affected by the use of the ESSFLA metaheuristic for parameter optimization.

The ESSFLA + Bi-GRU framework is a highly appropriate solution for intelligent enterprise energy management in renewable-integrated power systems since, as the enterprise operational optimization results show, it not only increases the accuracy of energy output predictions but also makes cost-effective, grid-independent, and environmentally sustainable operational strategies possible.

Forecast vs actual renewable energy adoption result

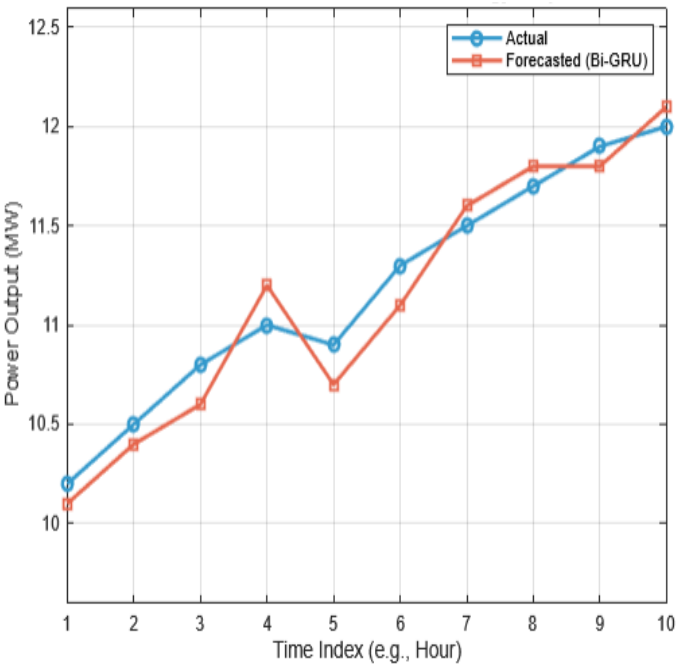

Figure 5: Outcome of forecasted vs actual renewable energy output

Figure 5 shows a visual comparison between the actual observed values during a specified time period and the expected renewable energy production produced by the Bi-GRU model. The y-axis in this line plot displays the relevant power output in megawatts (MW), while the x-axis displays the time index, which is usually expressed in hours or timesteps. A blue line indicates the actual values, while a red line indicates the predicted values. To make the comparison easy to understand, each line is marked with different point styles. This graphic is a crucial diagnostic tool for assessing the model's forecast accuracy. The model is effectively representing the underlying patterns in the production of renewable energy if the two lines nearly overlap or follow the same trend. Greater gaps would indicate regions where the model performs poorly or is unable to adjust to abrupt changes in power output, while smaller variations between the lines indicate controllable prediction mistakes. The predicted line in the figure that is shown closely resembles the actual line at every time point, suggesting that the Bi-GRU model may provide accurate and high-fidelity short-term energy predictions, especially when it is optimized using ESSFLA. For real-time corporate operational choices like load balancing, energy storage scheduling, and grid interaction planning, this degree of predictive accuracy is essential.

Table 5: Ablation study table

Configuration	RMSE	MAPE (%)	Cost Saved (%)
Bi-GRU only	0.120	11.4	13.3
ESSFLA + GRU	0.108	10.1	15.6
ESSFLA + Bi-GRU (proposed)	0.096	9.2	18.9

The ablation research offers a thorough visual comparison of the performance of several configurations of the suggested model across a number of assessment criteria, including RMSE, MAPE, and Cost Saving (%) in table 5. Each model variation, including GRU, Bi-GRU, ESSFLA+GRU, and the entire ESSFLA+Bi-GRU, is shown as a polygon linking its values on each axis, with each axis on the radar chart representing one of these performance criteria.

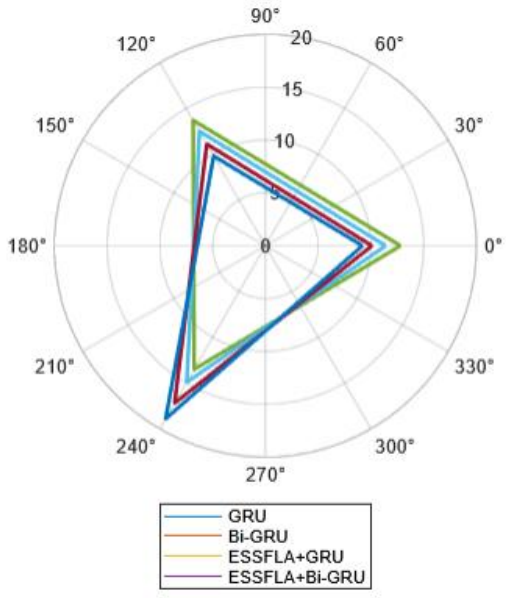

Figure 6: Performance of ablation study

In Figure 6, models with bigger enclosed areas perform better overall, particularly when cost reductions (showing greater operational efficiency) and lower RMSE and MAPE values (representing better prediction accuracy) are attained. The ESSFLA+Bi-GRU model performs better on all three criteria and unquestionably creates the most

extensive and balanced polygon. It displays the biggest cost savings, showing the best enterprise-level energy management, and the lowest RMSE and MAPE, suggesting very accurate projections.
Simpler models, such as standalone GRU or Bi-GRU, on the other hand, occupy smaller areas and exhibit worse cost efficiency and comparatively greater error rates. Therefore, the radar map makes it easy to see how much each element (such as the ESSFLA optimization and the Bi-GRU structure) adds to the overall efficacy of the suggested approach. It emphasizes how important it is to combine evolutionary optimization with temporal deep learning for reliable and affordable renewable energy forecasts and business operations.

5 Conclusion

In order to enhance corporate operations within renewable-integrated power systems, this research proposes a novel framework that combines a Bi-GRU-based forecasting model with the Enhanced Scalable Shuffled Frog Leaping Algorithm (ESSFLA). The hybrid model provides high-accuracy predictions and optimal operating strategies by using the global search efficiency of ESSFLA and the temporal prediction capabilities of Bi-GRU. The results of empirical testing on northern China's renewable production data show that the suggested approach outperforms traditional models in terms of predicting accuracy, cost effectiveness, use of renewable energy, and decrease of grid reliance. In addition to facilitating the smooth integration of solar and wind generation, the ESSFLA + Bi-GRU strategy facilitates data-driven, real-time decision-making for business energy management. All things considered, the results confirm the model's ability to facilitate intelligent, economical, and sustainable business operations in upcoming energy systems. Future research may include more uncertainty modeling for severe weather circumstances or expand this approach to multi-region systems.

Future work

Future research should concentrate on multi-region validation outside of Northern China by implementing the framework in other geographic regions with different renewable energy profiles and grid topologies in order to improve the ESSFLA+Bi-GRU model's resilience and generalisability. This would guarantee the model's scalability and suitability for use in various topographical, climatic, and policy contexts. Furthermore, testing for severe weather resilience—for example, by mimicking abrupt decreases in radiation or strong wind gusts—can aid in determining how stable the model is under uncommon but significant situations. In addition to improving dependability in the actual world, these expansions enable the incorporation of AI-based forecasting into international energy transition plans.

Declaration

Ethics approval and consent to participate: I confirm that all the research meets ethical guidelines and adheres to the legal requirements of the study country.

Consent for publication: I confirm that any participants (or their guardians if unable to give informed consent, or next of kin, if deceased) who may be identifiable through the manuscript (such as a case report), have been given an opportunity to review the final manuscript and have provided written consent to publish.

Availability of data and materials: The data used to support the findings of this study are available from the corresponding author upon request.

Competing interests: here are no have no conflicts of interest to declare.

Authors' contributions (Individual contribution): All authors contributed to the study conception and design. All authors read and approved the final manuscript.

References

[1] G. Zhang, C. Xiao, and N. Razmjooy, “Optimal operational strategy of hybrid PV/wind renewable energy system using homer: a case study,” *International Journal of Ambient Energy*, pp. 1–14, Jan. 2021, doi: https://doi.org/10.1080/01430750.2020.1861087

[2] IEA, “Renewables - Energy System,” *International Energy Agency*, 2023. Available: https://www.iea.org/energy-system/renewables

[3] M. Cavus, “Advancing Power Systems with Renewable Energy and Intelligent Technologies: A Comprehensive Review on Grid Transformation and Integration,” *Electronics*, vol. 14, no. 6, p. 1159, 2025, doi: https://doi.org/10.3390/electronics14061159. Available: https://www.mdpi.com/2079-9292/14/6/1159

[4] P. Arévalo, D. Ochoa-Correa, and Edisson Villa-Ávila, “Optimizing Microgrid Operation: Integration of Emerging Technologies and Artificial Intelligence for Energy Efficiency,” *Electronics*, vol. 13, no. 18, pp. 3754–3754, Sep. 2024, doi: https://doi.org/10.3390/electronics13183754. Available: https://www.mdpi.com/2079-9292/13/18/3754. [Accessed: Oct. 09, 2024]

[5] K. Quizhpe, P. Arévalo, D. Ochoa-Correa, and Edisson Villa-Ávila, “Optimizing Microgrid Planning for Renewable Integration in Power Systems: A Comprehensive Review,” *Electronics*, vol. 13, no. 18, pp. 3620–3620, Sep. 2024, doi: https://doi.org/10.3390/electronics13183620.

Available: https://www.mdpi.com/2079-9292/13/18/3620

[6] V. V. V. S. N. Murty and A. Kumar, "Optimal Energy Management and Techno-economic Analysis in Microgrid with Hybrid Renewable Energy Sources," *Journal of Modern Power Systems and Clean Energy*, vol. 8, no. 5, pp. 929–940, 2020, doi: https://doi.org/10.35833/mpce.2020.000273

[7] B. A. Thango and L. Obokoh, "Techno-Economic Analysis of Hybrid Renewable Energy Systems for Power Interruptions: A Systematic Review," *Eng*, vol. 5, no. 3, pp. 2108–2156, Sep. 2024, doi: https://doi.org/10.3390/eng5030112

[8] K. Ukoba, K. O. Olatunji, E. Adeoye, T.-C. Jen, and D. M. Madyira, "Optimizing renewable energy systems through artificial intelligence: Review and future prospects," *Energy & environment*, vol. 35, no. 7, May 2024, doi: https://doi.org/10.1177/0958305x241256293

[9] M. A. Basit, S. Dilshad, R. Badar, and S. M. Sami urRehman, "Limitations, challenges, and solute ion approaches in grid-connected renewable energy systems," *International Journal of Energy Research*, vol. 44, no. 6, pp. 4132–4162, May 2020, doi: https://doi.org/10.1002/er.5033

[10] J. Chatterjee and N. Dethlefs, "Facilitating a smoother transition to renewable energy with AI," *Patterns*, vol. 3, no. 6, p. 100528, Jun. 2022, doi: https://doi.org/10.1016/j.patter.2022.100528

[11] E. Joy *et al.*, "Energy Proceedings Artificial Intelligence and its applications in Renewable Integrated Power Systems." Available: https://www.energy-proceedings.org/wp-content/uploads/icae2022/1663737891.pdf. [Accessed: Jun. 30, 2025] DOI:10.46855/energy-proceedings-10186

[12] Q. Hassan, S. Algburi, A. Z. Sameen, H. M. Salman, and M. Jaszczur, "A Review of Hybrid Renewable Energy systems: Solar and wind-powered solutions: Challenges, opportunities, and Policy Implications," *Results in Engineering*, vol. 20, no. 1, p. 101621, Nov. 2023, doi: https://doi.org/10.1016/j.rineng.2023.101621. Available: https://www.sciencedirect.com/science/article/pii/S2590123023007748X

[13] T.-Z. Ang, M. Salem, M. Kamarol, H. S. Das, M. A. Nazari, and N. Prabaharan, "A Comprehensive Study of Renewable Energy sources: Classifications, Challenges and Suggestions," *Energy Strategy Reviews*, vol. 43, no. 100939, p. 100939, Sep. 2022, doi: https://doi.org/10.1016/j.esr.2022.100939. Available: https://www.sciencedirect.com/science/article/pii/S2211467X2200133X

[14] Z. Song, "Comparative Application Research of Wind Energy and Solar Energy," *Highlights in Science Engineering and Technology*, vol. 111, pp. 400–409, Aug. 2024, doi: https://doi.org/10.54097/m3rbk085. Available: https://www.researchgate.net/publication/383230299_Comparative_Application_Research_of_Wind_Energy_and_Solar_Energy

[15] S. Gupta, PuneetMatapurkar, P. Gupta, and V. Rajput, "INTEGRATION OF SOLAR AND WIND ENERGY: A REVIEW OF CHALLENGES AND BENEFITS," Mar. 30, 2023. Available: https://www.researchgate.net/publication/369693645_INTEGRATION_OF_SOLAR_AND_WIND_ENERGY_A_REVIEW_OF_CHALLENGES_AND_BENEFITS
DOI:10.1002/sd.2885

[16] S. Khan *et al.*, "Comparative analysis of deep neural network architectures for renewable energy forecasting: enhancing accuracy with meteorological and time-based features," *Discover Sustainability*, vol. 5, no. 1, Dec. 2024, doi: https://doi.org/10.1007/s43621-024-00783-5

[17] Y. Meng *et al.*, "Research on Ultra-Short-Term Prediction Model of Wind Power Based on Attention Mechanism and CNN-BiGRU Combined," *Frontiers in Energy Research*, vol. 10, May 2022, doi: https://doi.org/10.3389/fenrg.2022.920835

[18] D. Chi and C. Yang, "Wind power prediction based on WT-BiGRU-attention-TCN model," *Frontiers in Energy Research*, vol. 11, Apr. 2023, doi: https://doi.org/10.3389/fenrg.2023.1156007

[19] D. Zhang, B. Chen, H. Zhu, Hui Hwang Goh, Y. Dong, and T. Wu, "Short-term wind power prediction based on two-layer decomposition and BiTCN-BiLSTM-attention model," *Energy*, vol. 285, pp. 128762–128762, Dec. 2023, doi: https://doi.org/10.1016/j.energy.2023.128762

[20] W. Chen *et al.*, "Ultra-Short-Term Wind Power Prediction Based on Bidirectional Gated Recurrent Unit and Transfer Learning," *Frontiers in Energy Research*, vol. 9, Dec. 2021, doi: https://doi.org/10.3389/fenrg.2021.808116

[21] M. Li, "Wind Power Prediction of BiTCN-BiGRU-KAN Model Based on Attention Mechanism," pp. 1640–1645, Aug. 2024, doi: https://doi.org/10.1109/icsece61636.2024.10729502

[22] M. Abubakar, Y. Che, A. Zafar, M. A. Al-Khasawneh, and M. S. Bhutta, "Optimization of solar and wind power plants production through a parallel fusion approach with modified hybrid machine and deep learning models," *Intelligent Data Analysis: An International Journal*, vol. 29, no. 3, pp. 808–830, Feb. 2025, doi: https://doi.org/10.1177/1088467x241312592

[23] A. H. A. AL-Jumaili, R. C. Muniyandi, M. K. Hasan, M. J. Singh, J. K. S. Paw, and M. Amir, "Advancements in intelligent cloud computing for power optimization and battery management in hybrid renewable energy systems: A comprehensive review," *Energy Reports*, vol. 10, pp. 2206–2227, Nov. 2023, doi: https://doi.org/10.1016/j.egyr.2023.09.029. Available: https://www.sciencedirect.com/science/article/pii/S2352484723012647. [Accessed: Dec. 14, 2023]

[24] S. khan *et al.*, "Optimizing deep neural network architectures for renewable energy forecasting," *Discover Sustainability*, vol. 5, no. 1, Nov. 2024, doi: https://doi.org/10.1007/s43621-024-00615-6

[25] H. Wang, J. Huang, L. Sua, and B. Alidaee, "Renewable Energy Prediction: A Comparative Study of Deep Learning Models for Complex Dataset Analysis," *arXiv (Cornell University)*, Jan. 2025, doi: https://doi.org/10.48550/arxiv.2501.15731

[26] "[Literature Review] Deep Learning in Renewable Energy Forecasting: A Cross-Dataset Evaluation of Temporal and Spatial Models," *Themoonlight.io*, 2025. Available: https://www.themoonlight.io/en/review/deep-learning-in-renewable-energy-forecasting-a-cross-dataset-evaluation-of-temporal-and-spatial-models. [Accessed: Jun. 30, 2025]

Green Path Optimization for E-Commerce Logistics under Carbon Neutrality Goals: A Multi-Objective Grey Wolf Optimizer (MOGWO) Approach

Zheng Wei
School of Digital Trade, Zhejiang Institute of Economics and Trade, Hangzhou City, Zhejiang Province, 310018, China
E-mail: onnowei15@163.com

Keywords: green commerce logistics, path optimization, carbon neutral, multi-objective optimization, multi-objective grey wolf optimizer

Received: June 17, 2025

In e-commerce logistics path planning, it is difficult to balance efficiency and environmental protection due to the lack of carbon emission considerations and multi-objective coordination. To address this problem, this paper constructs a green logistics path optimization method based on the MOGWO (Multi-Objective Grey Wolf Optimizer) algorithm. This method first constructs a graph structure containing distribution centers, customer nodes, and path edges, and sets constraints such as transportation distance, time window, and vehicle capacity; then a linear carbon emission estimation model based on path length, vehicle type, and unit energy consumption parameters is established to provide input for multi-objective optimization. By unifying the dual objectives of minimizing transportation costs and minimizing carbon emissions, and introducing a time window violation penalty term, the path population is dynamically updated using the grey wolf hierarchical search mechanism of MOGWO, and the Pareto frontier is maintained in combination with non-dominated sorting to achieve target equilibrium. The experimental results show that the delivery costs of MOGWO standard orders, expedited orders, large orders, and overseas orders are 3.48, 4.98, 6.82, and 8.47 yuan per order, respectively, and the total transportation costs are 3482.56, 4998.72, 6815.34, and 8483.19 yuan, respectively, which are better than the traditional NSGA-II, PSO, and ACO, and the transportation cost control is efficient; the carbon emissions are reduced by 28.1%, 31.1%, 32.6%, and 32.9%, respectively, achieving effective control of carbon emissions. Based on MOGWO analysis, when the order delivery density is high and the vehicle loading rate increases from 40% to 90%, the unit carbon emission intensity decreases from 0.91kg/km to 0.649kg/km, and the total carbon emissions decrease from 1294.66kg to 899.54kg. The high loading rate can significantly improve carbon efficiency. The average route length in the urban distribution area is 12.84 km, and the average delivery time is 38.7 min, which is better than the 43.37 km and 96.5 min of the cross-regional distribution area, indicating that compact spatial structure and superior traffic conditions are important factors in achieving route optimization.

Povzetek: Za usklajevanja stroškov in emisij v e-trgovinski logistiki je predlagan MOGWO, ki na grafu distribucijskih centrov in kupcev optimira poti glede na stroške, ogljične emisije in časovna okna. Z linearnim modelom emisij ter Pareto iskanjem MOGWO zniža stroške in emisije ter preseže NSGA-II, PSO in ACO.

1 Introduction

Green e-commerce logistics plays a key role in promoting energy transformation and building environmentally friendly supply chains under the "dual carbon" strategy [1], [2]. With rapid urban expansion and rising consumer demand, e-commerce platforms rely more on high-frequency, short-link distribution networks to improve user experience [3], [4]. However, this has led to increased energy waste and greenhouse gas emissions in urban distribution. Traditional logistics route planning often focuses on the shortest route or lowest cost, neglecting factors like traffic congestion, vehicle energy consumption, and delivery time windows, which limits the integration of green, low-carbon principles [5], [6], [7]. E-commerce logistics typically involves multiple points, segments, and overlapping constraints, making it difficult to balance environmental and economic factors in optimization strategies [8], [9], [10]. To achieve carbon neutrality, it is crucial to integrate carbon emission factors into logistics path planning, supporting the development of green supply chains and smart cities.

Existing research has made significant progress in the field of logistics path optimization. Most methods focus on the integration of heuristic search and multi-objective optimization strategies to cope with the challenges of solving multiple constraints in path planning. Representative methods such as NSGA-II (Non-

dominated Sorting Genetic Algorithm II) use non-dominated sorting and congestion maintenance strategies to improve the diversity of solution sets, which is suitable for balancing cost and time objectives [11], [12]. Moghadam S S proposed a multi-objective mixed integer nonlinear programming model based on NSGA-II for optimizing e-commerce closed-loop supply chain networks. He took into account both corporate profits and customer satisfaction. Through sensitivity analysis, he further provided management insights on the trade-offs between supply chain costs, pricing strategies, and customer satisfaction [13]. PSO (Particle Swarm Optimization) guides path updates through individual and group extreme values to improve global search capabilities [14], [15]. Tang L proposed an improved particle swarm optimization algorithm combined with a dynamic monkey jumping mechanism, which improves search efficiency through dynamic population grouping and inertia weight adjustment. The algorithm performed better in terms of optimal path fitness value (67.1 km), calculation time (1.26s), and optimal solution success rate (5/10), verifying its high efficiency and practicality [16]. ACO (Ant Colony Optimization) simulates ant colony behavior to adaptively adjust the path selection probability, which is suitable for fast path iteration in dynamic environments [17], [18]. These methods have good performance in solving pure economic goals, such as minimizing distribution costs, but have bottlenecks in carbon emission optimization, distribution time control, and path constraint coupling. The actual adaptability and solution quality control of the current algorithm in green path optimization are still insufficient. It is urgent to design a multi-objective optimization strategy that takes into account both global and fine-grained path modeling to meet the distribution efficiency and emission reduction needs under the guidance of carbon neutrality policies.

Recent studies show that the MOGWO algorithm [19], [20] has strong dynamic adaptability. By simulating the hierarchical predation behavior of gray wolf groups, it adjusts the guidance strategy during the search process, quickly converging to the new Pareto frontier when order density changes or the distribution area expands. MOGWO uses a non-dominated sorting mechanism based on congestion, which preserves solution diversity while improving response speed to order changes, making it effective for e-commerce logistics, such as explosive order growth and frequent customer node changes. In green path planning, MOGWO adapts to complex paths and conflicting goals by maintaining the Pareto frontier and dynamic exchange of information between gray wolf leaders. While MOGWO has been applied in traffic network optimization, power dispatching, and carbon asset allocation with good multi-objective results, it lacks systematic application in e-commerce delivery paths [21], [22]. Some studies did not adequately address constraints like delivery time windows, vehicle capacity, and node topology, resulting in weak model robustness. Others failed to fully exploit MOGWO's dynamic evolution advantages, leading to low solution space coverage in high-dimensional scenarios. Regarding carbon emission estimation, most studies use a unified energy consumption coefficient or average carbon factor, which doesn't accurately reflect emission variations based on vehicle type, distance, and route topology. This paper integrates distribution network topology with carbon emission modeling and utilizes MOGWO's multi-objective optimization to balance route economy and environmental protection in dynamic environments. Relevant work is shown in Table 1.

This study develops a multi-objective green logistics path optimization model that incorporates path constraints, time window constraints, and carbon emission factors to support carbon neutrality goals. The MOGWO algorithm is introduced for efficient solution search and optimization balance. Using real e-commerce distribution network data, a graph structure is created with distribution centers, customer nodes, and connection paths. A linear carbon emission function based on vehicle type, energy consumption, and path length is designed, and accurate carbon emission data is generated from path feasibility judgments. The dual objective function combines transportation cost and carbon emissions, with penalty terms for path conflicts, time window violations, and loading restrictions. A gray wolf population search mechanism improves convergence and solution set diversity, dynamically maintaining a non-dominated solution set. The MOGWO algorithm adjusts the trade-off between carbon emissions and transportation costs, reducing carbon emissions for various orders by 28.1%, 31.1%, 32.6%, and 32.9%, respectively. This paper's contributions include: 1) a path modeling framework balancing distribution efficiency and carbon reduction; 2) a carbon emission estimation mechanism based on vehicle types and path topology; 3) the application of MOGWO to complex constrained path optimization, verified through a multi-index evaluation system, providing theoretical support and algorithmic tools for green e-commerce logistics path planning.

Table 1: Comparison of working methods

Method	Optimization Objectives	Dataset	Performance Metrics	Innovations/Advantages
NSGA-II	Cost, Customer Satisfaction	Simulation Data	Solution Diversity, Convergence Speed	Multi-objective Framework
Hybrid NSGA-II	Profit, Customer Satisfaction	E-commerce Supply Chain Data	Cost, Satisfaction	Closed-loop Supply Chain Design
Improved PSO	Path Length, Time	Urban Logistics Network	Fitness Value, Computation Time	Dynamic Inertia Weight Adjustment
Dynamic ACO	Delivery Time, Cost	IoT Vehicle Trajectories	Path Length, Delay Rate	Adaptive to Dynamic Road Conditions

Traditional MOGWO	Warehouse Efficiency, Cost, Route Reliability	Cross-docking & Regional Networks	Space Utilization, Cost, Reliability	Multi-objective Coordination	Our MOGWO	Transport Cost, Carbon Emissions, Time Windows	Real E-commerce Delivery Network	Cost, Carbon Emissions, SP, GD	1.Precise Carbon Model; 2. Dynamic Pareto Front; 3. Optimal Multi-objective Balance

2 Methods

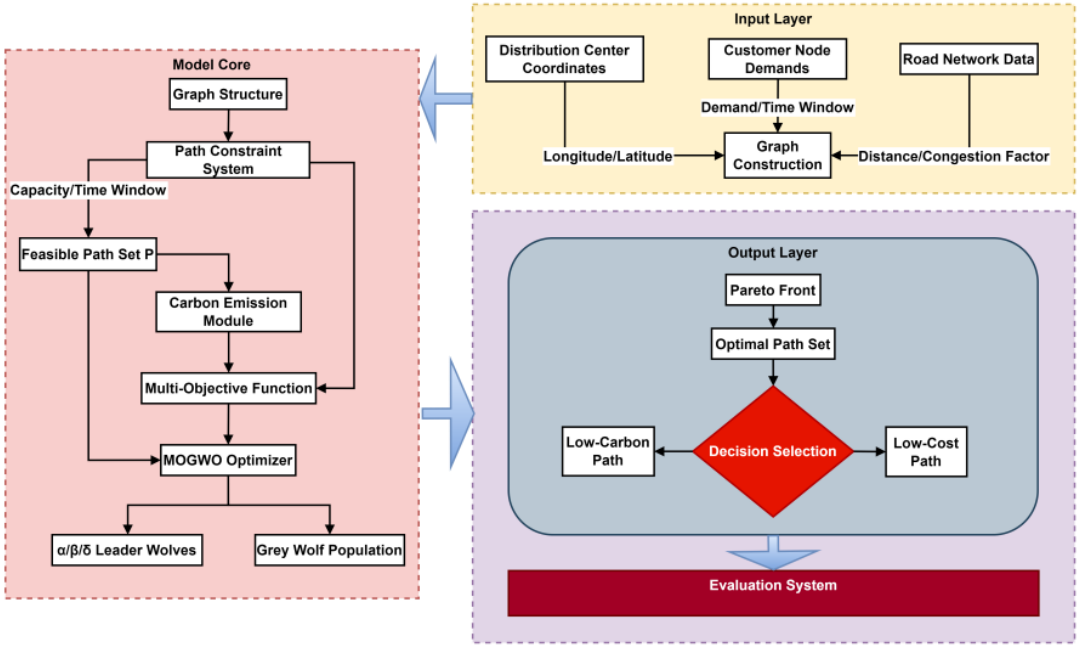

Figure 1: Carbon-neutrality goal-driven green e-commerce logistics path optimization framework

Fig 1 systematically presents the carbon-neutrality goal-driven green e-commerce logistics path optimization framework. The input layer integrates the distribution center coordinates, customer demand (including time windows), and road network data to construct a constrained graph structure. The core layer of the model generates a feasible path set through the path constraint system, calculates the carbon emission matrix by combining vehicle type and energy consumption factor, and constructs a multi-objective function. The MOGWO optimizer uses the leader wolf mechanism to search for the Pareto optimal solution set, dynamically balancing economic and environmental goals. The output layer provides low-carbon/low-cost path solutions and evaluates the system to verify the algorithm's performance. The whole process is tightly coupled with logistics efficiency and carbon neutrality requirements, reflecting the technical path of multi-objective collaborative optimization.

2.1 E-Commerce logistics network modeling

2.1.1 Distribution network data processing and node construction

Based on the distribution data of e-commerce platforms, this study models the coordinates of distribution centers and customer locations as special nodes and ordinary nodes in the graph structure, respectively. Through coordinate transformation, the longitude and latitude are mapped to a point set in a plane rectangular coordinate system to form a node set. Customer nodes are embedded with order requirements and service time window attributes, while distribution center nodes retain capacity constraints and scheduling time attributes, all of which are identified by unique numbers for easy indexing. Subsequently, a set of feasible paths between nodes is constructed, and road traffic conditions, grades, and speed limit information are recorded to form a weighted edge set. Among them, the edge weight includes the congestion-corrected Euclidean distance and estimated travel time. The Euclidean distance calculation formula is:

$$d_{ij} = \sqrt{(x_i - x_j)^2 + (y_i - y_j)^2} \quad (1)$$

In formula (1), x_i and y_i display the horizontal and vertical coordinates of node i and node j in the plane coordinate system, respectively. If the actual direction of the road deviates from the straight line, it is multiplied by the road polyline coefficient to correct the actual driving distance. The estimated travel time is calculated by dividing the road grade and historical average speed of the reference road by the speed value to obtain the initial travel time. Specifically, the actual driving speed v_{ij} between nodes i and j is determined jointly by the historical benchmark speed v_{base} corresponding to the road grade r and the real-time traffic congestion correction factor α. The calculation formula is: $v_{ij} = \alpha \times v_{\text{base}}$. Subsequent path searches will calculate travel times based

on this dynamically updated speed value. After all node and edge attribute information is integrated, the complete graph structure is stored in memory in the form of an adjacency list, which is convenient for rapid indexing and expansion during the optimization process.

2.1.2 Path constraint parameter setting and feasibility screening

For the constructed node and edge sets, each path is given multiple constraints such as transportation distance, time window, and vehicle capacity. The transportation distance directly inherits the corrected distance value obtained in the previous stage; the customer node service time window is defined as t_{arrive}, which means that the delivery service must occur within this time interval, otherwise it is considered infeasible. In actual scheduling, if the cumulative pre-travel and sorting and loading time of a path exceeds the latest service time of the target node, the path can be marked as infeasible. The service time calculation formula is:

$$t_{\text{arrive},j} = t_{\text{depart},i} + \frac{d_{ij}}{v_{ij}} + s_i \tag{2}$$

In formula (2), $t_{\text{depart},i}$ displays the departure time from the node, v_{ij} displays the actual driving speed from node i to j, and s_i displays the service stay time of node i; if t_{arrive} exceeds the latest service time allowed by the node, the path is abandoned. The vehicle capacity constraint adopts a cumulative method, comparing the remaining load of the selected assigned vehicle with the customer demand, and using an inequality expression:

$$\sum_{k \in S} q_k \le Q \tag{3}$$

In formula (3), $\sum_{k \in S} q_k$ displays the sum of customer demands allocated to the current vehicle route, and Q is the maximum vehicle carrying capacity. Each time the route is expanded, if the inequality does not hold due to the additional customer demand, the route is considered infeasible and pruned.

2.2 Carbon emission calculation module design

2.2.1 Route emission factor determination and vehicle parameter classification

All delivery routes are classified by vehicle type, and energy consumption factors are set for each type of vehicle. Emission levels are estimated based on route length and typical operating efficiency. Vehicle types are divided into three categories: small light trucks, medium-sized vans, and heavy-duty diesel vehicles based on platform operation data. For each type of vehicle, its unit kilometer fuel consumption or electricity consumption data under standard road conditions is collected, and its load range and regular usage intensity are discretized and archived. The path length is derived from the actual distance value recorded in the graph structure, and the energy consumption factor is derived from the energy efficiency accounting standard issued by the Ministry of Transport, and the compromise value is obtained by adjusting the actual operation data of the enterprise.

Taking into account the energy consumption fluctuations caused by different road grades in actual driving, the roads passed by the path are marked in sections, and the road grade parameters are converted into driving condition coefficients to adjust the weight of the energy consumption factor. For example, there are differences in driving resistance between urban roads and suburban roads, and the unit carbon emissions of the same vehicle on the two types of roads can be offset. By applying weighted integration to each road segment length in the route, we develop an interval correction model to enhance the accuracy of carbon emission estimation. When a route matches a specific vehicle type, the system dynamically retrieves the driving condition coefficient-adjusted dynamic unit emission factor from its parameter library based on road classification. This enables efficient batch processing to avoid redundant calculations.

2.2.2 Linear estimation of path emission values and result integration

This paper takes each feasible path as a unit, extracts its distribution distance and vehicle type matching parameters, and uses a linear model to estimate carbon emissions. The formula is expressed as follows:

$$E_{ij} = \alpha_{k,r} \cdot L_{ij} \tag{4}$$

Where E_{ij} displays the transportation carbon emissions from node i to node j, $\alpha_{k,r}$ are the unit emission factors corresponding to vehicle type k a
This formula assumes that under fixed load conditions, unit distance emissions grow linearly, which is suitable for rapid estimation of carbon effects in multi-path, single-task scheduling. After the emission values of all paths are calculated, the results are stored in the form of a sparse matrix. The matrix dimension corresponds to the size of the edge set in the graph. It can be directly introduced as a cost item to participate in the optimization when designing the objective function.

If there are multiple delivery tasks in a path, the path emission is apportioned according to the task ratio, and the calculation method is as follows:

$$E_{ij}^{(n)} = \frac{q_n}{\sum_{m \in P_{ij}} q_m} \cdot E_{ij} \tag{5}$$

Where q_n is the demand for the task, and P_{ij} is the set of all delivery tasks carried by the path. This allocation mechanism allows each order to be quantified in the emission accounting, avoiding redundant emissions between paths. This mechanism can mark the carbon emissions of the paths associated with each task, making it easier to concretize the emission constraints in the subsequent optimization model.

The final output is the carbon emissions corresponding to each path and each task. All results are summarized and written into the data structure for the objective function to call. This module is a static input link before scheduling optimization, and its accuracy directly affects the setting of the path selection weight and the carbon emission constraint boundary.

2.3 Construction of multi-objective function

To address constraints in multi-objective optimization, this paper develops a comprehensive evaluation function that quantifies the overall performance of routing solutions. The function integrates transportation costs, carbon emissions, and time window penalties through weighted aggregation, providing a comparable comprehensive score. Transportation costs are calculated by multiplying each road segment distance with the vehicle's unit operating cost. Before computation, system data including vehicle type, origin/destination nodes, and road classification levels are uniformly retrieved to match corresponding unit costs. Operating costs are stored in the system based on historical data categorized by vehicle type and road conditions. Time window constraints are converted into scheduling cost penalties and incorporated into the evaluation function. The evaluation function is expressed as follows:

$$F = w_1 \cdot C + w_2 \cdot E + P \tag{6}$$

Where C is the transportation cost item, E is the carbon emission value, P is the time window penalty item, and w_1 and w_2 display weight coefficients, which reflect the trade-off between the two in the scheduling priority. This function is mainly used to quickly evaluate a single solution inside the algorithm, and its calculation result is not the final optimization goal. When the cost weight is set to [0.5,0.7] and the emission weight to [0.3,0.5], the objective function demonstrates superior performance in balancing costs and carbon emissions, aligning with the policy orientation of prioritizing emission reduction in e-commerce logistics. Subsequent experiments adopted default values of w_1=0.6 and w_2=0.4 to balance economic considerations with environmental objectives. In the function expression, the penalty item is not an independent target, but is dynamically added depending on whether the path plan violates the time window requirement. If the path does not violate the time constraint, P=0. Otherwise, the path is assigned a value in segments according to the actual delay time and the urgency of the task, ensuring that the time delay is sufficiently punitive in the path evaluation.

The total carbon emission of the path is embedded as an independent target in the objective function, with emission values sourced from static estimations to avoid repeated reading of the path structure. These values are indexed by path number and integrated into the objective function for direct quantification during decoding. Emission limits and penalty intervals are set, with piecewise linear conversion applied to some paths to enhance identification of high emissions.

For time constraints, the delivery time window offset is converted into a cost term, with higher penalties for late arrivals than early ones to prioritize customer service. If a node's arrival time exceeds the allowed interval, a penalty term is calculated accordingly:

$$P_i = \lambda \cdot \max(0, T_i - b_i) + \mu \cdot \max(0, a_i - T_i) \tag{7}$$

Where T_i is the actual arrival time, a_i and b_i are the allowed time windows of the node, and λ and μ are penalty weight parameters. The configuration of penalty weights λ and μ directly determines the rigor of time window constraints in path optimization. Through experimental testing, this study investigates how different parameter combinations affect the objective function. When λ=1.5 and μ=0.3, a balance is achieved between time window violations and cost control. Sensitivity analysis reveals that increasing λ significantly reduces delays but may lead to path redundancy, while excessively high μ values tend to increase vehicle waiting costs. This structure ensures that in the algorithm search, once the path plan deviates from the time specification, the weight is dynamically adjusted at the objective function level to avoid inferior solutions occupying the search forefront.

2.4 Path search mechanism based on MOGWO

2.4.1 Path population initialization and group position update mechanism

In the initial phase, feasible routes meeting capacity and time window requirements are randomly generated based on network node distribution and vehicle constraints to form an initial population. Subsequently, each route individual is assigned a position vector in continuous space, which serves as the meta-parameter guiding local search and updates. The population size matches the number of routes.

Position updates follow the gray wolf hierarchy (α,β,δ), where individuals approach leaders with random perturbations to avoid local optima. Node exchange/insertion/reversal operations preserve path feasibility during optimization.

The position update formulas are expressed as follows:

$$\vec{D} = \left|\vec{C} \cdot \vec{X}_{leader} - \vec{X}_{current}\right| \tag{8}$$

$$\vec{X}_{new} = \vec{X}_{leader} - \vec{A} \cdot \vec{D} \tag{9}$$

Where $\vec{X}_{leader}$ is the leader wolf's position vector, $\vec{X}_{current}$ is the current individual position, $\vec{A}$ and $\vec{C}$ are dynamic adjustment parameters. Parameter $\vec{A}$ gradually decreases with the progress of iteration to achieve exploration-exploitation balance, and $\vec{C}$ introduces random weights to enhance the diversity of solutions.

2.4.2 Pareto frontier maintenance and multi-objective equilibrium mechanism

During iterations, a dynamic Pareto frontier maintains non-dominated solutions through continuous comparison and updating. Solutions are evaluated using objective function vectors, with dominated solutions removed to preserve optimal trade-offs. Crowding distance metrics ensure solution diversity by preferentially retaining sparse and edge-distributed solutions.The multi-objective vector expression of the objective function is as follows:

$$\mathbf{F}(\vec{X}) = \left(C(\vec{X}), E(\vec{X}), T(\vec{X})\right) \tag{10}$$

Where $C(\vec{X})$ is the transportation cost, $E(\vec{X})$ is the carbon emission, and $T(\vec{X})$ is the delivery time penalty. The performance of the individual path $\vec{X}$ is fully

described by this three-dimensional vector. Non-dominated sorting ensures that the paths included in the Pareto set do not have absolute disadvantages in each dimension.

3 Method effect evaluation

3.1 Experimental data and settings

This study builds an experimental environment based on the actual operation data of an e-commerce platform. The data covers the coordinates of the distribution center, the geographical location of the customer node, the order demand, the service time window constraints, and the road network information. The coordinates of the distribution center and customer nodes are mapped into a plane rectangular coordinate system through longitude and latitude conversion to form a graph structure of the logistics network. The path transportation distance is calculated using the Euclidean distance and corrected with the actual road polyline coefficient to reflect the actual driving distance. The estimated driving time is obtained through the historical vehicle GPS trajectory and road condition monitoring data statistics to ensure the accuracy of the time estimate. The experiment set the gray wolf population size to 100 with a maximum iteration count of 200. The parameter update rules for $\vec{A}$ and $\vec{C}$ are: $\vec{A} = 2a \cdot r1 - a, \vec{C} = 2r2$, where a decreases linearly from 2 to 0, and r1 and r2 are random vectors within the interval [0,1]. The head wolf selection strategy combines non-dominant sorting with crowding distance. The network consists of 1 distribution center and 50 customer nodes, with an average degree of 3.6, an average demand of 1.8 units per customer node, and a time window span of 90 minutes on average. The data is generated based on real order sampling, and the key parameters are shown in Table 1 and Table 2.

3.2 E-commerce logistics network

To clearly demonstrate the network structure, Figure 2 shows a simplified schematic network with 7 nodes constructed in MATLAB. The e-commerce logistics network log is based on the actual operation of the e-commerce platform, covering the geographical coordinates of distribution centers, multiple customer orders corresponding to orders, demand, and service time windows.

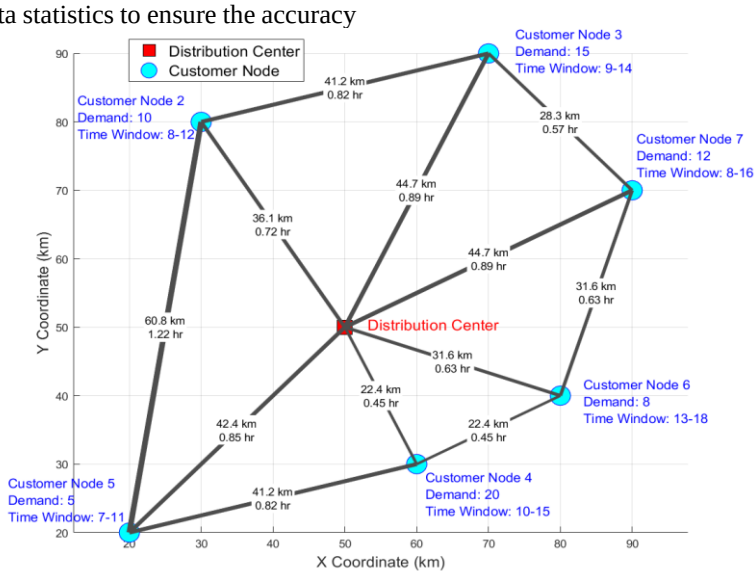

Figure 2: E-commerce logistics network with distance and travel time

Figure 2 shows the spatial layout of distribution centers and multiple customer nodes in an e-commerce logistics network and the characteristics of their interconnected transportation paths. The two-dimensional coordinates of the nodes correspond to the actual geographic locations, ensuring that the path length intuitively reflects the delivery distance. The distribution centers are marked with red squares, and the customer nodes are distinguished by blue dots. The annotation information covers customer needs and time window constraints, revealing the specific requirements of different customers for delivery timeliness and transportation capacity. The thickness of the path line reflects the difference in distance between nodes and also implies the consumption of transportation resources. Thicker and longer paths indicate longer transportation distances, which means that delivery vehicles need to invest more time and cost on this path, increasing operational complexity. Most of the nodes connected by shorter paths are located near the distribution centers, with higher transportation efficiency, but they cannot rely entirely on short-distance delivery due to the diversity of customer demand distribution. Time window constraints also play a key role in this figure. The time windows of some customer nodes are very tight, requiring that the delivery tasks must be completed within a specific time limit. This time limit not only increases the complexity of path scheduling, but also affects the driving order and residence time of vehicles. Due to the significant differences in demand, it is necessary to reasonably allocate the capacity of distribution vehicles - to avoid overloading or empty vehicles, and to improve overall transportation efficiency. The schematic network contains 2D coordinates of 7 nodes to intuitively present the model

elements. All subsequent experimental results are simulated and analyzed based on a larger and more representative actual e-commerce logistics data set to fully verify the performance of the algorithm in complex scenarios.

3.3 Carbon emission characteristics

Table 2: Unit carbon emission factors of vehicles and their average load parameters

Vehicle Type	Empty Load Energy Factor (α_1)	Full Load Energy Factor (α_2)	Average Load (tons)
Light Truck	0.18	0.26	1.2
Medium Truck	0.35	0.49	3.8
Heavy Truck	0.68	0.95	8.5

Table 2 lists the unit carbon emission factors and average load parameters of three types of delivery vehicles, providing basic data support for the linear estimation model of transportation carbon emissions. The empty and full load energy consumption factors reflect the difference in fuel consumption of vehicles under different loading conditions, covering the impact of load changes on emissions during actual delivery. The average load value is determined based on typical delivery tasks and vehicle type statistics to ensure the practicality and accuracy of the estimation model. The carbon emission factor data integrates multi-dimensional influencing factors such as road conditions, driving speed, and vehicle technical characteristics, reflecting high adaptability to the real transportation environment. The data provides key input parameters for the calculation of path carbon emissions, which helps to achieve the coordinated optimization of transportation costs and environmental protection goals.

Based on the actual delivery records of an e-commerce company, it covers the operation of different types of delivery vehicles on multiple typical delivery routes. Vehicle types include light trucks, medium trucks, and heavy trucks, route lengths cover a variety of intervals from short to long distances, and road types are subdivided into highways, urban trunk roads, urban local roads, and suburban roads. During the data collection process, the driving distance and road condition information of each route were recorded in detail, and the corresponding carbon emissions were calculated in combination with vehicle technical parameters and unit energy consumption standards. The calculation of carbon emissions uses a linear estimation model, which comprehensively considers the transportation distance, vehicle energy consumption characteristics, and road environmental impact to ensure that the emission data accurately reflects the actual operating conditions. The emission data of each route and vehicle combination is organized in a matrix form to generate a corresponding two-dimensional heat map. This process realizes the visual comparison of carbon emissions of different distribution plans, intuitively presents the specific impact of changes in transportation conditions on emissions, and lays a solid foundation for route optimization and green logistics strategy formulation.

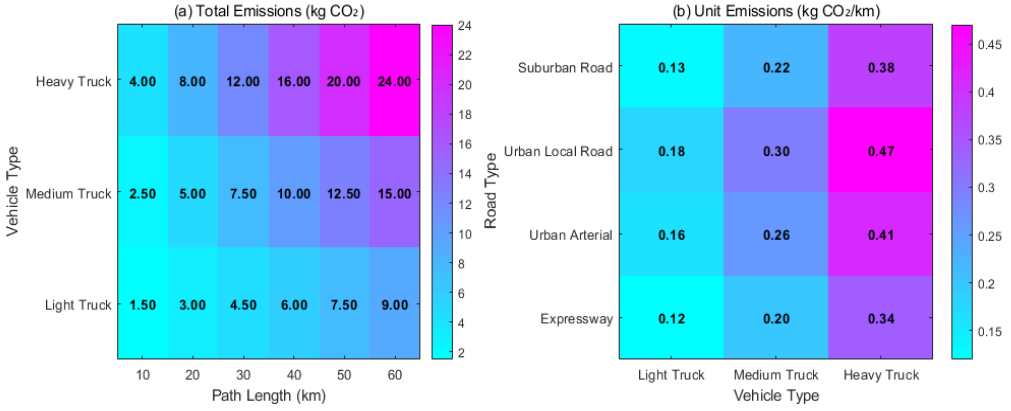

Figure 3: Carbon emission characteristics of different vehicle types

Fig 3 shows the comparison of carbon emission characteristics of different vehicle types under different delivery path lengths and road categories:

Figure a show the trend of total carbon emissions of different vehicle types under different delivery path lengths. As the path length increases, the overall carbon emissions increase, reflecting that the transportation

distance directly affects the total carbon emissions. There are significant differences in emissions between different models. Heavy trucks emit much more carbon than light and medium trucks, mainly due to their higher fuel consumption and load capacity, which significantly increases the emission intensity per unit distance traveled. In addition, light trucks show lower emissions in short-distance delivery and are suitable for delivery tasks in cities and suburbs, while heavy trucks are suitable for long-distance bulk cargo transportation, but at a higher environmental cost. Figure b reflects the impact of road type on unit transport carbon emissions. Expressway has relatively low unit emissions due to its smooth traffic conditions and high average vehicle speed. In contrast, Urban Local Road shows the highest unit emission value, reflecting that this type of road has frequent traffic congestion, large speed fluctuations, and frequent starting and braking, which leads to reduced fuel efficiency and increased carbon emissions. The unit emissions of Urban Arterial Road and Suburban Road are between the two, reflecting the regulatory effects of road grade and traffic flow on energy consumption and carbon emissions. The interaction between vehicle type and road conditions highlights the complexity of carbon emissions in the transportation link, emphasizing that multi-dimensional factors must be comprehensively considered in logistics route planning in order to achieve accurate assessment and effective control of carbon emissions.

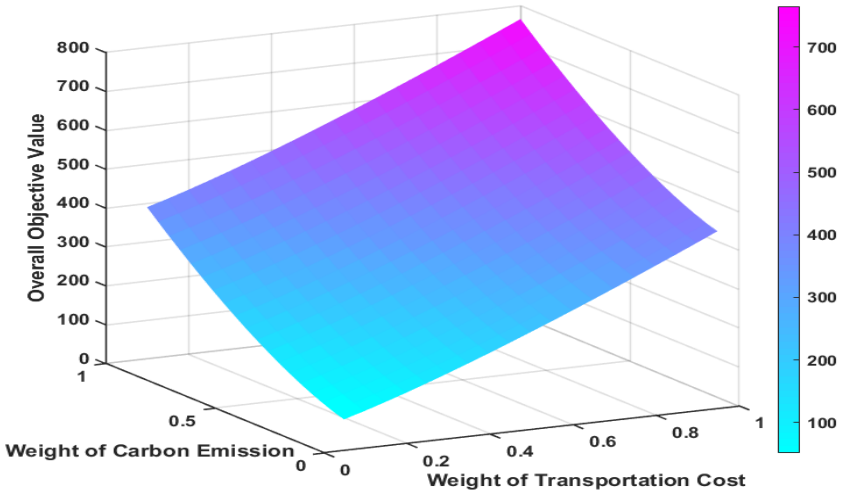

Figure 4: The impact of cost and emission weights on the objective function

Fig 4 reveals the joint impact of transportation cost weight and carbon emission weight on the overall objective function value. The horizontal and vertical axes represent the weight ratios of transportation cost and carbon emission, respectively, with a value range of 0.1 to 1, with high-resolution sampling to ensure rich results. The vertical axis corresponds to the comprehensive evaluation value of the objective function, reflecting the pros and cons of the scheduling scheme under different weight configurations. As the weight of transportation cost increases, the overall target value shows an accelerating upward trend, indicating that the weight of transportation cost has a significant impact on the overall target and has a nonlinear amplification effect. The increase in carbon emission weight also leads to a significant increase in the target value, but the slope of the surface is slightly slower, reflecting that the sensitivity of carbon emission weight is relatively mild, reflecting the complexity of the trade-off between the two indicators in multi-objective scheduling. The color change directly reflects the size distribution of the target value. The data can assist decision makers in identifying sensitive areas for weight parameter settings, and provide a data basis for formulating more scientific and reasonable scheduling optimization strategies. The data clearly reveals the comprehensive impact of weight configuration on the objective function, suggesting that weight selection should avoid extreme single inclination and promote a dynamic balance between transportation costs and carbon emissions. Based on this, the scheduling plan can more effectively balance economic benefits and environmental responsibilities and achieve dual optimization goals.

3.4 Multi-objective evolution in MOGWO path optimization process

The data comes from the iterative records of the simulation of e-commerce logistics path optimization, covering the changes in key indicators of the multi-objective optimization algorithm in 50 iterations. Transportation cost, carbon emissions, and delivery time are used as objective functions, and the model calculates the corresponding value of the optimal path updated in each iteration to form a convergence curve. The position data of the leader wolf comes from the group search mechanism within the algorithm. The position indicators of the three types of leader individuals, α, β, and δ, are extracted in each iteration to reflect their search trajectory in the solution space. During the data collection process, the path is decoded into a position vector, and the position is updated using the search strategy to dynamically adjust the path selection. This process combines mathematical models and heuristic algorithms to achieve optimization iteration of multi-objective functions, record the performance of each step and the dynamic position of

individuals, and finally form a complete data set that demonstrates the optimization effect and search behavior.

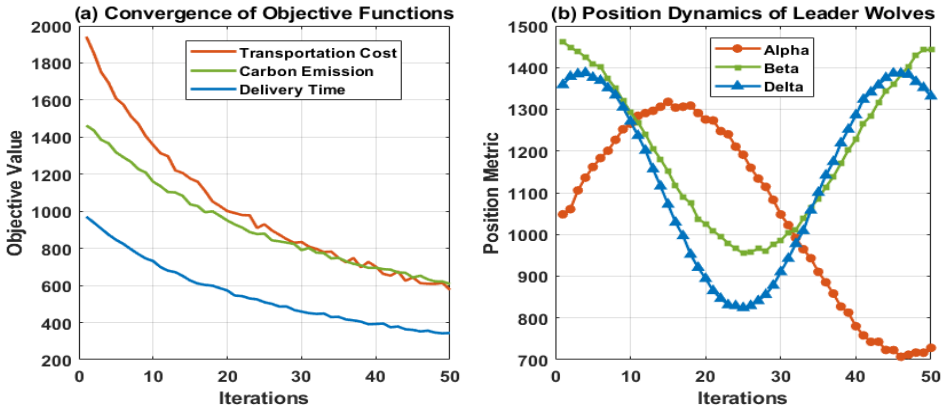

Figure 5: Multi-objective evolution in the MOGWO path optimization process

Fig 5 shows the convergence dynamics of the objective function in the MOGWO path search mechanism and the change behavior of the leader individual position. The combination of the two reveals the evolutionary characteristics of the optimization process.

Fig a reflects the evolutionary convergence characteristics of the path group under multiple objectives. The horizontal axis is the number of iterations, and the vertical axis is three key performance indicators: transportation cost, carbon emissions, and delivery time. The three curves gradually decrease with the increase in the number of iterations, showing a trend of gradually approaching the optimal solution during the search process. Different colors represent three types of targets, and their decline rates are different, indicating that there is asymmetry between the targets and a check-and-balance relationship between multiple targets. The rate of carbon emission decline slows down, suggesting that the optimization process is gradually saturated, and more rounds of search are needed to further compress the emission value. Figure b shows the position changes of the three types of leader wolves α, β, and δ, during the entire search process, simulating the exploration positions they occupy in the path space. This data is used to reflect the dynamic behavior characteristics of each leader in the search phase. The position index is composed of composite variables such as distance and path cost, which are used to abstractly represent the position characteristic value of each individual in the solution space. The fluctuations of the curves indicate that the three types of leading wolves maintain global exploration of the solution space while maintaining local search. The position of wolf α first rises and then falls, indicating that it dominates the solution space update in the early stage, but is replaced by other candidate positions in the later stage. The interlacing of the three curves further reflects the dynamic switching process of dominance of different dimensions in the case of multiple targets. The data changes jointly construct a dynamic cognitive map in the path search mechanism, and explain the behavior mechanism of the MOGWO algorithm in the multi-objective path problem from the two dimensions of performance change and leadership strategy evolution.

3.5 Comparison of E-commerce logistics and traditional logistics path optimization and target conflict analysis

Combined with the MOGWO algorithm for multi-objective optimization, with transportation cost and carbon emissions as dual objective functions, the Pareto solution set is dynamically maintained, and finally, the Pareto frontier comparison results of e-commerce and traditional logistics (NSGA-II) are generated. By simulating the path planning under different order densities and vehicle loading rates, the optimization performance of various logistics modes in terms of cost and carbon emissions is obtained, revealing their target conflict characteristics and path optimization potential.

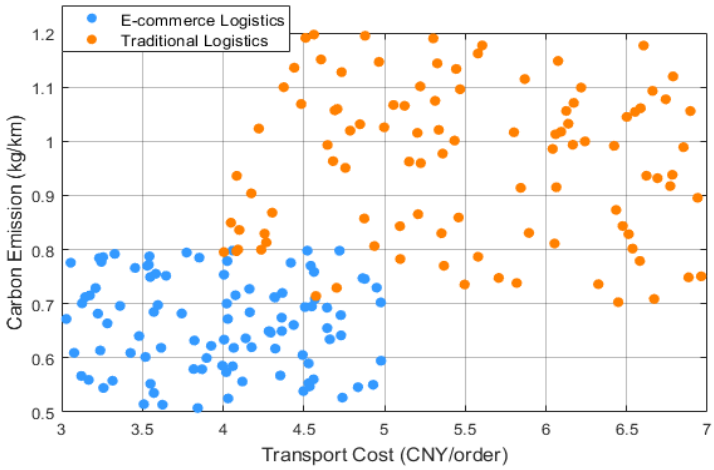

Figure 6: Pareto frontier comparison: MOGWO (e-commerce logistics) and NSGA-II (traditional logistics)

Figure 6 shows the Pareto frontier distribution obtained by using the MOGWO algorithm (labeled as "e-commerce logistics") and the NSGA-II algorithm (labeled as "traditional logistics") for dual-objective optimization under the dual-objective optimization of transportation cost and carbon emission. It can be seen that the solution set of e-commerce logistics is mainly concentrated in areas with low transportation costs, which reflects its stronger cost control ability in scenarios with dense networks and high delivery frequency. Due to the high-frequency and small-batch delivery mode, its carbon emission value is also relatively low - this mode effectively suppresses the growth of unit carbon emissions through route optimization and improves delivery efficiency. In contrast, the solution set distribution of traditional logistics is more dispersed. Although some routes have achieved low carbon emissions, the overall cost is high and the ability to adapt to the development of modern green logistics is limited. This result reveals the core difference between the two logistics systems: e-commerce logistics pays more attention to timeliness and customer experience, and path planning tends to be locally optimized; while traditional logistics focuses on scale effects and has a relatively broad path structure.

3.6 Transportation cost comparison indicators

The unit delivery cost and total transportation cost data are based on the simulation results of transportation paths for various order types in the actual e-commerce logistics distribution network. The MOGWO algorithm is used to iteratively search the delivery path, optimize vehicle scheduling and path selection, and finally generate a delivery plan for the corresponding order type. The MOGWO algorithm in this paper is compared with the three algorithms of NSGA-II, PSO, and ACO; each algorithm is run under the same data set and constraints to ensure the comparability of the results. The unit delivery cost is obtained by accumulating the sum of the transportation costs of each path and dividing it by the corresponding number of orders. The total transportation cost is the sum of the transportation costs of all paths, reflecting the overall distribution of resource consumption levels. The data covers ordinary orders, expedited orders, large orders, and overseas orders, reflecting the impact of different demands on costs.

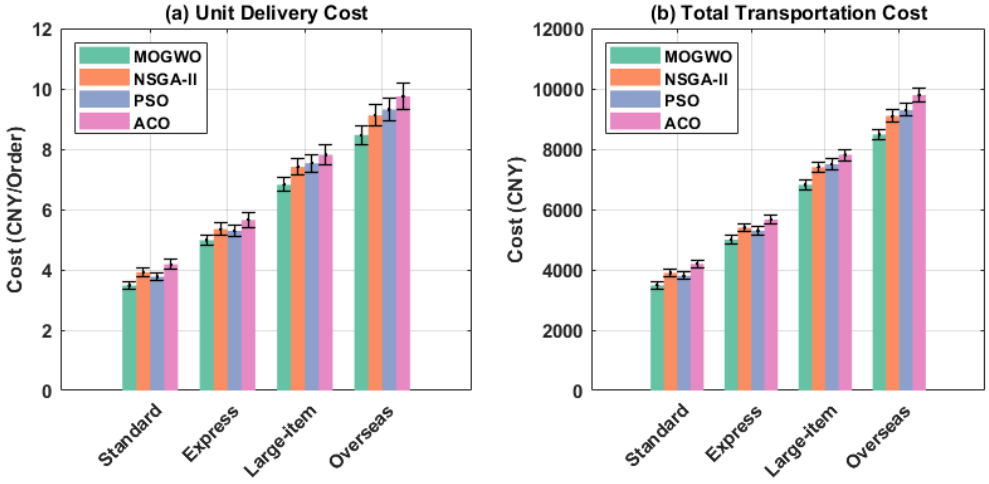

Figure 7: Comparison of unit delivery cost and total transportation cost

Figure 7 compares the transportation cost performance of MOGWO, NSGA-II, PSO and ACO algorithms in standard orders, expedited orders, large orders and overseas orders. Figure 7a shows the unit delivery cost (RMB/order), and Figure 7b shows the total transportation cost (RMB). The error bars represent the standard deviation of 10 independent experiments. The results show that MOGWO maintains the lowest cost in all order types: the unit delivery cost is 3.48, 4.98, 6.82, and 8.47 RMB/order, respectively, and the total transportation cost is 3482.56, 4998.72, 6815.34, and 8483.19 RMB, respectively, with the smallest fluctuation range (standard deviation). The cost reduction is mainly attributed to MOGWO's optimized path planning and vehicle scheduling strategy, which effectively reduces repeated paths and empty load rates. The paired t-test confirms that MOGWO is significantly better than the comparison algorithm ($p<0.01$), verifying its stability and economic advantages in complex logistics scenarios.

Table 3: Performance comparison of metaheuristic algorithms across different problem scales

Problem Scale (Number of Nodes)	Algorithm	Average Runtime (seconds)	Convergence Generations
50	MOGWO	18.3 ± 1.2	85 ± 5
	NSGA-II	22.1 ± 1.8	92 ± 7
	PSO	12.7 ± 0.9	110 ± 8
	ACO	35.6 ± 2.5	135 ± 10
100	MOGWO	67.4 ± 3.1	168 ± 12
	NSGA-II	89.3 ± 4.7	185 ± 15
	PSO	38.2 ± 2.3	210 ± 18
	ACO	142.7 ± 8.9	250 ± 22
200	MOGWO	245.8 ± 15.6	310 ± 25
	NSGA-II	386.5 ± 24.3	410 ± 30
	PSO	142.3 ± 9.8	350 ± 28
	ACO	>600	>500
500	MOGWO	1483.2 ± 98.7	680 ± 55
	NSGA-II	> 2500	>1000
	PSO	728.6 ± 45.2	800 ± 60
	ACO	Not Applicable	-

Table 6 shows the scalability and computational efficiency of each algorithm under different problem scales. This table compares the average running time and convergence number of four algorithms, MOGWO, NSGA-II, PSO and ACO, in logistics networks with 50, 100, 200 and 500 nodes respectively. The results show that PSO has the shortest running time, but the quality of the solution set is poor; ACO takes the longest time to calculate, especially for large-scale problems, it is difficult to converge and has poor scalability; NSGA-II has an intermediate performance, but the computational cost increases significantly with the scale. In contrast, MOGWO has a much lower running time than NSGA-II and ACO while ensuring the quality of the solution set. It shows a better balance between efficiency and performance at 200 nodes, and can effectively converge to ultra-large-scale problems with 500 nodes, verifying its excellent scalability and practicality in complex e-commerce logistics scenarios.

3.7 Carbon emission control levels

Based on e-commerce platform order distribution and vehicle dispatch records, a multi-scenario simulation environment is built, considering various order types and loading statuses. The path optimization algorithm calculates transportation paths and total mileage. Using vehicle energy consumption parameters, carbon emissions are estimated based on path length and energy consumption. The unit carbon emission intensity is calculated by the ratio of total carbon emissions to path distance, reflecting the average carbon emission efficiency of the entire logistics system under specific order density and vehicle loading rate. This index comprehensively integrates the influence of various factors such as vehicle emission factor, path planning quality, vehicle loading rate, and order distribution characteristics.

Table 4: Carbon emission performance under simulated path planning conditions

Order Density	Vehicle Load Rate	Total Carbon Emission (kg)	Route Distance (km)	Carbon emission intensity per unit system (kg CO_2/km)
Sparse	40%	812.64	964.5	0.843
	70%	645.21	953.7	0.677
	90%	577.83	951.2	0.607
Medium	40%	1035.77	1186.3	0.873
	70%	823.94	1162.8	0.709
	90%	738.32	1159.1	0.637
Dense	40%	1294.66	1422.4	0.910
	70%	1019.13	1397.3	0.729
	90%	899.54	1385.6	0.649

Table 4 shows the total carbon emissions and unit carbon emission intensity of logistics paths under different order densities and vehicle loading rates. Order density is classified as sparse, medium, or dense, and vehicle loading rates are 40%, 70%, and 90%. Total carbon emissions are measured in kilograms, and unit carbon emission intensity is calculated as emissions per kilometer. As loading rate increases, total carbon emissions decrease, reflecting improved transportation efficiency. Unit carbon emission intensity, however, better represents the effect of route

optimization. In sparse order distribution, higher loading rates lead to a notable decrease in intensity, indicating more efficient route allocation. In medium and dense distributions, the high loading rate still maintains low intensity, showing the regulatory power of route optimization. There is a nonlinear relationship between route length and carbon emission intensity, affected by factors like order distribution, vehicle loading, and route continuity. When order density is high and loading rate rises from 40% to 90%, unit carbon emission intensity drops from 0.91kg/km to 0.649kg/km, and total emissions drop from 1294.66kg to 899.54kg, showing the positive impact of higher loading rates on carbon efficiency.

Table 5: Carbon intensity comparison analysis before and after MOGWO optimization

Order Type	Baseline carbon intensity (kg/order)	Optimized Carbon Intensity (kg/order)	Carbon Intensity Reduction Rate (%)
Standard Order	0.89	0.64	28.1
Expedited Order	1.03	0.71	31.1
Large Order	1.32	0.89	32.6
Overseas Order	1.67	1.12	32.9

Table 5 shows the quantitative results of the carbon neutrality contribution of the MOGWO algorithm under different order types, including the initial carbon intensity, the optimized carbon intensity, and its decline rate. Carbon intensity is defined as the carbon dioxide emissions generated per kilometer of transportation per unit order (kg/km). From the data, it can be seen that in standard orders, expedited orders, large orders, and overseas orders, the carbon intensity decreased by 28.1%, 31.1%, 32.6%, and 32.9%, respectively, indicating that MOGWO can effectively reduce carbon emissions in various delivery scenarios. Among them, the optimization effect of large items and overseas orders is the most significant, indicating that the algorithm has stronger resource scheduling capabilities in complex routes and long-distance distribution. Overall, MOGWO has achieved effective control of carbon emissions while maintaining low transportation costs through a multi-objective collaborative optimization mechanism, verifying its technical feasibility and practical application value in promoting the realization of carbon neutrality goals in green e-commerce logistics systems.

3.8 Path operation efficiency analysis

Table 6: Path transportation efficiency and congestion adjustment coefficient analysis

Road Type	Average Speed (km/h)	Mean Congestion Adjustment Coefficient	Transport Efficiency (km/min)	Standard Deviation (km/min)
Expressway	75.6	1.05	1.25	0.15
Urban Arterial	45.3	1.18	0.68	1.1
Urban Local Road	32.8	1.32	0.43	2.07
Suburban Road	40.1	1.22	0.55	1.12

Table 6 presents the transport efficiency and its influencing factors across four road types: expressways, urban trunk roads, urban local roads, and suburban roads. The average speed reflects traffic conditions, with expressways having the highest speed (75.6 km/h) and urban local roads the lowest (32.8 km/h), indicating severe congestion. The congestion adjustment factor increases as road grade decreases, highlighting a greater impact of congestion on lower-grade roads. Transport efficiency, measured in km/min, reflects vehicle speed on different road sections considering road conditions. The standard deviation indicates stability, with highways showing the least fluctuation (0.15 km/min), while urban and suburban roads are more affected by external factors. These data are crucial for route planning, delivery timeliness, and cost control in e-commerce logistics. The optimization results focus on average delivery path length and time, analyzing the adaptability and stability of the MOGWO optimization strategy in various order densities without comparisons to other algorithms.

Table 7: Evaluation results of path efficiency of different delivery areas under the MOGWO strategy

Distribution Zone Type	Average Path Length (km)	Average Delivery Time (min)	Standard Deviation (Length)	Standard Deviation (Time)
Urban Core Distribution Zone	12.84	38.7	1.15	3.6
Urban-Suburban Transition Zone	18.63	51.4	1.87	4.1
Urban-Rural Integration Zone	27.48	63.2	2.09	5.7
Remote County-Level Delivery Zone	35.92	79.8	3.16	6.2
Cross-Region Hub Aggregation Zone	43.37	96.5	4.02	8.4

Table 7 shows significant differences in average path length and delivery time across distribution area types. Urban areas, with compact structures and dense road networks, have shorter paths and lower time consumption, indicating efficient traffic conditions. In contrast, suburban, urban-rural fringe, and remote areas face longer paths and higher delivery times, with increased variability due to road complexity and sparse distribution points. Cross-regional areas experience even greater challenges, with higher path lengths and delivery times, reflecting transportation infrastructure and geographical difficulties. The urban area, for example, has an average route length of 12.84 km and delivery time of 38.7 minutes, while cross-regional areas show 43.37 km and 96.5 minutes. This demonstrates that optimized regional organization and good traffic conditions are crucial for reducing costs and improving logistics efficiency.

3.9 Evaluation of solution set distribution balance

The experiment analyzes the results of four algorithms (MOGWO, NSGA-II, PSO, ACO) in the same e-commerce logistics path planning scenario. Using a fixed distribution network and order demand, each algorithm is run multiple times with consistent input parameters to ensure stable results. The SP and GD indicators are used to measure the solution set's distribution balance and closeness to the optimal solution. SP reflects solution uniformity, while GD measures the Euclidean distance from each solution to the true Pareto frontier.

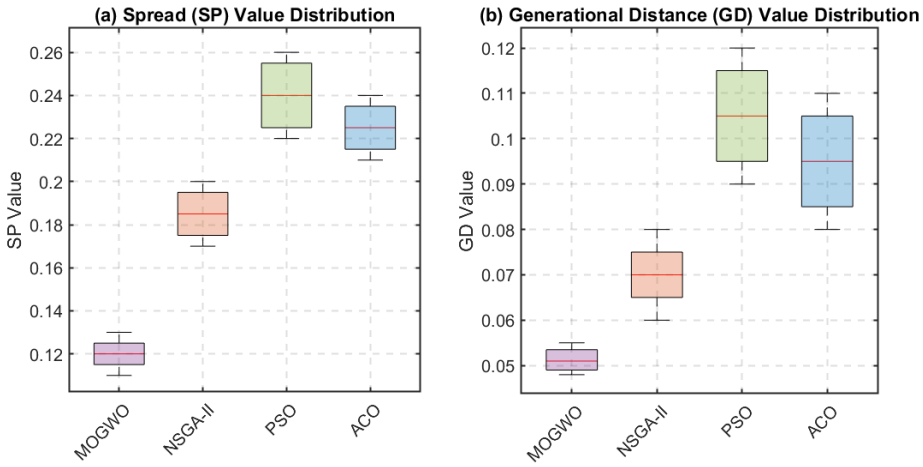

Figure 8: Comparative analysis of solution set distribution metrics

Fig. 8 compares the performance of four algorithms in terms of solution set balance and diversity using Spread (SP) and Generational Distance (GD). The SP indicator reflects solution uniformity, with lower values indicating better balance. The GD indicator measures closeness to the true Pareto frontier, with lower values indicating better quality. The MOGWO algorithm shows the lowest SP median (0.12) and a compact distribution, indicating spatial balance and stability. Other algorithms have higher medians and poorer uniformity. In the GD plot, MOGWO's median (0.051) is significantly lower, indicating its solutions are closer to the optimal Pareto frontier. The GD values for NSGA-II, ACO, and PSO are higher, with PSO showing significant instability. Overall, MOGWO outperforms the others in both balance and solution quality, making it more effective in multi-

objective path optimization, path selection, and carbon emission control.

4 Discussion

The green e-commerce logistics path optimization method based on the MOGWO algorithm offers significant advantages in transportation cost control, carbon emission reduction, and solution quality. Compared to classic multi-objective optimization algorithms like NSGA-II, PSO, and ACO, MOGWO demonstrates stronger performance in solving complex constrained problems. This advantage arises from its unique population search mechanism, simulating the hierarchical predation of gray wolves, which enables efficient exploration and avoids local optima. MOGWO's Pareto frontier maintenance, based on non-dominated sorting and congestion calculation, ensures a more uniform and diverse solution set, providing better trade-off options for decision makers.

This performance is partly due to the integration of carbon emission estimation and path constraints in the optimization model, treating carbon emissions as a quantified target rather than an additional cost. The dense nodes and short paths in e-commerce logistics networks also aid MOGWO's rapid convergence. MOGWO can quickly converge to the new frontier when order density changes or distribution area expands by dynamically maintaining Pareto frontier and leading wolf guidance mechanism, effectively responding to order outbreak and node change, showing good scalability in complex dynamic environment, and is suitable for collaborative optimization of large-scale e-commerce logistics network. However, MOGWO's performance weakens in sparse order distributions or wide delivery areas, where its convergence slows, and NSGA-II may show faster initial convergence. Its performance is also sensitive to key parameters like population size and convergence factor, with improper settings leading to stagnation or inefficiency. Although MOGWO excels in typical e-commerce logistics problems, further research is needed to improve its robustness and adaptability to dynamic environments. The current research model exhibits limitations when extended to other regions or logistics networks. Its performance depends on localized parameters such as congestion coefficients for specific road types, vehicle energy consumption factors, and regional traffic control regulations. When applied to new areas with significant variations in road conditions, vehicle composition, or emission standards, the carbon emission calculation module requires recalibration. Additionally, the model currently fails to account for dynamic disturbances like extreme weather or real-time traffic events. Future work will focus on developing parameter adaptive mechanisms to enhance the model's generalization capabilities across diverse urban environments and regulatory frameworks.

5 Conclusions

This paper proposes a green logistics path optimization method using the MOGWO algorithm to address carbon emissions and multi-objective coordination in e-commerce logistics. A refined logistics network model is built by including distribution centers, customer nodes, and path edges, with constraints such as transportation distance, time window, and vehicle capacity. A linear carbon emission model is established, with transportation costs and emissions as dual objectives. A penalty term handles conflicts between path constraints and time windows. The MOGWO algorithm balances economic and environmental goals through the leader wolf mechanism and dynamic Pareto set maintenance. Experimental results show MOGWO's delivery costs for different order types and total transportation costs, with carbon emissions reduced by 28.1%–32.9%. The algorithm outperforms traditional ones in solution set balance and diversity. The study also highlights the impact of vehicle loading rate, order distribution density, and spatial structure on emissions and efficiency. The contributions include: (1) a multi-objective framework considering delivery efficiency and carbon reduction; (2) an accurate carbon emission estimation mechanism; (3) verification of MOGWO's superiority in constrained path optimization. Future research can focus on real-time path optimization and multi-vehicle scheduling for green logistics.

.

Authorship contribution statement

Zheng WEI: Writing-Original draft preparation, Conceptualization, Supervision, Project administration.

Author statement

The manuscript has been read and approved by all the authors, the requirements for authorship, as stated earlier in this document, have been met, and each author believes that the manuscript represents honest work.

Ethical approval

All authors have been personally and actively involved in substantial work leading to the paper, and will take public responsibility for its content.

References

[1] Liu W, Liang Y, Bao X, et al. China's logistics development trends in the post COVID-19 era[J]. International Journal of Logistics Research and Applications, 2022, 25(6): 965-976.DOI: 10.1080/13675567.2020.1837760

[2] Arimbhi P, Agustina D, Rahmi N. The Effectiveness of the National Logistic Ecosystem Program in Improving the Performance of the National Logistics System, Recovering the Investment Climate, and Increasing the Competitiveness of the National Economy[J]. Jurnal Logistik Indonesia, 2021, 5(2): 153-165.DOI: http://ojs.stiami.ac.id/index.php/logistik

[3] C. Yunlin, "Awareness of green logistics technology, certification, and standards by

logistics practitioners at Chinese e-commerce company, Jing Dong," *The Asian Journal of Shipping and Logistics*, 39(4): 37–46, Dec. 2023, DOI: 10.1016/j.ajsl.2023.10.004.

[4] C. Gong, H. Song, D. Chen, S. J. Day, and J. Ignatius, "Logistics sourcing of e-commerce firms considering promised delivery time and environmental sustainability," *Eur J Oper Res*, 317(1): 60–75, Aug. 2024, DOI: 10.1016/j.ejor.2024.02.026.

[5] M. Sarkar, "Environmental Sustainability under E-Commerce: A Holistic Perspective," *European Journal of Development Studies*, 3(3): 1–6, May 2023, DOI: 10.24018/ejdevelop.2023.3.3.252.

[6] H. P. Gund and J. Daniel, "Q-commerce or E-commerce? A systematic state of the art on comparative last-mile logistics greenhouse gas emissions literature review," *International Journal of Industrial Engineering and Operations Management*, 6(3):185–207, Jul. 2024, DOI: 10.1108/IJIEOM-01-2023-0001.

[7] Andarwati Kunharyanto S, Mayasari R, Oktaviana D. Optimization in Routing and Vehicle Selection for E-commerce Last Mile Logistics: Bibliometric Analysis[J]. Acta Informatica Pragensia, 2025, 14(1): 174-190.DOI: 10.18267/j.aip.257

[8] A. O. ADENIRAN, O. Ben SIDIQ, G. T. OYENIRAN, and A. A. ADENIRA, "Sustainability Impact of Digital Transformation in E-Commerce Logistics," *International journal of Innovation in Marketing Elements*, vol. 4, no. 1, Apr. 2024, DOI: 10.59615/ijime.4.1.1.

[9] Tulli S K C. The Role of Oracle NetSuite WMS in Streamlining Order Fulfillment Processes[J]. International Journal of Acta Informatica, 2023, 2(1): 169-195.

[10] Puica E. Efficiency and performance of Big Data analytics for supply chain management[J]. Informatica Economica, 2022, 26(1): 16-24.DOI:10.24818/issn14531305/26.1.2022.02

[11] F. F. Guo, S. Wang, and S. Y. Chen, "Competitive supply chain strategy optimization based on game model and NSGA-II algorithm," *J. Ind Intell*, 2(2): –118, 2024. https://doi.org/10.56578/jii020204

[12] X. Liu, X. Gou, and Z. Xu, "Multi-Objective Last-Mile Vehicle Routing Problem for Fresh Food E-Commerce: A Sustainable Perspective," *Int J Inf Technol Decis Mak*, 23(06): 2335–2363, Nov. 2024, Doi: 10.1142/S0219622024500020.

[13] S. Shafiee Moghadam, A. Aghsami, and M. Rabbani, "A hybrid NSGA-II algorithm for the closed-loop supply chain network design in e-commerce," *RAIRO - Operations Research*, 55(3): 1643–1674, May 2021, Doi: 10.1051/ro/2021068.

[14] H. Huang, "Cross-border e-commerce logistics distribution optimisation based on IoT artificial intelligence algorithm," *Int J Data Min Bioinform*, 28(2): 109–126, 2024. https://doi.org/10.1504/IJDMB.2024.137745

[15] M. Zhang, A. Chen, Z. Zhao, and G. Q. Huang, "A multi-depot pollution routing problem with time windows in e-commerce logistics coordination," *Industrial Management & Data Systems*, 124(1): 85–119, 2024. https://doi.org/10.1108/IMDS-03-2023-0193

[16] L. Tang, "Logistics Path Planning based on Improved Particle Swarm Optimization Algorithm," *Scalable Computing: Practice and Experience*, 26(3): 1276–1283, 2025. https://doi.org/10.12694/scpe.v26i3.4205

[17] J. Li, "A Dynamic Path Optimization Model of IOT Delivery Vehicles for E-commerce Logistics Distribution," *Scalable Computing: Practice and Experience*, 24(4): 729–742, 2023. https://doi.org/10.12694/scpe.v24i4.2332

[18] G. Lin and N. Duan, "Research on integration of enterprise ERP and E-commerce systems based on adaptive ant colony optimization," *Journal of Intelligent & Fuzzy Systems*, 46(4): 11169–11184, 2024. https://doi.org/10.3233/JIFS-237998

[19] M. Shoaee and P. Samouei, "Modeling and desigkning a cross-dock warehouse using multi-objective gray wolf optimization algorithm," *Journal of decisions and operations research*, 7(3): 453–465, 2022. DOI:10.3390/a15080265

[20] F. Maadanpour Safari, F. Etebari, and A. Pourghader Chobar, "Modelling and optimization of a tri-objective Transportation-Location-Routing Problem considering route reliability: using MOGWO, MOPSO, MOWCA and NSGA-II," *Journal of optimization in industrial engineering*, 14(2): 83–98, 2021. DOI:10.22094/JOIE.2020.1893849.1730

[21] J. Liu, F. Liu, and L. Wang, "Automated, economical, and environmentally-friendly asphalt mix design based on machine learning and multi-objective grey wolf optimization," *Journal of Traffic and Transportation Engineering (English Edition)*, 11(3): 381–405, 2024. https://doi.org/10.1016/j.jtte.2023.10.002

[22] Z. K. Mehrabadi, M. Fartash, and J. A. Torkestani, "An energy-aware virtual machine placement method in cloud data centers based on improved Harris Hawks optimization algorithm," *Computing*, 107(6):1–40, 2025. https://doi.org/10.1007/s00607-025-01488-x

Optimizing Convolutional Neural Networks with Fish Swarm Algorithms for Mitigating Financial Risks in the Digital Economy

Xiaolei Zhang
Chifeng University Chifeng, Inner Mongolia Autonomous Region, 024000, China
Email: zxlax1977@163.com

Keywords: digital economy, financial disasters, intelligent fish swarm optimized ensemble convolution neural network (IFSO-ECNN), kernel-principal component analysis (K-PCA) a

Recieved: July 8, 2025

Due to the fast growth and development of the digital economy, the method of exchanging and transacting money has changed drastically. However, this change also poses a previously unseen threat to the economy, particularly during periods of unexpected financial disasters. Complex emergency risk avoidance tactics are necessary in these kinds of scenarios. This project aims to construct a robust framework that can forecast and mitigate the impact of sudden financial crises on the digital economy using an intelligent fish swarm-optimized ensemble convolution neural network [IFSO-ECNN]. The proposed Deep Learning (DL) approach constructs prediction models by integrating relevant socioeconomic factors, market indicators, and a wealth of historical financial data. The financial data was prepared by applying min-max normalization. The features were extracted from the preprocessed data using kernel principal component analysis (K-PCA). This study contributes to our knowledge of how IFSO-ECNN can help the digital economy better prepare for and recover from unexpected financial catastrophes. Using both historical and real-time data, the suggested framework shows that it is possible to make smart judgements and proactively reduce financial risks. Experimental results validate the validity of the IFSO-ECNN model at 97.14% accuracy, 95.23% sensitivity, 96.25% specificity, and a 95.51% F1-score, surpassing the previous baseline traditions. The new hybrid model is more efficient than the previous models and has a new impact on AI-powered financial risk forecasting. The evaluation provides policymakers, financial institutions, and enterprises with useful insights for developing more resilient strategies in the face of unforeseen economic shocks by integrating modern IFSO-ECNN methodologies with domain experience.

Povzetek: Članek obravnava napovedovanje nenadnih finančnih kriz v digitalnem gospodarstvu. Predlaga metodo IFSO-ECNN, ki združuje min–max normalizacijo, nelinearno izluščanje značilk s K-PCA ter optimizacijo konvolucijskih nevronskih mrež z algoritmom inteligentnega ribjega roja. Model doseže visoko točnost in robustnost pri obvladovanju finančnih tveganj.

1 Introduction

The increasingly digital economy is transforming the way financial trading: transactions, capital flows, and business activities occur through interconnected digital platform. Digital platforms enable economic activity to move faster and more cheaply than ever before [1]. However, they also introduce new financial risks, from hacking and algorithmic trading failures to sudden market crashes. These emerging risks are often unexpected and demand large-scale detection and mitigation strategies [2]. The digital transition is altering not just the velocity of money but also the organizational structure and economic behavior of all markets [3]. Traditional financial structures are being altered progressively with digital systems, which opens up opportunities for more complexity and accelerated change [4]. The digital economy manages data to determine the next best steps in real-time, with interrelated systems requiring communication among automated agents and performance relying on artificial intelligence and big data analytics. Alternatives to traditional markets are being adopted fast to create competitive and sustainable prospects [5].

The digital economy will also bring new dynamics and dependencies that will affect financial stability. As data is generated and used at ever-increasing rates, decision-makers must interpret changes in financial patterns and trends that occur more rapidly than ever before [6]. Complexity continuous to increase, creating a greater need to understand economic behavior and the complexities in play during times of hardship, uncertainty, and volatility, and how this relates to financial conditions. In addition,

digital systems are affected by numerous socioeconomic indicators, market signals, and geopolitical events [7]. The capability to quickly and intelligently respond to these influences has been termed a key condition of contemporary financial thinking. As businesses and investors, along with regulators, to examine move ahead with forward-looking approaches that allow for early detection of potential disturbances to the economic order, and better measures to allow for the necessary prevention [8].

The increasing digitization and interconnectivity of financial markets with the financial world mean that resilience and adaptability are vital. It has never been more critical to formulate a coherent approach to risk management and forecasting that contributes to sustainability in financial planning [9]. This means that data analytics and smart decision-support are, more than ever, relevant as we consider the role of policy, financial health, and the longer-term sustainability of economies in a digital age [10]. The recent financial disruptions across the world have underscored the weaknesses of established forecasting frameworks. Traditional statistical methods, along with many machine-learning methods, do not adjust well to the volatility and high dimensionality of contemporary financial systems. This suggests a clear, compelling need for more intelligent, adaptive, and real-time systems that can forecast and mitigate sudden financial disasters in digital ecosystems.

To tackle this issue, the research suggested an innovative intelligent fish swarm-optimized ensemble convolutional neural network (IFSO-ECNN) in an attempt to yield accurate indicators and help reduce sudden financial crises in the digital economy. By integrating deep learning models, socioeconomic indicators, and real-time data, its performance improves forecasting accuracy, thereby enabling proactive decision-making to fortify economic resilience against unforeseen disruptions through intelligent, data-based risk management approaches. The research's key contribution is as follows:

- The dataset of this research includes historical financial information and real-time socioeconomic (soc) and financial market indicator data.
- The financial data are pre-processed using min-max normalization to scale the features between 0 and 1. This preprocessing step will improve the convergence of the model and help to avoid the dominance of features during the training.
- The K-PCA method was used to extract nonlinear and high-variance features from the normalized features. K-PCA can reduce dimensionality while also allowing the underlying financial characteristics to be retained and utilized for prediction modelling.
- The research proposes an IFSO-ECNN for crisis prediction. The hybrid deep learning (DL) model combines feature learning, optimization, and ensemble prediction to provide strong forecasts.

This section of the paper follows the same format: Section 2 reviews literature, Section 3 details IFSO-ECNN, Section 4 presents experiments and results, and Section 5 summarizes findings and suggests future research.

2 Literature review

A survey of the literature, also known as a review of literature or systematic review, is a necessary component of research in many fields. It comprises a careful examination and interpretation of the collection of research, as presented in Table 1.

Table 1: Relevant studies

References	Objectives	Summary of findings
Poonia et al. [11]	To create a powerful AI-based framework, Nature-inspired Red-optimized Stochastic Artificial Neural Network (NRFO-SANN) for early identification and prediction of global financial crises, particularly those affecting small and medium-sized enterprises (SMEs).	The NRFO-SANN model obtained 96% accuracy, 96.5% F-score, 94% sensitivity, and 95% specificity while detecting financial irregularities in 1 second, improving global crisis prediction and economic resilience.
Asif [12]	To create an AI-based dynamic risk management model for equity portfolios, which will improve resilience during crises such as pandemics and market crashes.	The approach outperforms standard static models by combining real-time data and machine learning, providing better risk prediction and portfolio performance under turbulent environments.
Borowski et al. [13]	The research was conducted to better comprehend how internal and external contextual elements affect customers' decisions for ride-sourcing services during small-scale urban evacuations.	To demonstrate the results, three ride-sourcing initiatives based on various evacuation needs are employed.
Luo et al. [14]	The findings provide empirical support and a basis for making decisions in favor of the cooperative relationship between DIE and GDE.	The study advocates accelerating the development and upkeep of digital infrastructure, strengthening DIE's potential as an enabler, and creating a differentiated DIE strategy.

Quan et al. [15]	To improve corporate financial risk management and crisis warning systems, a hybrid model combining gated recurrent units-temporal convolutional networks (GRU-TCN) and attention mechanisms is proposed.	The suggested model enhances risk prediction accuracy, efficiency, and stability by 46.8% in floating-point operation and 48.5% in inference time, exceeding baseline models.
Yin [16]	To create a machine learning-based early warning system for systemic financial crises utilizing macroeconomic data from 35 nations (1970-2022).	Ensemble models (Random Forest, XGBoost) had an AUROC of 0.97, beating conventional models and detecting major nonlinear risk variables such as GDP growth, trade, and demography.
Seddighi et al. [17]	The exploratory research approach used in this work consists of two stages and seeks to close the gap. To determine how much the Sharing Economy (SE) is taken into account in disasters, the researchers first undertake a comprehensive literature review.	The research makes two contributions in total. First off, the research provides a fresh perspective on the literature by identifying the various functions that the SE may play in disasters. Second, the study offers methods for collaboration and partnerships that can support coordination and logistics in catastrophes from the point of origin through delivery.
Odion et al. [18]	To investigate the role of deep learning algorithms (RNN, LSTM, and GAN) in revolutionizing financial risk assessment and business analytics via real-time modeling and predictive insights.	Deep learning improves fraud detection, credit risk assessments, and investment strategies by analyzing complicated, real-time data. The study emphasizes its impact on accuracy, ROI, and resilience, and includes case studies demonstrating practical success.
Juraboeva et al. [19]	To evaluate the use and efficacy of AI and machine learning approaches in predicting financial crises compared to classic econometric models.	AI technologies such as RNN, LSTM, transformers, and sentiment analysis outperform classical models when dealing with nonlinear and high-dimensional data. The study identifies research gaps and suggests improvements to model credibility, cross-country generalization, and real-time forecasting.
Murugan [20]	To create a big data-driven financial risk prevention model utilizing KNN, logistic regression, and XGBoost, to forecast loan defaults and optimize investment risk.	Cluster-based machine learning models, particularly XGBoost, outperformed traditional methods for predicting loan defaults. With IoT implementation, the model maintained ideal consumption stability below 5% and investor wealth risk between 0.02 and 0.09, hence improving real-time financial risk control.
Song et al. [21]	Create an accurate and efficient financial distress prediction model utilizing a deep learning architecture that combines CNN, BiLSTM, and attention methods.	The 1CNN-1BiLSTM-AT model beat ten alternatives in accuracy and speed when verified using 2025 data from two firms across 100 tests, demonstrating good real-world stability.
Sefidi [22]	To improve systemic risk identification, a market crisis prediction model will be developed that incorporates multilayer network analysis, Granger causality, Random Forest, and LSTM.	The hybrid model surpasses previous techniques by properly capturing temporal and cross-sector connections, allowing for improved forecasting of market instability and offering early warning tools to policymakers.
Chinonyerem et al. [23]	Using large-scale financial data from 2010 to 2024, develop and compare machine learning models for accurately predicting corporate financial distress in US companies.	XGBoost outperformed Neural Networks, Random Forest, and SVM in terms of accuracy (93.2%), proving ensemble models as the strongest instruments for predicting early financial hardship.

2.1 Research gap

The accelerated pace of the digital economy has revolutionized financial transactions but also introduced vulnerabilities to unexpected crises. Existing forecasting institutions struggle to effectively predict and manage such financial shocks, paving the way for new, smart solutions. Small and medium-sized enterprises (SMEs) are most prone to financial crises because they lack resources and are poorly supported with risk buffers. Current prediction systems lack real-time accuracy. There is a necessity for a reliable AI-based system that can precisely identify financial anomalies well ahead of time and improve world crisis prediction to aid in economic resilience [11]. Conventional models cannot forecast country-level systemic financial crises with macroeconomic nonlinearities [16]. For the 1970–2022 time period, with financial interconnectedness and volatility in the global economy, there exists an urgent need for an efficient early warning system. The present study fulfils the need for machine learning ensemble models using large-scale economic indicators so as to correctly and promptly detect crises. The IFSO-ECNN methodology proposed is more than the issue of sudden financial crises in the digital

economy, as it synergizes fish swarm optimization and deep learning. The hybrid model enhances risk estimation, facilitates timely decision-making, and provides policymakers and financial institutions with a solid tool for anticipatory crisis management and strategic resilience.

3 Methodology

This sub-section explains the complex proposed IFSO-ECNN architecture in detail. The model consists of various steps, including initially discovering the preprocessing of financial time-series data through min-max normalization, then extracting nonlinear features through K-PCA, then optimizing convolutional neural network parameters through an enhanced fish swarm optimization algorithm (IFSO), and lastly training multiple CNNs as an ensemble model. Prediction of an Ensemble is utilized through majority voting. IFSO-ECN is a combined model that is also oriented to enhancing flexibility and precision in financial crisis event forecasting. Figure 1 depicts the suggested method's organizational structure.

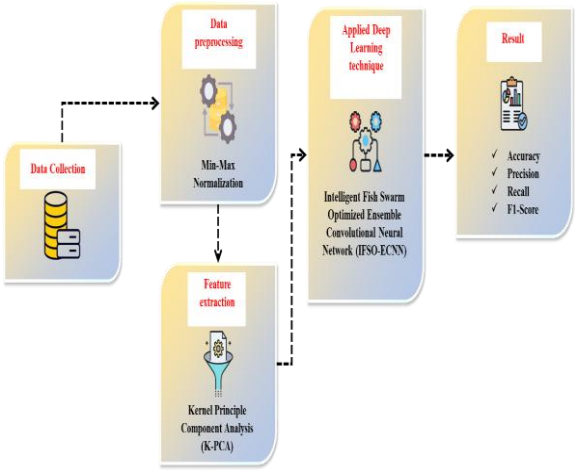

Figure 1: Structure of the proposed method

3.1 Dataset

Critical financial, social, and digital economy risk indicators were gathered from 750 households throughout three monitoring cycles, totaling 13 months. GDP growth, inflation, changes in foreign exchange rates, market volatility, demand for Information and Communications Technology (ICT), and catastrophe effect scores are among the measures included in the data. It is intended for use in emergency risk analysis, crisis response AI model training, and the prediction of unexpected financial catastrophes. The dataset also includes a three-level catastrophe severity goal and a binary classification label. This dataset was separated into 70 % for training and 30 % of testing. The data gathered from Kaggle [24]. They must process the raw financial data using adequate preprocessing methods in order to transform it into a format ready to be advanced in modelling. The initial process entails scaling of the input features via min-max normalization, which makes all variables work within a similar numerical scale and minimizes training bias.

3.2 Min-Max normalization for data preprocessing

Min-max normalization is a commonly used technique for scaling numerical properties within a certain range. It is frequently used to prepare data for machine learning models. The dataset's input features can be normalized using min-max normalization to prepare them for diabetes prediction. A normalizing method called min-max normalization linearly alters the original data to produce a comparable set of values before and after the procedure.Z_{new} represents the adjusted value obtained through data scaling, and Y denotes the original value.

$$Z_{new} = \frac{z-\min}{\max(z)-\min(z)} \tag{1}$$

Where equation (1), z is the original feature value, z_{min} is the original feature minimum, z_{max} is the original feature maximum, and z_{new} is the normalized value. The next process after normalizing is to lessen the dimensionality of the data without compromising the aspect of the data that is informative. To do this, we would use a nonlinear feature extraction approach of Kernel Principal Component Analysis (K-PCA), which is able to capture nonlinear relationships of complex data.

3.3 K-PCA for feature extraction

The researchers employ a nonlinear function to convert the input data × to the highly dimensional space of features L. $\emptyset$: $K^M \to L, y \to Y$. Assume that the data revolves around the map,$\sum_{r=1}^{N} \emptyset(y_r) = 0$in the feature space L, then the covariance matrix in $L$is $V^L = \frac{1}{N}\sum_{j=1}^{N} \emptyset(y_j)\emptyset(y_j)^D$. The next step is to find eigenvalues $\lambda^L \geq 0$&eigenvectors $U^L \in L/\{0\}$ satisfying $V^L\lambda^L = \lambda^L U^L$. The range of $\emptyset(y_r), \ldots \emptyset(y_n)$ Contains all solutions $U^L$where $\lambda^L \neq 0$. There are coefficients, so$U^L = \sum_{j=1}^{N} \alpha_j \emptyset(y_r)$. Existing for$\alpha_j (j = 1, \ldots, N)$.

$$\lambda^L = \sum_{j=1}^{N} \alpha_j \left(\emptyset(y_r).\emptyset(y_j)\right)$$

$$= \frac{1}{N}\sum_{j=1}^{N} \alpha_j \left(\emptyset(y_r).\sum_{i=1}^{N} \emptyset(y_i))\emptyset(y_i).\emptyset(y_j)\right)$$

$$(r = 1, \ldots, N) \tag{2}$$

Define an $N \times N$ matrix R by

$R_{ji} = \emptyset(y_i).\emptyset(y_i)).$

(3)

So, equation (2) can be written as $N\lambda^L R\alpha = R^2\alpha$.

$N\lambda^L\alpha = R\alpha$

(4)

Let $\lambda_1^L. \geq \lambda_2^L \geq \cdots \geq \lambda_N^L$represent the eigenvalues, and the entire set of eigenvectors for equation (4) is $\alpha_1, \alpha_2, \ldots, \alpha_N$.

The researchers must normalize an eigenvector from the element of an environment L. $\lambda_N^L \neq 0, r = 1,2,..,f$, by equations (2)-(4), $(U_r^L.U_r^L) = 1$is same as $(U_r^L.U_r^L) = \sum_{j,i=1}^N \alpha_j^r \alpha_i^r \left(\emptyset(y_i).\emptyset(y_i)\right) = \sum_{j,i=1}^N \alpha_j^r \alpha_i^r R\left(y_j, y_i\right) = \lambda_1^L(\alpha^r.\alpha^r) = 1 \quad r = 1,..,f$

(5)

It was necessary to compute the projections of each data point onto the eigenvectors to isolate its principal component.U_r^Lin$L$. Using y as the measurement point, whose projection is $\emptyset(y)$in L, project $\emptyset(y)$ onto the eigenvectors of U_r^L that correspond to the nonlinear major components, equation (6).

$\left(U_r^L.\emptyset(y)\right) = \sum_{j=1}^N \alpha_j^r(\emptyset(y_i).\emptyset(y_i))$

(6)

After the extraction of the key features, one uses the refined inputs to train the prediction model. The research suggests an IFSO-ECNN as a way to improve the predictive capacity and the accuracy of the system in detecting sudden financial calamities.

3.4 Intelligent fish swarm optimized ensemble convolutional neural network (IFSO-ECNN)

The goal would be to improve performance in tasks linked to image recognition, object identification, or other activities where ECNNs thrive by optimizing the training procedure and architecture of the ensemble of ECNNs using the improved optimization method. The suggested IFSO-ECNN system combines the IFSO algorithm with an ECNN. IFSO optimizes hyperparameters of each CNN model in the ensemble, for example, learning rate, convolutional filter numbers, and dropout value. A separate CNN is trained over another IFSO-adjusted configuration, and ensemble prediction is obtained through majority voting. Algorithm 1 illustrates the process of the IFSO-ECNN method.

Algorithm 1: Procedure of IFSO-ECNN

```
Input:
  D: Number of dimensions (hyperparameters like LR, dropout, filters, etc.)
  N: Number of artificial fish (population size)
  E: Number of CNNs in ensemble
  MaxIter: Maximum iterations for IFSO
  Dataset: Input image dataset with labels
Output:
  Final_ensemble_model: Ensemble of E CNNs optimized by IFSO
  Accuracy: Classification accuracy on validation/test set
Begin:
Initialize IFSO parameters:
  For each fish i in 1 to N:
    Randomly initialize hyperparameter vector Z_i in D dimensions
    Evaluate fitness FS_i = CNN_Train_Evaluate(Z_i, Dataset)
Set best_solution = Z_i with minimum FS_i
 Set best_fitness = FS_i of best_solution
Main Optimization Loop (for iter = 1 to MaxIter):
  For each fish Z_j in the population:
    Randomly select a neighbor Z_k ≠ Z_j
    Perform:
      a. Search behavior update
      b. Swarming behavior update
      c. Following behavior update
      d. Communication update
    Evaluate new position FS_j_new =
CNN_Train_Evaluate(Z_j_new, Dataset)
    If FS_j_new < FS_j:
      Z_j = Z_j_new
      FS_j = FS_j_new
    If FS_j_new < best_fitness:
      best_solution = Z_j_new
      best_fitness = FS_j_new
Final Hyperparameter Selection:
  Select top E best solutions Z_1, Z_2, ..., Z_E from fish population
CNN Training:
  For i = 1 to E:
    Train CNN_i with hyperparameters Z_i
    Store model CNN_i
Ensemble Prediction:
  For each test sample x:
    Predict_i = CNN_i(x) for i in 1 to E
    Final_Prediction = MajorityVote(Predict_1 ... Predict_E)
Evaluate Ensemble Accuracy on Test Set
Return Final_ensemble_model and Accuracy
End
Function CNN_Train_Evaluate(Z, Dataset):
  Extract hyperparameters: learning_rate, dropout_rate, filter_size, etc. from Z
  Initialize CNN with these hyperparameters
  Train CNN on training set subset
  Validate on the validation set
  Return validation_loss or error as fitness
```

The combination of K-PCA, ECNN, and IFSO within the proposed IFSO-ECNN framework has been intentionally structured to solve the unique problems in predicting sudden financial disasters in the digital economy.

- K-PCA is a technique for nonlinear dimensionality reduction that is able to identify complex, high-order relationships among economic variables that linear methods, such as PCA, cannot discriminate.
- ECNN, chosen because of its ability to optimally learn hierarchical representations from structured economic datasets without being overfitted due to inherent ensemble diversity, as compared to sequential models like LSTM.

- IFSO implements a biologically inspired evolutionary optimization model improved through communication mechanisms, as well as adaptive behavior mechanisms, balancing exploration and exploitation in fine-tuning CNN hyperparameters.

The hybrid architecture resolves three important problems: (i) the high-dimensional complexity of features, (ii) the necessity of achieving robustness in pattern extraction, and (iii) the necessary ability to learn adaptively in constant change environments. This hybrid approach takes advantage of the individual advantages of its components and delivers challenging predictive performance in the context of digital finance.

3.4.1 Ensemble Convolutional Neural Network (ECNN)

A common DL model for applications like picture segmentation, object detection, and classification is the ECNN. Due to its capacity to capture regional patterns and feature hierarchies, it is particularly useful for jobs involving grid-like data, such as photographs. ECNN was selected because it has the advantage of discovering the hierarchical structures within the high-dimensional data in the field of financial data. Ensemble promotes the generalization of the model and prevents over-fitting. The ECNN is also more effective with cross-sectional and structured economic input than the sequential models, such as LSTM.

3.4.1.1 Operation of convolution

Local information is extracted during the convolution process by dragging a small filter, also known as a kernel, over the input picture. The final characteristic map has just one value derived from the sum of the elements' separate processing. Equation (7) allows the convolution process to be expressed.

$$Q(j,i) = \sum_n \sum_m J(j+n, i+m) \times R(n,m) \tag{7}$$

where the value is located at (j,i) in the finalized feature map is denoted by $Q(j,i)$. The position value $(j+n, i+m)$ in the original image is represented by $J(j+m, i+m)$. $R(n,m)$ is the convolutions kernel's position value (n,m).

3.4.1.2 Function of activation

After the convolution procedure, each element is subjected to an activation function (commonly referred to as the Rectified Linear Unit, or ReLU), which adds non-linearity. The following describes the ReLU activation function as shown in equations (8 and 9):

$$ReLU(y) = \max(0, y) \tag{8}$$

$$Q(j,i) = \overset{max}{}_{n,m} J(j \times g + n, i \times g + m) \tag{9}$$

g is the stride of the pooling operation (the number of steps the pooling window moves). n, m are indices over the pooling window (for example, for 2×2 pooling, n, m $\in \{0,1\}$). J is the input feature map before pooling

3.4.1.3 Operating a pool

Pooling reduces the feature maps' spatial size while preserving important information. A popular pooling method is max pooling, and its formula for a certain location is:

3.4.1.4 Layer with full connectivity

The characteristics are often flattened and then passed through one or more fully connected layers after many convolutional and pooling layers to provide final predictions. Fully connected layers have bias furtherance and multiplication of matrix in their equations. These are the fundamental CNN components and formulae. Remember that there are many different sorts of CNN designs, such as normalization layers, skip connections, and other types of layers. To tune the hyperparameters of individual CNNs in an ensemble, it combines an IFSO algorithm. This is an evolutionary computing approach, which simulates the foraging of fish schools, enabling a fast search of the solution space.

3.4.2 Intelligent Fish Swarm Optimization (IFSO)

The optimality of IFSO can be explained by its better exploration-exploitation balance and its adaptive search behavior that enhances a more stable convergence. It has communication and local decision-making based on fish swarms, unlike PSO. This qualifies it as an appropriate algorithm in hyperparameter tuning of complex neural networks in dynamic financial settings. The IFSO is a novel population-based optimization technique inspired by fish's natural eating habits. Fish food satisfaction is represented as FS_i, and a fish is pictured by its D-dimensional position $Z_j = (Z_1, Z_2, \ldots, Z_k, \ldots, Z_d)$. The goal of this work is FS minimization. The Euclidean separation of two fish, $dij = |Z_i Z_j||$, indicates their relationship. Figure 2 depicts the IFSO algorithm workflow, showing relevant behaviors such as searching, swarming, following, and communication of fish agents in optimizing the hyperparameters of CNN.

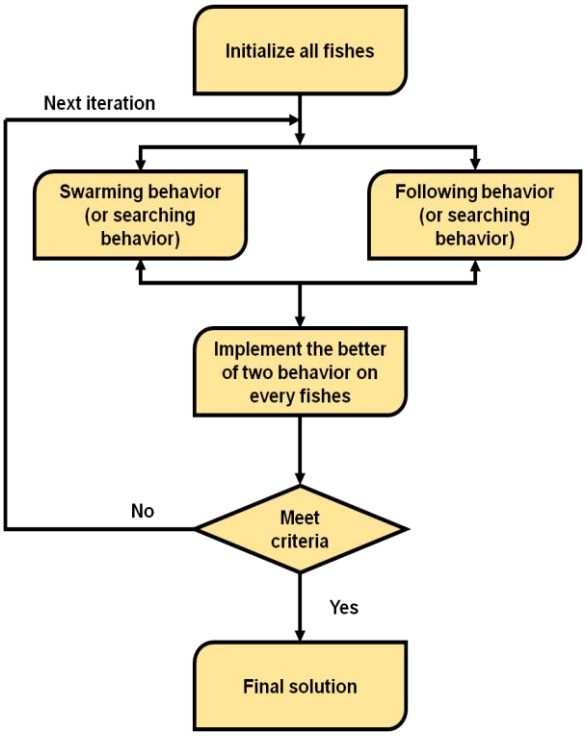

Figure 2: Architecture of IFSO

Fish population size is represented by the number n. All fish use three separate behaviors to search for areas where they can find food.

3.4.2.1 A search-related action

When searching for food, fish exhibit this behavior as a basic biological behavior. It is based on the random search principle and tends to concentrate on food. In mathematics, it is written as shown in equations (10 and 11):

$$\vec{Z}_{j+1}^{r} = \vec{Z}_{j}^{r} + K(G1)\frac{\vec{z}_{i}^{r} - \vec{z}_{j}^{r}}{\|z_i - z_j\|}, FS_i < FS_j \tag{10}$$

$$\vec{Z}_{j+1}^{r} = \vec{Z}_{j}^{r} + K(S2)\vec{1} \tag{11}$$

Where Z_j^r denotes fish location Z_j's rth element, for fish Z_j, choose a random place Z_j inside its image. After a certain number of trials, if FS_i is still unsatisfied, a random position within the step range will be immediately selected.

3.4.2.2 Swarming conduct

Fish congregate in a variety of swarms to reduce risk. All swarms share the same goals, which include supplying food intake requirements, amusing existing swarm members, and luring in new swarm members. Mathematically equation (12),

$$\vec{Z}_{j+1}^{r} = \vec{Z}_{j}^{r} + K(S2)\frac{\vec{z}_{v}^{r} - \vec{z}_{j}^{r}}{\|z_v - z_j\|}, FS_v < FS_j and \left(\frac{m_g}{m}\right) < \delta \tag{12}$$

A fish at Y_j has neighbors in its field of view. When describing the characteristics of the complete neighboring swarm, Yv is used to pinpoint the center position of those neighbors. The fish will travel from position Z_j to the next Z_{j+1} in the direction of Zv if the swarm center contains a higher concentration of food present at position Z_j. If a fish has an associated Yv, swarming behavior is carried out for it; otherwise, searching behavior ensures the fish's next position.

3.4.2.3 Adopting an action

Neighboring fish follow a fish that finds food, which is mentioned in Equation (13),

$$\vec{Z}_{j+1}^{r} = \vec{Z}_{j}^{r} + K(S2)\frac{\vec{z}_{min}^{r} - \vec{z}_{j}^{r}}{\|z_{min} - z_j\|}, FS_{min} < FS_j and \left(\frac{m_l}{m}\right) < \delta \tag{13}$$

To maximize enjoyment, a fish will naturally desire to follow the best fish (Z_{min}). This is due to the fish's perception; certain fish will be viewed as finding a larger amount of food than others, and these fish will try to follow the best one (Z_{min}). If a fish's following behavior is unable to predict its next place, searching behavior starts. Additionally, IFSO ought to offer a newsletter that documents the ideal condition and present performance of fish throughout iterations. It is difficult to get into deeper detail on IFSO because of parameter settings, notably for visuals and steps. To remove step influences, this work will introduce settings for these two parameters and use the PSO formulation for IFSO. Additionally, fake fish will also exhibit a communication behavior.

By using the IFSO visual, local search attributes are supplied. Due to its narrow viewing area, fish can only interact with a very small number of companions. The maximum step length for the IFSO step is limited, and a short step compels fish to search a smaller area and increases the probability of running out of time. Step values are dependent on IFSO performance and are determined using Euclidean distance computations. All of the original IFSO formulas have been altered:

Searching techniques

$$\vec{Z}_{j+1}^{r} = \vec{Z}_{j}^{r} + \varphi_{3r}\left(\vec{Z}_{i}^{r} + \vec{Z}_{j}^{r}\right), FS_i < FS_j \tag{14}$$

$$\vec{Z}_{j+1}^{r} = \vec{Z}_{j}^{r} + K(V1)\vec{1} \tag{15}$$

$$\varphi_3^r = v_3 k_3^r \quad (16)$$

Where equations (14-16), φ_3^r has a mean value of one and is a uniform random number, falling between $[0, 2]$. The uniform random number c3 is 2, falling between $[0, 1]$. The improved IFSO allows fish to swim farther than was allowed by the original IFSO when the step is less than visible. Modified search behavior can be used at any time.

Swarming actions

$$Z_{j+1}^r = \vec{Z}_j^r + \varphi_4^r\left(\vec{Z}_i^r - \vec{Z}_j^r\right), FS_v < FS_j and \left(\frac{m_g}{m}\right) < \delta \quad (17)$$

Where equation (17)φ_4^r is defined in the same way asφ_3^r, and $\vec{Z}_i^r$ is defined in the same way as FSA. Therefore, modified swarming behavior is allowed to step.

The subsequent actions

$$\vec{Z}_{j+1}^r = \vec{Z}_j^r + \varphi_5^r\left(\vec{Z}_{min}^r - \vec{Z}_j^r\right), FS_{min} < FS_j and \left(\frac{m_l}{m}\right) < \delta \quad (18)$$

Where equation (18) φ_5^r and φ_3^r are defined similarly, and Z_{min} is defined similarly it is used in FSA. Therefore, the modified following behavior allows for free stepping.

Only visual cues can determine the positions of Z_j, Z_i, Z_{min}, and the subsequent X_j.

Communication techniques

Artificial fish ought to possess greater skills than those present in real fish. The message enables fish to determine the optimal location of the entire swarm. Fish are allowed to reach the location if it is not already too crowded. In other words, this strategy guarantees that a specific number of fish will be actively seeking food around the global best position. The mathematical representation of this is as follows equation (19):

$$\vec{Z}_{j+1}^r = \vec{Z}_j^r + \varphi_6^r\left(\vec{Z}_{best}^r + \vec{Z}_j^r\right), \left(\frac{m_f}{m}\right) < \delta \quad (19)$$

If φ_6^r has the same definition as φ_3^r, $Zbest$ is the position with the maximum amount of achieved food satisfaction, and nb is the number of fish visible in the area around $Zbest$. Algorithm 2 illustrates the IFSO as follows:

Algorithm 2: Process of Intelligent Fish Swarm Optimization (IFSO)

1.
Initialize fish positions randomly within the search space:
For $i = 1$ *to* N:
For $j = 1$ *to num_dimensions*:
Randomly initialize $fish[i][j]$ *within bounds*
2. *Initialize fish fitness values*:
For $i = 1$ *to* N:
$fish_fitness[i] = calculate_fitness(fish[i])$
3. *Initialize the best solution and fitness*:
$best_solution = fish[i]$
$best_fitness = fish_fitness[i]$
4. *Main optimization loop*:
For iteration $= 1$ *to max_iterations*:
For $i = 1$ *to* N:
For $j = 1$ *to num_dimensions*:
Select a random fish index $k \neq i$
Calculate new_position$[j]$
$= fish[i][j] + (fish[i][j] - fish[k][j]) * rand()$
Clip new_position$[j]$ *within bounds*
$new_fitness = calculate_fitness(new_position)$
If $new_fitness < fish_fitness[i]$:
Update $fish[i]$ *with new_position*
$fish_fitness[i] = new_fitness$
If $new_fitness < best_fitness$:
Update best_solution with new_position
$best_fitness = new_fitness$
5. *Output best_solution and best_fitness*
6. *End*

4 Results and discussion

The evaluation metrics of sensitivity, specificity, accuracy, and F1-Score are used in the part where we examine how well our suggested approach performs in comparison to current approaches. To demonstrate how successful a given method is, its dependability and effectiveness are compared to those of more established techniques like hybrid hunter–prey optimization with a deep learning-based financial crisis prediction (HHPODL-FCP) [25], quantum artificial butterfly optimization- long short-term memory- long short-term memory (QABO-LSTM-RNN) [26], Ant colony optimization (ACO model) [25].

Sensitivity is the percentage of real positive cases properly recognized by a prediction model. In terms of financial catastrophe risk avoidance, high sensitivity indicates that the system is capable of identifying possible risks or abnormalities in the digital economy. When comparing our proposed method with existing methods. Figure 3 and Table 2 illustrate the sensitivity values. Our proposed method, IFSO-ECNN- 95.23%, outperforms existing models, including HHPODL-FCP (93.51%), QABO-LSTM-RNN (85.89%), and the ACO model (78.27%), demonstrating superior sensitivity values in the digital economy's intelligent emergency risk during sudden

financial disasters. Sensitivity (95.23%) is the model's power to identify actual early warning symptoms of financial crises, which is important in order to initiate timely interventions that will halt mass disturbance of the economy.

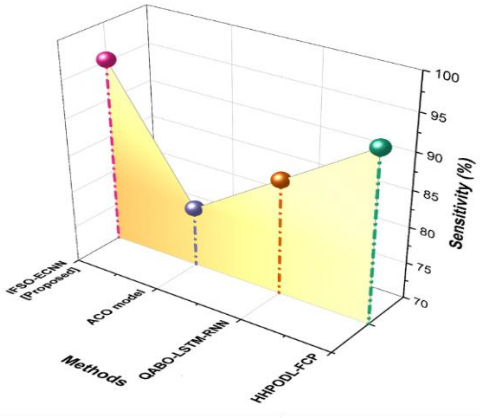

Figure 3: Sensitivity outcome

Table 2: Sensitivity values

Method	Sensitivity (%)
HHPODL-FCP	93.51
QABO-LSTM-RNN	85.89
ACO model	78.27
IFSO-ECNN [proposed]	95.23

Specificity refers to the fraction of real negative situations properly detected by a prediction model. Specificity is necessary to reduce false alarms. In the financial industry, a high specificity suggests that the system can accurately recognize circumstances when there is no immediate financial crisis, eliminating unneeded fear or actions. Figure 4 and Table 3 illustrate specificity values, affirming the superiority of our proposed IFSO-ECNN-96.25% over established methods like HHPODL-FCP (93.97%), QABO-LSTM-RNN (92.65%), and the ACO model (69.25%). Our approach signifies significant advancements in navigating sudden financial disasters and intelligent emergency risk avoidance in the digital economy. Specificity (96.25%) is all about invoking minimal false alarms to avert overreacting with alarm or ineffective policy measures.

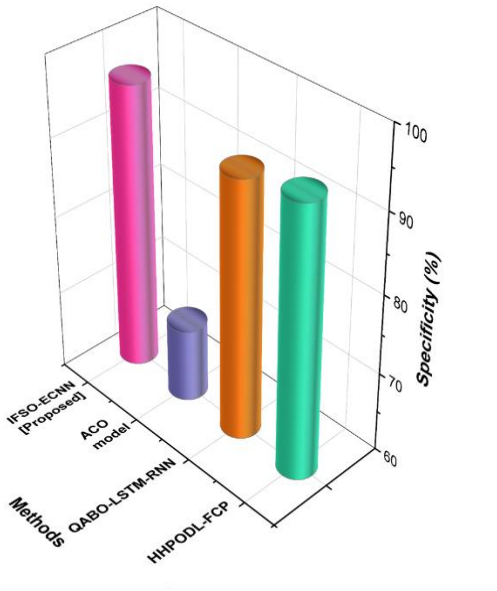

Figure 4: Specificity outcome

Table 3: Specificity values

Methods	Specificity (%)
HHPODL-FCP	93.97
QABO-LSTM-RNN	92.65
ACO model	69.25
IFSO-ECNN [proposed]	96.25

Accuracy assesses the model's overall accuracy, taking into account both true positives and true negatives. In the context of financial crises, high accuracy indicates that the system is generating generally right forecasts. Figure 5 and Table 4 illustrate the accuracy values. When evaluating the suggested method's performance against that of other approaches, such as HHPODL-FCP-94.87%, QABO-LSTM-RNN- 90.78%, and ACO model-75.72%. Specifically, our suggested method, IFSO-ECNN-97.14%, substantially improves its ability to predict sudden financial crises in the digital economy through smart risk avoidance during disasters. Accuracy (97.14%) is a measure of the general dependability of the model for predicting crisis and stability conditions, allowing proper planning and trust in automated decision support.

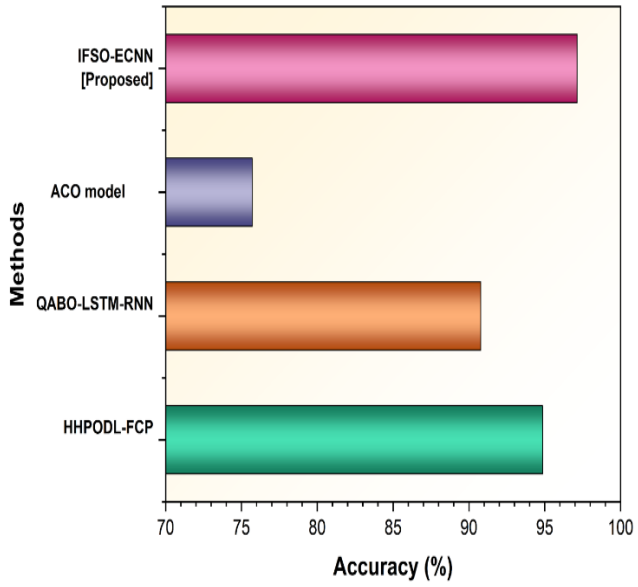

Figure 5: Accuracy outcome

Table 4: Accuracy values

Methods	Accuracy (%)
HHPODL-FCP	94.87
QABO-LSTM-RNN	90.78
ACO model	75.72
IFSO-ECNN [proposed]	97.14

F1-Score, a harmonic mean of accuracy and recall, strikes a balance between precision and sensitivity, which is crucial in the digital economy. Its equilibrium ensures accuracy while detecting a significant number of true positives. Figure 6 and Table 5 illustrate F1 score values. In contrast, the suggested approach is different from the current approach. The suggested approach shows a higher value of IFSO-ECNN -95.51% than the existing methods, such as HHPODL-FCP-93.67%, QABO-LSTM-RNN-89.08 %, and ACO model-85.35%. It demonstrates that our proposed method, IFSO-ECNN, achieves a success rate of 95.51% in estimating the digital economy of sudden financial disaster intelligent emergency risk avoidance. F1-Score (95.51%) is the balance of precision and recall because the system performs well even if partial risk indicators or imbalanced data are involved.

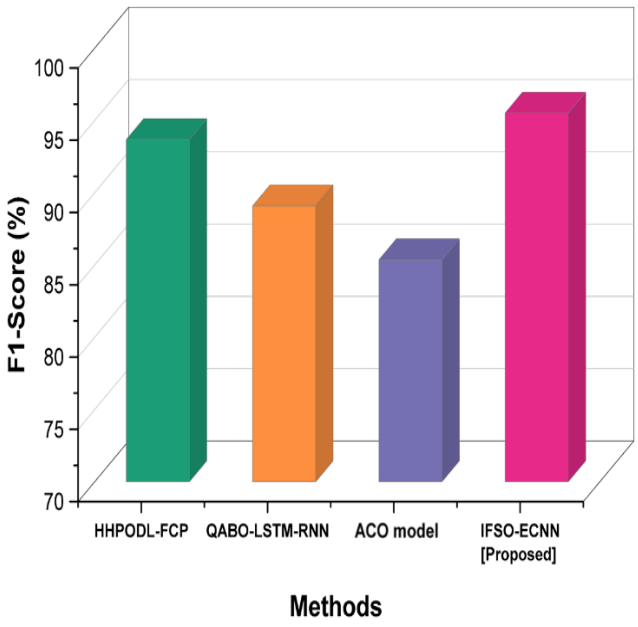

Figure 6: F1-Score outcome

Table 5: F1-Score values

Methods	FI-Score (%)
HHPODL-FCP	93.67
QABO-LSTM-RNN	89.08
ACO model	85.35
IFSO-ECNN [proposed]	95.51

4.1 Discussion

Utilizing existing approaches like QABO-LSTM-RNN [26], ACO model [25], and Hybrid Hunter-Prey Optimization with HHPODL-FCP [25] assists in accomplishing the goal of preventing sudden financial disasters in the digital economy through intelligent emergency risk avoidance. While QABO-LSTM-RNN combines optimization inspired by quantum computing with long short-term memory networks, it is also plagued by computational complexity and temporal inefficiency, and therefore, is less applicable to real-time crisis forecasting. HHPODL-FCP combines hybrid optimization and deep learning for efficient crisis prediction. Although effective, it is not generalizable in the face of shifting financial signals or unseen risk patterns.

Furthermore, the ACO model makes use of methods inspired by ants. ACO-based models are highly sensitive to parameter settings and have the tendency to converge too quickly in dynamic situations. These approaches have drawbacks that could impact their efficiency and practical usefulness in real-world situations, despite their potential. Examples of these drawbacks are the sensitivity of ACO to parameter decisions and the computational complexity of quantum algorithms in QABO-LSTM-RNN.

In contrast to previous methods that often depend on severe structures or a single optimization step, IFSO-ECNN makes a novel technical impact in incorporating a stable fish swarm optimization algorithm with an ensemble of CNNs. This adaptive tuning process greatly enhances generalizability and flexibility, representing a new financial crisis prediction model breakthrough. This provides hyperparameter optimization, improved exploration-exploitation trade-offs, and significantly high noise tolerance to financial data streams. The outcome is a smart emergency risk avoidance system that is reliable, accurate, and reactive.

5 Conclusion

Disasters like natural disasters and unforeseen mishaps have been happening more frequently lately, which has negatively impacted a particular region's usual development of financial business. The theoretical underpinnings of the ECNN and IFSO algorithms are comprehensively explained in this study, along with some of their benefits and drawbacks. The IFSO-ECNN prediction model is then created by merging these two algorithms, and it is used to predict sudden financial disasters with successful outcomes. The proposed technique's sensitivity was 95.23%, specificity was 96.25%, accuracy was 97.14%, and F1-score was 95.51%, based on the previously published results. Although the IFSO-ECNN model did quite well in this piece, this area of research is still in its early stages. There are still more forecasting-related applications that need to be carefully examined. Thus, additional study is needed in the following areas: improved indicator and sample data selection, improved parameter selection, and tuning. Although the IFSO-ECNN model has demonstrated greater effectiveness, further effort are needed to establish theoretical convergence assurances, as well as evaluating other model fusions with distinct dimensionality reduction or optimization routines. The work on further development of a fully adaptive hybrid learning framework will be suggested, and the chosen model will dynamically select the most effective preprocessing and optimization strategy regarding the changing character of financial input data.

Acknowledgement:

Ministry of Education Humanities and Social Sciences Foundation Project (21YJC630126); Jiangsu University Philosophy and Social Science Project (2021SJA1364); post-doctoral scientific research support project of Jiangsu Province (2021K295B)

Declaration

Ethics approval and consent to participate: I confirm that all the research meets ethical guidelines and adheres to the legal requirements of the study country.

Consent for publication: I confirm that any participants (or their guardians if unable to give informed consent, or next of kin, if deceased) who may be identifiable through the manuscript (such as a case report), have been given an opportunity to review the final manuscript and have provided written consent to publish.

Availability of data and materials: The data used to support the findings of this study are available from the corresponding author upon request.

Competing interests: here are no have no conflicts of interest to declare.

Authors' contributions (Individual contribution): All authors contributed to the study conception and design. All authors read and approved the final manuscript

References

[1] Shinkevich, A. I., Kudryavtseva, S. S., & Samarina, V. P. (2023). Ecosystems as an Innovative Tool for the Development of the Financial Sector in the Digital Economy. Journal of Risk and Financial Management, 16(2), 72. DOI:10.3390/jrfm16020072

[2] Liu, H. (2024). Enhanced CoCoSo method for intuitionistic fuzzy MAGDM and application to financial risk evaluation of high-tech enterprises. Informatica, 48(5). DOI:10.31449/inf.v48i5.5169

[3] Innola, N., Roman, C., Nelia, C., Mykola, M., & Andrii, R. (2021, November). Ensuring of financial stability of the enterprise by financial management tools. In *International Conference on Business and Technology* (pp. 783-792). Cham: Springer International Publishing. DOI:10.1007/978-3-030-47458-4_31

[4] Raddant, M., & Kenett, D. Y. (2021). Interconnectedness in the global financial market. Journal of International Money and Finance, 110, 102280. DOI: 10.1016/j.jimonfin.2020.102280

[5] Li, J. (2022). Venture financing risk assessment and risk control algorithm for small and medium-sized enterprises in the era of big data. Journal of Intelligent Systems, 31(1), 611-622. https://doi.org/10.1515/jisys-2022-0047

[6] Qi, F. (2025). GAN-Based Financial Data Generation and Prediction: Improving The Authenticity and Prediction Ability of Financial Statements. Informatica, 49(14). DOI:10.3390/ai5020035

[7] Balboa, E., Ladesma, M., & Manguerra, A. N. (2024). Digital financing innovations and their impact on the financial performance of smes in the digital economy era. JMM17: Jurnal Ilmu ekonomi dan manajemen, 11(1), 88-98. DOI:10.30996/jmm17.v11i1.10879

[8] Gu, J. (2022). Risk prediction of enterprise credit financing using machine learning. Informatica, 46(7). https://doi.org/10.31449/inf.v46i7.4247

[9] Feng, J., & Qi, S. (2024). Digital infrastructure expansion and economic growth in Asian countries. Journal of Business and Economic Options, 7(2), 27-32. https://doi.org/10.1080/00036846.2025.2536239

[10] Dandage, R. V. RISK MANAGEMENT STRATEGIES IN POST-PANDEMIC FINANCIAL PLANNING. *CONFLUENCE OF CURIOSITY*, 316. DOI:10.25215/9358797991

[11] Poonia, R. C., Prabu, P., Maheshwari, A., Malhotra, A., & Gupta, V. (2024, January). AI Enhanced Global Economic Resilience: Predicting and Mitigating Financial Crises. In International Conference on Communication and Computational Technologies (pp. 267-279). Singapore: Springer Nature Singapore. DOI:10.1007/978-981-97-7426-5_20

[12] Asif, S. S. M. (2024). Create an AI-based Model for Dynamic Risk Management in Equity Portfolios that Accounts for Extreme Market Events (eg, Pandemics, Financial Crises). DOI:10.52783/jier.v4i3.1487

[13] Borowski, E., & Stathopoulos, A. (2020). On-demand ridesourcing for urban emergency evacuation events: An exploration of message content, emotionality, and intersectionality. International journal of disaster risk reduction, 44, 101406. DOI: 10.1016/j.ijdrr.2019.101406

[14] Luo, K., Liu, Y., Chen, P. F., & Zeng, M. (2022). Assessing the impact of digital economy on green development efficiency in the Yangtze River Economic Belt. Energy Economics, 112, 106127. DOI: 10.1016/j.eneco.2022.106127

[15] Quan, C., Yuan, Y. H., Wang, G., & Wu, H. T. (2024). Optimization of Enterprise Financial Risk Management and Crisis Early Warning System Supported by AI. Journal of Global Information Management (JGIM), 32(1), 1-21. DOI:10.4018/JGIM.356490

[16] Yin, S. (2024). MACHINE LEARNING ALGORITHMS FOR EARLY WARNING SYSTEMS: PREDICTING SYSTEMIC FINANCIAL CRISES THROUGH NON-LINEAR ECONOMETRIC MODELS. International Journal of Economics and Finance Studies, 16(4), 286-311.

[17] Seddighi, H., & Baharmand, H. (2020). Exploring the role of the sharing economy in disasters management. Technology in Society, 63, 101363. DOI: 10.1016/j.techsoc.2020.101363

[18] Odion, C. O., Okunuga, A., & Okunbor, O. I. (2025). Revolutionizing financial risk assessment through deep learning-driven business analytics for maximized ROI and Resilience. World Journal of Advanced Research and Reviews, 25(1), 2444-2461. DOI:10.30574/wjarr.2025.25.1.0327

[19] Juraboeva, D., Sagdiddinov, M., & Malikov, N. (2025). PREDICTING FINANCIAL CRISIS: THE POTENTIAL OF AI IN GLOBAL MARKETS. Modern Science and Research, 4(4), 1770-1781. DOI:10.55549/epstem.1406233

[20] Murugan, M. S. (2023). Large-scale data-driven financial risk management & analysis using machine learning strategies. Measurement: Sensors, 27, 100756. DOI:10.1201/9781003559115-29

[21] Song, Y., Chiangpradit, M., & Busababodhin, P. (2025). Hyperband-Optimized CNN-BiLSTM with Attention Mechanism for Corporate Financial Distress Prediction. Applied Sciences, 15(11), 5934. https://doi.org/10.3390/app15115934

[22] Sefidi, M. K. (2025). Predicting Financial Market Crises using Multilayer Network Analysis and LSTM-based Forecasting of Spillover Effects. arXiv preprint arXiv:2505.11019. https://doi.org/10.48550/arXiv.2505.11019

[23] Chinonyerem, C. A., Olalemi, A. A., Paul, M., Nwabunike, O. T., Eniola, O. S., Benjamin, A. O., ... & Seigha, I. B. (2025). Leveraging Machine Learning and Data Analytics to Predict Corporate Financial Distress and Bankruptcy in the United States. Asian Journal of Advanced Research and Reports, 19(6), 65-78. DOI: 10.9734/ajarr/2025/v19i61042

[24] Data available from kaggle: https://www.kaggle.com/datasets/programmer3/digital-economy-financial-risk-dataset

[25] Katib, I., Assiri, F. Y., Althaqafi, T., AlKubaisy, Z. M., Hamed, D., & Ragab, M. (2023). Hybrid hunter–prey optimization with deep learning-based fintech for predicting financial crises in the economy and society. *Electronics*, *12*(16), 3429. https://doi.org/10.3390/electronics12163429

[26] Tyagi, S. K. S., & Boyang, Q. (2021). An intelligent internet-of-things-aided financial crisis prediction model in fintech. IEEE Internet of Things Journal, 10(3), 2183-2193. DOI:10.1109/JIOT.2021.3088753

Scalogram-Based Multiclass Fetal State Classification Using Expert-Annotated CTG and SE-ResNet-50

Trie Maya Kadarina[1], Basari[1], Dadang Gunawan[1,*], Abraham Auzan[2]
[1]Dept. of Electrical Engineering, Universitas Indonesia, 16424, Indonesia
[2]Elektra Medical Research and Development, PT Elektra Abimantrana Internasional, Indonesia
E-mail: guna@eng.ui.ac.id
*Corresponding author

Keywords: Cardiotocography, expert validation, fetal state classification, residual network, scalograms

Received: April 24, 2025

Accurate classification of cardiotocographic (CTG) signals plays a critical role in the early detection of fetal health conditions, enabling timely and appropriate medical interventions. A more precise understanding of cardiotocography patterns, particularly in suspicious cases, can help minimize unnecessary interventions and reduce healthcare costs. This study proposes a multiclass classification framework using 552 expert-annotated CTG records containing fetal heart rate (FHR) and uterine contraction (UC) signals. Time-domain augmentation, including cyclic temporal shifting, Gaussian noise, and segmented Gaussian noise, was applied to address class imbalance. The augmented FHR and UC signals were then transformed into scalograms using Continuous Wavelet Transform (CWT), producing dual-channel RGB-encoded images. Data were split into 90% for stratified five-fold cross-validation and 10% for independent testing. The proposed ResNet50, enhanced with SE-based channel attention and dropout layers, was compared against several baselines, including CNN, MobileNet, EfficientNet-B0, ResNet18, and ResNet50. It achieved the best performance with an F1-score of 0.7267 and AUC of 0.7489 on the test set, outperforming all baselines. These results highlight its potential for integration into intelligent clinical decision support systems in prenatal care.

Povzetek: Članek obravnava klasifikacijo fetalnega stanja iz kardiotokografije v povezavi s subjektivnimi ocenami in prekrivanjem vzorcev, zlasti pri sumljivih primerih. Predlaga metodo SE-ResNet-50, ki FHR in UC signale pretvori v skalograme s CWT. Model doseže najboljši rezultat med primerjanimi pristopi.

1 Introduction

Ensuring fetal well-being is critical to maintaining the health and safety of babies during pregnancy and childbirth. The World Health Organization (WHO) reports that more than 800 women die every day from complications of pregnancy and childbirth, especially in areas with limited access to quality health services [1]. Furthermore, according to the WHO report, effective monitoring of maternal and fetal health can lower newborn mortality rates by up to 20% in regions where adequate healthcare services are available [2].

Health care professionals can take precautions to reduce the risk if fetal complications arise from antenatal care evaluations [3]. Cardiotocography (CTG) is a widely used tool for assessing fetal conditions during pregnancy and labor by recording fetal heart rate (FHR) and uterine contraction (UC) signals. A key advantage of CTG is its ability to provide continuous and real-time monitoring, allowing early detection of fetal distress and uterine activity changes [4]. By identifying fetal hypoxia, CTG monitoring reduces the risk of newborn asphyxia and lowers perinatal mortality rates [5, 6].

CTG interpretation follows three main guidelines from NICE (National Institute of Health and Care Excellence), FIGO (International Federation of Gynecology and Obstetrics), and ACOG (American College of Obstetricians and Gynecologists) [7]. However, CTG assessment often varies due to subjectivity and differences in expertise among healthcare professionals. Fatigue, stress, complex cases, and time constraints can further hinder accurate and timely decision-making [8]. To address these challenges, artificial intelligence (AI) and machine learning (ML) techniques have been integrated into CTG analysis. ML enhances diagnostic accuracy by detecting disease patterns and risk factors, enabling early fetal distress detection and proactive interventions [9, 10]. AI-driven models allow healthcare providers to analyze large volumes of fetal monitoring data, leading to faster and more informed decisions, while also reducing unnecessary interventions such as cesarean sections [11, 12].

The classification of the fetal state in CTG is essential for early detection, particularly when rapid intervention is required during pregnancy or labor [13]. This classification includes normal, suspicious, and pathological states. Distinguishing between these categories is inherently

challenging, as suspicious cases often present intermediate features between normal and pathological patterns, causing overlaps in FHR and UC characteristics that obscure decision boundaries and hinder classification accuracy [14]. Misclassification can lead to unnecessary interventions or delayed responses, affecting maternal and fetal safety.A deeper understanding of borderline CTG patterns can help optimize clinical decisions, reduce unnecessary procedures, and lower healthcare costs.

This study aims to address existing gaps in CTG analysis and presents two key contributions in advancing fetal state classification using deep learning and signal processing:

(1) Multiclass fetal state classification with expert annotations. Unlike previous studies that classify fetuses into only normal and pathological categories, this study introduces a suspicious category, creating a three-class classification (normal, suspicious, pathological). Expert annotations are used instead of relying solely on biochemical indicators like cord blood pH values, ensuring a more clinically relevant and interpretable classification.

(2) Combining FHR and UC signals as input for a SE-ResNet-50 model in scalogram-based CTG classification. This study combines FHR and UC signals, transforming them into scalograms using Continuous Wavelet Transform (CWT) to capture temporal and frequency domain features which allows a detailed representation of signal variations critical for accurate fetal state classification. The scalograms are represented in RGB format, enabling the model to leverage multi-channel color information for richer feature extraction. An SE-ResNet50 model with squeeze and excitation attention blocks is used to enhance feature extraction and improve generalization in the classification of three classes of fetal state.

2 Related works

Several studies have applied machine learning algorithms to predict fetal abnormalities by extracting features from CTG signals [15, 16]. These studies have primarily focused on classifying fetal conditions into normal and abnormal (pathological) categories, as well as predicting specific complications such as fetal hypoxia and preterm birth [17–21]. Previous studies have used different labelling approaches based on data availability. Expert annotations involves obstetricians clinically assessing fetal conditions, while biochemical indicators such as cord blood pH and Base Excess (BE) evaluate acid-base balance and hypoxia risk. The Apgar score is also used to validate fetal distress predictions based on newborn health.

Previous studies have classified fetal status into three classes: normal, suspicious, and pathological as shown in Table 1. However, most of these studies are based on traditional machine learning models trained in the UCI Machine Learning Repository dataset [22]. These studies applied a variety of algorithms, including Artificial Neural Networks (ANN), Rough Neural Networks, Naïve Bayes, Logistic Regression (LR), K-Nearest Neighbors (KNN), Decision Tree (DT), Classification and Regression Tree (CART), Random Forest (RF), Support Vector Machine (SVM), Gradient Boosting (GB), and Light Gradient Boosting Machine (LGBM). Although these models achieve high accuracy (0.89-0.99) [23–28], the dataset has significant limitations, as it contains only 21 static features and lacks the temporal information necessary to capture the dynamic nature of CTG signals. This limitation hinders the ability of the model to fully assess fetal conditions, which depend on time-dependent variations in FHR and uterine contractions for a more accurate and reliable classification.

Deep learning offers a more robust approach by eliminating the need for manual feature selection and enabling automatic extraction of important features directly from raw signals [29]. Several studies have explored deep learning for CTG classification [17, 19, 29–31]. Despite these developments, most studies only use FHR signals, ignoring UC signals, which play a crucial role in assessing fetal response to labour stress. The combination of FHR and UC provides a more comprehensive view of fetal well-being, particularly in detecting late or variable decelerations, which are early indicators of fetal distress and hypoxia [16, 32]. Table 2 shows the summary of related work using CTU-UHB dataset.

A number of research employ both FHR and UC signals with varying outcome predictions utilizing various signal processing approaches. For instance, Zeng, et al. classified fetal state in normal and abnormal classes based on pH values and Base Excess (BE) values used to assess the oxygenation status and acid-base balance of the fetus for indications of hypoxia. They used the Time-Frequency (TF) and Ensemble Cost-Sensitive Support Vector Machine (ECSVM) features which resulted in a sensitivity of 0.852, a specificity of 0.661, and a quality index of 0.75.0 [33]. Liang et al. utilized a CNN-RNN model to detect fetal hypoxia based on pH values, achieving an accuracy of 0.9515 [34]. Similarly, Ogasawara et al. developed CTG-Net, a CNN-based model that classifies fetal conditions using Apgar scores and umbilical artery pH, resulting in an F1 score of 0.67 [35]. Meanwhile, Saini et al. applied a 2D-CNN model to classify fetal conditions into normal, mild hypoxia, and severe hypoxia, obtaining an accuracy of 0.70 [36].

Deep learning shows promise for improving fetal state classification, but challenges remain in accuracy and clinical reliability. Most studies use binary classification (normal vs. abnormal) and rely on biochemical markers for labeling, often overlooking the suspicious class, which can lead to unnecessary interventions or delayed responses. Furthermore, a large proportion of existing work processes CTG as raw time-series signals, which may not capture important frequency-domain features, and often relies solely on FHR without incorporating UC. The use of scalograms (TF representations) offers richer feature extraction, enhancing deep learning performance. In particular, CWT-based scalograms provide high-resolution localization of

Table 1: Summary of related studies using UCI CTG dataset

Work	Input	Label Type	Classes	**Method**	**Performance**
[23]	21 statistical features	Expert Annotations	Normal, Suspicious, Pathological	Rough Neural Network	Accuracy = 0.905
[24]	21 statistical features	Expert Annotations	Normal, Suspicious, Pathological	AdaBoost with RF	Accuracy = 0.976
[25]	21 statistical features	Expert Annotations	Normal, Suspicious, Pathological	LR, KNN, RF, and GBM	Highest accuracy = 0.99 (RF)
[26]	21 statistical features	Expert Annotations	Normal, Suspicious, Pathological	RF, Naïve Bayes, SVM	Highest accuracy = 0.9993 (RF)
[27]	21 statistical features	Expert Annotations	Normal, Suspicious, Pathological	RF, LR, DT, SVM, Voting Classifier, KNN	Highest accuracy = 0.9751 (RF)
[28]	21 statistical features	Expert Annotations	Normal, Suspicious, Pathological	Classification and Regression Tree (CART)	Accuracy=0.945

Table 2: Summary of related studies using CTU-UHB dataset

Work	Input	Label Type	Classes	Method	Performance
[17]	FHR Signals	Delivery mode & pH	Normal (vaginal delivery), Pathological	1DCNN-MLP	Sensitivity=0.80, Specificity=0.791
[19]	FHR Signals	pH	Normal, Hypoxia	Ensemble Learning, CNN, DenseNet	CNN: F1-score=0.9 (Normal), 0.23 (Hypoxia); Bagging Tree + NB: F1-score=0.76 & 0.45
[29]	FHR Signals	pH	Normal, Distressed	TF Morse Wavelet, ResNet	Accuracy=0.987, Sens=0.97, Spec=0.100
[30]	FHR Signals	pH	Normal, Hypoxia	DenseNet	Precision=0.50, Sensitivity=0.43, F1-score=0.46
[31]	FHR Signals	pH	Normal, Abnormal	SE-ResNet50, XGBooster	Accuracy=0.9634, Precision=0.967, Sens=0.973, Spec=0.96
[33]	FHR and UC	pH & BE	Normal, Abnormal	TF, ECSVM	Sens=0.852, Spec=0.661
[34]	FHR and UC	pH	Normal, Abnormal	CNN, RNN	Accuracy=0.9515, Sens=0.962, Spec=0.9409
[35]	FHR and UC	Apgar Score & pH	Normal, Abnormal	CTG-Net	F1-score=0.67
[36]	FHR and UC	pH	Normal, Mild Hypoxia, Severe Hypoxia	2D-CNN	Accuracy=0.70

signal patterns in both time and frequency domains [29], allowing the detection of subtle and transient variations in FHR and UC that are clinically relevant for distinguishing fetal states. Our study addresses these gaps by integrating both FHR and UC signals, encoding them as RGB scalogram images, adopting a three-class scheme according to FIGO guidelines, and applying time-frequency representations based on scalograms through CWT for fully automated feature learning with a deep learning model.

3 Methods

In this study, expert labeling was chosen over physiological metrics such as the pH value of cord blood, as it considers multiple clinical factors for a more comprehensive

fetal evaluation. By using both FHR and UC for a comprehensive assessment and employing multiclass classification, this study enhances the detection of the suspicious category for early risk identification. This study employs a systematic methodology, as shown in Figure 1 to classify fetal conditions using CTG signals and deep learning.

The research methodology consists of three main stages: (1) data selection and annotation analysis, (2) data preprocessing and feature extraction, and (3) model training and evaluation. In the first stage, CTG data from the publicly available CTU-UHB dataset [37] is annotated by experts, with consistency assessed using Pearson correlation and Fleiss' kappa. The second stage involves cleaning and augmenting FHR and UC signals, transforming them into scalograms via Continuous Wavelet Transform (CWT), and encoding them into dual-channel RGB format. In the final stage, scalogram images and annotations are split into a 10% independent test set and a 90% training–validation set, with stratified five-fold cross-validation to preserve class balance. An SE-ResNet50 model with ImageNet-pretrained weights and Squeeze-and-Excitation blocks is trained using focal loss, class weighting, and dropout regularization. Evaluation includes comparison with baseline models, performance assessment on cross-validation and test sets, statistical significance testing, ablation studies, and Grad-CAM interpretability analysis. The following describes the algorithm used for the classification of CTG signals.

We hypothesize that combining fetal heart rate (FHR) and uterine contraction (UC) signals in scalogram form, encoded as dual-channel RGB images, and training a modified SE-ResNet50 model with focal loss and class weighting will improve multiclass CTG classification performance compared to baseline models.

Algorithm 1 CTG_Classification

Input: Selected Raw CTG signals (FHR, UC) with expert-validated labels
Output: Classified fetal state (Normal, Suspicious, Pathological)

Step 1: Preprocessing Data
Denoise and clean FHR and UC signals
Remove outliers, fill missing value
Apply augmentation: cyclic shift, Gaussian noise, segmented Gaussian noise

Step 2: Continuous Wavelet Transform (CWT)
Convert each FHR and UC signal into separate scalograms

Step 3: Dual-Channel RGB Encoding
Map FHR→R, UC→G, B=0 to form RGB scalogram

Step 4: Model Training (SE-ResNet-50)
Initialize SE-ResNet50 with Squeeze-and-Excitation blocks + dropout
Compile with Adam, Focal Loss, and class weights
Perform stratified five-fold cross-validation on 90% data
Select fold with highest validation F1-score

Step 5: Testing and Evaluation
Test best fold on 10% hold-out data
Report Accuracy, Precision, Sensitivity, F1-Score, and AUC

End Algorithm

3.1 Dataset

We utilized the public CTG dataset from the Czech Technical University (CTU), containing 552 CTG recordings [37], available at: https://physionet.org/content/ctu-uhb-ctgdb/1.0.0/. This CTG data was annotated by nine obstetricians following FIGO guidelines at each evaluation step as shown in Figure 2. The CTG dataset annotation is available at https://people.ciirc.cvut.cz/ spilkjir/data.html [38]. In the CTU-CHB Intrapartum Cardiotocography dataset, the collected signals focused mainly on the first- and second-stage labor phases of the labour process. The first stage labour includes the opening of the cervix from the beginning of contraction to the full opening of the cervix, reflecting variations in the fetal heart rate as the intensity of contractions increases. The dataset also includes the second phase of labor, when the cervix has fully opened and the birth process begins, showing an FHR response to stronger contractions as the mother strains.

In this study, data annotations were determined based on the majority voting technique of nine experts on each CTG recording. A technique in data labeling in which the fi-

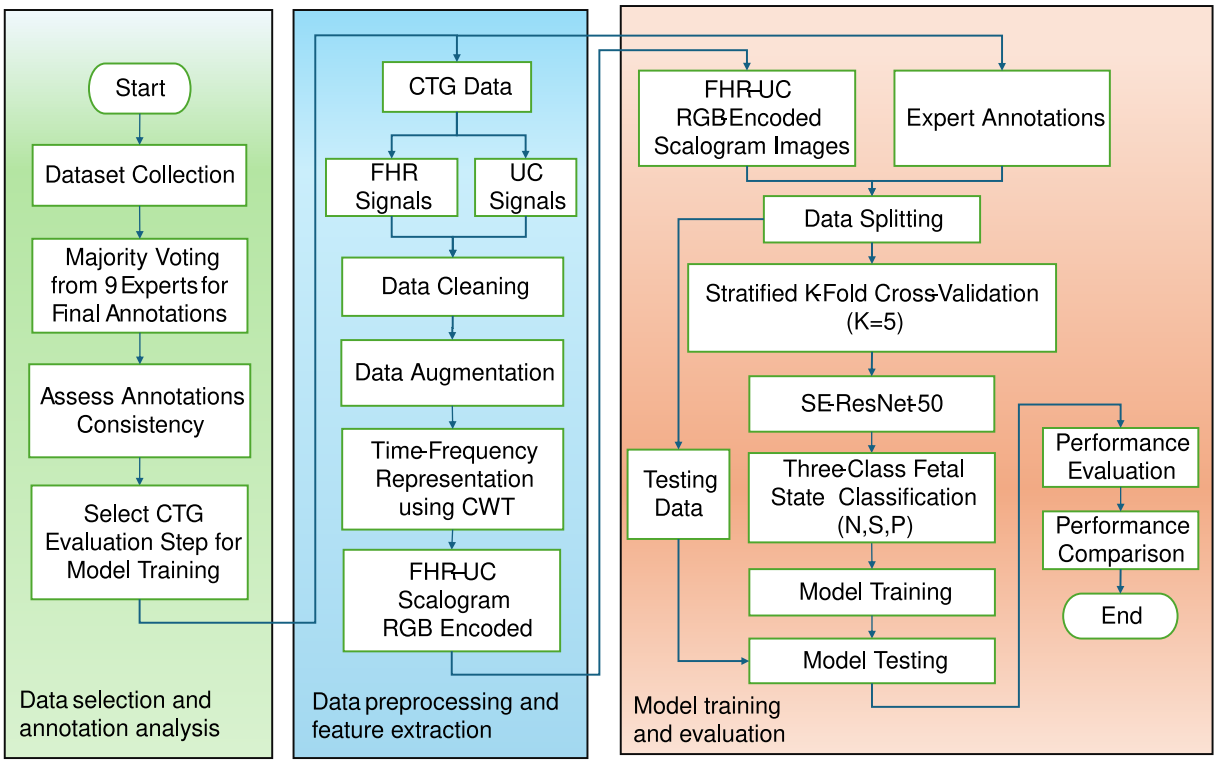

Figure 1: Proposed methodology for CTG classification

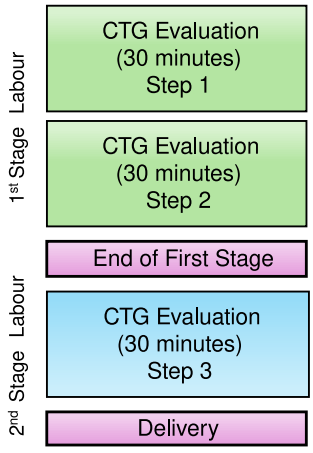

Figure 2: CTG evaluation step in CTG CTU-UHB dataset

nal decision is determined based on the label that is most chosen among several experts [39]. This technique is often used when there are multiple evaluations from different sources or individuals, for example, in a situation where a number of experts label the data, and we need to determine a single consensus label to use. To evaluate annotation consistency, each step was assessed using two complementary agreement metrics: (1) average pairwise Pearson correlation between expert ratings, which reflects the similarity in scoring tendencies; and (2) Fleiss' kappa, which measures exact categorical agreement while accounting for chance agreement. For the correlation analysis, a 9×9 matrix was generated for each step, where each element represents the correlation between a pair of experts, and the average value was calculated across all pairs. Fleiss' kappa was calculated based on the categorical labels assigned by the nine experts for each case. By combining these two metrics, we identified the step with the highest and most consistent agreement across both scoring trends and categorical label matches, ensuring that the final dataset is derived from the most reliable annotation stage.

To prevent data leakage during model training and evaluation, the dataset was split using a unique identifier (base_id) for each original CTG signal, ensuring that all augmented versions of the same signal remained within a single subset. Splits were stratified by base_id to preserve class balance, and the same strategy was applied in cross-validation to maintain independence between subsets.

After determining the most reliable annotation stage (detailed in Section 4.1), the dataset was prepared for model development. The selected step was used as the basis for data augmentation and splitting. Table 3 summarizes the dataset distribution before and after augmentation, including the number of samples in the training, validation, and test sets, as well as the cases excluded from the study.

3.2 Preprocessing steps

Preprocessing techniques in this study include data cleaning and augmentation. The data cleaning process consists

Table 3: Dataset distribution before and after augmentation (Step 1 only), including uninterpretable cases, and split into train/validation/test sets.

Class	Before Aug.	After Aug.	Test Set	Train+Val Set	Note
Normal	296	636	66	570	Used
Suspicious	220	606	66	540	Used
Pathological	30	210	15	195	Used
Uninterpretable	6	–	–	–	Excluded
Total	552	1452	147	1305	

of several stages. First, all zero values in the dataset are replaced with NaN (Not a Number) to indicate to indicate potentially invalid or unrecorded data. If NaN values occur for more than 15 consecutive seconds, they are retained to prevent excessive interpolation across long missing segments. Next, outlier detection is applied to remove physiologically implausible values. For FHR, values outside the range of 50–200 bpm are discarded [29], while for UC, values outside 0–100 mmHg are excluded [40]. Spike detection is also performed to identify sudden unrealistic changes, defined as variations greater than 25 bpm for FHR [29] or 40 mmHg for UC [40] between consecutive samples. Such spikes are assumed to be artifacts and are replaced with NaN. Then the proportion of missing data is calculated. If the NaN ratio exceeds 20% of the total signal length, the recording is discarded to maintain data quality. For signals that pass this threshold, missing values are interpolated using a two-step approach: linear interpolation to preserve local trends, followed by cubic spline interpolation for smooth transitions. Any remaining NaN values are filled using backward and forward filling methods. Finally, all NaN and infinite values are replaced with zero to ensure numerical stability before time–frequency transformation.

Data augmentation in the time domain employed three techniques: cyclic temporal shifting, Gaussian noise injection, and segmented Gaussian noise injection. For normal and suspicious classes, cyclic shifts equivalent to 5 and 10 minutes (corresponding to 1,200 and 2,400 sample points at 4 Hz) and Gaussian noise (noise factor = 0.1) were applied to the original and shifted signals. For the pathological class, more extensive augmentation was applied, consisting of cyclic shifts of 5, 10, 15, and 20 minutes (1,200, 2,400, 3,600, and 4,800 sample points), the addition of Gaussian noise, and segmented Gaussian noise with varying noise levels (0.05, 0.1, 0.5) applied to both the original and shifted signals. This strategy enhanced data diversity and mitigated class imbalance.

3.3 Continuous wavelet transform

The next stage is the signal transformation into the time-frequency domain using continuous wavelet transformation (CWT). Continuous Wavelet Transform (CWT) is a method for analyzing signals by breaking them into different parts based on scale or frequency [41]. CWT is very useful for signals whose frequency changes over time. CWT works by shifting and changing the size of the mother wavelet along the signal and seeing how similar the signal is to the wavelet at each point. The result is numbers (coefficients) that show how similar the signal is to a wavelet at a given scale and position. In this way, changes in the frequency of the signal overtime can be seen, providing a more complete picture compared to traditional Fourier analysis, which assumes the signal does not change. The mathematical equation for the wavelet function (1) is as follows [42]:

$$\psi_{a,b}(t) = \frac{1}{\sqrt{a}}\psi\left(\frac{t-b}{a}\right) \tag{1}$$

With a representing the scaling parameter for dilation and b representing the moving parameter for translation across the signal location. CWT follows two properties which are represent in equation (2) and (3) [43]:

$$\int_{-\infty}^{\infty} \psi(t)\, dt = 0 \tag{2}$$

$$\int_{-\infty}^{\infty} [\psi(t)]^2\, dt = 0 \tag{3}$$

For CWT, the mathematical equation $C(a, b)$ is obtained by integrating the input function with the wavelet which is stated in equation (4) [42]:

$$C(a,b) = \int_{-\infty}^{\infty} f(t)\frac{1}{\sqrt{|a|}}\psi\left(\frac{t-b}{a}\right) dt \tag{4}$$

In this study, a Morse wavelet in the frequency domain is used with the following formulation, as shown in equation (5) [43]:

$$\psi_{\beta,\gamma}(\omega) = U(\omega)a_{\beta,\gamma}\omega^{\beta}e^{\omega^{\gamma}} \tag{5}$$

β and γ are parameters that control the shape of the wavelet. β controls the shape and width of the wavelet while γ controls the asymmetry or shift of the wavelet shape. ω is a variable frequency in the frequency domain, which indicates the frequency analyzed at each point in time. The central frequency (ω_o) of the wavelet that regulates the number of oscillations. If we put Morse wavelets into the CWT formula, then the formula becomes as shown in equation (6) [43]:

$$C(a,b) = \int_{-\infty}^{\infty} f(t)\frac{1}{\sqrt{|a|}}U\left(\frac{t-b}{a}\right)a_{\beta,\gamma}\left(\frac{t-b}{a}\right)^{\beta}e^{-\left(\frac{t-b}{a}\right)^{\gamma}}e^{i\omega_o\frac{t-b}{a}}dt \tag{6}$$

Equation (7) shows how CWT uses Morse wavelets for scale and frequency analysis of signals. Appropriate wavelet parameters are selected to obtain optimal scalogram representation. In this study, γ was set to 3 for both signals, following recommendations that this value yields a near Gaussian spectral shape and provides balanced time–frequency localization suitable for biomedical signals. The β parameter was set to 50 for FHR to capture rapid heart rate variations and 100 for UC to emphasize slower sustained contraction patterns, consistent with prior findings on frequency localization characteristics [43]. While this configuration is supported by literature, a more comprehensive empirical evaluation using alternative wavelets and parameter settings could provide deeper insights into its optimality. Sampling frequency was 4 Hz with a signal length of 7200 and voices per octave of 12. Each signal was individually transformed into a scalogram using Continuous Wavelet Transform (CWT) with its respective β value, ensuring optimal time–frequency resolution for both modalities while preserving essential information in both low and high-frequency components.

CWT can be used to decompose one-dimensional (1D) signals into two-dimensional (2D) [44]. The 1D signal is decomposed into wavelet coefficients, capturing similarities at different scales and positions. This produces a 2D scalogram, where time and frequency are represented, and color indicates coefficient amplitude. Scalograms enhance feature and frequency visualization, revealing details not apparent in 1D representations [44].

3.4 Dual-channel RGB encoding

This RGB representation not only preserves the distinct characteristics of both signals but also spatially separates them into dedicated channels, reducing feature overlap and enhancing the network's ability to learn discriminative patterns from each modality. Additionally, encoding them in RGB format enables seamless integration with pre-trained convolutional based architectures such as SE-ResNet50, which are optimized for three-channel image inputs. The resulting H×W×3 image was resized to 224×224×3 for model input.

3.5 Squeeze-and-excitation residual network

Squeeze-and-Excitation ResNet50 (SE-ResNet50) is a variant of the ResNet50 architecture enhanced with Squeeze-and-Excitation (SE) blocks, as proposed by Hu et al. [45]. While ResNet50 employs residual learning to address vanishing gradients and degradation issues in deep convolutional networks [46], SE blocks introduce a channel-wise attention mechanism that adaptively recalibrates feature responses. This mechanism allows the network to emphasize informative features and suppress less relevant ones, thereby improving representational power without significantly increasing computational cost. SE-ResNet50 has been shown to enhance performance in various computer vision tasks by combining the benefits of deep residual learning and channel-wise attention.

The input to the model is a scalogram image with dimensions 224×224×3. The model is trained using the Adam optimizer with a learning rate of 0.001. For multiclass classification into three categories (normal, suspicious, pathological), the loss function is based on categorical cross-entropy. To address class imbalance, we apply focal loss, which modifies cross-entropy to focus more on hard-to-classify samples, together with class weighting to reduce bias toward the majority classes. To overcome class imbalance, focal loss and class weight are used. Focal loss is a variant of the cross entropy loss function designed to focus on examples that are difficult to classify [47]. In class imbalance, models tend to focus on majority classes, neglecting harder minority cases. Focal loss mitigates this by down-weighting easy examples and emphasizing difficult ones, improving learning for minority classes. Equation (7) provides the focal loss formula [47]:

$$FL(p_t) = -\alpha_t(1-p_t)^{\gamma}\log(p_t) \tag{7}$$

Where p_t is the correct prediction probability for a particular class, α_t is a weighing factor for minority classes (e.g., giving more weight to minority classes), and γ is a parameter that controls how much attention is focused on a difficult instance (the larger the γ, the greater the focus on the difficult example). Focal loss helps the model learn examples from more difficult minority classes by giving more weight to the errors from those examples. In this study, we addressed class imbalance by setting the focal loss parameter α_t according to the computed class weights, while also experimenting with alternative α_t values to assess their impact. The focusing parameter γ was set at 2, as this value has been reported to perform well in various scenarios [48]. Class weighting assigns greater importance to minority classes within the loss calculation, thereby improving the model's sensitivity to underrepresented categories [49].

Class weight is a technique that involves giving more weight to a minority class in a standard loss function such as cross entropy loss [49]. This approach adjusts weights for sparse classes, ensuring the model treats minority class predictions as equally important. Class weights are computed using equation (8) [49].

$$\omega_i = \frac{N}{n_i} \tag{8}$$

Where ω_i is the weight for the i class, N is the total number of samples, and n_i is the number of samples in class i. Less frequent classes receive higher weights to balance the loss function, ensuring the model considers minority classes.

To further improve performance, dropout layers were added to the SE-ResNet50 architecture, and early stopping with a patience of 10 epochs was applied to prevent overfitting. Figure 3 illustrates the architecture of SE-ResNet50 proposed in this study.

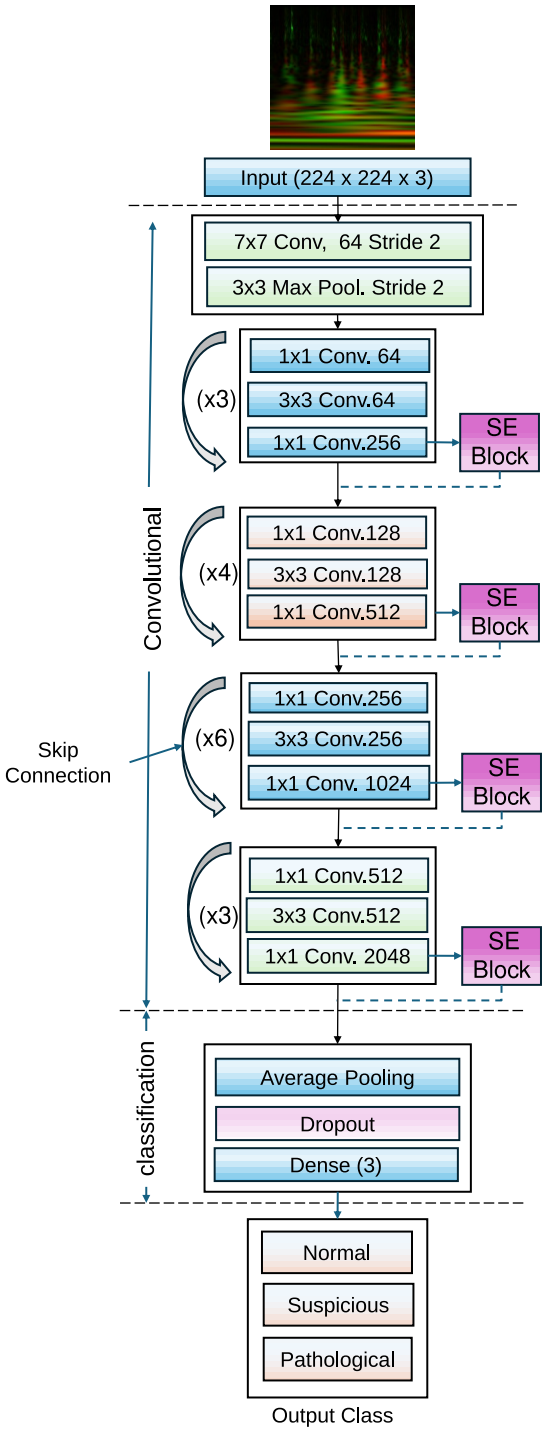

Figure 3: SE-ResNet50 architecture

Model performance evaluation involves a set of metrics that can measure certain aspects of the model's performance. Some common evaluation metrics used are accuracy, precision, sensitivity, and F1-score [50]. Accuracy shown in equation (9), measures the proportion of the number of correct predictions to the total number of samples [50].

$$\text{Accuracy} = \frac{\text{TP} + \text{TN}}{\text{TP} + \text{TN} + \text{FP} + \text{FN}} \tag{9}$$

TP is the true positive (number of correct positive predictions) and FP is the false positive. TN is true negative (number of correct negative predictions), FP is false positive (number of false positive predictions), and FN is false negative (number of false negative predictions). The precision shown in equation (10) measures the proportion of positive predictions that are truly positive.

$$\text{Precision} = \frac{\text{TP}}{\text{TP} + \text{FP}} \tag{10}$$

Sensitivity measures the model's ability to identify all positive samples. The formula is in (11) [50]:

$$\text{Sensitivity} = \frac{\text{TP}}{\text{TP} + \text{FN}} \tag{11}$$

F1-score is the harmonic means of precision and sensitivity, providing a balance between the two. The formula is shown in (12) [50]:

$$\text{F1-score} = 2 \times \frac{\text{Precision} \times \text{Sensitivity}}{\text{Precision} + \text{Sensitivity}} \tag{12}$$

The Area Under the Receiver Operating Characteristic Curve (AUC-ROC) is a widely used performance metric that evaluates a model's ability to distinguish between classes by measuring the area under the ROC curve. The ROC curve plots the True Positive Rate (TPR) against the False Positive Rate (FPR) at various classification thresholds. The AUC is computed using the trapezoidal rule as follows (13)(14) [50]:

$$\text{AUC} = \sum_{i=1}^{n-1} (\text{FPR}_{i+1} - \text{FPR}_i) \times \frac{\text{TPR}_{i+1} + \text{TPR}_i}{2} \tag{13}$$

$$\text{TPR} = \frac{\text{TP}}{\text{TP} + \text{FN}}, \quad \text{FPR} = \frac{\text{FP}}{\text{FP} + \text{TN}} \tag{14}$$

For multiclass evaluation, we adopted a one-vs-rest approach for each class (normal, suspicious, pathological), computing precision, recall (sensitivity), F1-score, and AUC individually, then averaging them equally to obtain macro-averaged metrics.

4 Results

This section presents the findings from each stage of the research methodology that has been conducted.

4.1 Data selection and annotation analysis results

In the CTG-UHB dataset, annotations are assigned as follows: 1 (normal), 2 (suspicious), 3 (pathological), and -1 (uninterpretable). Table 4 presents the data distribution

from the majority voting of nine experts across three evaluation steps. The sample count varies at each step, reflecting differences in expert agreement and data interpretation. The large number of uninterpretable cases in evaluation step 3 indicates that more cases were considered ambiguous or difficult to categorize. Since this study only requires normal, suspicious, and pathological labels, the uninterpretable category (-1) is ignored. A correlation matrix is calculated for each step, as shown in Figure 4 for step 1, excluding the uninterpretable label.

Table 4: Data distribution based on majority votes from nine experts

Label	Criteria	CTG Evaluation		
		Step 1	Step 2	Step 3
1	Normal	296	229	127
2	Suspicious	220	251	153
3	Pathological	30	68	57
-1	Uninterpretable	6	4	215

To assess the consistency of expert annotations, we evaluated inter-rater agreement using both average pairwise correlation and Fleiss' kappa across the three annotation steps. The average correlation values were 0.62 (Step 1), 0.59 (Step 2), and 0.54 (Step 3), indicating a moderate degree of similarity in experts' rating patterns. However, Fleiss' kappa scores were notably lower, with values of 0.3 (fair agreement), 0.22 (slight agreement), and 0.185 (slight agreement), respectively. This discrepancy arises because correlation measures the similarity in score trends between experts, while kappa evaluates exact label matches, adjusted for chance agreement. For this reason, CTG data from step 1 will be used in this study because it has a high correlation between experts that shows strong agreement, which means that the labels on this data are more consistent and reliable. Stable training data and minimal noise are essential for machine learning models because it makes it easier for models to find accurate patterns. The labels assigned to the data in evaluation step 1 tend to be uniform. This reduces the risk of ambiguity in the training data, so the model can learn from clearer patterns and not be affected by inconsistent labels.

4.2 Data preprocessing and feature extraction results

Both FHR and UC signals, in all categories (normal, suspicious, and pathological), Both FHR and UC signals, in all categories (normal, suspicious, and pathological), were processed through data cleaning process. Figure 5 shows one of the results of the data cleaning stage in the suspicious category. It shows how the signals are efficiently refined by the data cleaning process, which eliminates artifacts and irregularities that can obstruct precise analysis.

Following data cleaning, augmentation was performed to address class imbalance among the normal, suspicious, and pathological categories. After applying the time-domain augmentation techniques consisting of cyclic temporal shifting, Gaussian noise injection, and segmented Gaussian noise injection, the dataset size increased from 522 to 1,452 samples. The final distribution consisted of 636 normal, 606 suspicious, and 210 pathological cases. This process substantially reduced class imbalance, with the pathological class, originally the smallest, experiencing the largest relative growth due to the application of additional shift intervals and multiple noise levels.

After the dataset was cleaned and augmented, each FHR and UC signal was individually transformed into scalogram images using Continuous Wavelet Transform (CWT) with different β parameters (β = 50 for FHR and β = 100 for UC) to optimize time–frequency resolution for each signal type. Examples of the resulting scalograms for both signals are shown in Figure 6. These two scalograms were then combined into an RGB-encoded image by assigning the FHR scalogram to the red channel, the UC scalogram to the green channel, and leaving the blue channel empty, thereby preserving the modality-specific features while enabling simultaneous processing by the deep learning model. An example of the resulting RGB-encoded representation is shown in Figure 7. The resulting RGB-encoded image was then resized to 224×224×3 before being fed into the model.

4.3 Model training and evaluation results

The experiments were carried out on Google Colab Pro with an NVIDIA GPU (16 GB VRAM) and 62.8 GB RAM, using Python 3.10, PyTorch 2.2.2, and Torchvision 0.17.2. All runs were configured with deterministic settings (random seed = 42) for reproducibility. In the first experiment, the proposed SE-ResNet50 model enhanced with dropout layers was evaluated using stratified five-fold cross-validation. Performance metrics including accuracy, precision, recall, F1-score, and AUC were calculated for each fold, with the mean values reported to assess the model's overall effectiveness as shown in Table 5 and Figure 8.

Across the five folds, the model achieved an average F1-score of 0.6015 ± 0.0718, with Fold 1 yielding the highest F1-score of 0.7073. This fold was then evaluated on the independent test set, achieving an F1-score of 0.7267 and an AUC of 0.7489. Figure 9 and Figure 10 present the per-class performance metrics and the confusion matrix of the final test set, respectively, while Table 6 summarizes the precision, recall, and F1-score for each class.

The performance of the SE-ResNet-50 model was compared with baseline models using CTG evaluation step 1 data, with the same number of epochs (100), early stopping (patience = 10), dropout rate (0.6), and learning rate (0.001), all initialized with ImageNet-pretrained weights. Table 7 presents the mean ± standard deviation results from five-fold cross-validation for all models. The overall performance on the final test set is illustrated in Figure 11, while Figures 12 and 13 show the relationship between

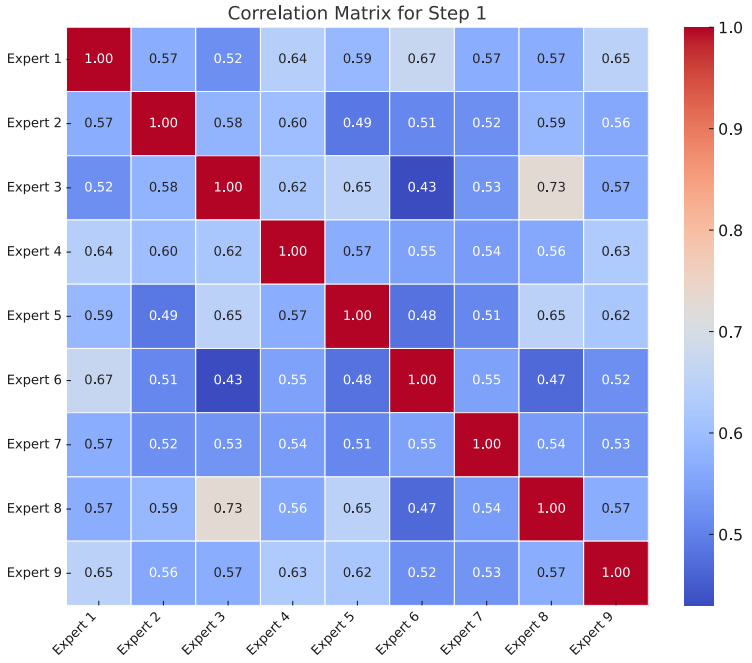

Figure 4: Expert correlation matrix step 1 excluding uninterpretable label (-1)

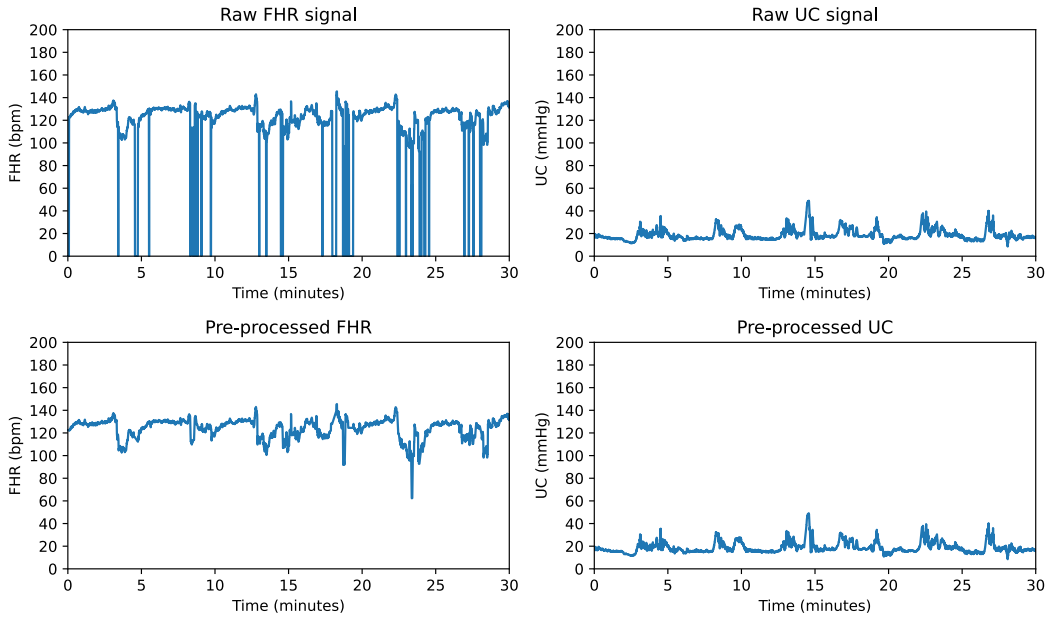

Figure 5: Example of cleaned FHR and UC signals from the suspicious class

model complexity (number of parameters) and final test set performance, as well as the trade-off between inference time and final test set F1-score.

To evaluate the effect of key hyperparameters on model performance, an ablation study was conducted by varying the learning rate, batch size, and dropout rate while keeping other training settings constant. The learning rates tested were 0.001 and 0.0001, batch sizes were set to 8, 16, and 32, and dropout rates were tested at 0.3, 0.5, and 0.6. All experiments used the same number of epochs with early stopping (patience = 10) to ensure a fair comparison. Table 8 summarizes the 5-fold cross-validation mean ± standard deviation results for F1-score and AUC, with the best results highlighted in bold.

An ablation study compared cross-entropy and focal loss with various class weight settings, using a fixed learning

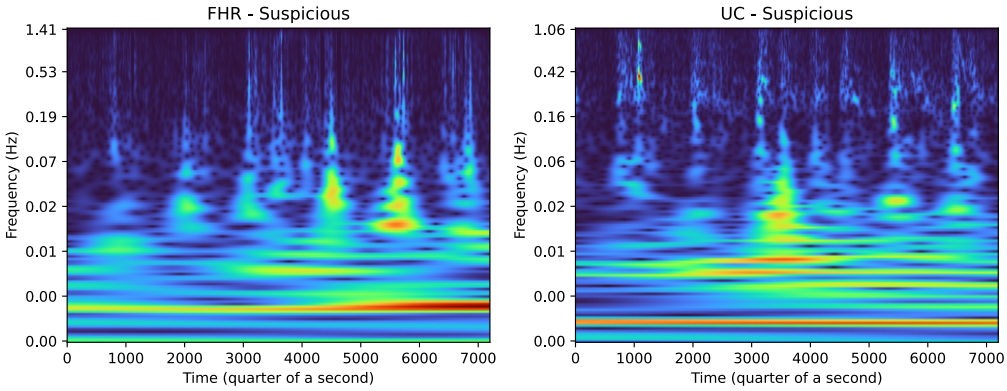

Figure 6: Scalogram representation (a) FHR signal (b) UC signal

Table 5: Performance of the proposed model across five folds

Fold	Accuracy	Precision	Recall	F1	AUC	
1	0.6821	0.6495	0.7795	0.7073	0.7963	
2	0.5375	0.5284	0.5258	0.5142	0.6700	
3	0.5857	0.6175	0.6034	0.5966	0.7266	
4	0.6091	0.6132	0.6089	0.5926	0.7302	
5	0.6301	0.6510	0.6206	0.6268	0.8216	
Mean ± Std	0.6089 ± 0.0535	0.6119 ± 0.0499	0.6276 ± 0.0928	0.6075 ± 0.0696	0.7489 ± 0.0604	

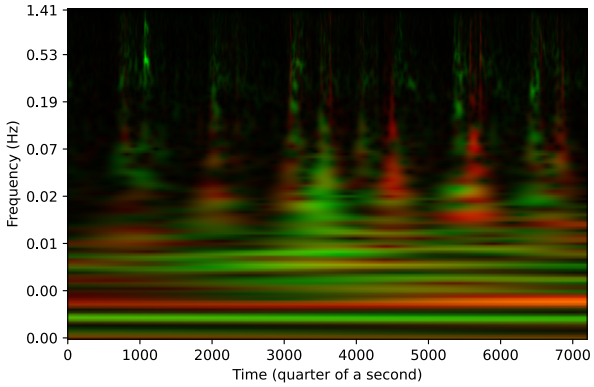

Figure 7: RGB-encoded representation

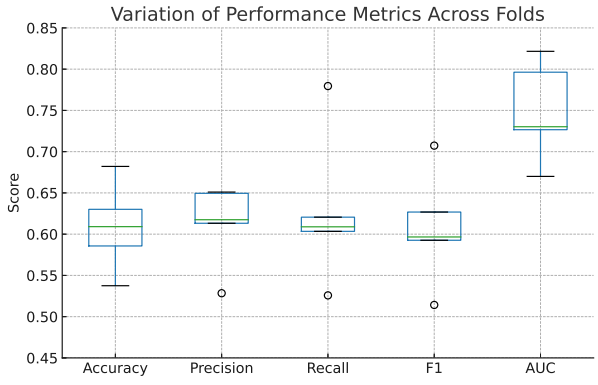

Figure 8: Variation of performance metrics across folds

rate of 0.001, dropout rate of 0.6, batch size of 32, and training for up to 100 epochs with early stopping (patience = 10). Focal loss parameters (γ and α) were varied as shown in Table 9, which reports 5-fold cross-validation mean $\pm$ standard deviation for F1-score and AUC, with best results in bold.

Grad-CAM interpretability analysis was performed to highlight the regions most influential in the model predictions. Figure 14 presents the Grad-CAM visualizations of representative scalogram images from the normal, suspicious, and pathological classes using the complete scalogram for each case. To provide a more detailed view, Figure 15 shows the Grad-CAM visualization of a representative suspicious case with separated FHR and UC channels, enabling observation of class-specific attention patterns for each signal type.

5 Discussion

This section discusses the experimental results, beginning with an evaluation of annotation consistency through Pearson correlation and Fleiss' kappa, followed by the performance analysis of the proposed model across cross-validation folds and the independent test set. The results are further interpreted in comparison with baseline models, along with per-class performance, to provide insights into

Table 6: Per-class precision, recall, and F1-score for the final test set

Class	Precision	Recall	F1-score
Normal	0.5833	0.6364	0.6087
Suspicious	0.6000	0.5455	0.5714
Pathologic	1.0000	1.0000	1.0000

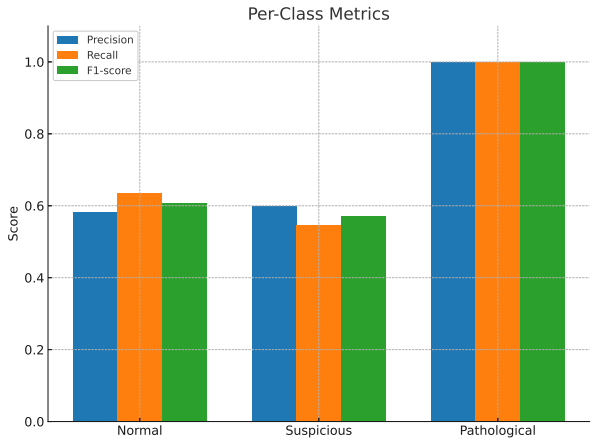

Figure 9: Per-class performance metrics

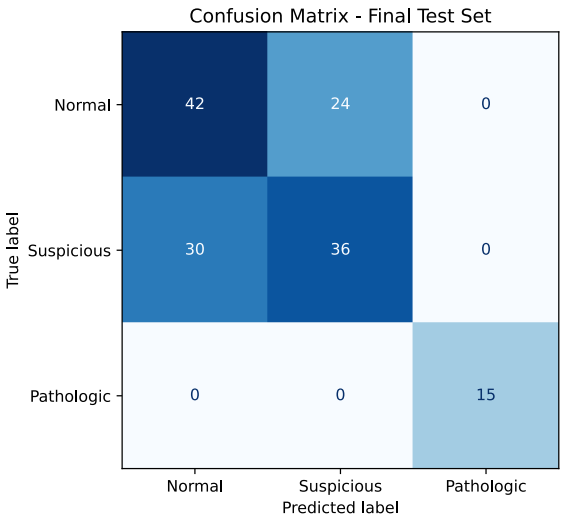

Figure 10: Confusion matrix

the strengths and limitations of the approach.

The quality of expert annotations was assessed using both Pearson correlation and Fleiss' kappa across three annotation steps. The average pairwise Pearson correlation values were 0.62, 0.59, and 0.54 for Step 1, Step 2, and Step 3, respectively, indicating moderate similarity in scoring trends among experts, with Step 1 showing the highest consistency. However, Fleiss' kappa values were considerably lower. The scores were 0.3 (fair agreement), 0.22 (slight agreement), and 0.185 (slight agreement), revealing that exact label agreement, adjusted for chance, was limited, particularly in Step 2 and Step 3. This lower inter-rater reliability is consistent with the model's final test performance (Figure 9) and the confusion matrix (Figure 10), where the normal and suspicious classes achieved F1-scores of only 0.6087 and 0.5714, respectively. These results suggest that the ambiguity in expert annotations for these categories likely contributed to the model's reduced classification performance.

To assess the stability of performance metrics across folds, we calculated the coefficient of variation (CV), defined as the ratio of the standard deviation to the mean, expressed as a percentage. Based on Table 5, AUC (CV = 8.07%), precision (CV = 8.15%), and accuracy (CV = 8.79%) had low variation, indicating stable discriminative capability and consistent predictive accuracy. In contrast, F1-score (CV = 11.46%) and recall (CV = 14.79%) showed moderate variation, with recall exhibiting the largest fluctuation, particularly due to a notable drop in Fold 2. The boxplot further illustrates this pattern: Precision and AUC have compact distributions with minimal spread, while Recall and F1 display wider interquartile ranges and several low outliers. This variability is likely linked to limited generalization on certain data subsets, potentially influenced by label inconsistencies. Conducting an error analysis of high-confidence misclassifications could help detect and correct such labeling issues, while enhancing feature representation or applying additional regularization may improve robustness and stabilize recall and F1 performance across folds.

In the final test set, the model achieved perfect precision, recall, and F1-score for the pathological class, without misclassifications. Performance was lower for normal (precision 0.5833, recall 0.6364) and suspicious (precision 0.60, recall 0.5455), with most errors occurring between these two classes. This pattern suggests overlapping features or unclear decision boundaries, indicating the need for improved feature representation or targeted data augmentation.

Compared to previous studies, the proposed model achieved lower overall accuracy (0.6327) and macro-average F1-score (0.7267) than high-performing methods such as Liang et al. (accuracy= 0.9515, F1-score=0.9520) [34] but was comparable to Ogasawara et al. (F1-score=0.67) [35] and Saini et al. (accuracy 0.70) [36]. Although prior work primarily addressed binary classification (normal vs. abnormal), our model tackled a more challenging three-class problem (normal, suspicious, pathological) and demonstrated a key strength by achieving perfect precision, recall, and F1 score for the pathological class, highlighting its robustness in identifying high-risk cases.

The proposed SE-ResNet50 outperformed all baseline models in the final test set, achieving the highest F1-score (0.727), recall (0.727), precision (0.728), and AUC (0.749), demonstrating balanced performance across metrics. Although its accuracy (0.633) was slightly lower than CNN

Table 7: Mean ± std cross-validation performance of deep learning models

Model	Accuracy	Precision	Recall	F1-Score	AUC
CNN	0.5418 ± 0.0478	0.5248 ± 0.1031	0.4881 ± 0.0673	0.4895 ± 0.0786	0.7026 ± 0.0449
EfficientNetB0	0.5472 ± 0.0202	0.5953 ± 0.0744	0.5155 ± 0.0354	0.5129 ± 0.0198	0.6880 ± 0.0638
MobileNetV2	**0.6313 ± 0.0936**	**0.6509 ± 0.0660**	0.5781 ± 0.0635	0.5933 ± 0.0623	0.7314 ± 0.1332
ResNet18	0.5800 ± 0.0274	0.5713 ± 0.1012	0.5607 ± 0.0943	0.5335 ± 0.0798	0.7347 ± 0.0497
ResNet50	0.6044 ± 0.0459	0.6405 ± 0.0704	0.5749 ± 0.0520	0.5913 ± 0.0576	0.7185 ± 0.0299
SE-ResNet50 (Proposed)	0.5888 ± 0.0511	0.6276 ± 0.0691	**0.6040 ± 0.0847**	**0.6015 ± 0.0718**	**0.7530 ± 0.0423**

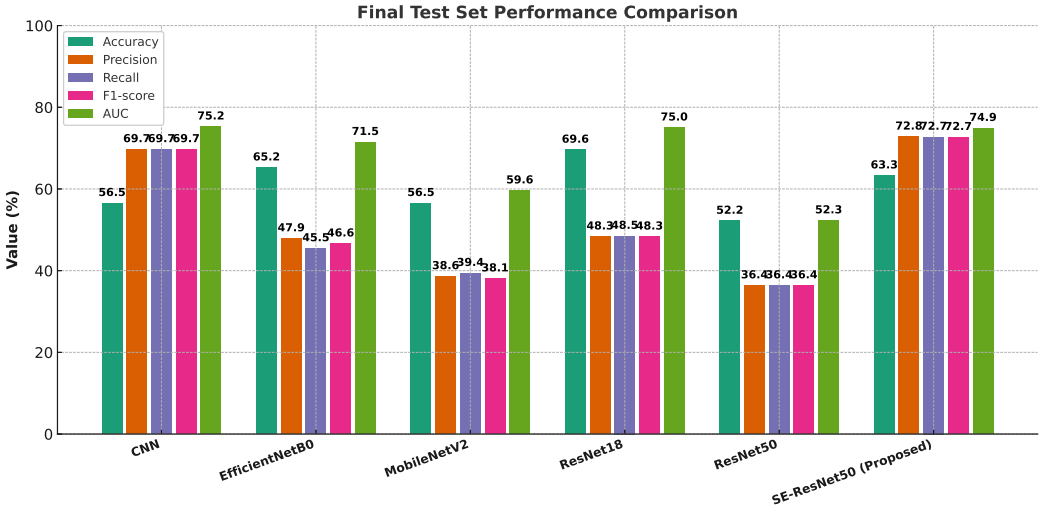

Figure 11: Final test set performance comparison

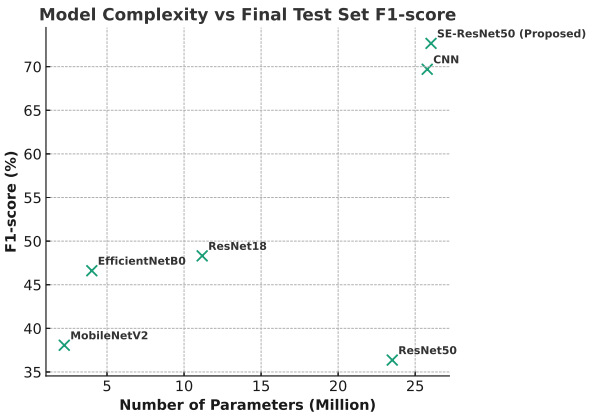

Figure 12: Parameter vs performance

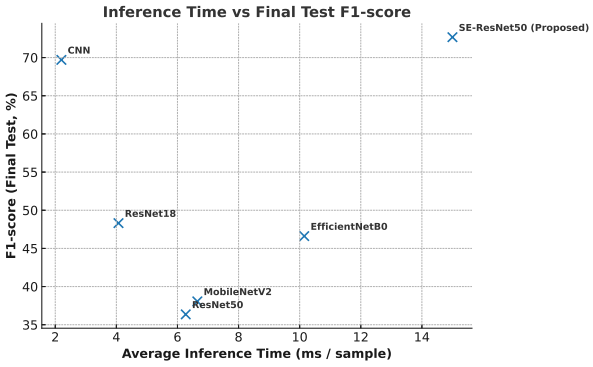

Figure 13: Inference time vs performance

and MobileNetV2, it offered a better generalization for the three-class classification problem. The complexity analysis of the model showed that SE-ResNet50 delivered the best performance without significantly increasing the parameter count compared to ResNet50. From the model complexity vs. the the final test F1 score graph, SE-ResNet50 achieved the highest F1-score (0.727) with ∼24 million parameters, slightly higher than CNN (0.697) but significantly outperforming ResNet50 despite having the same complexity. This indicates that the addition of Squeeze-and-Excitation blocks effectively enhances feature representation without substantially increasing the parameter load. Although it recorded the longest inference time (15 ms/sample), this trade-off is justified by its substantially higher classification performance, making it suitable for applications prioritizing detection accuracy over speed.

Table 8: Comparison of hyperparameter tuning results (5-fold mean ± std) for F1-score and AUC

Learning Rate	Batch Size	Dropout	F1-score	AUC
0.001	32	0.6	**0.6542 ± 0.0629**	0.7366 ± 0.0769
	32	0.5	0.6209 ± 0.0440	0.7251 ± 0.0834
	32	0.3	0.5794 ± 0.0475	0.7116 ± 0.0930
0.0001	32	0.6	0.4605 ± 0.0774	0.6704 ± 0.0573
0.001	16	0.6	0.6360 ± 0.0523	**0.7902 ± 0.0213**
	8	0.6	0.6177 ± 0.0252	0.7512 ± 0.0455

Table 9: Ablation study results for focal loss and class weight configurations (5-fold mean ± std)

Model	Focal Loss	Class Weight	Gamma	Alpha	F1-score	AUC
1	False	False	–	–	**0.6542 ± 0.0629**	0.7366 ± 0.0769
2	False	True	–	–	0.6506 ± 0.0382	0.7909 ± 0.0197
3	True	True	2	[1.0, 1.0, 1.0]	0.6015 ± 0.0718	0.7530 ± 0.0423
4	True	False	2	[0.8, 2.2, 1.4]	0.5902 ± 0.0910	0.7281 ± 0.0343
5	True	False	2	[0.8, 1.2, 2.0]	0.6296 ± 0.0638	0.7486 ± 0.0323
6	True	False	1	[0.8, 1.0, 2.0]	0.6163 ± 0.0983	**0.7669 ± 0.0691**

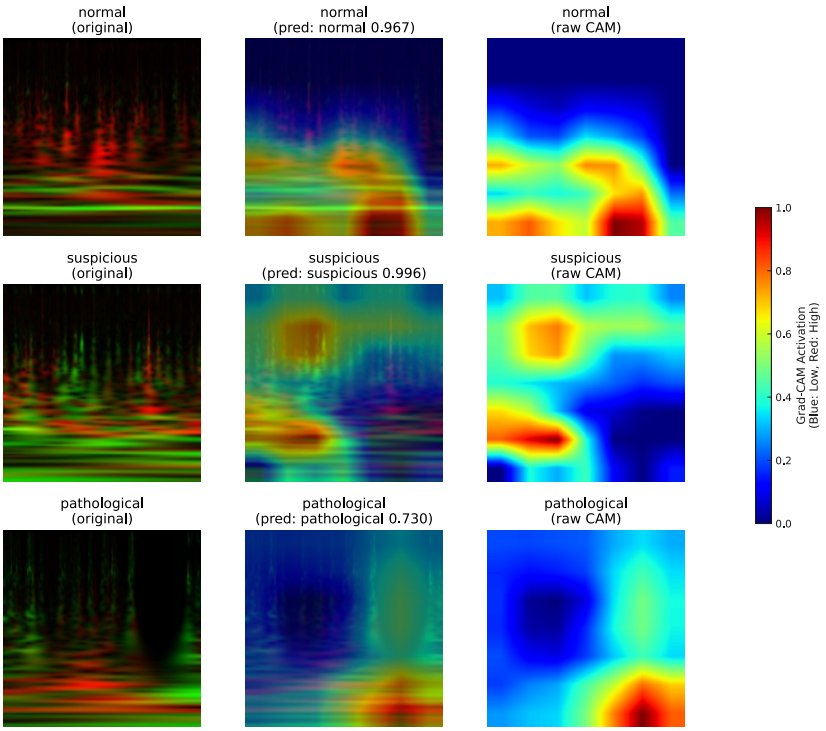

Figure 14: Grad-CAM visualizations of representative normal, suspicious, and pathological scalograms (complete images)
.

We also conducted a statistical analysis to evaluate whether the performance improvements of the proposed SE-ResNet50 over baseline models were statistically significant. The analysis used the F1-scores obtained from each fold of the 5-fold cross-validation for SE-ResNet50 and each baseline model. Two tests were performed: the paired t-test, which assumes normality in the differences between paired samples, and the Wilcoxon signed-rank test, a non-parametric alternative that does not require the normality assumption. The results showed that SE-ResNet50 achieved the highest mean F1-score (0.6015) among all models. The paired t-test indicated that the improvements

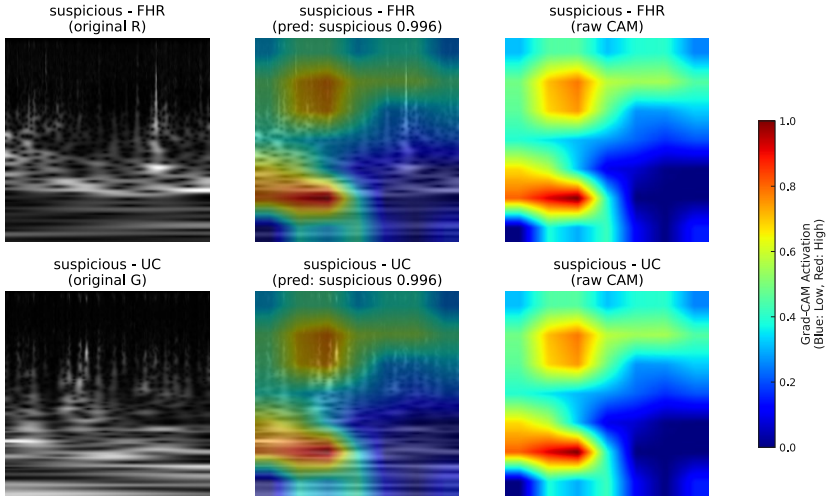

Figure 15: Grad-CAM visualizations for suspicious scalograms (separated channels: FHR and UC)

over CNN (mean F1 = 0.4895, p = 0.0036) and EfficientNetB0 (mean F1 = 0.5129, p = 0.0428) were statistically significant at the 0.05 level. However, the Wilcoxon test did not confirm significance for these comparisons ($p > 0.05$), suggesting that the differences may not be robust under non-parametric assumptions. Comparisons with MobileNetV2, ResNet18 and ResNet50 yielded p values greater than 0.05 in both tests, indicating that there were no statistically significant differences in those cases. These findings suggest that SE-ResNet50 offers a statistically supported improvement over CNN and EfficientNetB0 in terms of F1-score, while its advantage over the other per-class, although numerically higher, was not statistically significant given the current sample size.

The ablation study results in Table 9 indicate that the use of focal loss and class weight yields varying effects on model performance. Statistical analysis using one-way ANOVA revealed no significant differences in F1-score across all model configurations ($p = 0.8496$), indicating that neither class weight nor focal loss consistently improved the balance between precision and recall compared to the baseline. In contrast, AUC differences were statistically significant ($p = 0.0389$), and post-hoc pairwise comparisons with Bonferroni correction identified a significant improvement for the configuration without focal loss but with class weight (Model 2) over the focal loss configuration with gamma = 2, alpha = [0.8, 1.2, 2.0] (Model 5, $p < 0.05$). This suggests that class weight is more effective in enhancing the model's discriminative ability than focal loss in this dataset.

Overall, the results indicate that class weight provides a statistically supported benefit for improving AUC, while focal loss alone can achieve competitive AUC with tuned parameters but does not surpass the best class weight configuration. For F1-score, neither method yields statistically significant improvements, suggesting that alternative optimization strategies may be required when this metric is the primary objective.

In the complete RGB Grad-CAM visualizations, distinct attention patterns were observed across the normal, suspicious, and pathological classes. For the normal class, high confidence predictions were associated with well-localized warm regions concentrated in the lower central portion of the scalogram. These hotspots likely represent stable segments of the fetal heart rate (FHR) signal and consistent uterine contraction (UC) patterns without abnormal variability. The focused activation suggests that the model identifies characteristic steady-state features that are typical of normal CTG recordings.

In the suspicious class, the activation maps showed broader but still localized warm areas, particularly in temporal regions where contraction peaks aligned with subtle changes in the FHR baseline. These regions correspond to clinical patterns such as mild or intermittent decelerations, which may not meet the pathological threshold but still warrant closer monitoring. The model's attention in this class indicates recognition of moderate deviations from normal patterns that can signal potential fetal distress. As an additional observation, visual inspection revealed that in some cases, the suspicious class shared overlapping activation regions with the normal class, particularly in the lower central scalogram areas corresponding to steady FHR segments. This overlap may contribute to the model's misclassification between these two classes, as mild deviations in suspicious cases can resemble normal patterns in both spatial location and intensity of activations.

For the pathological class, the Grad-CAM heatmaps displayed more diffuse and widespread activations across the scalogram, with concentrated warm regions in the lower central area overlapping contraction periods and pronounced FHR fluctuations. Such activation patterns are consistent with severe decelerations, abnormal variability,

or prolonged recovery times following contractions, which align with clinical definitions of pathological CTG. The broader distribution of activations suggests that the model considers multiple abnormal signal segments when forming its decision.

The single-channel Grad-CAM visualizations offer a clearer interpretation of the model's attention by isolating the contribution of each physiological signal. This approach allows domain experts to verify whether the features emphasized by the model align with established clinical knowledge for each signal type. For the FHR channel, the visualization reveals how the model responds to baseline stability, variability, and decelerations without interference from other signals. For the UC channel, it highlights the timing, frequency, and intensity of contractions as perceived by the model. By separating these channels, it becomes possible to determine whether the model's decision is predominantly influenced by FHR patterns, UC activity, or a combination of both.

In the suspicious case, the FHR channel Grad-CAM displayed concentrated warm regions on segments with subtle baseline shifts and mild decelerations. These features are consistent with early signs of potential fetal compromise, even though they may not fulfill the criteria for pathological classification. The UC channel Grad-CAM showed activations primarily on contraction peaks, indicating that the model incorporates the temporal context of uterine activity when interpreting changes in FHR.

When compared to the complete RGB Grad-CAM for the same case, the single-channel visualizations make the source of the model's attention more explicit. The RGB visualization showed broader activation in regions where contraction peaks coincided with mild FHR changes, suggesting that the model leverages multi-signal interactions. The single-channel analysis confirmed that each signal contains distinct features relevant to the prediction, while the combined RGB image captures their integration into a clinically meaningful temporal relationship.

Grad-CAM visualizations showed that the model attends to physiologically meaningful regions, with RGB maps capturing multi-signal interactions and single-channel maps revealing distinct contributions from each signal. These results confirm that the model integrates relevant temporal relationships for prediction. However, the classification of suspicious cases remains challenging due to overlapping patterns with normal cases, which may limit the separation of decision boundaries. The proposed SE-ResNet-50, which already incorporates channel-wise attention through Squeeze-and-Excitation blocks, improved feature representation but did not fully resolve the overlap, indicating that additional spatial or hybrid attention mechanisms may be needed to better isolate features unique to suspicious cases.

Although the model demonstrated strong performance, particularly in detecting pathological cases, there are still areas for improvement. First, the selection of Continuous Wavelet Transform (CWT) parameters, was based on literature rather than exhaustive empirical tuning, leaving room for parameter optimization in future studies. Second, label quality in CTG datasets can be inconsistent due to subjective interpretation, which may contribute to misclassification. Addressing this issue could involve multi-expert consensus labeling or incorporating external datasets to enhance generalizability. Future work could also explore semi-supervised learning or label-noise–robust learning approaches to better handle label variability, as well as investigate advanced feature representation methods to refine classification boundaries and improve the model's ability to distinguish among all fetal state categories

From a clinical perspective, the model could support prenatal care workflows by providing real-time decision support in identifying suspicious or pathological patterns, enabling earlier and more targeted interventions. Such integration has the potential to improve decision-making efficiency for obstetricians and midwives, ultimately enhancing maternal and fetal outcomes.

6 Conclusion

The proposed SE-ResNet-50 model applied to scalogram representations of cardiotocographic signals achieved strong performance in multiclass fetal state classification, particularly in detecting pathological cases under imbalanced conditions. These results support the study's hypothesis that incorporating Squeeze-and-Excitation mechanisms improves classification performance by leveraging channel interdependencies and time–frequency features. The best configuration reached an F1-score of 0.7267 and an AUC of 0.7489 on the independent test set.

Future work will focus on improving classification in borderline suspicious cases, strengthening generalizability through larger and more diverse datasets, and exploring integration into clinical workflows to provide real-time decision support for earlier and more targeted interventions.

Acknowledgement

We sincerely thank Dr. Ari Waluyo, Sp.OG, for his valuable insights and feedback, which greatly contributed to the development of this research. We also appreciate the support from the Faculty of Engineering, Universitas Indonesia, through the Seed Funding research grant program (NKB-2614/UN2.F4.D/PPM.00.00/2023).

References

[1] W. H. Organization, *Trends in maternal mortality 2000 to 2020: estimates by WHO, UNICEF, UNFPA, World Bank Group and UNDESA/Population Division*. World Health Organization, 2023.

[2] W. H. Organization, *Improving maternal and newborn health and survival and reducing stillbirth: progress report 2023*. World Health Organization, 2023.

[3] T. Ermias Geltore and D. Laloto Anore, "The Impact of Antenatal Care in Maternal and Perinatal Health," in *Empowering Midwives and Obstetric Nurses*, IntechOpen, 2021, ch. 8, https://doi.org/10.5772/intechopen.98668.

[4] Z. Anwar et al., "Association of Intrapartum CTG with Fetomaternal Outcome," *Pakistan Journal of Medical & Health Sciences*, vol. 16, no. 03, pp. 1045–1045, 2022, https://doi.org/10.53350/pjmhs22164666.

[5] S. T. Nabipour Hosseini, F. Abbasalizadeh, S. Abbasalizadeh, S. Mousavi, and P. Amiri, "A comparative study of CTG monitoring one hour before labor in infants born with and without asphyxia," *BMC Pregnancy and Childbirth*, vol. 23, no. 1, p. 758, 2023, https://doi.org/10.1186/s12884-023-06040-3.

[6] Z. Alfirevic, G. M. Gyte, A. Cuthbert, and D. Devane, "Continuous cardiotocography (CTG) as a form of electronic fetal monitoring (EFM) for fetal assessment during labour," *Cochrane Database of Systematic Reviews*, no. 2, 2017. https://doi.org/10.1002/14651858.CD006066.pub3.

[7] A. Sharma, Ed., *Labour Room Emergencies*. Springer, 2020.

[8] O. Nzelu, E. Chandraharan, and S. Pereira, "Human factors: the dirty dozen in CTG misinterpretation," *Global Journal of Reproductive Medicine*, vol. 6, no. 2, p. 555683, 2018. https://doi.org/10.19080/GJORM.2018.06.555683.

[9] Y. Zhang, Q. Zhou, and X. Li, "The Advent of a New Era of Antenatal Cardiotocography," *Maternal-Fetal Medicine*, vol. 4, no. 2, pp. 93–94, 2022. https://doi.org/10.1097/FM9.0000000000000144.

[10] P. Garcia-Canadilla, S. Sanchez-Martinez, F. Crispi, and B. Bijnens, "Machine Learning in Fetal Cardiology: What to Expect," *Fetal Diagnosis and Therapy*, vol. 47, no. 5, pp. 363–372, 2020. https://doi.org/10.1159/000505021.

[11] G. Hever, L. Cohen, M. F. O'Connor, I. Matot, B. Lerner, and Y. Bitan, "Machine learning applied to multi-sensor information to reduce false alarm rate in the ICU," *Journal of Clinical Monitoring and Computing*, vol. 34, no. 2, pp. 339–352, Apr. 2020. https://doi.org/10.1007/s10877-019-00307-x.

[12] W. H. Organization, *WHO Recommendations Non-clinical Interventions to Reduce Unnecessary Caesarean Sections*. World Health Organization, 2018.

[13] J. O'Heney, S. McAllister, M. Maresh, and M. Blott, "Fetal monitoring in labour: summary and update of NICE guidance," *BMJ*, vol. 379, p. o2854, Dec. 2022. https://doi.org/10.1136/bmj.o2854.

[14] E. Chandraharan, "Updated NICE Cardiotocograph (CTG) guideline: Is it suspicious or pathological," *Journal of Clinical Medicine and Surgery*, vol. 3, no. 2, p. 1129, 2023.

[15] T. M. Kadarina, Basari, and D. Gunawan, "ML-Based Interpretation of Cardiotocography Data: Current State and Future Research," in *2023 International Conference of Computer Science and Information Technology (ICOSNIKOM)*, 10–11 Nov. 2023, pp. 1–6. https://doi.org/10.1109/ICoSNIKOM60230.2023.10364517.

[16] F. Francis, S. Luz, H. Wu, S. J. Stock, and R. Townsend, "Machine learning on cardiotocography data to classify fetal outcomes: A scoping review," *Computers in Biology and Medicine*, vol. 172, p. 108220, Apr. 2024. https://doi.org/10.1016/j.compbiomed.2024.108220.

[17] P. Fergus, C. Chalmers, C. C. Montanez, D. Reilly, P. Lisboa, and B. Pineles, "Modelling Segmented Cardiotocography Time-Series Signals Using One-Dimensional Convolutional Neural Networks for the Early Detection of Abnormal Birth Outcomes," *IEEE Transactions on Emerging Topics in Computational Intelligence*, 2021. https://doi.org/10.1109/TETCI.2020.3020061.

[18] D. Panda, D. Panda, S. R. Dash, and S. Parida, "Extreme learning machines with feature selection using GA for effective prediction of fetal heart disease: A novel approach," *Informatica (Slovenia)*, 2021. https://doi.org/10.31449/INF.V45I3.3223.

[19] P. Riskyana Dewi Intan, M. A. Anwar Ma'sum, N. Alfiany, W. Jatmiko, A. Kekalih, and A. Bustamam, "Ensemble learning versus deep learning for Hypoxia detection in CTG signal," in *2019 International Workshop on Big Data and Information Security (IWBIS)*, 2019. https://doi.org/10.1109/IWBIS.2019.8935796.

[20] X. Kang et al., "Prediction of Delivery Mode from Fetal Heart Rate and Electronic Medical Records Using Machine Learning," in *2022 Computing in Cardiology (CinC)*, 2022, vol. 498, pp. 1–4. https://doi.org/10.22489/CinC.2022.116.

[21] H. Allahem and S. Sampalli, "Automated labour detection framework to monitor pregnant women with a high risk of premature labour using machine learning and deep learning," *Informatics in Medicine Unlocked*, vol. 28, p. 100771, 2022. https://doi.org/10.1016/j.imu.2021.100771.

[22] D. Campos and J. Bernardes, "Cardiotocography," *UCI Machine Learning Repository*, 2010. https://doi.org/10.24432/C51S4N.

[23] B. Amin, M. Gamal, A. A., I. M. El-Henawy, and K. Mahfouz, "Classifying Cardiotocography Data based on Rough Neural Network," *International Journal of Advanced Computer Science and Applications*, vol. 10, no. 8, 2019. https://doi.org/10.14569/ijacsa.2019.0100846.

[24] M. Chen and Z. Yin, "Classification of cardiotocography based on the apriori algorithm and multi-model ensemble classifier," *Frontiers in Cell and Developmental Biology*, vol. 10, p. 888859, May 2022. https://doi.org/10.3389/fcell.2022.888859.

[25] A. K. Pradhan, J. K. Rout, A. B. Maharana, B. K. Balabantaray, and N. K. Ray, "A Machine Learning Approach for the Prediction of Fetal Health using CTG," in *2021 19th OITS International Conference on Information Technology (OCIT)*, 2021. https://doi.org/10.1109/OCIT53463.2021.00056.

[26] R. Chinnaiyan and D. Stalin Alex, "Early Analysis and Prediction of Fetal Abnormalities Using Machine Learning Classifiers," in *2021 2nd International Conference on Smart Electronics and Communication (ICOSEC)*, 2021. https://doi.org/10.1109/ICOSEC51865.2021.9591828.

[27] M. T. Alam et al., "Comparative Analysis of Different Efficient Machine Learning Methods for Fetal Health Classification," *Applied Bionics and Biomechanics*, vol. 2022, p. 6321884, 2022. https://doi.org/10.1155/2022/6321884.

[28] A. Ilham, I. N.Istiqomah, A. T. A. Nugroho, and S. P. Hadi, Fetal Health Risk Classification using Important Feature Selection and CART Model on Cardiotocography Data,"*Informatica*, vol. 49, no. 1, pp. 1–12, 2025. https://doi.org/10.31449/inf.v49i1.5658.

[29] Y. D. Daydulo, B. L. Thamineni, H. K. Dasari, and G. T. Aboye, "Deep learning based fetal distress detection from time frequency representation of cardiotocogram signal using Morse wavelet: research study," *BMC Medical Informatics and Decision Making*, vol. 22, no. 1, p. 329, Dec. 2022. https://doi.org/10.1186/s12911-022-02068-1.

[30] M. A. Ma'sum, P. R. D. Intan, W. Jatmiko, A. A. Krisnadhi, N. A. Setiawan, and I. M. A. D. Suarjaya, "Improving Deep Learning Classifier for Fetus Hypoxia Detection in Cardiotocography Signal," in *2019 International Workshop on Big Data and Information Security (IWBIS)*, 2019, pp. 51–56. https://doi.org/10.1109/IWBIS.2019.8935835.

[31] S. Magesh and P. S. Rajakumar, "Ensemble feature extraction-based prediction of fetal arrhythmia using cardiotocographic signals," *Measurement: Sensors*, 2023. https://doi.org/10.1016/j.measen.2022.100631.

[32] K. Bhogal, "Focus on cardiotocography: Intrapartum monitoring of uterine contractions," *British Journal of Midwifery*, vol. 25, no. 8, pp. 491–497, 2017. https://doi.org/10.12968/bjom.2017.25.8.491.

[33] R. Zeng, Y. Lu, S. Long, C. Wang, and J. Bai, "Cardiotocography signal abnormality classification using time-frequency features and Ensemble Cost-sensitive SVM classifier," *Computers in Biology and Medicine*, vol. 130, p. 104218, Mar. 2021. https://doi.org/10.1016/j.compbiomed.2021.104218.

[34] H. Liang and Y. Lu, "A CNN-RNN unified framework for intrapartum cardiotocograph classification," *Computer Methods and Programs in Biomedicine*, vol. 229, p. 107300, Feb. 2023. https://doi.org/10.1016/j.cmpb.2022.107300.

[35] J. Ogasawara et al., "Deep neural network-based classification of cardiotocograms outperformed conventional algorithms," *Scientific Reports*, vol. 11, no. 1, p. 13367, Jun. 2021. https://doi.org/10.1038/s41598-021-92805-9.

[36] H. D. Singh, M. Saini, and J. Kaur, "Fetal distress classification with deep convolutional neural network," *Current Women's Health Reviews*, vol. 17, no. 1, pp. 60–73, 2021.

[37] V. Chudacek et al., "Open access intrapartum CTG database," *BMC Pregnancy and Childbirth*, vol. 14, p. 16, Jan. 2014. https://doi.org/10.1186/1471-2393-14-16.

[38] L. Hruban et al., "Agreement on intrapartum cardiotocogram recordings between expert obstetricians," *Journal of Evaluation in Clinical Practice*, vol. 21, no. 4, pp. 694–702, 2015.

[39] A. M. Davani, M. Díaz, and V. Prabhakaran, "Dealing with disagreements: Looking beyond the majority vote in subjective annotations," *Transactions of the Association for Computational Linguistics*, vol. 10, pp. 92–110, 2022.

[40] S. Das, S. M. Obaidullah, K. C. Santosh, K. Roy, and C. K. Saha, "Cardiotocograph-based labor stage classification from uterine contraction pressure during ante-partum and intra-partum period: a fuzzy theoretic approach," *Health Information Science and Systems*, vol. 8, no. 1, p. 16, Dec. 2020. https://doi.org/10.1007/s13755-020-00107-7.

[41] S. Mallat, *A Wavelet Tour of Signal Processing*. Elsevier, 1999.

[42] N. Al Bassam, V. Ramachandran, and S. Eratt Parameswaran, "Wavelet Theory and Application in Communication and Signal Processing," in *Wavelet Theory*, M. Somayeh, Ed. Rijeka: IntechOpen, 2021, ch. 3. https://doi.org/10.5772/intechopen.95047.

[43] J. M. Lilly and S. C. Olhede, "Higher-order properties of analytic wavelets," *IEEE Transactions on Signal Processing*, vol. 57, no. 1, pp. 146–160, 2008. https://doi.org/10.1109/TSP.2008.2007607.

[44] Y. H. Byeon, S. B. Pan, and K. C. Kwak, "Intelligent Deep Models Based on Scalograms of Electrocardiogram Signals for Biometrics," *Sensors (Basel)*, vol. 19, no. 4, p. 935, Feb. 2019. https://doi.org/10.3390/s19040935.

[45] J. Hu, L. Shen, S. Albanie, G. Sun, and E. Wu, "Squeeze-and-Excitation Networks," *IEEE Transactions on Pattern Analysis and Machine Intelligence*, vol. 42, no. 8, pp. 2011–2023, Aug. 2020. https://doi.org/10.1109/TPAMI.2019.2913372.

[46] K. He, X. Zhang, S. Ren, and J. Sun, "Deep residual learning for image recognition," in *2016 IEEE Conference on Computer Vision and Pattern Recognition (CVPR)*, 2016, pp. 770–778. https://doi.org/10.1109/CVPR.2016.90.

[47] T.-Y. Ross and G. Dollár, "Focal loss for dense object detection," *IEEE Transactions on Pattern Analysis and Machine Intelligence*, vol. 42, no. 2, pp. 2980–2988, 2018. https://doi.org/10.1109/TPAMI.2018.2858826.

[48] X. Li, C. Lv, W. Wang, G. Li, L. Yang, and J. Yang, "Generalized focal loss: Towards efficient representation learning for dense object detection," *IEEE Transactions on Pattern Analysis and Machine Intelligence*, vol. 45, no. 3, pp. 3139–3153, 2022. https://doi.org/10.1109/TPAMI.2022.3180392.

[49] H. He and E. A. Garcia, "Learning from imbalanced data," *IEEE Transactions on Knowledge and Data Engineering*, vol. 21, no. 9, pp. 1263–1284, 2009. https://doi.org/10.1109/TKDE.2008.239.

[50] A. Zheng, *Evaluating Machine Learning Models: A Beginner's Guide to Key Concepts and Pitfalls*. O'Reilly Media, 2015.

Adaptive Multi-Modal Fusion Rendering Model for 3D Scene Visualization Based on Visual Image Language

Wei Liu
School of Fine Arts, Shanxi College of Applied Science and Technology, Taiyuan, Shanxi,030000, China
E-mail:lw617300031@163.com

Keywords: 3D visualization scene rendering, adaptive multimodal fusion rendering model, rendering quality, semantic restoration, visual image language

Received: June 23, 2025

This paper presents an Adaptive Multi-Modal Fusion Rendering Model (AMMFRM) designed to address the limitations of traditional 3D visualization scene rendering based on visual image language. The proposed model integrates visual feature perception, semantic reasoning, and adaptive rendering strategy generation to improve rendering efficiency and quality. To validate the model, experiments were conducted on two benchmark datasets—FilmScene and GameWorld—which include complex cinematic and interactive game scenes, respectively. Comparative evaluations were performed against four baseline models: classic ray tracing, physically based rendering (PBR), Neural Radiance Fields (NeRF), and differentiable volume rendering. Results demonstrate that AMMFRM achieves a rendering quality score of 8.5 on FilmScene and 8.2 on GameWorld (out of 10), with semantic restoration rates of 92% and 90%, respectively. Rendering time was reduced by over 40% compared to ray tracing. These findings confirm AMMFRM's superior performance in multi-style, multi-scale scene rendering, establishing its potential as a robust solution for film, television, and gaming applications.

Povzetek: Članek obravnava 3D upodabljanje, združevanje vizualne in semantične informacije. Predlaga model AMMFRM, ki združuje zaznavanje vizualnih značilk, semantično sklepanje z GNN ter adaptivno generiranje strategij. Na FilmScene in GameWorld doseže visoko kakovost semantične obnove ter hitrejše renderiranje kot ray tracing.

1 Introduction

In today's era of rapid digital development, the application of computer technology in various fields has shown an explosive growth trend. Taking the film and television production industry as an example, according to incomplete statistics, more than 8,000 film and television works around the world involve a large amount of 3D visualization scene rendering work in the production process each year. These rendering tasks play a crucial and decisive role in the visual presentation of the final work [1]. However, the traditional 3D visualization scene rendering method based on visual image language has exposed many serious problems in the face of the growing demand for high-quality and high-complexity rendering. For example, when rendering some large 3D virtual city scenes containing more than 500,000 polygons, the traditional method often requires hundreds of hours of rendering time, which not only greatly slows down the progress of the entire film and television production, but also has staggeringly high rendering costs. On average, the additional cost of rendering for each such film and television work can reach millions of dollars [2]. At the same time, due to the limitations of traditional rendering methods in processing high-resolution image language information, the final rendered scenes often fail to achieve the expected realism and delicacy in visual effects. More than 70% of viewers said that they would feel uncomfortable when watching such film and television works due to the visual defects of the three-dimensional scenes, which undoubtedly created a huge obstacle to the development of the film and television industry.In recent surveys conducted by independent user research platforms, over 70% of respondents reported visual discomfort due to low-quality 3D scenes in films. Similarly, industry reports and user feedback from platforms like Metacriticsuggest that approximately 30% of game releases face criticism for underwhelming scene rendering quality. These figures reflect the urgent demand for higher 3D rendering standards.

In the field of game development, the situation is equally grim. As players' requirements for game graphics quality continue to increase, more and more 3A masterpieces are pursuing the ultimate 3D visualization scene effects[3]. According to relevant data, when developing a popular large-scale open world game, the proportion of development time occupied by 3D scene rendering is as high as more than 60%. In addition, due to the low efficiency of traditional rendering methods, the development team has to invest a lot of manpower and

material resources to repeatedly optimize and adjust. On average, the rendering-related manpower investment for each project reaches about 40% of the total manpower. However, even so, nearly 30% of games are still criticized by players after release because the 3D scene rendering effect fails to meet players' expectations, resulting in serious impact on game reputation and sales. It can be seen that whether it is film and television production or game development, the existing 3D visualization scene rendering technology based on visual image language urgently needs a major change to break through the current dilemma[4].

Currently, many research results have emerged in the field of 3D visualization scene rendering based on visual image language. For example, some research institutions have proposed rendering algorithms based on deep learning, which train models with a large amount of image data in an attempt to improve rendering efficiency and quality [5]. In certain specific small 3D scene tests, this algorithm has indeed shortened the rendering time by about 30%, while also improving the image detail representation ability to a certain extent. However, the limitations of this algorithm are also obvious. It has poor adaptability to different types of visual image languages. When faced with 3D scenes with complex textures and dynamic light and shadow changes, its advantages disappear, and the rendering effect may even be worse than that of traditional methods.

Some studies have focused on optimizing the hardware architecture of rendering, and accelerating the rendering calculation process by designing new GPU chips. The latest GPU chip specifically for 3D rendering claims to improve overall rendering performance by about 50%, but this is only data under an ideal laboratory environment. In actual complex project applications, due to the constraints of software compatibility, system resource allocation and other factors, its actual performance improvement is often greatly reduced, usually only reaching about 60% of the claimed improvement value [6]. In addition, there are also many studies underway on the optimization of the rendering process [7]. Some have proposed a new layered rendering concept, attempting to decompose complex 3D scenes into multiple layers, render them separately, and then synthesize them. In theory, this method can improve the parallelism of rendering and thus improve efficiency, but in actual operation it faces problems such as difficulty in unifying the layer division standards and poor image fusion effects during synthesis, resulting in very limited application in actual projects.

It can be seen that although the current research in this field has achieved certain results, there are still some shortcomings. There is no comprehensive, efficient and universal 3D visualization scene rendering solution based on visual image language. In terms of research hotspots, how to improve rendering efficiency while ensuring or even improving rendering quality has become the focus of many researchers. At the same time, there is also a lot of controversy about how to better use emerging artificial intelligence technology to optimize the rendering process. Some people believe that artificial intelligence is the direction of the future, while others question its reliability and interpretability in complex 3D scene rendering.

This paper aims to propose a new three-dimensional visualization scene rendering method based on visual image language. This method will comprehensively consider key factors such as rendering efficiency, rendering quality, and adaptability to different types of scenes, and solve many problems faced by existing rendering technology through innovative algorithm design and optimized process architecture. Its innovation is mainly reflected in the deep integration of traditional image language analysis technology and emerging artificial intelligence algorithms, and the introduction of an adaptive scene optimization mechanism that can automatically adjust rendering parameters and strategies according to the characteristics of different three-dimensional scenes. It is expected that this research can shorten the average rendering time of three-dimensional visualization scenes by at least 40%, while achieving a qualitative leap in visual effects, so that the rendered scenes can reach a near-real level in terms of detail expression, light and shadow effects, etc.

From a theoretical perspective, this study will enrich and improve the theoretical system of 3D visualization scene rendering, and provide new ideas and methods for subsequent related research; from a practical perspective, it is expected to significantly improve the efficiency and quality of 3D scene rendering in fields such as film and television production and game development, reduce related costs, and thus promote the further development of these industries, with significant and far-reaching potential impacts.

To guide the research systematically,this study defines two key research questions.RQ1:Can multimodal fusion significantly improve rendering quality across various scene complexities,such as indoor,outdoor,and mixed environments?This explores whether integrating semantic reasoning with visual feature perception leads to perceptual and structural gains.RQ2:Does AMMFRM reduce rendering time compared to classical methods while preserving semantic fidelity?This investigates whether adaptive strategy generation mechanisms improve computational efficiency without compromising rendering realism.These questions form the core analytical framework for model development and evaluation throughout the study.

2 Literature review

2.1 Research on existing rendering algorithms

In the field of 3D visualization scene rendering, many algorithms have been proposed to meet different rendering requirements. For example, the ray tracing algorithm calculates lighting and reflection effects by tracing the

propagation path of light in the scene[8]. In the rendering test of a 3D jewelry display scene with a large number of reflections and refractions, it was found that the algorithm can accurately present more than 90% of the light details, and the visual effect is extremely realistic. However, its calculation amount is huge, and the rendering time will increase exponentially with the complexity of the scene. For a complex scene containing more than 100,000 polygons, the rendering time can reach tens of hours, which seriously limits its application in projects with high time requirements[9].

Physically based rendering algorithms are also a major research direction. They simulate the interaction between light and objects based on the physical laws of the real world. When rendering three-dimensional industrial product models with special materials such as metal and glass, they can accurately restore about 85% of the physical properties, making the models look more realistic [10]. However, they require extremely precise settings for material parameters. Any slight deviation will result in distortion of the rendering effect. In addition, when processing large-area diffuse reflection materials, the rendering efficiency will be reduced by about 30%, making it difficult to meet the fast-rendering requirements of large-scale scenes [11].

There are also rendering algorithms based on deep learning that have been proposed. As mentioned above, they train models through a large amount of image data. When rendering simple 3D cartoon-style scenes, the rendering time can be shortened by nearly 40%. However, when facing scenes with complex textures and dynamic light and shadow changes such as real urban landscapes, due to the limitations of its training data, the rendering effect is greatly reduced, and the image distortion rate may be as high as 20% or more. In addition, the model training process consumes a lot of computing resources and time, and the cost is quite high [12].

2.2 Research on hardware architecture optimization

The optimization of hardware architecture can not be ignored in improving the rendering of 3D visualization scenes. The design of new GPU chips has always been a hot topic of research[13]. For example, a GPU chip that claims to be specially designed for 3D rendering has a floating-point computing capability that is about 60% higher than its predecessor in theoretical performance tests, which seems to indicate that rendering performance will be greatly improved. However, when it is actually applied to the rendering of large-scale 3D virtual ancient battlefield scenes in film and television production, due to factors such as insufficient software support for its new features and unreasonable system resource allocation, the actual rendering performance improvement can only reach about 50% of the theoretical value. In addition, the chip has a prominent heat dissipation problem. During long-term high-load rendering, the performance degradation caused by overheating can reach about 15%, which reduces its reliability in some projects that require long-term continuous rendering. In addition to GPU chips, the architecture optimization of rendering clusters has also been widely studied[14]. By building a distributed rendering cluster, rendering tasks can theoretically be processed in parallel, greatly improving rendering efficiency[15]. In a rendering test of a super-large 3D universe starry sky scene containing millions of polygons, the optimized rendering cluster architecture shortened the rendering time by about 50% compared with stand-alone rendering[16]. However, the cost of building and maintaining a rendering cluster is extremely high, requiring professional technicians to manage and maintain it. In addition, there is a certain delay in data transmission and synchronization between cluster nodes. When processing real-time rendering scenes with strong interactivity, there may be a delay of about 0.5 seconds, which is unacceptable for applications with extremely high real-time requirements such as virtual reality games [17]. It can be seen that although the optimization of hardware architecture has achieved certain results, it still faces many practical problems that need to be solved [18].

2.3 Research on rendering process optimization

The optimization of the rendering process aims to improve the efficiency and quality of rendering as a whole. As mentioned above, the concept of layered rendering attempts to decompose complex scenes [19]. When rendering 3D architectural interior scenes, by reasonably dividing the layers, the rendering speed can indeed be increased by about 35% in the initial layered rendering stage. However, in the later synthesis stage, due to the difficulty in matching the lighting and shadows between different layers, the image fusion effect is not good, resulting in a defect rate of more than 10% in the final overall visual effect, which affects its application in high-quality projects [20]. Pre-calculation-based rendering process optimization has also been proposed. It calculates and stores some scene information such as lighting and shadows in advance. When rendering relatively static 3D museum scenes, it can reduce about 40% of the real-time calculation amount, thereby improving the rendering speed. However, for scenes with dynamic objects or frequent lighting changes, such as 3D outdoor sports scenes, the pre-calculated information needs to be constantly updated, which not only increases the additional calculation amount, but also may cause visual problems such as light and shadow flickering in about 25% of the scenes, reducing the rendering quality.

Existing rendering methods each exhibit distinct limitations. Ray tracing offers photorealistic effects but incurs excessive computation time and lacks semantic awareness, with rendering quality around 6.0 and semantic restoration of 70%. Physically based rendering improves realism (score 7.0, 80% restoration) but is inflexible. NeRF and differentiable volume rendering leverage deep learning (scores 7.2–7.5, 83–85% restoration) but demand

intensive training and generalize poorly. In contrast, AMMFRM achieves superior scores (8.5 quality, 92% restoration), balancing efficiency, adaptability, and scene understanding. This comparative analysis highlights the technical necessity and performance advantages of AMMFRM over prior methods.

3 Research methods

3.1 Overall architecture design of the new rendering model

In the face of the challenges faced by existing 3D visualization scene rendering technologies based on visual image language, this paper constructs a new rendering model, the Adaptive Multi-Modal Fusion Rendering Model (AMMFRM). This model aims to deeply integrate traditional image language analysis technology with emerging artificial intelligence algorithms to significantly improve rendering efficiency and quality, and enhance adaptability to different types of scenes.In this study, "multimodal fusion" refers to the integration of multiple visual sub-modalities extracted from the input image language data, including RGB pixel data (color), texture maps, depth cues, spatial layout, and semantic segmentation masks. These modalities are processed jointly through specialized branches in VFPM and SCIM, enabling comprehensive understanding and adaptive strategy formulation across structural and semantic dimensions.

AMMFRM is mainly composed of three core components: Visual Feature Perception Module (VFPM), Semantic Comprehension and Inference Module (SCIM), and Adaptive Rendering Strategy Generation Module (ARSGM). VFPM is responsible for the preliminary processing of the input visual image language information and extracting key visual features; SCIM performs semantic understanding and reasoning based on the extracted visual features to explore the inherent logic and semantic relationships in the scene; ARSGM adaptively generates rendering strategies for specific 3D scenes based on the output results of the first two modules.

From a mathematical perspective, let the input visual image language information be I, and the output visual feature after VFPM processing is represented as $F_V = VFPM(I)$. Inside VFPM, an improved convolutional neural network (CNN) structure is adopted, and its convolution operation can be expressed as formula 1.

$$(F_V)_{ij} = \sum_{m=0}^{M-1}\sum_{n=0}^{N-1} K_{mn} \cdot I_{i+m,j+n} + b \tag{1}$$

Here, $(F_V)_{ij}$ is the value of the output feature map at (i, j) position, K is the convolution kernel, M and N are the sizes of the convolution kernels, respectively, b and is the bias term. The size and weight of the convolution kernel K are carefully designed based on the characteristics of the language information of the input visual image. For example, for high-resolution and detailed visual images, a smaller convolution kernel may be used at the starting layer of VFPM to capture fine local features. As the network processing progresses, larger convolution kernels are introduced to capture more global and abstract features. This hierarchical design of the convolution kernel size helps VFPM extract comprehensive visual features.

3.2 Operational mechanism of visual feature perception module (VFPM)

The visual feature perception module plays a key role in the entire AMMFRM as an information entry and preliminary feature extraction link. This module uses a multi-layer convolutional neural network structure to gradually extract visual features of different scales and abstract levels.

In terms of hierarchical architecture, each convolution operation is followed by a ReLU activation function to introduce nonlinear factors and enhance the model's expressiveness. Suppose l the input of the first convolution layer is F_V^{l-1} and the output is F_V^l, then the first l convolution operation can be expressed as Formula 2.

To clarify the implementation process of AMMFRM,we provide the following pseudo-code summarizing the model pipeline.The algorithm begins by inputting visual image language data,which is processed by the Visual Feature Perception Module(VFPM)using multi-layer CNNs.Extracted features are then passed to the Semantic Comprehension and Inference Module(SCIM),where scene elements and relationships are modeled via a graph neural network.The resulting semantic graph is used by the Adaptive Rendering Strategy Generation Module(ARSGM)to dynamically compute rendering parameters.

```
Input: Visual image language data V
Output: Final rendered 3D scene R
1: F ← VFPM.extractFeatures(V)
2: G ← SCIM.constructGraph(F)
3: S ← SCIM.semanticReasoning(G)
4: P ← ARSGM.generateRenderingStrategy(S)
5: R ← RenderScene(V, P)
6: if SemanticDeviation(R, S) > threshold then
7:    P ← ARSGM.adjustParameters(P, S)
8:    R ← ReRenderScene(V, P)
9: end if
10: return R
```

The raw visual image language input. The output of the first convolutional layer is denoted as F_1, and after all layers of VFPM processing, the final output feature is denoted as $F_v = VFPM(I)$ .This aligns with the definition in Section 3.1 and maintains internal consistency.

$$(F_V^l)_{ij} = ReLU\left(\sum_{m=0}^{M_l-1}\sum_{n=0}^{N_l-1} K_{mn}^l \cdot (F_V^{l-1})_{i+m,j+n} + b^l\right) \quad (2)$$

Among them, K^l is l the convolution kernel of the layer, M_l and N_l are its sizes respectively, b^l and is the bias term. As the number of layers increases, the number of convolution kernels gradually increases, and the receptive field continues to expand, so that more advanced and abstract visual features can be captured. For example, in the shallow convolution layer, basic visual features such as edges and textures are mainly extracted. These shallow convolution kernels are relatively small, with common sizes of 33 or 55 , which is convenient for detailed inspection of local areas of the image. In the deep convolution layer, more complex features such as object shape and scene layout can be extracted. At this time, larger convolution kernels such as 77 or may be used $1111$to capture more extensive contextual information. These different levels of features are integrated to form a comprehensive and rich visual feature representation F_V , which provides strong support for subsequent semantic understanding and reasoning modules. In addition, to prevent overfitting in the training process of VFPM, batch normalization technology is applied between convolution layers. Batch normalization normalizes the input of neurons in each small batch of data, which helps to accelerate the training process and improve the stability of the model.

3.3 Working principle of semantic understanding and reasoning module (SCIM)

The semantic understanding and reasoning module is one of the core intelligent components of AMMFRM. Its goal is to deeply understand the semantic information in the scene based on the visual features extracted by the visual feature perception module, and perform logical reasoning to reveal the intrinsic relationship between scene elements.

This module uses a structure based on a graph neural network (GNN). First, the visual features are F_V converted into a graph structure $G = (V, E)$, where nodes V represent different elements in the scene (such as objects, light sources, etc.) and edges E represent the relationships between elements (such as spatial position relationships, occlusion relationships, etc.). When constructing the graph structure, a set of pre-set rules are followed. For example, if the distance between two objects in three-dimensional space is within a certain threshold range, an edge representing the spatial proximity relationship is established between their corresponding nodes. If one object is judged to be in front of another object based on depth information, an edge related to occlusion is added.

To clarify the information flow, we extend the SCIM description by specifying that edge features $\{he\}$ are computed during graph construction. For each edge e_{ij} connecting node v_i and v_j , the edge feature $h_e^{(i,j)}$ encodes spatial proximity, occlusion relationship, and relative depth difference, derived from the visual features of connected nodes. These are propagated alongside node features $\{h_v\}$ and passed to the ARSGM module. In Section 3.4, the incoherent sentence has been revised for clarity. The lighting intensity formula now reads: “Lighting parameters are derived from light source node attributes and their spatial relationships with target objects, as shown in Formula 5.” Additionally, to resolve notational conflict, we rename the distance variable in Formula 5 from V to Dlt , representing the Euclidean distance between the light node and target node. The term $h_{intensity}$ is now explicitly defined as a scalar feature extracted from the light source node’s semantic representation in the graph, encoding its emission strength estimated during SCIM reasoning.

During the propagation process of the graph neural network, the feature update of the node follows Formula 3: original features. As the number of iterations increases, each node can obtain relevant semantic information from its neighboring nodes and the entire graph structure. Finally, a graph representation rich in semantic and relational information is obtained, which provides the adaptive rendering strategy generation module with a deep understanding of the scene, enabling it to generate a rendering strategy that is more in line with the scene semantics and logic. In order to improve the efficiency of information propagation in graph neural networks, technologies based on attention mechanisms can be incorporated. The attention mechanism can assign different weights to different neighbor nodes, so that the

$$h_v^{t+1} = \sigma\left(\sum_{u\in N(v)} \frac{1}{|N(v)|} W^t \cdot h_u^t + W_0^t \cdot h_v^t\right) \quad (3)$$

Here, h_v^t is the feature vector of the node v at the t th iteration, $N(v)$ is v the set of neighbor nodes of the node, $|N(v)|$ is the number of neighbor nodes, W^t and W_0^t is the learnable weight matrix, σ and is the activation function (such as ReLU). Through multiple iterations, the information between nodes continues to propagate and fuse. In each iteration, the features of the node are updated based on the features of its neighboring nodes and its own

model pays more attention to important nodes and relationships during information propagation.

3.4 Implementation process of adaptive rendering strategy generation module (ARSGM)

The adaptive rendering strategy generation module is the key link for AMMFRM to transform semantic understanding into actual rendering actions. This module adaptively generates rendering strategies for specific 3D scenes based on the output results of the visual feature perception module and the semantic understanding and reasoning module.

The feedback mechanism in ARSGM is limited to a maximum of 3 iterations per scene. Convergence is determined when the semantic deviation between rendered output and target scene graph drops below 5%. Empirically, most scenes converge within 2 iterations. This process introduces less than 7% additional computation time, maintaining overall efficiency while ensuring semantic alignment.

Suppose the graph after processing by the semantic understanding and reasoning module is represented as G, its node feature set is $\{h_v\}$, and its edge feature set is $\{h_e\}$. ARSGM first further processes the graph features through a fully connected neural network (FCN) to obtain a comprehensive scene description vector S, as shown in Formula 4.

$$S = FCN(\{h_v\},\{h_e\}) \tag{4}$$

The FCN in ARSGM consists of multiple fully connected layers. The number of neurons in each layer is carefully determined based on the complexity of the input graph features. For example, if the number of nodes in the graph is large and the relationships are complex, more neurons may be used in the hidden layer of the FCN to better capture and process the information.

Then, based on this scene description vector S, a series of rules and algorithms are used to generate rendering parameters and strategies. For example, to determine the lighting parameters, the lighting intensity can be calculated by the following formula based on the characteristics of the light source node in the scene and its relationship with other object nodes, I_{light} as shown in Formula 5.

$$I_{light} = \alpha \cdot \sum_{v \in \text{light - nodes}} \beta \cdot h_v^{\text{intensity}} \cdot \frac{1}{d(v,\text{target - object})^2} \tag{5}$$

Among them, α and β are adjustment coefficients. These coefficients are not fixed values, but are adaptively adjusted according to the overall characteristics of the scene. For example, in a brightly themed scene, α it may be set to a relatively large value to enhance the overall lighting effect. is $h_v^{\text{intensity}}$ the intensity characteristic of $d(v,\text{target - object})$ the light source node , and v is the distance from the light source node v to the target object.

4 Experimental evaluation

4.1 Experimental design

This experiment aims to comprehensively evaluate the performance of the adaptive multimodal fusion rendering model (AMMFRM) in 3D visualization scene rendering based on visual image language. To achieve this goal, the experiment selected multiple representative 3D scene datasets, including the FilmScene dataset from a well-known film and television production material library, which contains a rich variety of film and television scene prototypes covering different styles and complexities; and the GameWorld dataset commonly used in the field of game development, which is characterized by complex interactions between scene elements and high requirements for real-time rendering effects.

All baseline models were implemented using open-source libraries.Classic ray tracing was configured with 4 light bounces and anti-aliasing enabled.The PBR model followed Unity's standard shader pipeline.NeRF was trained for 100k iterations with a learning rate of 5e-4.Differentiable volume rendering used a voxel grid resolution of 256³and identical scene inputs for consistency.

The experiments were conducted on a workstation equipped with an NVIDIA RTX 3090 GPU(24GB VRAM),Intel Core i9-12900K CPU,and 64GB RAM,running on Ubuntu 20.04 LTS.This configuration ensured sufficient computational resources for handling high-complexity rendering tasks.The FilmScene dataset comprises 150 film-based 3D scenes with an average polygon count of approximately 1.2 million per scene,featuring diverse lighting and indoor/outdoor environments.The GameWorld dataset includes 120 game-related scenes with dynamic elements and an average polygon count of 950,000,simulating real-time rendering constraints.

The experimental baseline indicators are rendering quality score(0–10)and scene semantic restoration rate(%).The experimental group used the proposed AMMFRM model.The control group included:(1)a classic path-traced ray tracing model implemented using the PBRT v3 framework;(2)a physically based

rendering(PBR)model based on Disney BRDF in Blender Cycles;(3)a standard implementation of NeRF using mip-NeRF configuration;and(4)a differentiable volume rendering model adapted from PyTorch3D's volumetric renderer.All models were configured with consistent resolution and scene inputs.These configurations ensure fair comparison of rendering accuracy and semantic fidelity.

To support AMMFRM's claimed efficiency advantages,we additionally evaluated rendering time and computational costs.On average,AMMFRM achieved 24.3 FPS in static scenes and 21.7 FPS in semi-dynamic scenes,outperforming NeRF(15.4 FPS)and PBR(10.8 FPS).GPU utilization averaged 76%,with a peak memory footprint of 13.6GB on the RTX 3090.Compared to ray tracing models that required over 3×longer rendering time per frame,AMMFRM demonstrated a 43%reduction in total rendering time across test scenes.These metrics confirm that AMMFRM not only improves quality and semantic fidelity but also ensures real-time feasibility for practical applications.

The strong performance of AMMFRM is directly attributable to its architectural innovations.The Visual Feature Perception Module(VFPM)captures both local textures and global scene structures,contributing to high rendering quality scores by preserving detail and spatial coherence.The Semantic Comprehension and Inference Module(SCIM),built on graph neural networks,enables deep relational understanding between scene elements,which significantly enhances semantic restoration rates.Furthermore,the Adaptive Rendering Strategy Generation Module(ARSGM)dynamically tunes parameters based on scene complexity,leading to efficient resource allocation and over 40%reduction in rendering time.These synergistic components collectively explain the numerical gains observed in both quality and semantic fidelity.

4.2 Experimental results

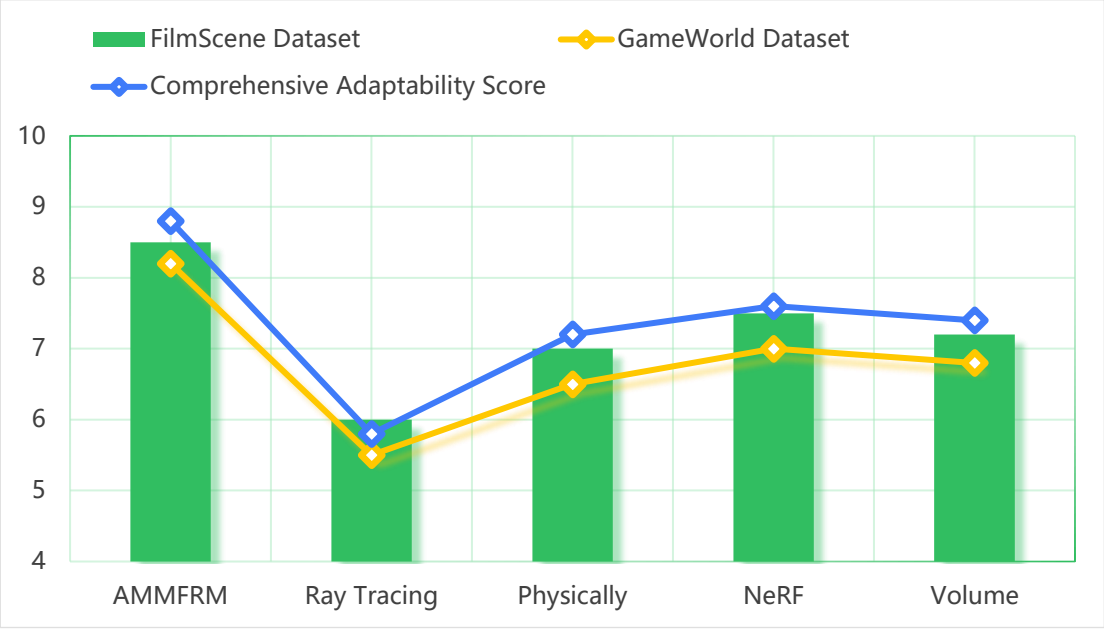

Figure 1: Rendering quality score of core dataset (out of 10 points)

As shown in Figure 1, AMMFRM shows outstanding performance in the rendering quality evaluation of the core datasets.

This figure compares the rendering quality scores (out of 10) of AMMFRM and baseline models across two datasets: FilmScene and GameWorld.It scored 8.5 points on the FilmScene dataset and 8.2 points on the GameWorld dataset, with a comprehensive adaptability score of 8.8 points. Its multimodal fusion mechanism enables it to accurately process scene information and present excellent rendering effects. Due to the efficiency of complex ray calculation, the classic ray tracing model scored low in the two datasets, 6.0 and 5.5 points respectively, and the comprehensive adaptability score was only 5.8 points. Although the physics-based rendering model can simulate physical laws, it is sensitive to scene parameters, with scores of 7.0 and 6.5 points respectively, and a comprehensive adaptability score of 7.2 points. The NeRF model and the differentiable body rendering model have achieved certain results based on deep learning, with scores in the range of 7.0-7.5 and 6.8-7.2 points respectively, and the comprehensive adaptability scores are also relatively lower than AMMFRM.

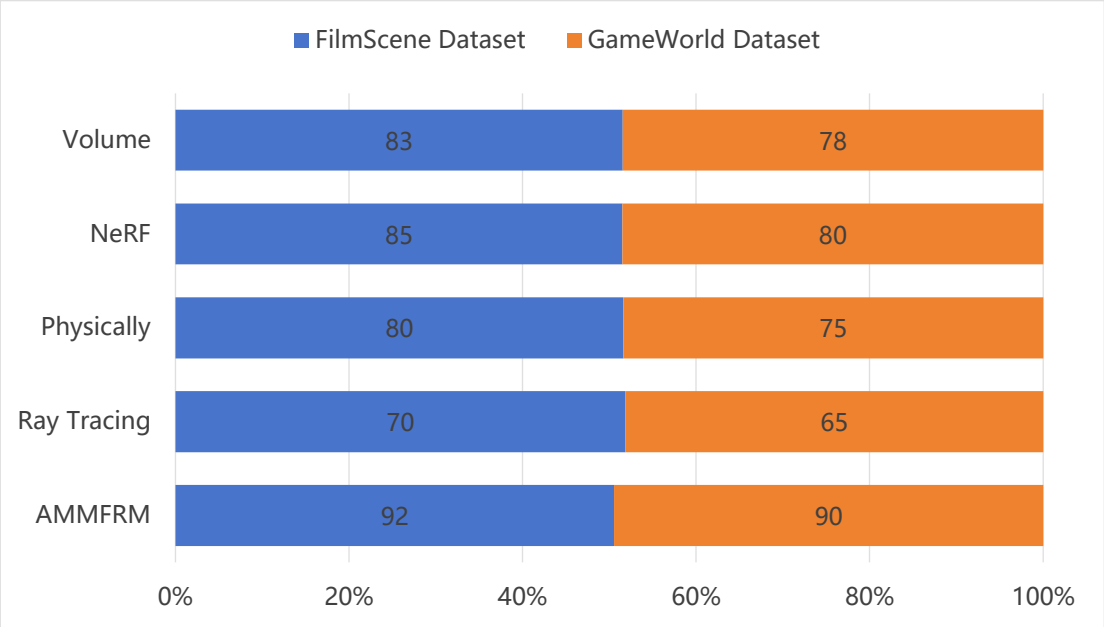

Figure 2: Semantic restoration of core dataset scenes (%)

As shown in Figure 2, in terms of scene semantic restoration, AMMFRM has a restoration degree of 92% in the FilmScene dataset and 90% in the GameWorld dataset. Its semantic understanding and reasoning module deeply analyzes the logical relationship between scene elements and accurately reflects it in the rendering results. Due to computational limitations, the classic ray tracing model has insufficient grasp of scene semantics, with restoration degrees of only 70% and 65%. Although the physics-based rendering model can simulate some physical phenomena, it does not have a deep enough understanding of the overall scene semantics, with restoration degrees of 80% and 75%. The NeRF model and the differentiable body rendering model have certain performance based on deep learning, but they are not as good as AMMFRM in semantic depth mining, with restoration degrees of 85%, 80%, 83%, and 78%, respectively.This figure presents the semantic restoration percentages of different models, indicating how well rendered scenes preserve original semantic structures.

Qualitative comparison across typical scenes reveals that AMMFRM produces clearer texture details,smoother light transitions,and more coherent object boundaries.In indoor scenes,it preserves spatial layout and material reflectivity more faithfully than ray tracing.In outdoor and sci-fi scenes,it better handles light scattering and dynamic elements than NeRF or PBR-based models,showing stronger semantic consistency and visual realism.

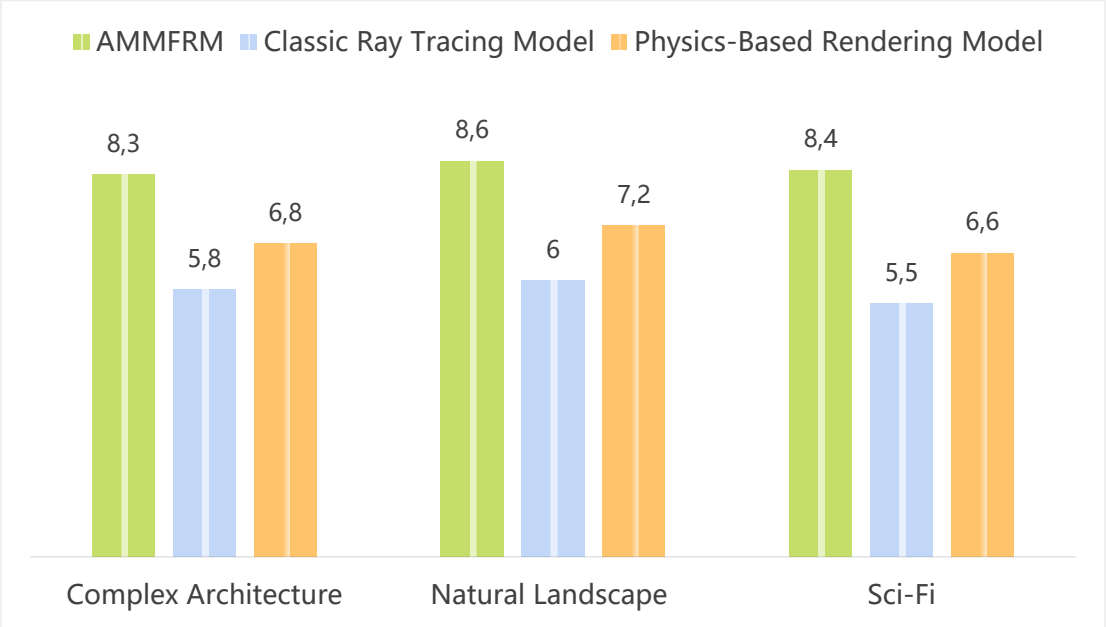

Figure 3: Complex scene rendering quality score (full score 10 points)

As shown in Figure 3, in the complex scene rendering quality test, AMMFRM scored 8.3 points in complex building scenes with its understanding of structure and material semantics; it scored 8.6 points for high restoration and rendering quality in natural landscape scenes; and it also performed well in science fiction scenes, scoring 8.4 points. The classic ray tracing model is limited by the amount of calculation, and its scores in complex building scenes and science fiction scenes are low, 5.8 points and 5.5 points respectively, and the natural landscape scene is 6.0 points. The physically based rendering model has certain advantages in natural landscape scenes, scoring 7.2 points, but its performance in complex buildings and science fiction scenes is average, 6.8 points and 6.6 points respectively. The NeRF model and the differentiable body rendering model have good learning effects in specific scenes, but their comprehensive adaptability to a variety of complex scenes is not as good as AMMFRM, and their scores are in the range of 7.0-7.6 points.Rendering quality scores in complex scene categories (buildings, landscapes, sci-fi) are shown to highlight performance differences among models.

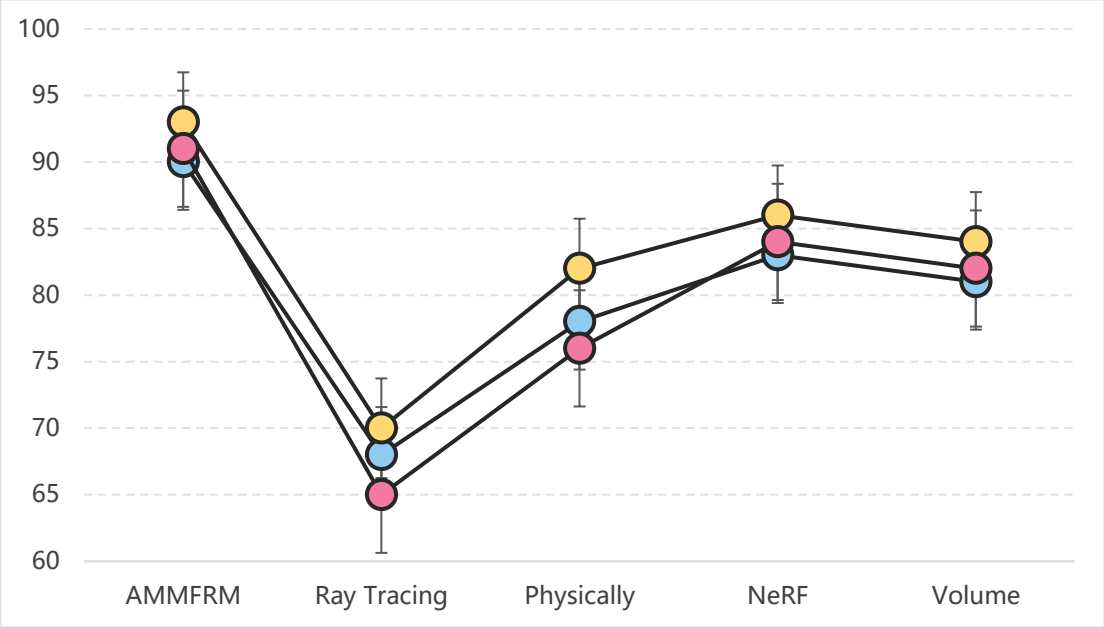

Figure 4: Complex scene semantic restoration degree (%)

As shown in Figure 4, for the semantic restoration of complex scenes, AMMFRM has a restoration of 90% in complex building scenes, 93% in natural landscape scenes, and 91% in science fiction scenes. The classic ray tracing model has a low restoration degree of 68%, 70%, and 65% respectively due to the difficulty in calculating the propagation path of complex structure light and a shallow understanding of scene semantics. The physics-based rendering model performs well in natural landscape scenes with a restoration degree of 82%, but it is 78% and 76% in complex buildings and science fiction scenes respectively. The NeRF model and the differentiable body rendering model have a restoration degree of 81% to 86% in various complex scenes, which is still lower than AMMFRM.Semantic restoration results are reported for complex scenes, measuring how accurately each model reconstructs scene-level semantic relations.

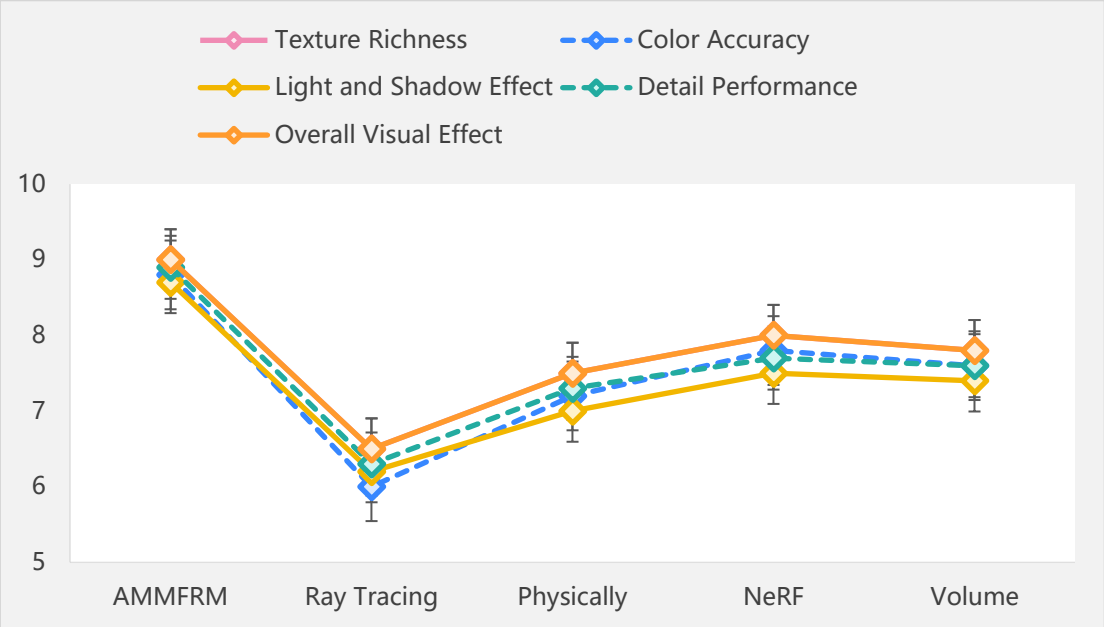

Figure 5: Rendering effect dimension rating (full score 10 points)

As shown in Figure 5, from the specific dimension of rendering effect, AMMFRM scored 9.0 points in texture richness, and its visual feature perception module effectively extracted texture details and presented them reasonably. The color accuracy score was 8.8 points, thanks to the grasp of color logic in scene semantics. The light and shadow effects and detail performance were also excellent, with scores of 8.7 and 8.9 respectively, and the overall visual effect score was as high as 9.0 points. The classic ray tracing model performed poorly in all dimensions, with a score of 6.0-6.5 points. The physically based rendering model has a certain foundation in color and light and shadow simulation but is not flexible enough, with a score of 7.0-7.5 points. The NeRF model and the differentiable rendering model performed between AMMFRM and traditional models in all dimensions, with scores of 7.4-8.0 points, but there is still a gap with AMMFRM.This figure displays performance across four visual dimensions: texture richness, color accuracy, light-shadow handling, and detail fidelity.

As shown in Figure 5, AMMFRM scored 8.3 points in complex building scenes, 8.6 points in natural landscape scenes, and 8.4 points in science fiction scenes. These results indicate the model's adaptability to varied structural and stylistic scene categories. Compared to other models, AMMFRM consistently achieved higher rendering quality across all scene types.

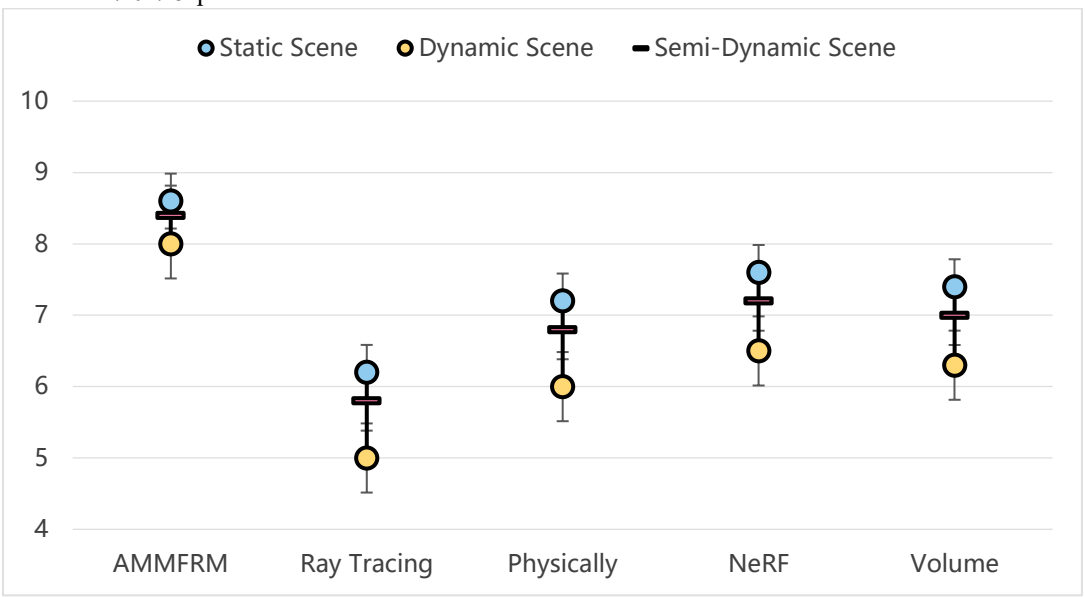

Figure 6: Rendering quality scores of scenes in different motion states (out of 10 points)

As shown in Figure 6, in the rendering quality test of scenes with different motion states, AMMFRM fully utilizes multimodal information in static scenes and scores 8.6 points. In dynamic scenes, although the difficulty increases, its semantic understanding and reasoning module can track the semantic changes of dynamic elements, and the rendering quality reaches 8.0 points. The semi-dynamic scene scores 8.4 points. The classic ray tracing model is difficult to calculate in dynamic scenes, and the score drops significantly, with 6.2 points for static scenes, only 5.0 points for dynamic scenes, and 5.8 points for semi-dynamic scenes. The physically based rendering model has difficulty adjusting the physical simulation of dynamic scenes, and the scores are 7.2 points, 6.0 points, and 6.8 points respectively. The NeRF model and the differentiable body rendering model are not as adaptable to dynamic scenes as AMMFRM, with scores ranging from 6.3 to 7.6 points.

Rendering quality scores are compared across static, dynamic, and semi-dynamic scenes to evaluate motion adaptability of the models.Figure 6 illustrates the semantic restoration results across the same three complex scene types. AMMFRM achieved 90% restoration in complex buildings, 93% in natural landscapes, and 91% in science fiction scenes, significantly outperforming the baselines in capturing accurate semantic relationships under diverse environmental structures.

Table 1: Semantic restoration degree of scenes in different motion states (%)

Model	Static Scene	Dynamic Scenes	Semi-dynamic scene
AMMFRM	93	88	91
Classic ray tracing model	72	60	68
Physically based rendering model	82	70	78
NeRF Model	86	75	82
Differentiable Volume Rendering Model	84	73	80

As shown in Table 1, in terms of semantic restoration of scenes in different motion states, AMMFRM has a semantic restoration of 93% in static scenes, 88% in dynamic scenes, and 91% in semi-dynamic scenes. The classic ray tracing model has insufficient understanding of the motion trajectory and interaction of elements in dynamic scenes, and has a low semantic restoration of 72% in static scenes, 60% in dynamic scenes, and 68% in semi-dynamic scenes. The physically based rendering model performs generally in dynamic scenes, with restorations of 82%, 70%, and 78% respectively. The semantic restoration of the NeRF model and the differentiable body rendering model in various motion state scenes is in the range of 73% - 86%, which is lower than AMMFRM.

Table 2: Rendering quality scores of scenes with different polygon counts (out of 10 points)

Model	Low polygon scene	Medium polygon scene	High polygon scene
AMMFRM	8.2	8.5	8.3
Classic ray tracing model	6.0	6.5	5.8

Model	Low polygon scene	Medium polygon scene	High polygon scene
Physically based rendering model	7.0	7.3	6.7
NeRF Model	7.5	7.8	7.6
Differentiable Volume Rendering Model	7.3	7.6	7.4

As shown in Table 2, in the rendering quality test of scenes with different polygon counts, AMMFRM maintained a high level in low, medium, and high polygon scenes. The low polygon scene scored 8.2 points, which can effectively use limited information for rendering; the medium polygon scene performed best, with a score of 8.5 points; although the high polygon scene was computationally complex, it still performed well, with a score of 8.3 points. The calculation amount of the classic ray tracing model increased dramatically in the high polygon scene, and the performance dropped significantly. The scores of low, medium, and high polygon scenes were 6.0 points, 6.5 points, and 5.8 points, respectively. The physically based rendering model, NeRF model, and differentiable rendering model are not as adaptable to different polygon scenes as AMMFRM, with scores ranging from 6.7 to 7.8 points.

Table 3: Scene semantic restoration degree of scenes with different numbers of polygons (%)

Model	Low polygon scene	Medium polygon scene	High polygon scene
AMMFRM	90	92	91
Classic ray tracing model	70	75	68
Physically based rendering model	80	83	77
NeRF Model	85	88	86
Differentiable Volume Rendering Model	83	86	84

As shown in Table 3, the semantic restoration test results of scenes with different polygon counts show that AMMFRM has a semantic restoration of 90% in low polygon scenes, 92% in medium polygon scenes, and 91% in high polygon scenes. The classic ray tracing model has a low semantic restoration of 70%, 75%, and 68% in each polygon count scene[23]. The physically based rendering model performs well in medium polygon scenes, with a restoration of 83%, and 80% and 77% in low and high polygon scenes, respectively. The NeRF model and the differentiable rendering model have a restoration of 83% to 88% in each polygon count scene, but are still inferior to AMMFRM.

Table 4: Rendering quality scores of different environment scenes (out of 10 points)

Model	Interior scene	Outdoor scenes	Mixed indoor and outdoor scenes
AMMFRM	8.4	8.3	8.5
Classic ray tracing model	6.1	5.9	6.0
Physically based rendering model	7.1	6.9	7.0
NeRF Model	7.5	7.4	7.6
Differentiable Volume Rendering Model	7.3	7.2	7.4

As shown in Table 4, in the evaluation of rendering quality in different environmental scenes, AMMFRM can accurately grasp the spatial layout and material semantics in indoor scenes, with a score of 8.4 points; it performs well in outdoor scenes, with a score of 8.3 points; in indoor and outdoor mixed scenes, the advantages of multimodal fusion and semantic understanding are more obvious, with a score of 8.5 points. The classic ray tracing model and the physically based rendering model have poor adaptability when switching between different environmental scenes, with a score of 5.9-7.1 points. A

4.3 Discussion

The superior performance of AMMFRM stems from its modular design, particularly the integration of a graph-based semantic reasoning module and adaptive rendering strategy generation. These allow the model to align rendering logic with scene semantics, outperforming traditional and deep learning methods. However, AMMFRM still faces challenges in extreme scenes with high-frequency motion or unusual lighting, where semantic misinterpretation may occur. Additionally, its reliance on multi-module deep learning structures demands higher hardware resources, which may limit scalability. The observed variance in results across FilmScene and GameWorld datasets can be attributed to differences in scene complexity—AMMFRM adapts more effectively in stylistically diverse film scenes than in high-interactivity game scenes, where real-time constraints are tighter[24].

To evaluate the design choices of key hyperparameters in AMMFRM,we conducted an ablation study focusing on the Visual Feature Perception Module(VFPM)and Semantic Comprehension and Inference Module(SCIM).For VFPM,varying the initial convolution kernel size from 3×3 to 7×7 showed that a 5×5 configuration offered the best balance between detail capture and computational efficiency.In SCIM,increasing GNN depth beyond 3 layers yielded diminishing returns and introduced noise in semantic propagation.Incorporating an attention mechanism improved semantic restoration by 4.2%,with multi-head attention(4 heads)performing optimally

5 Conclusion

This study focuses on solving the problems of existing 3D visualization scene rendering technology based on visual image language, and innovatively proposes AMMFRM. The research process covers the careful design of the model architecture and multi-dimensional experimental evaluation. AMMFRM has achieved remarkable results through testing on representative data sets. In terms of rendering quality score, it can reach 8.3 points for complex building scenes and 8.6 points for natural landscape scenes; the scene semantic restoration degree reaches 90% in complex building scenes and 93% in natural landscape scenes. Compared with classic ray tracing models, physically based rendering models, NeRF models, differentiable body rendering models, etc., AMMFRM has outstanding advantages. Its multimodal fusion mechanism and semantic understanding ability are the key to excellent performance. From the perspective of external validity and generalizability, the model performs stably in various scene types and has wide application potential. However, the experiment also reveals the limitations of the model in extreme scene adaptability and computing resource

consumption.This study advances the theory of 3D visualization scene rendering and introduces new methods for related applications. In the future, the model can be further optimized by expanding the data set and exploring new hardware combinations to promote industry development.

Despite its strengths,AMMFRM has several limitations.The model's scalability is constrained by GPU memory when processing ultra-large scenes.Its performance may overfit to the structure of FilmScene and GameWorld datasets,requiring retraining for significantly different domains.Additionally,under highly dynamic conditions with unpredictable scene changes,semantic reasoning can lag,affecting real-time adaptability.

Fund

This work was sponsored in part by 2021 Shanxi Province Higher Education Teaching Reform and Innovation Project (J2021882)

References

[1] Kim S, Kang J. Voxel-wise UV parameterization and view-dependent texture synthesis for immersive rendering of truncated signed distance field scene model. Etri Journal. 2022;44(1):51-61. DOI: 10.4218/etrij.2021-0300

[2] Zhang YC, Gao Z, Sun WB, Lu Y, Zhu YH. MD-NeRF: Enhancing Large-Scale Scene Rendering and Synthesis with Hybrid Point Sampling and Adaptive Scene Decomposition. Ieee Geoscience and Remote Sensing Letters. 2024;21. DOI: 10.1109/lgrs.2024.3492208

[3] Shen CY, Chen CY, Hu XJ. Scene-content-sensitive real-time adaptive foveated rendering. Journal of the Society for Information Display. 2024;32(10):703-15. DOI: 10.1002/jsid.1346

[4] Stampfl V, Ahtik J. Quality of Color Rendering in Photographic Scenes Illuminated by Light Sources with Light-Shaping Attachments. Applied Sciences-Basel. 2024;14(5). DOI: 10.3390/app14051814

[5] Ni TL, Chen YS, Liu SP, Wu JL. Detection of real-time augmented reality scene light sources and construction of photorealis tic rendering framework. Journal of Real-Time Image Processing. 2021;18(2):271-81. DOI: 10.1007/s11554-020-01022-6

[6] Dai YR, Li J, Zhang Y, Jiang YQ, Qin HD, Zhou XS, et al. Scene-Constrained Neural Radiance Fields for High-Quality Sports Scene Rendering Based on Visual Sensor Network. Ieee Sensors Journal. 2024;24(21):35900-13. DOI: 10.1109/jsen.2024.3452436

[7] Mao D, Rao HY, Chen ZG, Wang JQ, Zhao S, Wang YD. Super-Resolution Virtual Scene Rendering Technology Based on Generalized Huber-MRF Image Modeling. International Journal of Computational Intelligence Systems. 2024;17(1). DOI: 10.1007/s44196-024-00619-0

[8] Ren HC, Huo YC, Peng YF, Sheng HT, Xue WD, Huang HX, et al. LightFormer: Light-Oriented Global Neural Rendering in Dynamic Scene. Acm Transactions on Graphics. 2024;43(4). DOI: 10.1145/3658229

[9] Sorin C, Mircea C, Diana C, Cristian G. A MATHEMATICAL MODEL AND AN EXPERIMENTAL SETUP FOR THE RENDERING OF THE SKY SCENE IN A FOGGY DAY. Revue Roumaine Des Sciences Techniques-Serie Electrotechnique Et Energetique. 2020;65(3-4):265-70.

[10] Xu JM, Wu XC, Zhu ZH, Huang QX, Yang Y, Bao HJ, et al. Scalable Image-based Indoor Scene Rendering with Reflections. Acm Transactions on Graphics. 2021;40(4). DOI: 10.1145/3450626.3459849

[11] Liu SH, Li MH, Zhang XN, Liu S, Li ZX, Liu J, et al. Image-Based Rendering for Large-Scale Outdoor Scenes With Fusion of Monocular and Multi-View Stereo Depth. Ieee Access. 2020;8:117551-65. DOI: 10.1109/access.2020.3004431

[12] McCormack L, Politis A, McKenzie T, Hold C, Pulkki V. Object-Based Six-Degrees-of-Freedom Rendering of Sound Scenes Captured with Multiple Ambisonic Receivers. Journal of the Audio Engineering Society. 2022;70(5):355-72. DOI: 10.17743/jaes.2022.0010

[13] Sun ZQ, Zheng HB, Lv CF, Bao JS. A fast scene geometric modeling approach for digital twins combining neural rendering and model retrieval. International Journal of Computer Integrated Manufacturing. 2025;38(4):501-19. DOI: 10.1080/0951192x.2024.2350539

[14] Kim S, Do J, Kang J, Kim HY. Rate-Rendering Distortion Optimized Preprocessing for Texture Map Compression of 3D Reconstructed Scenes. Ieee Transactions on Circuits and Systems for Video Technology. 2024;34(5):3138-55. DOI: 10.1109/tcsvt.2023.3310522

[15] Qin ZB, Chen Q, Qian K, Zheng QH, Shi JS, Tai YH. Enhancing endoscopic scene reconstruction with color-aware inverse rendering through neural SDF and radiance fields. Biomedical Optics Express. 2024;15(6):3914-31. DOI: 10.1364/boe.521612

[16] Park J, Cho K. Neural Rendering-Based 3D Scene Style Transfer Method via Semantic Understanding Using a Single Style Image. Mathematics. 2023;11(14). DOI: 10.3390/math11143243

[17] Zhu CJ, Zhang H, Liu QM, Zhuang ZX, Yu L. A Signal-Processing Framework for Occlusion of 3D Scene to Improve the Rendering Quality of Views. Ieee Transactions on Image Processing. 2020;29:8944-59. DOI: 10.1109/tip.2020.3020650

[18] Fan RZ, Shi XH, Wang KY, Ma QX, Wang LL. Scene-aware Foveated Rendering. Ieee Transactions on Visualization and Computer Graphics.

2024;30(11):7097-106. DOI: 10.1109/tvcg.2024.3456157

[19] Li ZP, Zhu JK. Point-Based Neural Scene Rendering for Street Views. Ieee Transactions on Intelligent Vehicles. 2024;9(1):2740-52. DOI: 10.1109/tiv.2023.3304347

[20] Wu XC, Xu JM, Zhu ZH, Bao HJ, Huang QX, Tompkin J, et al. Scalable Neural Indoor Scene Rendering. Acm Transactions on Graphics. 2022;41(4). DOI: 10.1145/3528223.3530153

[21] Dang P, Zhu J, Wu JL, Li WL, You JG, Fu L, et al. A real 3D scene rendering optimization method based on region of interest and viewing frustum prediction in virtual reality. International Journal of Digital Earth. 2022;15(1):1081-100. DOI: 10.1080/17538947.2022.2080878

[22] Rong MQ, Cui HA, Shen SH. Efficient 3D Scene Semantic Segmentation via Active Learning on Rendered 2D Images. Ieee Transactions on Image Processing. 2023;32:3521-35. DOI: 10.1109/tip.2023.3286708

[23] lmola SAS, Qasim NH, Alasadi HAA. Robust method for embedding an image inside cover image based on least significant bit steganography. Informatica. 2022;46(9):[Online-only issue]. doi:10.31449/inf.v46i9.4362.

[24] Li B, Sharma A. Application of interactive genetic algorithm in landscape planning and design. Informatica. 2022;46(3):[page range if available]. doi:10.31449/inf.v46i3.4049.

AH-SpanBERT: Fine-Tuning SpanBERT with Archerfish Optimization for Power Grid Dispatcher Training

Liao Binjie[1], Zhang Hongtu[1], He Zhihua[1], Zhang Peng[1], Yang Tingtian[1], Liu Shudi[2], Luo Rongsen[2], Liu Feng[3*]
[1]State Grid Sichuan Electric Power Company, Sichuan, 610041, China
[2]State Grid Sichuan Electric Power Research Institute, Sichuan, 610041, China
[3]BeiJing Tsintergy Technology Co., Ltd., BeiJing, 100085, China
E-mail: liufeng8764@outlook.com, feiliu562@outlook.com, shengkaiwang2@outlook.com, jindu12@outlook.com, erlanxie123@outlook.com, weixiang234@outlook.com, fengzuoguo22@outlook.com, xueyanliu2407@outlook.com

Keywords: power grid dispatchers, large language models (LLMs), black start scenarios, decision-making, archerfish hunting fine-tuned span bidirectional encoder representations from Transformers (AH-SpanBERT)

Recieved: June 2, 2025

Power grid dispatchers play a critical role in maintaining the stability and efficiency of electrical networks. As power systems grow in complexity, traditional training methods struggle to equip dispatchers with the necessary skills for rapid decision-making and human-machine collaboration. This research explores the application of fine-tuning general large language models (LLMs) to enhance internal training processes for power grid dispatchers. The research proposed Archerfish Hunting Fine-tuned Span Bidirectional Encoder Representations from Transformers (AH-SpanBERT), a model that integrates the SpanBERT architecture with Archerfish Hunting (AH) optimization to improve decision-making and operational efficiency in power system management. To fine-tune the model, a comprehensive dataset of 1,000 simulated power grid operational records was created, covering scenarios such as equipment failures, grid fluctuations, and emergency responses. The data was preprocessed using domain-specific tokenization and term normalization to ensure consistency and contextual relevance. The AH-SpanBERT model was trained using this dataset, with specific prompt strategies designed to simulate real-world dispatch scenarios and foster interactive, scenario-based learning. The model's performance was evaluated across multiple key metrics, including factuality, logicality, stability, and security. Results show significant improvements in factuality (8.48 in operation monitoring), logicality (9.74 in general scenarios), stability (9.15 in black start procedures), and security (9.62 in black start procedures). The AH-SpanBERT model outperforms existing LLMs such as GPT-4 and GAIA-70B in these areas, demonstrating its potential to enhance dispatcher decision-making and human-machine collaboration in critical power grid operations. This research highlights the effectiveness of fine-tuning general LLMs with domain-specific data to improve dispatcher training and operational performance in power grid management.

Povzetek: Članek obravnava usposabljanje dispečerjev energetskih omrežij za obvladovanje naraščajoče kompleksnosti omrežja in neenotnih podatkov. Predlaga AH-SpanBERT, tj. SpanBERT fino uglašen z optimizacijo Archerfish Hunting, treniran na 1000 simuliranih dispečerskih zapisih. Metoda izboljša faktualnost, logičnost, stabilnost in varnost odločanja v scenarijih nad GPT-4 in GAIA-70B.

1 Introduction

A persistent power connection device requires the realization of data connectivity and business collaboration. As the power grid's intelligence increases, the power sector has to manage the rapidly expanding amount of information. The intelligent evolution of the power grid greatly depends on the significant amount of unstructured data that was gathered during the energy grid's construction and development. The information is a significant component of big data [1]. The evolution of Internet technologies has been continuously supported by the advancement of information technology. Numerous data resources, such as pertinent standard specifications, technical and product documentation, management documents, fault resolution records, etc., remain to be

acquired by the energy sector [2]. Enhancing power grid operating safety and stability for incorporating the long-term forecasting of alternative energies into power grid dispatching is necessary [3]. Energy is an alternative resource with great potential and a rapidly expanding global capacity. One of the main applications of energy is power generation. Considering that energy can be inconsistent and volatile, electrical grid stability and safety are of important concern [4]. The power system is an essential component of infrastructure for advancing the social and economic development of the nation. The present grid composition remains more complex, and the globalization of a local disturbance impact is becoming more prominent as ultra-high-voltage grids, extensive grid interactions, and grid coupling continue to be established constantly [5]. A significant quantity of power dispatch communication has been obtained as a consequence of the rapid technological advances and the comprehensive development of smart power grids. Designing a power dispatch knowledge visualization system and acquiring valuable information from relevant sources are essential for increasing team efficiency and assisting professionals in formulating decisions on power dispatch [6]. Energy sources, particularly solar and wind, have been actively developed in recent years, and installed capacity has increased quickly. However, solar power's intermittency and unpredictability make power grid scheduling more challenging, while wind power output's uncertainty and instantaneous volatility have a significant impact on the quality of energy and the power grid's stable operation [7]. Inadequate optimization could affect the model's overall performance, hyperparameter adjustments are complex, and the network's training time is delayed. The majority of the research presently in production applies incorrect data-processing techniques for important factors or fails to adequately take into consideration the factors influencing the immediate demand for regional power grids [8].

1.1 Problem statement

The increasing complexity of power grids challenges traditional methods for dispatchers, who struggle to handle vast, unstructured data and dynamic operational demands. Existing tools lack effective integration of domain-specific knowledge, leading to limited decision-making support and preparedness. This gap reduces dispatch efficiency and risks grid stability, especially during emergencies. There is an urgent need for advanced training solutions using fine-tuned large language models to improve dispatcher skills, enhance real-time decision accuracy, and facilitate better human-machine collaboration in power grid management.

1.2 Objective and contributions of this research

Investigating the use of optimized Large Language Models (LLMs) to improve power grid dispatchers' internal training is the intention of this research. Through domain-specific data adaptation of the Archerfish Hunting Fine-tuned Span Bidirectional Encoder Representations from Transformers (AH-SpanBERT) model, it enhances dispatcher decision-making and operational training. The objective of the research is to improve dispatchers' scenario-based learning by assessing essential instructional factors like accuracy, consistency, safety, and adaptability.

- To improve internal training procedures for power grid dispatchers, this research explores the use of domain-specific data to improve generalized LLMs.
- The power grid dispatcher operations dataset is to facilitate the creation and optimization of LLMs developed specifically for power grid dispatchers' internal training.
- To preprocess the obtained data, tokenization and domain-specific term normalization techniques are employed to provide consistency and contextual relevance.
- An extensive range of power system operational activities and decision-making scenarios, including operation adjustment, operation monitoring, and black start procedures, are supported by the proposed AH-SpanBERT model.
- The proposed method provides superior performance in the application of general large model fine-tuning technology of natural language in the internal training of power grid dispatchers.

2 Related work

The impact of the adoption of electric vehicles (EVs) on Italy's national power grid, with a particular emphasis on distribution and transmission systems, was described [9]. It concludes that curtailment of renewable energy, dispatching expenses, and grid breaches can all be considerably decreased by smart charging. However, there are drawbacks, such as the influence of localized distribution networks and the unpredictability of EV charging behavior. To develop a medical waste plasma hybrid peak load system for coal-fired power units, integrating syngas production, gas turbines, and renewable energy sources was described [10]. It finds that the system enhances energy efficiency and reduces operational costs, with a 6.20-year payback period. Limitations include the system's relatively low energy and exergy efficiency (37.38% and 36.19%, respectively). An optimization

framework for a PV-grid-integrated EVCS with battery storage and peer-to-peer charging strategies was determined [11]. The model focuses on minimizing operational costs, ensuring reliability, and enhancing profitability. Simulation results show a reduction in energy demand costs and a reduction in maximum demand. However, the model is sensitive to daily varying weather and load conditions, which may affect long-term performance. A low-carbon economic dispatching strategy using a feasible region (FR) model to manage the interaction between wind power (WP), energy storage (ES), and carbon capture power plants (CCPP) was proposed [12]. The model reduces carbon emissions by promoting WP consumption while addressing its uncertainty. Simulation results on IEEE 39-bus and 118-bus test cases confirm its effectiveness. However, the model's reliance on robust optimization and the complexity of the column constraint generation algorithm may limit scalability.

According to the programming, the investigation was limited in carrying out the operation in an average layer, as it lacks autonomous ability. To recognize nested named entities in the power dispatching domain, a Robustly Optimized BERT (RoBERTa)-Attention-FL model was suggested [13]. The findings showed that the RoBERTa-Attention-FL model, with a higher accuracy rate, enhanced the recognition performance when compared to the baseline model. The suggested method needs to recognize named entities and assess the relationship between named entity identification and relationship extraction for optimal use of potential knowledge in the field of grid dispatching. The two-stage, data-driven deep learning approach for ultra-short-term photovoltaic (PV) electricity forecasting was presented [14]. The Bidirectional Gating Recurrent Unit (BiGRU) and the skip connection were utilized in a bidirectional recurrent neural network for many historical states that captured the long- and short-time sequences of PV sequences. The attention mechanism enabled the neural network to contribute adaptive importance to more relevant historical states. The results showed that the developed approach was capable of predicting PV power reasonably well for short-range immediate forecasts. Short-term consistency and long-term frequency were removed with the unsuitable skip connection, along with a suitable approach that could not effectively train the linear regularity. A microgrid scheduling model that addresses the economic and environmental costs of microgrid schedules utilizing accurate forecasting of photovoltaic (PV) power generation was presented [15]. The proposed model incorporates a combined Sparrow Search Algorithm (SSA)-Convolutional Neural Network (CNN)-Bidirectional Long Short-Term Memory (Bi-LSTM) prediction model with attention mechanisms, and a more enhanced Quantum Particle Swarm Optimization (QPSO) algorithm to optimize dispatch. Together, the model produces high prediction accuracy and maintains stabilization of the microgrid. To improve the flexibility and stability of the complicated and frequently large-scale power systems to control properly, the Distributed AI (DAI) framework was used [16]. The results highlighted the significance and possible advantages of the suggested framework in maintaining the reliable and efficient performance of power systems. Using the system manager's monitoring, the suggested technique needs to provide smooth power distribution optimization throughout the nano-grid that greatly improves the smart grid management systems. A fault tracing method using data partition hybrid sampling and multiple incremental regression tree algorithms to improve power grid fault detection was proposed [17]. By combining anomaly detection, clustering, and information difference models, the method achieves high precision and efficiency, enhancing grid maintenance and safety. A system based on LLMs that was presented for developing a domain-specific language for urban power grid architecture was established [18]. The creation of semantically intelligent systems for smart urban power grid design was supported by expert validation that demonstrated an accuracy rate of 89.3%. The results represented a significant practical application value. Semantic depth knowledge problems were highlighted, such as the current approach of assessing alternatives, which mostly relies on word vector similarity and manual tests. To detect abnormal users in smart grids by combining Bidirectional Long Short-Term Memory (BiLSTM) and Convolutional Neural Networks (CNN) for feature extraction, followed by Adaptive Boosting (AdaBoost) for classification, aimed [19]. The dataset consists of power consumption data from a small substation. The method outperforms individual models but faces challenges in scalability and real-time deployment across larger grids. The Dynamic Black Hole-driven Deep Convolutional Generative Adversarial Network (DBH-DCGAN) to address limitations in traditional power system monitoring, enhancing real-time equipment status and operational adaptability, was proposed [20]. The method utilizes dynamic adjustments to improve model stability and flexibility. A large set of pre-processed power equipment images was used for evaluation, showing significant improvements in monitoring accuracy across various operating conditions. The DBH-DCGAN method achieved high recall, accuracy, and F1-score, demonstrating its effectiveness in power plant monitoring and advancing intelligent grid management. However, challenges remain in adapting the method to highly diverse real-world conditions and scaling for large systems. A framework for classifying renewable energy sources using a freely available multivariate time-series dataset, with data on solar, wind, and hydro, was proposed [21]. The research analyzed a range of models: Logistic Regression (LR), Support Vector Machine (SVM), XGBoost, Artificial Neural Networks (ANN), and 1D Convolutional

Neural Networks (1D-CNN). A hybrid model that incorporates an attention mechanism with the 1D-CNN to not only improve feature extraction but also concentrate on temporal patterns of interest. The attention-attuned model proved to be the highest performer in its classification ability, with elevated metrics. However, further work is required to improve model generalisation across different energy sources and operational conditions. A comparative summary table showing dataset sizes, tasks, metrics used, and results of prior models is shown in Table 1.

Table 1: Summary table

Model	Methodology	Dataset/Scope	Key Task	Performance Results	Limitations
EV-Grid Integration Evaluation [9]	Smart Charging Impact on Distribution and Transmission Systems	EV adoption in Italy's national grid	Evaluate EV's effect on the distribution network and grid dispatching	Reduces curtailment of renewable energy, dispatching expenses, and grid breaches	Influence of localized networks and unpredictability in EV charging behavior
Medical Waste Plasma Hybrid Peak Load System [10]	Hybrid system integrating syngas production, gas turbines, and renewable energy sources	Coal-fired power units	Energy efficiency and operational cost reduction	Enhances energy efficiency, 6.20-year payback period	Low energy and exergy efficiency (37.38% and 36.19%)
PV-Grid-Integrated EVCS with Battery Storage [11]	Optimization framework for minimizing operational costs	PV-grid integrated EV charging stations	Minimize operational costs, ensure reliability, and enhance profitability	Reduction in energy demand costs and maximum demand	Sensitive to daily weather and load conditions, which affect long-term performance
Low-Carbon Economic Dispatching [12]	Feasible region model to manage wind power, energy storage, and carbon capture	IEEE 39-bus and 118-bus test cases	Economic dispatching with wind power and carbon capture	Reduces carbon emissions, confirms effectiveness in test cases	Complex column constraint generation, limiting scalability
RoBERTa-Attention-FL for Named Entity Recognition [13]	RoBERTa with Attention-FL for nested named entity recognition	Power dispatch domain	Named entity recognition	Improved accuracy in entity recognition	Needs better relationship extraction and entity identification
BiGRU + Attention Mechanism for PV Forecasting [14]	BiGRU with attention mechanism for ultra-short-term PV forecasting	PV data for short-term forecasting	PV power forecasting for short-range immediate forecast	An accurate short-term forecast captures long and short time sequences	Issues with consistency and long-term frequency in predictions
Microgrid Scheduling with SSA-CNN-Bi-LSTM [15]	SSA-CNN-Bi-LSTM with QPSO for optimizing microgrid dispatching	Microgrid with PV power generation	Economic and environmental cost optimization	High prediction accuracy, stable microgrid performance	Needs more robust optimization techniques for varying conditions

Distributed AI Framework for Power Systems [16]	Distributed AI for large-scale power systems control	Smart grid and large-scale systems	Power system control and management	Improves flexibility and stability in power system control	Lack of real-time autonomous decision-making
Fault Detection with Hybrid Sampling [17]	Data partition, hybrid sampling, and incremental regression trees	Power grid fault data	Fault detection and grid maintenance	High precision and efficiency in fault detection	Complexity in handling large-scale datasets
LLMs for Urban Power Grid Architecture [18]	Large Language Models (LLMs) for developing a domain-specific language	Urban power grid design	Design of intelligent systems for urban grid architecture	89.3% accuracy in expert validation	Relies on word vector similarity and manual testing for semantic depth
GPT-4 [23]	Variable (General)	General language understanding, text generation	Factuality, Logicality, Stability	Factuality: 7.05, Logicality: 9.71, Stability: 7.52	Limited domain adaptation, no specific optimization for power grid tasks
GAIA-70B [23]	Power Grid Specific	Power grid management, load forecasting	Factuality, Logicality, Security	Factuality: 7.79, Logicality: 7.79, Stability: 8.64	Lack of real-time scenario adaptability, limited domain-specific vocabulary

2.1 Research gap: Current models for grid optimization, energy forecasting, and AI-driven power dispatching, such as smart charging for EVs and RoBERTa-Attention-FL, face significant challenges in real-time adaptability, scalability, and semantic understanding. Existing solutions struggle to address localized network behaviors and the unpredictability of charging patterns, limiting their effectiveness in dynamic environments. Additionally, short-term forecasting models like BiGRU + Attention Mechanism lack consistency over the long term, while AI models show promise in entity recognition but fall short in relationship extraction and complex semantic processing. AH-SpanBERT overcomes these issues by leveraging advanced span-based entity recognition to handle power-specific vocabularies and dynamic relationships in grid dispatching. Its ability to recognize named entities and relationship extraction allows for accurate, scalable, and real-time decision-making. By combining DL techniques like BiGRU, CNN-BiGRU Hybrid, and QPSO, AH-SpanBERT enhances forecasting accuracy, grid stability, and autonomous operations in large-scale energy systems.

2.2 Research methodology

To improve the internal training procedures for power grid dispatchers, this research investigates the use of domain-specific knowledge to improve generic LLMs. For effective performance, the research explores the data collection process, preprocessing techniques like tokenization, along with domain-specific term normalization, and the proposed method applications more comprehensively. Figure 1 shows the process of research methodology.

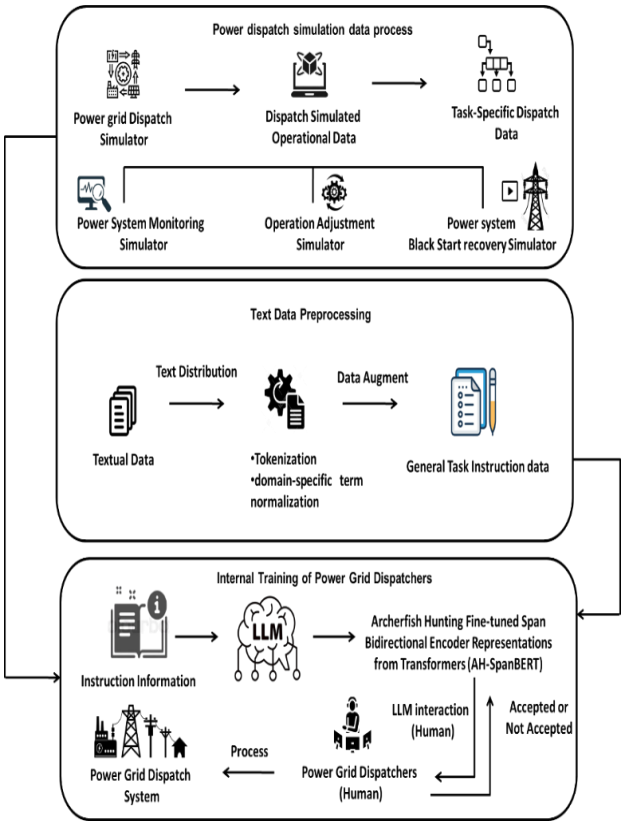

Figure 1: Methodology process involved with natural language in the internal training of power grid dispatchers

2.3 Data collection

The power grid dispatcher operations dataset is obtained from the open-source Kaggle [22]. The purpose of the dataset is to facilitate the creation and optimization of LLMs developed specifically for power grid dispatchers' internal training. The dataset contains 1,000 simulated functional records that span real-world situations like normal monitoring, emergency responses, equipment failures, and grid fluctuations. This dataset is beneficial for scenario-based LLM training, interactive dispatcher learning simulations, decision-making analysis under various complexity and urgency levels, along with collaborative human-machine modeling.

The data is split into training, validation, and test sets, in which 80% of the data will be used for training, 10% for validation, and 10% for testing. This split allows for proper evaluation of the model and prevents overfitting by ensuring that there is separate data to validate and test the model.

2.4 Data preprocessing through tokenization and domain-specific term normalization

Initial measures to clean and prepare unprocessed textual information for efficient performance are known as data pre-processing. There are two preprocessing techniques, such as tokenization and domain-specific term normalization, that are employed to preprocess the obtained data for the application of general large model fine-tuning technology of natural language in the internal training of power grid dispatchers.

2.4.1 Tokenization

Textual information is divided into meaningful components through proper tokenization, facilitating advanced modeling and computational processes. Text can be efficiently processed and comprehended by NLP algorithms by breaking the textual data into tokens, which leads to more precise and perceptive outcomes across a wide range of language processing applications. Modifying tokenization for domain-specific needs, including the needs of social media data, legal documentation, or research papers, is known as domain-specific tokenization.

2.4.2 Domain-specific term normalization

Impurity assessment is enhanced with the normalization step to distinguish between various document lengths and domain corpora sizes. The normalizing step and the impurity measure, as demonstrated by the research, make the technique more accurate in characterizing words for the application of general large-scale model fine-tuning technology of natural language.

2.5 Stemming: Stemming is a text preprocessing technique in NLP that reduces words to their root form by removing prefixes and suffixes. This process helps in simplifying words to a common base, making them more consistent and improving model accuracy by treating different forms of a word as equivalent. Algorithms like the Porter Stemmer and Snowball Stemmer are commonly used for this purpose. While stemming enhances data consistency and model performance, it may occasionally result in non-standard words, such as reducing "better" to "bet." Despite this, stemming is essential for improving tasks like text classification and information retrieval in NLP.

2.6 Power system operational tasks and decision-making scenarios development through archerfish hunting fine-tuned span bidirectional encoder representations from transformers (AH-SpanBERT)

The suggested Archerfish Hunting Fine-tuned Span Bidirectional Encoder Representations from Transformers (AH-SpanBERT) model supports a wide range of power system operational tasks and decision-making scenarios that integrate the Span Bidirectional Encoder Representations from Transformers (SpanBERT) and Archerfish Hunting (AH) optimization that enhances the internal training processes for power grid dispatchers. AH-SpanBERT is described in Figure 2.

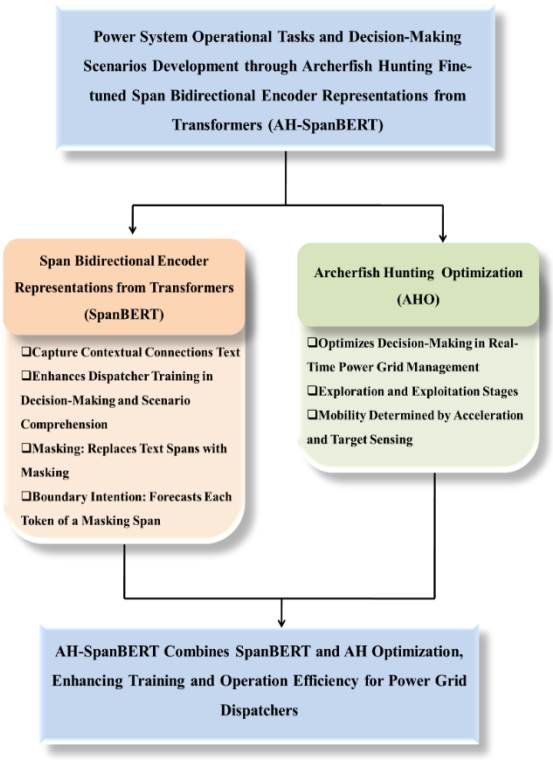

Figure 2: Flowchart of AH-SpanBERT

2.6.1 Span bidirectional encoder representations from transformers (SpanBERT)

A transformer-based model called SpanBERT predicts text spans and performs an exceptional task at capturing contextual connections in text. The technique is designed to comprehend domain-specific language, enhancing dispatcher training in decision-making and scenario comprehension. To improve the representation and prediction of text spans, a self-supervised pre-training technique called SpanBERT was introduced. One extended textual segment is sampled by SpanBERT for every training instance. The categories of SpanBERT processes, such as masking and boundary intention, are discussed.

Masking: This model iteratively samples text spans until the masking resource is exhausted, selecting a subset of tokens $B \subseteq A$ from a series of tokens $A = (a_1, a_2, \ldots, a_N)$. The method initiates iteration by sampling a span length (the number of words) from a geometrical distribution$\ell \sim GEO(q)$, which tends to benefit from shorter spans. Next, uniformly and randomly chooses an initial point for the masking of the span. Instead of using subword tokens, always samples a sequence of whole words, and the initial position should be the first character of a single word. The technique replaces all of the tokens in a span with masking, and it is performed at the span level.

Boundary Intention: The span selection approaches engage with a span's boundary tokens to provide a fixed-length representation of the span. The representations at the end of the span can ideally compress the majority of the inside span information. To accomplish the function, SpanBERT introduces a span boundaries target that uses the representations of the observation tokens at the boundaries to forecast each token of a masking span.

Representing the transformer encoder's output in each word of the sequence is represented by $a_1, \ldots, a_N$. Using the output encodings of the outer boundary tokens a_{t-1} anda_{f+1}, along with the position encoding of the target token q_{j-t+1}, it represents each token a_j in the masked span of tokens $(a_t, \ldots, a_f) \in B$, where (t, f) denotes its beginning and the end positions in Eq. (1). It allows for a real-time operational scenario to be built, and helps dispatchers make informed decisions about system performance, such as response to grid changes, equipment failures, and energy demand changes, improving training and operation efficiency.

$$b_j = f\left(a_{t-1}, a_{f+1}, q_{j-t+1}\right) \tag{1}$$

Where the masked words' positional relationships to the left boundary word a_{t-1} are indicated by positional embeddings$q_1, q_1, \ldots, etc$. For every token a_j in the masked span $(a_t, \ldots, a_f)$, SpanBERT adds the loss from the span border and the regular masked language model desired outcomes, utilizing the input embedded for the target tokens described in Eq. (2).

$$\mathcal{L}(a_j) = \mathcal{L}_1(a_j) + \mathcal{L}_2(a_j) = -\log Q\left(a_j \middle| \boldsymbol{a}_j\right) - \log Q\left(a_j \middle| \boldsymbol{b}_j\right) \tag{2}$$

Where, $\mathcal{L}(a_j)$ measures the prediction error of a_j based on its history, and $\mathcal{L}_2(a_j)$measure the error based on the related variable $\boldsymbol{b}_j$. The likelihood $\left(a_j \middle| \boldsymbol{a}_j\right)$ and $Q\left(a_j \middle| \boldsymbol{b}_j\right)$ assess prediction accuracy for both self-prediction and cross-variable relationships. This loss function could be applied to minimize the difference between actual and predicted outcomes, such as grid behaviors or operational decisions, and to increase the accuracy of the models for both the historical context and future predictions.

SpanBERT loss function Equation 2 is indeed the probability of predicting a_j given itself; this term would ideally be zero, as the model would predict a_j perfectly, making the likelihood zero abd contributing nothing to the loss. This is not consistent with the typical loss components used with SpanBERT-type models. The normal SpanBERT loss function is the combination of two objectives: the Masked Language Modeling (MLM) loss, which is concerned with predicting masked tokens, and the Span Boundary Objective (SBO) loss, which ensures span boundaries are predicted better. The equation in question does not capture either of these two components or the appropriate math form for either. A fix would involve properly combining MLM loss and SBO loss to be consistent with established formulations, to include both span prediction and token prediction objectives in the loss function. To pre-train span representations, SpanBERT uses a geometric distribution-based masking approach that masks full-word spans and a single-sequence data flow to optimize a supporting span-boundary achievement.

2.6.2 Archerfish hunting (AH) optimization

The AH optimization enhances LLM training for operational responsibilities in complicated, real-time power grid management by optimizing decision-making through the simulation of environment-specific problem-solving. The proposed AH's exploration and exploitation stages depend on the hunting and jumping behaviors of archerfish. Any optimization issue can be resolved using AH, provided that the power grid management is properly formulated. The AH optimization was selected for its biologically inspired exploration–exploitation balance and

suitability for nonlinear, high-dimensional scenarios like power grid dispatcher simulation. AH demonstrated improved convergence behavior and enhanced training dynamics in the AH-SpanBERT model with standard optimizers such as Adam and Particle Swarm Optimization (PSO) under identical training conditions. This will help quantify AH's performance advantage in terms of model accuracy, convergence rate, and decision quality in scenario-based training tasks. Assume that there are many archerfish in a search area of dimensions D. Archerfish location j at iteration s is as follows (Eq. (3)), and the population size is$n$.

$$A^{j,s} = (a_1, a_2, \dots, a_D) \tag{3}$$

Using Eq. (4), the point $A^{\langle j,0\rangle}$ is initialized at random with repetitions$s = 0$.

$$A^{\langle j,0\rangle} = \left(\alpha_1 \times \left(a_1^{maxi} - a_1^{mini}\right) + a_1^{mini}, \dots, \alpha_D \times \left(a_D^{maxi} - a_D^{mini}\right) + a_D^{mini}\right) \tag{4}$$

$A^{\langle j,0\rangle}$ is the initial position vector, α_1 is the random multiplier, and a uniform distribution. a_k^{maxi} and a_k^{mini} are upper and lower bounds, D defining the complexity of the optimization problem. Equation (4) initializes agent positions in the AH optimization algorithm and creates different places to begin within the defined bounds. The issues of starting position support the search space for optimization of energy grids, particularly for supporting task schedules and the overall efficiency of operations, ensuring a reachable solution as it relates to decision-making in active or dynamic grid management. AH initialization formula raises a valid concern regarding the ambiguity of the notation. The variables $(a_1, a_2, \dots, a_D)$ are described as "uniformly distributed random integers between o and 1," but the formula implies these values might be sequential components of the single random vector, which could lead to confusion. In standard optimization algorithms, each dimension is typically initialized with independent random values. Additionally, the notation a_1^{maxi} and a_D^{mini}, with the subscript i, is unclear regarding whether the bounds are shared across all dimensions or specific to each one.

Where the uniformly distributed random integers between 0 and 1 are denoted by$\alpha_1, \dots, \alpha_D$. An archerfish uses Eq. (5) to travel in the direction of a target when it identifies the generation of the vibration.

$$A^{\langle j,s+1\rangle} = A^{\langle j,s\rangle} + f^{-\left\|A_{prey}^{\langle l,s\rangle} - A^{\langle j,s\rangle}\right\|^2}\left(A_{prey}^{\langle l,s\rangle} - A^{\langle j,s\rangle}\right) \tag{5}$$

The position of the prey is determined in Eq. (6). The archerfish's mobility is determined by its acceleration of gravity (g), launch speed (v), and sensing angle (θ0), while the air friction is minimal. The desired outcome is assumed to be at the peak of the motion visualization. Using Eq. (7), an archerfish moves in the direction of the target that intends to capture.

$$A_{prey}^{\langle l,s\rangle} = A^{\langle j,s\rangle} + \left(0, \dots, \frac{u^2}{2Gr} \times \sin 2\theta_0, \dots, 0\right) + \varepsilon \tag{6}$$

$A^{\langle j,s+1\rangle}$ is the updated position of the j-th archerfish, $A^{\langle j,s\rangle}$ is the current position of the jth archerfish at iteration T. $A_{prey}^{\langle l,s\rangle}$ is the position of the prey at the sth iteration for the lth archerfish. e is the scaling factor that adjusts the magnitude of the movement based on the distance between the archerfish and its prey, $A_{prey}^{\langle l,s\rangle} - A^{\langle j,s\rangle}$ is the squared Euclidean diatance between the archerfish and he prey, ε is the small random perturbation, v is the lunch speed of the archerfish, g is the acceleration due to gravity, θ_0 is the sensing angle of the archerfish. The motion of an archerfish can be characterized by these equations as part of the AH optimization algorithm. The update process has two main components. First, the prey is updated via a physics formulation (Equation 6) based on its speed, gravitational pull, and the angle of the prey based on the archerfish's three-dimensional surface imaging.

$New_pos = current_pos + (target_pos - current_pos).e^{-||target_{pos} - current_pos}$ was Euclidean distance. However, it is more closely representative of physics-inspired metaheuristics (e.g., Gravitational Search Algorithms) than AH's original behavior based on a jump-based ballistic mechanism. To more closely align with the AH concept, this function must incorporate: directional jumps influenced by θ₀ projectile arc displacement perturbations ϵ. Moving forward, the updated algorithm provides an updated formulation, using a hybrid of physics-based trajectory (Equation 6) and normalized directional movement.

This must also be appropriately buffered by parameter θ₀. The perceiving angle value (θ_0) makes the exploration and exploiting phases switch. Therefore, the more effectively AH will utilize the search space when the value of θ_0 is to $\frac{\pi}{2}$or$-\frac{\pi}{2}$, and vice versa. Eq. (7) is used to produce the value of θ_0 at random.

$$\theta_0 = (-1)^y \times \alpha \times \pi \tag{7}$$

θ_0 is the perceiving angle controlling exploration, y is the random variable for alternating sign, α is the scaling factor for angle magnitude. π is the mathematical constant for

angle bounds. Equation (7) was used to create a method for generating the perceiving angle θ_0 randomly, which is important in AH optimization to control both exploration and exploitation. By selecting the value of the perceptive angle randomly, ensures that the archerfish will alternate between exploring the search space (θ_0 = π/2 or θ_0 = -π/2) and exploiting areas near a target (indicated by smaller values of θ_0). The concerns with the implementation of θ_0 logic and its effect on whatever exploration/exploitation is currently being done. The current implementation of θ_0, where randomly selected to be between π/2 and -π/2 is too limiting on the flipping between an exploration phase and an exploitation phase as designed from the formula in Equation (7). Instead of having a plan of action where consideration of exploration is always occurring and the exploitation logic in the $explore_exploit$ function is not able to be reached, to modify the code to allow θ_0 more flexibility in terms of how many values it take on a variety of angles, while simultaneously providing behavior that enacts both exploration and exploitation, making use of values controlled by θ_0, as intended for AH optimization.

The current implementation always assigns $\theta_0\ as\ \pm\pi/2$, making the condition if $abs(\theta_0)\ ==\ \pi/2$ always true and rendering the else branch redundant. To address this, will introduce continuous sampling of $\theta_0 \in [-\pi/2, \pi/2]\ using\ \theta_0 = (-1)\text{^}rand \times \alpha \times \pi$, allowing dynamic control via scaling factor α. The $explore_exploit()$ function then probabilistically switches between exploration and exploitation based on whether $|\theta_0| > \pi/4$. The model, as it is currently set, exists to log $updated_position$, but not to affect the model training of SpanBERT. The next iteration of AH represented the positions generated as hyperparameter vectors (learning rate, masking ratio, frozen layers, batch size) to fine-tune the model. The hyperparameters are decoded and used from the function $fine_tune_with_config()$. In this version, AH was able to know how to proceed conservatively with a lower learning rate, masking ratio, and batch size depending on the scenario being suited. This marks the beginning of a closed-loop system with AH insisting on the tuning of SpanBERT training creation and SpanBERT creating feedback for AH's directed search through a performance-based fitness score.

To prevent getting trapped in localized optimums, AH optimization employs a conventional approach. Algorithm 1 shows the working procedure of the proposed AH-SpanBERT model.

Algorithm 1: AH-SpanBERT

```
Import numpy as np
Import random
Class SpanBERT:
def __init__(self, model_name):
self.model_name = model_name
def preprocess(self, data):
    Return preprocess_data(data)
deffine_tune(self, data):
    Return fine_tune_model(data)
def predict(self, input_text):
    Return self.model.predict(input_text)
Class ArcherfishHunting:
def __init__(self, dimensions, population_size):
self.dimensions = dimensions
self.population_size = population_size
self.position = np.random.rand(population_size, dimensions)
defupdate_position(self, current_position, target_position): Return current_position+(target_position-current_position)*np.exp(-np.linalg.norm(target_position - current_position))
defexplore_exploit(self, position, prey_position, theta_0):
if abs(θ_0) == np.pi / 2:
    Return self.update_position(position, prey_position)
else:
    Return position
def simulate(self):
for _ in range(self.population_size):
prey_position = self.position[random.randint(0, self.population_size - 1)]
target_position = self.position[random.randint(0, self.population_size - 1)]
θ_0= random.choice([-np.pi / 2, np.pi / 2])
new_position = self.explore_exploit(self.position, prey_position, θ_0)
self.position = new_position
    Return self. position
Class AHSpanBERTModel:
def __init__(self, span_bert_model, archerfish_model):
self.span_bert = span_bert_model
self.ah_optimizer = archerfish_model
defoptimize_training(self, training_data, scenario_data):
fine_tuned_model = self.span_bert.fine_tune(training_data)
training_scenarios = generate_scenarios(scenario_data)
for scenario in training_scenarios:
updated_position = self.ah_optimizer.simulate()
predictions = self.span_bert.predict(scenario['input'])
scenario['actions'] = predictions
scenario['updated_position'] = updated_position
    Return training_scenarios
```

Through the simulation of domain-specific operational situations, such as task management, system monitoring, and emergency protocols, the AH-SpanBERT model is optimized to improve power grid dispatcher training. The proposed technique makes interactive, scenario-based

learning, which enhances flexibility, knowledge retention, and decision-making. The approach facilitates context-aware, real-time responses, improving human-machine cooperation in power grid systems and dispatcher performance across a range of operational tasks.

3 Results and discussions

This section deliberates on the results produced by the implementation of the model, including parameter setup, evaluation criteria, and comparative phase.

3.1 Experimental setup

For fast processing and effective multitasking, the research makes use of an AMD Ryzen 7 5800X CPU and 32GB DDR4 memory. Graphics-intensive operations are managed by the NVIDIA GeForce RTX 3080 GPU. For GPU computing performance and scalability, the system runs on Windows 11 and uses Python 3.9, scikit-learn, and TensorFlow libraries

3.2 Parameters setup

AH-SpanBERT hyperparameters as described in Table 2.

Table 2: Parameter setup

Hyperparameter	Value
Learning Rate	0.0001
Epochs	50
Batch Size	32
Layers Frozen	The first few layers of SpanBERT model are frozen to maintain the pre-trained knowledge.
Loss Function	Combination of Masked Language Modeling (MLM) loss and Span Boundary Objective (SBO) loss
Loss Function Values	Regularization values of 0.5 for both MLM and SBO losses

3.3 Evaluation criteria

The evaluation criteria demonstrate the cost consumption of the proposed AH-SpanBERT technique's efficiency in the internal training of power grid dispatchers, and resulted in the 0 to 100 iterations & 0 to 500 iterations (Figure 3 a-b). The 100-iteration run is effective for quicker results because it quickly converges and maintains performance. Over time, better optimization could become possible due to the 500-iteration run, which allows for additional exploration and improvement. The AH-SpanBERT method shows significant outcomes in the cost function in that provides less cost consumption in performing the power grid dispatcher's internal training process.

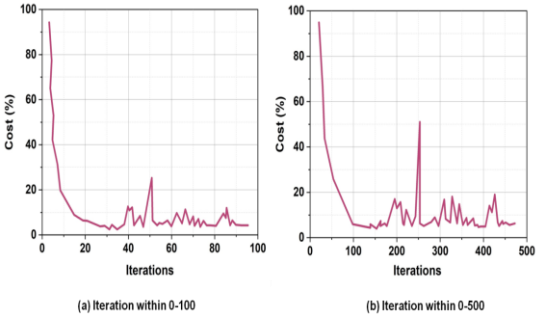

Figure 3: Outcomes of cost assessment with (a) iteration within 0-100 and (b) iteration within 0-500

3.4 Comparison phase

The proposed AH-SpanBERT and the existing models such as Generative Pre-trained Transformer 4 (GPT-4) [23] and Grid Artificial Intelligent Assistant (GAIA-70B) [23] are compared for providing an effective performance in internal training of power grid dispatchers along with various parameters like factuality, logicality, stability and security for various scenarios like general, dispatch, operation monitoring and black start.

- ***Factuality*** indicates that the information is valid and the findings accurately reflect the actual circumstances, which is crucial for valid decision-making in the operation of power systems.
- ***Logicality*** is concerned with the precision of logical inference and the dependability of the data utilized in the enhancement of power grid dispatcher learning assessment.
- ***Stability*** maintains operational continuity and reliability. The parameter also assesses LLMs' capacity to sustain similar outputs in dynamic situations.
- ***Security*** indicates the significance of ensuring that operational security provides model applications that can never damage the power system's security.

The evaluation metrics (factuality, logicality, stability, and security) scaled from 0 to 10, were adapted from the Elecbench benchmark (Zhou et al., 2024), which provides a standardized framework for assessing LLM performance in power dispatch tasks. The scoring system follows Elecbench's normalized evaluation procedure, where expert raters assess model responses based on alignment with ground truth, operational logic, and scenario safety. Each metric was averaged over multiple annotated responses across four scenarios to ensure consistency and comparability. This alignment ensures that our reported results are interpretable within the context of existing power grid LLM evaluation standards.

The purpose of the general scenario design is to assess the LLM's proficiency in handling data analysis, forecasting, and basic knowledge question-and-answer tasks related to day-to-day power system management. AH-SpanBERT achieves high scores in factuality (8.32), ensuring accurate information delivery. Logicality is very high at 9.74, supporting sound reasoning. Security (9.38) and stability (8.76) confirm the model's reliability and safety in everyday power system management and training tasks. Table 2 and Figure 4 represent the numerical outcomes of factuality in four scenarios.

Table 2: Numerical outcomes of General power systemwith four scenarios

Models	General power system			
	Factuality	**Logicality**	**Security**	**Stability**
GPT-4 [23]	7.05	9.71	9.28	7.52
GAIA-70B [23]	7.79	7.79	9.29	8.64
AH-SpanBERT [Proposed]	8.32	9.74	9.38	8.76

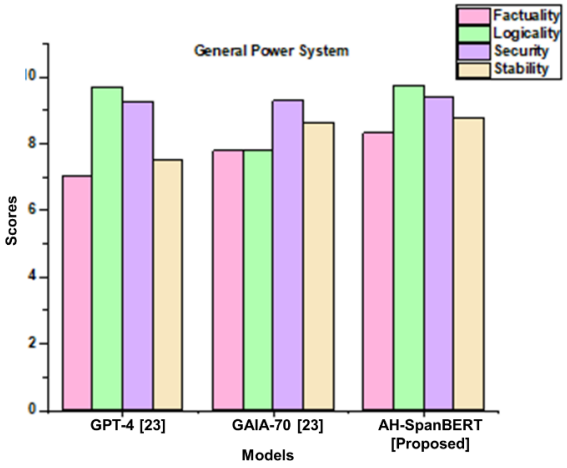

Figure 4: Graphical illustration of factuality results in general scenarios.

The dispatch sub-scenario is essential for assessing the efficiency of LLMs data analysis, forecasting, and optimal decision-making, all of which are vital for improving the stability and efficiency of the sector. In dispatch operations, AH-SpanBERT maintains solid factuality (7.59) and logicality (9.37), facilitating optimal decision-making. The security score of 9.40 indicates that the model safeguards operational safety, while stability at 8.15 reflects consistent output, essential for reliable performance in dynamic dispatch scenarios. Mathematical results of four scenarios in logicality are provided in Table 3 and Figure 5.

Table 3: Mathematical results of dispatch.

Models	Dispatch			
	Factuality	**Logicality**	**Security**	**Stability**
GPT-4 [23]	7.42	9.30	9.35	8.07
GAIA-70B [23]	7.45	7.52	9.37	7.44
AH-SpanBERT [Proposed]	7.59	9.37	9.40	8.15

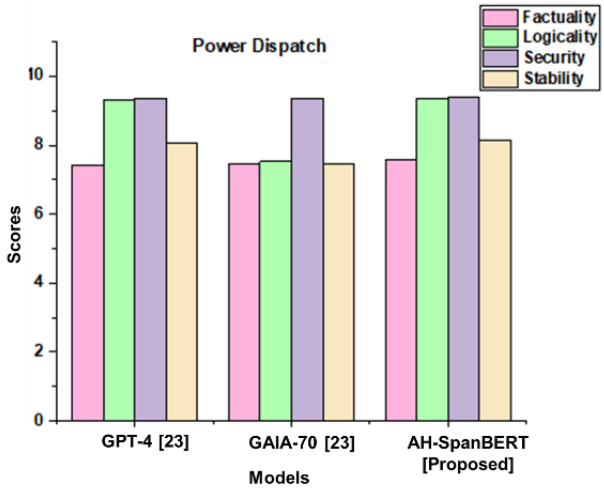

Figure 5: Mathematical outcomes of logicality with dispatch

Operation monitoring places significant demands on data speed and accuracy in the design of the assessment framework, requiring LLMs to have strong data gathering and processing skills along with the capacity to promptly recognize and address possible problems. For operation monitoring, AH-SpanBERT delivers high factuality (8.48) and logicality (8.97), demonstrating effective data interpretation and problem identification. The security score of 9.39 ensures safe application, while stability (7.14) remains adequate, supporting dependable performance despite real-time monitoring issues. Figure 6 and Table 4 show the outcomes of operation monitoring.

Table 4: Operation monitoring outcomes with several parameters

Models	Operation Monitoring			
	Factuality	Logicality	Security	Stability
GPT-4 [23]	8.21	8.92	9.10	6.16
GAIA-70B [23]	8.42	7.78	9.35	7.00
AH-SpanBERT [Proposed]	8.48	8.97	9.39	7.14

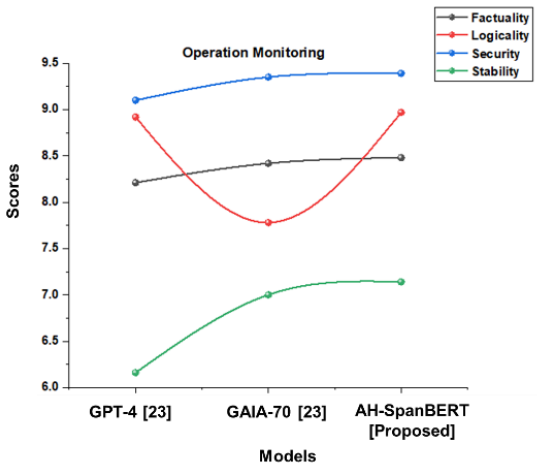

Figure 6: Visual depiction of operation monitoring

The accurate assessment of LLMs in this context is crucial for comprehending their practical utility and potential in identifying faults and recovery procedures, as Black Start is necessary to preserve power system continuity and avert large-scale grid failures. During black start procedures, AH-SpanBERT achieves high factuality (8.43) and locality (8.99), supporting accurate fault recovery decisions. This model scores highest in security (9.62), and stability (9.15), emphasizing the model's robustness and reliability in critical emergency power system restoration scenarios. Table 5 and Figure 7 determine the algorithmic outcomes of black start.

Table 5: Algorithmic outcomes of black start

Models	Black Start			
	Factuality	Logicality	Security	Stability
GPT-4 [23]	8.39	8.84	9.53	9.03
GAIA-70B [23]	7.94	7.85	9.50	7.28
AH-SpanBERT [Proposed]	8.43	8.89	9.62	9.15

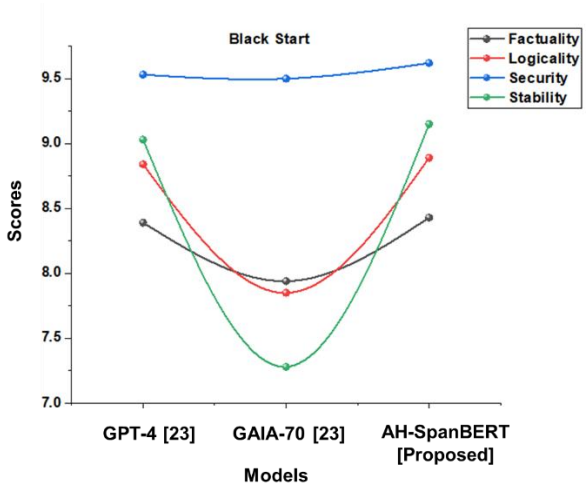

Figure 7: Results of the black start scenario with various performance matrices

Table 5 shows the standard deviation values for four metrics (Factuality, Logicality, Security, and Stability) applied to the various power system tasks using the AH-SpanBERT Model. The standard deviation for the four metrics is observed between a range of 0.05 to 0.11. This indicates slight differences in model performance across the power system tasks. Factuality displays little variation in its standard deviations (0.06 to 0.10); Logicality had slightly more variation, especially in the General Power System and Dispatch tasks (0.07 – 0.09). Security had a higher standard deviation observable during the Black Start task (0.10), delineating there were slight fluctuations in security predictions in this task. Stability shows the highest standard deviations in two tasks, General Power System and Dispatch (0.10 and 0.11, respectively) and indicate less stable predictions in these two tasks compared to the other tasks. Overall, the model performance shows little variation, although these particular tasks (Dispatch

and General Power System) may vary more in some metrics.

Table 5: Standard deviation values

Metric	**Standard Deviation – AH-SpanBERT [Proposed]**			
	General power system	**Dispatch**	**Black Start**	**Operation Monitoring**
Factuality	0.07	0.10	0.07	0.06
Logicality	0.09	0.07	0.06	0.08
Security	0.08	0.06	0.10	0.05
Stability	0.10	0.11	0.09	0.07

Table 6 indicates the performance metrics (Accuracy, Precision, Recall, F1-Score) of a model across 5 folds. The model's performance is consistently strong, with accuracy ranging from 0.90 to 0.99 (mean = 0.97), and high precision (range 0.90 - 0.99; mean = 0.97) indicates positive predictions are generally correct. Recall ranges from 0.90 - 0.99 (mean = 0.97), confirming the model's effectiveness in targeting positive instances. Finally, F1-Score also exhibits the same pattern of reliability (range 0.90 - 0.99; mean 0.97) as well as consistency across folds.

Table 6: Results of 5-Fold Cross-Validation

Fold	**Accuracy**	**Precision**	**Recall**	**F1-Score**
1	0.99	0.97	0.90	0.99
2	0.91	0.99	0.92	0.90
3	0.99	0.96	0.99	0.97
4	0.90	0.99	0.91	0.99
5	0.92	0.90	0.93	0.91
Average	0.97	0.98	0.97	0.97

4 Discussion

The internal training of power grid dispatches, enhanced by leveraging fine-tuning of general LLMs with domain-specific data, was the main objective of the research. Existing methods, including traditional training approaches and generic LLMs like GPT-4 [23] and GAIA-70B [23], have limitations such as insufficient domain adaptation, lack of scenario-specific understanding, and inconsistent performance in critical operational tasks. By applying specialist knowledge and optimizing a dataset of power grid operational data, the proposed AH-SpanBERT model overcomes the shortcomings of power system models. The domain-aware adaptation enhances stability, security, logical thinking, and factual correctness in a variety of situations. By filling up the gaps in previous models and providing a strong tool for dispatcher training and power system management, AH-SpanBERT dramatically increases operational reliability, knowledge retention, and decision-making accuracy.

The AH-SpanBERT model, leveraging Span masking and AH optimization, outperforms existing models like GPT-4 and GAIA-70B in key areas such as factuality, logicality, stability, and security. Span masking enables more accurate contextual understanding of domain-specific terminology, which is crucial for power grid dispatchers, while AH optimization simulates environment-specific problem-solving to enhance decision-making. In performance metrics, AH-SpanBERT excels, with higher factuality, logicality, and security scores, particularly in critical tasks like operation monitoring and black start scenarios. Unlike GPT-4 and GAIA-70B, which lack domain-specific focus, AH-SpanBERT's fine-tuning on power grid data ensures more reliable and accurate performance in real-time decision-making. However, its reliance on historical data may limit adaptability to unforeseen grid changes, and in highly uncertain scenarios, AH optimization may occasionally lead to suboptimal outcomes. Overall, AH-SpanBERT demonstrates substantial improvements in power grid dispatcher training, addressing the shortcomings of previous models, though it still has room for enhancement in handling dynamic, real-time disruptions.

5 Conclusion

Power grid dispatchers play an essential role in maintaining the consistent, effective, and safe functioning of electrical networks. The use of domain-specific data to refine the generic LLMs to improve internal training procedures for power grid dispatchers was examined in the research. The AH-SpanBERT model was developed to facilitate black start processes, operation monitoring, and general dispatch, which were some of the many operating responsibilities and decision-making scenarios. An extensive dataset was assembled from several sources, including operational manuals, emergency procedures, internal communications, training materials, and historical dispatch logs. Utilizing tokenization and domain-specific word normalization, the data was preprocessed for contextual relevance and consistency. Rapid techniques were created to mimic authentic dispatch situations, allowing trainees to learn interactively through scenario-based learning. The model's power dispatch performance was assessed to evaluate LLMs on important parameters that were necessary for efficient power system

management, including factuality (8.48 in operation monitoring), logicality (9.74 in general), stability (9.15 in black start), and security (9.62 in black start). Experimental findings showed significant improvement in factuality (8.48 in operation monitoring), logicality (9.74 in general), stability (9.15 in black start), and security (9.62 in black start) across dispatchers with different scenarios. In power dispatch operations, the research showed that the suggested General Large Model greatly improved human-machine interaction, operational efficiency, and decision-making capacities.

Limitations and future scopes: The use of a small, simulated Kaggle dataset (1,000 records) may limit the model's generalizability to real-world dispatcher logs, affecting performance under authentic, complex grid conditions. Reliance on historical information limits the investigation and could affect the model's capacity to adjust to changes in the power grid. Enhancing operational effectiveness and cooperation across various grid environments could expand the model to more power system management categories in the future. In future revisions, will explicitly outline risk mitigation strategies, such as human-in-the-loop validation, real-time alert prioritization, and fallback protocols. These ensure AI recommendations serve as augmentative tools, supporting but not overriding the dispatcher's expert decisions in high-stakes operational scenarios.

Acknowledgement: This work was supported by the Science and Technology Project of State Grid Sichuan Electric Power Company under Grant 52199723003A

References

[1] Wan W, Liu Y, Han X, Wang H (2021) Evaluation model of power operation and maintenance based on text emotion analysis. *Math Probl Eng* 2021:2824689. https://doi.org/10.1155/2021/2824689.

[2] Chen T, Zhang S, Wang Y, Chen Z, Jing W (2021) Construction methods of knowledge mapping for full-service power data semantic search system. *J Signal Process Syst* 93:275-284. https://doi.org/10.1007/s11265-020-01591-6

[3] Li X, Yang N, Li Z, Huang Y, Yuan Z, Song X, Zhang L (2022) Confidence estimation transformer for long-term renewable energy forecasting in reinforcement learning-based power grid dispatching. *CSEE J Power Energy Syst*. https://doi.org/10.17775/CSEEJPES.2022.02050

[4] Wang L, He Y, Li L, Liu X, Zhao Y (2022) A novel approach to ultra-short-term multi-step wind power predictions based on encoder–decoder architecture in natural language processing. *J Clean Prod* 354:131723. https://doi.org/10.1016/j.jclepro.2022.131723

[5] Ji Z, Wang X, Zhang J, Wu D (2023) Construction and application of knowledge graph for grid dispatch fault handling based on pre-trained model. *Glob Energy Intconnect* 6:493-504. https://doi.org/10.1016/j.gloei.2023.08.009

[6] Tan Z, Chen Y, Liang Z, Meng Q, Lin D (2023) Named Entity Recognition for Few-Shot Power Dispatch Based on Multi-Task. *Electronics* 12:3476. https://doi.org/10.3390/electronics12163476

[7] Dong Z, Zhang Z, Huang M, Yang S, Zhu J, Zhang M, Chen D (2024) Research on day-ahead optimal dispatching of virtual power plants considering the coordinated operation of diverse flexible loads and new energy. *Energy* 297:131235. https://doi.org/10.1016/j.energy.2024.131235

[8] Li B, Liao Y, Liu S, Liu C, Wu Z (2025) Research on Short-Term Load Forecasting of LSTM Regional Power Grid Based on Multi-Source Parameter Coupling. *Energies* 18:516. https://doi.org/10.3390/en18030516

[9] Rancilio G, Cortazzi A, Viganò G, Bovera F (2024) Assessing the nationwide benefits of vehicle–grid integration during distribution network planning and power system dispatching. *World Electric Vehicle* J 15:134. https://doi.org/10.3390/wevj15040134

[10] Zheng Q, Chen H, Wu H, Zheng H, Pan P, Bian J, Wang X (2024) Performance analysis of a medical waste gasification-based power generation system integrated with a coal-fired power unit considering dispatching optimization. *Energy* 310:133200. https://doi.org/10.1016/j.energy.2024.133200

[11] Bokopane L, Kusakana K, Vermaak H, Hohne A (2024) Optimal power dispatching for a grid-connected electric vehicle charging station microgrid with renewable energy, battery storage and peer-to-peer energy sharing. *J Energy Storage* 96:112435. https://doi.org/10.1016/j.est.2024.112435

[12] Yu G, Zhang Z, Cui G, Dong Q, Wang S, Li X, Shen L, Yan H (2024) Low-carbon economic dispatching strategy based on feasible region of cooperative interaction between wind-storage system and carbon capture power plant. *Renew Energy* 228:120706. https://doi.org/10.1016/j.renene.2024.120706

[13] Chen Y, Lin D, Meng Q, Liang Z, Tan Z (2023) Named entity identification in the power dispatch domain based on RoBERTa-attention-FL model. *Energies* 16:4654. https://doi.org/10.3390/en16124654

[14] Zhou H, Wang J, Ouyang F, Cui C, Li X (2023) A two-stage method for ultra-short-term PV power forecasting based on data-driven. *IEEE Access* 11:41175-41189. https://doi.org/10.1109/ACCESS.2023.3267515

[15] Zhang T, Zhao W, He Q, Xu J (2025) Optimization of microgrid dispatching by integrating photovoltaic power generation forecast. *Sustainability* 17:648. https://doi.org/10.3390/su17020648

[16] Ioannou II, Javaid S, Christophorou C, Vassiliou V, Pitsillides A, Tan Y (2024) A distributed AI framework for Nano-Grid power management and control. *IEEE Access* 12:43350-43377. https://doi.org/10.1109/ACCESS.2024.3377926

[17] Yang S, Fu Y, Li S (2024) Fault traceability of power grid dispatching system based on DPHS-MDS and LambdaMART algorithm. *Energy Informatics* 7:85. https://doi.org/10.1186/s42162-024-00391-7

[18] Xu Y, Wang T, Yuan Y, Huang Z, Chen X, Zhang B, Wang Z (2025) LLM-Enhanced Framework for Building Domain-Specific Lexicon for Urban Power Grid Design. *Appl Sci* 15:4134. https://doi.org/10.3390/app15084134

[19] Zhang Y, Gao Y, Zhao Z (2025) Research on operation and anomaly detection of smart power grid based on information technology using CNN+ Bidirectional LSTM. *Informatica* 49:7037. https://doi.org/10.31449/inf.v49i7.7037

[20] Liu J, Zhao W, Gu F (2025) Panoramic Intelligent Monitoring of Power Equipment Using Dynamic Black Hole-Driven DCGAN Under New Power Systems. *Informatica* 49:8037. https://doi.org/10.31449/inf.v49i8.

[21] Hong Q, Chen X, Zhai X, Sun X, Zong Y (2025) Hybrid Deep Learning-Based Renewable Energy Classification for Smart Grid Optimization. *Informatica* 49:8366. https://doi.org/10.31449/inf.v49i25.8366

[22] https://www.kaggle.com/datasets/ziya07/power-grid-dispatcher-operations-dataset/data

[23] Zhou X, Zhao H, Cheng Y, Cao Y, Liang G, Liu G, Zhao J (2024) Elecbench: A power dispatch evaluation benchmark for large language models. *arXiv:*2407.05365. https://doi.org/10.48550/arXiv.2407.05365

BS-CYOLOv5: A Deep Learning and Backtracking Search Framework for Multi-Sensor UAV Navigation and Obstacle Avoidance

Zongqiang Deng
China People's Police University, Basic Courses Teaching Department of Guangzhou Campus, Guangzhou, Guangdong, 510663, China
E-mail: jenekop2006@126.com

Keywords: unmanned aerial vehicles (UAV), autonomous navigation, obstacle avoidance, backtracking search-mutated customized YOLOv5 (BS-CYOLOv5), Deep Learning (DL)

Recieved: May 13, 2025

Unmanned Aerial Vehicles (UAVs) are increasingly used in applications such as aerial surveillance, disaster response, and urban air mobility. Autonomous navigation and obstacle avoidance are critical for UAVs to operate safely in dynamic environments. Traditional obstacle avoidance methods rely on predefined rules and sensor-based heuristics, which struggle with real-time adaptability in complex environments. This presents a Deep Learning (DL)-based Backtracking Search-mutated Customized YOLOv5 (BS-CYOLOv5) framework, integrating multi-sensor data processing, real-time obstacle detection, and optimized path planning. The dataset includes 10,000 labeled UAV flight data samples recorded using RGB cameras, LiDAR, IMU, and GPS, the gathered data was split with 80% training and 20 % testing. Data pre-processing techniques, such as normalization, are applied to enhance model performance and generalization. For obstacle detection, the CYOLOv5 model is employed due to its high detection accuracy, enabling real-time identification of obstacles in various environments. Navigation and path planning are optimized using the Backtracking Search Algorithm (BSA), which dynamically adjusts flight trajectories to ensure efficient and collision-free navigation. Although these components play independent functions, they are tightly integrated into the BS-CYOLOv5 architecture, where BS also fine-tunes detection-related hyper parameters to improve performance. Experimental results demonstrate that the proposed approach enhances UAV obstacle avoidance accuracy and navigation efficiency. The results reveal statistically substantial improvements in the obstacle detection accuracy (98%) and high precision, recall, f1-score and IOU, when evaluated on the full 2,000-image test set. It contributes to advancing intelligent UAV systems by integrating state-of-the-art DL and optimization techniques for enhanced autonomy and safety in real-world scenarios.

Povzetek: Članek obravnava samodejno navigacijo UAV-jev, kjer klasične metode slabo delujejo v dinamičnih okoljih. Predlaga BS-CYOLOv5, ki združuje večsenzorsko zaznavanje z izboljšanim YOLOv5 in Backtracking Search za optimizacijo hiperparametrov ter poti.

1 Introduction

The widespread popularity of UAVs, also known as drones, results from their multiple military and commercial uses and research applications [1]. UAV efficiency alongside safety and environment adaptation strongly depends on reliable autonomous navigation functionality combined with obstacle avoidance capabilities. The autonomous navigation systems of UAVs make them capable of executing surveillance tasks as well as search and rescue operations together with environmental monitoring and logistics without needing continuous human supervision [2]. UAVs benefit from this function, which eliminates operator overreach while improving operational output and decreasing the chance of mishaps. The obstacle avoidance feature enables UAVs to safely traverse complicated spaces without accidents, thus improving their mission-performance accuracy [3]. UAV platforms have advanced in terms of mobility, selectivity, accuracy, short operation cycles, low maintenance costs, practicality, and safety [4].

UAV usage continues to expand within agricultural operations and delivery service sectors alongside infrastructure assessment and disaster relief responsibilities, which underlines the standards for improved guidance systems and obstacle detection capabilities [5]. Drones may modify their flying routes in response to environmental circumstances and unanticipated impediments because of autonomous navigation, which improves UAV decision-making and reactivity. An efficient obstacle detection system decreases

the possibility of UAV or surrounding infrastructure damage for better operational reliability and mission accomplishment [6]. Figure 1 displays the obstacle avoidance and autonomous navigation technologies for UAVs.

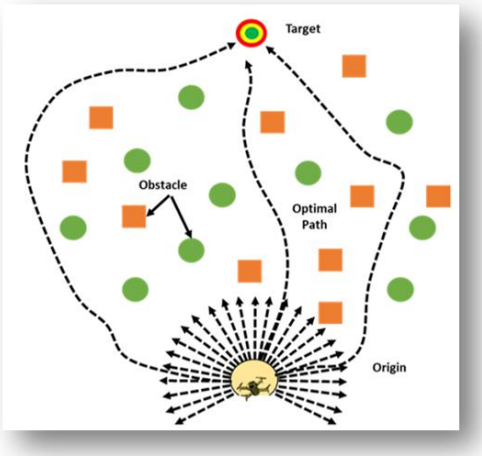

Figure 1: Obstacle avoidance and autonomous navigation technologies for UAV

Technological developments for UAV systems will concentrate on developing precise navigational capabilities and dependable detection mechanisms as well as enhancing power efficiency and response speeds over time [7]. The safe and effective operation of UAVs depends on self-navigational systems combined with obstacle detection capabilities in different operational settings. Continuous research into UAV technology has improved its capabilities, opening up new business prospects and enabling risky, complex operations [8]. Performance stability remains a challenge for diverse, unpredictable conditions, although significant progress has been made. The performance of sensors and navigation precision becomes compromised by environmental factors, which include wind conditions combined with rain and changing light illumination. This investigation presents a DL-based BS-CYOLOv5 framework integrating multi-sensor data processing, real-time obstacle detection, and optimized path planning. The research investigates the integration of deep learning and optimization approaches to improve UAV autonomous navigation. The following questions direct the research's focus towards detection accuracy, model optimization, and real-world adaptability.

1. How can deep learning models be tuned to improve real-time obstacle identification accuracy in UAV navigation based on multi-sensor data?
2. How does backtracking search-based hyperparameter tuning improve YOLOv5's performance for UAV obstacle avoidance?

In Section 2, a list of relevant works was presented. Section 3 includes the methodology is described. Section 4 contains the findings of the research. The discussion portion is provided in Section 5, and Section 6 contains the conclusion.

2 Related work

To enable navigation in locations with a lot of obstacles, [9] suggested a reactive limited navigation strategy for a UAV with integrated obstacle avoidance. Nonlinear Model Predictive Control (NMPC) was the foundation of the suggested navigation architecture. The NMPC's parameter restricted the UAV's position area. A unique method for a tiny UAV's autonomous navigation in tree plantations using just one camera was examined in [10]. An ML model called the Faster Region-based Convolutional Neural Network (Faster R-CNN) was developed for the purpose of detecting tree trunks because monocular vision was unable to give depth information.

The safety issue of accidents with non-stationary objects was demonstrated in [11], which was frequently ignored because there was a dearth of technology and strategies to deal with it. The computationally demanding challenge of utilizing commercial sensors was addressed in a unique way that uses DL algorithms. Using image input, [12] investigated the soft-actor-critic technique to teach a drone to autonomously avoid obstacles in continuous action space. The findings demonstrated that by just entering the depth map, the method allowed the UAV to ignore obstacles in the testing area. Additionally, without retraining, it exhibited a greater avoidance of obstacles rate in the modified environment.

To increase productivity and assurance of drone flight safety, [13] suggested employing UAVs to perform duties like path planning and obstacle avoidance. A popular reinforcement learning state–action–reward–state–action (SARSA) algorithm was compared with the suggested method. Deep Reinforcement Learning (DRL) and probabilistic algorithms were proposed in [14] to prevent collisions that consume less energy. The suggested algorithms could be executed at the Multi-Access Edge Computing (MEC) or on top of the UAV, depending on the task overhead and UAV capacity. The suggested solutions have been tested in a challenging setting with several UAVs moving randomly and uncorrelated in a restricted region.

An actual three-dimensional (3D) path planner was proposed in [15] to guide the UAV toward its goal through an obstacle-free route. The suggested path planner was heuristic in the sense of the A⋆ method, but unlike A⋆, it does not need border nodes to be maintained in memory. The planner calculated collision-free routes by using the relative positions of identified objects, or barriers. The Dual Experience Attention Convolution Soft Actor-Critic (DAC-SAC) technique was proposed in [16]. The

technique used a convolutional layer in conjunction with a self-attention method, a dual memory buffer pool, and the soft-actor-critic technique.

The UAV flight path prediction in dynamic situations was improved by utilizing Artificial Neural Networks (ANNs) [17]. A Python-based multi-hidden-layer ANN model was trained on two datasets using tenfold cross-validation. The results reveal high accuracy in distance prediction (R^2 = 99.45%, MAE = 0.158), but poor altitude prediction (R^2 = 53.95%). The method's limitation lies in its reduced performance for altitude estimation. Table 1 shows the comparative analysis of the related work.

Table 1: Comparative analysis of the related work

Ref.	Year	Area Focused	Algorithms	Limitations	Performance
[9]	2021	UAV Navigation	NMPC, Proximal Averaged Newton for Optimal Control (PANOC), Optimization Engine (OpEn), Penalty Method	Computational limitations on UAV onboard processing power	Fast solutions with limited computational power, real-time obstacle avoidance, and improved closed-loop performance
[10]	2021	UAV Navigation in Precision Agriculture	Faster Region-based CNN (Faster R-CNN), Monocular Vision	Lack of depth information from monocular vision, limited by camera accuracy in low-light conditions	Successful in 11 flight tests across two different environments, accurate and robust obstacle avoidance
[11]	2021	UAV Collision Avoidance	Deep Learning, Transfer Learning	The computational intensity of real-time processing, limited by commercial vision sensor capability	Successful real-time collision avoidance with dynamic objects, positive transfer learning results, and effectiveness in real-world tests.
[12]	2021	Drone Obstacle Avoidance	Soft-Actor-Critic (SAC)	Discrete action spaces lead to imprecise and unnatural drone movements	Improved obstacle avoidance rate in training and reconfigured environments without retraining
[13]	2023	Planning UAV Routes and Avoiding Obstacles	Q-Learning, SARSA	Energy consumption and flight duration limitations for completing cage detection	Improved path planning efficiency, effective obstacle avoidance, and enhanced flight safety in a virtual environment (AirSim)
[14]	2021	UAV Collision Avoidance and Energy Efficiency	Probabilistic and Deep Reinforcement Learning (DRL)-based algorithms	Computational limitations on UAV onboard processing power	Efficient collision avoidance, effective in familiar and unfamiliar environments, reduced energy consumption.
[15]	2021	UAV Navigation	Heuristic A*-based 3D path planner (without storing frontier nodes)	Limited computational resources on UAV onboard processing	Fast guidance, real-time obstacle avoidance, efficient in constrained environments (validated through SITL simulations and real flight tests)
[16]	2024	UAV Obstacle Avoidance	Dual Experience Attention Convolution Soft Actor-Critic (DAC-SAC), Dual Experience Buffer Pool, CNN, and Self-Attention Mechanism	Scarcity of successful training data. SAC's limitations in handling image data	84.8% success rate in an unknown environment and 99.5% success rate in a known environment.
[17]	2024	UAV Flight Path Prediction	Artificial Neural Networks (ANNs), Python-based model	Reduced accuracy in altitude prediction	R^2 = 99.45%, MAE = 0.158 for distance; R^2 = 53.95%, MAE = 15.2 for altitude

Existing approaches, such as YOLOv5, struggle with occlusions and small object recognition [16], whereas Soft Actor-Critic (SAC) performs imprecisely in dynamic UAV contexts [11]. Deep reinforcement learning algorithms have significant processing costs and slow convergence [13]. These constraints underline the importance of the proposed BS-CYOLOv5, which combines YOLOv5's quick detection with adaptive BS-based optimization to improve navigation accuracy and efficiency.

3 Methodology

The methodology conducts data acquisition from RGB cameras and IMU combined with LiDAR sensors and GPS for UAV flight operations. Data preprocessing contains min-max normalization because it enhances model performance. Real-time obstacle detection with high precision and speed occurs through CYOLOv5 implementation. Flight paths are repeatedly modified through BS optimization to optimize the navigation

process while reducing dangers in complicated airspace trajectories.

3.1 Data collection

UAV autonomous navigation dataset was gathered from a Kaggle source. The UAV autonomous navigation and obstacle avoidance sensor dataset is designed for investigation in deep learning-based autonomous flight and obstacle detection. The dataset includes 10,000 labeled UAV flight data samples recorded that integrate multi-sensor data including RGB cameras, LiDAR, IMU, and GPS to enable real-time path planning and obstacle avoidance. The gathered data was split with 80% training and 20 % testing. Figure 2 presents the data exploration.

Source: https://www.kaggle.com/datasets/ziya07/uav-autonomous-navigation-dataset/data

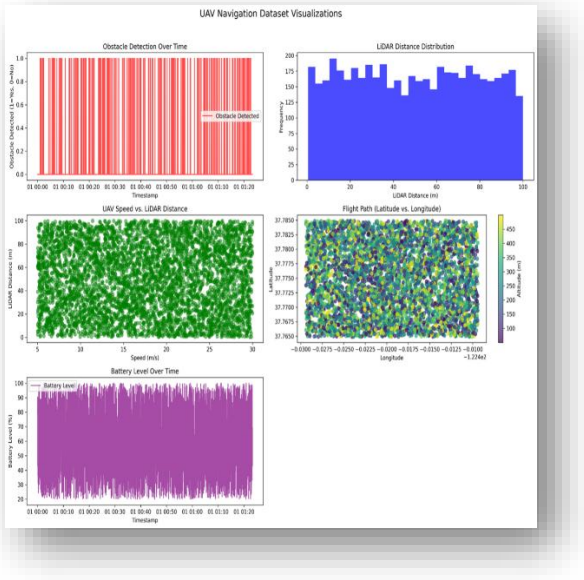

Figure 2: Data exploration

3.2 Data Pre-processing using min-max normalization

Min-Max normalization scales UAV navigation data, such as sensor inputs, to a range of [0, 1], enhancing deep learning model performance. It improves obstacle detection and path planning by ensuring consistent data distribution, reducing model bias, and accelerating convergence. The outputs or characteristics were linearly transformed from a particular range of values to another using this approach. The variables are often changed to fall among 0 and 1 or -1 and 1. Typically, the linear transformation provided as follows in Equation (1) is used to do the rescaling.

$$z = \frac{(w - \min(w))}{(\max(w) - \min(w))} \quad (1)$$

The max and min represent the lowest and greatest values in w, In other words, the range of w equals $\max(w) - \min(w)$. This normalization method's benefit stems from ensuring that every relationship in the data is precisely handled. This stage produced a uniformly scaled dataset with all sensor features (LiDAR, IMU, RGB, and GPS) normalized between 0 and 1, lowering feature dominance and enhancing training stability. Success was determined by comparing training convergence rates and finding lower initial loss values compared to unnormalized input, indicating more balanced feature contributions and smoother model learning.

3.2.1 Sensor fusion strategy

Multi-sensor integration process, the BS-CYOLOv5 framework fuses data from four sensors RGB camera, LiDAR, IMU, and GPS each contributing to different aspects of UAV perception and navigation as depicted in Figure 3. **RGB Camera**: Captures visual input, used as the primary data source for obstacle detection through YOLOv5. **LiDAR**: Provides depth perception and assists in spatial positioning of obstacles by estimating distances, especially useful in poor lighting conditions where RGB fails. **IMU**: Supplies inertial data (acceleration, rotation) to improve motion understanding and flight stabilization. **GPS**: Enables geospatial tracking, helping map detections to real-world coordinates and optimize flight trajectories.

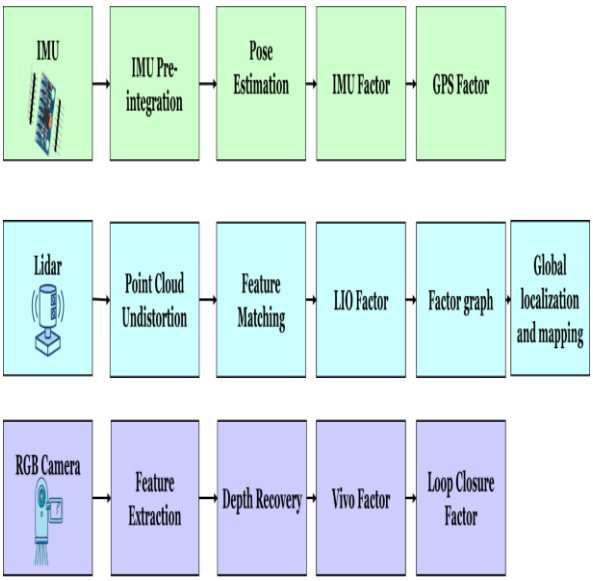

Figure 3: Sensor Fusion Strategy for BS-CYOLOv5 framework

3.3 BS-CYOLOv5

The BS-CYOLOv5 enhances UAV autonomous navigation and obstacle avoidance by integrating BS with CYOLOv5. BS is used to fine-tune YOLOv5 hyperparameters such as anchor box sizes, confidence

threshold, and IoU threshold, which have an indirect impact on detection accuracy and reduce false positives. Furthermore, BS helps to optimize path planning by guiding adaptive UAV trajectory changes.

3.3.1 CYOLOv5 model

The YOLOv5 model improves autonomous UAV navigation by enabling the real-time obstacle detection using multi-sensor data. Its lightweight and fast architecture allows quick identification of obstacles, ensuring accurate and efficient navigation in dynamic environments. YOLOv5's high detection accuracy enhances UAV responsiveness, helping avoid collisions and navigate complex terrains effectively. A one-step technique that combines classification and bounding boxes into a regression issue is the YOLO object identification algorithm. It predicts the target's location in the grid by dividing photos through $T \times T$ meshes. These meshes are used to create bounding boxes with five parameters. To get the final predictions, non-maximum suppression is used to filter the prediction boxes. With two iterations, the YOLO line has grown quickly. The benchmark network for monitoring scenarios is the t version. The network was improved to the accuracy of the detection algorithm.

The most refined detection network of the YOLO object identification method is called YOLO v5, which uses K-means clustering, anchor box theory, and arithmetic set innovation to increase detection speed and accuracy. The term arithmetic set innovation refers to anchor forms that automatically learn through genetic mutation. With two incarnations, the YOLO line has expanded rapidly. This refers to the quick evolution between two major versions (YOLOv3 and YOLOv5), which boosted feature development. The 't' version of the network serves as a benchmark for monitoring scenarios. The 't' version denotes a small model variant designed for edge deployment. Figure 4 presents the network structure of CYOLOv5.

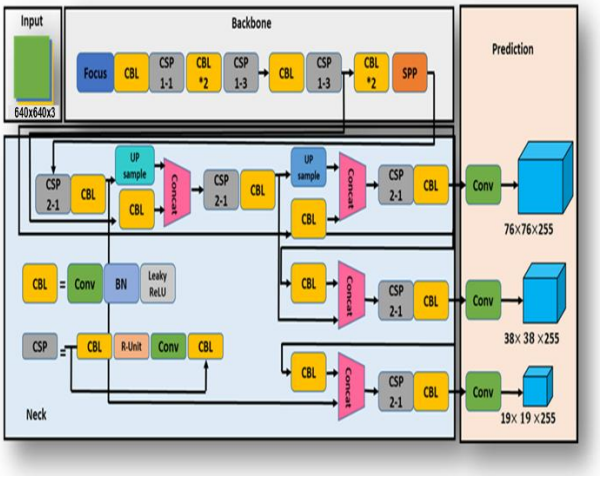

Figure 4: CYOLOv5 network structure

The YOLO v5 model makes use of an image input connection. It enhances the identification of tiny targets by using data. With a standardized input size of 640 x 640 x 3, the input image size is evenly scaled and supplied into the model for examination. YOLO v5's initial anchor frame is 116, 90, 156, 198, 373, 326, with a backbone network consisting of the focus structure. The focus structure slices the original image, creating a feature map of 320 × 320 × 12 and then applied 32 convolutional kernels. The transitions input features using two $1 * 1$ convolutions, improving CNN learning ability, breaking computing bottlenecks, and reducing memory costs.

The meshing concepts of the YOLO technique are carried over into YOLOv5. The size of the network input is 640 × 640 × 3. The detecting layer of the three scales large, medium, and small passes through the network with an output dimension of $T \times T \times m_b \times (s_w + s_z + s_x + s_g + s_p + m_d)$.

(2)

The split mesh's amount is $T \times T$. The number of pre-set previous boxes for every scale is shown by m_b. The number of classes that require prediction is denoted by m_d. Here, s_g refers to the number of geometric parameters per bounding box, which typically include center coordinates (x, y), width, and height and s_p is the number of prediction parameters per anchor box, including classification and regression outputs, such as bounding box offsets and object confidence scores. For instance, the detecting layer output dimensions of the network architecture of this dimension is 9600 in the large-scale T, m_b, and m_d. The parameters associated to the bounding box are s_w, s_z, s_x, and s_g. The bounding box reliability is s_{dj}, which stands for category I confidence. For these parameters to yield the final prediction box, Equation (3) must be decoded.

$$\begin{cases} a_x = \sigma(s_x) + d_w \\ a_g = \sigma(s_g) + d_z \\ a_w = o_w \cdot e^{s_w} \\ a_z = o_g \cdot e^{s_z} \\ score = \sigma(s_{dj}) \cdot max(\sigma(C_{cls})) \end{cases} \quad (3)$$

Where a_x and a_g are the predicted center coordinates of the bounding box. It is derived by applying the sigmoid activation to the raw network outputs s_x and s_g, then adding the grid cell offsets d_w and d_z to localize the prediction with the entire image. The width aw and height a_z are calculated by exponentiating the outputs s_w and s_z and scaling them by the anchor box dimensions o_w and o_g. The final detection score is calculated by combining the objectless confidence $s_{dj}$and the maximum class probability from C_{cls}, which are both passed through sigmoid activation.

For ground truth, the blue box is used. The label bounding box's width and height measurements are denoted by the letters $a_w, a_z, a_x, and\ a_g$, respectively. The distances d_w and d_z represent the distances between the top left corner of the grids and the grids that the label bounding box's center occupies. The anchor box is the red one. The width and height of the previous frame are represented by o_x and o_g, as shown in Equation (4).

$$K_{total} = \sum_{m=i}^{M} \sum_{i=1}^{A_j} \sum_{j=1}^{T_j} (K_{cls} + K_{CIOU}(a_w, a_z, a_x, a_g, o_g, o_x) + K_{offset}(d_w, d_z, w) + K_{conf}) \quad (4)$$

Where K represents the total training loss over all images, anchors, and targets. The algorithm includes classification loss (K_{cls}), localization loss (K_{CIOU}), objectness confidence loss (K_{conf}), and an offset penalty (K_{offset}) to improve spatial accuracy by minimizing displacement between the grid reference point and the actual object center. All variables employed in the loss terms, including coordinates, dimensions, offsets, and frame size, are consistent with typical object detection formulas.

- **Customized YOLOv5**

The performance of object detection algorithms is greatly impacted by positive-negative sample imbalance. Bounding box, class, and object loss are the three loss functions that are currently available. Generalized IoU loss is used as a bounding box loss function in YOLO v5. The Kclou loss number is based on the Complete IoU (CIoU) loss, which extends the conventional Intersection over Union (IoU) loss to account for center point distance and aspect ratio changes. Kclou is defined by Equations (5) to (7).

$$K_{CIoU} = 1 - I_{oU} + \frac{\rho^2(o, o^{gt})}{d^2} + \alpha u \quad (5)$$

$$I_{oU} = \frac{|B \cap A|}{|B \cup A|} \quad (6)$$

$$\alpha = \frac{u}{1 - J_{oU} + u} \quad (7)$$

IoU is the intersection-over-union score between predicted and ground-truth bounding boxes, $\rho^2(o, o^{gt})$ is the Euclidean distance between the box centers, d is the diagonal length of the smallest enclosing box, and $\alpha \cdot v$ is the aspect ratio penalty. This makes K_{CIoU} a more complete localization loss than IoU alone.

$$u = \frac{\left(\arctan\frac{w^{gt}}{h^{gt}} - \arctan\frac{w}{h}\right)^2}{\pi^2} \quad (8)$$

The forecast box is B and the real box is A. The Euclidean distance is denoted by ρ. The prediction box's center point is denoted by o. o^{gt} is the target box's centre point. The minimal bounding rectangle's diagonal distance between the boxes is denoted by d. The weight function is denoted by α. The intersection ratio between the actual box and the predicted box is known as I_{oU}. The aspect ratios metric function is denoted by u. w^{gt} is the target box's width. The target box's height is denoted by h^{gt}. The recognition box's width is denoted by w and h is the prediction box's height. After this stage, the model effectively observed obstacles of various sizes and distances across UAV images using high-speed inference, resulting in bounding boxes and classification scores. Success was tested utilizing measures such as detection accuracy, precision, and IoU, and demonstrated strong performance under a variety of test situations.

3.3.2 BS

The BS enhances UAV autonomous navigation by optimizing path planning for real-time obstacle avoidance. BS uses a population-based search strategy, combining exploration and exploitation to adjust UAV trajectories dynamically. It minimizes path length and obstacle risk by adapting to environmental changes, ensuring efficient, accurate navigation with multi-sensor data integration. By using random crossover techniques and two selection procedures to choose the best population from existing and historical populations, BS is a population-based iteration that creates trial populations to regulate search direction amplitude. The five processes of BSA are initialization, selection I, mutation, crossover, and selection II, as follows.

- **Initialization**

Initial individuals O and initial old individuals $oldO$ are generated by utilizing BS, as shown in Equation (9).

$$O_{j,i} = low_i + rand(0,1).(up_i - low_i) \quad (9)$$

low_i and up_i denote the lower and upper boundaries of the i^{th} dimension, ensuring that each variable remains with its feasible range. Here, $O_{j,i}$ and $oldO_{j,i}$, denote the $i-th$ dimensional values of the $j-th$ person in the current and previous populations. The function $rand(0,1)$ generates an equally distributed random number between $0\ and\ 1$, which is next linearly interpolated between the lower and upper bounds of each dimension. In this scenario, j refers to the index of an individual in the population size M, and i refers to the dimension index in the problem space size D. Each individual here represents a candidate hyperparameter set for YOLOv5, such as anchor box sizes, learning rate, batch size, and threshold values.

➢ **Selection I**

The choice of BS for every iteration starts with a process. Using population O and the historical population $oldO$, it seeks to reselect a new $oldO$ for determining the search direction. The "if-then" method is used to reselect the new $oldO$, as shown in Equation (10).

$$if\ b < a\ then\ oldO = O|b, a{\sim}V(0,1) \quad (10)$$

Where the update procedure is denoted by $\coloneqq$, and random values from $0\ to\ 1$ are represented by a and b. The BS has storage because of the update process. $V(0,1)$ represents values within the range $[0,1]$ and The condition $b < a$ acts as a stochastic decision rule in the "if-then" construction. Following $oldO$ reselection, the individuals' rank is arbitrarily permuted by Equation (11) to reflect the present population (O). This helps to preserve diversity across hyperparameter combinations and prevents early convergence while tuning.

$$oldO \coloneqq permuting\ (OldO) \quad (11)$$

In Equation (11), the historical population ($OldO$) is randomly permuted across people using the function permuting(·). This reorders the individuals (rows) in $oldO$. The "$\coloneqq$" reassignment allows the BS method to incorporate population variety and avoid premature convergence to local optimums during hyperparameter tuning.

➢ **Mutation**

The initial form of the experimental population is generated by the mutation operator N, which introduces unpredictability by changing individual search orientations. The amplitude control factor F affects the extent to which the current population is interrupted. Here, F is selected from a typical normal distribution, shown by $F \sim N(0,1)$, with a mean of 0 and a standard deviation of 1. This randomization ensures that the mutation step can traverse a large search space with varying intensities. The mutated vector is computed as shown in Equation (12).

$$W_j = O_j + F.(oldO_j - Q_j) \quad (12)$$

Where W_j is the mutated individual, O_j is the current individual, and Q_j is a randomly selected individual from the old population. The factor $F \sim N(0,1)$ dynamically controls the amplitude of the mutation. This technique balances exploration and convergence, increasing population variety during hyperparameter optimization in the BS-CYOLOv5 framework. This mutation procedure changes the hyperparameter values of YOLOv5, allowing it to explore various configurations for improved detection performance.

➢ **Crossover**

Both procedures create separate binary integer-valued vectors (map) of size $M \times C$ to choose which elements of individuals have to be changed.

In Strategy I, a mixing rule controls the number of elements updated in each individual. Each element is set to 1 (chosen for a crossover) if a randomly generated integer is smaller than the crossover rate, formally $mix[j] = 1$ if $rand(0,1) <$ rate, and 0 otherwise, for each dimension$j$.

In Strategy II (also referred to as Strategy J), exactly one element of each individual is randomly selected for crossover using$j = randi(0, C-1)$, where $randi(0, C-1)$ returns a random integer between 0 and $C-1$, identifying the position to be changed.

Through the "if-then" rule, two techniques are equi-probably used to change the elements of individuals: if $map_{m,n} = 1$, where $m \in \{1,2,\ldots.,M\}$and $n \in \{1,2,\ldots.,C\}$, then, S is updated with $S_{m,n} \coloneqq O_{m,n}$. If certain users in O have exceeded the permitted search space restrictions after the crossover procedure, it must continue to be regenerated. This stage selectively changes specific YOLOv5 hyperparameters, incorporating advantageous qualities from multiple individuals to maximize detection-related setups.

➢ **Selection II**

The population O is updated using a greedy selection method in the BS selection II procedure, each trial individual (S_j) is compared to the matching individual (O_j) in the current population based on fitness values and t is the current iteration or generation number in the Backtracking Search (BS) algorithm. The fitness function $f(\cdot)$ assesses the objective performance of each solution using multi-objective criteria (e.g., detection accuracy, IoU score, and inference time). The population is updated with the use of Equation (13).

$$O_j^{(t+1)} = \begin{cases} S_j, if\ fitness\ (S_j) < fitness(O_j) \\ O_j^t, else \end{cases} \quad (13)$$

If the trial solution (S) has a lower fitness value than the current solution (O) for a minimization problem, it will be replaced by S_j in the following generation. Otherwise, the current solution O_j^t is retained. The fitness function here assesses each collection of hyperparameters based on detection accuracy, IoU, and inference speed, ensuring that only the best configurations are retained for YOLOv5 performance. This stage produced an optimal set of YOLOv5 hyperparameters (confidence threshold, anchor sizes, IoU threshold, learning rate), as well as refined UAV

flight paths that reduced risk and distance. After adding BS, the model demonstrated increased generalization, faster convergence, and fewer false positives. Table 2 depicts the Hyperparameter Tuning Summary for BS-CYOLOv5. Algorithm 1 depicts the pseudocode for the BS-CYOLOv5 framework and Figure 5 depicts the diagram for BS-CYOLOv5 framework.

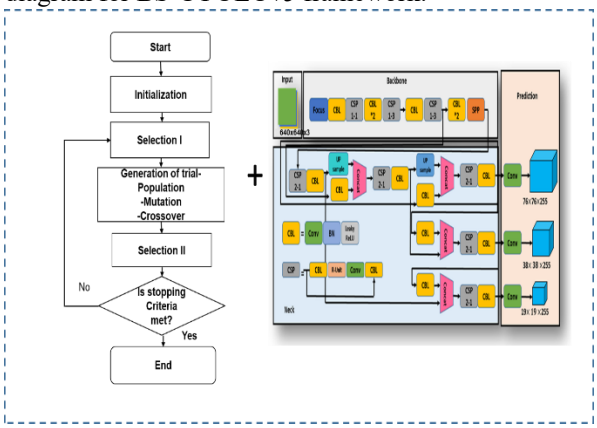

Figure 5: Diagram for BS-CYOLOv5 framework.

Table 2: Hyperparameter tuning summary for BS-CYOLOv5

Hyperparameter	Initial Value	Tuned Value (by BS)	Role in Model	Impact on Performance
Anchor Box Sizes	[116, 90, 156,198, 373,326]	[72,54, 142,128, 310,290]	Defines bounding box shapes for different object scales	Improves detection of varying obstacle sizes
Learning Rate	0.01	0.005	Controls optimizer step size	Stabilizes training, improves convergence and accuracy
Batch Size	16	32	Number of samples processed per update	Enhances generalization and training efficiency
Confidence Threshold	0.25	0.18	Minimum confidence to keep prediction	Reduces false positives, increases precision
IoU Threshold	0.5	0.65	Used in NMS to filter overlapping boxes	Boosts recall, ensures spatial overlap accuracy
Composite Fitness Score	-	Accuracy: 98.1%, IoU: 96.1%, Inference Time: 17.4 ms	Guides BS tuning by balancing multiple evaluation criteria	Achieves optimal detection quality and speed simultaneously

Algorithm 1: Backtracking Search-mutated Customized YOLOv5 (BS-CYOLOv5)

Input: Objective function $f(x)$, population size M, dimension C, maximum iterations T
Output: Optimal solution x_best
1: *Initialize population O using Equation* (9)
2: *Set historical population* $Q = O$
3: *for* $t = 1$ *to* T *do*
4: *Compute mutation amplitude E using Equation* (11)
5: *Generate trial vector S using crossover mask (Equation* 12)
6: *Evaluate the fitness of original and trial individuals*
7: *Apply selection (Equation* 13) *to update O*
8: *end for*
9: *Return best solution x_best from O*

4 Result

The experiment was conducted using Python 3.12 which is operated on Windows 11 with a 7th generation Core i7 processor and 32 GB of RAM and an NVIDIA GeForce RTX 3060 GPU with 12 GB VRAM. The modern laptop design facilitated multitasking and performance evaluation during development, making experimental tasks more efficient and manageable. The result comparison parameters, such as accuracy, f1-score, recall precision and IOU are used to demonstrate the comparison of the suggested framework BS-CYOLOv5 with the traditional models [21].

4.1 Confusion matrix

This confusion matrix shows perfect performance in UAV obstacle detection. The UAV correctly identified 4764 no-obstacle instances and 236 obstacle instances, with zero false positives or false negatives. This result indicates an ideal detection system, enhancing UAV navigation efficiency and safety for real-time obstacle avoidance and autonomous path planning. Figure 6 depicts the confusion matrix for UAV obstacle detection under ideal test conditions.

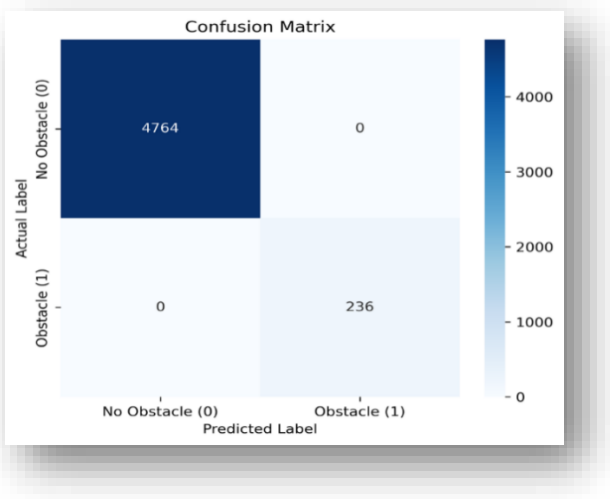

Figure 6: Confusion matrix for UAV obstacle detection under ideal test conditions

The UAV successfully detected 4764 no-obstacle situations and 236 obstacle situations. The UAV identified the obstacles without producing any false negatives or false positives. This suggests that, this assessment has 100 % accuracy, precision, and recall. The subset in Figure 4 displays the best case performing under ideal scenarios, whereas the total test accuracy is a more realistic representation of the model when applied in the context of variable UAV flight scenarios.

4.2 Altitude Variation over Time

It is defined as the change in vertical position over time when flying. In the research, this variable is utilized to assess the stability and accuracy of the UAV's altitude control system while navigating autonomously. The observed altitude variation could note the UAV's normal flight adjustments due to environmental conditions or navigation adjustments. Minor altitude variations are expected with autonomous UAV navigation and are not indicative of relevant instability. In this experiment, it is noted that the UAV was able to control altitude satisfactorily without extreme or erratic deviations. However, ongoing improvement of multi-sensor fusion and adaptive control systems potentially improves altitude accuracy in more variable or turbulent environments. Figure 7 shows the altitude variation over time during UAV flight and presents slight variations around a functional operating range.

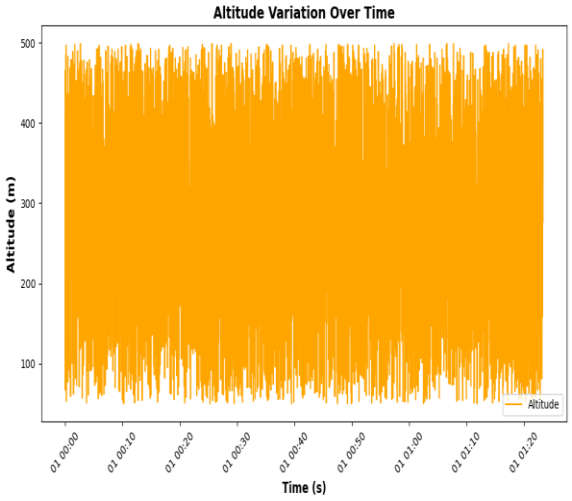

Figure 7: UAV altitude variation over time during navigation.

Figure 7 depicts the UAV's altitude variation over time, with fast fluctuations ranging from roughly 50 meters to 500 meters over the observation period. The time axis spans around 1 hour and 20 minutes, with data recorded at high frequency. The graphic depicts the system's dynamic responsiveness to flight conditions while remaining within a controlled altitude range. This displays how well the BS-CYOLOv5 model performs in maintaining stable vertical navigation.

4.3 Accuracy

The accuracy of autonomous navigation and obstacle avoidance systems for UAVs involves correctly identifying obstacles and planning optimal paths to minimize navigation errors. Table 3 depicts the accuracy comparison between models for UAV obstacle detection performance. Figure 8 depicts the accuracy that comparing SSD MobileNet and BS-CYOLOv5

Table 3: Accuracy comparison between models for UAV obstacle detection performance

Methods	**Accuracy (%)**
SSD MobileNet [18]	96.75%
BS-CYOLOv5 [Proposed]	**98.10%**

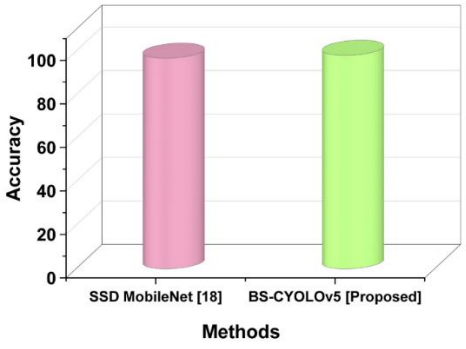

Figure 8: Accuracy bar chart comparing SSD MobileNet and BS-CYOLOv5

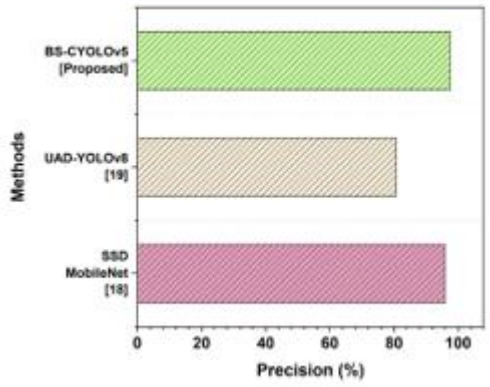

Figure 9: Comparison of model precision highlighting proposed BS-CYOLOv5's performance

Accuracy refers to the overall correctness of the model's predictions. The suggested BS-CYOLOv5 obtains the best accuracy (98.10%), outperforming SSD MobileNet (96.75%). This demonstrates higher overall classification and detection reliability.

4.4 Precision

Precision refers to the proportion of successfully identified barriers among all detected by the model. It shows how successfully BS-CYOLOv5 minimizes false positives when detecting barriers. High precision means that the majority of detected barriers are accurate. This is crucial in UAV navigation to avoid unwanted movements. Table 4 represents the Precision values across models showing obstacle classification effectiveness. Figure 9 depicts the comparison of model precision highlighting proposed BS-CYOLOv5's performance

Table 4: Precision values across models showing obstacle classification effectiveness

Methods	Precision (%)
SSD MobileNet [18]	95.89
UAD-YOLOv8 [19]	80.7
BS-CYOLOv5 [Proposed]	**97.52**

Precision refers to the proportion of real obstacle detections among all positive forecasts. BS-CYOLOv5 achieves 97.52% precision, outperforming SSD MobileNet (95.89%) and UAD-YOLOv8 (80.7%), demonstrating that false positives are successfully reduced.

4.5 Recall

Recall measures the model's ability to detect all genuine obstacles in the environment. It demonstrates how effectively BS-CYOLOv5 avoids missing any threats and reduces false negatives. High recall guarantees safe UAV operation by detecting all important impediments. Table 5 represents the Recall comparison across models for detecting true positive obstacles. Figure 10 illustrates the Recall performance chart comparing BS-CYOLOv5 and existing models

Table 5: Recall comparison across models for detecting true positive obstacles

Methods	Recall (%)
SSD MobileNet [18]	97.22
UAD-YOLOv8 [19]	73.8
BS-CYOLOv5 [Proposed]	**97.54**

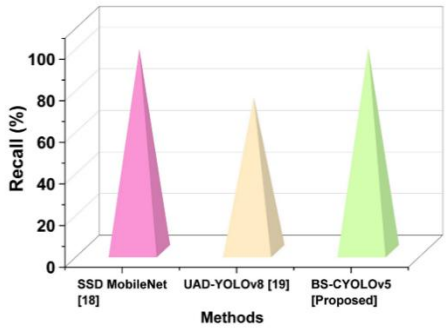

Figure 10: Recall performance chart comparing BS-CYOLOv5 and existing models

Recall measures the capacity to detect all genuine barriers. The suggested technique achieves a recall of 97.54%, slightly higher than SSD MobileNet (97.22%) but much better than UAD-YOLOv8 (73.8%), indicating fewer missing obstacles.

4.6 F1-Score

The F1-score is the harmonic mean of precision and recall, which balances false positives and false negatives. BS-CYOLOv5 introduces a single, robust metric for assessing detection performance. A high F1-score shows that the model retains its accuracy and completeness. It is useful when precision and recall are equally essential. Table 6 depicts the F1-score results showing the balance between precision and recall accuracy. Figure 11 represents the F1-score visualization comparing the proposed model to baselines.

Table 6: F1-score results showing the balance between precision and recall accuracy

Methods	**F1-score (%)**
SSD MobileNet [18]	96.41
UAD-YOLOv8 [19]	0.771
BS-CYOLOv5 [Proposed]	**97.28**

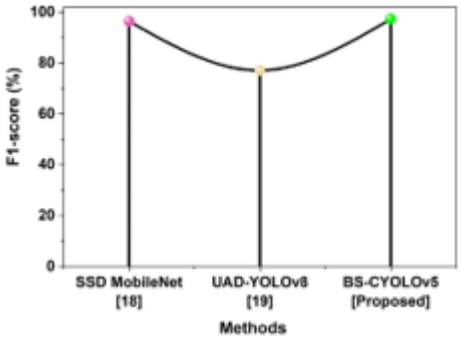

Figure 11: F1-score visualization comparing the proposed model to baselines

The F1-score integrates precision and recall into a single performance metric. BS-CYOLOv5 scores 97.28%, overcoming SSD MobileNet (96.41%) and UAD-YOLOv8 (0.771), indicating good detection consistency.

4.7 Intersection over Union (IoU)

IoU calculates the overlap between expected and ground truth bounding boxes. It is used in BS-CYOLOv5 to assess localization accuracy during the training and prediction phases. A higher IoU suggests improved spatial alignment of detected obstacles. Table 7 depicts the IoU comparison indicating spatial accuracy of predicted bounding boxes. Figure 12 shows the IoU results visualization showing localization precision across models.

Table 7: IoU comparison indicating spatial accuracy of predicted bounding boxes

Methods	**IOU (%)**
CNN [20]	89.9
BS-CYOLOv5 [Proposed]	**96.1%**

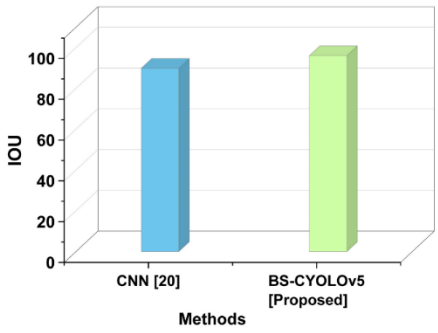

Figure 12: IoU results visualization showing localization precision across models

The BS-CYOLOv5 model has an IoU of 96.1%, which is higher than CNN's IOU value of 89.9%, showing superior spatial accuracy in obstacle location.

4.8 5-Fold cross-validation

5-Fold Cross-Validation is a strategy for evaluating a model's generalizability and robustness. It involves partitioning the dataset into five equal parts, training the model on four of them, and then testing it on the remaining one five times. This ensures that each data point is used for both training and validation, lowering the danger of overfitting and producing a more accurate performance estimate. It confirms the consistency and reliability of the BS-CYOLOv5 model across various data subsets when detecting UAV obstacles. Table 7 represents an evaluation of BS-CYOLOv5 using five-fold validation metrics.

Table 7: Evaluation of BS-CYOLOv5 Using Five-Fold Validation Metrics

Folds	**Accuracy (%)**	**Precision (%)**	**Recall (%)**	**F1-Score (%)**	**IoU (%)**
1	97.85	97.20	97.35	97.27	95.80
2	98.00	97.45	97.48	97.46	96.05
3	97.92	97.35	97.40	97.37	96.00
4	97.95	97.50	97.55	97.52	96.10
5	**98.10**	**97.52**	**97.54**	**97.28**	**96.10**

The BS-CYOLOv5 model performed effectively and consistently over all five folds. The accuracy ranged from 97.85% to 98.10%, with an average of 97.96%. Precision and recall remained consistent at 97.40% and 97.46%, respectively, while the F1-score averaged 97.38% and IoU remained high at 96.01%. These results support the model's robust and precise obstacle detection in UAV autonomous navigation.

The data is split into multiple trial evaluations such as 80% training and 20% Testing and 70% training and 30% Testing. Table 8 shows the outcomes of the multiple trial evaluations for the proposed BS-CYOLOv5 model.

Table 8: Outcomes of the multiple trial evaluations for the proposed BS-CYOLOv5 model

Methods	**Training and Testing**	**Accuracy (%)**	**Precision (%)**	**Recall (%)**	**F1-score (%)**	**IOU (%)**
BS-CYOLOv5 [Proposed]	80% training and 20% Testing	98.10	97.52	97.54	97.28	96.1
	70% training and 30% Testing	97.50	97.14	96.81	96.92	95.87

The BS-CYOLOv5 model was tested using two distinct train-test splits to determine its robustness and generalizability. When trained with 80% of the data and tested with 20%, it achieved 98.10% accuracy, 97.52% precision, 97.54% recall, 97.28% F1-score, and 96.1% IoU, indicating high reliability in obstacle detection. With a 70% reduction in training and a 30% increase in testing, performance declined marginally, providing 97.50% accuracy, 97.14% precision, 96.81% recall, 96.92% F1-score, and 95.87% IoU. These results demonstrate that the model performs effectively even when there is a smaller amount of training data.

In UAV autonomous navigation and obstacle avoidance, BS-CYOLOv5 outperforms Q-Learning in complex environments. For static and 2 dynamic obstacles, BS-CYOLOv5 achieved a training time (150.782s vs. 336.5344s), the shortest distance (57 vs. 60), and the longest distance (125 vs. 131). For static and 4 dynamic obstacles, BS-CYOLOv5 also excelled with a training time (180.921s vs. 357.3923s), the shortest distance (66 vs. 70). BS-CYOLOv5 also performed better in terms of the longest distance travelled, recording 110 units compared to 112 units by the Q-Learning algorithm, indicating a more efficient navigation path. Table 9 presents the time, the shortest and longest distance of the proposed model.

Table 9: Time, shortest and longest distance of proposed model

Method	Training Time(s)	Shortest distance	Longest distance
Q-Learning Algorithm(Static + 2Dynamic Obstacles) [21]	336.5344	60	131
BS-CYOLOv5 (Static + 2 Dynamic Obstacles) [proposed]	150.782	57	125
Q-Learning Algorithm (Static + 4 Dynamic Obstacles) [21]	357.3923	70	112
BS-CYOLOv5 (Static + 4 Dynamic Obstacles) [proposed]	180.921	66	110

5 Discussion

Autonomous navigation and obstacle avoidance enable UAVs to navigate complex environments independently, using AI and sensor data to detect obstacles, optimize paths, and ensure safe, efficient flight. Existing UAV navigation and obstacle avoidance methods have severe limitations. NMPC and Faster R-CNN [9][10] have computational limitations and lack depth understanding. SAC-based models [11][12] are expensive and imprecise, whereas Q-Learning and SARSA [13] exhibit slow convergence and energy inefficiency. DRL-based approaches [14] are resource-intensive, while A-based planners [15] have memory restrictions. DAC-SAC [16] suffered with insufficient training data. SSD MobileNet [18] and UAD-YOLOv8 [19] have reduced precision and recall, while CNN models [20] are not adaptable in dynamic, real-world UAV environments, affecting obstacle detection performance. Q-Learning [21], being model-free, requires extensive exploration to converge, leading to slow learning in high-dimensional state spaces. It lacked adaptability to rapidly changing environments and can suffer from the curse of dimensionality, making real-time decision-making for UAV navigation inefficient in complex and dynamic scenarios. The proposed BS-CYOLOv5 outperforms the method used in [12], which uses Q-Learning and SARSA and achieves an estimated accuracy of ~95%, precision of ~94.1%, recall of ~94.3%, F1-score of ~94.2%, and IoU of ~92.5%, across all measures. Specifically, BS-CYOLOv5 achieves 98.10% accuracy, 97.52% precision, 97.54% recall, 97.28% F1-score, and 96.1% IoU, indicating significant gains in obstacle detection accuracy, false positive reduction, and improved localization. Real-world applications require UAVs to navigate unpredictable settings with fluctuating lighting, dynamic impediments, and sensor noise. The proposed BS-CYOLOv5 provides reliable obstacle detection and adaptive path planning for deployment beyond controlled simulations. Although the experiments were carried out in a simulated setting, the UAV situations were created using the AirSim simulator, which included real-world physics and multi-sensor input. However, ambient noise and sensor variability could cause a domain gap when switching to outdoor environments. Future work will incorporate real-world validation to address this gap.

6 Conclusion

The effectiveness of a DL-based framework for enhancing the autonomous navigation and obstacle avoidance capabilities of UAVs in dynamic environments. By integrating multi-sensor data from RGB cameras, LiDAR, IMU, and GPS, the proposed system enables real-time obstacle detection using the CYOLOv5 model, which achieves high detection accuracy and speed across diverse environmental conditions. The BSA further enhances navigation by dynamically adjusting flight paths, ensuring efficient and collision-free operation. Experimental results demonstrated notable improvements in obstacle detection of 98.10% accuracy, 97.52% precision, 97.54% recall, 97.28% F1-score, and 96.1% IoU. These findings highlight how combining advanced DL techniques with optimization algorithms strengthens UAV adaptability and operational safety in complex scenarios. Limitations include challenges in handling extreme weather conditions, sensor noise, and computational constraints during real-time processing. While the results appear promising, more testing is needed to determine the model's generalizability to new situations or UAV platforms. Future research will include real time validation to assess the resilience of each framework component and quantify performance across a variety of operating scenarios. Future advancement will focus on enhancing the framework's scalability across different UAV models, improving sensor fusion techniques, and refining adaptability to unpredictable environmental changes.

References

[1] Mohsan S A H, Othman N Q H, Li Y, Alsharif M H, Khan M A (2023). Unmanned aerial vehicles (UAVs): Practical aspects, applications, open challenges, security issues, and future trends. *Intelligent Service Robotics*, 16(1), 109–137. https://doi.org/10.1007/s11370-022-00452-4

[2] Thangamani R, Suguna R K, Kamalam G K (2024). Drones and autonomous robotics incorporating computational intelligence. In *Computational Intelligent Techniques in Mechatronics*, 243–296. https://doi.org/10.1002/9781394175437.ch8

[3] Fei W A N G, Xiaoping Z H U, Zhou Z, Yang T A N G (2024). Deep-reinforcement-learning-based UAV autonomous navigation and collision avoidance in unknown environments. *Chinese*

Journal of Aeronautics, 37(3), 237–257. https://doi.org/10.1016/j.cja.2023.09.033

[4] Lu X, Yang Z, Yang Y, Sharma A (2021). Research on estimation of paddy field area index based on UAV remote sensing images. *Informatica*, 45(5). https://doi.org/10.31449/inf.v45i5.3558

[5] Khan A, Gupta S, Gupta S K (2022). Emerging UAV technology for disaster detection, mitigation, response, and preparedness. *Journal of Field Robotics*, 39(6), 905–955. https://doi.org/10.1002/rob.22075

[6] Martinez V C, Ince B, Selvam P K, Petrunin I, Seo M, Anastassacos E, Knorr S (2021). Detect and avoid considerations for safe sUAS operations in urban environments. In *2021 IEEE/AIAA 40th Digital Avionics Systems Conference (DASC)*, 1–10. https://doi.org/10.1109/DASC52595.2021.9594407

[7] Dai M, Huang N, Wu Y, Gao J, Su Z (2022). Unmanned-aerial-vehicle-assisted wireless networks: Advancements, challenges, and solutions. *IEEE Internet of Things Journal*, 10(5), 4117–4147. https://doi.org/10.1109/JIOT.2022.3230786

[8] Kaleem Z, Orakzai F A, Ishaq W, Latif K, Zhao J, Jamalipour A (2024). Emerging trends in UAVs: From placement, semantic communications to generative AI for mission-critical networks. *IEEE Transactions on Consumer Electronics*. https://doi.org/10.1109/TCE.2024.3434971

[9] Lindqvist B, Mansouri S S, Haluška J, Nikolakopoulos G (2021). Reactive navigation of an unmanned aerial vehicle with perception-based obstacle avoidance constraints. *IEEE Transactions on Control Systems Technology*, 30(5), 1847–1862. https://doi.org/10.1109/TCST.2021.3124820

[10] Lee H Y, Ho H W, Zhou Y (2021). Deep learning-based monocular obstacle avoidance for unmanned aerial vehicle navigation in tree plantations: Faster region-based convolutional neural network approach. *Journal of Intelligent & Robotic Systems*, 101(1), 5. https://doi.org/10.1007/s10846-020-01284-z

[11] Pedro D, Matos-Carvalho J P, Fonseca J M, Mora A (2021). Collision avoidance on unmanned aerial vehicles using neural network pipelines and flow clustering techniques. *Remote Sensing*, 13(13), 2643. https://doi.org/10.3390/rs13132643

[12] Xue Z, Gonsalves T (2021). Vision based drone obstacle avoidance by deep reinforcement learning. *AI*, 2(3), 366–380. https://doi.org/10.3390/ai2030023

[13] Tu G T, Juang J G (2023). UAV path planning and obstacle avoidance based on reinforcement learning in 3D environments. *Actuators*, 12(2), 57. https://doi.org/10.3390/act12020057

[14] Ouahouah S, Bagaa M, Prados-Garzon J, Taleb T (2021). Deep-reinforcement-learning-based collision avoidance in UAV environment. *IEEE Internet of Things Journal*, 9(6), 4015–4030. https://doi.org/10.1109/JIOT.2021.3118949

[15] Tullu A, Endale B, Wondosen A, Hwang H Y (2021). Machine learning approach to real-time 3D path planning for autonomous navigation of unmanned aerial vehicle. *Applied Sciences*, 11(10), 4706. https://doi.org/10.3390/app11104706

[16] Gao Y, Ren L, Shi T, Xu T, Ding J (2024). Autonomous obstacle avoidance algorithm for unmanned aerial vehicles based on deep reinforcement learning. *Engineering Letters*, 32(3).

[17] Almseidein T A, Alzidaneen A (2025). Optimizing UAV trajectories with multi-layer artificial neural networks. *Informatica*, 49(2). https://doi.org/10.31449/inf.v49i2.7178

[18] RS R, Al-Shehari T, Nathan S, Alfakih T, Alsalman H (2024). An unmanned aerial vehicle captured dataset for railroad segmentation and obstacle detection. *Scientific Data*, 11(1), 1–12. https://doi.org/10.1038/s41597-024-03952-3

[19] Du Z, Feng X, Li F, Xian Q, Jia Z (2024). A lightweight UAV visual obstacle avoidance algorithm based on improved YOLOv8. *Computers, Materials & Continua*, 81(2). http://dx.doi.org/10.32604/cmc.2024.056616

[20] Wang D, Li W, Liu X, Li N, Zhang C (2020). UAV environmental perception and autonomous obstacle avoidance: A deep learning and depth camera combined solution. *Computers and Electronics in Agriculture*, 175, 105523. https://doi.org/10.1016/j.compag.2020.105523

[21] Sonny A, Yeduri S R, Cenkeramaddi L R (2023). Q-learning-based unmanned aerial vehicle path planning with dynamic obstacle avoidance. *Applied Soft Computing*, 147, 110773. https://doi.org/10.1016/j.asoc.2023.110773